

**UCLA**

**UCLA Electronic Theses and Dissertations**

**Title**

Tectonic Evolution of the Northeastern Tibetan Plateau

**Permalink**

<https://escholarship.org/uc/item/7jc5d3tq>

**Author**

Zuza, Andrew Vincent

**Publication Date**

2016

**Supplemental Material**

<https://escholarship.org/uc/item/7jc5d3tq#supplemental>

Peer reviewed|Thesis/dissertation

UNIVERSITY OF CALIFORNIA

Los Angeles

Tectonic Evolution of the  
Northeastern Tibetan Plateau

A dissertation submitted in partial satisfaction of the  
requirements for the degree Doctor of Philosophy  
in Geology

by

Andrew Vincent Zuza

2016

© Copyright by  
Andrew Vincent Zuza  
2016

## ABSTRACT OF THE DISSERTATION

Tectonic Evolution of the  
Northeastern Tibetan Plateau

by

Andrew Vincent Zuza

Doctor of Philosophy in Geology

University of California, Los Angeles, 2016

Professor An Yin, Chair

How the Tibetan Plateau was constructed and evolved in response to ongoing India-Asia convergence since 65-55 Ma is fundamental in understanding processes of continental tectonics. Furthermore, the kinematics and mechanisms of plateau formation and continental deformation have implications for the complex interactions between tectonics, erosion, and climate change in Earth's most recent history. To provide insights into these processes, my research is focused on the development of the northern margin of the Tibetan Plateau, which is defined by the 350-km-wide and 1300-km-long Cenozoic Qilian Shan-Nan Shan thrust belt. This active fold and thrust system overprinted a region that has a complex pre-Cenozoic tectonic history involving multiple phases of Proterozoic basement deformation and early Paleozoic orogeny. In this work, I integrate geologic mapping, balanced cross section construction and restoration, seismic reflection interpretation, geochronology, thermobarometry, geodetic data analysis, and analogue modeling to investigate the tectonic development of northern Tibet over a range of timescales,

from the Proterozoic evolution of central Asian cratons to the active deformation that is shaping the northern margin of the Tibetan Plateau.

The magnitude, style, and distribution of Cenozoic shortening strain across northern Tibet can be used to test competing models of continental deformation. The shortening distribution across the Qilian Shan-Nan Shan thrust belt, derived from surface mapping and subsurface seismic reflection profiles, suggests that the modern thickness and elevation of the northern plateau has developed as a result of southward continental underthrusting of Asia beneath Tibet and distributed crustal thickening. The thrust systems in northern Tibet link to the east with  $> \sim 1000$ -km-long parallel left-slip strike-slip faults (i.e., the Haiyuan, Qinling, and Kunlun faults). The along-strike variation of fault offsets and pervasive off-fault deformation along these strike-slip faults create a strain pattern that departs from the expectations of the classic plate-like rigid-body motion and flow-like distributed deformation models of continental deformation. Instead, I propose that the major strike-slip faults formed as a non-rigid bookshelf-fault system where clockwise rotation of northern Tibet drives left-slip bookshelf faulting and related off-strike-slip fault deformation. In addition, I employ a stress-shadow model that uses the characteristic spacing of strike-slip faults and seismogenic-zone thickness estimates across northern Tibet and central Asia to estimate fault strength and the regional stress state. The strike-slip faults in Asia have a low coefficient of fault friction ( $\sim 0.15$ ), which may explain why deformation penetrates more than 3500 km into Asia from the Himalayan collisional front, and why the interior of Asia is prone to large ( $M > 7.0$ ) devastating earthquakes along major strike-slip faults.

A well-constrained understanding of Cenozoic deformation across northern Tibet allows for better reconstructions of the Proterozoic and Paleozoic tectonics. Field relationships and

geochronologic studies reveal that the early Paleozoic Qilian suture, which bounds the southern margin of the North China craton, records the Ordovician-early Silurian closure of the Qilian Ocean via south-dipping subduction beneath the Qaidam continent. The evolution of this ocean and North China's southern margin has implications for reconstructions of Neoproterozoic and Paleozoic Earth, including the development of the Tethyan and Paleo-Asian Oceanic Domains. By restoring the Phanerozoic deformation along the northern and southern margins of the Tarim and North China cratons, I propose and test a hypothesis that these cratons once stretched westward across present-day Asia, possibly as far west as Baltica, as a continuous Neoproterozoic continent.

The dissertation of Andrew Vincent Zuza is approved.

T. Mark Harrison

Craig E. Manning

Yongwei Sheng

An Yin, Committee Chair

University of California, Los Angeles

2016

## TABLE OF CONTENTS

|  |    |
|--|----|
| <b>Chapter 1: Introduction</b>   | 1  |
| 1.1. Introduction  | 2  |
| 1.2. The Cenozoic evolution of the northern Tibetan Plateau (Chapters 2 and 3)   | 5  |
| 1.3. Spacing and strength of active continental strike-slip faults (Chapter 4)   | 7  |
| 1.4. The Proterozoic-Paleozoic tectonic evolution of northern Tibet and central Asia (Chapters 5 and 6)                                      | 9  |
| 1.5. References  | 17 |
| <br>   |    |
| <b>Chapter 2: Testing models of Tibetan Plateau formation with Cenozoic shortening estimates across the Qilian Shan-Nan Shan thrust belt</b> | 24 |
| 2.1. Abstract  | 25 |
| 2.2. Introduction  | 26 |
| 2.3. Regional Geology  | 29 |
| 2.3.1. The early Paleozoic Qilian orogen and related basement rocks  | 30 |
| 2.3.2. Jurassic and Cretaceous Extensional Setting   | 31 |
| 2.3.3. Cenozoic structures   | 32 |
| 2.4. Testing plateau formation models with shortening estimates  | 33 |
| 2.4.1. Models and implications for shortening along the plateau's northeastern margin  | 34 |
| 2.4.2. Existing shortening Estimates across the Qilian Shan-Nan Shan thrust belt   | 36 |
| 2.4.3. Shortening across Qaidam Basin and the North Qaidam thrust belt   | 39 |
| 2.5. Geologic mapping of the central Qilian Shan   | 40 |
| 2.5.1. Map units   | 40 |
| 2.5.1.1. Sedimentary units   | 41 |
| 2.5.1.2. Metamorphic and mélangé units   | 44 |
| 2.5.1.3. Igneous units   | 45 |
| 2.5.2. Regional unconformities   | 47 |
| 2.5.3. Structural geology  | 49 |
| 2.5.3.1. Shule Nan Shan  | 50 |
| 2.5.3.2. Tuo Lai Nan Shan  | 52 |
| 2.5.3.3. Tuo Lai Shan  | 55 |
| 2.5.3.4. Structural data from the metamorphic basement   | 57 |
| 2.5.4. Balanced cross sections   | 58 |
| 2.6. Seismic reflection profiles across the North Qilian Shan  | 59 |
| 2.6.1. Surface geology in the North Qilian Shan  | 60 |
| 2.6.2. Timing of Cenozoic deformation  | 62 |
| 2.6.3. Approximate vertical scale of seismic sections and associated uncertainties   | 63 |
| 2.6.4. Seismic reflection profiles   | 64 |
| 2.7. Cenozoic shortening estimates across the central Qilian Shan  | 68 |
| 2.7.1. Shortening based on geologic mapping of the central Qilian Shan   | 69 |
| 2.7.2. Shortening based on seismic reflection profiles   | 71 |
| 2.8. Discussion  | 74 |



|  |            |
|--|------------|
| 2.8.1. Cenozoic shortening across the northeastern Tibetan Plateau                                     | 74         |
| 2.8.2. Crustal shortening, thickening, and denudation  | 77         |
| 2.8.3. Model for Cenozoic development of the northeastern Tibetan Plateau                              | 81         |
| 2.8.4. Accommodation mechanisms of India-Asia convergence  | 83         |
| 2.8.5. Similar deformational styles along northern and southern<br>plateau margins                     | 84         |
| 2.9. Conclusions   | 86         |
| 2.10. References   | 129        |
| <br>   |            |
| <b>Chapter 3: Non-rigid passive bookshelf faulting in northern Tibet</b>                               | <b>144</b> |
| 3.1. Abstract  | 145        |
| 3.2. Introduction  | 146        |
| 3.3. Cenozoic left-slip faults in northern Tibet   | 148        |
| 3.3.1. Initiation age and along-strike variation of fault offsets and slip rates                       | 149        |
| 3.3.2. Protracted regional clockwise rotation of northern Tibet  | 152        |
| 3.3.3. Extension and shortening within fault-bounded domains   | 154        |
| 3.4. Non-rigid bookshelf fault model   | 155        |
| 3.4.1. Active and passive bookshelf faulting   | 156        |
| 3.4.2. Non-rigid bookshelf faulting in northern Tibet: passive and stretchy                            | 160        |
| 3.4.3. Active bookshelf faulting: the Garlock fault in California                                      | 163        |
| 3.5. Discussion  | 165        |
| 3.5.1. Driving mechanism for clockwise rotation  | 165        |
| 3.5.2. Implications for the Cenozoic development of northern Tibet                                     | 166        |
| 3.5. Conclusions   | 169        |
| 3.6. References  | 184        |
| <br>   |            |
| <b>Chapter 4: Spacing and strength of active continental strike-slip faults</b>                        | <b>193</b> |
| 4.1. Abstract  | 194        |
| 4.2. Introduction  | 195        |
| 4.3. Generating parallel strike-slip faults  | 196        |
| 4.3.1. Existing models   | 196        |
| 4.3.2. Stress-shadow model for extensional joints  | 197        |
| 4.3.3. Stress-shadow model for strike-slip faulting  | 198        |
| 4.4. Analogue modeling   | 202        |
| 4.4.1. Experimental materials  | 203        |
| 4.4.2. Scaling considerations  | 204        |
| 4.4.3. Experimental procedure and results  | 205        |
| 4.4.4. Analogue experiments and the stress-shadow model  | 206        |
| 4.5. Continental strike-slip faults  | 207        |
| 4.5.1. Strike-slip faults in California and Asia   | 208        |
| 4.5.2. Seismogenic zone thickness observations   | 209        |
| 4.6. Discussion  | 211        |
| 4.6.1. Minimum and maximum thickness cutoffs for generating<br>strike-slip faults                      | 211        |
| 4.6.2. Effects of a diffuse brittle-ductile transition and fault-healing on<br>brittle-crust thickness | 213        |

|  |            |
|--|------------|
| 4.6.3. Formation of irregularly-spaced strike-slip faults  | 214        |
| 4.6.4. Role of the lower crust driving strike-slip faulting                                      | 215        |
| 4.6.5. Estimates of absolute fault friction from fault spacing and<br>seismogenic zone thickness | 216        |
| 4.7. Conclusions   | 218        |
| 4.8. References  | 232        |
| <b>Chapter 5: Pre-Mesozoic tectonic evolution of the Qilian Shan</b>                             | <b>236</b> |
| 5.1. Abstract  | 237        |
| 5.2. Introduction  | 238        |
| 5.3. Deformation history of northern Tibet   | 240        |
| 5.3.1. Cenozoic deformation  | 241        |
| 5.3.2. Mesozoic extension  | 242        |
| 5.3.3. Paleozoic tectonics   | 242        |
| 5.4. Regional geologic setting of the Qilian Shan  | 244        |
| 5.4.1. Geology of the Qilian Shan  | 244        |
| 5.4.2. Geology of the North Qaidam metamorphic belt  | 247        |
| 5.4.3. Tectonic models for the Qilian orogen   | 248        |
| 5.5. Geologic mapping of the central Qilian Shan   | 249        |
| 5.5.1. Proterozoic and Paleozoic map units   | 249        |
| 5.5.2. Field relationships   | 252        |
| 5.6. Geochronology   | 254        |
| 5.6.1. U-Pb zircon geochronology   | 254        |
| 5.6.1.1. Methods   | 254        |
| 5.6.1.2. Sample description and results  | 256        |
| 5.6.2. In-situ Th-Pb monazite geochronology  | 261        |
| 5.6.2.1. Methods   | 262        |
| 5.6.2.2. Sample description and results  | 263        |
| 5.7. Whole-rock geochemistry   | 266        |
| 5.7.1. Methods   | 266        |
| 5.7.2. Results and discussion  | 268        |
| 5.8. Thermobarometry   | 272        |
| 5.8.1. Methods   | 272        |
| 5.8.2. Sample description and mineral composition  | 275        |
| 5.8.3. THERMOCALC <i>P-T</i> histories   | 279        |
| 5.8.4. Pseudosection <i>P-T</i> histories  | 282        |
| 5.9. Deformation history of the central Qilian Shan  | 286        |
| 5.10. Discussion   | 288        |
| 5.10.1. Lateral extent of the Qilian suture  | 288        |
| 5.10.2. Nature of the Qilian arc   | 290        |
| 5.10.3. Mesoproterozoic-Paleozoic tectonic evolution of northern Tibet                           | 291        |
| 5.11. Conclusion   | 295        |
| 5.12. References   | 344        |

|  |          |
|--|----------|
| <b>Chapter 6: The tectonic history of central Asia: The Balkatach hypothesis and a new model for the evolution of the Paleo-Pacific, Tethyan, and Paleo-Asian Oceans</b> | 360      |
| 6.1. Abstract  | 361      |
| 6.2. Introduction  | 362      |
| 6.3. Methods and regional tectonic analysis  | 365      |
| 6.3.1. Data handling   | 365      |
| 6.3.2. Assembly of tectonic domains  | 367      |
| 6.3.3. Tectonic modification of Precambrian cratons  | 368      |
| 6.3.4. Paleomagnetic considerations  | 369      |
| 6.4. Geology of the major pre-Mesozoic tectonic domains of central Asia  | 370      |
| 6.4.1. The Central Asian Orogenic System (COAS)  | 371      |
| 6.4.2. Baltica   | 374      |
| 6.4.3. Turan   | 378      |
| 6.4.4. Karakum   | 380      |
| 6.4.5. Tarim   | 381      |
| 6.4.6. The Qilian-Qaidam-Kunlun (Qinling-Dabie) continent and orogens  | 386      |
| 6.4.7. North China   | 390      |
| 6.5. Systematic restoration of central Asia and evidence for the Neoproterozoic Balkatach continent  | 394      |
| 6.5.1. Late Mesozoic-Cenozoic intracontinental deformation   | 395      |
| 6.5.2. Late Paleozoic-Mesozoic intracontinental deformation and ocean closure  | 398      |
| 6.5.3. Neoproterozoic rifting and Paleozoic orogeny  | 399      |
| 6.5.4. The origin of the Qaidam-Qilian-Kunlun and CAOS microcontinents   | 400      |
| 6.5.5. Paleomagnetic data  | 401      |
| 6.6. Tectonic evolution of Balkatach   | 402      |
| 6.6.1. Paleoproterozoic  | 402      |
| 6.6.2. Mesoproterozoic (Fig. 6.13)   | 403      |
| 6.6.3. Neoproterozoic (Fig. 6.14)  | 403      |
| 6.6.4. Early-Middle Paleozoic (Fig. 6.15)  | 405      |
| 6.6.5. Late Paleozoic (Fig. 6.16)  | 405      |
| 6.6.6. Mesozoic-Cenozoic (Fig. 6.17)   | 406      |
| 6.7. Discussion  | 407      |
| 6.7.1. Neoproterozoic Balkatach in Rodinia   | 408      |
| 6.7.2. Tectonic calving and CAOS microcontinent formation  | 410      |
| 6.8. Conclusions   | 412      |
| 6.9. References  | 437      |
| <b>Appendices: Auxiliary figures, text, and data tables</b>  | 474      |
| <b>Supplementary Materials: Full-size geologic maps and cross sections</b>   | Attached |

## LIST OF FIGURES

|   |     |
|---|-----|
| 1.1. Simplified tectonic map of Asia  | 13  |
| 1.2. Regional map of the northern Himalaya-Tibetan orogen   | 14  |
| 1.3. End-member models for the development of the Tibetan Plateau                                 | 15  |
| 1.4. Evenly-spaced strike-slip fault domains in California and Asia                               | 16  |
|   |     |
| 2.1. Regional map of the northern Himalaya-Tibetan orogen   | 89  |
| 2.2. Competing models for the development of the northern Tibetan Plateau                         | 91  |
| 2.3. Cenozoic fault map and regional geologic map of central Qilian Shan-Nan Shan thrust belt     | 93  |
| 2.4. Existing shortening estimates across northern Tibet  | 95  |
| 2.5. Example cross sections and shortening estimates across northern Tibet                        | 96  |
| 2.6. Lithostratigraphy of the central Qilian Shan   | 100 |
| 2.7. Geologic map of the Shule Nan Shan and Hara Lake basin                                       | 102 |
| 2.8. Geologic map of the Tuo Lai Nan Shan and Tuo Lai Shan  | 105 |
| 2.9. Field photographs from the central Qilian Shan   | 108 |
| 2.10. Geologic map of the North Qilian Shan frontal thrust system                                 | 110 |
| 2.11. Google Earth view of the North Qilian Shan range  | 111 |
| 2.12. Balanced cross section across the Shule Nan Shan  | 112 |
| 2.13. Balanced cross sections across the Tuo Lai Nan and Tuo Lai Shan                             | 113 |
| 2.14. Seismic reflection profile #1 and interpreted cross section                                 | 116 |
| 2.15. Seismic reflection profile #2 and interpreted cross section                                 | 118 |
| 2.16. Seismic reflection profile #3 and interpreted cross section                                 | 120 |
| 2.17. Reconstructed pre-Cenozoic northern margin of the frontal Qilian Shan                       | 122 |
| 2.18. Plot of topography, crustal thickness, and shortening across northern Tibet                 | 123 |
| 2.19. Model for the development of the northern margin of the Tibetan Plateau                     | 124 |
|   |     |
| 3.1. Cenozoic fault map of the northern Himalayan-Tibetan orogen                                  | 171 |
| 3.2. Models for space-issue accommodation at the panel ends in a bookshelf fault system           | 172 |
| 3.3. Models for the role of strike-slip faulting and deformation ages in northern Tibet           | 173 |
| 3.4. Clockwise rotation of northern Tibet from global positioning system (GPS) data               | 174 |
| 3.5. Four-quadrant deformation pattern associated with fault rotation                             | 176 |
| 3.6. Conceptual models for active and passive bookshelf faulting                                  | 177 |
| 3.7. Velocity field for active and passive bookshelf faulting                                     | 178 |
| 3.8. Kinematic model of fault-parallel strain at one end of a bookshelf panel                     | 179 |
| 3.9. The Garlock fault as an active bookshelf fault   | 180 |
| 3.10. Driving mechanisms for passive bookshelf faulting in northern Tibet                         | 181 |
| 3.11. Cenozoic tectonic evolution of northern Tibet as a non-rigid passive bookshelf fault system | 182 |
|   |     |
| 4.1. Evenly-spaced strike-slip fault domains in California and Asia                               | 219 |
| 4.2. Conceptual model for the formation of evenly-spaced joints                                   | 220 |
| 4.3. Model parameters and boundary conditions for strike-slip fault formation                     | 221 |
| 4.4. Effects of stress-shadow model parameters  | 222 |
| 4.5. Analogue experiment setup and representative trials  | 223 |

|  |     |
|--|-----|
| 4.6. Earthquake locations and depths in California and Asia  | 225 |
| 4.7. Fault spacing vs brittle-crust thickness for California and Asia and<br>fault friction estimates        | 227 |
| 4.8. Conceptual model for maximum and minimum brittle-crust thicknesses for<br>nucleating strike-slip faults | 228 |
| 5.1. Tectonic maps of Asia showing the Tethyan and Paleo-Asian Domains                                       | 297 |
| 5.2. Regional map of the northern Himalaya-Tibetan orogen  | 299 |
| 5.3. Tectonic models for the early Paleozoic Qilian arc and orogen   | 300 |
| 5.4. Tectonostratigraphy of the central Qilian Shan  | 301 |
| 5.5. Simplified geologic map of the Tuo Lai Nan Shan and Tuo Lai Shan  | 302 |
| 5.6. Regional geologic map of the central Qilian Shan  | 305 |
| 5.7. Field photographs of the deformed metamorphic unit  | 306 |
| 5.8. Field photographs from the ophiolite complex of the central Qilian Shan                                 | 308 |
| 5.9. U-Pb concordia plots  | 309 |
| 5.10. Representative synkinematic garnet with included monazite grain  | 313 |
| 5.11. In-situ Th-Pb monazite geochronology results   | 314 |
| 5.12. AFM plot and geochemical discrimination diagrams   | 315 |
| 5.13. Trace element geochemistry   | 316 |
| 5.14. Geochemical discrimination for the metamorphic rock samples  | 317 |
| 5.15. X-ray maps and compositional profiles across garnet grains   | 318 |
| 5.16. Amphibole classification   | 322 |
| 5.17. Average <i>P-T</i> THERMOCALC estimates for selected metamorphic samples                               | 323 |
| 5.18. Pseudosections for selected metamorphic samples  | 324 |
| 5.19. Estimated depth history for basement rocks in the central Qilian Shan                                  | 329 |
| 5.20. Block models for the Proterozoic-Paleozoic tectonic evolution of the Qilian Shan                       | 330 |
| 6.1. Tectonic maps of Asia showing the Tethyan and Paleo-Asian Domains                                       | 414 |
| 6.2. Map of Balkatach domains  | 415 |
| 6.3. Correlation chart showing major tectonic events along Balkatach margins                                 | 416 |
| 6.4. Detrital zircon probability density plot for Balkatach domains  | 418 |
| 6.5. Neoproterozoic stratigraphic columns for the margins of Balkatach                                       | 419 |
| 6.6. Major Paleozoic events tectonic and magmatic events in the Urals  | 420 |
| 6.7. Tectonic divisions near the Caspian Sea and boundary of the Turan domain                                | 421 |
| 6.8. Tarim suture and tectonic evolution of the inferred Tarim arc   | 422 |
| 6.9. The Qilian suture and possible configurations of the Qilian Ocean                                       | 423 |
| 6.10. The Precambrian North China craton   | 424 |
| 6.11. The restoration of the Balkatach continent   | 425 |
| 6.12. Paleolatitude estimates for various Balkatach domains  | 426 |
| 6.13. Paleoproterozoic tectonic reconstruction of Western and Eastern Balkatach                              | 427 |
| 6.14. Neoproterozoic through Cambrian tectonic reconstructions of central Asia                               | 428 |
| 6.15. Paleozoic tectonic reconstructions of central Asia   | 430 |
| 6.16. Kazakhstan orocline and the closure of the Paleo-Asian Ocean   | 432 |
| 6.17. Cretaceous to present-day reconstruction of central Asia   | 433 |
| A.1. Uninterpreted seismic reflection profiles from Chapter 2  | 475 |

|  |     |
|--|-----|
| A.2. Physical and mechanical properties of experimental materials in Chapter 4                     | 478 |
| A.4. Schematic diagrams of stress-shadow model applied to the analogue experiments in Chapter 4    | 482 |
| A.5. Earthquake depths for California and Asia   | 483 |
| A.6. Cathodoluminescence (CL) images of zircon with locations of U-Pb spot analyses from Chapter 5 | 484 |

## LIST OF TABLES

|   |     |
|---|-----|
| 2.1. Model predictions for the formation the Tibetan Plateau  | 125 |
| 2.2. Cross sections and shortening estimates across northern Tibet  | 126 |
| 2.3. Mesozoic and Cenozoic stratigraphy of the Hexi Corridor  | 128 |
| 3.1. Physical and mechanical properties of experimental materials   | 230 |
| 3.2. Observed fault spacing and seismogenic zone thickness in Asia and California                             | 231 |
| 5.1. Tectonic model predictions for the early Paleozoic Qilian arc and orogen                                 | 333 |
| 5.2. Summary of zircon geochronology results  | 334 |
| 5.3. Monazite isotopic data for central Qilian Shan samples   | 335 |
| 5.4. Whole-rock geochemical composition of samples  | 336 |
| 5.5. <i>P-T</i> data from THERMOCALC for selected metamorphic rocks   | 342 |
| 6.1. Proterozoic timescale commonly used in the Chinese literature following Chinese Geological Survey (2014) | 435 |
| 6.2. Selected paleomagnetic poles and paleolatitudes for Central Asian continents                             | 436 |
| A.7. U-Pb isotopic data for central Qilian Shan igneous samples from Chapter 5                                | 486 |
| A.8. Representative electron-microprobe analyses metamorphic samples for thermobarometry from Chapter 5       | 495 |

## ACKNOWLEDGEMENTS

I will start by thanking the members of my committee for their support, encouragement, patience, and guidance. I thank Professor Yongwei Sheng for serving as an inquisitive outside committee member. Craig Manning and T. Mark Harrison asked probing and thoughtful questions. Through interactions with both Craig and Mark, I learned how to defend and/or question my fundamental research assumptions. Some of my earliest interactions with Craig had me questioning my interpretations of field observations related to the Qilian suture zone, and he forced me to think critically about the geologic predictions of my interpretations. I learned almost everything I know about geochronology and thermochronology from Mark Harrison's classic Thermochronometry course. He was also an excellent mentor during my first trip to Tibet in 2012, and I am glad that I had the chance to learn about the geology and especially the history of geologic investigations in Tibet.

An Yin is an amazing and creative geologist, and simply put, my success as a geologic researcher would not be possible without his leadership, friendship, dedication to my work, and guidance. He pushed me constantly to grow as a critical, curious, and creative scientist. Working with An, I learned to focus on everything from big picture geologic problems, such as the evolution of major oceanic domains in central Asia, to the smallest details, like how the characteristic spacing of Riedel shears in sandbox experiments may be an important property.

My research was assisted by numerous individuals at UCLA. I want to thank Frank Kyte and Rosario Esposito for help on the electron microprobe, Winnie Wu for assistance during my first attempts at monazite dating, Axel Schmidt, Matt Weilicki, Rita Economos, and Ming-Chang Liu for their assistance in acquiring and interpreting U-Th-Pb isotopic data, Yuxiu Zhang, Chen Wu, and Long Wu for carrying out the detrital zircon analysis and offering me this data prior to



its publication, and Jade Star Lackey for assistance with XRF analysis at Pomona College. I must save a dedicated sentence for Chen Wu. He has been a generous field companion over three field seasons, a go-to contact in China for logistical support, an enormous help with sample organization, preparation, and analysis in China, and a great friend over the last five years. Other collaborators and colleagues in China—including Jinhua Li, Haiyan Wang, Xiaosong Xiong, and Junfeng Gong—made my research both possible and thoroughly enjoyable.

I will always cherish my time at UCLA, and especially my interactions with everyone in the structural geology group, including Robin Reith, Paul Burgess, Peter Haproff, Jessica Watkins, Jennifer Scully, and Erin Leonard. The other geologists in the department were equally influential in my graduate career, including Dallon Stang, Nate Brown, Evan Wolf, and Ivy Curren. Together, we gathered around many campfires during long nights in the desert regions of California, Utah, Nevada, and Arizona. I will always appreciate the discussions I have had with all of my UCLA colleagues. I learned a lot from these folks! Furthermore, my time at UCLA was shaped by all of the graduate and undergraduate students in the Department of Earth and Space Sciences (now Earth, Planetary, and Space Sciences). I learned so much from all of my teaching experiences interacting with several generations of undergraduate geology majors. On a related note, I am grateful for having the opportunity to attend graduate school in the western United States. Over the last five years, I have been exposed to such amazing geology over the course my numerous day- to month-long field trips across the western states.

I thank Robin Reith for her patience and support over the years. Her mapping and research in the central Qilian Shan is a critical component of this dissertation. Furthermore, Robin has been persistently encouraging throughout my graduate work, especially during the more stressful periods. Lastly, she has always been around and willing to embark on fun,

distracting, and necessary adventures during much needed breaks from research, academics, and geology. Thank you. I also want to thank all of my family and friends for their support. During the completion of my graduate work, I was not always around, accessible, or responsive.

Last but not least, I thank the previous generation of An Yin students that served as role models, sources of inspiration, and reminders that success in graduate school is possible.

Although, during my time at UCLA, I never overlapped with Mike Murphy, Paul Kapp, Eric Cowgill, Mike Taylor, Matt Spurlin, Alex Webb, Stephanie Briggs, or Sara Cina, I constantly looked up to their legacy and work.

About half of Chapter 2 was published in *Geosphere* (Zuza et al., 2016) with Xiaogan Cheng and An Yin as coauthors. Thorough reviews by William Craddock and Delores Robinson, and the editorial handling of Raymond Russo, improved this text. Chapter 3 was originally published in *Tectonophysics* (Zuza and Yin, 2016) with An Yin as a coauthor. Paul Mann, an anonymous reviewer, and editor Jean-Philippe Avouac helped to clarify the ideas and logic presented in this publication and Chapter 3. Chapter 4 is currently in revision in *EPSL* at the time this dissertation was submitted (Zuza et al., 2016), with An Yin, Jessica Lin, and Ming Sun as coauthors. The text from this chapter was greatly improved by comments from two anonymous reviewers and editor Peter Shearer.

The research presented in this dissertation was supported by the National Science Foundation's (NSF) East Asia Pacific Summer Institute (EAPSI) summer fellowship and a Dissertation Year Fellowship funded by UCLA, both awarded to me. There were also contributions from the China University of Geosciences (Beijing) and grants from the SinoProbe Program administered by the Chinese Academy of Geological Sciences. Even when funding was tight, the always creative An Yin found ways to come up with research money: Fiat Lux trips,

running field conferences, and hosting international visitors during the UCLA summer field camp. For all of these efforts that allowed me to not just run through the motions of geologic research, but to follow my curiosity in any direction that it wandered, I am grateful.

## VITA

|                      |   |
|----------------------|---|
| 2009                 | Geology of the Central Andes Field Camp (Argentina), Cornell University   |
| 2010                 | Frontiers Abroad New Zealand Field Mapping  |
| 2010                 | University of Canterbury Semester Abroad Christchurch, New Zealand  |
| 2011                 | B. S., <i>Magna Cum Laude</i> , Science of Earth Systems: Geologic Sciences, Distinction in Research Cornell University, Ithaca, NY |
| 2012, 2014, and 2015 | Teaching assistant for UCLA Summer Field White Mountains, California  |
| 2012-2015            | Teaching assistant, UCLA  |

## PUBLICATIONS

- Zuza, A. V.**, Yin, A., Lin, J., Ming, S., 2016 in revision, Spacing and strength of active continental strike-slip faults: EPSL.
- Zuza, A. V.**, Yin, A., 2016, Continental deformation accommodated by non-rigid passive bookshelf faulting: An example from the Cenozoic tectonic development of northern Tibet: *Tectonophysics*, 677-678, p. 227-240.
- Wu, C., Yin, A., **Zuza, A. V.**, Zhang, J., Liu, W., Ding, L., 2016, Pre-Cenozoic geologic history of the central and northern Tibetan Plateau and the role of Wilson cycles in constructing the Tethyan orogenic system: *Lithosphere*, in press.
- Zuza, A. V.**, Cheng, X., Yin, A., 2016, Testing models of Tibetan Plateau formation with Cenozoic shortening estimates across the Qilian Shan-Nan Shan thrust belt: *Geosphere*, v. 12, no. 2, p. 501-532.
- Yin, A., **Zuza, A. V.**, Pappalardo, R. T., 2016, Mechanics of evenly spaced strike-slip faults and its implications for the formation of tiger-stripe fractures on Saturn's moon Enceladus: *Icarus*, v. 266, p. 204-216.
- Gao, R., Wang, H., Yin, A., Kang, Z., **Zuza, A. V.**, Li, W., Xiong, X., 2013, Tectonic Development of the northeastern Tibetan Plateau as constrained by high-resolution deep seismic-reflection data: *Lithosphere*, v. 5, no. 6, p. 555-574.
- Zuza, A. V.**, 2011, Late Cenozoic Volcanism in the Hövsgöl Rift Basin: Source, Genesis, and Evolution of Intraplate Volcanism in Mongolia [B.S. honor thesis]: Cornell University, 31 p.

## SELECTED PRESENTATIONS

- Zuza, A. V.**, 2016, Testing Tibetan Plateau formation models: Insights from the Qilian Shan-Nan Shan thrust belt: University of Nevada, Reno, NV, March 2016.
- Wu, C., Yin, A., **Zuza, A. V.**, Liu, W., 2015, U-Pb zircon geochronology from the basement of the Central Qilian Shan: Implications for tectonic evolution of northeastern Tibetan Plateau: AGU Fall Meeting Abstracts.
- Zuza, A. V.**, Yin, A., Lin, J., 2015, The stress shadow effect: a mechanical analysis of the evenly-spaced parallel strike-slip faults in the San Andreas fault system: AGU Fall Meeting Abstracts.

- Yin, A., **Zuza, A. V.**, Pappalardo, R., 2015, The Stress Shadowing Effect of the Tiger-stripe Fractures on Saturn's Moon Enceladus: AGU Fall Meeting Abstracts.
- Lin, J., **Zuza, A.V.**, Yin, A., 2015, Quantifying the Relationship between Strike-slip Fault Spacing and Brittle Crust Thickness in Continental Settings based on Sandbox Experiments: AGU Fall Meeting Abstracts.
- Zuza, A. V.**, Yin, A., Wu, C., 2015, The Neoproterozoic-Paleozoic tectonic history of the Qilian Shan and its control on the development of the Tibetan Plateau's northern margin: GSA Abstracts with Programs, v.47, n. 7.
- Zuza, A. V.**, Cenozoic tectonic evolution of the northeastern Tibetan Plateau: Insights from the Qilian Shan thrust belt: Caltech Geology Club Seminar, Pasadena, CA, April 2015.
- Zuza, A. V.**, Yin, A., Li, Jianhua, 2014, Deciphering the coupled Paleozoic and Cenozoic tectonic history of the Qilian Shan, northeastern Tibetan Plateau: AGU Fall Meeting Abstracts, v. 1, p. 4563.
- Zuza, A. V.**, Yin, A., 2014, Initial and Boundary Conditions for the Evolution of the Central Asian Orogenic System (CAOS): The Balkatach Hypothesis: GSA Abstracts with Programs, v. 46, n. 6, p.789.
- Zuza, A. V.**, Yin, A., 2013, Ductile bookshelf faulting: A new kinematic model for Cenozoic deformation in northern Tibet: AGU Fall Meeting Abstracts, v. 1, p. 2.
- Zuza, A. V.**, Yin, A., 2013, Testing the TWINS hypothesis: Were Greater North China and Laurentia linked in the Archean and Proterozoic?: GSA Abstracts with Programs, v. 45, n. 7, p. 463.
- Zuza, A. V.**, Reith, R. C., Yin, A., Dong, S., Liu, W., Zhang, Y., Wu, C., 2013, Structural and tectonic framework of the Qilian Shan-Nan Shan thrust belt, northeastern Tibetan Plateau: GSC-GSA Joint Meeting, Chengdu, China, June 2013.
- Zuza, A. V.**, Yin, A., 2013, The Greater China: A Sequential Palinspastic Reconstruction through the Phanerozoic: GSC-GSA Joint Meeting, Chengdu, China, June 2013.
- Zuza, A. V.**, Yin, A., Reith, R. C., Dong, S., Liu, W., Wu, C., Wu, L., Gong, J., Zhang, J., 2012, Cenozoic tectonic development of the Qilian Shan-Nan Shan (northeastern Tibetan Plateau): A preliminary synthesis: AGU Fall Meeting Abstracts, v. 1, p. 2635.
- Zuza, A. V.**, Reith, R. C., 2012, Tectonic Evolution of the Qilian Shan in Northern Tibet: A Paleozoic Orogen Reactivated in the Cenozoic: Seismology-tectonics seminar, Department of Earth and Space Sciences, University of California, Los Angeles, CA, October 2012.
- Zuza, A.**, Bat-Erdence, A., 2011, Late Cenozoic Volcanism in the Hövsgöl Rift Basin: Source, Genesis, and Evolution of Intraplate Volcanism in Mongolia, in Keck Geology Consortium Proceedings of the Twenty-Fourth Annual Keck Research Symposium in Geology, edited by Varga, R. J., p. 272-280.
- Zuza, A.**, Andronicos, C. L., Kay, S. M., 2011, Late Cenozoic Volcanism in the Hövsgöl Rift Basin: Source, Genesis, and Evolution of Intraplate Volcanism in Mongolia: Keck Geology Consortium, Schenectady, New York, April 2011.
- Gravley, D. M., Wandres, A., Bova, S.C., House, B., Kravitz, K.A., Spera, S., Walsh, D., Windham, C.J., **Zuza, A.**, Dohaney, J., 2010, Undergraduate research projects on Mt. Doom in New Zealand: A new model for study abroad experiences: GSA meeting, Denver, Colorado, October 2010.

**-Chapter 1-**  
**Introduction**

## 1.1. Introduction

Eurasia was the only continent assembled during the Phanerozoic (e.g., Şengör and Natal'in, 1996), and understanding its formation and evolution greatly impacts our knowledge of continental tectonics (Molnar, 1988; Yin, 2010). The Eurasian continent developed through the Neoproterozoic to the present over a span of one billion years (Scotese and McKerrow, 1990; Yin and Nie, 1996; Şengör and Natal'in, 1996; Yin and Harrison, 2000). The construction of this continent was accomplished by several continental collisions associated with the closure of the Paleo-Asian and Tethyan ocean domains in north-central and southern Asia, respectively (e.g., Zonenshain et al. 1990; Yin and Nie, 1996; Şengör and Natal'in, 1996; Heubeck, 2001; Badarch et al. 2002; Stampfli and Borel, 2002; Biske and Seltsmann, 2010; Wu et al., 2016) (Fig. 1.1). The most recent of these collisions, between the Indian and Eurasian continents, led to the development of the archetypal continental collision: the Himalayan-Tibetan orogen (e.g., Yin and Harrison, 2000; Yin, 2010).

This dissertation revolves around topics of intracontinental deformation, repeated collision and ocean closure, and the tectonic reorganization of northern Tibet, from the early Neoproterozoic collisions of cratons that formed the supercontinent Rodinia to the most recent development of the modern Tibetan Plateau. In this work, I provide insight into these events, and contribute to our understanding of the geology of the northeastern Tibetan Plateau, through detailed study of the Qilian Shan-Nan Shan thrust belt (Fig. 1.2). This active fold and thrust system, which presently defines the northeastern margin of the Tibetan Plateau (Figs. 1.1 and 1.2), is one of the widest active thrust belts in Tibet. The Qilian Shan exposes Precambrian basement, an early Paleozoic orogen, Mesozoic extensional basins, and Cenozoic thrust and strike-slip fault systems. Despite its important and complex tectonic position along the northern

margin of the plateau, this region has not been thoroughly examined with modern structural methods, leaving many first-order problems unresolved. The interaction between Paleozoic and Cenozoic structures in this region requires a holistic approach to unravel the regional tectonic history. It is impossible to accurately interpret the Paleozoic history without understanding the more recent Cenozoic deformation and reorganizational events, and tectonic reconstructions of Cenozoic deformation must be made in the context of the pre-Cenozoic configuration. This dissertation is comprised of five main chapters, and the topics generally progress from youngest (i.e., active Cenozoic shortening) to oldest (i.e., Proterozoic craton reconstructions) in terms of the geologic history.

Throughout this dissertation, I use the name Qilian Shan (Shan = Mountains in Chinese) to refer to the geographical and physiographical region that is comprised of the northernmost mountain range on the Tibetan Plateau. The Qilian Shan-Nan Shan is the name given to the Cenozoic thrust belt that occupies the region of the Qilian Shan, and this active thrust belt is responsible for its present-day geomorphology of the Qilian Shan (i.e., northwest-trending ranges and intermontane basins). Although the Qilian Shan and associated mountains are sometimes referred to as the Nan Shan (Nan Shan = Southern Mountains, which were to the south of the Silk Road as it ran through the Hexi Corridor; Fig. 1.2) (e.g., Tapponnier and Molnar, 1977) and the Cenozoic thrust belt is variably given a combination of these names (e.g., Nan Shan thrust belt, Qilian Shan thrust belt, etc), in this dissertation I refer to the mountain range or geographic location as the Qilian Shan and the active Cenozoic thrust belt as the Qilian Shan-Nan Shan. The Qilian orogen, Qilian suture, and remnants of the Qilian Ocean refer to the early Paleozoic features that are distributed throughout the Qilian Shan. The exposure of these early Paleozoic tectonic features is the result of uplift and erosion across the Cenozoic Qilian Shan-Nan Shan



thrust belt. Lastly, note that there are numerous ranges and major river valleys within the Qilian Shan or Qilian Shan-Nan Shan thrust belt (e.g., the Shule Nan Shan, Tuo Lai Shan, etc.), which I discuss in more detail in Chapter 2.

This dissertation is based primarily on detailed field mapping across northern Tibet, which included two summers of mapping in the central Qilian Shan and one two-week period of reconnaissance mapping where the northeastern Tibetan Plateau abuts against the North China craton (Figs. 1.1 and 1.2). In the summer of 2012, Robin Reith, Chen Wu, Junfeng Gong, Jinyu Zhang, myself, and a team of other geologists mapped the Tuo Lai and Shule river valleys in the central Qilian Shan. Our focus was primarily on establishing the tectonostratigraphic units, mapping Cenozoic thrust faults, and collecting samples for geochronology. We also completed several traverses across the metamorphic basement rocks. During this field season, Robin Reith and I focused on mapping the regionally extensive unconformities at the base of the Carboniferous (sometimes Permian or Triassic) strata, with the goal of using this marker horizon to help restore Cenozoic deformation. In addition, Chen Wu and I noted that metamorphic rocks in the Tuo Lai Nan Shan made up a large vertically oriented right-slip shear zone. Initially, we thought that this right-slip shear zone could have originally been a thrust fault from the early Paleozoic Qilian orogen that was rotated during Cenozoic deformation. This hypothesis was later refuted through focused mapping in 2013 and thermobarometry analysis.

During the summer of 2013, Chen Wu and I expanded our work from the previous summer, revisited key contacts, and focused our mapping in the Tuo Lai Shan, north of the town of Yanglong, which is bounded by the Tuo Lai and Heihe Rivers to the south and north, respectively. In this field season, we continued mapping the late Paleozoic unconformity surface that is regionally extensive throughout most of the central Qilian Shan. We also focused on the

early Paleozoic features of the Qilian orogen and suture, including Neoproterozoic passive continental margin rocks, Yushiguo ophiolite (e.g., Song and Su, 1998; Hou et al., 2006), and deformed Ordovician forearc strata.

On a two week field trip at the end of the summer of 2014, An Yin, Chen Wu, and I examined the southwestern margin of the North China craton near Wuwei and Jinchong. Interpretation of this field season's data is still ongoing, but we did identify several Proterozoic deformational events within the North China craton (possibly Paleo- and Mesoproterozoic events) and a large north-facing passive margin sequence. This passive margin represents the southernmost boundary of the Paleo-Asian oceanic domain (Fig. 1.1).

## **1.2. The Cenozoic evolution of the northern Tibetan Plateau (Chapters 2 and 3)**

Although investigations of Cenozoic crustal shortening along the southern and eastern margins of the Tibetan Plateau have been robust (e.g., Burchfiel et al., 1995; Murphy et al., 1997; Johnson, 2002; DeCelles et al., 2002; Robinson et al., 2006; McQuarrie et al., 2008; Hubbard and Shaw, 2009; Webb et al., 2011; Webb, 2013), our understanding of Cenozoic deformation along the northern plateau margin is lacking. Well-constrained shortening estimates provide a first-order test of plateau formation mechanisms (e.g., Hubbard and Shaw, 2009; Wang et al., 2011; Lease et al., 2012) (Fig. 1.3). Existing shortening studies across northern Tibet suggest a low magnitude of Cenozoic deformation across the Qilian Shan-Nan Shan thrust belt (Gaudemer et al., 1995; Meyer et al., 1998; Lease et al., 2012; Craddock et al., 2014). However, the lack of detailed structural observations in these aforementioned works, including systematic geologic mapping and subsurface seismic data, necessitated further examination.

In Chapter 2, I present data from detailed field mapping, balanced cross section construction and restoration, and seismic reflection analysis to provide robust minimum Cenozoic shortening strain estimates across the Qilian Shan-Nan Shan thrust belt. I show that the North Qilian Shan thrust system and adjacent Hexi Corridor have accumulated >53% Cenozoic strain (>50 km shortening), whereas the interior of the Qilian Shan-Nan Shan has accommodated >34% Cenozoic strain (>53 km shortening). Based on this observed strain distribution across northern Tibet, with higher strain along the northern frontal thrust zones and lower strain within the thrust belt interior, I suggest that a combination of distributed crustal shortening and minor (<250 km) southward underthrusting of the Asian lithosphere is responsible for the development of the northern Tibetan Plateau. About half of this chapter, related to the seismic reflection analysis across the northern Qilian Shan, was published in *Geosphere* (Zuza et al., 2016a) with Xiaogan Cheng and An Yin as coauthors. Thorough reviews by William Craddock and Delores Robinson, and the editorial handling of Raymond Russo, improved this text.

The kinematics of continental deformation have been related to plate-like rigid-body motion (e.g., Tapponnier et al., 1982; Weldon and Humphreys, 1986; Avouac and Tapponnier, 1993; Meade, 2007) and flow-like distributed deformation via viscous flow (e.g., England and Houseman, 1986; Yin and Taylor, 2011). These two end-member models have been extensively tested in Tibet against structures created during the Cenozoic India-Eurasia collision (e.g., Yin and Harrison, 2000; Zhu et al., 2005; Yin, 2010; van Hinsbergen et al., 2011; Yin and Taylor, 2011). Specifically, debates have been centered on whether the >1000-km-long east-striking left-slip Haiyuan, Qinling, and Kunlun faults in northern Tibet (Fig. 1.2) (Molnar and Tapponnier, 1975; Tapponnier and Molnar, 1977; Tapponnier et al., 2001; Taylor and Yin, 2009) have acted as rigid-block boundaries (Tapponnier et al., 1982; Avouac and Tapponnier et al., 1993;

Tapponnier et al., 2001) or transfer-fault structures linking dip-slip fault systems (e.g., Burchfiel et al., 1991; Yin, 2000; Duvall and Clark, 2010). These major strike-slip faults have a maximum slip in the central fault segment exceeding 10s to ~100 km but a much smaller slip magnitude ( $\sim < 10\%$  of the maximum slip) at their terminations. The along-strike variation of fault offsets and pervasive off-fault deformation create a strain pattern that departs from the expectations of the classic plate-like rigid-body motion and flow-like distributed deformation approximations for continental deformation.

In Chapter 3, I present a non-rigid bookshelf-fault model for the Cenozoic development of northern Tibet. This model, which relates left-slip faulting to distributed off-strike-slip fault deformation during regional clockwise rotation, explains several puzzling features, including (1) clockwise rotation of east-striking left-slip faults against the northeast-striking left-slip Altyn Tagh fault along the northwestern margin of the Tibetan Plateau, (2) alternating fault-parallel extension and shortening in the off-fault regions, and (3) eastward-tapering map-view geometries of the Qimen Tagh, Qaidam, and Qilian Shan thrust belts that link with the three left slip faults. I refer to this non-rigid bookshelf fault system as passive bookshelf-faulting because the rotating bookshelf panels are detached from the rigid bounding domains (e.g., Tarim Basin and North China). Chapter 3 was originally published in *Tectonophysics* (Zuza and Yin, 2016) with An Yin as a coauthor. Paul Mann, an anonymous reviewer, and editor Jean-Philippe Avouac helped to clarify the ideas and logic presented in this publication and Chapter 3.

### **1.3. Spacing and strength of active continental strike-slip faults (Chapter 4)**

The strike-slip faults in northern Tibet are parallel and remarkably evenly spaced (~150 km). Throughout Asia there are numerous examples of other parallel evenly-spaced strike-slip

fault systems, including right-slip faults across Central Asia, V-shaped conjugate faults across central Tibet, and right-slip faults in Iran (Fig. 1.4). Parallel strike-slip faulting occurs widely in nature, from a few meters to >100s km in length and spacing (e.g., Segall and Pollard, 1983; Davy and Cobbold, 1988; Swanson, 1988; Martel and Pollard, 1989; Dickinson, 1996; Yin, 2010). Regularly spaced strike-slip faults are observed along plate transform boundaries (e.g., the San Andreas fault system; Fig. 1.4A) (e.g., Nur et al., 1986; Dickinson, 1996), across collisional orogens (e.g., the Himalayan-Tibetan orogen; Fig. 1.4B) (Molnar and Tapponnier, 1975; Taylor and Yin, 2009; Yin, 2010), in analogue experiments (e.g., Tchalenko, 1970; Freund, 1974; Naylor et al., 1986; Yin and Taylor, 2011), and on icy satellites (e.g., Yin et al., 2016). Despite their common existence, the fundamental question of what controls fault spacing remains unanswered.

In Chapter 4, I explore the above issue through analogue and numerical modeling, and explain strike-slip fault spacing using a stress-shadow model (e.g., Lachenbruch, 1961; Yin et al., 2016). I present a mechanical model for the generation of parallel strike-slip faults that relates fault spacing to the following parameters: brittle-crust thickness, fault strength, crustal strength, and the crustal stress state. Scaled analogue experiments using dry sand, crushed walnut shells, and viscous putty were employed to test the key assumptions of this quantitative model. I ultimately apply this model to crustal-scale strike-slip faults on Earth using fault spacing and the seismogenic-zone thickness obtained from high-resolution earthquake-location data to estimate absolute fault friction of active strike-slip faults in Asia and along the San Andreas fault system in California. I show that the average friction coefficient of strike-slip faults in the India-Asia collisional orogen is lower than that of faults in the San Andreas fault system. Weaker faults explain why deformation penetrates >3500 km into Asia from the Himalaya and why the interior

of Asia is prone to large ( $M > 7.0$ ) devastating earthquakes along major strike-slip faults (Fig. 1.4).

The ideas and stress-shadow concepts of Chapter 4 were first presented at the JPL-UCLA Planetary Science Workshop (Yin and Zuza, 2015), where An Yin and I modified a stress-distribution solution for extensional jointing (Pollard and Segall, 1987) to apply to strike-slip faulting. The formal derivation of this stress-shadow model, as applied to Enceladus's ice shell, was published in *Icarus* (Yin, Zuza, and Pappalardo, 2016), with An Yin and Robert Pappalardo as coauthors. This derivation was further modified to apply to active continental strike-slip faults on Earth, and the model assumptions were tested and validated through analogue experiments with the assistance of Jessica Lin and Ming Sun at UCLA. Our updated ideas were presented together at AGU in 2015 (Zuza et al., 2015; Yin et al., 2015; Lin et al., 2015).

Chapter 4 is currently in revision in *EPSL* at the time this dissertation was submitted (Zuza et al., 2016b), with An Yin, Jessica Lin, and Ming Sun as coauthors. The text from this chapter was greatly improved by comments from two anonymous reviewers and editor Peter Shearer. Jessica Lin and Ming Sun helped with the execution of the experimental work, and Robin Reith and Ivy Curren are acknowledged for setting up the Virtual Tibet analogue modeling apparatus (now known as the Laboratory for Analogue Modeling of Planetary Surfaces or "LAMP").

#### **1.4. The Proterozoic-Paleozoic tectonic evolution of northern Tibet and central Asia (Chapters 5 and 6)**

Northern Tibet represents the boundary between the Tethyan Orogenic System to the south and the Paleo-Asian Oceanic Domain to the north (Fig. 1.1) (e.g., Şengör and Natal'in,

1996; Yin and Harrison, 2000; Heubeck, 2001; Stampfli and Borel, 2002). Extensive research has focused on the tectonic evolution these two domains but relatively little attention has been paid to the tectonic history and role of the cratonal units that lie between these two orogenic systems (e.g., the Tarim and North China cratons). The lack of studies on the “intermediate units” of Şengör and Natal’in (1996) (Fig. 1.1) has limited our ability to use a process-based approach to reconstruct the tectonic history of the two major orogenic systems in Asia.

In Chapter 5, I examine the southern margin the Tarim and North China cratons. The Kunlun-Qaidam continent collided against this margin during the early Paleozoic Qilian orogen. The abundance of ophiolite-bearing mélangé and blueschist assemblages across the Qilian Shan led early workers to suggest that this region represents the site of the closed Qilian Ocean (Wang and Liu, 1976; Xiao et al., 1978) that once separated North China from Qaidam. More recent work has shown that this ocean opened in the Neoproterozoic and closed during the early Paleozoic Qilian orogen (e.g., Yin and Harrison, 2000; Gehrels et al., 2003a, 2003b, 2011; Yin et al., 2007; Xiao et al., 2009; Song et al., 2013, 2014). There is little consensus regarding the timing and style (e.g., subduction polarity, number of arcs involved, relationship of continents) of the opening and closing of the Qilian Ocean. To better constrain the evolution of the Qilian orogen and resulting closure of the Qilian Ocean, I present geologic mapping across the central Qilian Shan integrated with U-Th-Pb zircon and monazite geochronology, whole-rock geochemistry of igneous rocks, thermobarometry of the metamorphosed basement rocks, and synthesis of existing datasets across northern Tibet. Here I show that two ocean-closure events affected this region—one in the early Neoproterozoic and the other in the early Paleozoic—and that the early Paleozoic Qilian orogen involved a single-south dipping subduction system. The

present-day configuration of the Qilian orogen has subsequently been tectonically modified by the early Paleozoic collisional event and later Cenozoic deformation.

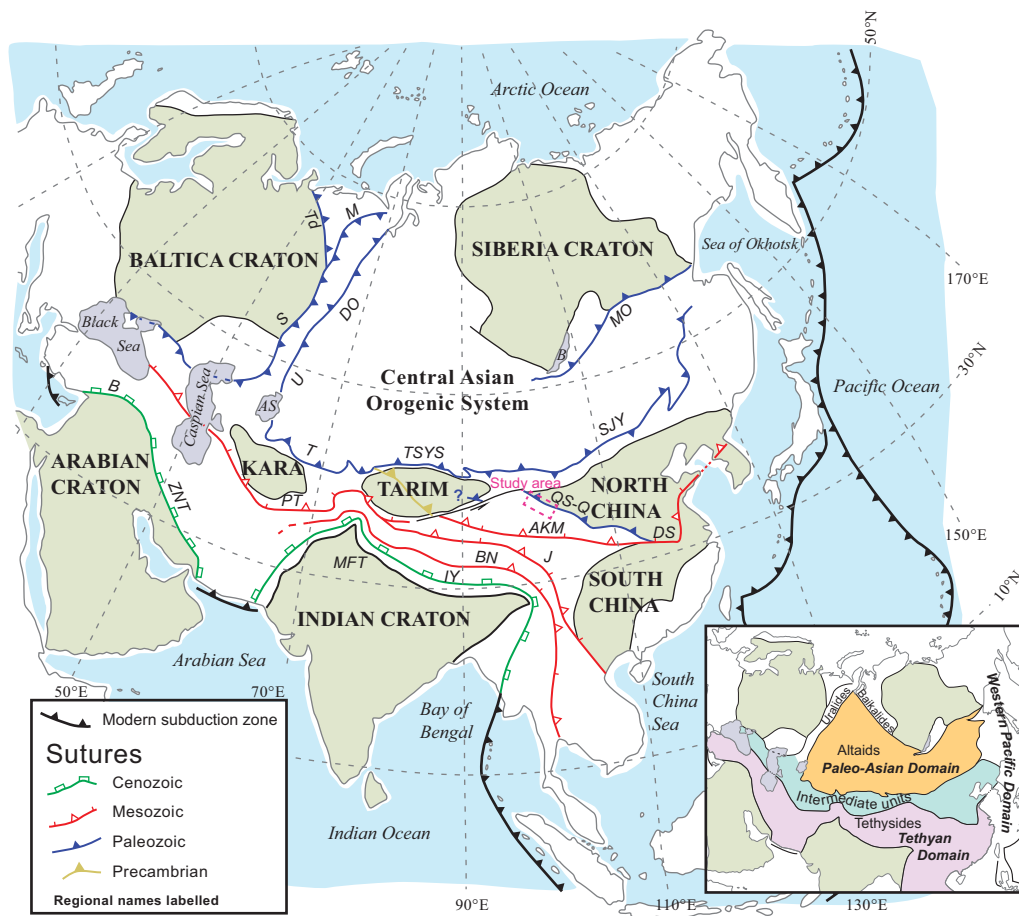
Chen Wu and Yuxiu Zhang shared unpublished U-Pb zircon ages from the Qilian Shan that were used in my reconstruction of the early Paleozoic Qilian orogen. Carrie Menold also provided unpublished U-Pb zircon ages and  $^{40}\text{Ar}/^{39}\text{Ar}$  cooling ages from the ultra-high pressure (UHP) rocks in the North Qaidam thrust belt to the south.

The reconstruction I present in Chapter 5 implies that the Qilian Ocean was not a major through-going ocean separating Laurasia from Gondwana (cf. Stampfli and Borel, 2002), but rather a small marginal sea that opened along an early Neoproterozoic suture zone along the southern margin of the linked Tarim-North China continent. However, existing supercontinent reconstructions treat North China, Tarim, and Qaidam as separate continents that collide in the Paleozoic (e.g., Li et al., 2008). Alternatively, An Yin and I speculated that these cratons were linked in the Neoproterozoic as part of a 6000-km-long continent (Zuza and Yin, 2013, 2014). A key test of this hypothesis is to restore Cenozoic and early Paleozoic deformation in the Qilian Shan region and evaluate whether the basement and continental margins correlate with Tarim and North China (e.g., Guo et al., 2005).

In Chapter 6, I review existing geologic literature on the Baltica, Karakum, Turan, Tarim, and North China cratons, including their mutual tectonic relationships and respective deformational histories during and after they became individual tectonic entities. I then systematically restore the geometry of these cratons from their present-day configuration through the Phanerozoic and into the Proterozoic using the Gplates software (Boyden et al., 2010). By removing the tectonic-distortion effects caused by intracontinental deformation and rifting events, I show that Baltica, Karakum, Turan, Tarim, and North China were once continuously

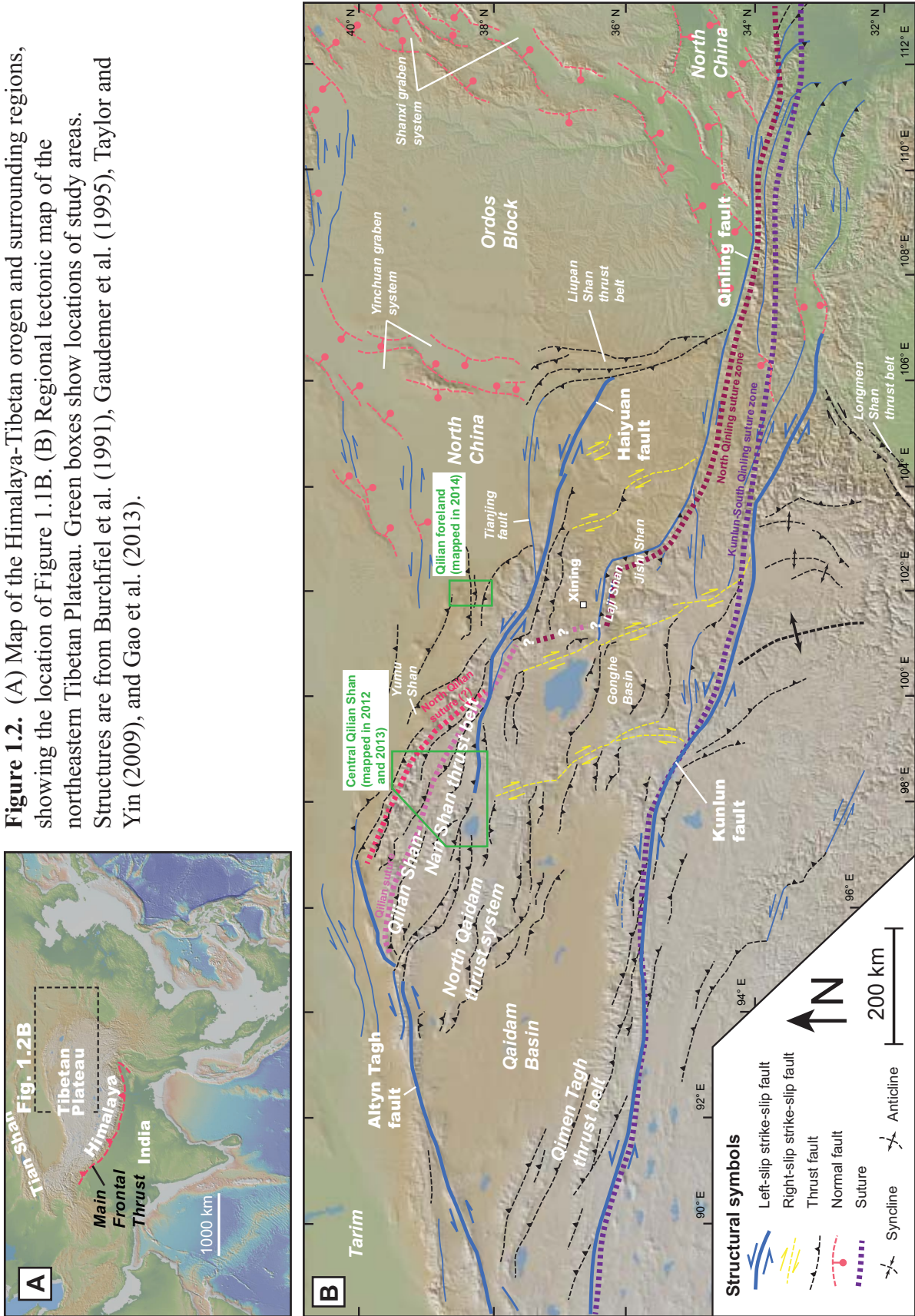


linked in the Neoproterozoic as a long continental strip that I refer to as Balkatach (named after the **Baltica-Karakum-Tarim-China** connection of traditionally-defined Precambrian cratons). In this chapter I show how the contiguous Balkatach continent, and the relative motion of its western and eastern arms (in present-day coordinates) in the Paleozoic, played an important role in the tectonic evolution of Asia. Neoproterozoic rifting along Balkatach's margins led to the genetically linked birth of the Paleo-Asian and Pacific Oceans, which were only separated when the eastern arm of the Balkatach continent wrapped around the closing Paleo-Asian Ocean in the latest Paleozoic.



**Figure 1.1.** Simplified tectonic map of Asia showing cratons, sutures, and modern subduction zones. Teeth on are on over-riding plate. For simplicity, the structures and sutures within the Central Asian Orogenic System are omitted. Purple box shows the approximate location of the study area. Pre-Neoproterozoic sutures within cratons are not shown. Inset map shows major tectonic division and oceanic domains. AS—Aral Sea, B—Lake Baikal, Kara—Karakum Craton, MFT—Main Frontal Thrust. Labeled sutures: AKM—Anyimaqen-Kunlun-Muztagh, B—Bitlis, BN—Bangong- Nuijiang, DO—Denisov-Oktyabrsk, DS—Dabie Shan, J—Jinsha, M—Magnitogorsk, MO—Mongol-Okhotsk, PT—Paleo-Tethys, S—Sakmara, SJY—Solonker-Jilin-Yanji, TSYS—Tian Shan-Ying Shan, T—Turketsan, Td—Timanide, U—Ural, QS-Q—Qilian Shan-Qinling, ZNT—Zagros-Neo-Tethys. After Yin and Nie (1996), Şengör and Natal'in (1996), Natal'in and Şengör (2005), Xiao et al. (2010), and Zheng et al. (2013).

**Figure 1.2.** (A) Map of the Himalaya-Tibetan orogen and surrounding regions, showing the location of Figure 1.1B. (B) Regional tectonic map of the northeastern Tibetan Plateau. Green boxes show locations of study areas. Structures are from Burchfiel et al. (1991), Gaudemer et al. (1995), Taylor and Yin (2009), and Gao et al. (2013).



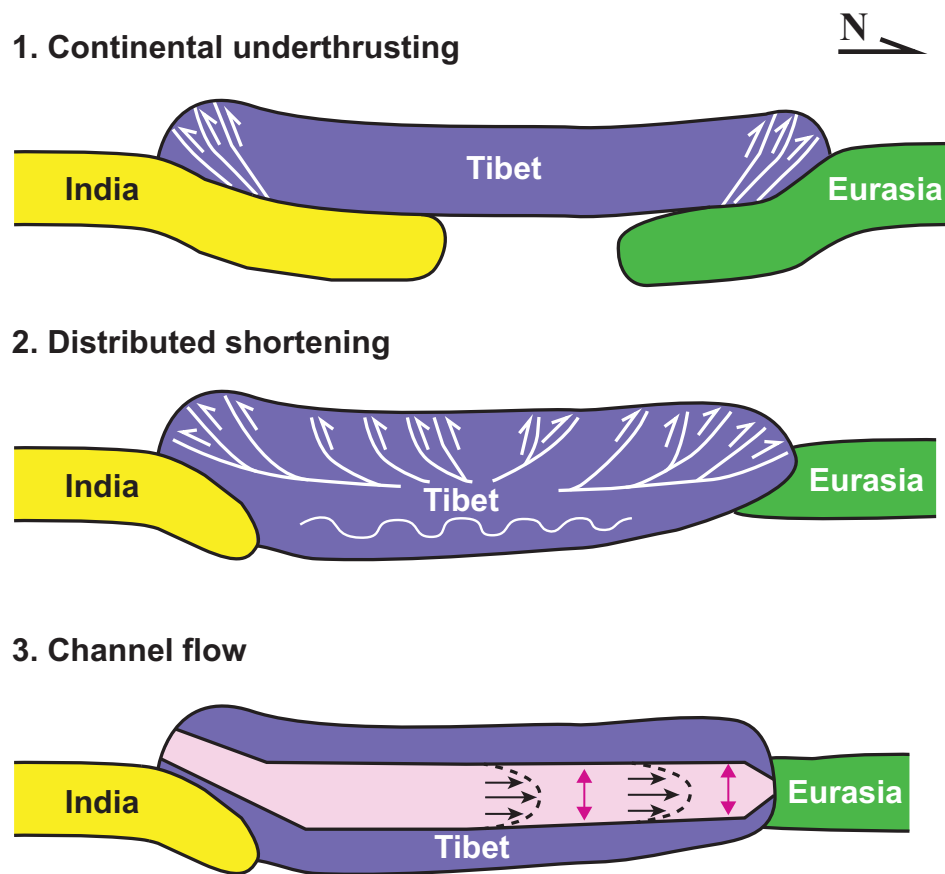


**Figure 1.3.** Three end-member tectonic models for the construction of the Tibetan Plateau.

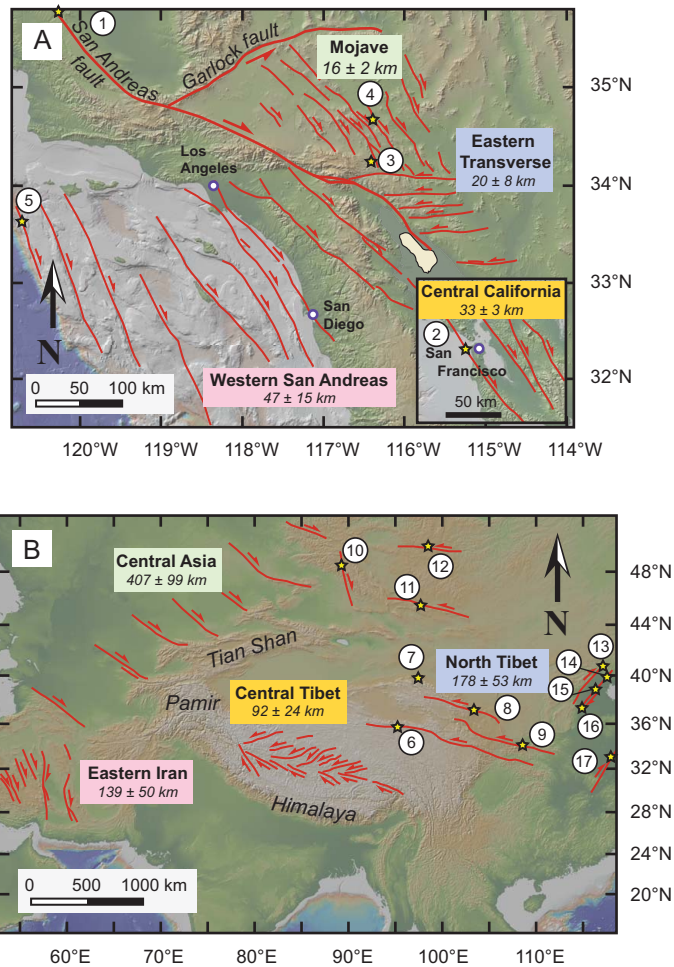


**Figure 1.4.** Evenly-spaced strike-slip domains in (a) California and (b) Asia and their average fault spacing. Inset in a shows parallel faults in central California. Histograms show fault spacing for each domain of strike-slip faulting in (c) California and (d) Asia. Locations (shown as yellow stars) and magnitudes of major intracontinental earthquakes along strike-slip faults in California and Asia: (1) 1857  $M = 7.9$  Fort Tejon earthquake, (2) 1906  $M = 7.8$  San Francisco earthquake, (3) 1992  $M = 7.3$  Landers earthquake, (4) 1999  $M = 7.1$  Hector Mine earthquake, (5) 1927  $M = 7.3$  Lompoc earthquake, (6) 2001  $M = 8.1$  Kunlun Pass earthquake, (7) 1932  $M = 7.6$  Changma earthquake, (8) 1920  $M = 7.8$  Haiyuan earthquake, (9) 1556  $M = 8.0$  Shaanxi earthquake, (10) 1931  $M = 8.0$  Fuyun earthquake, (11) 1957  $M = 8.1$  Gobi Altai earthquake, (12) 1905  $M = 8.4$  Bulnay earthquake, (13) 1679  $M = 8.0$  Sanhe-Pinggu earthquake, (14) 1976  $M = 7.8$  Tanshan earthquake, (16) 1966  $M = 7.2$  Xingtai earthquake, (16) 1830  $M = 7.5$  Cixian earthquake, and (17) 1668  $M = 8.0$  Tancheng earthquake.

## 1.5. References

- Avouac, J.P., and Tapponnier, P., 1993, Kinematic model of active deformation in central Asia: *Geophysical Research Letters*, v. 20, no. 10, p. 895-898.
- Badarch, G., Cunningham, W.D., and Windley, B.F., 2002, A new terrane subdivision for Mongolia: implications for the Phanerozoic crustal growth of Central Asia: *Journal of Asian Earth Sciences*, v. 21, no. 1, p. 87-110.
- Boyden, J.R., Müller, R.D., Gurnis, M., Torsvik, T.H., Clark, J., Turner, M., Ivey-Law, H., Watson, R., and Cannon, J., 2010, Next-generation plate tectonic reconstructions using GPlates, in *Geoinformatics*, eds, R. Keller and C. Baru: Cambridge, U.K., Cambridge University Press, p. 96-113.
- Burchfiel, B.C., Zhang, P., Wang, Y., Zhang, W., Song, F., Deng, Q., Molnar, P., and Royden, L., 1991, Geology of the Haiyuan fault zone, Ningxia-Hui Autonomous Region, China, and its relation to the evolution of the northeastern margin of the Tibetan Plateau: *Tectonics*, v. 10, no. 6, p. 1091-1110.
- Burchfiel, B.C., Zhiliang, C., Yupinc, L., and Royden, L.H., 1995, Tectonics of the Longmen Shan and adjacent regions, central China: *International Geology Review*, v. 37, no. 8, p. 661-735.
- Craddock, W.H., Kirby, E., Zhang, H., Clark, M.K., Champagnac, J.D., and Yuan, D., 2014, Rates and style of Cenozoic deformation around the Gonghe Basin, northeastern Tibetan Plateau: *Geosphere*, v. 10, no. 6, p. 1255-1282.
- Davy, P., and Cobbold, P. R., 1988, Indentation tectonics in nature and experiment. 1. Experiments scaled for gravity: *Bulletin of the Geological Institutions of Uppsala*, v. 14, p. 129-141.
- DeCelles, P.G., Robinson, D.M., and Zandt, G., 2002, Implications of shortening in the Himalayan fold-thrust belt for uplift of the Tibetan Plateau: *Tectonics*, v. 21, no. 6.
- Dickinson, W.R., 1996, Kinematics of transrotational tectonism in the California Transverse Ranges and its contribution to cumulative slip along the San Andreas transform fault system: *Geological Society of America Special Paper*, v. 305, p. 1-46.
- Duvall, A.R., and Clark, M.K., 2010, Dissipation of fast strike-slip faulting within and beyond northeastern Tibet: *Geology*, v. 38, no. 3, p. 223-226.
- England, P., and Houseman, G., 1986, Finite strain calculations of continental deformation: 2. Comparison with the India-Asia collision zone: *Journal of Geophysical Research: Solid Earth*, v. 91, no. B3, p. 3664-3676.
- Fielding, E., Isacks, B., Barazangi, M., and Duncan, C., 1994, How Flat is Tibet?: *Geology*, v. 22, p. 163-167

- Freund, R., 1974, Kinematics of transform and transcurrent faults: *Tectonophysics*, v. 21, no. 1, p. 93-134.
- Gaudemer, Y., Tapponnier, P., Meyer, B., Peltzer, G., Shunmin, G., Zhitai, C., Huagung, D., and Cifuentes, I., 1995, Partitioning of crustal slip between linked, active faults in the eastern Qilian Shan, and evidence for a major seismic gap, the 'Tianzhu gap,' on the western Haiyuan fault, Gansu (China): *Geophysical Journal International*, v. 120, p. 599-645.
- Gehrels, G. et al., 2011, Detrital zircon geochronology of pre-Tertiary strata in the Tibetan-Himalayan orogen: *Tectonics*, v. 30, no. 5.
- Gehrels, G.E., Yin, A., and Wang, X.-F., 2003a, Detrital-zircon geochronology of the northeastern Tibetan plateau: *Geological Society of America Bulletin*, v. 115, p. 881-896.
- Gehrels, G.E., Yin, A., and Wang, X.-F., 2003b, Magmatic history of the northeastern Tibetan Plateau: *Journal of Geophysical Research*, v. 108, p. 2423.
- Guo, Z.-J., Yin, A., Robinson, A., and Jia, C.-Z., 2005, Geochronology and geochemistry of deep-drill-core samples from the basement of the central Tarim basin: *Journal of Asian Earth Sciences*, v. 25, p. 45-56.
- Heubeck, C., 2001, Assembly of central Asia during the middle and late Paleozoic, in *Paleozoic and Mesozoic Tectonic Evolution of Central Asia: From Continental Assembly to Intracontinental Deformation*, Hendrix, M.S., and Davis, G.A. (eds): *Geological Society of America Memoir* 194, p. 1-22.
- Hou, Q., Zhao, Z., Zhang, H., Zhang, B., and Chen, Y., 2006, Indian Ocean-MORB-type isotopic signature of Yushigou ophiolite in North Qilian Mountains and its implications: *Science in China Series D*, v. 49, no. 6, p. 561-572.
- Hubbard, J., and Shaw, J.H., 2009, Uplift of the Longmen Shan and Tibetan plateau, and the 2008 Wenchuan (M= 7.9) earthquake: *Nature*, v. 458, no. 7235, p. 194-197.
- Johnson, M.R.W., 2002, Shortening budgets and the role of continental subduction during the India-Asia collision: *Earth-Science Reviews*, v. 59, no. 1, p. 101-123.
- Lachenbruch, A. H., 1961, Depth and spacing of tension cracks: *Journal of Geophysical Research*, v. 66, no. 12, p. 4273-4292.
- Lease, R.O., Burbank, D. W., Zhang, H., Liu, J., and Yuan, D., 2012, Cenozoic shortening budget for the northeastern edge of the Tibetan Plateau: Is lower crustal flow necessary?: *Tectonics*, v. 31, no. 3.
- Li, Z.X. et al., 2008, Assembly, configuration, and break-up history of Rodinia: A synthesis: *Precambrian Research*, v. 160, p. 179-210.

- Lin, J., Zuza, A.V., and Yin, A., 2015, Quantifying the Relationship between Strike-slip Fault Spacing and Brittle Crust Thickness in Continental Settings based on Sandbox Experiments: AGU Fall Meeting Abstracts.
- Martel, S. J., and Pollard, D. D., 1989, Mechanics of slip and fracture along small faults and simple strike-slip fault zones in granitic rock: *Journal of Geophysical Research: Solid Earth*, v. 94, no. B7, p. 9417-9428.
- McQuarrie, N., Ehlers, T. A., Barnes, J. B., and Meade, B., 2008, Temporal variation in climate and tectonic coupling in the central Andes: *Geology*, v. 36, no. 12, p. 999-1002.
- Meade, B.J., 2007, Present-day kinematics at the India-Asia collision zone: *Geology*, v. 35, no. 1, p. 81-84.
- Meyer, B., Tapponnier, P., Bourjot, L., Métivier, F., Gaudemer, Y., Peltzer, G., Shunmin, G., and Zhitai, C., 1998, Crustal thickening in Gansu-Qinghai, lithospheric mantle subduction, and oblique, strike-slip controlled growth of the Tibet Plateau: *Geophysical Journal International*, v. 135, p. 1-47.
- Molnar, P., and Tapponnier, P., 1975, Cenozoic tectonics of Asia: effects of a continental collision: *Science*, v. 189, no. 4201, p. 419-426.
- Molnar, P., 1988, Continental tectonics in the aftermath of plate tectonics: *Nature*, v. 335, no. 6186, p. 131-137.
- Murphy, M.A., Yin, A., Harrison, T. M., Dürr, S. B., Chen, Z., Ryerson, F. J., Kidd, S. F., Wang, X., and Zhou, X., 1997, Did the Indo-Asian collision alone create the Tibetan plateau?: *Geology*, v. 25, p. 719-722.
- Naylor, M. A., Mandl, G. T., and Supesteijn, C. H. K., 1986, Fault geometries in basement induced wrench faulting under different initial stress states: *Journal of Structural Geology*, v. 8, no. 7, p. 737-752.
- Nur, A., Ron, H., and Scotti, O., 1986, Fault mechanics and the kinematics of block rotations: *Geology*, v. 14, no. 9, p. 746-749.
- Pollard, D.D., and Segall, P., 1987, Theoretical displacements and stresses near fractures in rock: with applications to faults, joints, veins, dikes, and solution surfaces: *Fracture mechanics of rock*, v. 277, no. 349, p. 277-349.
- Robinson, D.M., DeCelles, P.G., and Copeland, P., 2006, Tectonic evolution of the Himalayan thrust belt in western Nepal: Implications for channel flow models: *Geological Society of America Bulletin*, v. 118, no. 7-8, p. 865-885.
- Scotese, C.R., and McKerrow, W.S., 1990, Revised world maps and introduction: *Geological Society of London Memoirs*, v. 12, no. 1, p. 1-21.



- Segall, P., and Pollard, D. D., 1983, Nucleation and growth of strike slip faults in granite: *Journal of Geophysical Research: Solid Earth*, v. 88, no. B1, p. 555-568.
- Şengör, A.M.C., and Natal'in, B.A., 1996, Paleotectonics of Asia: fragments of a synthesis, in Yin, A. and Harrison, T.M., eds., *Tectonic Evolution of Asia*: New York, Cambridge Univ. Press, p. 486-640.
- Song, S., Niu, Y., Su, L., and Xia, X., 2013, Tectonics of the North Qilian orogen, NW China: *Gondwana Research*, v. 23, no. 4, p. 1378-1401.
- Song, S., Niu, Y., Su, L., Zhang, C., and Zhang, L., 2014, Continental orogenesis from ocean subduction, continent collision/subduction, to orogen collapse, and orogen recycling: The example of the North Qaidam UHPM belt, NW China: *Earth-Science Reviews*, v. 129, p. 59-84.
- Song, S., and Su, L., 1998, Rheological properties of mantle peridotites at Yushigou in the North Qilian Mountains and their implications for plate dynamics: *Acta Geologica Sinica (English edition)*, v. 72, no. 2, p. 131-141.
- Swanson, M. T., 1988, Pseudotachylyte-bearing strike-slip duplex structures in the Fort Foster Brittle Zone, S. Maine: *Journal of Structural Geology*, v. 10, no. 8, p. 813-828.
- Stampfli, G.M., and Borel, G.D., 2002, A plate tectonic model for the Paleozoic and Mesozoic constrained by dynamic plate boundaries and restored synthetic oceanic isochrones: *Earth and Planetary Science Letters*, v. 196, no. 1, p. 17-33.
- Tapponnier, P., and Molnar, P., 1977, Active faulting and tectonics in China: *Journal of Geophysical Research*, v. 82, no. 20, p. 2905-2930.
- Tapponnier, P., Peltzer, G., Le Dain, A.Y., Armijo, R., and Cobbold, P., 1982, Propagating extrusion tectonics in Asia: New insights from simple experiments with plasticine: *Geology*, v. 10, no. 12, p. 611-616.
- Tapponnier, P., Zhiqin, X., Roger, F., Meyer, B., Arnaud, N., Wittlinger, G., and Jingsui, Y., 2001, Oblique stepwise rise and growth of the Tibet Plateau: *Science*, v. 294, no. 5547, p. 1671-1677.
- Taylor, M., and Yin, A., 2009, Active structures of the Himalayan-Tibetan orogen and their relationships to earthquake distribution, contemporary strain field, and Cenozoic volcanism: *Geosphere*, v. 5, p. 199-214.
- Tchalenko, J. S., 1970, Similarities between shear zones of different magnitudes: *Geological Society of America Bulletin*, v. 81, no. 6, 1625-1640.
- van Hinsbergen, D.J., Kapp, P., Dupont-Nivet, G., Lippert, P.C., DeCelles, P.G., and Torsvik, T.H., 2011, Restoration of Cenozoic deformation in Asia and the size of Greater India: *Tectonics*, v. 30, no. 5.

- Wang, Q., and Liu, X.Y., 1976, The ancient oceanic crust and its tectonic implications, North Qilian Mountains, China: *Scienta Geologica Sinica*, v. 1, p. 42–55 (in Chinese with English abstract).
- Wang, C., Gao, R., Yin, A., Wang, H., Zhang, Y., Guo, T., Li, Q., and Li, Y., 2011, A mid-crustal strain-transfer model for continental deformation: A new perspective from high-resolution deep seismic-reflection profiling across NE Tibet: *Earth and Planetary Science Letters*, v. 306, no. 3, p. 279-288.
- Webb, A.A.G., Yin, A., Harrison, T.M., C  l  rier, J., Gehrels, G.E., Manning, C.E., and Grove, M., 2011, Cenozoic tectonic history of the Himachal Himalaya (northwestern India) and its constraints on the formation mechanism of the Himalayan orogen: *Geosphere*, v. 7, no. 4, p. 1013-1061.
- Webb, A.A.G., 2013, Preliminary balanced palinspastic reconstruction of Cenozoic deformation across the Himachal Himalaya (northwestern India): *Geosphere*, v. 9, no. 3, p. 572-587.
- Weldon, R., and Humphreys, E., 1986, A kinematic model of southern California: *Tectonics*, v. 5., no. 1, p. 33-48.
- Wu, C., Yin, A., Zuza, A.V., Zhang, J., Liu, W., and Ding, L., 2016, Pre-Cenozoic geologic history of the central and northern Tibetan Plateau and the role of Wilson cycles in constructing the Tethyan orogenic system: *Lithosphere*, in press.
- Xiao, X.C., Chen, G.M., and Zhu, Z.Z., 1978, A preliminary study on the tectonics of ancient ophiolites in the Qilian Mountain, Northwest China: *Acta Geologica Sinica*, v. 52, no. 4, p. 281-295.
- Xiao, W., Windley, B.F., Yong, Y., Yan, Z., Yuan, C., Liu, C., and Li, J., 2009c, Early Paleozoic to Devonian multiple-accretionary model for the Qilian Shan, NW China: *Journal of Asian Earth Sciences*, v. 35, p. 323–333.
- Yin, A., 2000, Mode of Cenozoic east-west extension in Tibet suggesting a common origin of rifts in Asia during the Indo-Asian collision: *Journal of Geophysical Research: Solid Earth*, v. 105, no. B9, p. 21745-21759.
- Yin, A., 2010, Cenozoic tectonic evolution of Asia: A preliminary synthesis: *Tectonophysics*, v. 488, no. 1, p. 293-325.
- Yin, A., and Harrison, T.M., 2000, Geologic evolution of the Himalayan-Tibetan orogen: *Annual Review of Earth and Planetary Sciences*, v. 28, no. 1, p. 211-280.
- Yin, A., Manning, C.E., Lovera, O., Menold, C.A., Chen, X., and Gehrels, G.E., 2007b, Early Paleozoic tectonic and thermomechanical evolution of ultrahigh-pressure (UHP) metamorphic rocks in the northern Tibetan Plateau, northwest China: *International Geology Review*, v. 49, p. 681-716.

- Yin, A., and Nie, S., 1996, A Phanerozoic palinspastic reconstruction of China and its neighboring regions, in Yin, A. and Harrison, T.M., eds., *Tectonic Evolution of Asia*: New York, Cambridge University Press, p. 442-485.
- Yin, A., and Taylor, M.H., 2011, Mechanics of V-shaped conjugate strike-slip faults and the corresponding continuum mode of continental deformation: *Geological Society of America Bulletin*, v. 123, no. 9-10, p. 1798-1821.
- Yin, A., and Zuza, A.V., 2015, Spacing of the Tiger-stripe Fractures on Saturn's Moon Enceladus: A Mechanical Model and its Implications for the Ice-shell Thickness of the South Polar Terrain: JPL-UCLA Planetary Science Workshop, Los Angeles, CA, May 2015.
- Yin, A., Zuza, A.V., and Pappalardo, R. T., 2016, Mechanics of evenly spaced strike-slip faults and its implications for the formation of tiger-stripe fractures on Saturn's moon Enceladus: *Icarus*, v. 266, p. 204-216.
- Yin, A., Zuza, A.V., and Pappalardo, R., 2015, The Stress Shadowing Effect of the Tiger-stripe Fractures on Saturn's Moon Enceladus: AGU Fall Meeting Abstracts.
- Zhu, B., Kidd, W.S., Rowley, D.B., Currie, B.S., and Shafique, N., 2005, Age of initiation of the India-Asia collision in the east-central Himalaya: *The Journal of Geology*, v. 113, no. 3, p. 265-285.
- Zonenshain, L.P., Kuzmin, M.I., Natapov, L.M., and Page, B.M., 1990, *Geology of the USSR: a plate-tectonic synthesis*: Washington, D.C., American Geophysical Union Geodynamics Series 21, 242 p.
- Zuza, A.V., and Yin, A., 2013, Testing the TWINS hypothesis: Were Greater North China and Western Laurentia linked in the Archean and Proterozoic?: *GSA Annual Meeting*, v. 45, no. 7, p. 463.
- Zuza, A.V., and Yin, A., 2014, Initial and boundary conditions for the evolution of the Central Asian orogenic system (CAOS): The Balkatach hypothesis: *Geological Society of America Abstracts with Programs*, v. 46, no. 6, p. 789.
- Zuza, A.V., Yin, A., Lin, J., 2015, The stress shadow effect: a mechanical analysis of the evenly-spaced parallel strike-slip faults in the San Andreas fault system: AGU Fall Meeting Abstracts.
- Zuza, A.V., and Yin, A., 2016, Continental deformation accommodated by non-rigid passive bookshelf faulting: An example from the Cenozoic tectonic development of northern Tibet: *Tectonophysics*, v. 677-678, p. 227-240.
- Zuza, A.V., Cheng, X., and Yin, A., 2016a, Testing models of Tibetan Plateau formation with Cenozoic shortening estimates across the Qilian Shan-Nan Shan thrust belt: *Geosphere*, v. 12, no. 2., p. 501-532.

Zuza, A.V., Yin, A., Lin, J., and Sun, M., 2016b, Spacing and strength of active continental strike-slip faults: EPSL, in revision.

**-Chapter 2-**

**Testing models of Tibetan Plateau formation with Cenozoic shortening estimates across the Qilian Shan-Nan Shan thrust belt**

## 2.1. Abstract

Competing models that account for the construction of the Tibetan Plateau include continental subduction, underthrusting, distributed shortening, channel flow, and older crustal-structure inheritance. Well-constrained estimates of crustal shortening strain serve as a diagnostic test of these plateau formation models and are critical to elucidate the dominant mechanism of plateau development. In this chapter I estimate the magnitude of Cenozoic shortening across the central Qilian Shan-Nan Shan thrust belt, along the northeastern plateau margin, based on detailed geologic mapping, high-resolution seismic reflection profile analysis, and balanced cross section construction and restoration. By integrating surface and subsurface geology with the regional tectonic history, I show that the North Qilian Shan thrust system and adjacent Hexi Corridor have accumulated >53% Cenozoic strain (>50 km shortening), whereas the interior of the Qilian Shan-Nan Shan has accommodated >34% Cenozoic strain (>53 km shortening). Based on this observed strain distribution across northern Tibet, with higher strain along the northern frontal thrust zones and lower strain within the thrust belt interior, I suggest that a combination of distributed crustal shortening and minor (<250 km) southward underthrusting of the Asian lithosphere is responsible for the development of the northern Tibetan Plateau. Overall, the Qilian Shan-Nan Shan, North Qaidam, and Qaidam Basin thrust systems have absorbed a minimum of 250-350 km north-south Cenozoic shortening, which is approximately double the commonly cited value of ~150 km. Focused shortening along the North Qilian Shan frontal thrust system accommodates much of the present-day convergence between Tibet and North China, which suggests that the northern plateau margin may have developed in a similar manner to that of southern Tibet across the Himalayan thrust belt. These similar deformational styles persist

despite vastly different erosion- and denudation-rate boundary conditions, and thus Himalayan-style orogeny may operate independent of climate.

## **2.2. Introduction**

Understanding how the Tibetan Plateau (Fig. 2.1) was constructed greatly affects our knowledge of continental tectonics (Molnar, 1988; Yin, 2010). End-member models for plateau formation and evolution include (Table 2.1) (1) Cenozoic distributed shortening of the Asian crust (Dewey and Bird, 1970; Dewey and Burke, 1973) or its entire lithosphere (England and Houseman, 1986), (2) Cenozoic underthrusting of Indian (Argand, 1924; Powell and Conaghan, 1973; Powell, 1986; DeCelles et al., 2002; van Hinsbergen et al., 2011, 2012) and/or Asian lithosphere (Willett and Beaumont, 1994; Kind et al., 2002; Zhao et al., 2011; Feng et al., 2014; Ye et al., 2015) beneath the Tibetan Plateau, (3) Cenozoic vertical inflation of Tibetan crust by lateral channel flow in the middle or lower crust (Zhao and Morgan, 1987; Bird, 1991; Royden et al., 1997, 2008; Clark and Royden, 2000), (4) discrete Cenozoic intracontinental subduction coupled with lateral extrusion along major strike-slip faults (Tapponnier et al., 2001), and (5) pre-Cenozoic crustal thickening (e.g., Worley and Wilson, 1996; Murphy et al., 1997; Wallis et al., 2003). These models make specific predictions regarding the spatial distribution, magnitude, and temporal variation of Cenozoic strain (Table 2.1; Fig. 2.2).

Estimates of shortening magnitude provide a quantitative and diagnostic test for differentiating between these tectonic models, especially along the plateau margins where the effects predicted by intracontinental subduction, underthrusting, and crustal inflation models are most pronounced (e.g., Clark and Royden, 2000; DeCelles et al., 2002; Hubbard and Shaw, 2009; Lease et al., 2012). For example, the predictions of the lower crustal flow model of Clark

and Royden (2000) were initially supported by early observations of minimal east-west horizontal crustal shortening across the Longmen Shan along the eastern margin of the plateau (Fig. 2.1B) (Burchfiel et al., 1995; King et al., 1997). More recent seismic reflection analysis and balanced cross-section restoration indicate that crustal shortening alone is significant enough to generate the elevation and crustal thickness of the eastern Tibetan Plateau (Hubbard and Shaw, 2009). In the Laji Shan-West Qinling of northeastern Tibet (Fig. 2.1B), the present-day crustal thickness (45-55 km) (Yue et al., 2012) can be reconciled with crustal shortening strain of 10-12% and pure shear crustal thickening (Lease et al., 2012).

Although investigations of Cenozoic shortening along the southern and eastern margins of the plateau have been robust (e.g., Burchfiel et al., 1995; Johnson, 2002; DeCelles et al., 2002; Robinson et al., 2006; McQuarrie et al., 2008; Hubbard and Shaw, 2009; Webb et al., 2011; Webb, 2013), our understanding of Cenozoic deformation along the northern plateau margin is lacking. This margin is defined by the 350-km-wide and 1300-km-long Qilian Shan-Nan Shan thrust belt (Molnar and Tapponnier, 1975; Gaudemer et al., 1995; Meyer et al., 1998; Yin and Harrison, 2000; Taylor and Yin, 2009), which occupies about one-fifth of the Himalayan-Tibetan orogen, and is one of the widest active thrust belts in the India-Asia collisional zone (Fig. 2.1) (Yin, 2010). The absence of detailed structural observations, including systematic geologic mapping and subsurface seismic data, inhibits our understanding of plateau growth mechanisms. The present-day development of the Qilian Shan may provide insight into how the interior of the plateau evolved prior to planation processes (Liu-Zeng et al., 2008), and thus this region may represent a snapshot of early and ongoing plateau development. The timing and magnitude of deformation in this region, which is located more than 1500 km north of the India-Asia



collisional front (Fig. 2.1), has implications for strain transfer and partitioning across the Tibetan-Asian lithosphere (e.g., Wang et al., 2011; Yuan et al., 2013).

In this chapter, I present detailed geologic mapping, balanced cross section construction and restoration, and high-resolution seismic-reflection-profile analysis across the central Qilian Shan-Nan Shan thrust belt and adjacent Hexi Corridor to the north (Fig. 2.3) to constrain the magnitude of shortening along the Tibetan Plateau's northern margin. Some of these constraints come from detailed geologic mapping (~1:50,000) and structural geology study conducted in the central Qilian Shan, near the Shule, Tuo Lai, and Heihe River Valleys (~38.5°N, ~98.5°E) in the Qinghai and Gansu Provinces of western China (Fig. 2.3). In addition, I have interpreted three seismic reflection profiles across the North Qilian Shan frontal thrust system (Fig. 2.1). The seismic profiles also image the Hexi Corridor foreland basin, which is rich in petroleum resources (e.g., Wang and Coward, 1993; Chen and Yang, 2010; He and Pang, 2013) and has been surveyed extensively by seismic reflection profiling (e.g., J. Wu et al., 2006; Yang et al., 2007a, 2007b). Strain estimates are derived by constructing and restoring balanced cross sections that adhere to the known surface geology, subsurface data, and regional tectonic history.

I integrate these shortening strain estimates with other published shortening estimates across northern Tibet (Figs 2.4 and 2.5; Table 2.2) to evaluate plateau construction mechanisms. Specifically, balanced cross sections from the interior of the Qilian Shan-Nan Shan thrust belt, based solely on field mapping, indicate that the region has absorbed a minimum of ~30-40% shortening strain, whereas seismic reflection profiling indicates that the North Qilian Shan frontal thrust system has absorbed a minimum of 53% shortening strain. Shortening magnitude estimates from the northern frontal thrust system are comparable to the results of a seismic reflection study ~450 km to the east (Gao et al., 2013). Other shortening studies from within the

Qilian Shan-Nan Shan thrust belt, mostly based on surface geologic mapping alone, yield much lower strain values (~5-30% strain) (e.g., Gaudemer et al., 1995; Meyer et al., 1998; Lease et al., 2012; Craddock et al., 2014) (Figs. 2.4 and 2.5).

These discrepancies may be due to a combination of factors. First, they may highlight the limitations of some regional structural studies, including the tendency for the actual shortening to be underestimated by surface-based studies that miss hidden structures (e.g., detachments, blind faults, and duplexes). Second, there may be a real difference in strain magnitude between the plateau margin and within the northern plateau interior, suggesting mixed plateau formation processes. By integrating my estimates with existing studies, I propose that the following mechanisms are operating in northern Tibet: (1) southward underthrusting of Asian mantle lithosphere by 200-250 km results in high strain (>53%) along the North Qilian Shan thrust system, and (2) 250-350 km of distributed crustal shortening throughout the Qaidam Basin, North Qaidam, and Qilian Shan-Nan Shan thrust belts (>30-45% strain) (Fig. 2.1) leads to pure-shear crustal thickening.

### **2.3. Regional Geology**

The high elevation (~5 km) of the Tibetan Plateau (Fielding et al., 1994) was created in the Cenozoic, as a result of the India-Asia collision (Yin and Harrison, 2000; Tapponnier et al., 2001; Royden et al., 2008), or in the Mesozoic, as suggested for the southern and possibly eastern portions of Tibet (e.g., Worley and Wilson, 1996; Murphy et al., 1997). The average elevation of the northeastern plateau is slightly lower (~4.5 km) and this high topography drops off rapidly to <1.5 km to the northeast in the Hexi Corridor foreland (Fig. 2.1D). The present-day Qilian Shan-Nan Shan thrust belt is composed of northwest-trending thrust-bounded ranges and

intermontane basins spaced at 30-40 km (Fig. 2.1B). Crustal thickness estimates across this area range from 55 to 65 km (Fig. 2.1C) as constrained by receiver function (Yue et al., 2012; Ye et al., 2015), seismic refraction (Zhao et al., 2001), and seismic reflection (Gao et al., 2013) studies. The Ordos Basin, northeast of the Hexi Corridor (Fig. 2.1B), has far fewer earthquakes than the adjacent plateau and thus is considered a relatively stable block with an average crustal thickness of ~42 km (Chen et al., 2005; Liu et al., 2006; Pan and Niu, 2011).

The Cenozoic Qilian Shan-Nan Shan thrust belt defines the northeastern margin of the Tibetan Plateau, more than 1500 km to the north of the Himalayan collision front, between the North China craton to the north and Qaidam Basin to the south (Fig. 2.1). The thrust belt is constructed in a region that has a complex pre-Cenozoic tectonic history involving multiple phases of Proterozoic basement deformation, early Paleozoic orogeny, and Jurassic-Cretaceous extension (e.g., Vincent and Allen, 1999; Gehrels et al., 2003a, 2003b; Yin and Harrison, 2000; Yin et al., 2007b).

### **2.3.1. The early Paleozoic Qilian orogen and related basement rocks**

The Qilian orogen records the early Paleozoic closure of the Qilian Ocean as the Kunlun-Qaidam microcontinent collided against the southern margin of the North China craton (Yin and Nie, 1996; Şengör and Natal'in, 1996; Sobel and Arnaud, 1999; Yin and Harrison, 2000; Gehrels et al., 2003a, 2003b; Yin et al., 2007b; Xiao et al., 2009; Song et al., 2013). The Qilian orogen is composed of Silurian flysch sequences, Ordovician-Silurian plutonic bodies and arc-type assemblages, ophiolitic mélangé, and low- to high-grade metamorphic rocks.

The distribution of ophiolitic material indicates that a Cambrian-Ordovician Qilian Ocean separated Qaidam and North China (Smith, 2006; Xiang et al., 2007; Tseng et al., 2007; Zhang et

al., 2007; Xia and Song, 2010; Song et al., 2013). The convergence of these continents was facilitated by middle Cambrian-Ordovician subduction and related arc magmatism (Qian et al., 1998; Cowgill et al., 2003; Gehrels et al., 2003a; Su et al., 2004; C. Wu et al., 2004, 2006, 2010; Hu et al., 2005; Y.J. Liu et al., 2006; Quan et al., 2006; He et al., 2007; Tseng et al., 2009; Dang, 2011; Xia et al., 2012; Xiong et al., 2012; Song et al., 2013); intracontinental deformation and ocean closure occurred in Late Ordovician-Silurian time (Song et al., 2006; Y.J. Liu et al., 2006; Zhang et al., 2007; Lin et al., 2010). The orogen is an important preexisting weakness that may have controlled Cenozoic structures in northern Tibet: the Qilian Shan-Nan Shan thrust belt and Haiyuan left-slip fault closely follow the surface trace of the early Paleozoic orogen and suture (Fig. 2.1B) (Taylor and Yin, 2009).

### **2.3.2. Jurassic and Cretaceous extensional setting**

The Mesozoic closure of the Paleo-Tethys and Meso-Tethys Oceans (Pullen et al., 2008; Zhang et al., 2014) and associated with slab rollback to the south may have led to regional extension that affected much of the continent to the north, including the Altyn Tagh range, Qaidam Basin, Qilian Shan-Nan Shan, and Hexi Corridor, from southwest to northeast, respectively (Fig. 2.1) (Huo and Tan, 1995; Vincent and Allen, 1999; Chen et al., 2003; Yin et al., 2008a, 2008b). This extension is expressed by the development of extensive Jurassic and Cretaceous extensional and transtensional basins in the Altyn Tagh range, Qaidam Basin, the Hexi Corridor, and North China (Vincent and Allen, 1999; Chen et al., 2003; Yin et al., 2008a, 2008b). Although no confirmed extensional faults have been documented at the surface in the Qilian Shan, Jurassic and Cretaceous strata are widespread and record a transition from marginal marine and lacustrine to mostly terrestrial sedimentation. Jurassic strata consist of sandstone

interbedded with siltstone, carbon-rich shale, and coal (Gansu Geological Bureau, 1989; Qinghai BGMR, 1991). Upper Jurassic beds are often lacustrine. Cretaceous terrestrial redbed strata fine upward from coarse sandstone to lacustrine deposits that are prominently exposed along many basins in northern Tibet, from the Xining Basin in the south to the Hexi Corridor in the north (Fig. 2.1B) (Horton et al., 2004; Pan et al., 2004).

### **2.3.3. Cenozoic structures**

Cenozoic shortening in northern Tibet is accommodated in the northwest-trending Qilian Shan-Nan Shan, North Qaidam, and Qimen Tagh thrust belts (Jolivet et al., 2003; Yin et al., 2007a, 2008a, 2008b), from north to south, respectively (Fig. 2.1B). These major thrust belts link with the active >1000-km-long east-striking Haiyuan, Qinling, and Kunlun left-slip faults (Fig. 2.1B) (e.g., Taylor and Yin, 2009). The Haiyuan fault and Qilian Shan-Nan Shan thrust belt define the northeastern margin of the Tibetan Plateau, and the Hexi Corridor foreland basin bounds the plateau to the northeast (Fig. 2.1B). Thrusting initiated locally at 50-45 Ma in the southern Qilian Shan-Nan Shan and North Qaidam thrust belts, and deformation migrated southward to the Qimen Tagh and northward to the North Qilian Shan thrust belts by 25-20 Ma (Mock et al., 1999; Jolivet et al., 2001; Dupont-Nivet et al., 2004; Horton et al., 2004; Yin et al., 2008a, 2008b; Clark et al., 2010; Duvall et al., 2011). The region underwent a major pulse of deformation marked by the development of left-slip fault systems by 20-15 Ma (Jolivet et al., 2001; Craddock et al., 2011; Duvall et al., 2013; Yuan et al., 2013). Along the outer plateau margins, thrust initiation occurred at 10-8 Ma (Zheng et al., 2006, 2010; Godard et al., 2009).

Inversion of the global positioning system (GPS) velocity field across the region yields a N30°E contractional strain field (Zhang et al., 2004; Allmendinger et al., 2007). GPS velocity

differencing between North China and Qaidam Basin suggests overall north-south convergence rates of  $\sim 5.5 \text{ mm yr}^{-1}$  across the Qilian Shan-Nan Shan thrust belt (Zhang et al., 2004). Fault slip and shortening rates across the Qilian Shan-Nan Shan thrust belt range from  $<1$  to  $5 \text{ mm yr}^{-1}$  (Hetzel et al., 2004; W.J. Zheng et al., 2009, 2013; D. Zheng et al., 2010; Champagnac et al., 2010; Yuan et al., 2011; Craddock et al., 2014). The variability and uncertainty of these rates arise because the magnitude of Cenozoic fault offset and total shortening remains poorly constrained throughout most of the Qilian Shan. A detailed description of existing Cenozoic crustal shortening estimates is discussed below.

#### **2.4. Testing plateau formation models with shortening estimates**

A combination of mechanisms (Table 2.1) probably operates to generate the modern Tibetan Plateau (e.g., Molnar et al., 1993; Yuan et al., 2013). Geophysical studies of the lithosphere are valuable to understand geologic processes operating in the subsurface, but indirect observations and nonunique interpretations of detailed structures limit the extent to which hypotheses can be satisfactorily tested (e.g., Ammon et al., 1990; Brown et al., 1996; Makovsky and Klempner, 1999; Vergne et al., 2002, 2003; Frederiksen et al., 2003; Sherrington et al., 2004). An alternative quantitative approach for distinguishing among plateau construction models is to evaluate the spatial and temporal variations in the magnitude and style of Cenozoic crustal shortening strain via balanced cross-section construction and restoration (Dahlstrom, 1969). Although strain estimates from balanced cross-section restoration can be associated with large uncertainties and the solutions are often nonunique (e.g., Yin, 2006; Yin et al., 2010a; Judge and Allmendinger, 2011), our understanding of thrust systems (Boyer and Elliott, 1982) allows for well-constrained minimum strain estimates that are based on direct field observations

(e.g., bedding truncations, fault cutoffs, unit juxtapositions, and fault geometry requirements). These strain estimates place constraints on the vertical thickening and possible outward growth of the plateau.

#### **2.4.1. Models and implications for shortening along the plateau's northeastern margin**

Below I briefly summarize the proposed tectonic models for the construction of the Tibetan Plateau (Table 2.1), including their predictions for the distribution, magnitude, and timing of Cenozoic crustal strain across the Qilian Shan-Nan Shan thrust belt. The distributed shortening model (Fig. 2.2B) predicts vertically uniform shortening and pure shear thickening of the Asian crust (Dewey and Bird, 1970; Dewey and Burke, 1973) or its entire lithosphere (England and Houseman, 1986). Following the onset of India-Eurasian collision in the south (Zhu et al., 2005; van Hinsbergen et al., 2011), deformation and crustal thickening propagates northward, either steadily throughout the Cenozoic (England and Houseman, 1986) or rapidly with deformation occurring in the north soon after collision (i.e., within millions of years) (e.g., Horton et al., 2002; Yin et al., 2008a, 2008b; Wang et al., 2008; Dayem et al., 2009; Rohrman et al., 2012). These models predict ~30-40% shortening strain throughout Tibet to explain the present-day crustal thickness.

Meyer et al. (1998) and Tapponnier et al. (2001) suggested that deformation propagates northward across the plateau in discrete steps. Preexisting Paleozoic and Mesozoic sutures (Fig. 2.1B) focus deformation in zones of intracontinental subduction that are associated with post-India-Asia collision volcanic belts that also young to the northeast. Furthermore, oblique convergence causes deformation to occur in a mixed mode of thrust and left-slip faulting (Fig. 2.2C). This concept is supported by the observation that active strike-slip faults follow the trace

of Phanerozoic sutures (Fig. 2.1B) (Taylor and Yin, 2009). Deformation predictions of the intracontinental subduction model include (1) northward-propagating deformation starting in the south in the early Cenozoic and reaching the northeastern margin of the plateau by Pliocene-Quaternary time, (2) focused deformation along Phanerozoic suture zones, and (3) coupled left-slip and oblique thrust faulting (Fig. 2.2C).

Receiver function analyses suggest that the Asian mantle lithosphere is underthrusting northern Tibet (Fig. 2.2D). Large-scale underthrusting models (Kind et al., 2002; Zhao et al., 2011) require as much as ~1400 km of crustal shortening (~80% strain) across the 350-km-wide Qilian Shan-Nan Shan thrust belt on the northern margin of the plateau to accommodate such motion of the Asian mantle lithosphere (Fig. 2.1A), whereas the smaller scale underthrusting models (Feng et al., 2014; Ye et al., 2015) suggest 300 km of shortening (~46% strain). Both iterations of these models involve a southward propagation of structures from the Hexi Corridor foreland and minimal Cenozoic strain in the Qaidam Basin and Qimen Tagh thrust belts to the south (Fig. 2.1B).

Several groups of models argue that a lateral pressure gradient drives lower crustal channel flow and vertical inflation of the crust (e.g., Zhao and Morgan, 1987; Bird, 1991; Royden et al., 1997, 2008; Clark and Royden, 2000; Clark et al., 2004) (Fig. 2.2E). These models predict the outward flux of low-viscosity material from the southern and central regions of the plateau and a similar outward propagation of surface uplift. Lateral channel flow should be decoupled from the upper crust so that Cenozoic crustal strain on the plateau surface must be minimal (<5%) and the upper crust undergoes only vertical motion (Fig. 2.2E). Although the channel flow model of Clark and Royden (2000) only predicts crustal flow in eastern Tibet and does not specifically refer to the Qilian Shan, the overall channel-flow process (Zhao and



Morgan, 1987; Bird, 1991; Royden et al., 2008) should be considered as a general mechanism for thickening and thinning of the Tibetan crust.

Although most of the present-day topography of the Tibetan Plateau (Fig. 2.1) was likely created in the Cenozoic as a result of the India-Asia collision (Yin and Harrison, 2000; Tapponnier et al., 2001; Royden et al., 2008), several regions inherited their crustal thickness from older collisional events (e.g., Worley and Wilson, 1996; Murphy et al., 1997). Based on the regional tectonic history, pre-Cenozoic crustal thickening in northern Tibet could have occurred either during the early Paleozoic Qilian orogen (e.g., Yin and Harrison, 2000; Gehrels et al., 2003a, 2003b; Xiao et al., 2009; Song et al., 2013) or as a result of far-field uplift during the latest Paleozoic-early Mesozoic collisions between North China and South China or Qiantang and Asia (e.g., Yin and Nie, 1993; Pullen et al., 2008). If either case is correct, topography in the region must have persisted until today (Fig. 2.2F), the majority of deformational structures should be pre-Cenozoic, and erosion must be minimal over a period of hundreds of millions of years.

#### **2.4.2. Existing shortening estimates across the Qilian Shan-Nan Shan thrust belt**

A compilation of existing Cenozoic shortening estimates across northern Tibet (Fig. 2.4) are listed in Table 2.2. Gaudemer et al. (1995) constructed a north-northwest-trending cross section in the eastern Qilian Shan based mainly on interpreted satellite images and existing regional geologic maps (Fig. 2.4 and 2.5A); their cross section (Fig. 2.5A) involves south-dipping thrust faults that sole into a 10°-20° south-dipping detachment surface that merges with the Haiyuan fault at ~25 km depth. Gaudemer et al. (1995) estimated a minimum of 25 km shortening of a section that has a restored length of 100 km (~25% strain) by restoring the

unconformity overlying early Paleozoic and older basement rocks back to subhorizontal (Fig. 2.5A). By using a regionally correlative marker horizon (i.e., the Paleozoic unconformity surface), strain within the pre-Cenozoic strata can be considered. Although the cross section is located near the Haiyuan fault (Fig. 2.4), out-of-plane motion (i.e., parallel to the Haiyuan fault) is unconstrained on the mapped faults.

The shortening estimates presented by Meyer et al. (1998) (Fig. 2.4) are based on two independent methods (Table 2.2). First, they developed several serial north-northeast-trending cross sections across the western Qilian Shan-Nan Shan (Fig. 2.4) using satellite image analysis with minor field checks. The restoration of Cretaceous and Cenozoic marker horizons yields 20-30% shortening strain with an overall minimum of 150 km north-south shortening (>31% strain) across the entire Qilian Shan-Nan Shan thrust belt. Second, Meyer et al. (1998) derived bulk shortening estimates of  $120 \pm 30$  km (Table 2.2) from a regional mass balance of eroded sediments, assuming isostatic compensation and an initial crustal thickness of 47.5 km. Meyer et al. (1998) noted that an unconstrained left-slip component on strike-slip faults (i.e., the Qinling and Haiyuan faults) adds uncertainties to their estimates.

In the North Qilian Shan, near the seismic-reflection profiles interpreted in this study, Zheng et al. (2010) used apatite (U-Th)/He (AHe) data (Fig. 2.4) to show rapid cooling ca. 10 Ma. The preservation of a paleo-partial retention zone (PRZ) in the hanging wall and growth strata in the footwall (Fig. 2.5C) allowed Zheng et al. (2010) to estimate the horizontal shortening magnitude of  $8.2 \pm 1.8$  km (26% strain) (Fig. 2.5C) and an average shortening rate of  $\sim 1$  mm yr<sup>-1</sup>. These estimates are based on the assumption that shortening was accommodated by a single 30° south-dipping planar thrust (Fig. 2.5C) initiated at ca. 10 Ma. Lease et al. (2012) constrained shortening across the West Qinling thrust fault using existing AHe ages (Clark et al.,

2010) to obtain a ca. 110 Ma marker horizon in the footwall and hanging wall. The restoration of this horizon along a single south-dipping fault (average dip of 45°-50°) yields 4.3 km of horizontal shortening of a section that has a restored length of 30.3 km (~14.2% strain). Similarly, AHe ages were used (Lease et al., 2011, 2012) to develop a north-east-trending cross section across the Jishi Shan (Fig. 2.4) and to estimate 14.4 km shortening of a section that has a restored length of 100.6 km (~14.2% strain) (Fig. 2.5B).

A seismic reflection analysis across the eastern Haiyuan fault was conducted by Gao et al. (2013) (Fig. 2.4); they balanced and restored a 26-km-long section of a 180-km-long seismic reflection profile to estimate Cenozoic strain (Fig. 2.5D). The section crosses the Baiyin fault, and despite having no kinematic data to determine if it is a thrust or strike-slip fault, Gao et al. (2013) inferred this fault to be a thrust on the basis of its low-angle geometry in cross-section view and an oblique relationship with the left-slip Haiyuan fault in map view (Fig. 2.1B). Line-length balancing of their cross-section model yielded a minimum of 22.3 km of shortening across a 25.7-km-long deformed-state section (~46% strain) (Fig. 2.5D).

Craddock et al. (2014) presented 10 line-length balanced north-south cross sections across the Qinghai and Gonghe Nan Shan, south of Qinghai Lake (Fig. 2.4), that are restored by bringing Neogene strata to horizontal (Fig. 2.5E). They suggested  $1.5 \pm 0.7$  km shortening across the Qinghai Nan Shan. Shortening estimates in the Gonghe Nan Shan to the south are higher, ranging from 5.1 to 6.9 km ( $6.0 \pm 0.9$  km). These estimates were coupled with low-temperature thermochronologic and stratigraphic data (Craddock et al., 2011; Zhang et al., 2012) to suggest relatively low north-south shortening rates of  $\sim 0.2$  mm yr<sup>-1</sup> and  $\sim 0.7$  mm yr<sup>-1</sup> across the Qinghai and Gonghe Nan Shan, respectively.

The diversity in strain and strain rate estimates across the northeastern margin of the plateau (Figs. 2.4 and 2.5) may be attributed to both real variations in plateau-construction and deformational processes and/or limitations of the balanced cross section restoration method. Due to the remoteness of northern Tibet, many estimates are based primarily on satellite image analysis and reconnaissance-scale surface mapping, which can miss important structures such as blind or hidden faults, detachments, and duplexes. In addition, many studies only consider slip estimates on faults that cut Cenozoic strata and rarely consider deformation of pre-Cretaceous rocks. Especially in the Qilian Shan-Nan Shan thrust belt, where deformation is often thick-skinned and duplicates successions of the early Paleozoic Qilian arc and orogen (e.g., Yin et al., 2007b), much of the Cenozoic strain is recorded as deformation that affects early Paleozoic and older metamorphic rocks. To overcome these issues, an integrated knowledge of subsurface geology and the regional geologic history is required to develop the most reasonable, testable, and restorable geologic cross-section models.

#### **2.4.3. Shortening across Qaidam Basin and the North Qaidam thrust belt**

The Qaidam Basin and the North Qaidam thrust belts are to the south of the Qilian Shan (Fig. 2.1B) (Yin et al., 2008a). Balanced cross sections developed primarily from geologic mapping in the North Qaidam thrust belt indicate heterogeneous northeast-southwest crustal shortening that varies from >20% to 60% (Yin et al., 2008a) (Fig. 2.4; Table 2.2). In another study, Yin et al. (2008b) used seismic reflection data to develop a series of northeast-trending balanced cross sections across Qaidam Basin that reveal an eastward-decreasing strain gradient, ranging from ~35% strain in the west to >11% in the east (Fig. 2.4; Table 2.2). Both of these

studies suggest that Cenozoic crustal shortening is the primary mechanism for developing the topography and crustal thickness of Qaidam Basin and the North Qaidam thrust belt.

## **2.5. Geologic mapping of the central Qilian Shan**

Geologic mapping was conducted in the central Qilian Shan, near the town of Yanglong (~38.5°N, ~98.5°E) (Figs. 2.1 and 2.3). Mapping was focused along the Shule, Tuo Lai, and Heihe Rivers, which drain the Tibetan Plateau to the northwest. The river valleys, at elevations of ~3500 m, are bounded by northwest-trending ranges with moderate relief (~0.5 to 1.0 km); peak elevations reach >5.5 km. The southernmost range, just north of the Hara Lake, is named the Shule Nan Shan. The ranges to the north have an average range spacing of 30-50 km, and are known as the Tuo Lai Nan Shan, Tuo Lai Shan, North Qilian Shan (e.g., Zheng et al., 2010), and Yumu Shan (e.g., Tapponnier et al., 1990), from south to north respectively (Fig. 2.3).

A detailed lithostratigraphy is presented in Figure 2.6 and the geologic maps of the Shule Nan Shan, Tuo Lai Nan Shan, and Tuo Lai Shan are shown in Figures 2.7 and 2.8. Page-size limitations require the geologic maps to be presented in a dissected format (Figs. 2.7 and 2.7), but full-size maps are attached as a supplementary file (Supplementary Files 1 and 2).

### **2.5.1. Map units**

The lithostratigraphic units mapped in the central Qilian Shan are shown in Figure 2.6. Stratigraphic age assignments of the major lithologic units are primarily from Pan et al. (2004), and the more detailed framework used in this study is based on Gansu Geological Bureau (1989), Qinghai BGMR (1991), a detailed stratigraphic review by Zhiyi and Dean (1996), unpublished detrital zircon data (Y. Zhang, W. Chen, A. Yin, and A. Zuza unpublished data), and my own

observations. Map units range in age from Mesoproterozoic to Quaternary, and are described below.

#### *2.5.1.1. Sedimentary units*

The oldest sedimentary strata exposed in the central Qilian Shan consist of massive-bedded limestone and dolostone interbedded with low-grade metamorphosed basalt and volcanoclastic layers. The carbonate rocks have a distinct massive blue/grey or orange appearance. The stratigraphic thickness of this unit possibly exceeds 3-7 km but is poorly constrained because its basal contact with the underlying metamorphosed basement is not observed and internal deformation has affected the original stratigraphy. The regional geologic map of Pan et al. (2004) give this unit a Changchengian age (i.e., Paleo- or Mesoproterozoic) on the basis of an older regional geologic survey (Gansu Bureau of Geology, 1974). However, I reassign a Neoproterozoic age (labelled Z) based on recent geochronology studies on the widespread basalt that is interbedded with carbonate strata (Mao et al., 1998; Xia et al., 1999), including new 600-580 Ma ages for these basalts (Xu et al., 2015). Compared to the higher-grade Mesoproterozoic gneiss, marble, and schist unit (discussed in section 2.5.1.2), the relatively low-grade deformation observed in these rocks corroborates a Neoproterozoic age.

Ordovician rocks consist of low-grade metamorphosed sandstone, siltstone, and limestone with minor volcanic and volcanoclastic rocks. A distinctive blue-gray limestone unit (labelled O<sub>lm</sub>) appears to conformably overlie the Ordovician volcano-siliciclastic strata (labelled O). The lowest part of this unit is intruded by granitoid and intermediate to mafic dikes. All Ordovician rocks are strongly deformed and the original sedimentary relationships are obscured. Zhiyi and Dean (1996) state that siltstone, volcanic, and volcanoclastic rocks overlie thick

limestone deposits ( $O_{lm}$ ). This relationship is not directly observed in this mapping area, but it may be obscured by later deformation. Ordovician rocks may represent a complex mélange of forearc, accretionary wedge, and foreland-basin strata (Xiao et al., 2009; Zhiyi and Dean, 1996).

Silurian strata (labelled S) are absent from the mapping area, but found elsewhere in the Qilian Shan. The rocks unconformably overlie Ordovician strata, and are often isoclinally folded and bedding is transposed. The strata consist of minor conglomerate layers interbedded with siltstone, shale, and sandstone (Yang et al., 2009; Yan et al., 2010). Conglomerate clasts and the sedimentary rocks are dominated by volcanic and granitic gneiss clasts and lithic grains respectively. Most of the observed sections appear to be turbidite successions with interfingering conglomerate beds (Yan et al., 2010). Silurian rocks are generally considered to represent a flysch basin that transitions into molasse deposits (Du et al., 2003).

Devonian strata (labelled D) are mostly absent from the central Qilian Shan, but where outcrops exist to the north and south, they unconformably overlie deformed Proterozoic-early Paleozoic rocks. They consist of terrestrial conglomerate, sandstone, mudstone, and minor volcanic rocks, and deposits do not exceed 300 m in thickness (Qinghai BGMR, 1991). These deposits are interpreted to represent molasse that was deposited in intermontane and/or foreland basins during the Qilian orogen (Xia et al., 2003; Yan et al., 2007), which implies that continental collision and deformation was occurring by this time. This unit is disconformably overlain by younger units.

Carboniferous strata (labelled C) overlie Ordovician-Devonian rocks and other non-sedimentary units as part of a regionally extensive angular unconformity. A basal coarse-grained quartz arenite, displaying prominent crossbedding, is overlain by quartz sandstone and interbedded siltstone, with minor carbon-rich shale and coal. The unit experienced strong internal

but localized deformation along the shaley coal layers. Carboniferous rocks are 400-500 m thick. Permian strata are mapped as a single unit (labelled P) that has a thickness of ~1 km. The lower section consists of distinctive pink-red and white-gray coarse sandstone and interbedded siltstone. The upper section is made up of arkosic and quartz sandstone interbedded with siltstone and shale, and sandy limestone.

Conformably overlying these rocks are Triassic strata, which are thick (> 4km) and are divided into the lower ( $\overline{T}_1$ ), middle ( $\overline{T}_2$ ), and upper ( $\overline{T}_3$ ) units. Lower Triassic ( $\overline{T}_1$ ) rocks have a basal unit of massive cross-bedded grey sandstone overlain by arkosic and quartz sandstone, sandy limestone, siltstone, and calcareous siltstone. The middle Triassic ( $\overline{T}_2$ ) strata are dominated by basal sandy conglomerate and cross-bedded arkosic and quartz sandstone with minor with siltstone. Upper Triassic rocks ( $\overline{T}_3$ ) consist of a basal conglomerate with overlying arkosic sandstone interbedded with calcareous siltstone, darker organic-rich shale, and distinctive coal layers.

The overlying Jurassic rocks (labelled J) are generally parallel to upper Triassic strata, although a regional disconformity between these two units exists (Yin et al., 2008b). Jurassic strata are 800 m thick and consist of a basal conglomerate overlain by arkosic sandstone interbedded with siltstone, organic-rich shale, and numerous coal beds. This unit is generally restricted to valleys in the central Qilian Shan and is not cliff forming.

Cretaceous rocks (labelled K) consist of polymictic conglomerate and coarse sandstone that is reddish in color. This unit is exposed on both sides of the Tuo Lai Shan and its absolute thickness is not known. Map-view relationships require Cretaceous strata to be >270 m thick. In the Hexi Corridor to the north, Cretaceous rocks are observed to be >3 km thick (Zhiyi and



Dean, 1996). They often exhibit a growth strata geometry and are interpreted to have been deposited in extensional grabens or rift basins (Yin et al., 2008b).

Cenozoic rocks are predominantly Miocene through Pliocene in age (labelled N, for Neogene) (Qinghai BGMR, 1991; Zhiyi and Dean, 1996; Bovet et al., 2009), although the southernmost deposits may be as old as late Oligocene (e.g., Zhuang et al., 2011). They consist of red fluvial and lacustrine sediments. Conglomerate, sandstone, and mudstone have a clay, marl, or limestone matrix. Gypsums is prevalent. Quaternary sediments consist of alluvial, fluvial, and glaciofluvial deposits (Li and Yang, 1998; Zhao et al., 2002). They are differentiated in my mapping as active axial river deposits (labelled Q<sub>ax</sub>), active alluvial deposits (labelled Q<sub>aly</sub>), and inactive alluvial deposits (labelled Q<sub>alo</sub>).

#### *2.5.1.2. Metamorphic and mélangé units*

Metamorphosed basement rocks are widespread in the mapping area, and are divided into three unit groups: gneiss, schist, and foliated granitoid. The paraschist unit (labelled sch) is characterized by mica ± garnet schist, quartzite, foliated garnet amphibolite, marble, and local phyllite and slate. These rocks have been interpreted as a Proterozoic passive margin (Gehrels et al., 2003a, 2003b). Detrital zircon analyses (discussed in Chapter 5) confirm a maximum Mesoproterozoic age. The gneiss unit (labelled gn) is composed of quartzofeldspathic gneiss, mylonitic orthogneiss, and paragneiss. These rocks are inferred to be Proterozoic in age based on previous geologic maps (Qinghai BGMR, 1991; Pan et al., 2004). Foliated granitoid rocks (labelled gr<sub>f</sub>) intrude both the gneiss and schist units. Foliation within the foliated granitoid rocks is parallel to that of the other metamorphic units across their lithologic contacts. All of these

metamorphic rocks are inferred to have Precambrian protolith ages (Qinghai BGMR, 1991; Gehrels et al., 2003a; Pan et al., 2004), and I provide further age constraints in Chapter 5.

An ophiolite complex, referred to locally as the Yushigou ophiolite suite (Shi et al., 2004; Hou et al., 2006; Song et al., 2013), is exposed in the northern portion of the mapping area. This complex variably consists of ophiolitic mélange and fragments of an incipient oceanic arc. The unit has been assigned a Cambrian age based on reported fossils (Xiao et al., 1978) and geochronology studies (Shi et al., 2004; Song et al., 2013; see Chapter 5), and is thus labelled Cambrian as **€** (Fig. 2.6). The unit consists of ultramafic to mafic rocks, pillow basalts, and limestone and quartzite-sandstone knockers with chert. In addition, there are outcrops of massive plagioclase-pyroxene gabbro, which were mapped separately (labelled ga). There is significant deformation within the complex and the lithologic contacts are highly sheared. Taken together, this unit represents part of the Qilian suture zone (Fig. 2.1) (e.g., Wu et al., 2016), which connects along its northwest strike with the Aoyougou ophiolite (Zhang et al., 2001; Xiang et al., 2007) to the northwest and the Dongcaohe ophiolite (Tseng et al., 2007) to the southeast.

### *2.5.1.3. Igneous units*

Numerous early Paleozoic granitoid plutons are exposed throughout the Qilian Shan region. These plutons have been assigned ages ranging from 516 Ma to 345 Ma, and most are attributed to arc and/or orogenic magmatism (Qinghai BGMR, 1991; Qian et al., 1998; Cowgill et al., 2003; Gehrels et al., 2003a; Su et al., 2004; Wu et al., 2004, 2006, 2010; Hu et al., 2005; Liu et al., 2006; Quan et al., 2006; He et al., 2007; Tseng et al., 2009; Dang et al., 2011; Xia et al., 2012; Xiao et al., 2012; Xiong et al., 2012; Song et al., 2013). Several large (10-50 km<sup>2</sup>) and many minor (1-10 km<sup>2</sup>) plutonic bodies are exposed in the mapping area. They range in

composition from alkali feldspar granite to quartz monzonite. These bodies intrude the Proterozoic gneiss and schist complex and the Ordovician strata, but are unconformably overlain by Carboniferous and younger strata. This relationship places a lower-age bound on plutonism, such that the granitoids must be older than Carboniferous. Geochronology presented in Chapter 5 indicates that these plutons crystallized between ~474 and ~445 Ma. One of the plutonic bodies has a previous K-Ar age of  $345 \pm 17$  Ma, as reported by Qinghai BGMR (1991), but new U-Pb zircon ages suggest a crystallization age ~450 Ma for this same granitoid. The units are mapped as undifferentiated granitoid (gr), except where a crystallization age has been determined, either from this study or other work, in which case I assign a specific granitoid age. For example, Or(gr) for Ordovician granitoid. Minor dikes with compositions similar to the granitoids were also mapped.

In the Tuo Lai Shan, gabbroic plutonic rocks, diabase dikes, and basaltic volcanic rocks are found in the Yushiguo ophiolitic complex of the Qilian suture. U-Pb zircon ages from gabbro range from 555 to 516 Ma (Shi et al., 2004; Song et al., 2013). Tholeiitic pillow basalts are also found within this mélangé and whole-rock geochemical data suggests that they are enriched mid-ocean ridge basalts (E-MORB) (Song et al., 2013).

Foliated granitoid bodies (granodiorite to quartz diorite) (labelled gr<sub>f</sub>) intrude the Proterozoic metamorphic rocks. This unit is variably mylonitized with well-defined stretching lineations. Geochronology results presented in Chapter 5 indicates that this foliated granitoid has a crystallization ages that span ~950-900 Ma. This age range provides a lower-age bound for the protolith of the metamorphic complex that it intrudes.

### 2.5.2. Regional unconformities

Four distinct Phanerozoic unconformities are recognized in the mapping area (Figs. 2.7 and 2.8). Herein, they are named for the unit that overlies the unconformity. These unconformities are important because (1) they represent periods of rock uplift (e.g., deformation), erosion and/or other reasons for nondeposition and (2) they can be used to illustrate the pre-unconformity geometries of the older rock units. For example, Carboniferous and Cretaceous unconformities in the Tuo Lai Shan both overlie Ordovician strata. This requires the Ordovician rocks to be at or near the surface in both the Carboniferous and Cretaceous times. Thus, these rocks were at exposed to the surface prior to Cenozoic deformation.

The oldest unconformity, which is also the most widespread, consists of Carboniferous strata (locally Devonian and/or Permian) overlying Proterozoic basement and Qilian arc/orogen rocks (i.e., Ordovician-Silurian rocks) (Figs. 2.7 and 2.8). It is prevalent throughout the Shule Nan Shan, Tuo Lai Nan Shan, and Tuo Lai Shan (Figs. 2.9A and 2.9C), where Carboniferous strata overlie the Pt, Z, and O units. Where this depositional relationships is observed, the local rocks must have been located at or near the surface by Carboniferous time. This unconformity is also a key marker horizon in the balanced cross section restorations presented in Section 2.7.

In one locality along the southern flank of the Tuo Lai Nan Shan, Triassic rocks ( $\overline{\mathbf{R}}_2$ ) unconformably overlie Carboniferous and Proterozoic rocks, including the aforementioned Carboniferous unconformity (Fig. 2.8). Triassic strata are discordant from the underlying Carboniferous strata by  $\sim 10^\circ$  (Fig. 2.8). Just to the south, in the overturned anticline, Permian and Triassic rocks (P- $\overline{\mathbf{R}}_3$ ) make up a conformable and continuous sequence. This suggests that this unconformity surface is at least below Permian strata in the anticline, and it cuts upsection to the north to its location within the Triassic rocks as a buttress unconformity. In this scenario, a

thin veneer of Carboniferous rocks were deposited on top of the basement that had topography following the early Paleozoic Qilian orogen. Deposition was restricted to topographic lows. Permian through lower Triassic rocks were deposited on this relatively flat surface, and there was either a topographic high to the north or the sediment deposition simply pinched out to the north. Middle and upper Triassic rocks were evenly deposited over the underlying strata. Further interpretation of the depositional setting of these rocks is not within the scope of this study.

The last two unconformities—at the base of Cretaceous and Cenozoic rocks—were caused by regionally extensive tectonic events. The Mesozoic unconformity is related to the initiation of widespread extension across northern Tibet (e.g., Vincent and Allen, 1999; Chen et al., 2003). This unconformity primarily consists of Jurassic and/or Cretaceous rocks unconformably overlying Paleozoic and Proterozoic strata, with a variety of angular unconformities. Along the southern flank of the Tuo Lai Shan, Cretaceous rocks are unconformably deposited on top of Ordovician rocks and Carboniferous strata. This observation suggests two things. First, the Ordovician and Carboniferous rocks were both at or near the surface at the time of Cretaceous deposition. In addition, an event is required to tilt the Carboniferous unconformity and Carboniferous-Permian rocks prior to the deposition in the Cretaceous. This unconformity surface is folded in a northwest-trending ~1-km-wavelength syncline (Fig. 2.8). Cretaceous rocks were also deposited unconformably on Proterozoic-Paleozoic rocks, along the northern flank of the same range, and the Heihe River valley makes up a large Cretaceous basin that stretches ~140 km to the southeast to the city of Qilian.

Cenozoic rocks are only exposed in the southern portions of the mapping areas (Figs. 2.7 and 2.8). They were deposited on top of Jurassic and upper Triassic strata, which indicates that prior to Cenozoic deformation, these Mesozoic rocks were closest to the surface. The

development of this unconformity represents the initiation of Cenozoic deformation related to the Himalayan-Tibetan orogen.

### **2.5.3. Structural geology**

Structures generally follow a dominant northwest-southeast structural trend, including the general strike of sedimentary units, strike of foliations within the metamorphic units, trend of the ranges, and surface trace of faults. Deformation can be categorized into three distinct regimes: (1) Cenozoic folds and faults, (2) early Paleozoic folds, faults, and unit juxtapositions, and (3) early Paleozoic ductile shearing and metamorphism. There is no direct evidence of Mesozoic deformation or normal faulting, but the field observations are consistent with work by others that suggests that Jurassic and Cretaceous sedimentation was caused by regional extension (Vincent and Allen, 1999; Chen et al., 2003; Yin et al., 2008b), including fining-upward sequences and growth strata.

I interpret deformation of Carboniferous and younger strata to be Cenozoic in age based on the following observations: (1) most observed faults and folds of Carboniferous and younger rocks merge with present-day range-bounding thrusts, (2) these same faults truncate Cenozoic terrestrial deposits and Quaternary alluvium, (3) shallow-marine, lacustrine, and continental shelf deposition of parallel Carboniferous through Triassic strata was not associated with any deformational structures during these time periods, and (4) Jurassic and Cretaceous strata are extension related (e.g., Vincent and Allen, 1999; Chen et al., 2003; Yin et al., 2008a,b) so contractional structures involving these rocks must be Cenozoic in age. This also implies that folding and duplication of the Carboniferous unconformity occurred in the Cenozoic.

Presented below is a detailed structural analysis of each range, including juxtaposition geometries, map-view relationships, kinematic indicators, and alternative interpretations, starting with the Shule Nan Shan in the south and progressing to the ranges to the north (Fig. 2.3).

#### 2.5.3.1. Shule Nan Shan

The ranges bounding Hara Lake to the northeast and northwest expose Ordovician and Proterozoic basement rocks that are overlain by Carboniferous through Triassic strata (Fig. 2.7; Supplementary Figure 1). The Shule Nan Shan range is bounded to the southwest by NW-striking thrust faults (Fig. 2.7) that place Proterozoic-Paleozoic rocks against Neogene-Quaternary rocks in the Hara Lake Basin. Structures under Hara Lake were inferred by projecting geometric relationships and bedding attitudes observed to the northwest of the lake. For convenience of description, the NW- to W-striking thrust faults are labelled  $f1$  through  $f6$ , from south to north respectively (Fig. 2.7), and are discussed in this order below.

Fault 1. The WNW-striking fault dips  $70^\circ$  to the NE, juxtaposes Triassic rocks ( $\bar{R}_2$ - $\bar{R}_3$ ) against Permian-Triassic strata (P- $\bar{R}_2$ ), and truncates overlying Neogene sediments (Fig. 2.7).

The observed juxtaposition must have accommodated <100s of meters of slip. The fault trace to the east is obscured by Hara Lake.

Fault 2. The WNW-striking fault dips  $60^\circ$  NNE and places Carboniferous rocks (C) against Permian strata (P) (Fig. 2.7). Units beneath Carboniferous rocks are not exposed, which constrains the maximum fault offset on  $f2$  to 100s of meters.

Fault 3. This S-dipping fault has a variable E-ENE strike. In the west, the fault places a ~8-km-wide hanging-wall anticline of Permian strata (P) over a footwall syncline of Permian-Triassic rocks (P- $\bar{R}_1$ ) (Fig. 2.7). Map view relationships suggest that offset increases to

the east, but exposure is obscured by Hara Lake and the surrounding basin. This fault appears to either be truncated by, or merge with, *f4*, although this relationship is not directly observed (Fig. 2.7).

*Fault 4.* The trace of this NE-dipping fault is readily identified in satellite images as a conspicuous fault scarp that cuts across abandoned Quaternary alluvial fans. It is also responsible for uplifting Neogene sediments (Fig. 2.7), and is likely an active structure. The fault merges with *f5* to the east, and is assumed to be south-dipping and merge with both *f5* and *f6* at depth.

*Fault 5.* This NW-striking NE-dipping range-bounding fault of the Shule Nan Shan places Carboniferous rocks over Permian strata and overlying Neogene sediments (Fig. 2.7). The fault merges to the east with the Haiyuan fault (Fig. 2.7) and represents the westernmost termination structure of this major strike-slip fault. Kilometer-scale folds are observed in the hanging wall of this fault, exposing Carboniferous-late Triassic rocks (C- $\bar{\text{T}}_3$ ) (Fig. 2.7). Although no direct fault kinematic measurements were made for this fault, the fold axes are parallel to the fault strike, which may suggest that this fault is primarily a dip-slip structure. Fault offset must be <1 km based on the map view relationships, and the tight (~1 km wavelength) hanging wall folds accommodate a similar magnitude of shortening. This fault is possibly a splay of *f6*, which accommodates larger magnitude offset associated with the growth of the Shule Nan Shan range (Fig. 2.7).

*Fault 6.* This NE-dipping thrust places the Proterozoic schist unit (Pt[sch]) over Permian rocks (P). The gently NE-dipping (15-20°) Carboniferous-Triassic strata are interpreted to parallel the hanging-wall flat of this south-directed thrust fault, and thus parallel the dip of the fault. A minor fault splay *f6a* links with *f6* to the east, and truncates the Ordovician



granitoid unit and overlying Carboniferous strata. *Fault 6a* cuts the granitoid and overlying sedimentary strata, but offset diminishes within the granitoid. The fault trace of *f6a* to the east is covered by Quaternary sediments, but it is assumed that the fault merges to the east with *f6* at depth.

#### 2.5.3.2. Tuo Lai Nan Shan

The Tuo Lai Nan Shan range bounds the Shule River valley to the north (Fig. 2.8; Supplementary Figure 2). Neogene outcrops are exposed along the margins of the valley, unconformably overlying Triassic strata (Fig. 2.8). Proterozoic-Paleozoic rocks are juxtaposed against the Neogene deposits by south-directed Cenozoic thrust faults. Discussion of these faults, which are labelled *f1* through *f4* from south to north respectively (Fig. 2.8), is given below.

*Fault 1.* This WNW-striking N-dipping thrust fault places Triassic rocks over Neogene sediments and other Triassic strata (Fig. 2.8). For convenience of description, the western and eastern traces of these faults are denoted *f1a* and *f1b* respectively. *Fault 1a* places an anticline of Triassic strata ( $\overline{\text{R}}_3$ ), which is likely cored by P- $\overline{\text{R}}_2$  as in the east, over Neogene sediments. A minor (~100 m wavelength) hanging-wall anticline forms in the hanging wall of this steeply dipping thrust fault. In the east, *f1b* branches into several fault splays, which variably place Triassic ( $\overline{\text{R}}_3$ ) rocks over Neogene sediments and other Late Triassic rocks ( $\overline{\text{R}}_3$ ) (Figs. 2.9E-2.9G). Offset on this fault is minor as evidenced by minor map-view offset of the  $\overline{\text{R}}_3$ - $\overline{\text{R}}_2$  contact and the duplication of similar-aged units. This fault is inferred to merge to the east with the range-bounding *f3*. The geometry of *f1b* at depth is constrained by the focal mechanism (thrust dipping 27°N) from a 1993  $M_w$

= 5.9 event that has been relocated by Chu et al. (2009) to have occurred at a depth of ~7 km (Fig. 2.8). In light of this observation, it is clear that *f1b* is an active structure.

*Fault 2.* The WNW-striking faults are anomalous in the mapping area because they involve a northward transport direction. In the west this fault is labelled as *f2a* (Fig. 2.8). It is south-dipping and places a hanging-wall anticline of Triassic strata ( $\overline{\mathbf{R}}_3$ ) over Jurassic rocks. Jurassic strata in the footwall of *f2a* are internally deformed, with numerous 100-m-wavelength folds and faults. *Fault 2a* must be relatively low angle (10-20°S) based on its map trace (Fig. 2.8).

In the east, this fault is labelled as *f2b*. This fault merges to the west and east with *f3*. There is a prominent ~5-km-wide anticline in the hanging wall of *f2b*, just to the south of the *f2b*'s surface trace, which is referred to as the Shule anticline because it is exposed along the northern bank of the Shule River (Fig. 2.8). The anticline is overturned and north-verging; its northern limb is overturned to the south and its southern limb dips to the south (50-60°S) (Fig. 2.8). *Fault 2b* truncates this anticline, and cuts upsection to the northwest through lower Triassic to upper Triassic rocks ( $\overline{\mathbf{R}}_1$ - $\overline{\mathbf{R}}_3$ ). This truncation relationship suggests that *f2b* is a south-dipping thrust, the Shule anticline is the hanging-wall anticline of this thrust, and the *fault 2b* accommodated top-to-the-north motion. However, where this fault is exposed in a north-trending drainage along the northern overturned limb of the Shule anticline, the fault dips to the north (Figs. 2.8 and 2.9D). At this locality, the fault surface dips 60°N, Jurassic strata in the hanging wall are parallel to the fault, and Triassic rocks in the footwall are oblique to the fault surface (Fig. 2.9D). This geometric relationship alone would suggest a hanging wall flat-footwall ramp in a north-dipping normal fault. Alternatively, this fault juxtaposition may be part of an

overturned thrust that was originally S-dipping and placed Triassic rocks over Jurassic strata. Following this interpretation, the Triassic rocks make up a hanging-wall ramp whereas the Jurassic strata are part the footwall flat, and the fault was overturned by south-directed shear. The north-verging Shule anticline and map-view truncation relationships support this second interpretation (Fig. 2.8), and the south-directed  $f3$  may have caused this overturning of  $f2b$ . A field photograph in Figure 2.9B shows the overturned thrust  $f2b$  and south-directed  $f3$ .

Fault 3. This NW-striking fault dips to the north and juxtaposes Triassic ( $\overline{\mathbf{R}}_2$ ) through Proterozoic rocks over Cenozoic-Triassic strata (N- $\overline{\mathbf{R}}_3$ ). The laterally continuous fault crosses the entire mapping region (Fig. 2.8). The hanging wall consists middle Triassic strata ( $\overline{\mathbf{R}}_2$ ) unconformably overlying Proterozoic basement rocks (Pt[sch] and Pt[gn]). There is a thin veneer of Carboniferous rock beneath the Triassic strata, that also unconformably overly the Proterozoic rocks (Fig. 2.8). In the west, this fault juxtaposes Triassic rocks ( $\overline{\mathbf{R}}_2$ ) over Jurassic-Neogene strata (J-N). Here the fault either merges with or truncates  $f2a$  (Fig. 2.8). The eastern portion of this fault cuts both up- and down-section through the Shule anticline, which requires this fault to be out-of-sequence with respect to north-verging  $f2b$ . I infer that these two faults merge above the erosional surface, or  $f3$  crosscuts  $f2b$ , although the duplication of  $f2b$  is not observed in the mapping area.

Fault 4. This N-dipping fault places metamorphic basement rocks over a syncline of Triassic strata ( $\overline{\mathbf{R}}_2$ - $\overline{\mathbf{R}}_3$ ). The surface trace of  $f4$  is readily identifiable along the southern flank of the highest peaks of the Tuo Lai Nan Shan as this fault defines a sharp change in slope: Triassic rocks in the footwall are less resistant than the metamorphic rocks in the hanging

wall. The Triassic footwall syncline is truncated by *f4* and map relationships suggest that this syncline is overturned in the west, above the erosional surface. *Fault 4* splits into two fault splays in the west: *f4a* and *f4b*. *Fault 4a* places undifferentiated marble and schist rocks over the southern limb of the Triassic syncline (Fig. 2.8). Based on its surface trace, *f4b* must be relatively low angle (10-20°N). This fault juxtaposes Proterozoic schist and gneiss against undifferentiated marble and schist rocks. There are no constraints as to whether this fault is Cenozoic in age or older. Northeast-dipping (35-45°NE) Carboniferous-Permian strata unconformably overly the Pt(sch) along the southern bank of the Tuo Lai River (Fig. 2.8), which indicates that this this unconformity horizon continues above the erosional surface to the southeast.

#### 2.5.3.3. *Tuo Lai Shan*

The Tuo Lai Shan is bounded by the Tuo Lai River to the south and Heihe River to the north (Fig. 2.8). This range was constructed primarily by south-directed thrusting of early Paleozoic rocks over Cretaceous and younger strata (Fig. 2.8). Numerous fault splays within non-bedded and highly deformed units make precise interpretation of these faults difficult, but below I discuss three major thrust faults. These are labelled *f5* through *f8*, from south to north respectively (Fig. 2.8).

*Fault 5.* The NW-striking NE-dipping thrust fault consists of Ordovician strata and early Paleozoic granitoid rocks in its hanging wall (units O, O[gr], and gr) and Proterozoic metamorphic rocks (Pt[sch], Pt[gn], and Pt[gr<sub>i</sub>]) in its footwall (Fig. 2.8). The main fault and related splays dip ~35-60°NE. The fault is covered by Quaternary river deposits in the west, and its eastern extent is unknown (Fig. 2.8).

Fault 6. This label is tentatively given to the major thrust fault(s) that place inferred Precambrian and/or high-grade metamorphic rocks (Z and sch) over strongly deformed Ordovician strata and early Paleozoic granitoid rocks (units O, O[gr], and gr) (Fig. 2.8). In the west, I use *f6a* to specifically refer to the fault that juxtaposes Z(sch) against Ordovician strata that are intruded by early Paleozoic plutons (Fig. 2.8). This NE-dipping thrust fault also has Cretaceous and Carboniferous rocks in its footwall. It merges to the east with *f6b*, which specifically places the undifferentiated sch unit over the combined Ordovician strata-pluton unit (O and gr) (Fig. 2.8). This fault is also N-dipping and has a syncline of Carboniferous and Cretaceous rocks in its footwall. *Fault 6b* also places the ophiolite complex over Ordovician strata in the farthest east portion of the mapping area (Fig. 2.8). To the south of the ophiolite complex, several splays of *f6b* duplicate a suite of Ordovician rocks that are intruded by O(gr) and overlain by Carboniferous-Permian rocks (Fig. 2.8).

Fault 7. This NW-striking SW-dipping fault places a complex of Neoproterozoic marble and schist and Cambrian ophiolitic rocks (Z and  $\epsilon$ ) over Ordovician and late Paleozoic strata (O, C, and P) (Fig. 2.8). Where observed, this fault dips 40°SW (Fig. 2.8). This fault is inferred to be a backthrust of *f6*, and thus they are expected to merge at depth. Footwall strata (C and P) are variably folded at wavelength of ~2-3 km. *Fault 7* merges to the west with *f6a* and *f8*.

Fault 8. This major NE-dipping fault brings Neoproterozoic marble and schist rocks (Z[sch] and Z[mb]) over footwall rocks that include Neoproterozoic and Ordovician rocks unconformably overlain by Carboniferous-Permian strata (Fig. 2.8). These late Paleozoic footwall strata are folded at a kilometer scale. In the west, several fault splays duplicate a

series of Neoproterozoic schist rocks overlain by Carboniferous strata (Fig. 2.8). *Fault 8*'s hanging-wall rocks are unconformably overlain by Mesozoic strata (J and K) (Fig. 2.8). Several faults observed in the hanging wall of *f8* are entirely within Paleozoic or older rocks, and the timing of their activity is unconstrained.

#### 2.5.3.4. Structural data from the metamorphic basement

The Proterozoic schist and gneiss unit has strongly developed foliations and stretching lineations. These fabrics are inferred to have developed in the early Paleozoic as a result of the Qilian arc and subsequent Qilian orogen. Foliations are defined by mica layering in the mica  $\pm$  garnet schist rocks, gneissic banding with relatively mafic (biotite and amphibole) and felsic (plagioclase and quartz) layers, plagioclase layering in foliated garnet amphibolite rocks, or weak-to-strong mineral alignment (mostly mica and amphibole grains) in the foliated granitoid rocks. Stretching lineations are observed within the foliation surface and stretched plagioclase is most evident in many outcrops. This deformation occurred in the Ordovician, and the age constraints are discussed in more detail in Chapter 5.

The foliation and stretching lineation data from the metamorphic basement rocks were compiled and analyzed in several stereonet (Fig. 2.8) using the Stereonet 9 software provided by Rick Allmendinger. In the metamorphic rocks to the north of *fault 4*, the foliations are all roughly parallel, near vertical, and strike northwest. Stretching lineations within these units are subhorizontal and trend northwest. South of *fault 4*, the data is more diverse. Foliations are variable, generally NW-striking, and most lineations are SE-trending and subhorizontal.

The attitudes of these Paleozoic fabrics have been significantly modified by later deformation. To examine their original orientation, I rotate the attitude data back to a pre-

Carboniferous state (Fig. 2.8B). Structural data from south of *fault 4* must first be rotated to account for the folding that occurred in the east-trending Triassic syncline. The Triassic rocks are rotated back to horizontal and all of the data from beneath the Triassic strata (e.g., Carboniferous beds and the metamorphic rocks) are rotated accordingly. Next, the Carboniferous strata and underlying metamorphic rocks are rotated together so that the Carboniferous strata are horizontal. The pre-Carboniferous structural data are more parallel than the uncorrected data (Fig. 2.8B). The foliations are steep to near vertical and strike to the northwest. Stretching lineations are subhorizontal and trend to the southeast.

A similar procedure was done for the metamorphic structural data to the north of *fault 4*. In this case, all of the data was rotated in order to bring the Carboniferous-Permian strata that outcrop on the northern flank of the Tuo Lai Nan Shan (Fig. 2.8A) back to horizontal. The average foliation attitude and lineation plunge-trend observations from all of the corrected pre-Carboniferous datasets are  $126/84^{\circ}\text{SW}$  and  $12/119$ , respectively (Fig. 2.8B). Kinematic indicators suggest that this nearly vertical shear zone had a right-slip sense of shear.

#### **2.5.4. Balanced cross sections**

Cross sections developed from surface geology alone are non-unique tectonic models (e.g., Yin et al., 2010a; Judge and Allmendinger, 2011), but their uncertainty can be minimized by conforming to direct field observations, including bedding truncations, fault cutoffs, unit juxtapositions, and fault-geometry requirements. Cross section profiles were chosen along traverses that had the best exposure of bedded strata (i.e., Carboniferous through Cenozoic rocks) and a high density of field measurements. A large amount of bedding-attitude measurements help

to tightly constrain the fold and fault geometries, and the along-strike projection of map relationships also aids in interpretation of structures at depth.

The ultimate goal of the balanced cross section construction was to restore the sections to an undeformed state to estimate Cenozoic shortening. Because of the relatively thick-skinned deformation and large variations/uncertainties in stratigraphic thicknesses, I use the line-balancing method to restore deformation, as opposed to an area balance (Chamberlin, 1923; Mitra and Namson, 1989; Judge and Allmendinger, 2011). Thus, I assume that parallel folding is accommodated by flexural slip along bedding horizons (Elliot, 1983; Suppe, 1983). Unlike the area balance technique, line-length balancing requires well-constrained knowledge of bedding geometry, particularly at depth below the erosional surface. I use the kink-band technique (Dahlstrom, 1969; Suppe, 1983) to approximate these geometries and adhere to the observed map relationships and empirical cross-section construction “rules” (Bally et al., 1966; Dahlstrom, 1969; Boyer and Elliot, 1982; Elliot, 1983; Suppe, 1983). By choosing cross-section-profile lines where I have a high density of bedding measurements, I strive to reduce dip-domain spacing to approximate circular folds.

Bedding thickness is kept constant, except where geologic observations show otherwise (e.g., the pinching out of specific units). When hanging-wall cutoffs are eroded, I assume minimum fault offset and develop a kink-band fold that conforms to this. Further cross-section restoration assumptions are discussed in section 2.7

## **2.6. Seismic reflection profiles across the North Qilian Shan**

Three seismic reflection profiles across the North Qilian Shan frontal thrust system and adjacent foreland were acquired by the China National Petroleum Company (see Figs. 2.1 and



2.10 for their locations) (e.g., J. Wu et al., 2006; Yang et al., 2007a, 2007b). All three uninterpreted high-resolution seismic reflection profiles can be found in the Appendix (Fig. A.1). A regional geologic map was compiled from unpublished 1:200,000 scale maps, satellite analysis (i.e., Google Earth and Landsat images), and my own field observations (Fig. 2.10). The structures imaged in the seismic reflection profiles must be compatible with the local surface geology. Where available, age assignments in the seismic profiles are from drill hole and magnetostratigraphy data (e.g., Yang et al., 1993; Li, 1994; Li and Yang, 1998; Fang et al., 2004; J. Wu et al., 2006; Yang et al., 2007a, 2007b), or surface geology are projected onto the seismic profiles.

### **2.6.1. Surface geology in the North Qilian Shan**

The North Qilian Shan thrust system and its frontal Yumu Shan thrust ~30 km to the northeast (e.g., Tapponnier et al., 1990) represent the northernmost structures of the Qilian Shan-Nan Shan thrust belt (Fig. 2.1B). The Yumu Shan is a diverging fault splay (Boyer and Elliott, 1982) that merges with the North Qilian Shan thrust fault to the southeast (Fig. 2.1B). These fault systems are bounded to the north by the Hexi Corridor foreland basin (Figs. 2.1, 2.3, and 2.10), which is dissected by several isolated backthrust systems (e.g., the Longshou Shan thrust). The south-dipping Qilian Shan frontal thrust system places Proterozoic-early Paleozoic rocks over the Cenozoic strata of the Hexi Corridor foreland basin (Figs. 5 and 6) (e.g., Li et al., 1998; Fang et al., 2004). Observations of downdip slickenlines and asymmetric folds indicate that the faults are primarily dip-slip thrust faults (e.g., Tapponnier et al., 1990). The left-slip Haiyuan fault is located >100 km to the south (Fig. 2.1) and does not appear to influence the local deformational regime of the North Qilian Shan.

Hanging-wall rocks are mostly related to the early Paleozoic Qilian orogen, which juxtaposed Proterozoic high-grade gneiss and schist against Ordovician-Silurian low-grade metasediments. It is difficult to determine the age of deformational structures that are mapped entirely within the early Paleozoic units (Fig. 2.10), and without direct crosscutting relationships or more detailed mapping, these structures may be Paleozoic and/or Cenozoic in age. Ordovician and Silurian strata are often isoclinally folded and bedding is transposed. Early Paleozoic plutons are also widespread throughout the Qilian Shan (e.g., Gehrels et al., 2003a; Song et al., 2013). Two of the seismic profiles cross a >60-km-long Silurian granitoid intrusion, known as the Jinfosi pluton (Zhang et al., 1995), that intrudes Ordovician-Silurian rocks (Gehrels et al., 2003a; Wu et al., 2010) (Fig. 2.10). This pluton is thrust to the north over Mesozoic-Cenozoic strata and was the focus of a nearby AHe traverse (Zheng et al., 2010) (Fig. 2.10). The early Paleozoic strata and the plutonic rocks provide no reflective surfaces and are difficult to interpret with seismic reflection analysis because they appear transparent. Because of this issue, my analysis is mostly focused on the geometry of late Paleozoic and younger bedded strata that provide strong reflectors.

Carboniferous (locally Devonian) through Triassic deposits unconformably overlie early Paleozoic rocks (Fig. 2.10). There are limited surface exposures of Triassic rocks in the study area, and the sedimentary relationship between Late Triassic strata and the overlying Jurassic-Cretaceous sediments is not directly observed in this region. Triassic strata are much more prevalent in the central Qilian Shan-Nan Shan to the southwest (Pan et al., 2004), where the beds are variably subparallel to discordant with the overlying Jurassic-Cretaceous strata. Cretaceous rocks often exhibit a growth strata geometry and are interpreted to have been deposited in extensional grabens (Yin et al., 2008b). Jurassic through Cenozoic strata (Table 2.3) display the

clearest reflectors in the seismic reflection profiles and are most useful for cross-section construction. Jurassic rocks consist of coal-rich sandstone and siltstone beds that reach a thickness of ~800-1000 m (Gansu Geological Bureau, 1989; Zhiyi and Dean, 1996). Lower Cretaceous strata are widespread along the North Qilian Shan and Hexi Corridor, consist of red conglomerate and coarse sandstone, and have a total thickness >2600 m. The more localized upper Cretaceous strata consists of fluvial and lacustrine sandstone that are generally <500 m thick (Zhiyi and Dean, 1996).

The Hexi Corridor foreland is made up of >2.5 km of Cenozoic sediments, mostly Miocene (locally Oligocene) through Pliocene in age (Li et al., 1998; Bovet et al., 2009; Zhuang et al., 2011). The Cenozoic strata are exposed along drainages and localized structural uplifts (e.g., Li, 1993; Bovet et al., 2009). Quaternary sediments are often >1 km thick (Zhang et al., 1990) and consist of alluvial, fluvial, and glaciofluvial deposits (Li and Yang, 1998; Zhao et al., 2002).

### **2.6.2. Timing of Cenozoic deformation**

Several lines of evidence suggest that contractional deformation and crustal shortening of post-Devonian units across the North Qilian Shan initiated in the middle Miocene. First, I infer that deformation of Carboniferous through Cretaceous strata occurred in the Cenozoic based on the following observations: (1) thrust faults link with the present-day range-bounding Qilian Shan frontal thrusts (Figs. 2.10, 2.11, and 2.14-2.16), (2) these faults truncate Cenozoic nonmarine deposits and offset Quaternary alluvium (Figs. 2.10 and 2.11), (3) regionally, Carboniferous-Triassic strata are conformable and parallel to subparallel, indicating that deformation involving these units was post-Triassic, and (4) Jurassic-Cretaceous strata are

extension related (e.g., Vincent and Allen, 1999; Chen et al., 2003; Yin et al., 2008a, 2008b), so contractional deformation of Jurassic-Cretaceous strata must be Cenozoic in age. Second, AHe apatite ages obtained along a nearby traverse (Fig. 2.10) suggest that rapid cooling across the Qilian Shan frontal thrust system began ca. 10 Ma (Zheng et al., 2010). Lastly, the Cenozoic strata in the seismic reflection profiles, generally Miocene and Pliocene sedimentary rocks, exhibit growth strata relationships with the frontal thrusts (see section 2.6.4)

### **2.6.3. Approximate vertical scale of seismic sections and associated uncertainties**

The vertical axes in the seismic profiles are two-way traveltime, and an approximate depth scale was created assuming an average P-wave velocity of 5.5 km/s (Liu et al., 2006; Gao et al., 2013). Although the use of a single average seismic velocity distorts the geometry of the structures, I assume these effects to be negligible given that the sections are imaging only the uppermost ~15 km of crust and that I am primarily interested in assessing horizontal motion and shortening. The sediment in the foreland may have a lower seismic velocity (e.g., He and Pang, 2013), and therefore the seismic-reflection profiles likely overestimate the apparent thickness of Cenozoic sediments. However, my choice of an average seismic velocity leads to very minor uncertainties for the horizontal calculations. By assuming that these approximation of an upper crustal seismic velocity of 5.5 km/s has an associated error of  $\pm 0.5$  km/s, which is reasonable based on other regional geophysical studies (e.g., Liu et al., 2006) and the global distribution upper crustal p-wave velocities (Christensen and Mooney, 1995), then these uncertainties in the vertical scale affect the actual length of any inclined reflectors. The magnitude of this distortion depends on the apparent dip angle of the reflector. The original length of reflector that dips  $45^\circ$  would be distorted by 3-4%, whereas more shallowly dipping beds would undergo less

elongation. Thus, the line-length balancing analyses of horizontal shortening produce conservative uncertainties of 3-4%. The conversion of traveltimes to depth yields apparent bed thicknesses that are consistent with what is observed at the surface (see preceding description), strengthening the validity of this assumption.

#### **2.6.4. Seismic reflection profiles**

Three seismic reflection profiles (Figs. 2.14-2.16) show sequences of finely laminated reflectors, which are interpreted to represent sedimentary strata, and zones of diffuse low reflectivity, which may represent either large plutons or the strongly deformed and transposed Ordovician-Silurian strata. The great density of highly reflective layers allows us to understand the subsurface geometry, and the truncation of these closely spaced reflectors is due to faulting, unconformable deposition, or pluton intrusion. Overall, these three profiles image a south-dipping thrust system involving two major thrust faults that places Paleozoic and older rocks over a relatively undeformed Hexi Corridor foreland to the northeast (Fig. 2.10). The foreland consists of Mesozoic-Cenozoic sedimentary rocks unconformably overlying older bedded units.

Jurassic strata display the strongest and most continuous reflectors (Figs. 2.14-2.16), possibly because of the laterally continuous coal seams in these rocks. These beds generally are 6-8 km below the surface of the Hexi Corridor, but also are exposed along the base of the North Qilian Shan range (Fig. 2.10). Cretaceous strata are subparallel to Jurassic strata and also display finely laminated reflectors (Figs. 2.14-2.16). Truncations of these reflectors are pronounced and highlight major structures. Growth strata relationships occur in both the Cretaceous and Cenozoic strata; sedimentary rocks thicken to the south-southwest. Sequences of strong reflectors that have apparent thicknesses similar to either the Jurassic or Cretaceous reflectors in

the undeformed foreland footwall are interpreted to be the same units in the hanging wall. No clear regional-scale detachment surface at depth is observed in any of the sections, although the hanging-wall and footwall flats are often confined to Cretaceous strata. The transparent granitoid and Ordovician-Silurian units are ambiguous and I refrain from overinterpreting structures within these units. Paleozoic units at depth cannot be subdivided further unless surface extrapolation is possible, and are assigned a general Paleozoic age (Pz).

Seismic reflection profile 1 (Fig. 2.14) (line S-S' in Fig. 2.10) is an ~31-km-long section that images two south-dipping thrusts, which place the Silurian pluton on relatively undeformed Mesozoic-Cenozoic sedimentary rocks in the Hexi Corridor (Fig. 2.10). The set of strongest reflectors are interpreted to be Jurassic strata (e.g., Yang et al., 1993; Li, 1994; Li and Yang, 1998), 6 km below the surface in the Hexi Corridor (label 1 in Fig. 2.14), which is conformably overlain by Cretaceous and Cenozoic rocks. Minor north-dipping faults disrupt Jurassic and older strata. Jurassic strata are interpreted to overlie Carboniferous-Triassic rocks with a minor ( $10^{\circ}$ - $15^{\circ}$ ) angular unconformity (between labels 1 and 6 in Fig. 2.14), although the distinct units beneath the Jurassic strata are not constrained. The coherent layer of Jurassic strata pinches out in the south end of the profile (Fig. 2.14). This interpretation is further supported by the lack of Jurassic rocks exposed at the surface to the south-southwest of this profile location (Fig. 2.10). The relatively transparent Silurian granitoid and Ordovician-Silurian metasedimentary rock compose most of the southern portion of the acquired image (label 5 in Fig. 2.14). The truncation of poorly organized, tightly folded, and diffuse reflectors represents an intrusive contact of granitoid against Ordovician-Silurian metasedimentary rocks.

This profile images two major thrust faults (Figs. 2.10 and 2.11). The most northern structure (f1 in Fig. 2.14) involves a nearly continuous and parallel set of south-dipping ( $25^{\circ}$ -

35°S) reflectors juxtaposed against horizontal reflectors near the middle of the image (3 and 4 in Fig. 2.14). I interpret this structure as a hanging-wall flat-footwall ramp thrust fault. Hanging-wall rocks are interpreted to be Cretaceous in age based on projecting surface geology to depth (Figs. 2.10 and 2.14). The Jurassic strata pinch-out could alternatively be interpreted as a footwall-ramp truncation, which would require a matching Jurassic cutoff in the hanging wall. I do not prefer this interpretation because this relationship is not observed. Slip along f1 is at least 15-20 km. The second major fault (f2 in Fig. 2.14) truncates the Cretaceous hanging-wall strata of fault f1 and places the relatively transparent Ordovician-Silurian units against the Cretaceous rocks (Fig. 2.14). Based on the observed fault geometries and unit juxtapositions, slip along this second fault, f2, is likely 5-10 km. Some of the observed unconformities (i.e., beneath the Jurassic strata) could be low-angle hanging-wall bedding-parallel thrusts, but I prefer the unconformity interpretation based on the regional geology and because this assumption minimizes estimated shortening.

Seismic reflection profile 2 (Fig. 2.15) (line T-T' in Fig. 2.10) is a ~39-km-long section located ~40 km to the southeast of profile 1 (Fig. 2.10). This section images the same south-dipping thrust structures and undeformed foreland observed in profile 1. Strongly reflective Jurassic strata are ~8 km below the surface of the Hexi Corridor (1 in Fig. 2.15) and are overlain by Cretaceous-Quaternary sedimentary rocks (2 in Fig. 2.15). Middle Miocene rocks at the base of the range (N in Fig. 2.10) are syntectonic because they unconformably overlie Cretaceous strata and are truncated by the current range-bounding thrust (Fig. 2.15). This supports middle Miocene fault initiation. Jurassic strata overlie Triassic or Paleozoic rocks with an apparent angular unconformity of ~15° (between 1 and 6 in Fig. 2.15), similar to profile 1 (Fig. 2.14). Minor south-dipping faults disrupt Paleozoic through Jurassic strata in the north.

The southwestern side of the seismic profile also shows two major faults. The first brings Jurassic strata from a depth of ~8 km to ~5 km along a thrust fault (f1 in Fig. 2.15). This juxtaposition, along with the observed fault geometry, requires a minimum fault slip of ~15 km. The hanging-wall rocks in f1 are truncated by another major fault (f2 in Fig. 2.15) that brings Ordovician-Silurian and Jurassic strata over Jurassic-Cretaceous rocks (3 in Fig. 2.15), which requires ~10-15 km of slip. Another minor south-dipping fault transports early Paleozoic rocks and truncates north-dipping Jurassic strata. Slip on this fault is poorly constrained but must be large enough (2-4 km) to expose Silurian rocks in this range (Fig. 2.10) and to cut through and obscure Jurassic strata at the surface (Fig. 2.15).

Seismic reflection profile 3 (Fig. 2.16) (line U-U' in Fig. 2.16) is an ~25 km-long section located ~10 km to the southeast of profile 2 (Fig. 2.10). This is the only section that is parallel and aligned with shortening in the Yumu Shan to the northeast (Figs. 2.1, 2.3, and 2.17), and the imaged structures may be kinematically linked with those to the north (Tapponnier et al., 1990). The prominent reflector sequence that is interpreted to represent Jurassic strata is located at a depth of 3-4 km below the Hexi Corridor (label 1 in Fig. 2.16), compared to depths of 6-8 km in the other two profiles (Figs. 2.14 and 2.15). Thus, Cretaceous-Cenozoic deposits in this section are 2-4 km thinner than the other sections, although the relative thickness of each different-aged deposit is ambiguous (e.g., Cretaceous versus Neogene versus Quaternary strata). This thickness difference may be caused by either a Cretaceous or Cenozoic paleohigh that impeded the deposition of Cretaceous or Cenozoic sediments, or earlier localized Cenozoic uplift that allowed for more erosion of the youngest sedimentary rocks. Jurassic strata overlie Triassic or Paleozoic rocks with an angular unconformity of ~10° (between labels 1 and 5 in Fig. 2.16).



Unlike the other profiles, at least five north-dipping faults cut through Hexi Corridor sedimentary rocks with small-magnitude offsets. These south-directed faults may originate from deformation in the Yumu Shan (Figs. 2.1, 2.3, and 2.17). Two major thrusts are imaged in the southern portion of this profile. The first thrust (f1 in Fig. 2.16) creates the geometric relationship of south-dipping Cretaceous strata in the hanging wall against nearly horizontal strata in the footwall, near the middle of the section (4 in Fig. 2.16). This juxtaposition requires a minimum ~3-5 km of slip. The second major thrust (f2 in Fig. 2.16) is imaged at the southern edge of profile 3 and involves the movement of Jurassic-Cretaceous rocks to within 1-2 km of the surface along a south-dipping fault. A backthrust in the hanging wall truncates Jurassic strata, and only Silurian rocks are exposed at the surface along the profile surface trace (Fig. 2.10). Jurassic beds are exposed south of profile 3 (Fig. 2.10).

## **2.7. Cenozoic shortening estimates across the central Qilian Shan**

Given that contractional deformation of Carboniferous and younger rocks is interpreted to be Cenozoic in age, the restoration of balanced cross sections provides constraints on the minimum magnitude of Cenozoic shortening strain. In addition to the assumptions previously stated for cross section construction, the following assumptions were involved in the restoration of all balanced cross sections. (1) Deformation is plane strain in the north-northeast-trending sections; this is validated by direct field observations of dip-slip fault kinematics (e.g., fault slickenlines and asymmetric minor folding analysis; my own field observations), present-day north-northeast-south-southwest convergence as indicated by GPS velocities, and a northeast contractional strain field (Zhang et al., 2004; Allmendinger et al., 2007). (2) Unconformity surfaces that were used for section restoration have no initial relief and are restored to horizontal,

except when evidence suggest otherwise. (3) The pin lines are placed in the most undeformed strata, in the footwall or hanging wall. (4) Shortening estimates are a minimum because of hanging-wall erosion (Boyer and Elliott, 1982), bed-length changes during deformation (Groshong et al., 2012), cleavage formation, unrecognized additional detachment surfaces at depth (e.g., Yin et al., 2008a), and unconstrained deformation in the early Paleozoic granite and metasediments. (5) Although significant pre-Cenozoic deformation affected the region, following the logic presented here, restoration of Jurassic-Cretaceous strata provides an estimate of Cenozoic strain.

### **2.7.1. Shortening based on geologic mapping of the central Qilian Shan**

The balanced and restored cross sections presented in Figures 2.12 and 2.13 are based on surface geological mapping alone. The deformed-state cross sections presented here adhere to the map-view relationships (Figs. 2.7 and 2.8) and structural observations (see section 2.5.3). The restoration of these sections involved restoring slip along the mapped faults to reposition the late Paleozoic unconformity surfaces back to horizontal. When hanging-wall cutoffs were eroded, minimum slip was assumed. Pinlines were placed through undeformed strata. Additional cross-section-specific explanations are presented along with the cross sections in Figures 2.12 and 2.13.

The minimum magnitude of shortening estimated in these sections was, from north to south, 16.5 km (26.5% strain), 15.5 km (47% strain), 6.3 km (38% strain), and 11 km (35% strain) (Figs. 2.3., 2.12 and 2.13; Table 2.2). The summation of these estimates, ignoring section C-C' which is parallel to section D-D' (Fig. 2.8), suggests that the mapping area accommodated 43 km of Cenozoic shortening or ~35% strain.

The section that spans E-E' (Fig. 2.3) is totally unconstrained as I have not mapped this region and very little post-Silurian bedded strata are exposed to constrain fault and fold geometries. That said, I provide a first-order shortening estimate by applying the average strain estimate (i.e., 35%) for the central Qilian Shan, taken from sections A-A' through D-D', to section E-E'. This approach yields a minimum shortening magnitude of ~8.6 km (35% strain) (Table 2.2).

The summation of these balanced and restored cross sections across the central Qilian Shan-Nan Shan thrust belt, from Hara Lake in the south to just-south of the northern frontal Qilian Shan thrust system (i.e., sections A-A', B-B', C-C', and E-E') (Figs. 2.1 and 2.3), indicates that the region has accommodated a minimum of ~52 km of Cenozoic shortening (~35% strain) (Table 2.2). The precise initiation age for this deformation is not constrained. The most direct evidence for shortening initiation is the truncation of Miocene terrestrial strata by thrust faults (Figs. 2.8, 2.9F, and 2.9G). Based on similar sedimentological evidence, Zhuang et al. (2011) suggest an early to middle Miocene (i.e., ~23-15 Ma) deformation initiation age. Using this initiation age yields a shortening rate across the central Qilian Shan-Nan Shan thrust belt of 2.2 mm yr<sup>-1</sup> to 3.5 mm yr<sup>-1</sup>. Alternatively, if deformation initiated early at ~50 Ma like in southern Qilian Shan and North Qaidam thrust belts (Yin et al., 2008a), the shortening rate would only be ~1.0 mm yr<sup>-1</sup>. Given the range of initiation ages, the interior of the central Qilian Shan-Nan Shan thrust belt experienced strain rates ranging from  $2.2 \times 10^{-16} \text{ s}^{-1}$  to  $7.4 \times 10^{-16} \text{ s}^{-1}$ .

### 2.7.2. Shortening based on seismic reflection profiles

Balanced cross sections constructed from the seismic reflection profiles were assumed to have horizontal length errors of <4%, due to the use of a single average seismic velocity. The balanced and restored cross sections are presented in Figures 2.14-2.16.

Because the Jurassic strata in seismic reflection profile 1 (Fig. 2.14) are not observed in the hanging wall, either because it pinches out or is truncated by a fault, and the Cretaceous hanging-wall cutoff is also eroded, line-length balancing of either of these units would lead to large uncertainties. An alternative method is required to constrain shortening. Profile 1 is located within 2 km of the parallel traverse by Zheng et al. (2010) (Fig. 2.10), allowing for the use of their AHe data in the deformed and restored cross-section models. Their study locates a ca. 10 Ma apatite paleo-PRZ in the hanging wall of the north-directed thrust system (e.g., Fig. 2.5C), which can be used to estimate the location of a ca. 10 Ma paleoland surface at ~2.6 km above the paleo-PRZ, assuming a typical continental geothermal gradient and reasonable AHe closure temperature (see discussion in Zheng et al., 2010). I place this paleo-PRZ and ca. 10 Ma paleoland surface in the deformed-state cross section (Figs. 2.14B-2.14C) and use it in the restoration to align this ca. 10 Ma marker horizon (i.e., the paleoland surface) within middle Miocene strata in the Hexi Corridor footwall (Fig. 2.14D). The same method was used by Zheng et al. (2010), but with only one fault strand and an oversimplified fault geometry. My seismic reflection interpretation and knowledge of the fault geometries at depth allows for a better constrained restoration. I restore the paleo-PRZ within the Silurian granitoid along the imaged thrust faults until the inferred ca. 10 Ma paleoland surface is at the same vertical position as the ca. 10 Ma strata in the footwall (Fig. 2.14D). This restoration requires a good vertical scale to be meaningful, but the vertical scale of the seismic sections is only an approximation. To overcome

this issue, I use three independent observations to verify the vertical position. First, I compare the relative scale of the cross-section model with that presented by Zheng et al. (2010) that shows that the paleo-PRZ in the hanging wall is located ~2.1 km above the ca. 10 Ma surface in the Hexi Corridor. The cross-section model shows a similar vertical relationship. Second, Cretaceous beds are ~3 km thick (see preceding discussion) and I can compare the apparent thickness of these beds in the seismic section to create a local vertical scale. Third, I note that the Carboniferous strata unconformably overlying the Silurian pluton (Figs. 2.10, 2.14B, and 2.14C) must be restored to a viable pre-Cenozoic position to avoid creating an unreasonable buttress unconformity, which would indicate large-scale relief during the deposition of Cretaceous strata.

I position the Silurian pluton to minimize shortening (Fig. 2.14D), although allowing more slip would give the implied unconformities a more realistic geometry with less pre-Cenozoic relief. To the south of the Silurian pluton, the lack of bedded units and coherent reflectors makes restoration difficult. Silurian and Ordovician strata are involved in imbricate thrusting that may be either Paleozoic or Cenozoic in age (Figs. 2.10 and 2.14). With this restoration method, I calculate a minimum horizontal shortening magnitude of 25 km with a deformed section length of 21 km, which yields a minimum shortening strain of 54% (Fig. 2.14D). Alternatively, if I ignore the AHe data and retrodeform the strata along the observed footwall fault geometries, minimum shortening is 22 km (53% strain). The latter method does not adequately restore the Carboniferous unconformity to a reasonable elevation, and so I prefer the former shortening estimate (i.e., 25 km or 54% strain). A line-length balance of Cretaceous strata yields a shortening magnitude of 15 km and a corresponding strain of 40%, which can be regarded as absolute minimum estimates. If the strain was accommodated over the past ~10 m.y.

(Zheng et al., 2010), the corresponding horizontal shortening rate and strain rate are 2.2-2.5 mm yr<sup>-1</sup> and  $1.7 \times 10^{-15} \text{ s}^{-1}$ , respectively.

Profile 2 (Fig. 2.15) is retrodeformed to an undeformed pre-Cenozoic state by restoring the Jurassic beds (i.e., the prominent reflectors labeled 1 in Figs. 2.15A and 2.15B) to a continuous and horizontal position (Fig. 2.15D). The minimum magnitude of horizontal shortening calculated by this restoration is ~33 km across a deformed section length of ~29 km (Fig. 2.15D), which yields a shortening strain of 53%. The surface exposure of Jurassic strata in the hanging wall in the Qilian Shan range (Fig. 2.10) and the reasonably constrained location of Jurassic rocks in the Hexi Corridor footwall (Fig. 2.15) require a minimum vertical throw of 8-10 km. This observation corroborates my interpretation and requires shortening of this approximate magnitude. Given that this strain was accommodated since ca. 10 Ma (Zheng et al., 2010), the corresponding horizontal shortening rate and strain rate are 3.3 mm yr<sup>-1</sup> and  $1.7 \times 10^{-15} \text{ s}^{-1}$ , respectively.

Seismic reflection profile 3 (Fig. 2.16) is also restored using the Jurassic unit as a marker horizon (i.e., the prominent sequence of reflectors labeled 1 in Fig. 2.16). Motion on fault f2 is poorly constrained because of erosion of the hanging-wall cutoff, but there must be enough slip on fault f2 to expose Silurian strata at the surface (e.g., Fig. 2.10). The minimum magnitude of horizontal shortening calculated in this restoration is ~12 km across a deformed section with a length of 21 km, yielding a minimum strain of 36%. Assuming that deformation initiated ca. 10 Ma (Zheng et al., 2010), the corresponding horizontal shortening rate and strain rate are 1.2 mm yr<sup>-1</sup> and  $1.1 \times 10^{-15} \text{ s}^{-1}$ , respectively.

## 2.8. Discussion

### 2.8.1. Cenozoic shortening across the northeastern Tibetan Plateau

Through balanced cross section construction and restoration, I have constrained north-south shortening across the interior of the central Qilian Shan-Nan Shan thrust belt and along the North Qilian Shan frontal thrust system. I estimate that the total minimum magnitude of Cenozoic shortening across a ~98-km-long traverse of the central Qilian Shan-Nan Shan thrust belt, based on the surface geology alone, is ~52 km (~35% strain). This magnitude is comparable to regional shortening estimates across the region (Meyer et al., 1998; Yin and Harrison, 2000). Because the thrust belt geometry and deformational style to the southwest of Hara Lake appear to be similar to my mapping area (Figs. 2.1 and 2.3), I tentatively suggest that the observed strain can be extrapolated across the entire ~350-km-wide Qilian Shan-Nan Shan thrust belt, with the exception of the North Qilian Shan thrust system, which experienced higher strain as discussed below. This approach yields a minimum shortening of ~210 km (35% strain) across all of the Qilian Shan ranges south of the North Qilian Shan.

Seismic reflection profile analysis along the North Qilian Shan frontal thrust system yields minimum north-south shortening estimates of 25 km (54% strain), 33 km (53% strain), and 12 km (36% strain), from west to east (Figs. 2.4 and 2.10). Although the seismic reflection interpretations, cross-section models, and section restorations are nonunique solutions, the geometric compatibility between the three sections adds robustness to my interpretations. All three profiles image two south-dipping strands of the North Qilian Shan frontal thrust system. In all three cross sections, Quaternary sediments cover *fault 1*, and *fault 2* represents the range-bounding fault (Fig. 2.10), suggesting that *fault 1* is inactive and *fault 2* is active. This trailing

imbricate system may have first exploited the relative weaknesses within the bedded Cretaceous rocks before cutting through early Paleozoic strata.

Profiles 1 and 2 yield similar shortening magnitude and strain estimates. One explanation for profile 3 having a lesser magnitude of Cenozoic shortening is that deformation may be partitioned between the Qilian Shan and Yumu Shan thrust systems, ~25 km northeast of profile 3 (e.g., Tapponnier et al., 1990) (Fig. 2.17). Profile 3 is the only section that is directly in line with the Yumu Shan. Estimated north-south shortening rates across the Yumu Shan are 0.4-1.9 mm yr<sup>-1</sup> (Tapponnier et al., 1990) and if faulting also initiated ca. 10 Ma, the magnitude of shortening should be between 4 and 19 km. Summation of the shortening magnitudes and rates from the Yumu Shan and the Qilian Shan frontal thrust system imaged in profile 3 yields 16-31 km (33-49% strain) and 1.6-3.1 mm yr<sup>-1</sup>, respectively, consistent with the shortening observed in profiles 1 and 2 to the west (Fig. 2.17).

Shortening estimates derived from the longest profile (i.e., profile 2; Fig. 2.15) indicate that the North Qilian Shan minimum Cenozoic shortening magnitude and strain were  $33 \pm 6$  km and  $52\% \pm 4\%$ , respectively, including the uncertainties associated with using a single uniform seismic velocity. Other seismic reflection analyses across the North Qilian Shan frontal thrust system obtain comparable strain values of 40-55% (J. Wu et al., 2006; Yang et al., 2007a, 2007b). Assuming that this strain can be applied across the width of the North Qilian Shan frontal range (40-50 km), a possible restored position of the northern margin of the Qilian Shan prior to Cenozoic shortening is shown in Figure 2.17. Note that all three profiles restore to a similar position.

The north-south shortening rate across the North Qilian Shan thrust system derived from this study,  $3.3 \pm 0.6$  mm yr<sup>-1</sup>, is much higher than most other rate estimates across northern Tibet



(Hetzl et al., 2004; W.J. Zheng et al., 2009, 2013; D. Zheng et al., 2010; Yuan et al., 2011), but is consistent with the estimates of Champagnac et al. (2010) (i.e.,  $\sim 2.5 \text{ mm yr}^{-1}$ ), also along the North Qilian Shan frontal thrust system. If correct, these high deformation rates indicate that deformation is currently focused along the northern margin of the plateau, and that the North Qilian Shan thrust faults accommodate more than half of the entire geodetic shortening across the Qilian Shan-Nan Shan thrust belt (i.e.,  $\sim 5.5 \text{ mm yr}^{-1}$ ) (Zhang et al., 2004). This result indicates that focused deformation along the northern margin of the Tibetan Plateau is similar to Himalayan shortening along the southern margin of the plateau, where strain is highly concentrated along the Main Frontal Thrust (Lavé and Avouac, 2000; Burgess et al., 2012).

The remaining contemporary convergence rate must be accommodated within the interior of the Qilian Shan-Nan Shan thrust belt. Because the initiation age of deformation within the thrust belt interior is poorly constrained, there is no way to precisely calculate the shortening rate across this region. However, by subtracting the shortening rate across the North Qilian Shan thrust system ( $3.3 \pm 0.6 \text{ mm yr}^{-1}$ ) from the present-day convergence rate across the Qilian Shan-Nan Shan thrust belt (i.e.,  $\sim 5.5 \text{ mm yr}^{-1}$ ) (Zhang et al., 2004), I note that 2.2-1.6  $\text{mm yr}^{-1}$  of shortening should be accommodated across this interior. The observed minimum shortening magnitudes suggest shortening rates that vary, depending on the initiation age, from  $\sim 1.0 \text{ mm yr}^{-1}$  (i.e.,  $\sim 50 \text{ Ma}$  initiation age) to  $3.5 \text{ mm yr}^{-1}$  (i.e.,  $15 \text{ Ma}$  initiation age), which fall within the expected range. In fact, the above information suggests that shortening probably started prior to  $\sim 24 \text{ Ma}$  (i.e.,  $\sim 2.2 \text{ mm yr}^{-1}$  shortening rate), or else the shortening rates would be too high across the entire Qilian Shan-Nan Shan thrust belt. Alternatively, it is possible that shortening rates may have varied in the past.

The Cenozoic shortening documented in this work (Table 2.2) is generally higher than other estimates around the northeastern Tibetan Plateau (Fig. 2.4). This disparity may be due to either a heterogeneous strain distribution in northern Tibet or an artifact of the limitations of strain estimates that are calculated from observations of the surface geology alone. Estimates derived from restoring only Cenozoic strata are significantly lower (<15% strain) (e.g., Lease et al., 2012; Craddock et al., 2014) than those that incorporate subsurface data (>40% strain) (J. Wu et al., 2006; Yang et al., 2007a, 2007b; Yin et al., 2008b; Gao et al., 2013; this study). However, the variable topography, eastward-tapering thrust belts (Fig. 2.1B), complex interaction between strike-slip and thrust faulting, and heterogeneous strain estimates in different cross sections from the same study (e.g., Fig. 2.4) suggest that strain is not spatially constant across northern Tibet. By integrating my estimates with other seismic analyses, detailed field-mapping-based estimates, and regional bulk shortening estimates (e.g., Yin et al., 2008b; Meyer et al., 1998; Gao et al., 2013), I suggest that the bulk Cenozoic strain across the Qilian Shan-Nan Shan thrust system is >30% (215-300 km shortening) (Fig. 2.4; Table 2.2), and higher strain (>53% or ~50 km shortening) is concentrated in the North Qilian Shan thrust belt along the plateau margin. Thus, the higher strain observed along the North Qilian Shan should not be extrapolated across the entire Qilian Shan-Nan Shan thrust belt.

### **2.8.2. Crustal shortening, thickening, and denudation**

To quantitatively evaluate plateau formation mechanisms, I first determine the significance of distributed shortening in crustal thickening and plateau development. A well-constrained estimate of the pre-Cenozoic crustal thickness of northern Tibet is required to assess the role that crustal shortening has in crustal thickening. Although such an estimate does not

exist, several lines of evidence suggest that the pre-Cenozoic thickness of the northern Tibet was ~40 km. The global average thickness of modern continental crust is  $41 \pm 6$  km (Christensen and Mooney, 1995). Although Mesozoic rifting is widespread across northern Tibet (Vincent and Allen, 1999; Chen et al., 2003) and rifted crust can be as thin as  $36 \pm 8$  km (Christensen and Mooney, 1995), nonmarine Cretaceous deposits require the crust to be at least 32-34 km thick to be above sea level, given Airy isostatic compensation (e.g., Schubert and Sandwell, 1989). Furthermore, the Ordos Basin to the northeast of the plateau (Fig. 2.1) represents relatively stable crust, with a lack of earthquakes and a lower average elevation (i.e., ~1.3 km). Its current crustal thickness of ~42 km (Liu et al., 2006) is a good approximation for crustal thickness in the adjacent northern Tibet prior to Cenozoic deformation.

The horizontal crustal shortening observed across northern Tibet (Table 2.2) contributes to crustal thickening of this initially ~40-km-thick crust, assuming that surface and mantle erosional processes and/or lateral material transport (i.e., not plane strain shortening) are not outpacing crustal thickening. Vertical thickening results from horizontal shortening assuming the following: (1) vertically uniform horizontal plane strain shortening of the crust (i.e., upper, middle, and lower crust), (2) two-dimensional (2-D) pure shear crustal thickening, and (3) minor, or at least well-constrained, denudation. Horizontal shortening strain,  $\epsilon_h$ , is defined as  $\epsilon_h = \frac{l_f - l_i}{l_i}$ , where  $l_f$  and  $l_i$  are the final and initial cross section lengths, respectively. Horizontal shortening strain can be converted to horizontal stretch strain,  $s_h = \frac{l_f}{l_i} = \epsilon_h + 1$ , which is inversely related to the vertical stretch strain,  $s_v = \frac{1}{s_h}$ . The apparent present-day crustal thickness,  $T_f$ , relates to vertical stretch strain ( $s_v$ ) as  $T_f = T_i \times s_v$ , where  $T_i$  is the initial crustal thickness. This same

approach can be used to back-calculate the apparent pre-deformational crustal thickness of the Tibetan Plateau (Table 2.2).

This simple approximation excludes the effects of denudation, but as shown below, there has been less than 5 km of Cenozoic denudation across northern Tibet. The Silurian-Carboniferous unconformity in the hanging wall of the North Qilian Shan frontal thrust system (Figs. 2.10 and 5.14) constrains how much material was removed to expose this marker horizon. Carboniferous-Jurassic strata are ~4-4.5 km thick and Jurassic-Cretaceous rocks record a transition from marginal marine to nonmarine deposits (Gansu Geological Bureau, 1989; Qinghai BGMR, 1991). The exposure of the base Carboniferous beds (i.e., the unconformity surface) requires 4-4.5 km denudation since the beginning of the Cretaceous, when terrestrial sedimentation began (Vincent and Allen, 1999) and erosion could have commenced. The magnitude of Cretaceous versus Cenozoic erosion and/or denudation is not constrained, and so this estimate provides a maximum Cenozoic denudation magnitude of 4.5 km. The AHe study of Zheng et al. (2010) shows erosion and denudation magnitudes of ~2 km since ca. 10 Ma. I assume a conservative maximum denudation magnitude of 5 km across the central Qilian Shan thrust system and assume that all of northern Tibet underwent a similar magnitude of denudation.

Other low-temperature thermochronology studies also indicate low magnitudes of denudation. Apatite fission-track (AFT) analysis across the northwestern Qilian Shan and Hexi Corridor by George et al. (2001) yields mostly Cretaceous and older cooling ages. AHe and AFT data from the western Haiyuan fault also yields Cretaceous or older ages (Duvall et al., 2013). These older cooling ages suggest that denudation >4-5 km did not occur across most of northern Tibet in the Cenozoic.

Assuming that the crustal thickness of northern Tibet prior to India-Asia collisions is ~40 km, I calculate the crustal thickness that develops due to horizontal shortening (Table 2.2), and compare this value to the present-day crustal thickness (55-65 km) (e.g., Fig. 2.1C) of northern Tibet (Fig. 2.18). When crustal shortening alone generates a crustal thickness that agrees with modern observations, no additional mechanisms are favored for plateau development, but if the shortening estimates overthicken or underthicken the crust, alternative processes, including channel flow or underthrusting (e.g., Fig. 2.2), are required. This analysis is conducted along two northeast-trending cross-section lines across northern Tibet (lines J-J' and K-K' in Fig. 2.4) (Fig. 2.18).

In the west, along line J-J' in Figure 2.4, the observed crustal shortening estimates in the Qimen Tagh, Qaidam Basin, and Qilian Shan-Nan Shan thrust belts can effectively explain the present-day crustal thickness (Fig. 2.18). The shortening observed in the seismic profiles at the northern edge of the Qilian Shan is high and predicts thicker crust (i.e., 75-80 km) than what is observed. In the east, along line K-K' in Figure 2.4, shortening estimates south of the Haiyuan fault near the Gonghe Basin (Fig. 2.4) are too low to adequately explain the observed crustal thickness (Fig. 2.18); an extra crustal thickness of ~10 km is needed. To the north of the Haiyuan fault crustal shortening is sufficient to develop the observed ~50-km-thick crust (Fig. 2.18). The higher shortening reported by Gao et al. (2013) predicts thicker crust than what is observed (~70-75 km) (Fig. 2.18). This integrated analysis can ascertain the importance of distributed shortening as a plateau formation mechanism. For most of northern Tibet, away from the plateau margins, distributed crustal shortening and pure shear thickening can adequately generate the observed 55-65 km crustal thickness (Fig. 2.18), which suggests that distributed shortening is the dominant crustal thickening process operating through most of this region. The higher strain

observed by the seismic reflection analysis along the plateau margin may result from either southward underthrusting of the Asian mantle lithosphere or continental subduction (Table 2.1). Given that this higher magnitude deformation is focused along the northern margin of the plateau and not along existing sutures (Fig. 2.1), the underthrusting model is favored. If the Asian mantle lithosphere is underthrust to a position near Qaidam Basin, as suggested by Ye et al. (2015) (Fig. 2.1A), ~300 km shortening (~50%) is required to accommodate this motion.

### **2.8.3. Model for Cenozoic development of the northeastern Tibetan Plateau**

By integrating existing work across northern Tibet, I develop a lithospheric-scale model for the Cenozoic construction of the northeastern Tibetan Plateau (Fig. 2.19). The crustal thickness and elevation of the northeastern Tibetan Plateau are the results of bulk north-south shortening of the Tibetan-Asian lithosphere by at least 250-350 km, from the Kunlun fault in the south to the Hexi Corridor in the north (Figs. 2.1 and 2.19). This shortening is accommodated by southward underthrusting of the Asian mantle lithosphere beneath the northern margin of the plateau and a similar magnitude of crustal shortening and pure shear crustal thickening (Fig. 2.19). Strain observed away from the margins of the northeastern plateau is  $>\sim 30\text{-}45\%$ , which is sufficient to thicken an initially ~40-km-thick crust to the present-day crustal thickness solely by distributed crustal shortening and pure shear thickening. With this scenario, the Tibetan crust has thickened by ~20 km via distributed contractional folding and faulting as a result of deformation that transferred rapidly from the south, as early as ca. 50 Ma (Yin et al., 2008a; Duvall et al., 2013). Localized higher strain ( $>53\%$ ) along the northern plateau margin results from southward underthrusting of the Asian mantle lithosphere to a position beneath northern Qaidam Basin. This is supported by receiver function studies that image the south-dipping North China mantle

lithosphere beneath the Tibetan Plateau (Feng et al., 2014; Ye et al., 2015). However, these observations are not consistent with the high magnitude of underthrusting envisioned by Kind et al. (2002) (Fig. 2.1A) that would require significantly more upper crustal shortening (Fig. 2.2D). The relatively recent initiation of faulting (Zheng et al., 2010) and high strain rates (Champagnac et al., 2010; this study) along the northern plateau margin suggest that this interpreted underthrusting is a young feature of plateau development that initiated at around 10 Ma.

Although most of the observed strain distribution (Fig. 2.18) can be explained by this lithospheric-scale model (Fig. 2.19), the low shortening magnitudes (<15%) near the Gonghe Basin and the Jishi-Laji Shan to the southeast require explanation (Lease et al., 2012; Craddock et al., 2014). These relatively low shortening estimates may be the result of shortening underestimation because of the lack of subsurface data, although Lease et al. (2012) argued that these low shortening magnitudes are sufficient to generate the observed crustal thickness from crust with an initial thickness of  $45 \pm 5$  km. Alternatively, these low strain magnitudes may indicate that a different mechanism is operating in this eastern region of northern Tibet (Fig. 2.1B), such as northeast-east-directed lower crustal flow around Sichuan Basin (Clark and Royden, 2000) that could lead to additional vertical crustal thickening without horizontal crustal strain at the surface. The lateral flow of low-viscosity material may be driven by the northward indentation of India into the Tibetan lithosphere from the south or the southward underthrusting of the Asian mantle lithosphere beneath northern Tibet.

#### **2.8.4. Accommodation mechanisms of India-Asia convergence**

There has been 2000-2500 km of convergence between India and Asia since the onset of collision at 65-55 Ma (e.g., Molnar and Tapponnier, 1975; Dewey et al., 1989; Le Pichon et al., 1992; Zhu et al., 2005; van Hinsbergen et al., 2011). Efforts to document this convergence in crustal shortening generally come up short, with 600-900 km shortening in the Himalaya (DeCelles et al., 2002; Robinson et al., 2006; Yin et al., 2010b; Long et al., 2011; Webb, 2013) and 300-400 km of north-south shortening reported across all of Tibet (e.g., Yakovlev and Clark, 2014). These low values for Tibetan shortening need to be reconsidered in light of detailed field and seismic subsurface data. By integrating my shortening estimates across the central Qilian Shan-Nan Shan thrust belt with other robust estimates discussed in this paper (e.g., Gaudemer et al., 1995; Meyer et al., 1998; Yin et al., 2008a, 2008b; Reith, 2013; Gao et al., 2013), I suggest that the entire 350-km-wide Qilian Shan-Nan Shan thrust belt accommodates a minimum of 215-300 km Cenozoic shortening. Higher strain of >53% is occurring along the northern plateau margin, whereas lower strain of >30-45% is occurring within the thrust belt interior (Table 2.2). Given that similar strain magnitudes have been documented in the Qimen Tagh, Qaidam Basin, and North Qaidam thrust belts (Yin and Harrison, 2000; Yin et al., 2007a, 2008a, 2008b; Wang et al., 2011) (Figs. 2.1 and 2.4; Table 2.2), at least 250-350 km of north-south Cenozoic shortening may have been absorbed between Hexi Corridor and the Kunlun fault (Figs. 2.1, 2.18, and 2.19). These extrapolations require further testing, but demonstrate that crustal shortening and the construction of the northeastern Tibetan Plateau play a significant role in accommodating the >2000 km convergence between India and Asia.



### **2.8.5. Similar deformational styles along northern and southern plateau margins**

The style of deformation operating along the northern margin of the Tibetan Plateau mimics what is inferred to be occurring along the southern margin, in the Himalaya. Although models for the development of the Himalaya are rigorously debated (e.g., Argand, 1924; Dewey and Burke, 1973; Zhao and Morgan, 1987; Burchfiel et al., 1992; Nelson, 1996; Beaumont, 2001, 2004; DeCelles et al., 2002), it has been widely argued that the Indian mantle lithosphere has been underthrust beneath the Tibetan lithosphere (i.e., beneath the Tibetan Plateau) (Argand, 1924; Powell and Conaghan, 1973; DeCelles et al., 2002). Furthermore, contemporary strain is highly concentrated along the Main Frontal Thrust (MFT); that is, all of the present-day convergence across the Himalaya ( $\sim 20 \text{ mm yr}^{-1}$ ) is accommodated by deformation along the MFT (Lavé and Avouac, 2000; Zhang et al., 2004; Burgess et al., 2012).

These above similarities persist despite vastly different boundary conditions affecting each margin of the plateau. The magnitude of deformation and continental underthrusting are very different, but broadly correlate with convergence rate. The convergence rate across the Himalaya ( $\sim 20 \text{ mm yr}^{-1}$ ) is four times as high as the rate across the Qilian Shan-Nan Shan ( $\sim 5 \text{ mm yr}^{-1}$ ), and the magnitude of continental underthrusting beneath the Himalaya ( $\sim 800 \text{ km}$ ) is also about four times as the inferred magnitude of underthrusting in northern Tibet ( $\sim 200 \text{ km}$ ) (DeCelles et al., 2002; Zhang et al., 2004; Robinson et al., 2006; Webb, 2013; Ye et al., 2015). In addition, the magnitudes and rates of precipitation, erosion, and denudation across northern Tibet are much lower than for the Himalaya. As discussed in Section 2.8.2., older cooling ages (i.e., Mesozoic and older) across northern Tibet imply a low magnitude and rate of denudation (e.g., George et al., 2001). Conversely, across the arc-length of Himalaya, a range of late Cenozoic cooling ages (e.g.,  $^{40}\text{Ar}/^{39}\text{Ar}$  mica, AFT, zircon fission track ages) indicate rather rapid erosion

and denudation (e.g., Thiede and Ehlers, 2013; McQuarrie and Ehlers, 2015). The cooling age distribution broadly correlates with climate, and the present-day climate maps show that the Himalaya receive an order of magnitude more precipitation than the Qilian Shan (Liu et al., 2009).

Over the past two decades, many workers have focused on testing the hypothesis that climate and erosion exert a first-order control on continental tectonics and style of continental deformation (e.g., Beaumont et al., 2001, 2004; Wobus et al., 2003; Thiede et al., 2004), which has led to the formulation of climate-driven tectonic models for the development of the Himalaya (e.g., Beaumont et al., 2001). The tectonic development of the Qilian Shan-Nan Shan and northern Tibet can represent a “dry-orogen” analogue to test of the influence, or lack thereof, of climate in developing a Himalayan-style orogen. To the first-order, the different climatic conditions acting on both the north and south margins of the plateau do not appear to influence continental tectonics because the style of deformation across the Qilian Shan-Nan Shan thrust belt mimics the Himalaya. Instead, the magnitude of deformation and continental underthrusting correlates with convergence magnitude and rate. Although further analysis beyond the scope of this current study, these insights suggest that the style of continental deformation may not be significantly affected by climate and erosion. Both margins of the plateau are deforming in a similar manner, and thus climate-driven mechanisms (e.g., Beaumont et al., 2001; Thiede et al., 2004) for the development of a Himalayan-style orogen may not be required.

## 2.9. Conclusions

The following conclusions can be drawn based on detailed geologic mapping, seismic-reflection profile analysis, cross section construction and restoration, and crustal shortening estimation across the Qilian Shan-Nan Shan thrust belt of northern Tibet.

- (1) Existing satellite- and field-based Cenozoic shortening estimates across the Qilian Shan-Nan Shan thrust belt are typically low (e.g., <15-20%). I posit that these studies generally underestimate crustal strain across northern Tibet by missing blind structures and detachments. More robust studies, including those based on detailed geologic mapping, seismic reflection analyses, and regional bulk mass balances, suggest that strain across most of northern Tibet, from the Qimen Tagh in the south to the North Qilian Shan in the north, is a minimum of ~30-53%.
- (2) Detailed geologic mapping across four ranges in the Qilian Shan-Nan Shan thrust belt reveals numerous predominately north-dipping thrust faults that juxtapose high-grade metamorphic and early Paleozoic arc rocks against late Paleozoic and younger bedded sedimentary strata. These thrust sheets reactive the early Paleozoic Qilian orogen, and Cenozoic deformation is highly concentrated along the Qilian suture zone.
- (3) The restoration of balance cross sections along a ~98-km-long traverse across interior of the Qilian Shan-Nan Shan thrust belt indicate that the region has accommodated a minimum of ~53 km Cenozoic shortening or ~35% shortening strain. This shortening is similar to regional shortening estimates (Meyer et al., 1998; Yin and Harrison, 2000), and I suggest that this strain can be extrapolated across the entire ~350-km-wide Qilian Shan-Nan Shan thrust belt, with the exception of the North Qilian Shan frontal thrust system that has absorbed >53% strain.

- (4) Seismic reflection analysis across the North Qilian Shan reveals a south-dipping Cenozoic thrust system that places Paleozoic and Mesozoic strata on undeformed Mesozoic-Cenozoic sediments in the Hexi Corridor foreland. I estimate 25 km (54% strain), 33 km (53% strain), and 12 km (36% strain) of upper-crustal north-south shortening across this range. The lowest shortening estimate is likely due to deformation being partitioned between the Qilian Shan and the Yumu Shan thrusts. I prefer the values from the longest seismic reflection profile and suggest that the North Qilian Shan accommodates a minimum crustal shortening strain, shortening rate, and strain rate of ~53%,  $3.3 \pm 0.6 \text{ mm yr}^{-1}$ , and  $1.7 \times 10^{-15} \text{ s}^{-1}$ , respectively. Assuming that this shortening strain can be extrapolated across the entire frontal North Qilian Shan range, there has been a minimum of 50 km of north-south Cenozoic shortening across the northern margin of the Tibetan Plateau.
- (5) The observed strain distribution across the northern Tibetan Plateau—i.e., >50% across the plateau margin and >35% within the Qilian Shan-Nan Shan thrust belt interior—suggests that the dominant processes of plateau construction operating in northern Tibet are a combination of distributed crustal shortening, pure shear thickening, and southward underthrusting of the Asian mantle lithosphere. Most of the modern crustal thickness across the region can be explained by 30-45% shortening of crust with an initial thickness of ~40 km. The higher strain recorded along the northern plateau margin may result from the southward underthrusting of Asian mantle lithosphere, which is supported by recent receiver function analysis (Ye et al., 2015). I present a 2-D lithospheric-scale model that relates these two deformation mechanisms to the observed strain in north Tibet.
- (6) Accordingly, I suggest that the 350-km-wide Qilian Shan-Nan Shan thrust belt has accommodated a minimum of 210-300 km of Cenozoic north-south shortening. By

incorporating other existing shortening estimates across northern Tibet, I tentatively extrapolate the observed strain distribution to suggest that more than 250-350 km of north-south Cenozoic shortening has been absorbed within the Tibetan Plateau between the Kunlun fault in the south and the Hexi Corridor in the north, which is almost double the commonly cited shortening value of ~150 km.

- (7) Most of the present-day convergence between North China and Tibet is focused along the northern plateau margin, similar to Himalayan shortening where strain is concentrated along the Main Frontal Thrust (Lavé and Avouac, 2000; Burgess et al., 2012). Although magnitude of deformation across the Qilian Shan-Nan Shan and Himalaya is quite different, which may simply reflect different magnitudes and rates of convergence across each orogen, both thrust systems involve continental underthrusting and focused shortening along the frontal thrust faults. The similarity of deformational styles along the southern and northern margins of the Tibetan Plateau exists despite vastly different erosion and denudation rates, which suggests that climate may not play a significant role in the development of a Himalayan-style orogen (cf. Beaumont et al., 2001; Thiede et al., 2004).

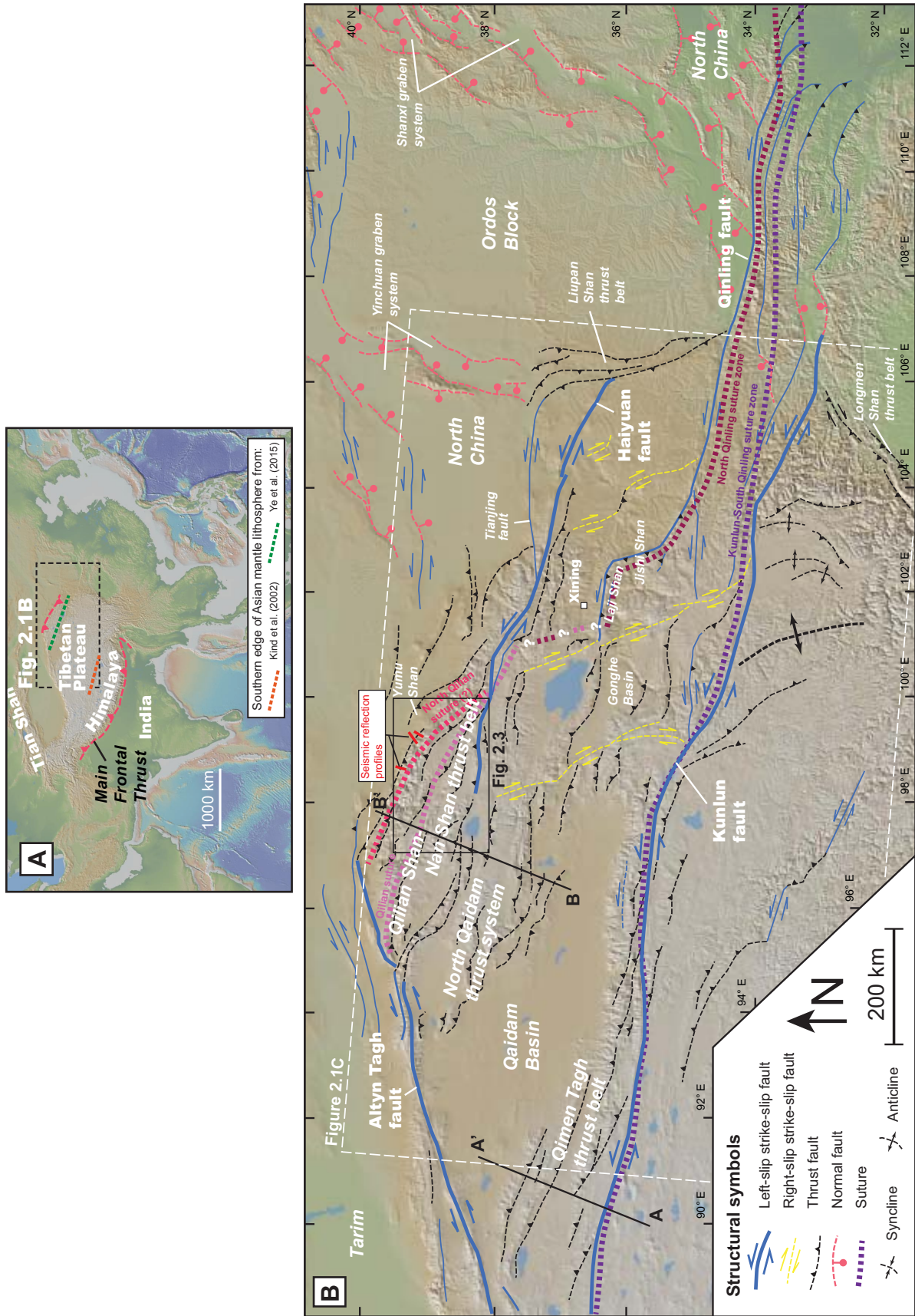


**Figure 2.1.** Complete caption on following page.

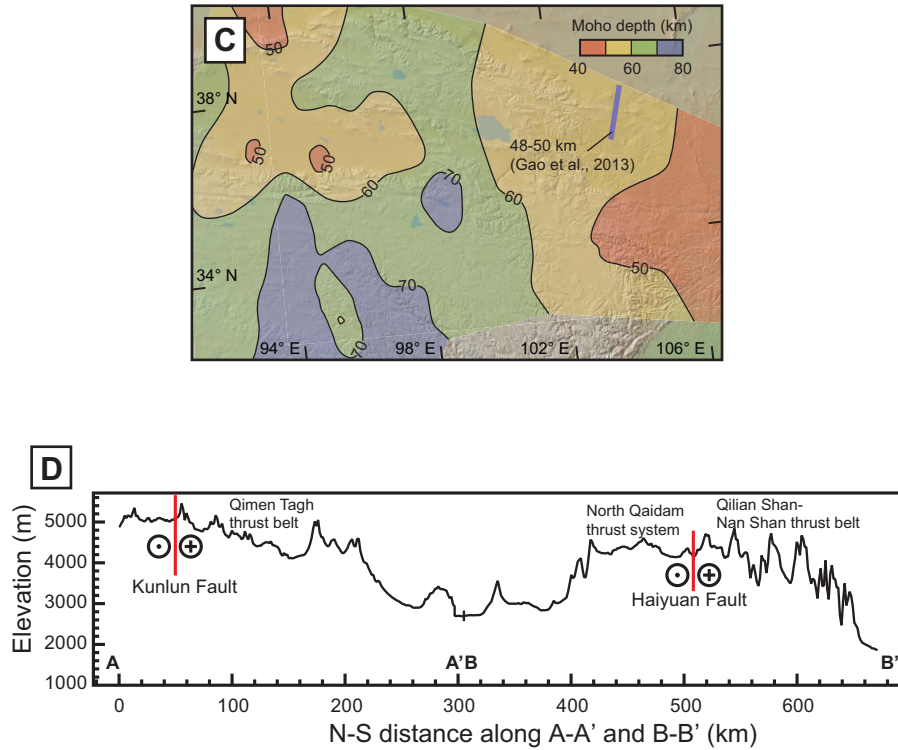


**Figure 2.1.** (A) Map of the Himalaya-Tibetan orogen and surrounding regions, showing the location of Figure 2.1B. The southern edge of Asian lithosphere is from Kind et al. (2002) and Ye et al. (2015). (B) Regional tectonic map of the northeastern Tibetan Plateau. Also shown are the locations of Figures 2.1C and 2.3 and the seismic reflection profiles (Figs. 2.14-2.16). Structures are from Burchfiel et al. (1991), Gaudemer et al. (1995), Taylor and Yin (2009), and Gao et al. (2013). (C) Contoured crustal thickness estimates derived from receiver-function analysis of Yue et al. (2012). Also shown for comparison is the Moho depth imaged by seismic reflection analysis of Gao et al. (2013). (D) Topographic profiles across northeastern Tibet (profiles A-A' and B-B' in Fig. 2.1B). The digital topographic basemaps and profiles from GeoMapApp software (Ryan et al., 2009) are available at <http://www.geomapapp.org/>.

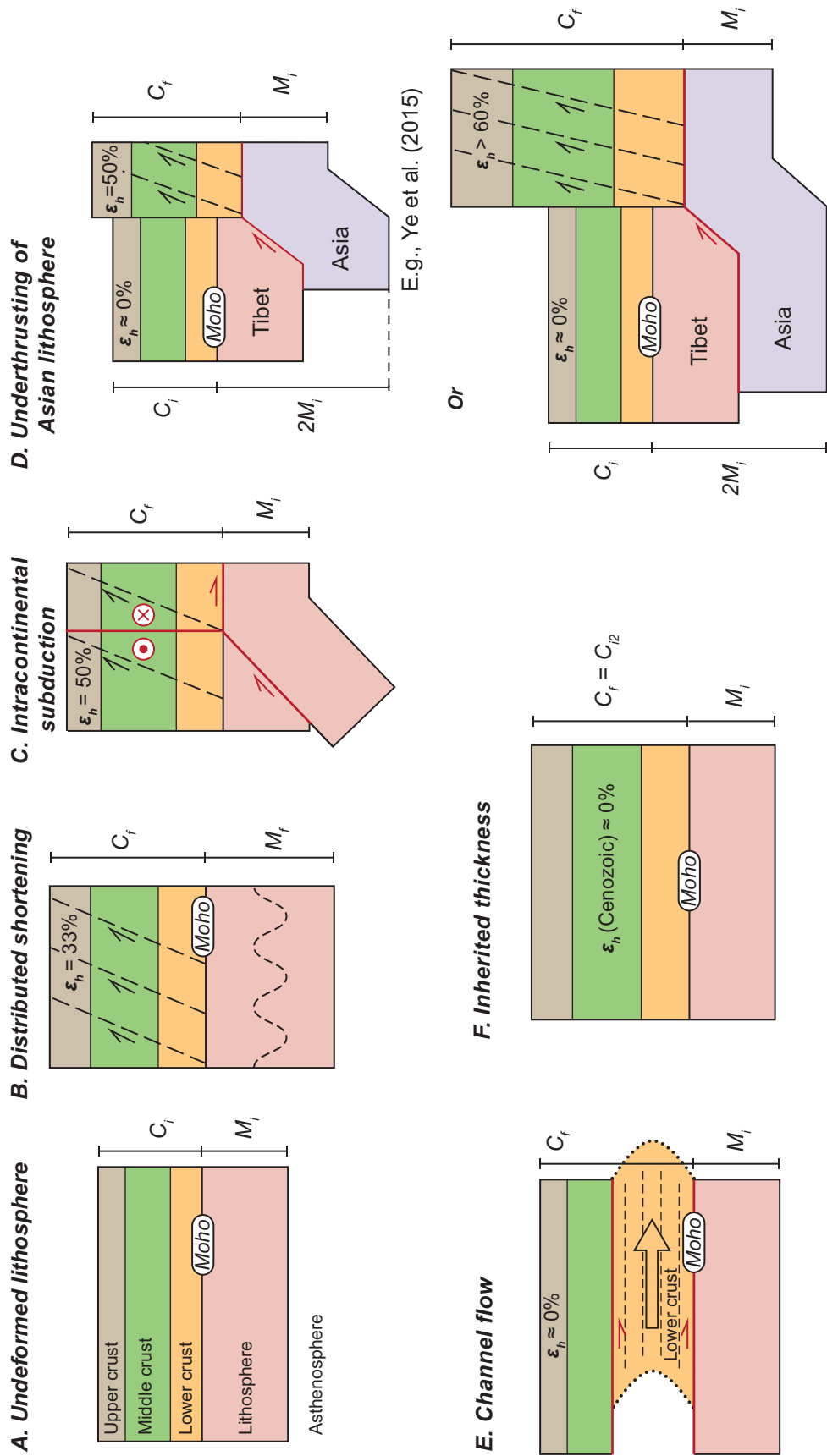


**Figure 2.2.** Complete caption on following page.



**Figure 2.2 (continued).** Competing end-member models for the continental deformation and the development of the northeastern Tibetan Plateau.  $C_i$  and  $C_f$  represent the initial and final thickness of the crust, respectively, and  $M_i$  and  $M_f$  represent the initial and final thickness of the mantle lithosphere, respectively (see text). Red lines indicate major detachment surfaces or strike-slip faults. (A) Continental lithosphere prior to deformation. (B) The distributed shortening model predicts vertically uniform strain, evenly spaced thrust faults, and pure shear thickening of the entire continental lithosphere. (C) The intracontinental subduction model requires subduction of the mantle lithosphere, which is decoupled from the deforming crust. The concentrated mixed-mode deformation (i.e., left-slip and thrust faulting) and subduction occur along older suture zones. (D) The underthrusting model predicts crustal shortening at the plateau margins to accommodate southward motion of the Asian mantle lithosphere: strain at this margin is either large ( $>60\%$  strain) if the Asian mantle lithosphere is underthrust to central Tibet (e.g., Kind et al., 2002) or more minor ( $\sim 50\%$  strain) if it is only underthrust to Qaidam Basin (e.g., Ye et al., 2015). Little crustal shortening should occur away from the plateau margins. (E) The channel flow models predict lateral motion of the lower crust and little shortening in the upper crust. Vertical inflation of a ductile channel leads to thickening of the crustal lithosphere. (F) The present-day thickness may be inherited from an older pre-Cenozoic collisional event; in this case, the final present-day crustal thickness  $C_f$  is equal to the pre-Cenozoic crustal thickness  $C_{i2}$ , which was attained during a pre-India-Asia collision thickening process.

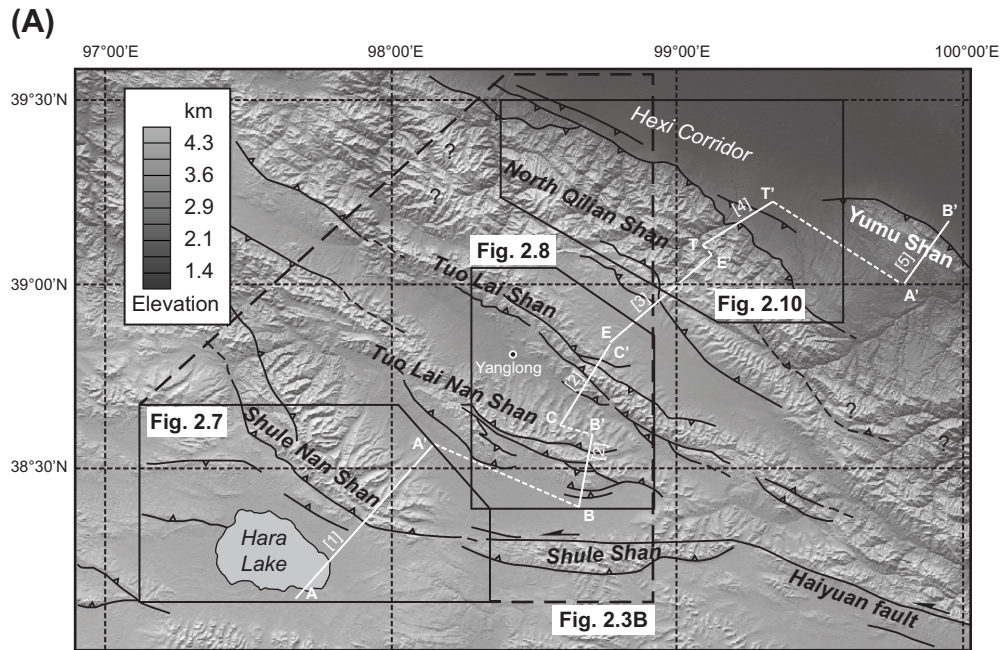


**Figure 2.3.** (A) Cenozoic fault map of northern Tibet after Yin et al. (2007a, 2008a, 2008b), Gao et al. (2013), and my own observations. Underlying basemap is from GeoMapApp software (Ryan et al., 2009). Boxes indicate the locations of map areas in Figure 2.3B, 2.7, 2.8, and 2.10. Also shown are the cross section lines across the central Qilian Shan-Nan Shan thrust belt. Cross section data: [1] cross section in Figure 2.12 based on mapping presented in Figure 2.7, [2] cross sections in Figure 2.13 based on detailed mapping presented in Figure 2.8, [3] inferred section and shortening based on compiled regional maps (Gansu Geological Bureau, 1989; Qinghai BGMR, 1991; Pan et al., 2004), [4] seismic reflection analysis in Figure 2.15 and mapping in Figure 2.10, and [5] work by Tapponnier et al. (1990).

(B)

### Regional geologic map of the Central Qilian Shan-Nan Shan thrust belt

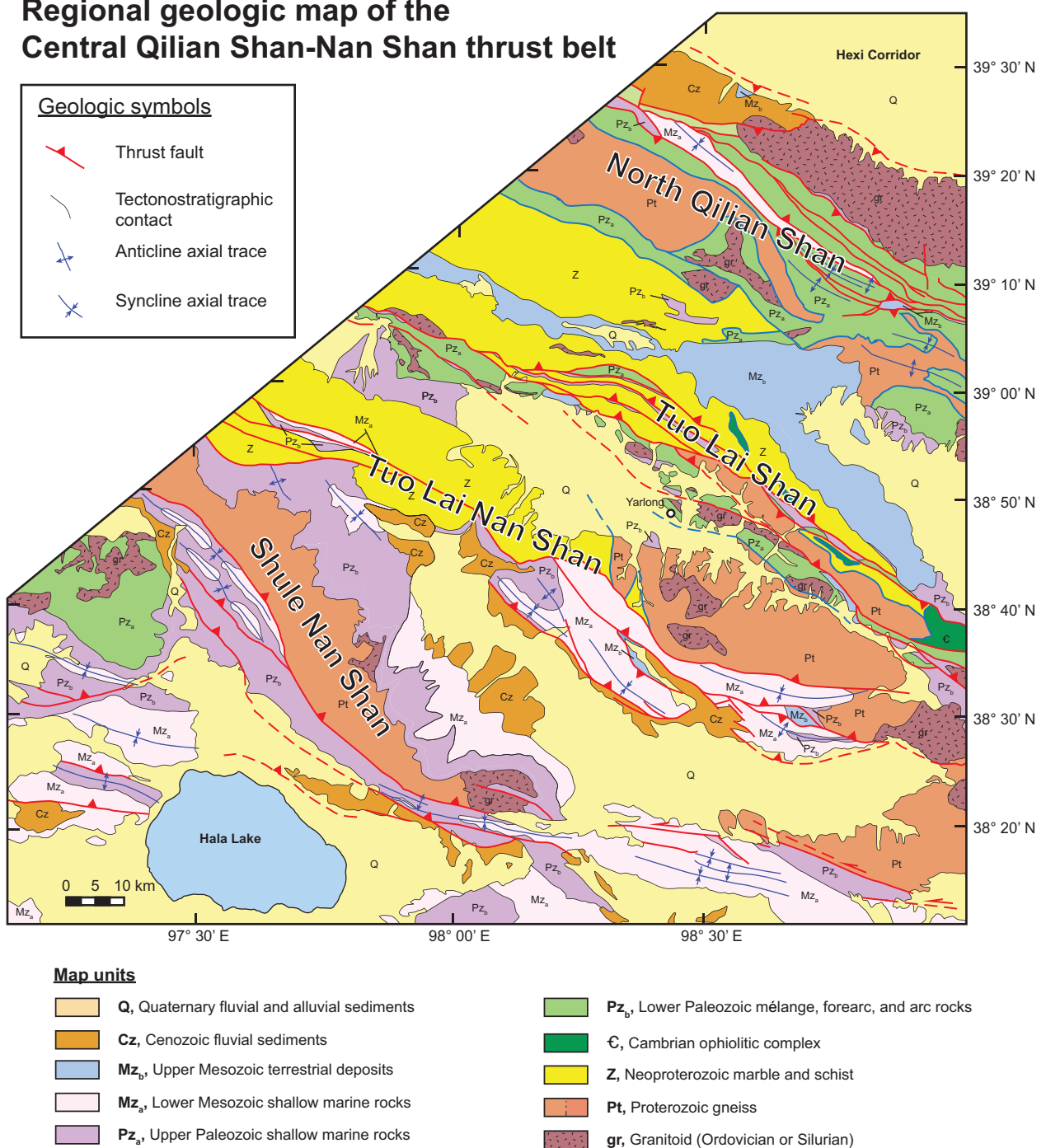


**Figure 2.3 (continued).** (B) Regional geologic map of the central Qilian Shan-Nan Shan thrust belt based on Gansu Geological Bureau (1989), Qinghai BGMR (1991), Pan et al. (2004), and my own geologic mapping and structural interpretations. Map units from a simplified tectonostratigraphic scheme. Location is shown in Figure 2.3A.

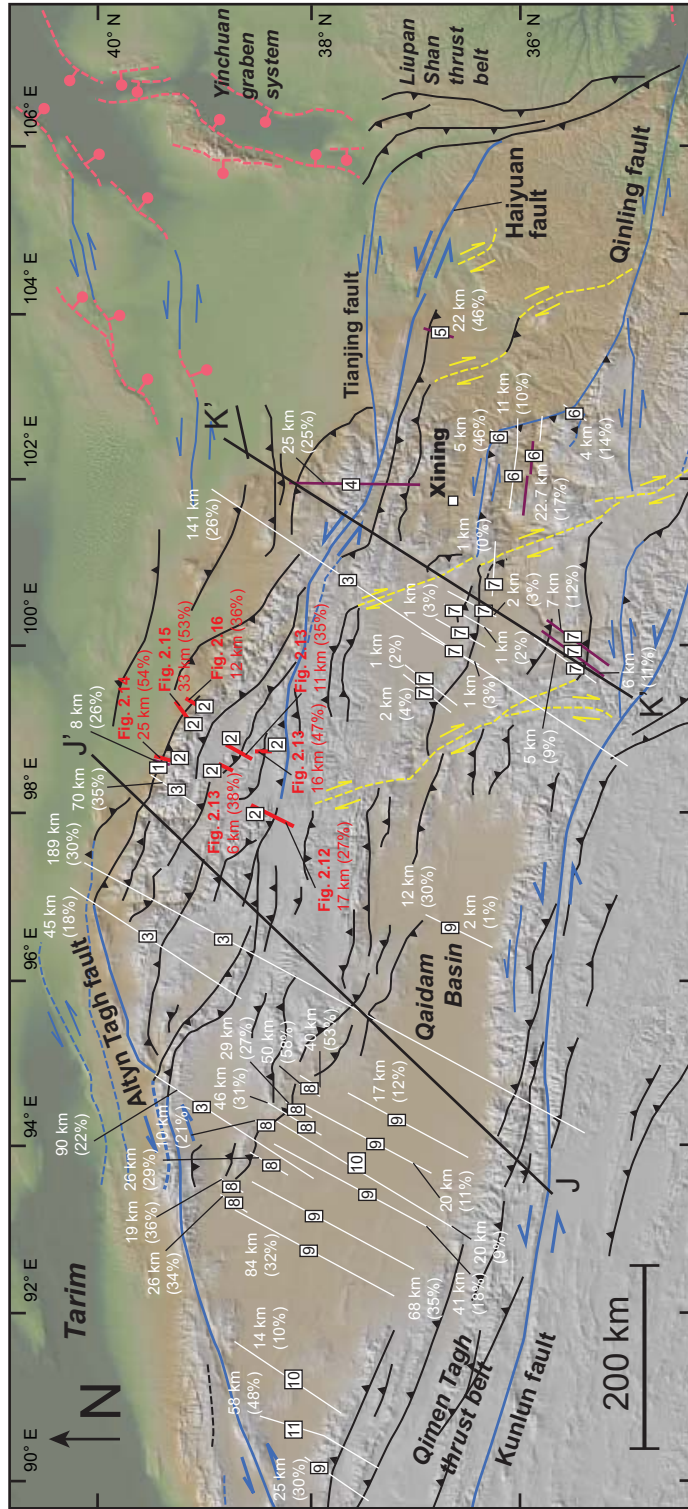
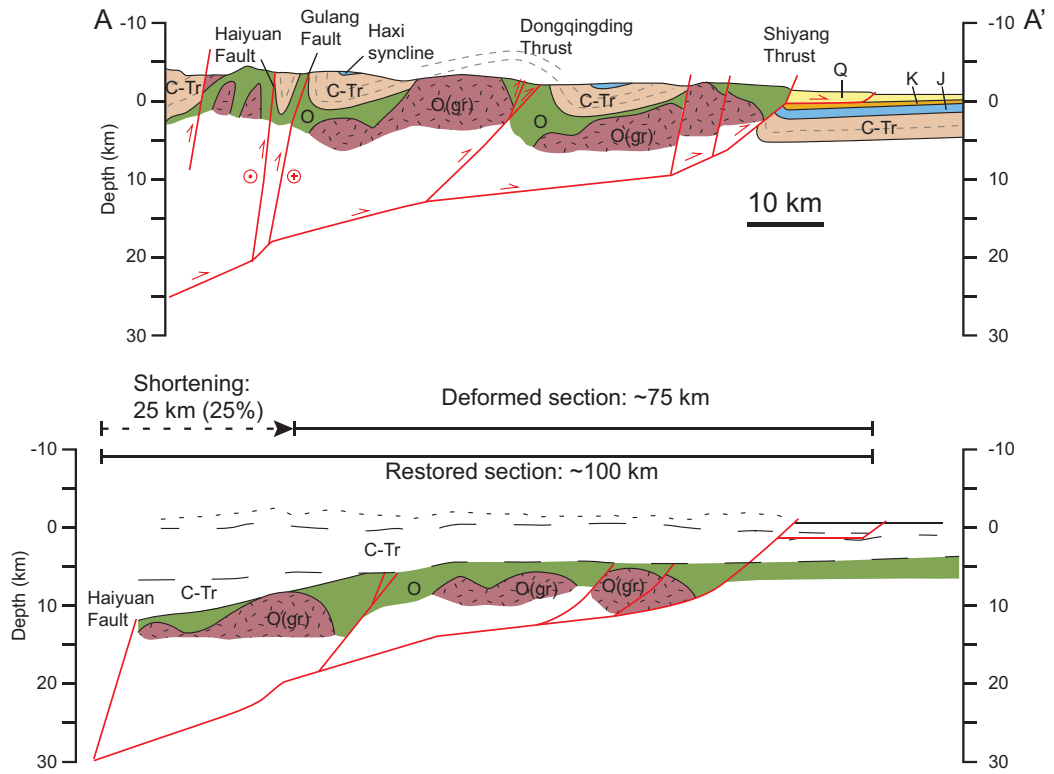


**Figure 2.4.** Simplified Cenozoic fault map of the northeastern Tibetan Plateau showing the existing shortening estimates that are compiled in Table 2.2. Purple section lines correspond to cross sections and shortening estimates that are shown as examples in Figure 2.5. Red lines show the cross sections and shortening estimates from this study. Symbols are as in Figure 2.1. For figure clarity some sections and shortening estimates from the North Qaidam thrust system (Yin et al., 2008a) have been omitted. The boxed numbers correspond to the reference for each shortening strain estimate: 1—Zheng et al. (2010), 2—this study, 3—Meyer et al. (1998), 4—Gaudemer et al. (1995), 5—Gao et al. (2013), 6—Lease et al. (2012), 7—Craddock et al. (2014), 8—Yin et al. (2008a), 9—Yin et al. (2008b), 10—Zhou et al. (2006), 11—Yin et al. (2007a). Section lines J–J' and K–K' correspond to the crustal thickness and shortening magnitude relationship explored in Figure 2.18.

**A. Gaudemer et al. (1995)**



**B. Lease et al. (2012)**

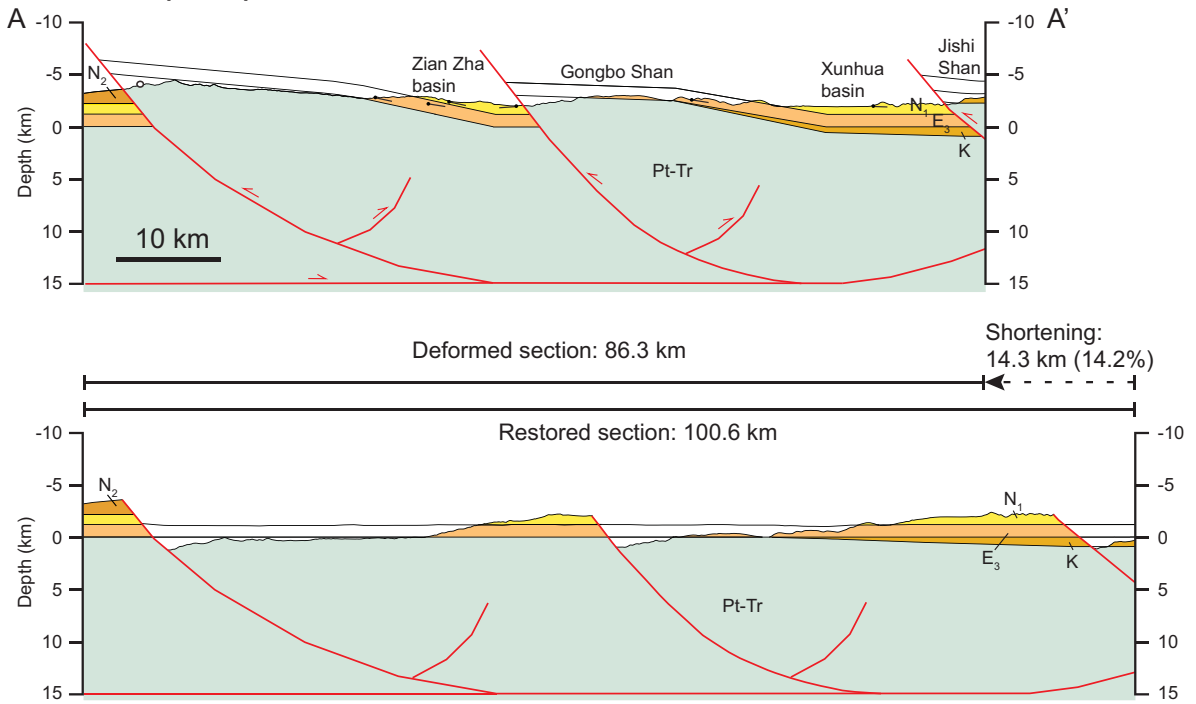
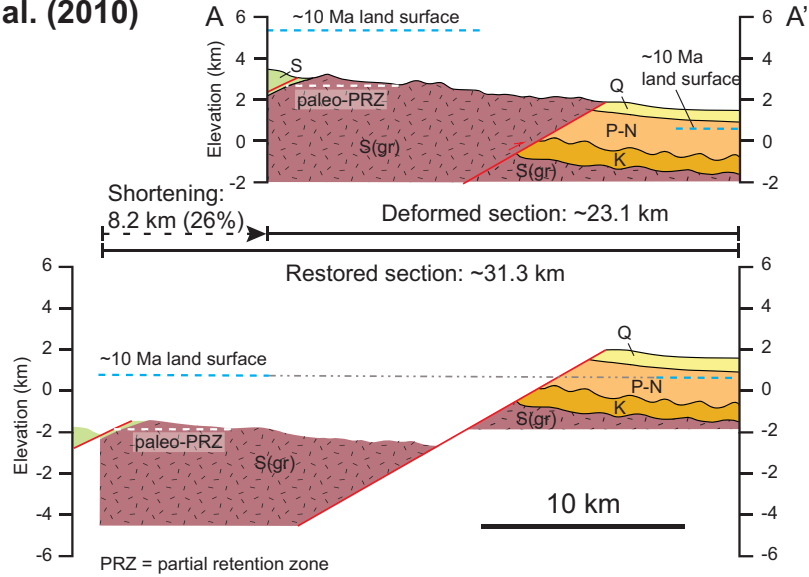


**Figure 2.5.** Complete caption can be found on page following (E).

**C. Zheng et al. (2010)**



**D. Gao et al. (2013)**

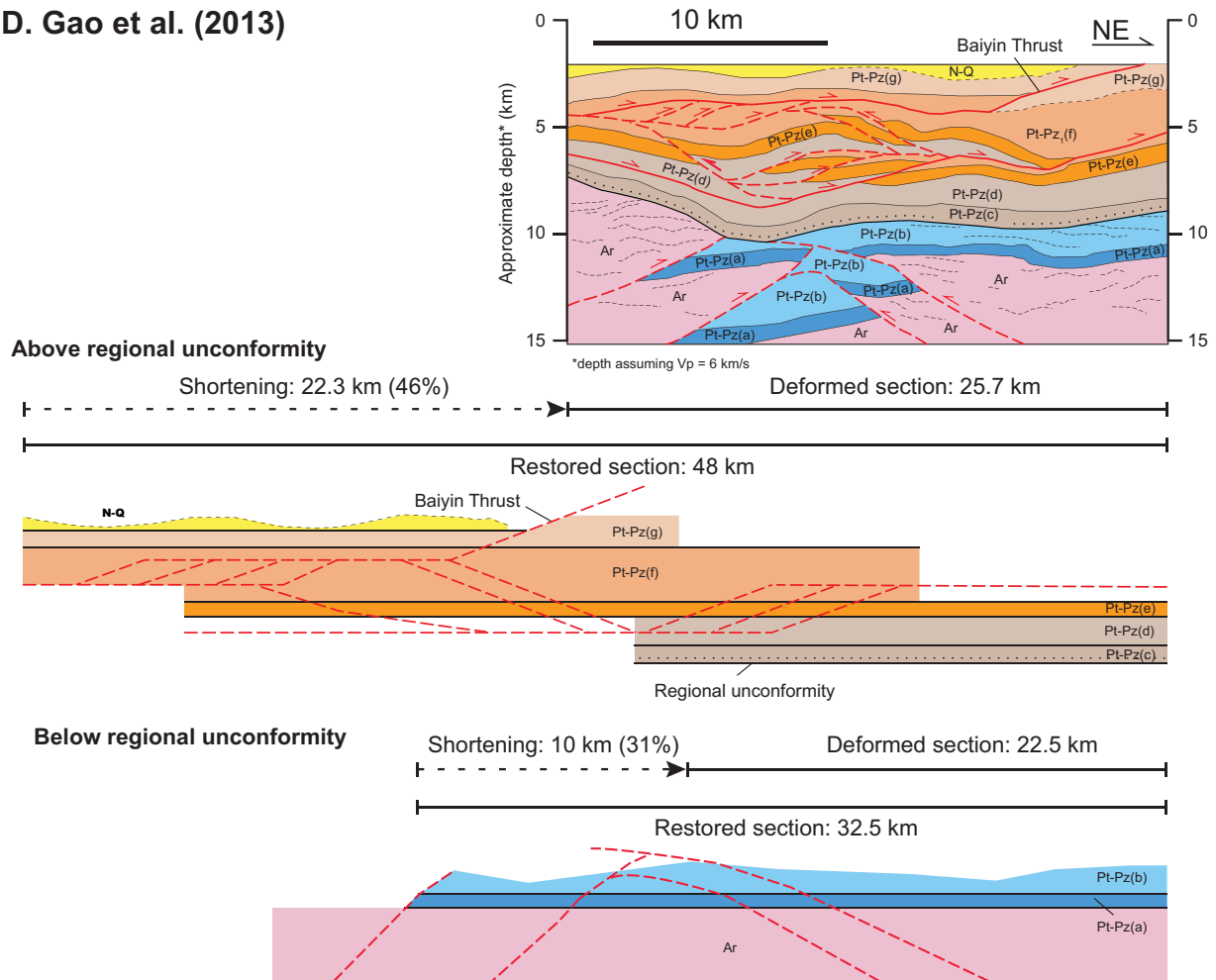


**Figure 2.5 (continued).** Complete caption can be found on page following (E).

E. Craddock et al. (2014)

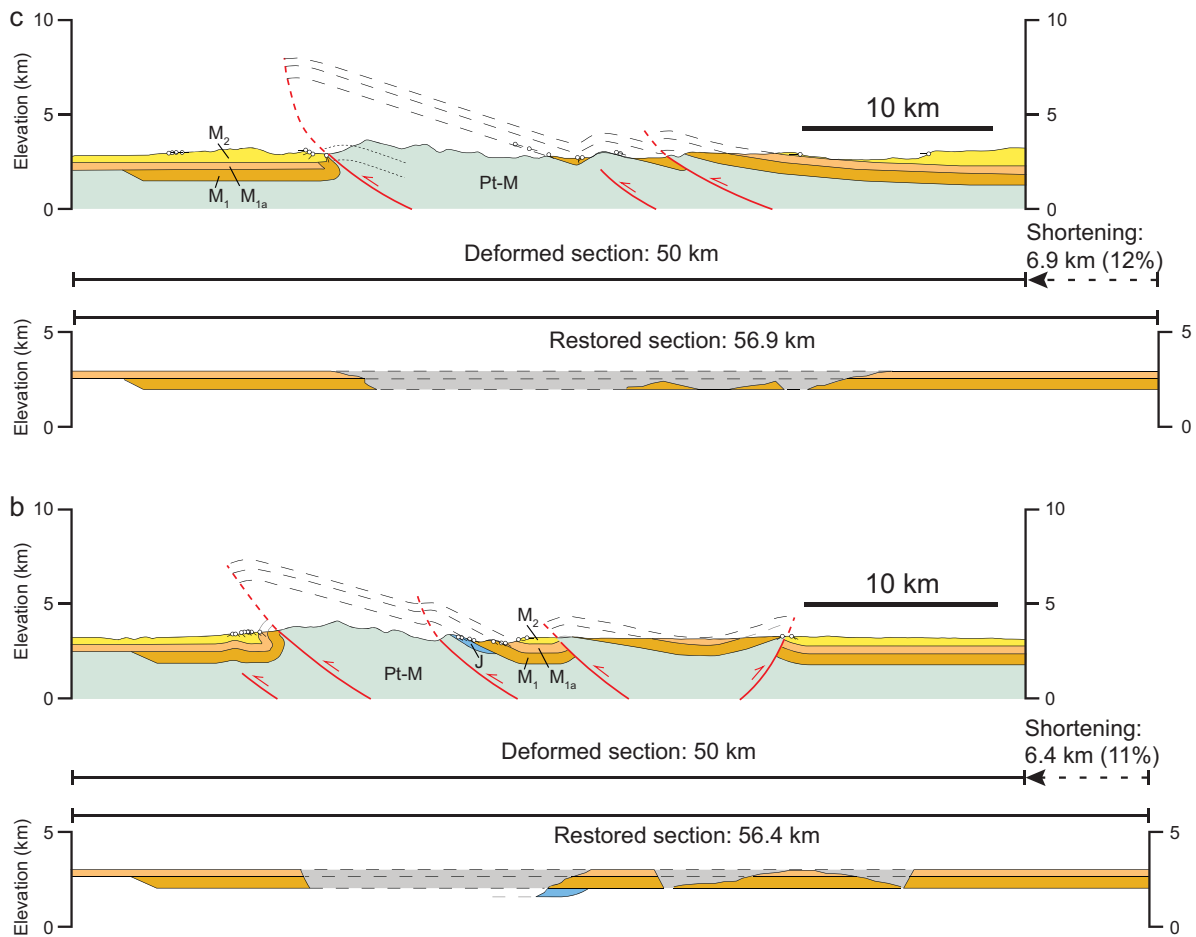


Figure 2.5 (continued). Complete caption on following page.

**Figure 2.5 (continued).** Selected examples of existing cross sections and shortening estimates across northern Tibet. Locations are shown in Figure 2.4. Cross sections were redrafted in original style and modified only to allow comparison among them (e.g., similar-age units are the same color). (A) Cross section across the eastern Qilian Shan from Gaudemer et al. (1995). Line-length restoration of the section used the base of the Carboniferous strata as a marker horizon and the section was not restored across the left-slip Haiyuan fault. (B) One of three west-east cross sections constructed across the Xunhua Basin-Jishi Shan by Lease et al. (2012). The restoration involved line-length restoration of the base of the Cenozoic strata, and deformation within pre-Cenozoic units is not considered. Note that the depth to detachment and the fault kinematics (oblique versus pure dip slip) on these west-east sections remain unconstrained. For explanation of subscripts 1-3, please see original text of Lease et al. (2012). (C) Schematic cross section across the northern Qilian Shan frontal thrust zone by Zheng et al. (2010). The section does not incorporate kinematic data, but restores an apatite helium paleo-partial retention zone (PRZ) in the hanging wall and growth strata in the footwall to constrain vertical fault throw. The assumption of a single fault with a constant dip (30°; Yang et al., 2007a) yields a minimum horizontal shortening estimate. (D) Upper crustal structures associated with the Baiyin thrust from a regional seismic reflection profile obtained by Gao et al. (2013). The interpreted section was constructed by analyzing prominent reflectors and extrapolating surface structures to depth. Note that the depth scale assumes a seismic velocity of 6 km/s throughout the section (e.g., Liu et al., 2006). Line-length restoration of the section, above and below an inferred Paleozoic unconformity, restores prominent reflectors to horizontal. For explanation of subscripts a-g, please see original text of Gao et al. (2013). (E) Two of three north-south cross sections across the Gonghe Nan Shan by Craddock et al. (2014). These sections assume that the tilted Cenozoic strata are forelimbs and backlimbs of fault-bend folds. Deformation within pre-Miocene units is not considered. Ar—Archean; C—Carboniferous; E—Eocene; J—Jurassic; K—Cretaceous; Mz—Mesozoic; N—Neogene; O(gr)—Ordovician granite; P—Paleogene; Pt—Proterozoic; Pz—Paleozoic; Q—Quaternary; S—Silurian; Tr—Triassic; Vp—P wave velocity.



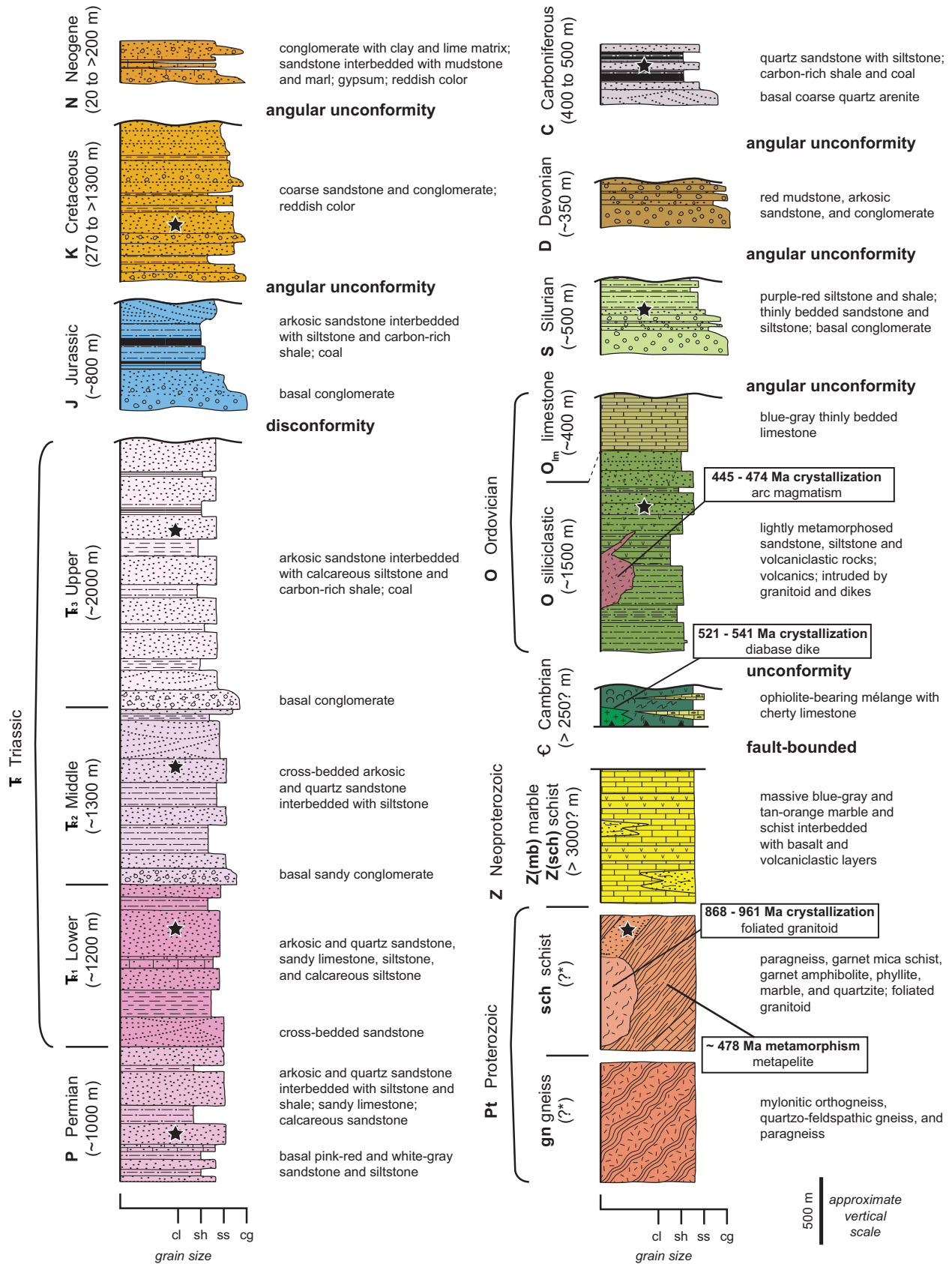


Figure 2.6. Complete caption on following page.

**Figure 2.6 (continued).** Lithostratigraphy of the central Qilian Shan, specific to the Tuo Lai and Shule Shan. Age assignments from Qinghai BGMR (1991), Pan et al. (2004), Xu et al. (2015), and our own observations. Also shown are U-Pb detrital zircon samples of major units (black stars) (Y. Zhang, unpublished data) and geochronology results from Chapter 5.

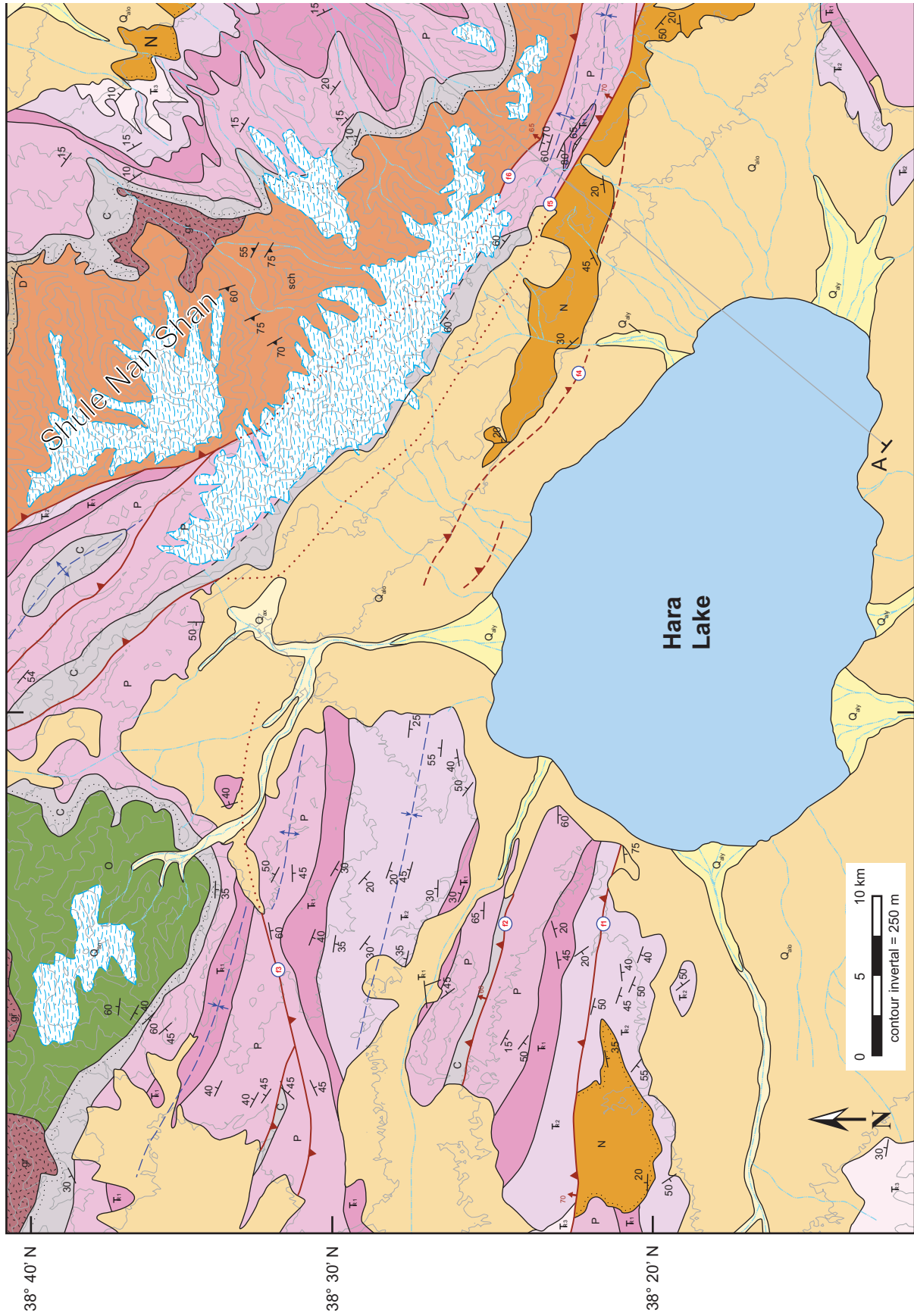
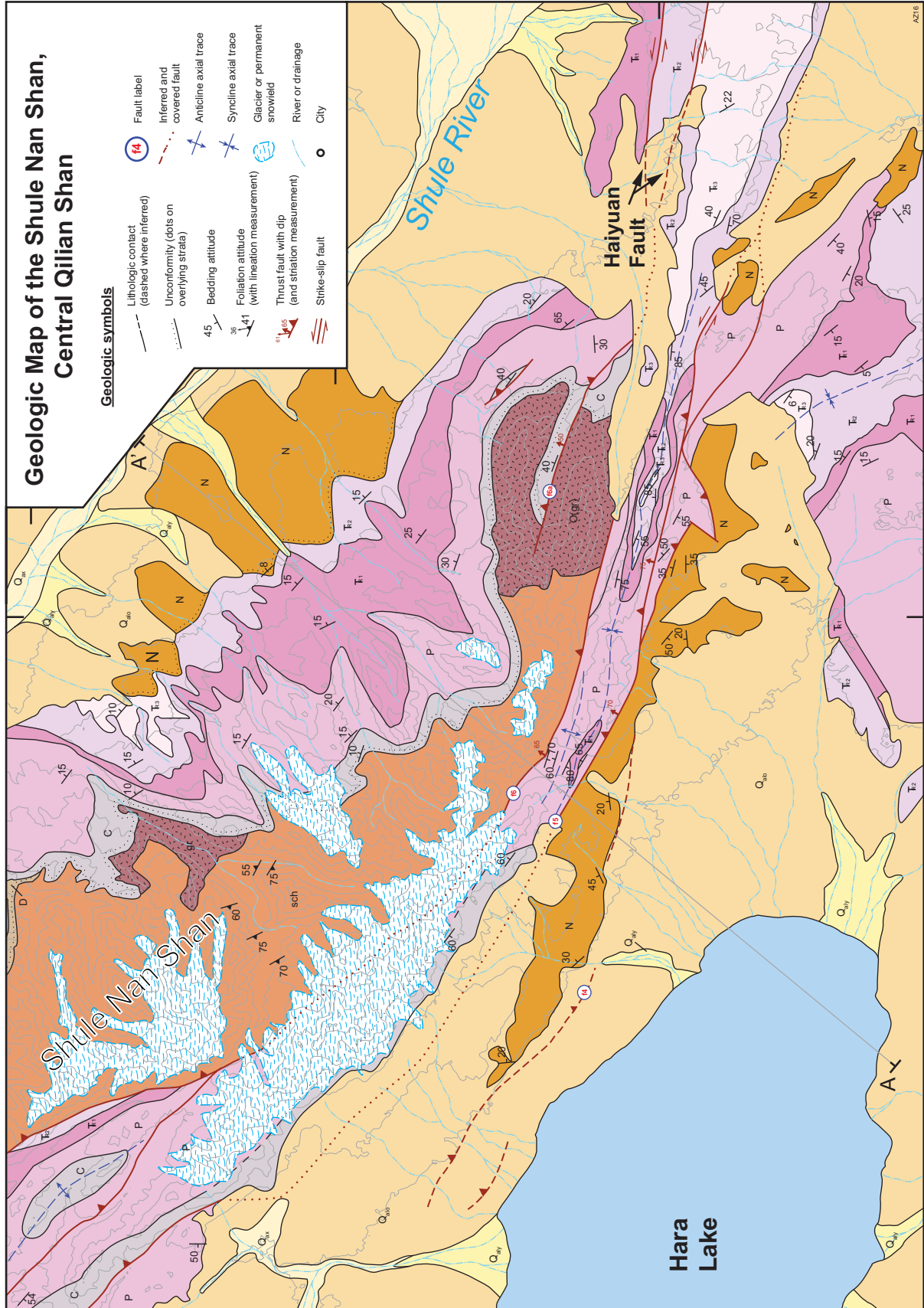
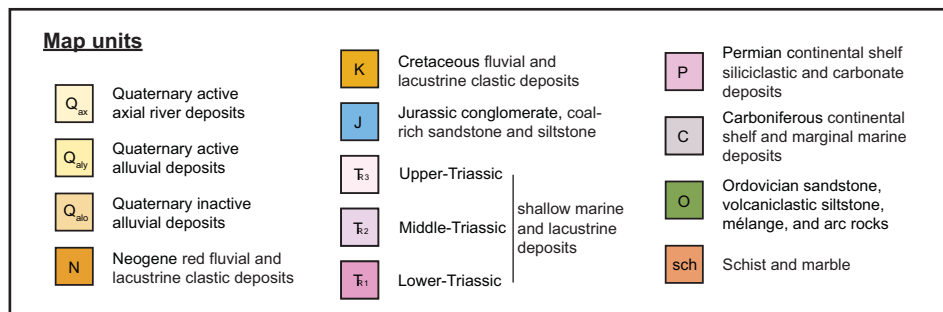


Figure 2.7. Complete caption can be found after map.



**Figure 2.7 (continued).** Complete caption on the following page. 98° 00' E



**Figure 2.7 (continued).** Geologic map of the Shule Nan Shan and Hara Lake basin (see Figures 2.1 and 2.2 for location) compiled from unpublished Chinese geologic maps, Gansu Geological Bureau (1989), Qinghai BGMR (1991), satellite-image analysis (e.g., Landsat 7 and 8, and Google Earth), and my own structural interpretations.

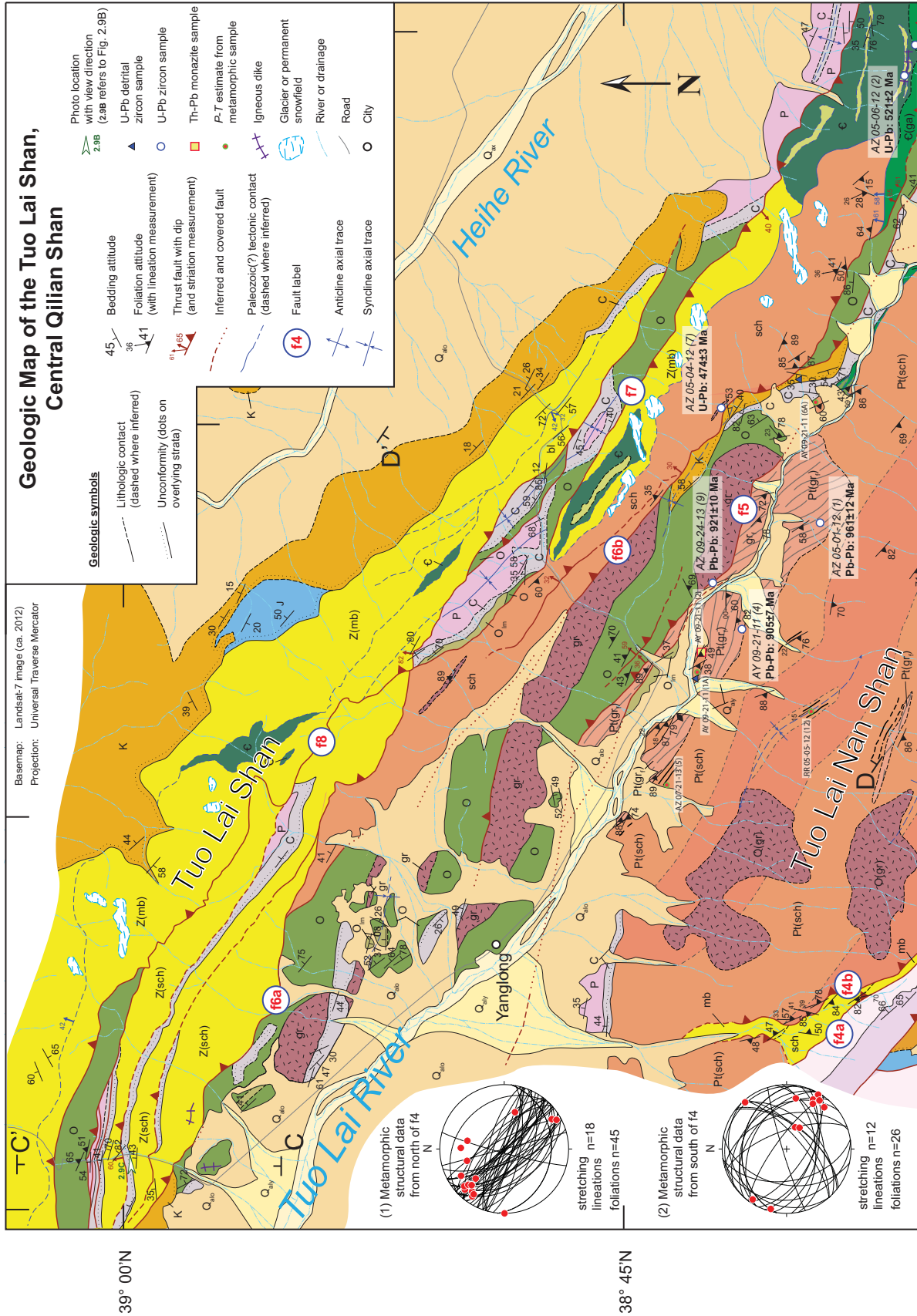


Figure 2.8. Complete caption can be found after map.

(A) (continued)

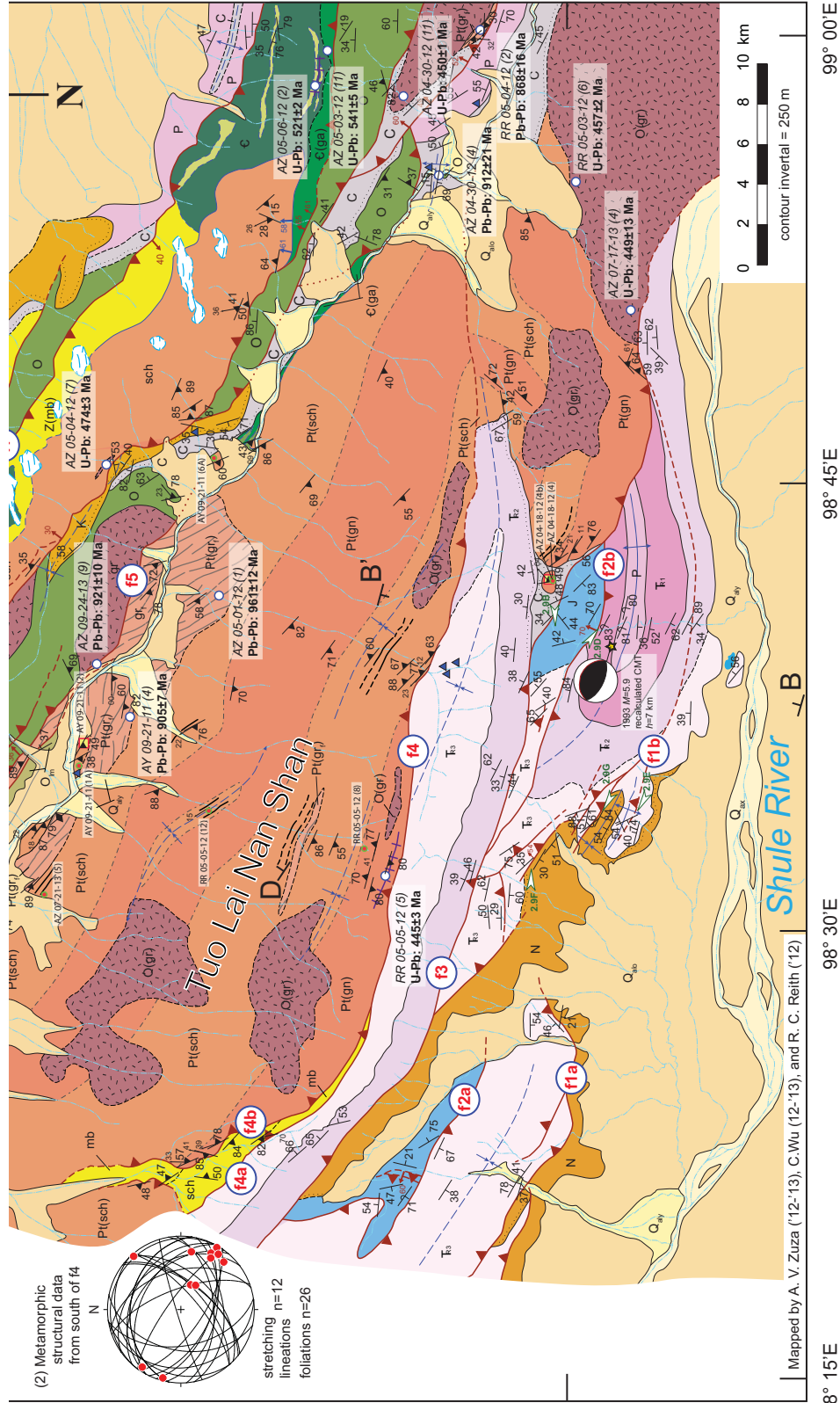
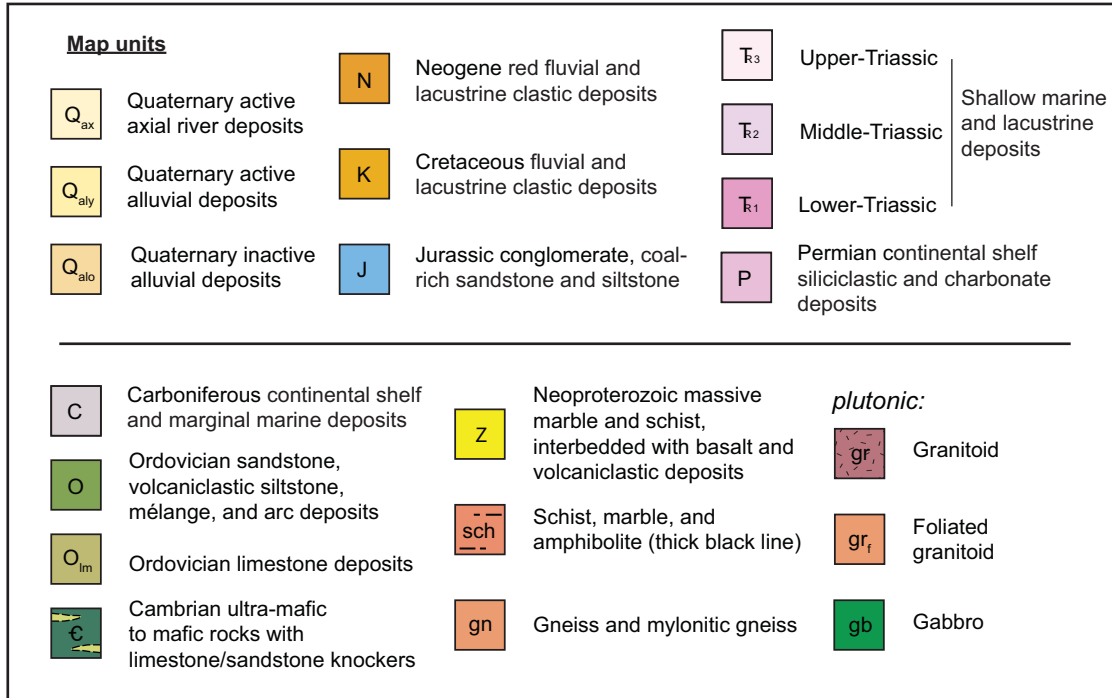
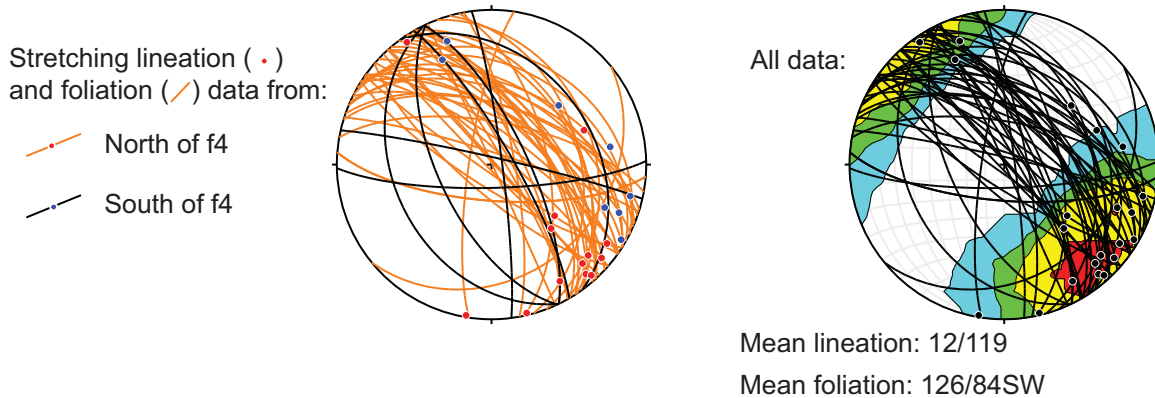


Figure 2.8. Complete caption can be found on following page.

**(A) (continued)**



**(B) Unfolded pre-Carboniferous structural data**



**Figure 2.8.** (A) Geologic map of the Tuo Lai Nan Shan and Tuo Lai Shan (see Figures 2.1 and 2.3 for location) based on compiled Chinese geologic maps (Gansu Geological Bureau, 1989; Qinghai BGMR, 1991), satellite-image analysis (e.g., Landsat 7 and 8, and Google Earth), and detailed mapping by A. Zuza, R. Reith (e.g., Reith, 2013), C. Wu, L. Wu, and J. Zhang. (B) Unfolded structural data (i.e., foliation and lineation attitudes) from the metamorphic basement units that represent the pre-Carboniferous state. Original data is in A.



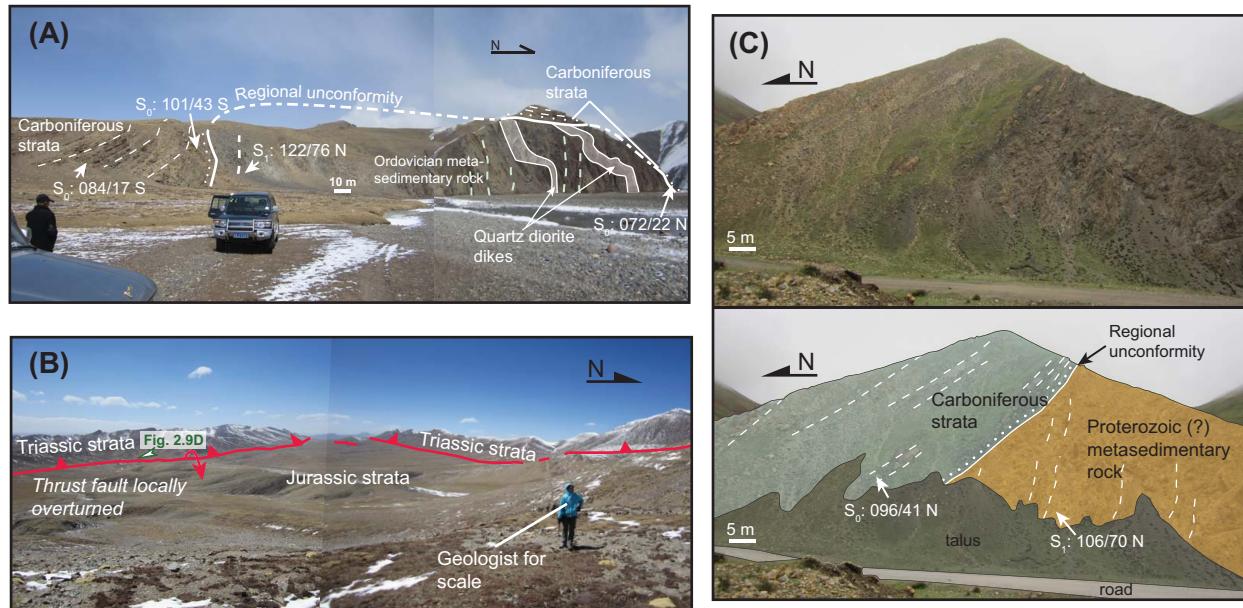


**Figure 2.9.** Field photographs from the central Qilian Shan. (A) Broad anticline showing regional unconformity at the base of the Carboniferous strata, which unconformably overlie Ordovician metasedimentary rocks. (B) Triassic strata thrust over a valley of Jurassic rocks from both the north and the south. Note that the north-vergent thrust in the south of this image places Lower Triassic rocks over Jurassic strata and is overturned. See Figure 2.9D for a close-up view. (C) The regional unconformity at the base of the Carboniferous strata, which unconformably overlie Proterozoic metasedimentary rocks.

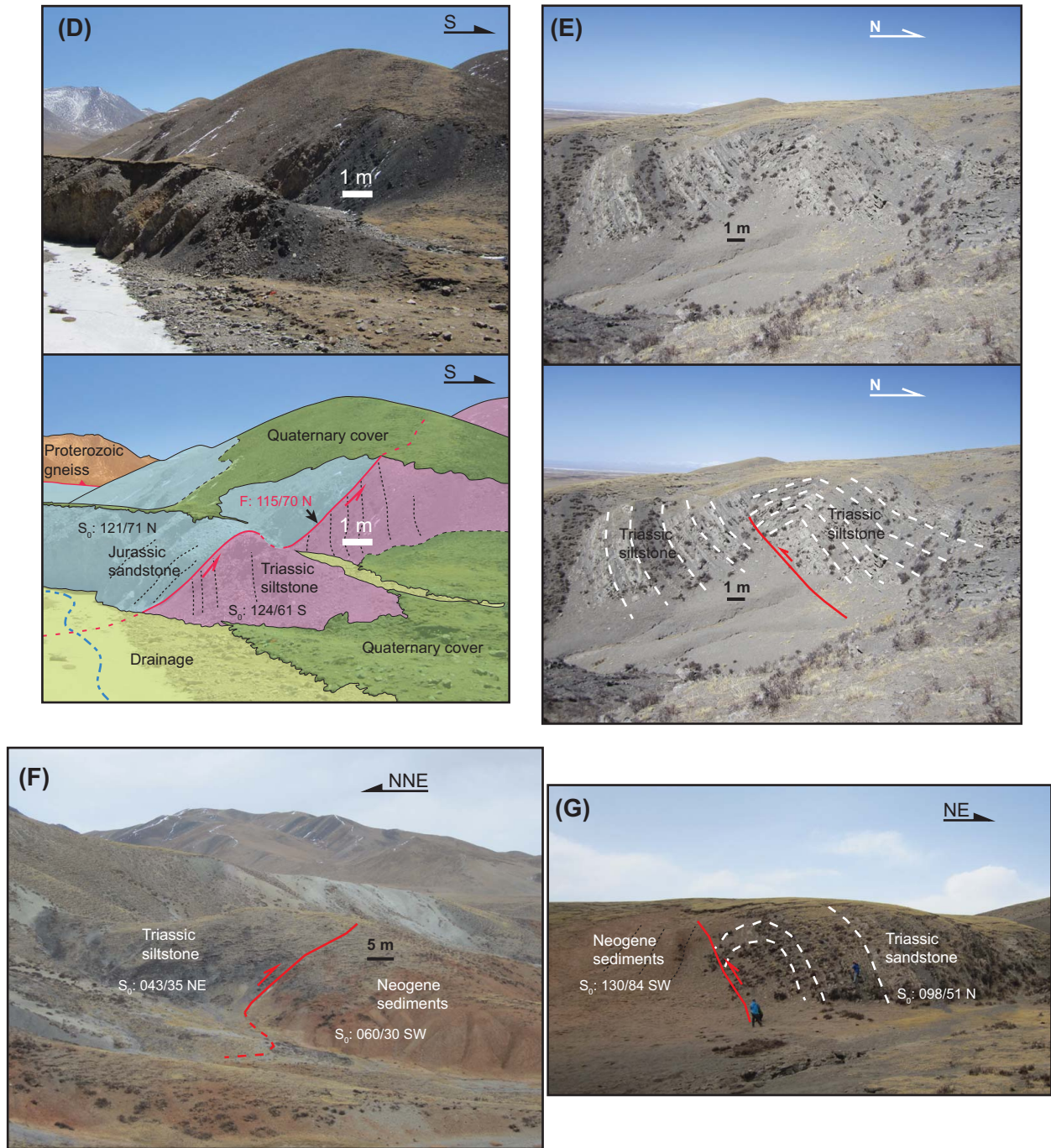


**Figure 2.9 (continued).** (D) Overturned thrust fault that originally placed Lower Triassic rocks on Jurassic strata. (E) Minor south-directed thrust fault within Triassic strata. (F-G) Thrust faults that place Triassic strata over Neogene sediments.

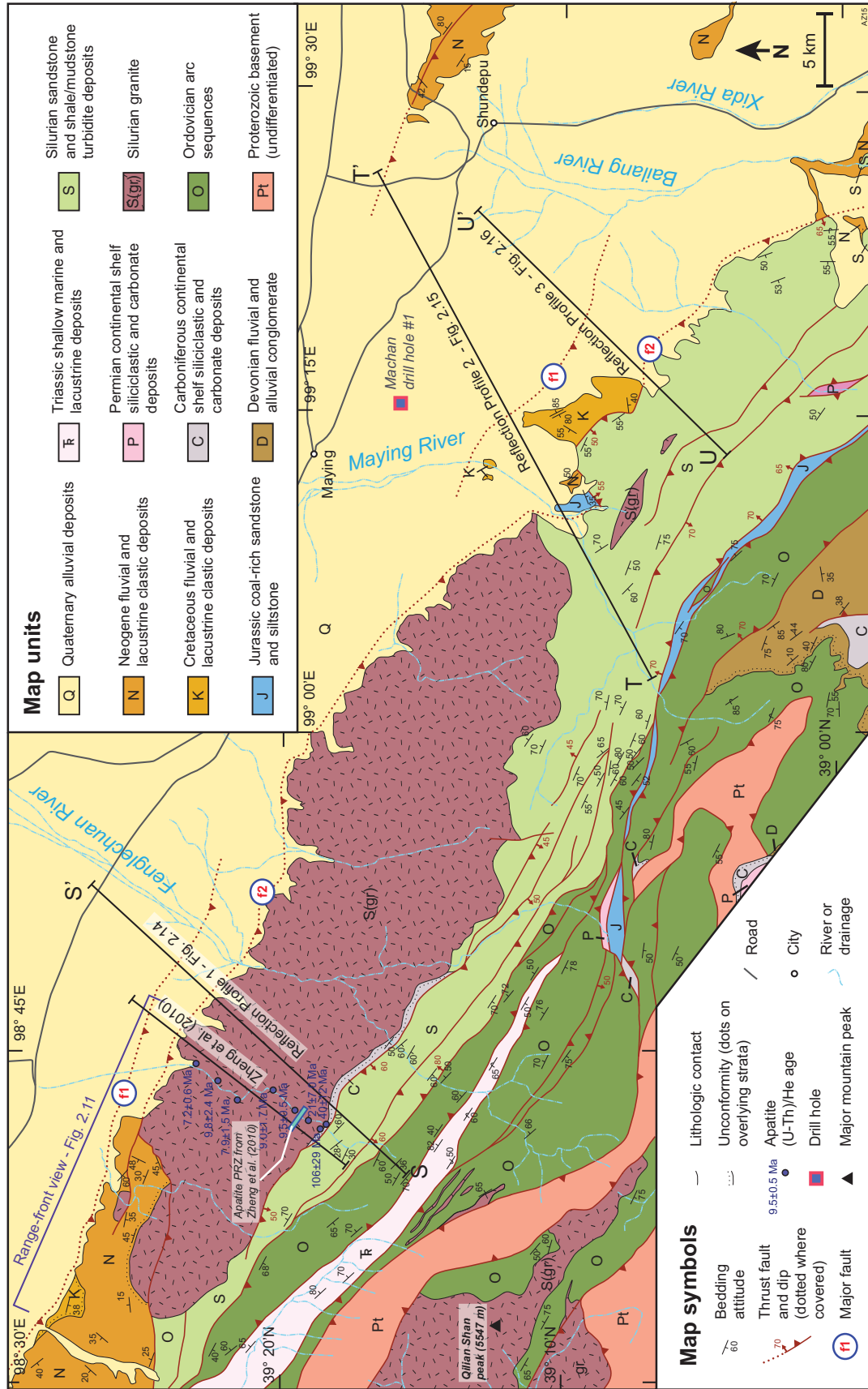


**Figure 2.10.** Geologic map of the northern Qilian Shan frontal thrust zone compiled from unpublished maps, Gansu Geological Bureau (1989), Qinghai BGM (1991), and our own structural interpretations. See Figure 2.3 for location. Satellite image viewpoint (Google Earth) of Figure 2.11 is shown. Also shown are the locations of three seismic reflection profiles (Figs. 2.14-2.16), a drill hole described in J. Wu et al. (2006), and the AHe traverse of Zheng et al. (2010). PRZ—partial retention zone.

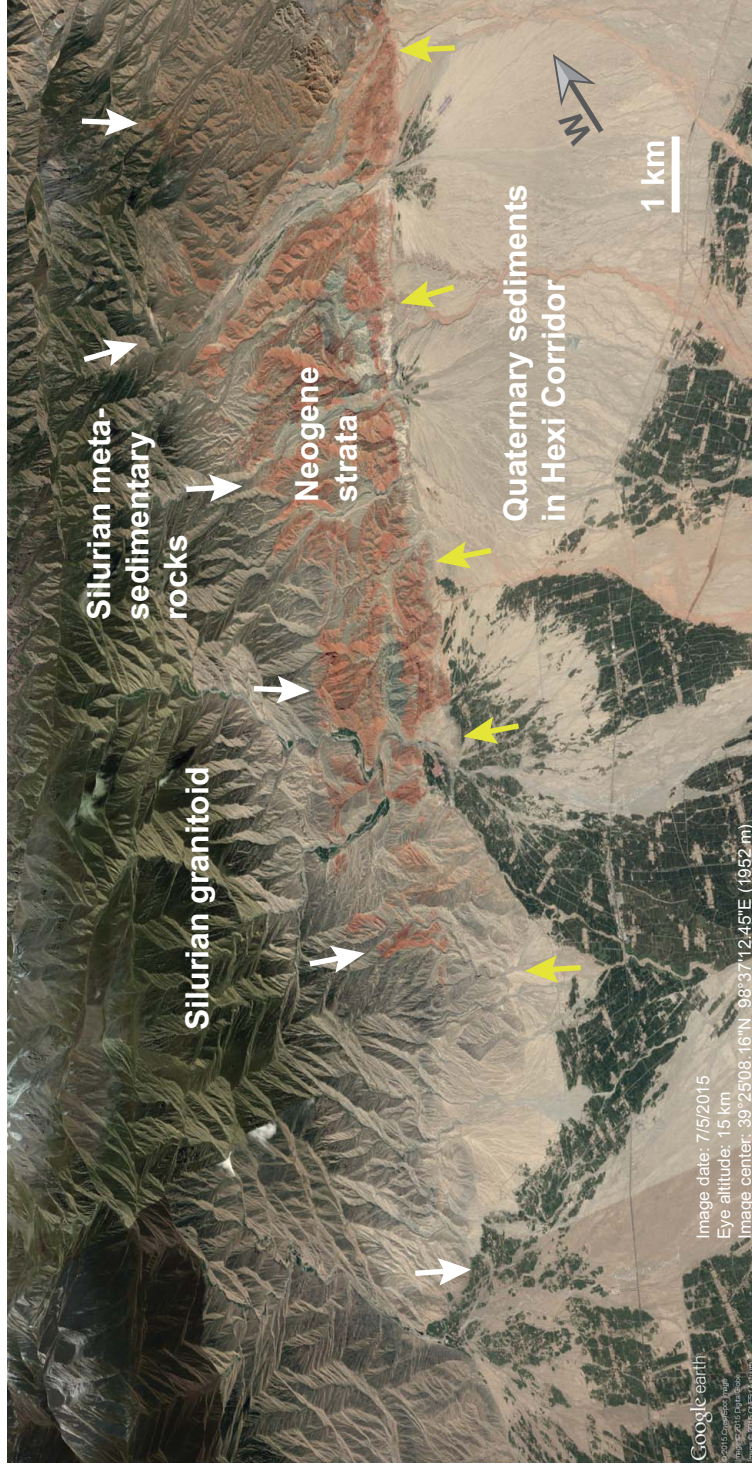
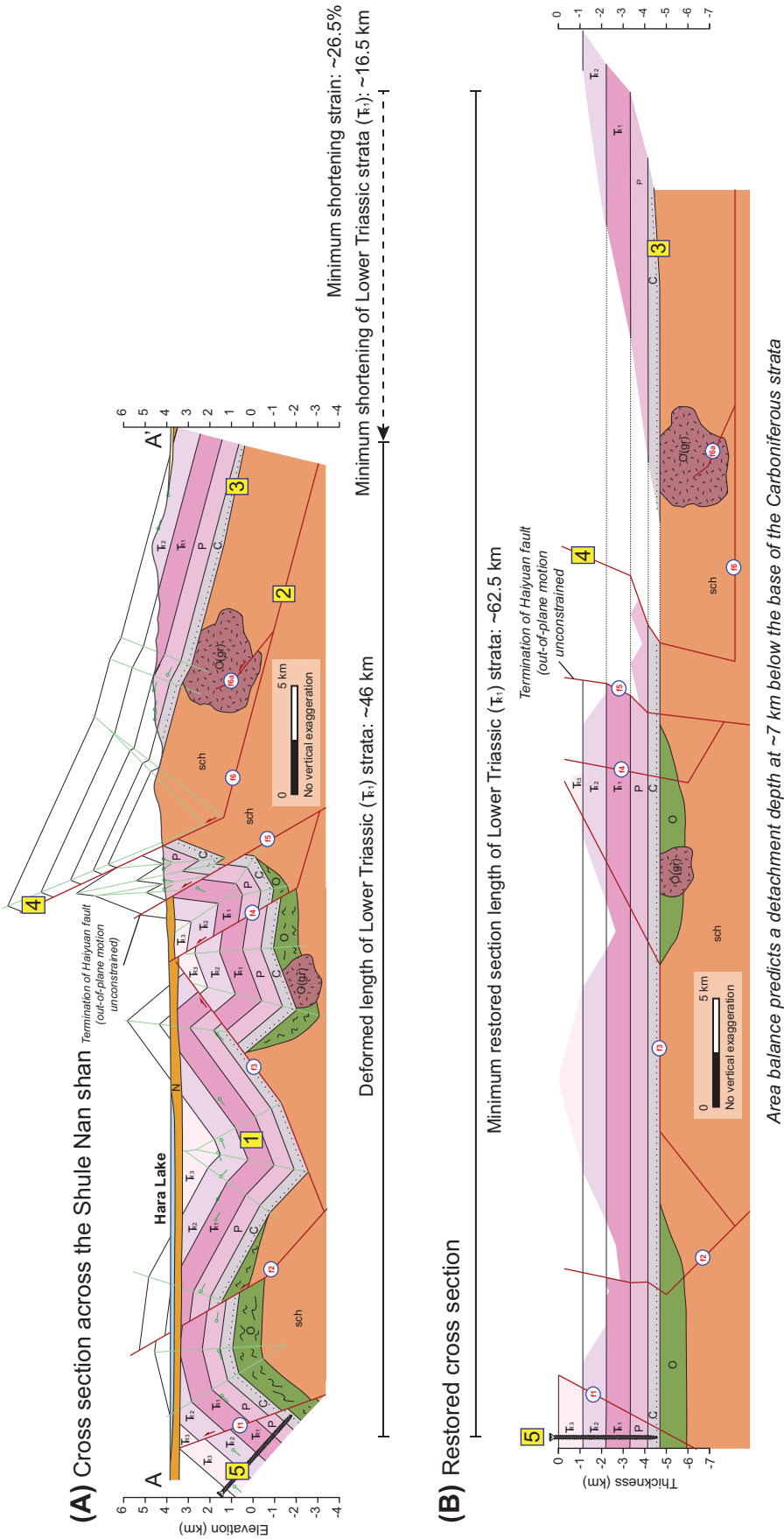


**Figure 5.11.** Southward-looking view of Qilian Shan range from Google Earth. White arrows point to a major thrust fault that juxtaposes Silurian granitoid and metasedimentary rocks against Neogene and Quaternary rocks; the yellow arrows point to a separate thrust fault splay that brings Jurassic–Neogene strata over Quaternary sediments. See Figure 2.10 for location.

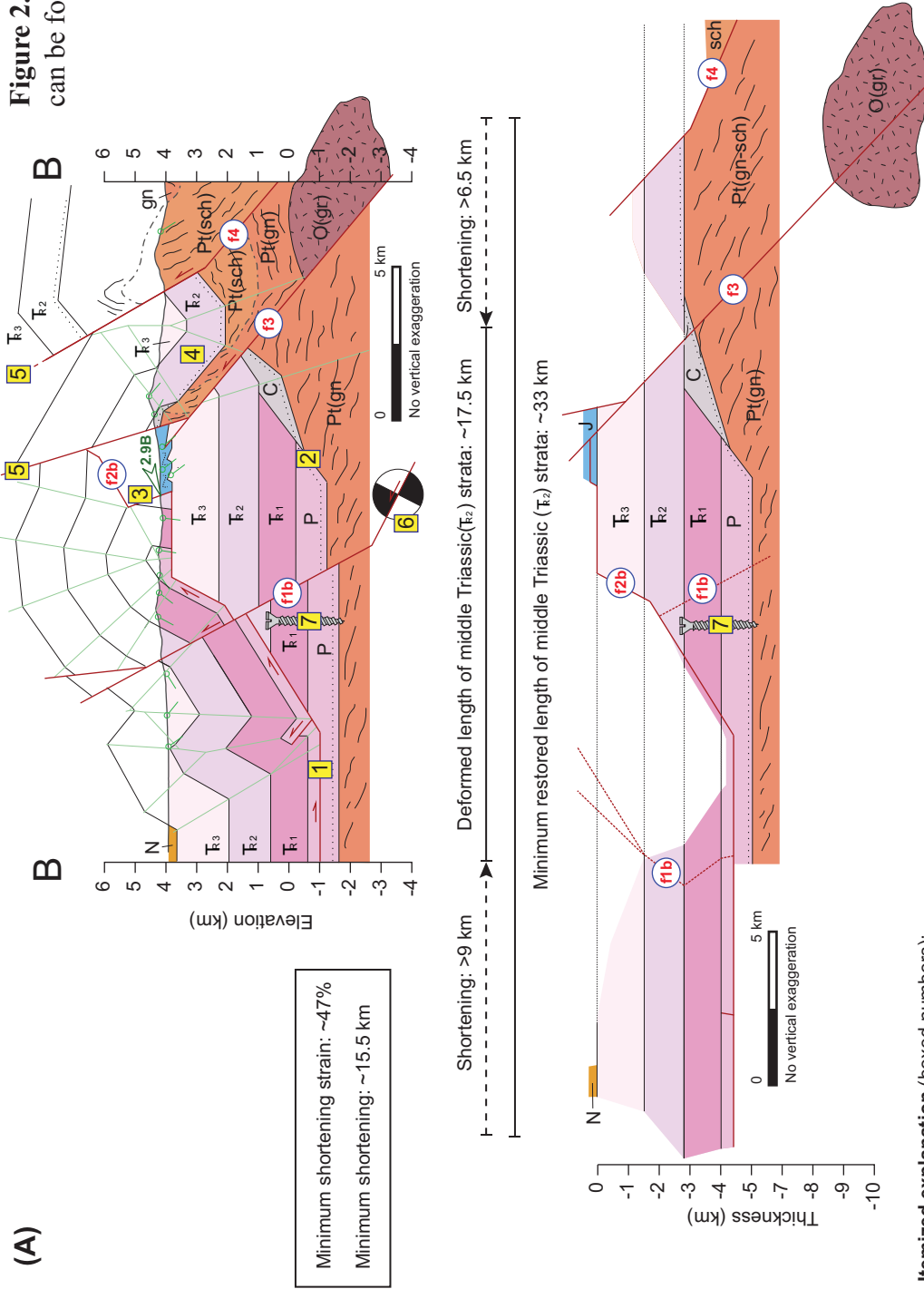


**Itemized explanation** (boxed numbers):

- (1) Geometries of faults and folds under Hara Lake were constrained by projecting structural data along strike.
- (2) Angle of hanging wall flat determined from the angle of the overlying P-R strata.
- (3) The assumed Carboniferous strata pinch-out to the north is part of the regional buttress unconformity underlying the C-P strata.
- (4) Minimum slip on the fault is restored due to hanging-wall cutoff erosion.
- (5) Pinline placed through undeformed hanging-wall strata.

**Figure 2.12.** Geologic cross section across the Shule Nan Shan in a (A) deformed and (B) restored state. Line-length restored cross section in B is based on the restored length of the Lower Triassic ( $T_1$ ) strata. Profile line shown in Figure 2.7.

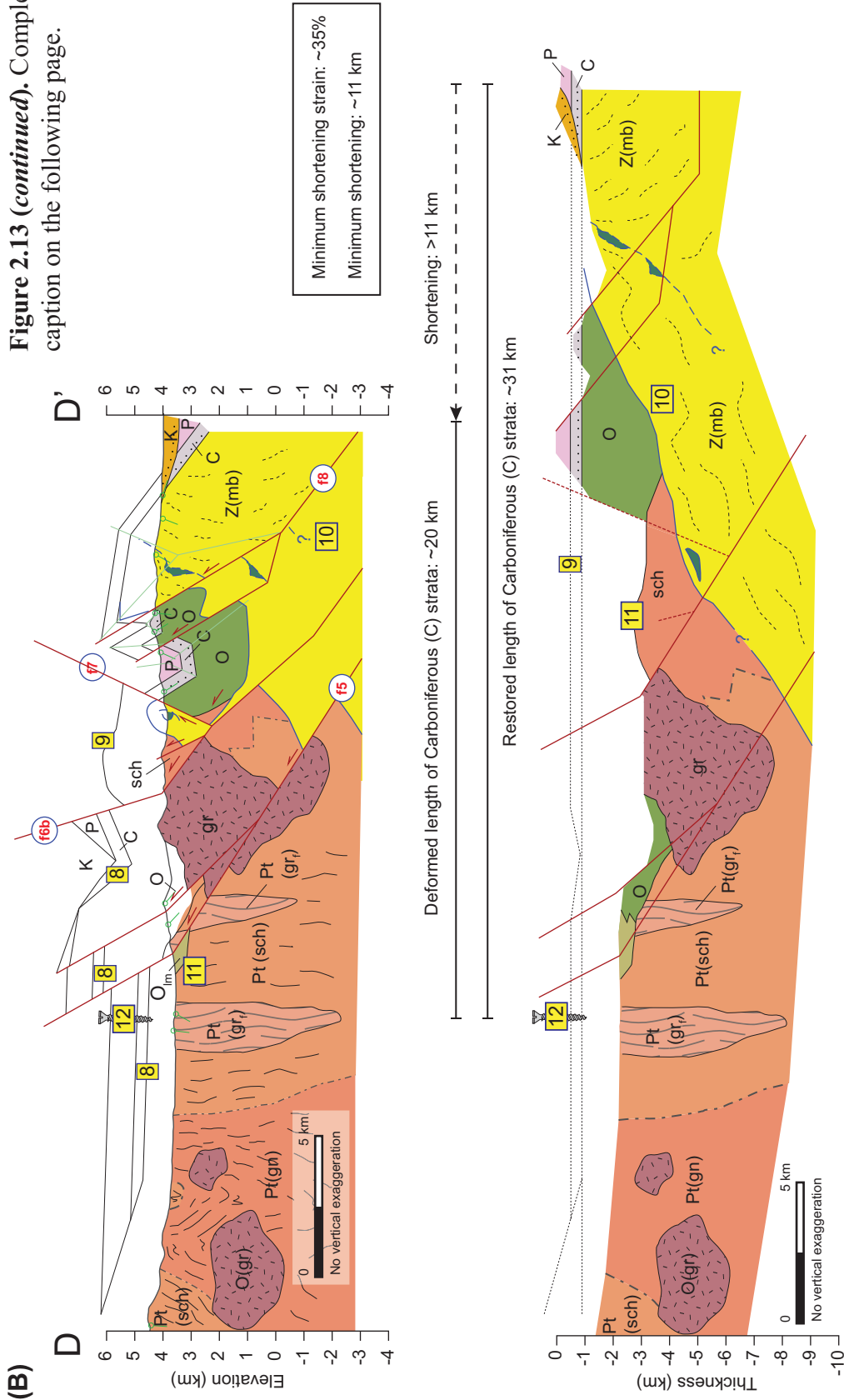
**Figure 2.13.** Complete caption can be found after cross sections.



**Itemized explanation** (boxed numbers):

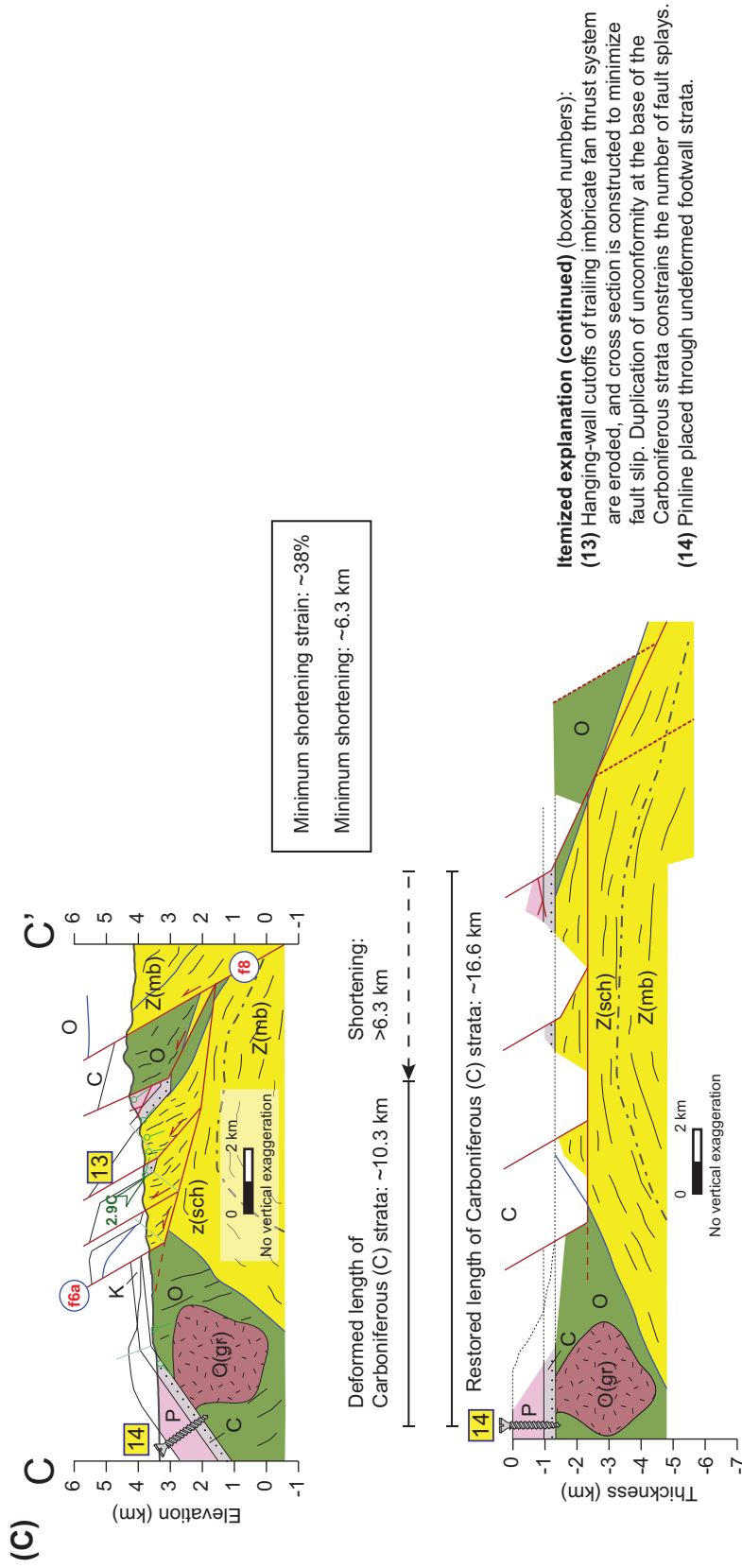
- (1) Fault 2b is interpreted to sole into Permian strata because this north-vergent thrust does not expose older/deeper rocks.
- (2) Nature of unconformity between Paleozoic strata and gn is unconstrained. Current cross section model implies ~1-2 km topography at the start of C-P. Note that adjusting this initial condition does not significantly alter our shortening estimates.
- (3) Overtuned thrust currently displays J over T relationship, but is interpreted to have been a J footwall-wall flat and P-T hanging-wall ramp. See field photograph in Figure 2.9D.
- (4) Footwall syncline shows T unconformably overlying sch-gn; the inferred absence of C-P strata is due to paleotopography of the basement rocks.
- (5) Minimum fault slip restored due to erosion of the hanging-wall cutoff.
- (6) Earthquake focal mechanism from 1993  $M_w=5.9$  event and preferred nodal plane of fault slip. Event position (focal depth) calculated by Chu et al. (2009).
- (7) Pinline placed through undeformed footwall strata.

**Figure 2.13 (continued).** Complete caption on the following page.



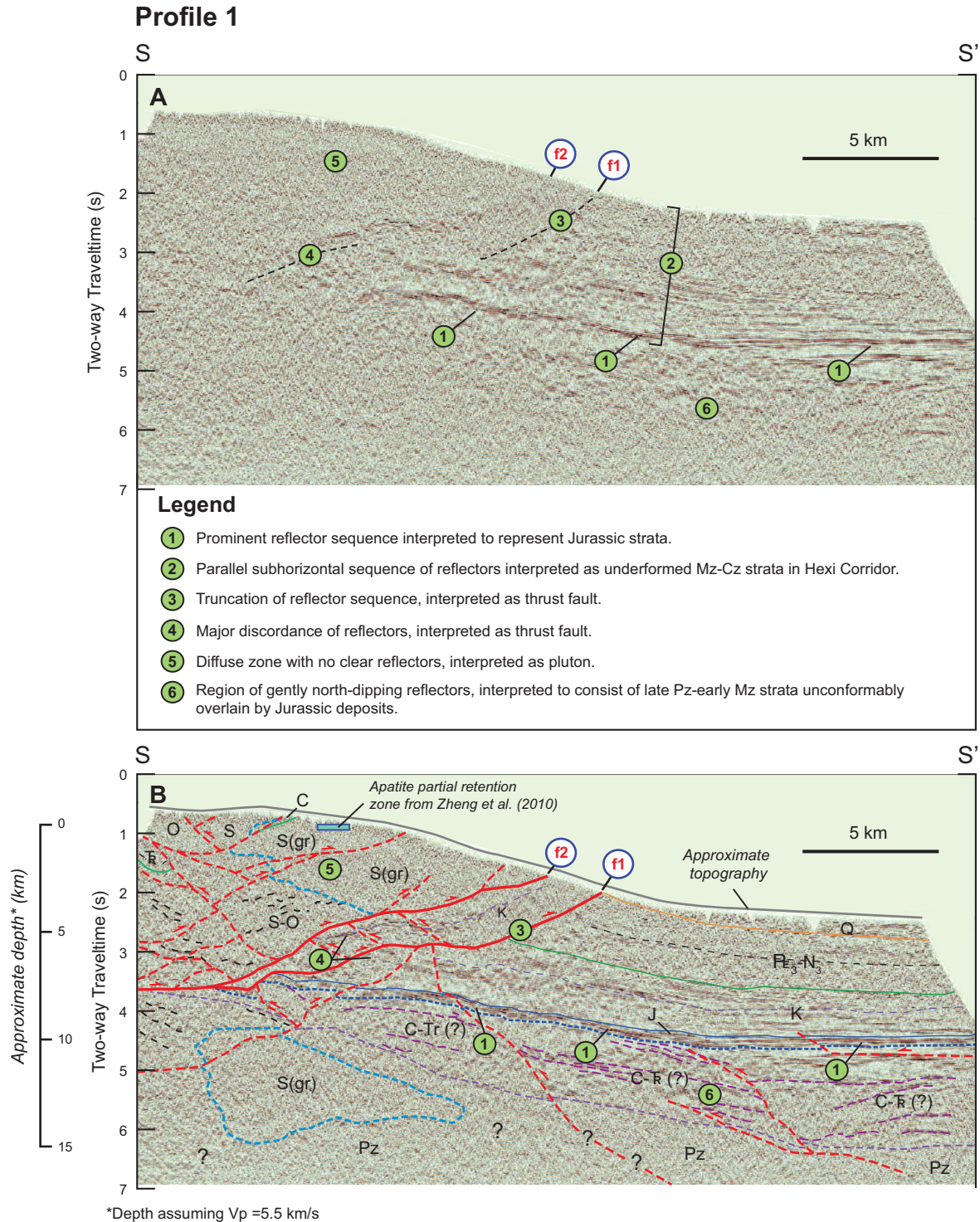
**Itemized explanation (continued)** (boxed numbers):

- (8) Eroded unconformity inferred from map relationships.
- (9) Minimum length of Carboniferous unconformity.
- (10) The pre-Cenozoic geology at depth is poorly constrained, especially the relationship between **Z(mb)** and **O** strata.
- (11) As drawn, this inferred contact implies that the Ordovician strata were deposited unconformably on Proterozoic basement and that the contact is intruded by a **O-S** pluton. This is supported by the absence of a major fault juxtaposing the basement and Ordovician units. Pre-Cenozoic upwarping of contact reduces Cenozoic shortening magnitude.
- (12) Pinline placed through inferred undeformed hanging-wall strata.



**Figure 2.13 (continued).** Geologic cross sections across the Tuo Lai Shan and Tuo Lai Nan Shan in a deformed and restored state. Profile lines shown in Figure 2.8.





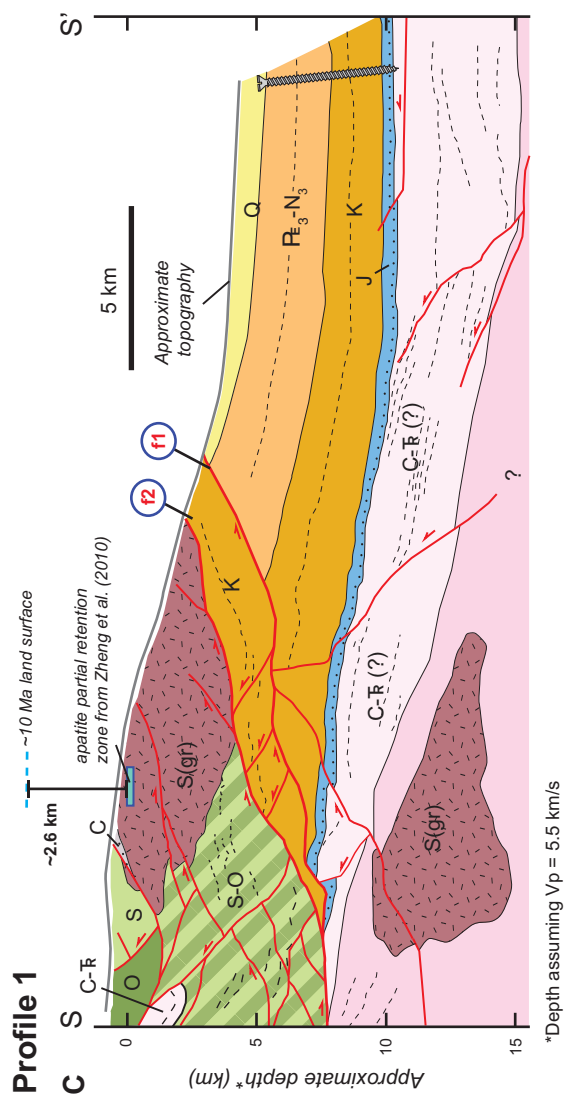
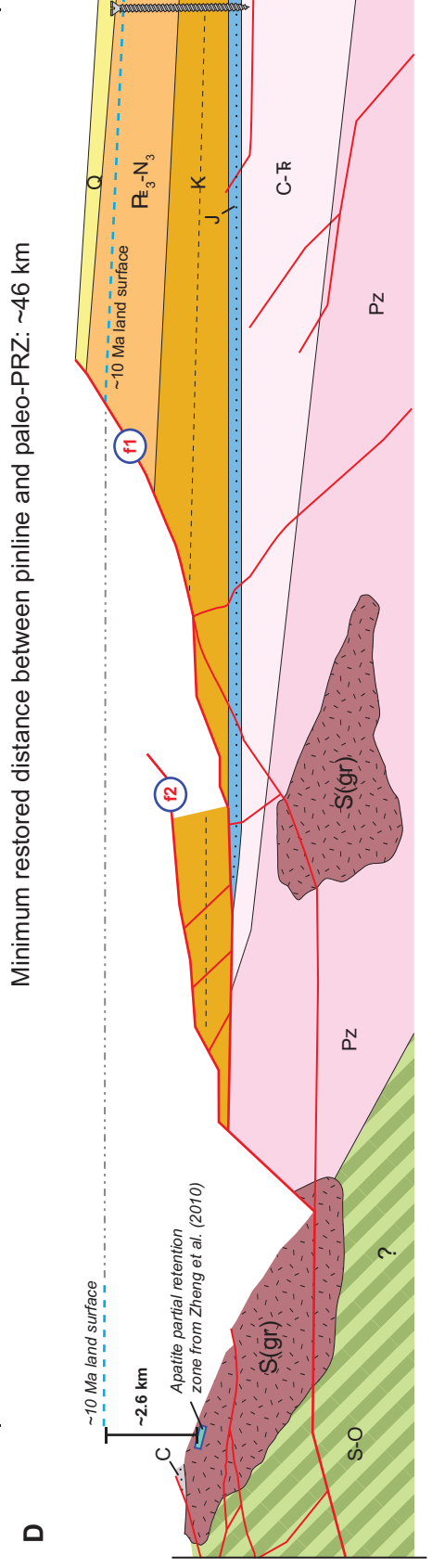


**Figure 2.14 (continued).** (C) Geologic cross section based on interpretations shown in Fig. 2.14B. (D) Restored cross section based on removing slip on imaged faults to move the paleo-partial retention zone (PRZ) and ca. 10 Ma paleoland surface in the hanging wall to a vertically aligned position with the ca. 10 Ma growth-strata surface in the Hexi Corridor footwall. See text for further discussion.

Minimum shortening: ~25 km (54% strain)

Deformed distance of pinline and paleo-PRZ: ~21 km



**Alternative minimum shortening estimates:**  
 Based on minimum required fault slip: 22 km (53% strain)  
 Based on restored length of Cretaceous strata (K): 15 km (40% strain)

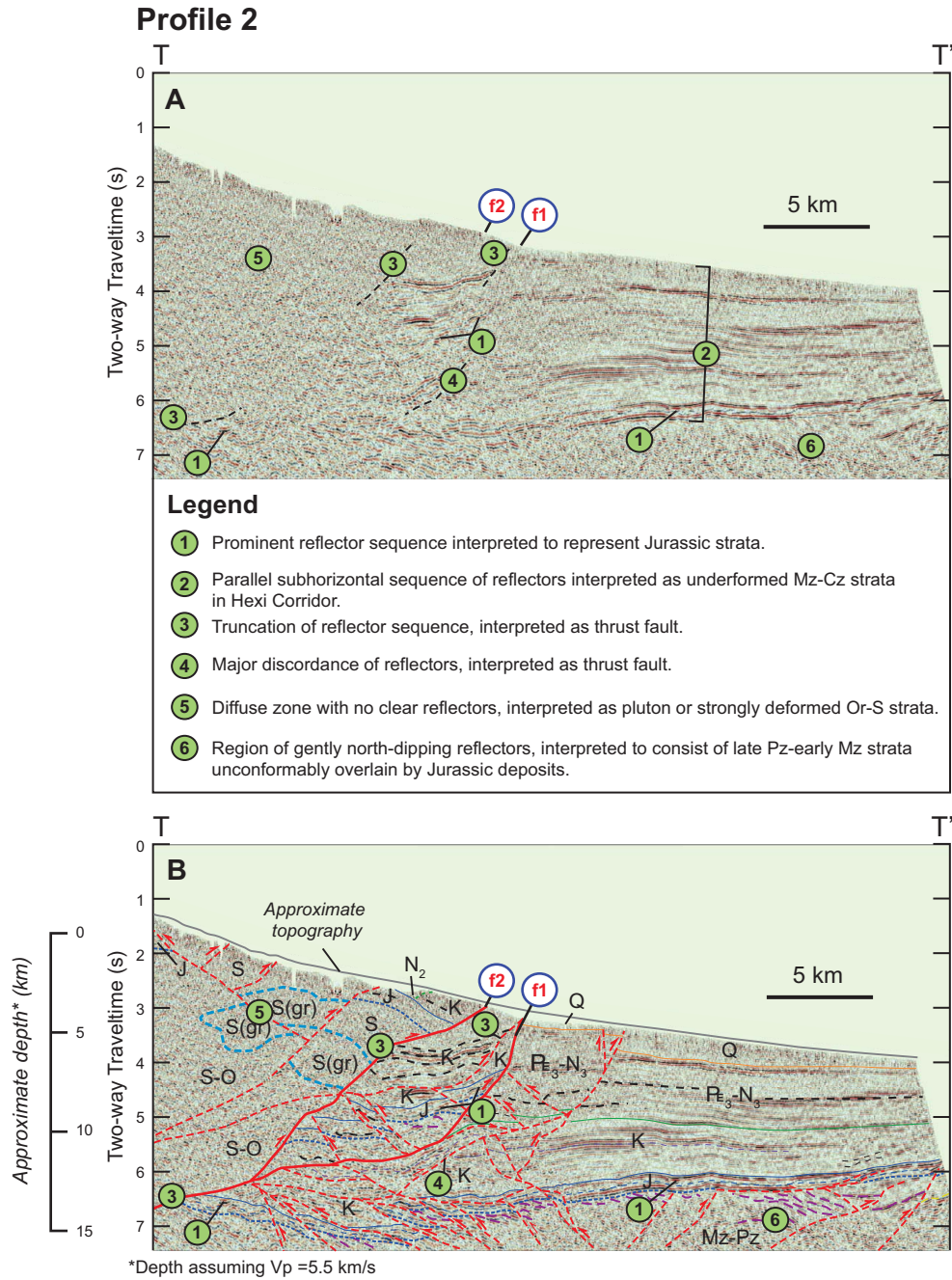


**Figure 2.15.** (A) Uninterpreted seismic reflection profile. See Figures 2.1, 2.3, and 2.10 for location. Key features, including reflectors and truncations, are labeled from 1 to 6 and described in the legend, and major faults are labeled for discussion in text (i.e., f1 and f2). (B) Interpreted seismic reflection profile. Important features are labeled as in Figure 2.15A. See Figure 2.10 for map unit age abbreviations.

**Profile 2**

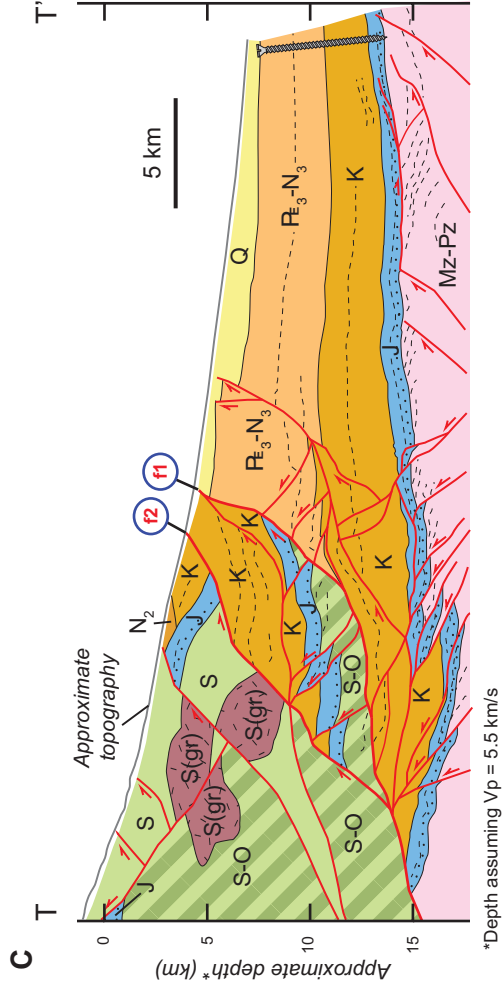
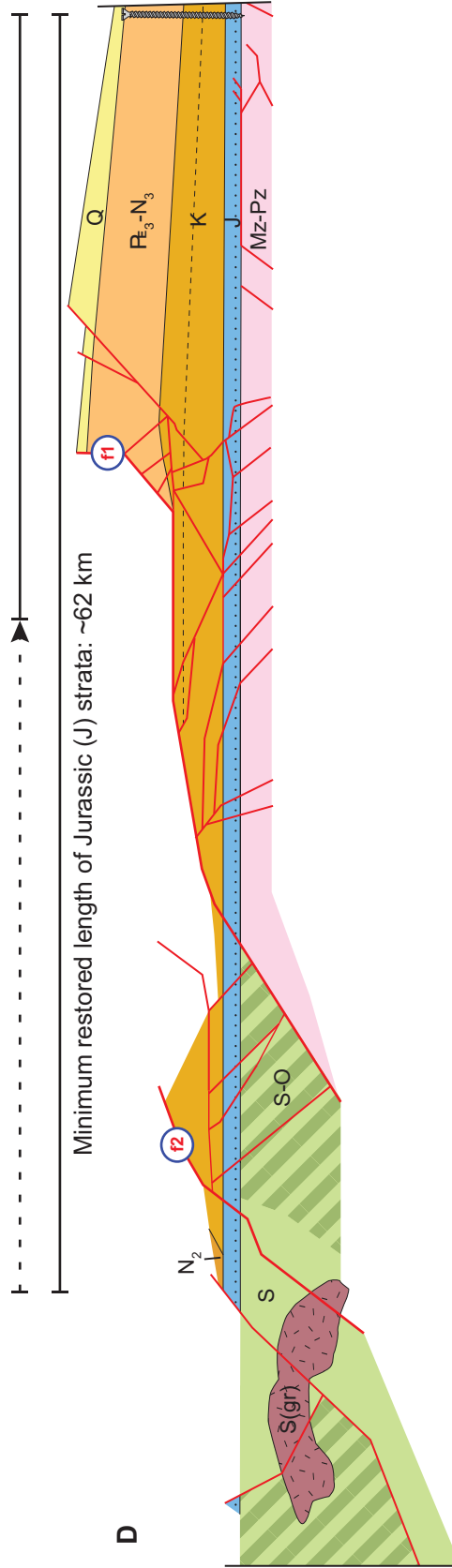


**Figure 2.15 (continued).** (C) Geologic cross section based on interpretations shown in Fig. 2.15B. (D) Line-length restored cross section from Fig. 15C based on restoring Jurassic strata.

Minimum shortening of Jurassic (J) strata: ~33 km (53% strain) Deformed length of Jurassic (J) strata: ~29 km



### Profile 3

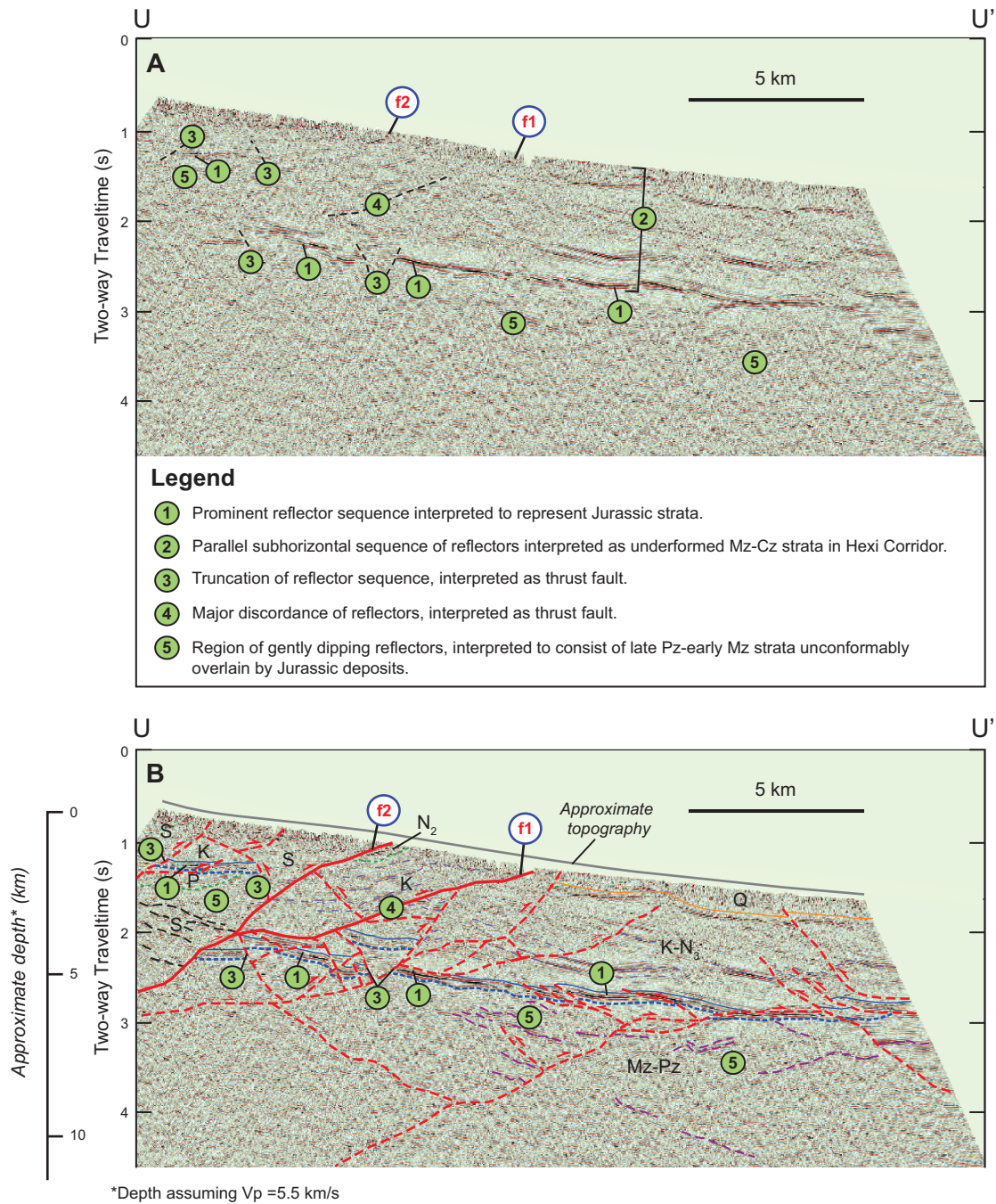


**Figure 2.16.** (A) Uninterpreted seismic reflection profile. See Figures 2.1, 2.3, and 2.10 for location. Key features, including reflectors and truncations, are labeled from 1 to 5 and described in the legend, and major faults are labeled for discussion in text (i.e., f1 and f2). (B) Interpreted seismic reflection profile. Important features are labeled as in Figure 2.16A. See Figure 2.10 for map unit age abbreviations.

**Profile 3**

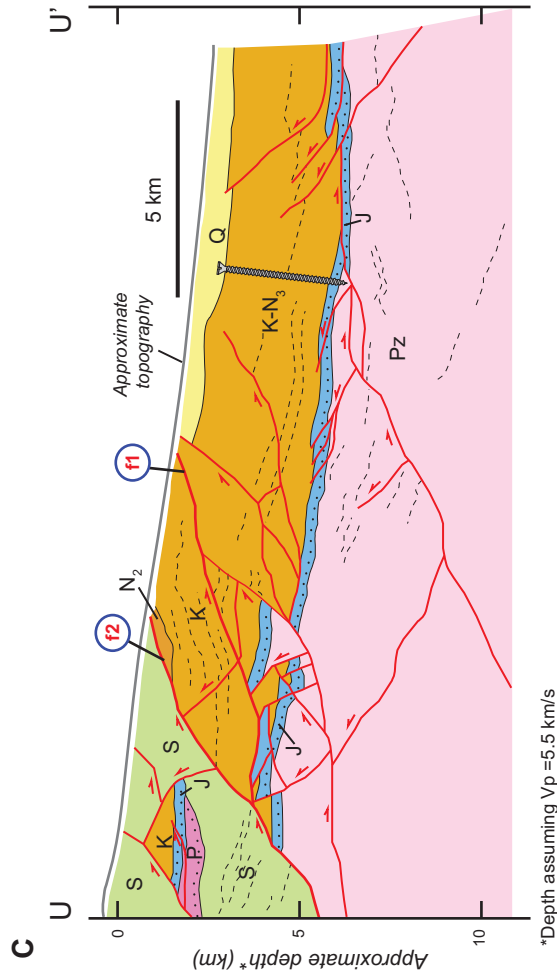
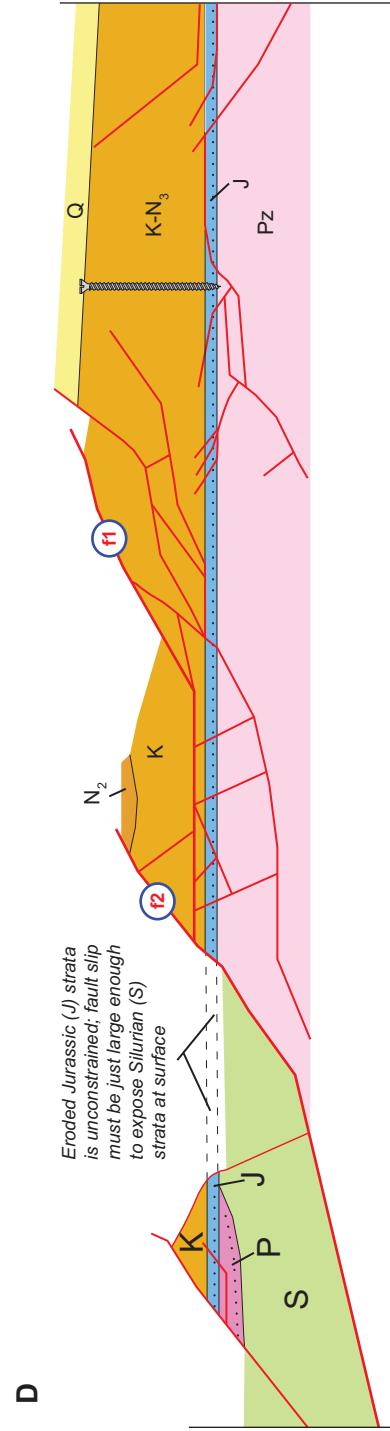


**Figure 2.16 (continued).** (C) Geologic cross section based on interpretations shown in Fig. 2.16B. (D) Line-length restored cross section from Fig. 16C based on the restoration of Jurassic strata.

Minimum shortening of Jurassic (J) strata: 12 km (36% strain)

Deformed length of Jurassic (J) strata: ~21 km

Minimum restored length of Jurassic (J) strata: ~33 km



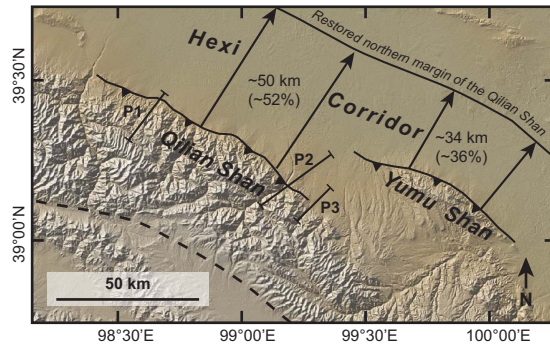


**Figure 2.17.** Sketch map showing reconstruction of the pre-Cenozoic northern margin of the frontal Qilian Shan relative to the present-day based on the shortening estimates obtained in this study. This map highlights the fact that lower magnitude shortening in the east are balanced by an overall wider zone of deformation, as strain is also occurring in the Yumu Shan. P1, P2, and P3 refer to profiles 1, 2, and 3, respectively. Note that P3 is in line with the Yumu Shan. Reconstructed pre-Cenozoic northern margin of the frontal Qilian Shan thrust system whereas the other seismic profiles are not.

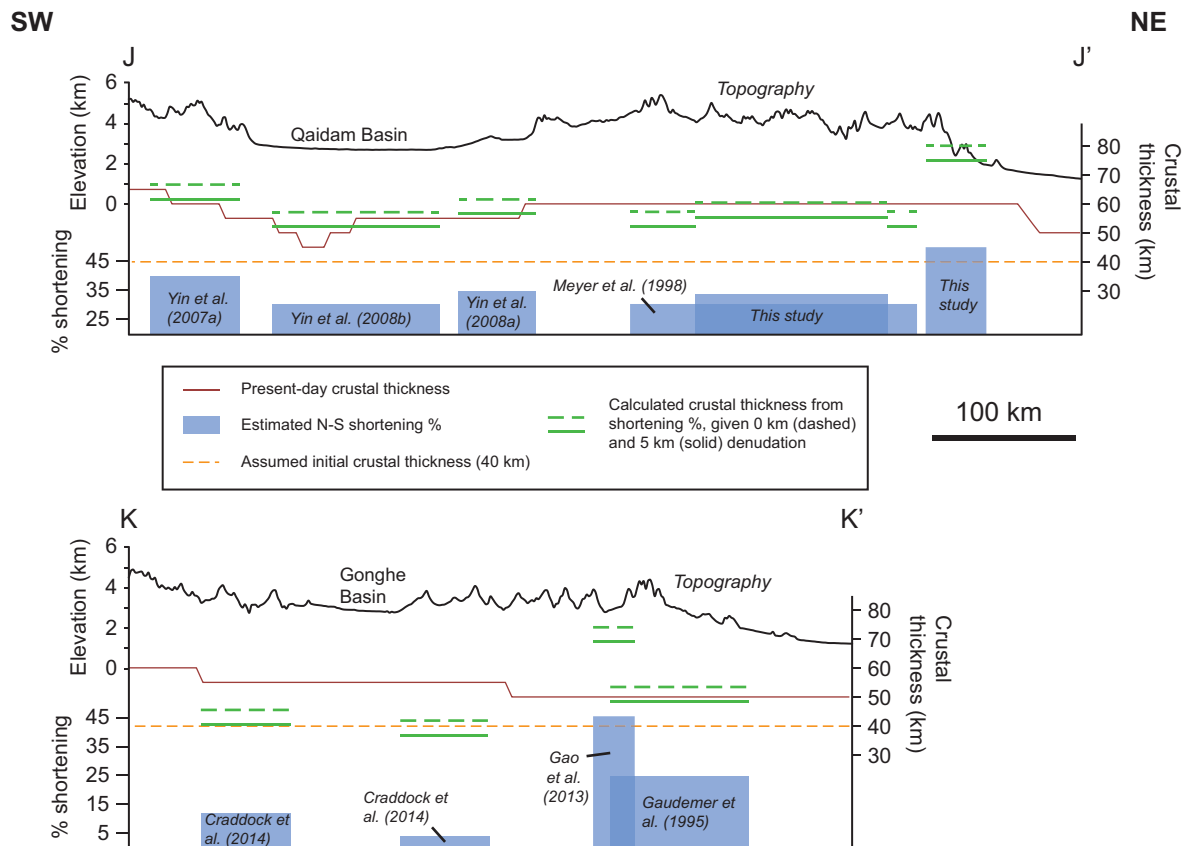


**Figure 2.18.** Comparison plot of topography (black lines), crustal thickness (red lines), estimated percent crustal shortening (blue boxes), and predicted present-day crustal thickness (dashed green line = no denudation; solid green line = 5 km denudation) given pure shear thickening at estimated shortening strain magnitude along the segment assuming an initial crustal thickness of 40 km (dashed orange line). Section lines J-J' and K-K' are shown in Figure 2.4. Crustal thickness values are from Yue et al. (2012) (Fig. 2.1C) and shortening estimates discussed in text. Note that when crustal shortening and pure shear thickening cannot account for the observed present-day crustal thickness, an alternative plateau formation mechanism is favored.



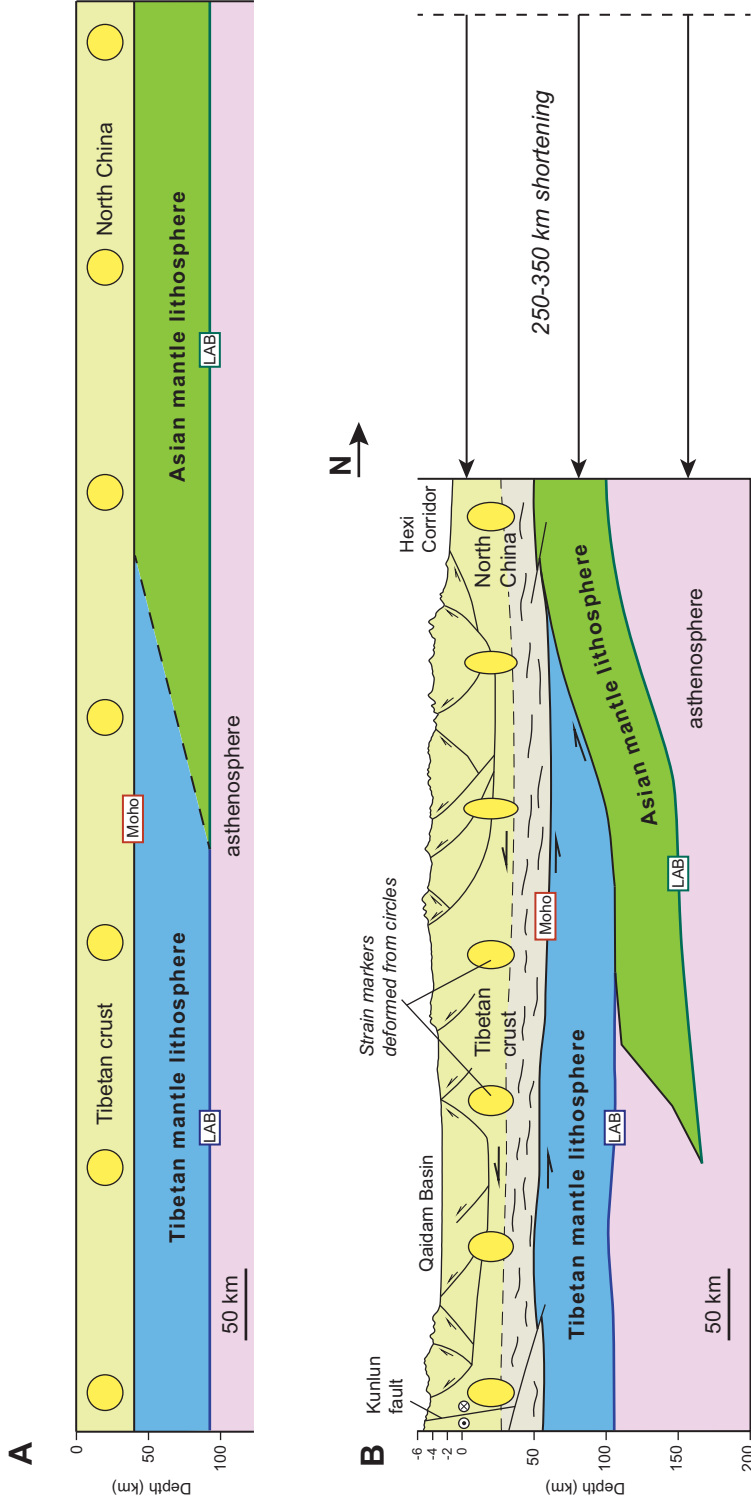


**Figure 2.19.** Lithospheric-scale model for the development of the northeastern Tibetan Plateau, between the Kunlun fault in the south and the Hexi Corridor in the north. (A) The pre-Cenozoic undeformed Tibetan and Asian continental lithosphere. (B) 250–350 km of Cenozoic convergence between Qaidam Basin and North China is accommodated by southward underthrusting of the Asian mantle lithosphere beneath Tibet and distributed vertically-uniform crustal shortening. The strain ellipses deformed from circles illustrate the relative magnitude of contractional strain along this profile. Note that with the exception of the top 6 km, there is no vertical exaggeration in this profile. Crustal structures, including subhorizontal shear zones, Moho depth, and lithosphere-asthenosphere boundary (LAB) positions are from Gao et al. (1999, 2013), Wang et al. (2011), Feng et al. (2014), and Ye et al. (2015).

**Table 2.1. Comparison of model predictions for the formation of the Tibetan Plateau**

| <b>Models</b>  | <b>Predictions</b>  |   |   | <b>References</b>  |
|--|---|---|---|--|
|  | <b>Temporal Evolution</b>   | <b>Spatial Distribution</b>   | <b>Shortening at Plateau Margins</b>  |  |
| <b>Distributed shortening</b>                            | Northward propagation of shortening across Tibet.   | Cenozoic thrusts and folds are uniformly distributed across Tibet.                    | 30-40% crustal shortening to explain the crustal thickness of Tibet.                | Dewey and Bird (1970); Dewey and Burke (1973); England and Houseman (1986)   |
| <b>Discrete intra-continental subduction</b>             | Stepwise, northward propagation of the intracontinental subduction zones.                                     | Cenozoic thrusts in discrete zones along older sutures and coeval strike-slip faults. | Little shortening away but >50% shortening along the subduction zones               | Meyer et al. (1998); Tapponnier et al. (2001)  |
| <b>Underthrusting of Indian and/or Asian lithosphere</b> | Shortening propagates inward from underthrust margins (e.g., north from Himalaya and south from Qilian Shan). | Cenozoic structures contributing to crustal thickening are minor features in Tibet.   | >50% crustal shortening along plateau margins but little shortening within plateau. | Argand (1924); Powell and Conaghan, (1973); Powell, (1986); Kind et al. (2002); Zhao et al. (2011); Ye et al. (2015) |
| <b>Vertical inflation by channel flow</b>                | Propagating surface uplift from plateau interior to plateau margins.  | Minor Cenozoic shortening particularly along plateau margins.                         | Little crustal shortening (<5%), particularly along plateau margins.                | Zhao and Morgan (1987); Bird (1991); Royden et al. (1997); Clark and Royden (2000); Karplus et al. (2011)            |
| <b>Inherited thickness</b>                               | Deformation and structures predate India-Eurasian collision.  | Structures related to pre-Cenozoic tectonic settings.                                 | Mainly pre-Cenozoic structures and minimal erosion.                                 | Worley and Wilson (1996); Murphy et al. (1997); Wallis et al. (2003)   |

**Table 2.2. Cross sections and shortening estimates across northern Tibet**

| Location                                | Section label*      | Orientation | Shortening<br>(km) [strain %] | Restored<br>length (km) | $T_i$ (km) <sup>®</sup> | Reference                            |
|---|---------------------|-------------|-------------------------------|-------------------------|-------------------------|--------------------------------------|
| <i>Qilian Shan-Nan Shan thrust belt</i> |                     |             |                               |                         |                         |                                      |
| North                                   | A-A'                | NE-SW       | 8.2 [26]                      | 31.3                    | 41-52                   | Zheng et al. (2010)                  |
|   | S-S'                | NNE-SSW     | 25 [54]                       | 46                      | 23-29                   |                                      |
| North                                   | T-T'                | NNE-SSW     | 33 [53]                       | 64                      | 26-34                   | This study (seismic profiles)        |
|   | U-U'                | NNE-SSW     | 12 [36]                       | 33                      | 35-45                   |                                      |
|   | A-A'                | NE-SW       | 16.5 [26.5]                   | 62.5                    | 44-48                   |                                      |
|   | B-B'                | NNE-SSW     | 15.5 [47]                     | 33                      | 32-34                   |                                      |
| Central                                 | C-C'                | NE-SW       | 6.3 [38]                      | 16.6                    | 37-40                   | This study (geologic cross sections) |
|   | D-D'                | NE-SW       | 11 [35]                       | 31                      | 41-45                   |                                      |
|   | E-E'                | NE-SW       | 8.6 [35]                      | 26                      | 41-45                   |                                      |
|   | b                   | NE-SW       | 90 [22]                       | 415                     | 43-55                   |                                      |
|   | d                   | NE-SW       | 35-45 [13-18]                 | 258-268                 | 46-59                   |                                      |
|   | f                   | NE-SW       | 50-70 [23-35]                 | 200-220                 | 39-50                   |                                      |
| Regional                                | Composite b, d, f   | NE-SW       | 150 [31]                      | 485                     | 38-48                   | Meyer et al. (1998)                  |
|   | C1                  | NE-SW       | 188.5 ± 98 [30]               | 630                     | 39-49                   |                                      |
|   | C2                  | NE-SW       | 141 ± 84 [26]                 | 540                     | 41-52                   |                                      |
|   | Mass balance        | NE-SW       | 120 ± 30 [14-23]              | 640                     | 45-57                   |                                      |
| Regional                                | -                   | NE-SW       | 360 [50]                      | 710                     | 28-35                   | Yin and Harrison (2000)              |
| East                                    | A-A'                | NNW-SSE     | 25 [25]                       | 100                     | 41-53                   | Gaudemer et al. (1995)               |
| Baiyin thrust                           | Fig. 6 <sup>1</sup> | NNW-SSE     | 22.3 [46]                     | 47.9                    | 30-38                   | Gao et al. (2013)                    |
|   | A-A'                | W-E         | 14.3 [14.2]                   | 100.6                   | 47-60                   |                                      |
| Jishi Shan                              | B-B'                | W-E         | 10.5 [10.4]                   | 100.8                   | 49-63                   | Lease et al. (2012)                  |
|   | C-C'                | W-E         | 8.4 [26]                      | 32.4                    | 41-52                   |                                      |
| West Qinling                            | D-D'                | NE-SW       | 4.3 [14.2]                    | 30.3                    | 47-60                   | Lease et al. (2012)                  |
| Laji Shan                               | E-E'                | NE-SW       | 5.1 [46]                      | 11.1                    | 30-38                   | Lease et al. (2011, 2012)            |
|   | a                   | NNE-SSW     | 2.2 [4.2]                     | 52.2                    | 53-67                   |                                      |
|   | b                   | NNE-SSW     | 0.8 [1.6]                     | 50.8                    | 54-69                   |                                      |
|   | c                   | NNE-SSW     | 1.4 [2.7]                     | 51.4                    | 54-68                   |                                      |
| Qinghai Nan Shan                        | d                   | NNE-SSW     | 1.3 [2.5]                     | 51.3                    | 54-68                   | Craddock et al. (2014)               |
|   | e                   | NNE-SSW     | 0.9 [1.8]                     | 50.9                    | 54-69                   |                                      |
|   | f                   | NNE-SSW     | 1.6 [3.1]                     | 51.6                    | 53-68                   |                                      |
|   | g                   | W-E         | 0.8 [0]                       | 32.3                    | 55-70                   |                                      |
|   | a                   | NE-SW       | 5.1 [9.3]                     | 55.1                    | 50-63                   |                                      |
| Gonghe Nan Shan                         | b                   | NE-SW       | 6.4 [11.3]                    | 56.4                    | 49-62                   | Craddock et al. (2014)               |
|   | c                   | NE-SW       | 6.9 [12.1]                    | 56.9                    | 48-62                   |                                      |
| <i>North Qaidam thrust system</i>       |                     |             |                               |                         |                         |                                      |
|   | (1)                 | NE-SW       | 26 [34]                       | 60                      | 36-46                   |                                      |
|   | (2)                 | NE-SW       | 19 [36]                       | 53                      | 35-45                   |                                      |
|   | (3)                 | NE-SW       | 26 [29]                       | 91                      | 39-50                   |                                      |
|   | (4)                 | NE-SW       | 10 [21]                       | 48                      | 43-55                   |                                      |
|   | (5)                 | NE-SW       | 46 [31]                       | 149                     | 38-48                   |                                      |
|   | (6)                 | NE-SW       | 29 [27]                       | 103                     | 40-51                   |                                      |
|   | (7)                 | NE-SW       | 50 [58]                       | 86                      | 23-29                   |                                      |
| North Qaidam                            | (8)                 | NE-SW       | 40 [53]                       | 68                      | 26-33                   | Yin et al. (2008a)                   |
|   | Gaoquan             | NE-SW       | 9.8 [63]                      | 15.6                    | 20-26                   |                                      |
|   | Lulehe              | NE-SW       | 31 [63]                       | 49                      | 20-26                   |                                      |
|   | Luliang Shan        | NE-SW       | 34 [55]                       | 62                      | 25-32                   |                                      |
|   | Gaqui               | NE-SW       | 22 [38]                       | 57.5                    | 34-43                   |                                      |
|   | Xiaoqaidam          | NE-SW       | 6.5 [23]                      | 33.5                    | 42-53                   |                                      |
|   | Lenghu-4            | NE-SW       | 1.6 [35]                      | 4.6                     | 36-46                   |                                      |
|   | Lenghu-4            | NE-SW       | 16 [39]                       | 41                      | 34-43                   |                                      |

**Table 2.2 (continued). Cross sections and shortening estimates across northern Tibet*****Qaidam Basin thrust system***

|                                      |       |       |             |        |       |                         |
|--------------------------------------|-------|-------|-------------|--------|-------|-------------------------|
| Qaidam Basin                         | 1     | NE-SW | 84 [32.3]   | 257    | 37-47 | Yin et al. (2008b)      |
|                                      | 2     | NE-SW | 68 [35.1]   | 270    | 36-45 |                         |
|                                      | 3     | NE-SW | 41 [17.7]   | 231    | 45-58 |                         |
|                                      | 4     | NE-SW | 20 [10.7]   | 187    | 49-63 |                         |
|                                      | 5     | NE-SW | 17 [12.1]   | 147    | 48-62 |                         |
|                                      | 6QB   | NE-SW | 2 [1]       | 52     | 54-69 |                         |
|                                      | 6QS   | NE-SW | 12 [30]     | 40     | 39-49 |                         |
| Qaidam Basin                         | 2     | NE-SW | 13.74 [9.6] | 143.06 | 50-63 | Zhou et al. (2006)      |
|                                      | 6 + 9 | NE-SW | 19.98 [9]   | 219.82 | 50-64 |                         |
| <b><i>Qimen Tagh thrust belt</i></b> |       |       |             |        |       |                         |
| West                                 | 7     | NE-SW | 25 [30]     | 74     | 39-49 | Yin et al. (2008b)      |
| West                                 | A-D   | NE-SW | 58 [48]     | 120    | 29-36 | Yin et al. (2007a)      |
| West                                 | -     | NE-SW | 270 [57]    | 470    | 24-30 | Yin and Harrison (2000) |

\*As reported in original reference

@Apparent initial pre-deformational crustal thickness given shortening estimate

<sup>1</sup>Restoration above regional Paleozoic unconformity

**Table 2.3. Mesozoic and Cenozoic stratigraphy of the Hexi Corridor**

| Unit Names                       | Symbol                         | Geologic time               | Age               | Description   |
|----------------------------------|--------------------------------|-----------------------------|-------------------|---|
| Quaternary<br>(undifferentiated) | Q                              | Quaternary                  | 2.5 Ma to present | Boulders and gravels                                  |
| Yumen Formation                  | N <sub>2</sub> -Q <sub>1</sub> | Pliocene-<br>Pleistocene(?) | ca. 4 - 2 (?) Ma  | Pebble to boulder<br>conglomerate with<br>minor sands |
| Shulehe Formation                | N <sub>1</sub>                 | Miocene to Pliocene         | 23 to ca. 4 Ma    | Reddish conglomerate,<br>sandstone, and<br>mudstone   |
| Baiyanghe Formation              | P <sub>E3</sub>                | Oligocene                   | ca. 28 to 23 Ma   | Red-orange sandstone<br>mudstone with<br>gypsum       |
| Huoshagou Formation              | P <sub>E3</sub>                | Oligocene                   | 33.9 to ca. 28 Ma | Red conglomerate,<br>mudstone, and<br>sandstone       |
| Xinminbao Group                  | K                              | Cretaceous                  | 145 - 66 Ma       | Red-orange<br>conglomerate and<br>coarse sandstone    |
| Bolou/Dashankou Group            | J                              | Jurassic                    | 201 - 145 Ma      | Coal-rich sandstone<br>and siltstone                  |

## 2.10. References

- Allmendinger, R.W., Reilinger, R., and Loveless, J., 2007, Strain and rotation rate from GPS in Tibet, Anatolia, and the Altiplano: *Tectonics*, v. 26.
- Ammon, C.J., Randall, G.E., and Zandt, G., 1990, On the nonuniqueness of receiver function inversions: *Journal of Geophysical Research*, v. 95, p. 15,303-15,318.
- Argand, E., 1924, *La Tectonique de l'Asie*: Proceedings of the 13th International Geological Congress, v. 7, p. 171-372.
- Bally, A.W., Gordy, P.L., and Stewart, G.A., 1966, Structure, seismic data, and orogenic evolution of southern Canadian Rocky Mountains: *Bulletin of Canadian Petroleum Geology*, v. 14, no. 3, p. 337-381.
- Beaumont, C., Jamieson, R.A., Nguyen, M. H., and Lee, B., 2001, Himalayan tectonics explained by extrusion of a low-viscosity crustal channel coupled to focused surface denudation: *Nature*, v. 414, no. 6865, p. 738-742.
- Beaumont, C., Jamieson, R.A., Nguyen, M.H., and Medvedev, S., 2004, Crustal channel flows: 1. Numerical models with applications to the tectonics of the Himalayan-Tibetan orogen: *Journal of Geophysical Research: Solid Earth*, v. 109, no. B6.
- Bird, P., 1991, Lateral extrusion of lower crust from under high topography in the isostatic limit: *Journal of Geophysical Research*, v. 96, p. 10,275-10,286.
- Bovet, P.M., Ritts, B.D., Gehrels, G., Abbink, A.O., Darby, B., and Hourigan, J., 2009, Evidence of Miocene crustal shortening in the north Qilian Shan from Cenozoic stratigraphy of the western Hexi Corridor, Gansu Province, China: *American Journal of Science*, v. 309, p. 290-329.
- Boyer, S.E., and Elliott, D., 1982, Thrust systems: *American Association of Petroleum Geologists Bulletin*, v. 66, p. 1196-1230.
- Brown, L.D., Zhao, Wenjin, Nelson, K.D., Hauck, M., Alsdorf, D., Ross, A., Cogan, M., Clark, M., Liu, Xianwen, and Cheet, Jinkai, 1996, Bright spots, structure and magmatism in southern Tibet from INDEPTH seismic reflection profiling: *Science*, v. 274, p. 1688-1690.
- Burchfiel, B. C., et al., 1991, Geology of the Haiyuan fault zone, Ningxia-Hui Autonomous Region, China, and its relation to the evolution of the northeastern margin of the Tibetan Plateau: *Tectonics*, v. 10, no. 6, p. 1091-1110.
- Burchfiel, B.C., Zhiliang, C., Hodges, K.V., Yuping, L., Royden, L.H., Changrong, D., and Jiene, X., 1992, The South Tibetan detachment system, Himalayan orogen: Extension contemporaneous with and parallel to shortening in a collisional mountain belt: *Geological Society of America Special Papers*, v. 269, p. 1-41.

- Burchfiel, B.C., Zhiliang, C., Yupinc, L., and Royden, L.H., 1995, Tectonics of the Longmen Shan and adjacent regions, central China: *International Geology Review*, v. 37, p. 661-735.
- Burgess, W. P., Yin, A., Dubey, C. S., Shen, Z. K., and Kelty, T. K., 2012, Holocene shortening across the Main Frontal Thrust zone in the eastern Himalaya: *Earth and Planetary Science Letters*, v. 357, p. 152-167.
- Chamberlin, R.T., 1923, On the crustal shortening of the Colorado Rockies: *American Journal of Science*, v. 33, p. 215-221.
- Champagnac, J.D., Yuan, D.Y., Ge, W.P., Molnar, P., and Zheng, W.J., 2010, Slip rate at the north-eastern front of the Qilian Shan, China: *Terra Nova*, v. 22, p. 180-187.
- Chen, J.H., Liu, Q.Y., Li, S.C., Guo, B., and Lai, Y.G., 2005, Crust and upper mantle S-wave velocity structure across northeastern Tibetan Plateau and Ordos block: *Chinese Journal of Geophysics*, v. 48, p. 369-379.
- Chen, Q.L., and Yang, Z.L., 2010, Petroleum geology of Pan-Hexi Corridor basins and exploration prospecting: *Natural Gas Geoscience*, v. 21, p. 186-192.
- Chen, X., Yin, A., Gehrels, G.E., Cowgill, E.S., Grove, M., Harrison, T.M., and Wang, X.-F., 2003, Two phases of Mesozoic north-south extension in the eastern Altyn Tagh range, northern Tibetan Plateau: *Tectonics*, v. 22, 1053.
- Chu, R., Zhu, L., and Helmberger, D.V., 2009, Determination of earthquake focal depths and source time functions in central Asia using teleseismic P waveforms: *Geophysical Research Letters*, v. 36, no. 17.
- Christensen, N., and Mooney, W., 1995, Seismic velocity structure and composition of the continental crust: A global view: *Journal of Geophysical Research Atmospheres*, v. 100, p. 761-9788.
- Clark, M.K., and Royden, L.H., 2000, Topographic ooze: Building the eastern margin of Tibet by lower crustal flow: *Geology*, v. 28, p. 703-706.
- Clark, M. K., Schoenbohm, L. M., Royden, L. H., Whipple, K. X., Burchfiel, B. C., Zhang, X., Tang, W., Wang, E., and Chen, L., 2004, Surface uplift, tectonics, and erosion of eastern Tibet from large-scale drainage patterns: *Tectonics*, v. 23.
- Clark, M.K., Farley, K.A., Zheng, D., Wang, Z., and Duvall, A.R., 2010, Early Cenozoic faulting of the northern Tibetan Plateau margin from apatite (U-Th)/He ages: *Earth and Planetary Science Letters*, v. 296, p. 78-88.
- Cowgill, E., Yin, A., Harrison, T.M., and Wang, X.F., 2003, Reconstruction of the Altyn Tagh fault based on U-Pb geochronology: the role of backthrusts, mantle sutures, and heterogeneous crustal strength in forming the Tibetan plateau: *Journal of Geophysical Research*, v. 108, 2346.

- Craddock, W., Kirby, E., and Zhang, H., 2011, Late Miocene-Pliocene range growth in the interior of the northeastern Tibetan Plateau: *Lithosphere*, v. 3, p. 420-438.
- Craddock, W.H., Kirby, E., Zhang, H., Clark, M.K., Champagnac, J.D., and Yuan, D., 2014, Rates and style of Cenozoic deformation around the Gonghe Basin, northeastern Tibetan Plateau: *Geosphere*, v. 10, p. 1255-1282.
- Dahlstrom, C.D.A., 1969, Balanced cross section: *Canadian Journal of Earth Sciences*, v. 6, p. 743-757.
- Dang, J., 2011, Geochemical characteristics and tectonic implications of Jinfosi granite in north Qilian: *Gansu Geology*, v. 20, p. 40-44.
- Dayem, K.E., Molnar, P., Clark, M.K., and Houseman, G.A., 2009, Far-field lithospheric deformation in Tibet during continental collision: *Tectonics*, v. 28.
- DeCelles, P.G., Robinson, D.M., and Zandt, G., 2002, Implications of shortening in the Himalayan fold-thrust belt for uplift of the Tibetan Plateau: *Tectonics*, v. 21, 1062.
- Dewey, J.F., and Bird, J.M., 1970, Mountain belts and the new global tectonics: *Journal of Geophysical Research*, v. 75, p. 2625-2647.
- Dewey, J.F., and Burke, K.C., 1973, Tibetan, Variscan, and Precambrian basement reactivation: products of continental collision: *Journal of Geology*, v. 81, p. 683-692.
- Dewey, J. F., Cande, S., and Pitman, W. C., 1989, Tectonic evolution of the India/Eurasia collision zone: *Eclogae Geologicae Helvetiae*, v. 82, no. 3, p. 717-734.
- Dupont-Nivet, G., Horton, B.K., Butler, R.F., Wang, J., Zhou, J., and Waanders, G.L., 2004, Paleogene clockwise tectonic rotation of the Xining-Lanzhou region, northeastern Tibetan Plateau: *Journal of Geophysical Research*, v. 109, no. B4.
- Duvall, A.R., Clark, M.K., van der Pluijm, B.A., and Li, C., 2011, Direct dating of Eocene reverse faulting in northeastern Tibet using Ar-dating of fault clays and low-temperature thermochronometry: *Earth and Planetary Science Letters*, v. 304, p. 520-526.
- Duvall, A.R., Clark, M.K., Kirby, E., Farley, K.A., Craddock, W.H., Li, C., and Yuan, D.Y., 2013, Low-temperature thermochronometry along the Kunlun and Haiyuan Faults, NE Tibetan Plateau: Evidence for kinematic change during late-stage orogenesis: *Tectonics*, v. 32, p. 1190-1211.
- Elliott, D., 1983, The construction of balanced cross-sections: *Journal of Structural Geology*, v. 5, no. 2.
- England, P., and Houseman, G., 1986, Finite strain calculations of continental deformation: 2. Comparison with the India-Asia collision zone: *Journal of Geophysical Research*, v. 91, no. B3, p. 3664-3676.



- Fang, X., Zhao, Z., Li, J., Yan, M., Pan, B., Song, C., and Dai, S., 2004, Late Cenozoic magnetostratigraphy of Laojunmiao anticlines of northern Qilian shan (Mts.) and its implications for uplift of northern Tibetan Plateau: *Science in China*, v. 34, no. 2, p. 97-106.
- Feng, M., Kumar, P., Mechie, J., Zhao, W., Kind, R., Su, H., Xue, G., Shi, D., and Qian, H., 2014, Structure of the crust and mantle down to 700 km depth beneath the East Qaidam basin and Qilian Shan from P and S receiver functions: *Geophysical Journal International*, v. 199, p. 1416-1429.
- Fielding, E., Isacks, B., Barazangi, M., and Duncan, C., 1994, How flat is Tibet?: *Geology*, v. 22, p. 163-167.
- Frederiksen, A.W., Folsom, H., and Zandt, G., 2003, Neighbourhood inversion of teleseismic Ps conversions for anisotropy and layer dip: *Geophysical Journal International*, v. 155, p. 200-212.
- Gansu Geological Bureau, 1989, Regional geology of Gansu Province: Beijing, Geological Publishing House, 692 p. (in Chinese).
- Gao, R., Cheng, X., and Wu, G., 1999, Lithospheric structure and geodynamic model of the Golmud-Ejn transect in northern Tibet, *in* Macfarlane, A., et al., eds., Himalaya and Tibet: Mountain roots to mountain tops: Geological Society of America Special Paper 328, p. 9-17.
- Gao, R., Wang, H., Yin, A., Dong, S., Kuang, Z., Zuzi, A.V., Li, W., and Xiong, X., 2013, Tectonic development of the northeastern Tibetan Plateau as constrained by high-resolution deep seismic-reflection data: *Lithosphere*, v. 5, p. 555-574.
- Gaudemer, Y., Tapponnier, P., Meyer, B., Peltzer, G., Shunmin, G., Zhitai, C., Huang, D., and Cifuentes, I., 1995, Partitioning of crustal slip between linked, active faults in the eastern Qilian Shan, and evidence for a major seismic gap, the 'Tianzhu gap,' on the western Haiyuan fault, Gansu (China): *Geophysical Journal International*, v. 120, p. 599-645.
- George, A.D, Marshall, S.J., Wyrwoll, K.H., Jie, C., and Yanchou, L., 2001, Miocene cooling in the northern Qilian Shan, northeastern margin of the Tibetan Plateau, revealed by apatite fission-track and vitrinite-reflectance analysis: *Geology*, v. 29, no. 10, p. 939-942.
- Gehrels, G.E., Yin, A., and Wang, X.F., 2003a, Detrital zircon geochronology of the northeastern Tibet: *Geological Society of America Bulletin*, v. 115, p. 881-896.
- Gehrels, G.E., Yin, A., and Wang, X.F., 2003b, Magmatic history of the Altyn Tagh, Nan Shan, and Qilian Shan region of western China: *Journal of Geophysical Research*, v. 108.
- Godard, V., Pik, R., Lavé, J., Cattin, R., Tibari, B., De Sigoyer, J., Pubellier, M., and Zhu, J., 2009, Late Cenozoic evolution of the central Longmen Shan, eastern Tibet: Insight from (U-Th)/He thermochronometry: *Tectonics*, v. 28.

- Groshong, R.H., Withjack, M.O., Schlische, R.W., and Hidayah, T.N., 2012, Bed length does not remain constant during deformation: recognition and why it matters: *Journal of Structural Geology*, v. 41, p. 86-97.
- He, G., and Pang, K., 2013, Seismic constraints on central Asian evolution of late Cenozoic: uplift rates and two-stage evolution of the northern Tibetan Plateau: *China Journal of Earth Science and Climate Change*, v. 4, no. 5.
- He, S., Wang, H., Xu, X., Zhang, H., and Ren, G., 2007, A LA-ICP-MS U-Pb chronological study of zircons from Hongtubu basic volcanic rocks and its geological significance in the east segment of North Qilian orogenic belt: *Advances in Earth Science*, v. 22, p. 143-151.
- Hetzl, R., Tao, M., Stokes, S., Niedermann, S., Ivy-Ochs, S., Gao, B., Stecker, M.R., and Kubik, P.W., 2004, Late Pleistocene/Holocene slip rate of the Zhangye thrust (Qilian Shan, China) and implications for the active growth of the northeastern Tibetan Plateau: *Tectonics*, v. 23.
- Horton, B.K., Yin, A., Spurlin, M.S., Zhou, J., and Wang, J., 2002, Paleocene-Eocene syncontractional sedimentation in narrow, lacustrine-dominated basins of east-central Tibet: *Geological Society of America Bulletin*, v. 114, p. 771-786.
- Horton, B.K., Dupont-Nivet, G., Zhou, J., Waanders, G.L., Butler, R.F., and Wang, J., 2004, Mesozoic-Cenozoic evolution of the Xining-Minhe and Dangchang basins, northeastern Tibetan Plateau: Magnetostratigraphic and biostratigraphic results: *Journal of Geophysical Research*, v. 109, no. B4.
- Hou, Q., Zhao, Z., Zhang, H., Zhang, B., and Chen, Y., 2006, Indian Ocean-MORB-type isotopic signature of Yushigou ophiolite in North Qilian Mountains and its implications: *Science in China Series D*, v. 49, no. 6, p. 561-572.
- Hu, N.G., Xu, A.D., and Yang, J.X., 2005, Characteristics and tectonic environment of Zhigoumen pluton in Longshoushan area: *Journal of Earth Sciences and Environment*, v. 27, p. 5-11 (in Chinese with English abstract).
- Hubbard, J., and Shaw, J.H., 2009, Uplift of the Longmen Shan and Tibetan plateau, and the 2008 Wenchuan (M= 7.9) earthquake: *Nature*, v. 458, no. 7235, p. 194-197.
- Huo, Y.L., and Tan, S.D., 1995, Exploration case history and petroleum geology in Jiuquan continental basin: Beijing, China, Petroleum Industry Press, 211 p.
- Johnson, M.R.W., 2002, Shortening budgets and the role of continental subduction during the India-Asia collision: *Earth-Science Reviews*, v. 59, p. 101-123.
- Jolivet, M., Brunel, M., Seward, D., Xu, Z., Yang, J., Roger, F., Tapponnier, P., Malavieille, J., Arnaud, N., and Wu, C., 2001, Mesozoic and Cenozoic tectonics of the northern edge of the Tibetan plateau: Fission-track constraints: *Tectonophysics*, v. 343, p. 111-134.

- Jolivet, M., Brunel, M., Seward, D., Xu, Z., Yang, J., Malavieille, J., Roger, F., Leyreloup, A., Arnaud, N., and Wu, C., 2003, Neogene extension and volcanism in the Kunlun fault zone, northern Tibet: New constraints on the age of the Kunlun Fault: *Tectonics*, v. 22, 1052.
- Kind, R., et al., 2002, Seismic images of crust and upper mantle beneath Tibet: Evidence for Eurasian plate subduction: *Science*, v. 298, no. 5596, p. 1219-1221.
- King, R.W., Shen, F., Burchfiel, B.C., Royden, L.H., Wang, E., Chen, Z., Liu, Y., Zhang, X.-Y., Zhao, J.-X., and Li, Y., 1997, Geodetic measurement of crustal motion in southwest China: *Geology*, v. 25, p. 179-182.
- Lavé, J., and Avouac, J. P., 2000, Active folding of fluvial terraces across the Siwaliks Hills, Himalayas of central Nepal: *Journal of Geophysical Research*, v. 105, no. B3, p. 5735-5770.
- Lease, R.O., Burbank, D.W., Clark, M.K., Farley, K.A., Zheng, D., and Zhang, H., 2011, Middle Miocene reorganization of deformation along the northeastern Tibetan Plateau: *Geology*, v. 39, p. 359-362.
- Lease, R.O., Burbank, D.W., Zhang, H., Liu, J., and Yuan, D., 2012, Cenozoic shortening budget for the northeastern edge of the Tibetan Plateau: Is lower crustal flow necessary?: *Tectonics*, v. 31.
- Le Pichon, X., Fournier, M., and Jolivet, L., 1992, Kinematics, topography, shortening, and extrusion in the India-Eurasia collision: *Tectonics*, v. 11, p. 1085-1098.
- Li, Y.L., 1993, Uplift of the Qinghai-Xizang Plateau and the affect to environment, *in* Bao, H.S., ed., *Proceedings of geography research*: Nanjing, Nanjing University Publishing House, p. 41-52 (in Chinese).
- Li, Y.L., 1994, Mechanism and evolution of tectonic landforms in Hexi Corridor, Gansu [PhD thesis]: Peking University (in Chinese).
- Li, Y.L., and Yang, J.C., 1998, Tectonic geomorphology in the Hexi Corridor, north-west China: *Basin Research*, v. 10, p. 345-352.
- Lin, Y.H., Zhang, L.F., Ji, J.Q., and Song, S.G., 2010,  $^{40}\text{Ar}/^{39}\text{Ar}$  age of Jiugequan lawsonite blueschists in northern Qilian Mountains and its petrologic significance: *Chinese Science Bulletin*, v. 55, p. 2021-2027.
- Liu, M., Mooney, W.D., Li, S., Okaya, N., and Detweiler, S., 2006, Crustal structure of the northeastern margin of the Tibetan plateau from the Songpan-Ganzi terrane to the Ordos basin: *Tectonophysics*, v. 420, p. 253-266.
- Liu, Y. J., Neubauer, F., Genser, J., Takasu, A., Ge, X. H., and Handler, R., 2006,  $^{40}\text{Ar}/^{39}\text{Ar}$  ages of blueschist facies pelitic schists from Qingshuigou in the Northern Qilian Mountains, western China: *Island Arc*, v. 15, no. 1, p. 187-198.

- Liu, X.D., Cheng, Z. G., and Zhang, R., 2009, The A1B scenario projection for climate change over the Tibetan Plateau in the next 30 to 50 years: *Plateau Meteorology*, v. 28, no. 3, p. 475-484 (in Chinese).
- Liu-Zeng, J., Tapponnier, P., Gaudemer, Y., and Ding, L., 2008, Quantifying landscape differences across the Tibetan plateau: Implications for topographic relief evolution: *Journal of Geophysical Research: Earth Surface*, v. 113, no. F4.
- Long, S., McQuarrie, N., Tobgay, T., and Grujic, D., 2011, Geometry and crustal shortening of the Himalayan fold-thrust belt, eastern and central Bhutan: *Geological Society of America Bulletin*, v. 123, p. 1427-1447.
- Makovsky, Y., and Klemperer, S.L., 1999, Measuring the seismic properties of Tibetan bright spots: Evidence for free aqueous fluids in the Tibetan middle crust: *Journal of Geophysical Research*, v. 104, p. 10,795-10,825.
- McQuarrie, N., Robinson, D., Long, S., Tobgay, T., Grujic, D., Gehrels, G., and Ducea, M., 2008, Preliminary stratigraphic and structural architecture of Bhutan: Implications for the along strike architecture of the Himalayan system: *Earth and Planetary Science Letters*, v. 272, p. 105-117.
- McQuarrie, N., and Ehlers, T.A., 2015, Influence of thrust belt geometry and shortening rate on thermochronometer cooling ages: Insights from thermokinematic and erosion modeling of the Bhutan Himalaya: *Tectonics*, v. 34, no. 6, p. 1055-1079.
- Meyer, B., Tapponnier, P., Bourjot, L., Métivier, F., Gaudemer, Y., Peltzer, G., Shunmin, G., and Zhitai, C., 1998, Crustal thickening in Gansu-Qinghai, lithospheric mantle subduction, and oblique, strike-slip controlled growth of the Tibet Plateau: *Geophysical Journal International*, v. 135, p. 1-47.
- Mitra, S., and Namson, J.S., 1989, Equal-area balancing: *American Journal of Science*, v. 289, no. 5, p. 563-599.
- Mock, C., Arnaud, N.O., and Cantagrel, J.M., 1999, An early unroofing in northeastern Tibet? Constraints from  $^{40}\text{Ar}/^{39}\text{Ar}$  thermochronology on granitoids from the eastern Kunlun range (Qianghai, NW China): *Earth and Planetary Science Letters*, v. 171, p. 107-122.
- Molnar, P., 1988, Continental tectonics in the aftermath of plate tectonics: *Nature*, v. 335, no. 6186, p. 131-137.
- Molnar, P., and Tapponnier, P., 1975, Cenozoic tectonics of Asia: Effects of a continental collision: *Science*, v. 189, no. 4201, p. 419-426.
- Molnar, P., England, P., and Martinod, J., 1993, Mantle dynamics, uplift of the Tibetan Plateau, and the Indian monsoon: *Reviews of Geophysics*, v. 31, p. 357-396.

- Murphy, M.A., Yin, A., Harrison, T.M., Dürr, S.B., Chen, Z., Ryerson, F.J., Kidd, S.F., Wang, X., and Zhou, X., 1997, Did the Indo-Asian collision alone create the Tibetan plateau?: *Geology*, v. 25, p. 719-722.
- Nelson, K.D., Zhao, W., Brown, L.D., Kuo, J., Che, J., Liu, X., Klemperer, S.L., Makovsky, Y., Meissner, R., Mechie, J., and Kind, R., 1996, Partially molten middle crust beneath southern Tibet: synthesis of project INDEPTH results: *Science*, v. 274, no. 5293, p. 1684-1688.
- Pan, G., Ding, J., Yao, D., and Wang, L., 2004, Geological map of Qinghai-Xiang (Tibet) plateau and adjacent areas: Chengdu, China, Chengdu Institute of Geology and Mineral Resources, China Geological Survey, Chengdu Cartographic Publishing House, scale 1:1,500,000.
- Pan, S., and Niu, F., 2011, Large contrasts in crustal structure and composition between the Ordos plateau and the NE Tibetan plateau from receiver function analysis: *Earth and Planetary Science Letters*, v. 303, p. 291-298.
- Powell, C.M., 1986, Continental underplating model for the rise of the Tibetan Plateau: *Earth and Planetary Science Letters*, v. 81, p. 79-94.
- Powell, C.M.A., and Conaghan, P.J., 1973, Polyphase deformation in Phanerozoic rocks of the Central Himalayan Gneiss, northwest India: *Journal of Geology*, v. 81, p. 127-143.
- Pullen, A., Kapp, P., Gehrels, G.E., Vervoort, J.D., and Ding, L., 2008, Triassic continental subduction in central Tibet and Mediterranean-style closure of the Paleo-Tethys Ocean: *Geology*, v. 36, p. 351-354.
- Qian, Q., Wang, Y.M., Li, H.M., Jia, X.Q., Han, S., and Zhang, Q., 1998, Geochemical characteristics and genesis of diorites from Laohushan, Gansu Province: *Acta Petrolei Sinica*, v. 14, p. 520-528 (in Chinese with English abstract).
- Qinghai BGMR (Bureau of Geology and Mineral Resources), 1991, Regional geology of Qinghai Province: Beijing, China, Geological Publishing House, 662 p.
- Quan, S., Jia, Q., Guo, Z., and Wang, W., 2006, Basic characteristics of granitoids related to tungsten mineralization in the Qilian mountain: *Mineralium Deposita*, v. 25, p. 143-146.
- Reith, R.C., 2013, Structural geology of a central segment of the Qilian Shan-Nan Shan thrust belt: Implications for the magnitude of Cenozoic shortening in the northeastern Tibetan Plateau [M.S. thesis]: Los Angeles, University of California, 73 p.
- Robinson, D.M., DeCelles, P.G., and Copeland, P., 2006, Tectonic evolution of the Himalayan thrust belt in western Nepal: Implications for channel flow models: *Geological Society of America Bulletin*, v. 118, p. 865-885.

- Rohrmann, A., Kapp, P., Carrapa, B., Reiners, P.W., Guynn, J., Ding, L., and Heizler, M., 2012, Thermochronologic evidence for plateau formation in central Tibet by 45 Ma: *Geology*, v. 40, p. 187-190.
- Royden, L.H., Burchfiel, B.C., King, R.W., Wang, E., Chen, Z., Shen, F., and Liu, Y., 1997, Surface deformation and lower crustal flow in eastern Tibet: *Science*, v. 276, no. 5313, p. 788-790.
- Royden, L.H., Burchfiel, B.C., and van der Hilst, R.D., 2008, The geological evolution of the Tibetan Plateau: *Science*, v. 321, no. 5892, p. 1054-1058.
- Ryan, W.B.F., et al., 2009, Global multi-resolution topography synthesis: *Geochemistry, Geophysics, Geosystems*, v. 10.
- Schubert, G., and Sandwell, D., 1989, Crustal volumes of the continents and of oceanic and continental submarine plateaus: *Earth and Planetary Science Letters*, v. 92, p. 234-246.
- Sengör, A.M.C., and Natal'in, B.A., 1996, Paleotectonics of Asia: Fragments of a synthesis, *in* Yin, A., and Harrison, T.M., eds., *The tectonics of Asia*: New York, Cambridge University Press, p. 486-640.
- Sherrington, H.F., Zandt, G., and Frederiksen, A., 2004, Crustal fabric in the Tibetan plateau based on waveform inversions for seismic anisotropy parameters: *Journal of Geophysical Research*, v. 109.
- Smith, A.D., 2006, The geochemistry and age of ophiolitic strata of the Xinglongshan Group: Implications for the amalgamation of the Central Qilian belt: *Journal of Asian Earth Sciences*, v. 28, p. 133-142.
- Sobel, E.R., and Arnaud, N., 1999, A possible middle Paleozoic suture in the Altyn Tagh, NW China: *Tectonics*, v. 18, p. 64-74.
- Song, S., Zhang, L.F., Niu, Y.L., Su, L., Song, B., and Liu, D.Y., 2006, Evolution from oceanic subduction to continental collision: A case study of the Northern Tibetan Plateau inferred from geochemical and geochronological data: *Journal of Petrology*, v. 47, p. 435-455.
- Song, S., Niu, Y., Su, L., and Xia, X., 2013, Tectonics of the North Qilian orogen, NW China: *Gondwana Research*, v. 23, p. 1378-1401.
- Su, J., Zhang, X., Hu, N., Fu, G., and Zhang, H., 2004, Geochemical characteristics and genesis of adakite-like granites at Yema Nanshan in the western segment of the Central Qilian Mountains: *Chinese Geology*, v. 31, p. 365-371.
- Suppe, J., 1983, Geometry and kinematics of fault-bend folding. *American Journal of Science*: v. 283, no. 7, p. 684-721.

- Shi, R.D., Yang, J.S., and Wu, C.L., 2004, First SHRIMP dating for the formation of the Late Sinian Yushigou Ophiolite North Qilian Mountains: *Acta Geologica Sinica*, v. 78, p.649–657 (in Chinese with English abstract).
- Tapponnier, P., et al., 1990, Active thrusting and folding in the Qilian Shan, and decoupling between upper crust and mantle in northeastern Tibet: *Earth and Planetary Science Letters*, v. 97, p. 382-403.
- Tapponnier, P., Zhiqin, X., Roger, F., Meyer, B., Arnaud, N., Wittlinger, G., and Jingsui, Y., 2001, Oblique stepwise rise and growth of the Tibet Plateau: *Science*, v. 294, no. 5547, p. 1671-1677.
- Taylor, M., and Yin, A., 2009, Active structures of the Himalayan-Tibetan orogen and their relationships to earthquake distribution, contemporary strain field, and Cenozoic volcanism: *Geosphere*, v. 5, p. 199-214.
- Thiede, R.C., Bookhagen, B., Arrowsmith, J.R., Sobel, E.R., and Strecker, M.R., 2004, Climatic control on rapid exhumation along the Southern Himalayan Front: *Earth and Planetary Science Letters*, v. 222, no. 3, p. 791-806.
- Thiede, R.C., and Ehlers, T.A., 2013, Large spatial and temporal variations in Himalayan denudation: *Earth and Planetary Science Letters*, v. 371, p. 278-293.
- Tseng, C.Y., Yang, H.J., Yang, H.Y., Liu, D.Y., Tsai, C.L., Wu, H.Q., and Zuo, G.C., 2007, The Dongcaohe ophiolite from the North Qilian Mountains: A fossil oceanic crust of the paleo-Qilian ocean: *Chinese Science Bulletin*, v. 52, p. 2390-2401.
- Tseng, C.Y., Yang, H.J., Yang, H.Y., Liu, D., Wu, C., Cheng, C.K., Chen, C.H., and Ker, C.M., 2009, Continuity of the North Qilian and North Qinling orogenic belts, central orogenic system of China: Evidence from newly discovered Paleozoic adakitic rocks: *Gondwana Research*, v. 16, p. 285-293.
- van Hinsbergen, D.J., Kapp, P., Dupont-Nivet, G., Lippert, P.C., DeCelles, P.G., and Torsvik, T.H., 2011, Restoration of Cenozoic deformation in Asia and the size of Greater India: *Tectonics*, v. 30, TC5003.
- van Hinsbergen, D.J., Lippert, P.C., Dupont-Nivet, G., McQuarrie, N., Doubrovine, P.V., Spakman, W., and Torsvik, T.H., 2012, Greater India Basin hypothesis and a two-stage Cenozoic collision between India and Asia: *National Academy of Sciences Proceedings*, v. 109, p. 7659-7664.
- Vergne, J., Wittlinger, G., Qiang, H., Tapponnier, P., Poupinet, G., Jiang, M., Herquel, G., and Paul, A., 2002, Seismic evidence for stepwise thickening of the crust across the NE Tibetan Plateau: *Earth and Planetary Science Letters*, v. 203, p. 25-33.
- Vergne, J., Wittlinger, G., Farra, V., and Su, H., 2003, Evidence for upper crustal anisotropy in the Songpan-Ganze (northeastern Tibet) terrane: *Geophysical Research Letters*, v. 30, 1552.

- Vincent, S.J., and Allen, M.B., 1999, Evolution of the Minle and Chaoshui Basins, China: Implications for Mesozoic strike-slip basin formation in Central Asia: *Geological Society of America Bulletin*, v. 111, p. 725-742.
- Wallis, S., Tsujimori, T., Aoya, M., Kawakami, T., Terada, K., Suzuki, K., and Hyodo, H., 2003, Cenozoic and Mesozoic metamorphism in the Longmenshan orogen: Implications for geodynamic models of eastern Tibet: *Geology*, v. 31, p. 745-748.
- Wang, C., Zhao, X., Liu, Z., Lippert, P.C., Graham, S.A., Coe, R.S., Yi, H., Zhu, L., Liu, S., and Li, Y.-l., 2008, Constraints on the early uplift history of the Tibetan Plateau: *National Academy of Sciences Proceedings*, v. 105, p. 4987-4992.
- Wang, C., Gao, R., Yin, A., Wang, H., Zhang, Y., Guo, T., Li, Q., and Li, Y., 2011, A mid-crustal strain-transfer model for continental deformation: A new perspective from high-resolution deep seismic-reflection profiling across NE Tibet: *Earth and Planetary Science Letters*, v. 306, p. 279-288.
- Wang, Q.M., and Coward, M.P., 1993, The Jiuxi basin, Hexi corridor, NW China: Foreland structural features and hydrocarbon potential: *Journal of Petroleum Geology*, v. 16, p. 169-182.
- Webb, A.A.G., 2013, Preliminary balanced palinspastic reconstruction of Cenozoic deformation across the Himachal Himalaya (northwestern India): *Geosphere*, v. 9, p. 572-587.
- Webb, A.A.G., Yin, A., Harrison, T.M., C  lerier, J., Gehrels, G.E., Manning, C.E., and Grove, M., 2011, Cenozoic tectonic history of the Himachal Himalaya (northwestern India) and its constraints on the formation mechanism of the Himalayan orogen: *Geosphere*, v. 7, p. 1013-1061.
- Willett, S.D., and Beaumont, C., 1994, Subduction of Asian lithospheric mantle beneath Tibet inferred from models of continental collision: *Nature*, v. 369, no. 6482, p. 642-645.
- Wobus, C.W., Hodges, K.V., and Whipple, K.X., 2003, Has focused denudation sustained active thrusting at the Himalayan topographic front?: *Geology*, v. 31, no. 10, p. 861-864.
- Worley, B.A., and Wilson, C.J., 1996, Deformation partitioning and foliation reactivation during transpressional orogenesis, an example from the Central Longmen Shan, China: *Journal of Structural Geology*, v. 18, p. 395-411.
- Wu, C.L., Yang, J.S., Yang, H.Y., Wooden, J., Shi, R.D., Chen, S.Y., and Zheng, Q.G., 2004, Dating of two types of granite from north Qilian, China: *Acta Petrolei Sinica*, v. 20, p. 425-432.
- Wu, C.L., Yao, S., Zeng, L., Yang, J., Wooden, J., Chen, S., and Mazadab, F., 2006, Double subduction of the early Paleozoic North Qilian oceanic plate: Evidence from granites in the central segment of North Qilian, NW China: *Geology in China*, v. 33, p. 1197-1208.



- Wu, C.L., Xu, X.Y., Gao, Q.M., Li, X.M., Lei, M., Gao, Y.H., Frost, B.R., and Wooden, J., 2010, Early Palaeozoic granitoid magmatism and tectonic evolution in North Qilian, NW China: *Yanshi Xuebao*, v. 26, p. 1027-1044 (in Chinese with English abstract).
- Wu, J., Tang, Q.S., Chen, H.L., Xiao, A.C., Cheng, X.G., and Mao, Q.M., 2006, The thrust deformation of pluton: Take the Jinfosi pluton in eastern Jiuquan Basin as an example: *Geological Journal of China Universities*, v. 12, p. 22-29 (in Chinese with English abstract).
- Xia, X.H., and Song, S.G., 2010, Forming age and tectono-petrogenesis of the Jiugequan ophiolite in the North Qilian Mountain, NW China: *Chinese Science Bulletin*, v. 55, p. 1899-1907.
- Xia, X.H., Song, S., and Niu, Y., 2012, Tholeiite-boninite terrane in the North Qilian suture zone: Implications for subduction initiation and back-arc basin development: *Chemical Geology*, v. 328, p. 259-277.
- Xiang, Z.Q., Lu, S.N., Li, H.K., Li, H.M., Song, B., and Zheng, J.K., 2007, SHRIMP U-Pb zircon age of gabbro in Aoyougou in the western segment of the North Qilian Mountains, China and its geological implications: *Geological Bulletin of China*, v. 26, p. 1686-1691.
- Xiao, W., Windley, B.F., Yong, Y., Yan, Z., Yuan, C., Liu, C., and Li, J., 2009, Early Paleozoic to Devonian multiple-accretionary model for the Qilian Shan, NW China: *Journal of Asian Earth Sciences*, v. 35, p. 323-333.
- Xiao, X.C., Chen, G.M., and Zhu, Z.Z., 1978, A preliminary study on the tectonics ancient ophiolites in the Qilian Mountain, northwest China: *Acta Geologica Sinica*, v.4, p. 279-295 (in Chinese with English abstract).
- Xiong, Z., Zhang, H., and Zhang, J., 2012, Petrogenesis and tectonic implications of the Maozangsi and Huangyanghe granitic intrusions in Lenglongling area, the eastern part of North Qilian Mountain, NW China: *Earth Science Frontiers*, v. 19, p. 214-227.
- Yakovlev, P.V., and Clark, M.K., 2014, Conservation and redistribution of crust during the Indo-Asian collision: *Tectonics*, v. 33, p. 1016-1027.
- Yang, J.C., Zheng, W.T., and Li, Y.L., 1993, Evolution model of the compressive basins in the Hexi Corridor, in Bao, H.S., ed., *Proceeding of geography research*: Nanjing, China, Nanjing University Publishing House, p. 133-144 (in Chinese).
- Yang, S., Cheng, X., Xiao, A., Chen, J., Fan, M., and Tain, D., 2007a, The structural characteristics of Northern Qilian Shan mountain thrust belt and its control on the oil and gas accumulation: Beijing, China, Science Press, p. 70-82 (in Chinese).
- Yang, S., Chen, H., Cheng, X., Xiao, A., He, G., Chen, J., and Tian, D., 2007b, Deformation characteristics and rules of spatial change for the Northern Qilianshan thrust belt: *Earth Science Frontiers*, v. 14, p. 211-221.

- Ye, Z., Gao, R., Li, Q., Zhang, H., Shen, X., Liu, X., and Gong, C., 2015, Seismic evidence for the North China plate underthrusting beneath northeastern Tibet and its implications for plateau growth: *Earth and Planetary Science Letters*, v. 426, p. 109-117.
- Yin, A., 2006, Cenozoic tectonic evolution of the Himalayan orogen as constrained by along-strike variation of structural geometry, exhumation history, and foreland sedimentation: *Earth-Science Reviews*, v. 76, p. 1-131.
- Yin, A., 2010, Cenozoic tectonic evolution of Asia: A preliminary synthesis: *Tectonophysics*, v. 488, p. 293-325.
- Yin, A., and Harrison, T.M., 2000, Geologic evolution of the Himalayan-Tibetan orogen: *Annual Review of Earth and Planetary Sciences*, v. 28, p. 211-280.
- Yin, A., and Nie, S., 1993, An indentation model for the North and South China collision and the development of the Tan-Lu and Honam fault systems, eastern Asia: *Tectonics*, v. 12, no. 4, p. 801-813.
- Yin, A., and Nie, S., 1996, A Phanerozoic palinspastic reconstruction of China and its neighboring regions, *in* Yin, A., and Harrison, T.M., eds., *The tectonics of Asia*: New York, Cambridge University Press, p. 442-485.
- Yin, A., Dang, Y.-Q., Zhang, M., McRivette, M.W., Burgess, W.P., and Chen, X.-H., 2007a, Cenozoic tectonic evolution of Qaidam Basin and its surrounding regions (part 2): Wedge tectonics in southern Qaidam Basin and the Eastern Kunlun Range, *in* Sears, J.W., et al., eds., *Whence the Mountains? Inquiries into the evolution of orogenic systems: A volume in honor of Raymond A. Price*: Geological Society
- Yin, A., Manning, C.E., Lovera, O., Menold, C.A., Chen, X., and Gehrels, G.E., 2007b, Early Paleozoic tectonic and thermomechanical evolution of ultrahigh-pressure (UHP) metamorphic rocks in the northern Tibetan Plateau, northwest China: *International Geology Review*, v. 49, p. 681-716.
- Yin, A., Dang, Y.-Q., Wang, L.-C., Jiang, W.-M., Zhou, S.-P., Chen, X.-H., Gehrels, G.E., and McRivette, M.W., 2008a, Cenozoic tectonic evolution of Qaidam Basin and its surrounding regions (part 1): The southern Qilian Shan-Nan Shan thrust belt and northern Qaidam Basin: *Geological Society of America Bulletin*, v. 120, p. 813-846.
- Yin, A., Dang, Y.Q., Zhang, M., Chen, X.H., and McRivette, M.W., 2008b, Cenozoic tectonic evolution of the Qaidam basin and its surrounding regions (Part 3): Structural geology, sedimentation, and regional tectonic reconstruction: *Geological Society of America Bulletin*, v. 120, p. 847-876.
- Yin, A., Dubey, C.S., Webb, A.A.G., Kelty, T.K., Grove, M., Gehrels, G.E., and Burgess, W.P., 2010a, Geologic correlation of the Himalayan orogen and Indian craton: Part 1. Structural geology, U-Pb zircon geochronology, and tectonic evolution of the Shillong Plateau and its neighboring regions in NE India: *Geological Society of America Bulletin*, v. 122, p. 336-359.

- Yin, A., Dubey, C.S., Kelty, T.K., Webb, A.A.G., Harrison, T.M., Chou, C.Y., and C  lerier, J., 2010b, Geologic correlation of the Himalayan orogen and Indian craton: Part 2. Structural geology, geochronology, and tectonic evolution of the Eastern Himalaya: Geological Society of America Bulletin, v. 122, p. 360-395.
- Yuan, D. Y., et al., 2011, Late Quaternary right-lateral slip rates of faults adjacent to the lake Qinghai, northeastern margin of the Tibetan Plateau: Geological Society of America Bulletin, v. 123, p. 2016-2030.
- Yuan, D.Y., et al., 2013, The growth of northeastern Tibet and its relevance to large-scale continental geodynamics: A review of recent studies: Tectonics, v. 32, p. 1358-1370.
- Yue, H., et al., 2012, Lithospheric and upper mantle structure of the northeastern Tibetan Plateau: Journal of Geophysical Research, v. 117, no. B5.
- Zhang, Z.H., 1990, Quaternary Geological Map of China and Adjacent Seas (1:2500000): Beijing, Cartographic Publishing House.
- Zhang, D.Q., Sun, G.Y., and Xu, H.L., 1995, Petrology and isotope chronology of the Jinfosi pluton, Qilian Mts., Gansu: Acta Geoscientia Sinica, v. 37, p. 375-385 (in Chinese with English abstract).
- Zhang, H.-P., Craddock, W.H., Lease, R.O., Wang, W.-T., Yuan, D.-Y., Zhang, P.-Z., Molnar, P., Zheng, D.-W., and Zheng, W.-J., 2012, Magnetostratigraphy of the Neogene Chaka Basin and its implications for mountain building processes in the north-eastern Tibetan Plateau: Basin Research, v. 24, p. 31-50.
- Zhang, J.X., Meng, F.C., and Wan, Y.S., 2007, A cold early Palaeozoic subduction zone in the North Qilian Mountains, NW China: Petrological and U-Pb geochronological constraints: Journal of Metamorphic Geology, v. 25, p. 285-304.
- Zhang, P.Z., et al., 2004, Continuous deformation of the Tibetan Plateau from global positioning system data: Geology, v. 32, p. 809-812.
- Zhang, Z.C., Zhou, M.F., Robinson, P.T., Mao, J.W., Yang, J.M., and Zuo, G.C., 2001, SHRIMP dating of the Aoyougou ophiolite in the west sector of the north Qilian Mountains and its geological significance: Acta Petrologica Sinica, v. 17, p. 222-226 (in Chinese with English abstract).
- Zhang, Z.M., Dong, X., Santosh, M., and Zhao, G.C., 2014, Metamorphism and tectonic evolution of the Lhasa terrane, Central Tibet: Gondwana Research, v. 25, p. 170-189.
- Zhao, R., Zhao, Z., Fan, W., Zhou, Z., and Mao, J., 2002, Geology of Gansu Province: Bureau of Geology and mineral resources of Gansu Province, in Geological Atlas of China: Beijing, China, Geological Publishing House, p. 325-332.
- Zhao, W., et al., 2001, Crustal structure of central Tibet as derived from project INDEPTH wide-angle seismic data: Geophysical Journal International, v. 145, p. 486-498.

- Zhao, W., et al., 2011, Tibetan plate overriding the Asian plate in central and northern Tibet: *Nature Geoscience*, v. 4, p. 870-873.
- Zhao, W.-L., and Morgan, W.J., 1987, Injection of Indian crust into Tibetan lower crust: A two-dimensional finite element model study: *Tectonics*, v. 6, p. 489-504.
- Zheng, D., Zhang, P.Z., Wan, J., Yuan, D., Li, C., Yin, G., Zhang, G., Wang, Z., Min, W., and Chen, J., 2006, Rapid exhumation at ~ 8 Ma on the Liupan Shan thrust fault from apatite fission-track thermochronology: Implications for growth of the northeastern Tibetan Plateau margin: *Earth and Planetary Science Letters*, v. 248, p. 198-208.
- Zheng, D., Clark, M.K., Zhang, P., Zheng, W., and Farley, K.A., 2010, Erosion, fault initiation and topographic growth of the North Qilian Shan (northern Tibetan Plateau): *Geosphere*, v. 6, p. 937-941.
- Zheng, W.J., Zhang, P.Z., Yuan, D.Y., Zheng, D.W., Li, C., Zhang, P., Yin, J., Min, W., Heermance, R., and Chen, J., 2009, Deformation on the northern of the Tibetan Plateau from GPS measurement and geologic rates of the late Quaternary along the major fault: *Chinese Journal of Geophysics*, v. 52, p. 2491-2508.
- Zheng, W.J., Zhang, P.Z., He, W.G., Yuan, D.Y., Shao, Y.X., Zheng, D.W., Ge, W.P., and Min, W., 2013, Transformation of displacement between strike-slip and crustal shortening in the northern margin of the Tibetan Plateau: Evidence from decadal GPS measurements and late Quaternary slip rates on faults: *Tectonophysics*, v. 584, p. 267-280.
- Zhiyi, Z., and Dean, W.T., 1996, Phanerozoic geology of northwest China: Beijing, China, Science Press, 316 p.
- Zhou, J., Xu, F., Wang, T., Cao, A., and Yin, C., 2006, Cenozoic deformation history of the Qaidam Basin, NW China: Results from cross-section restoration and implications for Qinghai-Tibet Plateau tectonics: *Earth and Planetary Science Letters*, v. 243, p. 195-210.
- Zhu, B., Kidd, W.S., Rowley, D.B., Currie, B.S., and Shafique, N., 2005, Age of initiation of the India-Asia collision in the east-central Himalaya: *Journal of Geology*, v. 113, p. 265-285.
- Zhuang, G., Hourigan, J.K., Ritts, B.D., and Kent-Corson, M.L., 2011, Cenozoic multiple-phase tectonic evolution of the northern Tibetan Plateau: constraints from sedimentary records from Qaidam basin, Hexi Corridor, and Subei basin, northwest China: *American Journal of Science*, v. 311, no. 2, p. 116-152.

**-Chapter 3-**

**Non-rigid passive bookshelf faulting in northern Tibet**

### 3.1. Abstract

Collision-induced continental deformation commonly involves complex interactions between strike-slip faulting and off-fault deformation, yet this relationship has rarely been quantified. In northern Tibet, Cenozoic deformation is expressed by the development of the >1000-km-long east-striking left-slip Kunlun, Qinling, and Haiyuan faults. Each have a maximum slip in the central fault segment exceeding 10s to ~100 km but a much smaller slip magnitude ( $\sim < 10\%$  of the maximum slip) at their terminations. The along-strike variation of fault offsets and pervasive off-fault deformation create a strain pattern that departs from the expectations of the classic plate-like rigid-body motion and flow-like distributed deformation end-member models for continental tectonics. Here I present a non-rigid bookshelf-fault model for the Cenozoic tectonic development of northern Tibet. This model, which quantitatively relates discrete left-slip faulting to distributed off-fault deformation during regional clockwise rotation, explains several puzzling features, including the: (1) clockwise rotation of east-striking left-slip faults against the northeast-striking left-slip Altyn Tagh fault along the northwestern margin of the Tibetan Plateau, (2) alternating fault-parallel extension and shortening in the off-fault regions, and (3) eastward-tapering map-view geometries of the Qimen Tagh, Qaidam, and Qilian Shan thrust belts that link with the three major left-slip faults in northern Tibet. I refer to this specific non-rigid bookshelf-fault system as a passive bookshelf-fault system because the bookshelf-panels rotation is detached from the rigid bounding domains. As a consequence, the wallrock of the strike-slip faults deforms to accommodate both the clockwise rotation of the left-slip faults and off-fault strain that arises at the fault ends. An important implication of this model is that the style and magnitude of Cenozoic deformation in northern Tibet vary drastically in the east-west direction. Thus, any single north-south cross section and its kinematic reconstruction

through the region do not properly quantify the complex deformational processes of plateau construction.

### **3.2. Introduction**

The fundamental mode of continental tectonics has been characterized by two end-member processes: plate-like rigid-body motion (e.g., Tapponnier et al., 1982; Weldon and Humphreys, 1986; Avouac and Tapponnier, 1993; Meade, 2007) and distributed deformation via viscous flow (e.g., England and Houseman, 1986; Yin and Taylor, 2011). In the rigid-plate model, continental deformation is quantified by rigid block rotation on a sphere about their respective Euler poles; the horizontal dimension of the blocks is much greater than the width of faults/shear zones that bound the blocks (e.g., Avouac and Tapponnier, 1993). In contrast, the viscous-flow model quantifies continental deformation by solving a boundary-value problem that requires the knowledge of lithospheric rheology (e.g., England and Houseman, 1986). This model envisions distributed continental deformation, with major faults approximated as zones of high strain within a continuum. These two end-member models have been extensively tested in Tibet against structures created during the Cenozoic India-Eurasia collision (e.g., Yin and Harrison, 2000; Zhu et al., 2005; Yin, 2010a; van Hinsbergen et al., 2011; Yin and Taylor, 2011). Debates have been centered on whether the >1000-km-long east-striking left-slip Haiyuan, Qinling, and Kunlun faults in northern Tibet (Fig. 3.1) have acted as rigid-block boundaries (Tapponnier et al., 1982; Avouac and Tapponnier, 1993; Tapponnier et al., 2001) or transfer-fault structures linking dip-slip fault systems (e.g., Burchfiel et al., 1991; Yin, 2000; Duvall and Clark, 2010).

One form of rigid-block models for deformation in northern Tibet is bookshelf faulting, which requires that the observed left-slip faulting is driven by regional right-lateral shear (Cobbold and Davy, 1988; England and Molnar, 1990). Applying the classic rigid bookshelf-fault model (Freund 1970) to explain the tectonic development of northern Tibet raises several important questions that have not yet been addressed. (1) Why do the parallel east-striking left-slip faults terminate at the northeast-striking left-slip Altyn Tagh fault rather than a right-slip northeast-striking shear zone as required by the bookshelf-fault model (Fig. 3.1)? (2) How are the required lithospheric-scale “gaps” and “overlaps” at the ends of the rotating blocks accommodated by off-strike-slip-fault deformation (e.g., Luyendyk et al., 1980; Onderdonk, 2005; Platt and Becker, 2013) (Fig. 3.2)? (3) What is the kinematic relationship between the east-striking left-slip faults and the triangular eastward-tapering thrust belts at the western ends of the strike-slip faults (i.e., the Qimen Tagh, Qaidam, and Qilian Shan-Nan Shan thrust belts) (Fig. 3.1)?

In this study I propose a non-rigid bookshelf-fault model (e.g., Yin and Pappalardo, 2015) to resolve the above issues. Specifically, I show that an eastward decrease in Cenozoic strain results in clockwise rotation and left-slip bookshelf faulting across northern Tibet. The detached rotation of these bookshelf faults against rigid bounding domains, a process which I refer to as passive bookshelf faulting, may explain why a left-slip bookshelf fault system is bounded by the left-slip Altyn Tagh fault (Fig. 3.1). Non-rigid wallrock deformation within the strike-slip-fault-bounded regions accommodates both the clockwise rotation of the strike-slip faults and the space issues that arise at the ends of the bookshelf panels. The model implies that thrust belt development and strike-slip faulting in the region are coeval and kinematically linked,



which contrasts an earlier suggestion that they represent two distinct stages of plateau development (e.g., Yuan et al., 2013).

### **3.3. Cenozoic left-slip faults in northern Tibet**

The ~N110°E-striking left-slip Kunlun, Qinling, and Haiyuan faults, extending for ~1500, ~1000, and ~1000 km respectively, are by far the longest and most continuous structures in northern Tibet (Fig. 3.1) (Tapponnier et al., 2001; Taylor and Yin, 2009). The faults are lithospheric structures (Wang et al., 2011; Gao et al., 2013) that closely follow the surface traces of the Paleozoic and Mesozoic Qilian, Qinling, and Kunlun suture zones (Yin and Harrison, 2000; Wu et al., 2016) (Fig. 3.1).

The kinematics of these major east-striking faults has been related to lateral extrusion (Tapponnier et al., 1982; 2001; Cheng et al., 2015), strain transfer between thrust belts (Burchfiel et al., 1991; Zhang et al., 1991; Duvall and Clark, 2010), and bookshelf faulting associated with clockwise fault rotation induced by broad and distributed north-trending right-lateral shear (England and Molnar, 1990; Zuza and Yin, 2013) (Fig. 3.3a). The extrusion fault model requires high slip rates ( $> 10\text{-}20$  mm/yr), large fault offsets (100s km) (Tapponnier et al., 1982; Avouac and Tapponnier, 1993), the presence of zipper thrusts at the western end of the left-slip faults (Peltzer and Tapponnier, 1988; Cheng et al., 2015), and a conjugate and coeval right-slip fault with a similar slip magnitude to assist eastward lateral extrusion (scenario 1 in Fig. 3.3a). In contrast, the transfer-fault model predicts transpressional deformation at the termination thrusts oriented obliquely to the strike-slip faults (scenario 2 in Fig. 3.3a). Finally, the bookshelf fault model predicts clockwise rotation of both the left-slip faults and the fault-bounded wallrock. If the bookshelf panels are rigid, the model predicts the formation of “gaps” and/or “overlaps” at

the end of the rotating blocks (scenario 3 in Fig. 3.3a); these gaps and overlaps can be reconciled by fault-parallel extension and/or shortening with non-rigid off-fault deformation (scenario 4 in Fig. 3.3a). Proposed solutions to the space issues of rigid bookshelf faulting (scenario 3 in Fig. 3a) include (1) extension leading to basin formation (Luyendyk et al., 1980) (Fig. 3.2b), (2) shortening within the terminal regions of the rotated blocks (e.g., Onderdonk, 2005) (Fig. 3.2c), or (3) fault-parallel stretching across the rotated blocks (e.g., Platt and Becker, 2010, 2013) (Fig. 3.2d).

### **3.3.1. Initiation age and along-strike variation of fault offsets and slip rates**

A summary of inferred fault initiation ages across northern Tibet is shown in Figure 3.3b (Yuan et al., 2013). The Haiyuan fault, which initiated at ~17-12 Ma in the west (Duvall et al., 2013) and ~8 Ma in the east (Zheng et al., 2006; Yuan et al., 2013) (Fig. 3.3b), is estimated to have  $95 \pm 15$  km left-lateral offset at the center (Gaudemer et al., 1995) and 10-15 km slip at the eastern end (Burchfiel et al., 1991; Zhang et al., 1991) (Fig. 3.1). Slip along the range-bounding thrusts at the western termination of the Haiyuan fault is  $\leq 10$  km (Reith, 2013; Zuza et al., 2014, 2016) (Fig. 3.1), requiring a significant decrease in fault slip from the center to the western end. The bidirectional decrease in the total fault offset along the Haiyuan fault correlates with the along-fault variation of Quaternary and global positional system (GPS) velocity field based slip rates: 11-19 mm/yr at the center (Gaudemer et al., 1995; Lasserre et al., 1999, 2002),  $< 5$  mm/yr in the east (Zhang et al., 1991; Cavalié et al., 2008; Li et al., 2009), and 2-4 mm/yr in the west (Duvall and Clark, 2010).

The western segment of the Qinling fault is a transpressional structure that initiated at ~50 Ma (Duvall et al., 2013; Yuan et al., 2013) (Fig. 3.3b), whereas the eastern segment of the

Qinling fault is a transtensional structure initiated in the Eocene with accelerated motion in the late Miocene (Mercier et al., 2013) (Fig. 3.1). Slip along the central and eastern sections of the Qinling fault is 20-30 km (Ratschbacher et al., 2003) with a Quaternary slip rate of  $7.2 \pm 2.2$  mm/yr (Zhang et al., 1995). The total fault offset in the west is constrained by east-west shortening magnitude estimates of 10-15 km across both the Jishi Shan and Liupan Shan thrust belts (Fig. 3.1) (Zhang et al. 1991; Burchfiel et al. 1991; Lease et al., 2012). The Jishi Shan and Liupan Shan thrust belts initiated at ~13 Ma and ~8 Ma respectively (Zheng et al., 2006; Godard et al., 2009; Lease et al., 2012), corresponding to an average slip rate on the western Qinling fault of about 1-1.5 mm/yr. This is significantly less than that of the central and eastern fault segments.

The Kunlun fault initiated diachronously at 35-30 Ma in the west (Mock et al., 1999; Jolivet et al., 2003; Clark et al., 2010), 20-15 Ma along its central segment (Yuan et al., 2006; Duvall et al., 2013), and ~8 Ma in the east (Duvall et al., 2013) (Fig. 3.3b). Offset along the fault decreases bidirectionally from ~120 km in the center (Kidd and Molnar, 1988) to <10s of km at the eastern and western ends when it links with minor dip-slip fault systems (Jolivet et al., 2003; Fu and Awata, 2007) (Fig. 3.1). Quaternary slip rates along the central Kunlun fault of 10-12 mm/yr (Van der Woerd et al., 1998, 2000, 2002; Fu et al., 2005; Li et al., 2005) decrease to < 2 mm/yr along the eastern segment (Kirby et al., 2007; Harkins and Kirby, 2008; Harkins et al., 2010). Given the fault initiation age of 35-30 Ma in the west and 20-30 km of slip along the fault (Mock et al., 1999; Jolivet et al., 2003), the average slip rate of the Kunlun fault in the west is also < 2 mm/yr. Thus, slip rates along the Kunlun fault must decrease bidirectionally from the center.

These east-striking left-slip faults terminate in the west at the northwest-trending Qilian Shan-Nan Shan, Qaidam Basin, and Qimen Tagh thrust belts and in the east at the north-trending Liupan Shan and Longmen Shan thrust belts (Fig. 3.1). Thrusting first started at ~50 Ma in the southern Qilian Shan and northern Qaidam Basin thrust systems, which was followed by activity in the Qimen Tagh and the northern Qilian Shan thrust belts at 25-20 Ma (e.g., Yin et al., 2008a; Duvall et al., 2013; Cheng et al., 2014) (Fig. 3.3b). The Longmen Shan thrust belt, which involves dip-slip thrusting and minor right-slip faulting (Densmore et al., 2007; Yin, 2010b), began to develop at 30-25 Ma and accelerated deformation occurred at 15-10 Ma (Godard et al., 2009; Wang et al., 2012). The Liupan Shan thrust belt initiated at ~8 Ma (Zheng et al. 2006). Existing studies indicate a north-south shortening magnitude of 200-450 km across the three northwest-trending thrust belts (i.e., the Qimen Tagh, Qaidam Basin, and Qilian Shan-Nan Shan) (Gaudemer et al., 1995; Meyer et al., 1998; Yin et al., 2007; Yin et al., 2008a, 2008b; Gao et al., 2013; Cheng et al., 2014; Zuza et al., 2016), which contrasts sharply to the 10-40 km of shortening across the north-trending Liupan Shan and Longmen Shan thrust belts (Fig. 3.1) (Zhang et al., 1991; Burchfiel et al., 1995; Hubbard and Shaw, 2009).

The major left-slip faults in northern Tibet also link with extensional zones and right-slip faults (Fig. 3.1). The Haiyuan fault merges with the north-trending Yinchuan rift system in the east and the southeast-striking right-slip Elashan and Riyueshan faults in the west (e.g., Zhang et al., 1998), whereas the Qinling fault links with the Shanxi rift system in the east and the right-slip Riyueshan-Gonghe faults in the west (e.g., Zhang et al., 1998). The Kunlun fault links with central Tibetan rifts in the west (Yin, 2000) and the right-slip Elashan and Gonghe faults along its eastern segment (Fig. 3.1). Note that both the obliquely oriented western thrust belts and right-slip faults and the orthogonally oriented rifts and eastern thrust belts accommodate

stretching and shortening parallel to the east-striking left-slip faults (Fig. 3.1). This off-fault strain pattern is inconsistent with the extrusion and transfer-fault models for the tectonic development of left-slip faulting in northern Tibet (scenarios 1 and 2 in Fig. 3.3a).

### **3.3.2. Protracted regional clockwise rotation of northern Tibet**

The restoration of a series of balanced cross sections indicates an eastward decrease in north-south Cenozoic shortening across the Qaidam Basin thrust belt (Yin et al., 2008a, 2008b). A similar eastward decrease in Cenozoic shortening strain may be inferred across the Qilian Shan-Nan Shan and Qimen Tagh thrust belts on the basis of an eastward decrease in the (1) number of thrusts, (2) thrust belt width, and (3) average elevation assuming all thrusts initiated at the same elevation and have experienced the same amount of erosion (Fig. 3.1). The eastward decrease in shortening strain implies clockwise rotation across northern Tibet throughout much of the Cenozoic (i.e., since thrust initiation at 50–45 Ma). This observation is consistent with paleomagnetic data that suggests 15°–20° total clockwise rotation across northern Tibet with respect to the Eurasian reference pole since the Cretaceous (Fig. 3.4b) at a rate of 0.3 to 0.5°/Ma (Frost et al., 1995; Halim et al., 1998, 2003; Cogné et al., 1999; Dupont-Nivet et al., 2004; Chen et al., 2002a, 2002b; Sun et al., 2006). Variability in clockwise rotation magnitudes, ranging from 0° to >20° across the region, results from heterogeneous Cenozoic deformation (Yin et al., 2008a).

Geodetic measurements (Gan et al., 2007) show clockwise rotation of northern Tibet about an Euler pole located ~500 km to the southeast of the Eastern Himalayan Syntaxis (Fig. 3.4). Other workers have placed the rotation poles for northern Tibet in the western South China

Sea (Peltzer and Saucier, 1996) and southwest China (Thatcher, 2007) to fit the global positional system (GPS) data with clockwise rotation rates of 0.5 to 1°/Ma.

I examined the velocity field across the region using the published GPS data of Gan et al. (2007) to constrain the rotation rates of the east-striking left-slip faults in northern Tibet. With this data, I derived the relative rotation and shear strain rates for four fault-bounded domains: the Qilian Shan (QS), North Qaidam (NQ), Qaidam Basin (QB), and East Central Tibet (ECT). The rotation rates of the above fault-bounded domains may approximate the fault rotation rates if present-day fault-perpendicular shortening and extension are negligible. Using the northern foreland of the Tibetan Plateau in the North China craton as a fixed reference frame (i.e., the star in Fig. 3.4b), I projected fault-perpendicular velocities (i.e., N20°E, referred to as the  $y$ -direction) of each fault-bounded domain onto a line trending N110°E (referred to as the  $x$ -direction) that approximates the strike-slip fault strike (Fig. 3.4b). Note that only stations to the north or south of the major left-slip faults (e.g., stations in the North Qaidam thrust belt were excluded) were chosen. In addition, stations that are less than ~50 km from the active strike-slip faults were avoided to avoid complications due to elastic behavior along locked faults (e.g., Savage and Burford, 1973).

Each domain displays a relatively linear east-west velocity gradient, shear strain rate ( $\dot{\gamma} = 2\dot{\epsilon}_{xy}$ ), and rotation rate ( $\dot{\omega}$ ) (Fig. 3.4c). Clockwise rotation rates are similar for the East Central Tibet, Qaidam Basin, and North Qaidam domains (i.e., 0.59°/Ma, 0.66°/Ma, and 0.64°/Ma, respectively) and decrease to 0.41°/Ma for the Qilian Shan domain in the north (Fig. 3.4c). The decrease in rotation rate across the Qilian Shan implies that central and northern Tibet are rotating in a clockwise sense relative to North China. The magnitudes of north-south right-lateral shear strain rates ( $\dot{\epsilon}_{xy}$ ) vary between  $1.0 \times 10^{-16} \text{ s}^{-1}$  and  $\sim 2.5 \times 10^{-16} \text{ s}^{-1}$  (Fig. 3.4c). These present-day

rotation rates are similar with those that are geologically and paleomagnetically derived (see above), although less than  $1\text{-}2^\circ/\text{Ma}$  estimated by England and Molnar (1990).

### **3.3.3. Extension and shortening within fault-bounded domains**

The wallrock of the major left-slip faults, defined as the crust bounded by the strike-slip faults, displays a distinctive four-quadrant strain distribution (Fig. 3.5). Each strike-slip fault can be divided into four quadrants that alternate between domains of fault-parallel stretching and domains of fault-parallel shortening (Fig. 3.5a). The northern wallrock of the Haiyuan fault experiences fault-parallel shortening through thrusting across the obliquely oriented Qilian Shan-Nan Shan thrust belt in the west and fault-parallel extension across the orthogonally oriented Yinchuan rift in the east (Figs. 3.1 and 3.5b). The southern wallrock of the Haiyuan fault experiences fault-parallel stretching via right-slip faulting in the west and fault-parallel shortening across the Liupan Shan thrust belt in the east (Figs. 3.1 and 3.5b). The northern and southern wallrock panels of the Qinling fault are dominated by fault-parallel contraction across the Jishi Shan and Liupan Shan thrust belts in the northwest and a contractional zone bounding the southeastern edges of the Qinling and Daba Shan in the east (Figs. 3.1 and 3.5). In contrast, the Qinling wallrock is characterized by fault-parallel extension along the Shanxi rift system to the northeast and a right-slip fault system to the southwest (Fig. 3.5b). The Kunlun fault also displays a four-quadrant deformation pattern expressed by shortening across the Qimen Tagh and Min Shan-Longmen Shan thrust belts and extension across north-striking Tibetan rifts and right-slip faulting (Kirby et al., 2000; Jolivet et al., 2003; Wang and Burchfiel, 2004; Yin et al., 2007, 2008b; Duvall and Clark, 2010; Cheng et al., 2014) (Fig. 3.5b).

The southeast-striking right-slip Elashan, Riyueshan and Gonghe faults may represent secondary bookshelf faults within this larger bookshelf fault system (e.g., Duvall and Clark, 2010) (Figs. 3.1 and 3.5b). The fault geometries and right-slip kinematics, consistent with left-slip shear between the Kunlun and Haiyuan faults, also suggest north-south shortening and east-west stretching (i.e., strike-slip fault-parallel extension and fault-perpendicular shortening).

### **3.4. Non-rigid bookshelf fault model**

As summarized above, existing work across northern Tibet indicates: (1) an eastward decrease in Cenozoic north-south shortening accompanied by clockwise rotation of the east-striking left-slip faults and their wallrock since the Eocene, (2) a bilateral decrease in strike-slip fault offset and slip rate along the left-slip faults that eventually almost disappears at the fault ends, and (3) a distinctive four-quadrant strain pattern in the wallrock of these faults. These observations can be tested against the existing models for the role of strike-slip faulting in accommodating India-Eurasia convergence across northern Tibet (Fig. 3.3a). The observed fault rotation is not explicitly required by the extrusion-fault and transfer-fault models (scenarios 1 and 2 in Fig. 3.3a), and neither of these models predict a four-quadrant strain pattern along the left-slip faults (Fig. 3.5). The observed bidirectional decrease in fault slip is also inconsistent with these models. The extrusion-fault model (scenario 1 in Fig. 3.3a) requires conjugate faults with comparable slip magnitudes, which is not observed in northern or central Tibet (Fig. 3.1) (cf. Cheng et al., 2015). Lastly, dip-slip north-south shortening in the western Qilian Shan-Nan Shan thrust belt near the western end of the Haiyuan fault, as indicated by fault plane solutions (Fig. 3.1) (e.g., Taylor and Yin, 2009) and field observations (Yin et al., 2008a; Reith, 2013; see



Chapter 2), is inconsistent with the transfer fault model that predicts left-slip transpression across this termination thrust system (scenario 2 in Fig. 3.3a).

At face value, the observations from northern Tibet may best be explained by a rotated-fault model. The rigid bookshelf-fault model (England and Molnar, 1990) (scenario 3 in Fig. 3.3a), based on the classic work on bookshelf faulting by Freund (1970), does not account for off-fault deformation and fails to quantify the relationship between strike-slip and dip-slip faulting. Below I propose a new non-rigid bookshelf-fault model for the development of linked left-slip faults and eastward-tapering thrust belts in northern Tibet.

### **3.4.1. Active and passive bookshelf faulting**

Traditionally, the sense of shear within a bookshelf fault system is opposite that of the bounding shear zone that drives bookshelf panel rotation (Freund, 1970). For example, a left-slip bookshelf fault system requires a right-slip bounding shear zone to drive clockwise panel rotation. In this case, right-lateral shear “drags” the fault-bounded domains in a clockwise fashion. I herein refer to this process as *active* bookshelf faulting, because at least one of the bounding “walls” is moving to drive panel rotation (Fig. 3.6a). Alternatively, I introduce a new self-rotating *passive* bookshelf fault system, where the rotating panels are detached from the fixed boundary “walls” (e.g., Yin and Pappalardo, 2015) (Fig. 3.6b). In this model, the kinematics of the boundary shear zones and the individual bookshelf faults can be the same when the rotation axis is fixed in the center of the bookshelf fault system and the bounding walls are fixed (middle panel of Fig. 3.6b). Qualitatively, if the active bookshelf system is driven by drag along the edges, then the passive system is driven by a push from behind (or upward as in Fig.

3.6b) or rotation from below. This model predicts that the top bounding surface in Figure 3.6b absorbs shortening strain, and the magnitude of this strain varies laterally due to block rotation.

Note that there are many possible variations of the passive bookshelf-fault model, depending on the relative magnitude of rigid-block rotation and rigid-block translation. For example, if the bookshelf fault system experiences both self-rotation at the panel centers and significant translation (upward in Fig. 3.6b), the sense of shear along one of the boundary shear zones may switch (bottom panel in Fig. 3.6b). Depending on the magnitude of translation, there may be little observable shear on the right boundary zone in Figure 3.6b.

The geometric relationships between the initial width of the system in the  $x$ -direction ( $L_o$ ), width of the panels in the  $y$ -direction ( $W$ ), panel rotation magnitude ( $\alpha$ ), translation velocity magnitude ( $v$ ), and boundary shear slip (e.g.,  $S_o$ ,  $S_1$ ,  $S_2$ , etc.) are quantified, assuming rigid-body motion, in Figure 3.6. For the active bookshelf fault system shown in Figure 3.6a, translation of the left wall by  $S_o$  relative to the right wall leads to right lateral shear strain (total shear strain of  $S_o/L$ ) and clockwise panel rotation ( $\alpha$ ), so that the variable width of the system ( $L$ ) is

$$L = W \sin \alpha + L_o \cos \alpha . \quad (1)$$

Half of the corners of the bookshelf panels remain in contact with the bounding-edge of the walls but they may slip in the  $y$ -direction (i.e.,  $S_1$  and  $S_6$  in Fig. 3.6a), so that the system can experience more shear than the panel rotation expresses. Given that all of left-side bookshelf panel corners move relative to the left boundary wall in the  $y$ -direction by  $S_1$ , and  $S_1 \geq 0$  (Fig. 3.6a), the slip of the other left-side corners relative to the left boundary wall is

$$S_2 = W / (\cos \alpha) - W + S_1 \quad (2a)$$

$$S_3 = 2W / (\cos \alpha) - 2W + S_1 . \quad (2b)$$

Slip of the right-side corners relative to the right boundary wall is similar, except that the magnitudes are related to  $S_6$  instead of  $S_7$  (Fig. 3.6a).

The width of the passive bookshelf fault system remains constant ( $L = L_o$ ) (Fig. 3.6b). Rotation of the panels in the passive bookshelf fault system of Figure 3.6b results in boundary zone slip magnitudes (i.e.,  $S_1$  and  $S_2$  on the left and right sides, respectively) of

$$S_1 = (2 \tan \alpha)/L_o \quad (3a)$$

$$S_2 = -(2 \tan \alpha)/L_o. \quad (3b)$$

Alternatively, if there is a component of translation in the  $y$ -direction ( $v$ ) (bottom panel of Fig. 3.6b), the resulting boundary zone slip magnitudes are described by:

$$S_1 = (2 \tan \alpha)/L_o + v \quad (4a)$$

$$S_2 = -(2 \tan \alpha)/L_o + v. \quad (4b)$$

First-order deformation in either the passive or active systems can be quantified as continuous velocity fields. The idealized velocity field (i.e., no discrete faults) across an active bookshelf system is

$$u = 0 \quad (5a)$$

$$v = -\frac{v_o}{h} x \quad (5b)$$

where  $u$  and  $v$  are the velocity components in the  $x$  and  $y$  directions perpendicular and parallel to the shear zone, respectively,  $h$  is the width of the shear zone, and  $v_o$  is the velocity on one side of the shear zone at  $x = -h$  relative to the other side of the shear zone (Fig. 3.7a). Note that in all of my derivations, the origin is placed at the right-side boundary, so that the left boundary is located at  $x = -h$  (Fig. 3.7). The corresponding strain-rate-tensor components are

$$\dot{\epsilon}_{xx} = \frac{\partial u}{\partial x} = 0 \quad (6a)$$

$$\dot{\epsilon}_{yy} = \frac{\partial v}{\partial y} = 0 \quad (6b)$$

$$\dot{\epsilon}_{xy} = \frac{1}{2} \left( \frac{\partial u}{\partial y} + \frac{\partial v}{\partial x} \right) = -\frac{v_o}{2h}, \quad (6c)$$

where  $\dot{\epsilon}_{xx}$  and  $\dot{\epsilon}_{yy}$  are extension strain rates in the  $x$  and  $y$  directions, perpendicular and parallel to the shear zone, and  $\dot{\epsilon}_{xy}$  is the shear strain rate (e.g., Ramsay and Huber, 1983). The rotation rate may be derived as follows:

$$\dot{\epsilon}_{xy} = \frac{\dot{\gamma}}{2} = \frac{\tan \dot{\omega}}{2} \quad (7a)$$

$$\dot{\omega} = \tan^{-1} \frac{-v_o}{h} \quad (7b)$$

where  $\dot{\omega}$  is rotation rate and  $\dot{\gamma}$  is engineering or total shear strain rate (Fig. 3.7a).

Deformation for the passive bookshelf system (Fig. 3.7b) can be quantified in a similar manner, except that the velocity in the  $y$ -direction is the sum of velocities related to translation and rotation (Figs. 3.6b and 3.7b), such that

$$v = v_r + v_t \quad (8a)$$

$$v_r = -v_{ro} \left( \frac{2x}{h} + 1 \right) \quad (8b)$$

$$v_t \geq 0 \quad (8c)$$

where  $v$  is the velocity component in the  $y$ -direction parallel to the shear zone,  $h$  is the width of the shear zone,  $v_r$  is velocity component related to rotation,  $v_{ro}$  is the rotation-related velocity at one side of the shear zone at  $y = -h$ , and  $v_t$  is the velocity component related to translation. In this approximation, I am only considering the  $y$ -component of the rotational velocity ( $v_r$ ). The complete corresponding velocity field is

$$u = 0 \quad (9a)$$

$$v = -v_{ro} \left( \frac{2x}{h} + 1 \right) + v_t \quad (9b)$$

where  $u$  is the velocity component in the  $x$ -direction perpendicular to the shear zone, and the other variables are the same as above (Fig. 3.7b). The strain-rate-tensor components are as follows:

$$\dot{\epsilon}_{xx} = \frac{\partial u}{\partial x} = 0 \quad (10a)$$

$$\dot{\epsilon}_{yy} = \frac{\partial v}{\partial y} = 0 \quad (10b)$$

$$\dot{\epsilon}_{xy} = \frac{1}{2} \left( \frac{\partial u}{\partial y} + \frac{\partial v}{\partial x} \right) = \frac{-v_{ro}}{h} \quad (10c)$$

from which the rotation rate is given by

$$\dot{\omega} = \tan^{-1} \frac{-2v_{ro}}{h}. \quad (11)$$

### 3.4.2. Non-rigid bookshelf faulting in northern Tibet: passive and stretchy

I propose that the clockwise rotating east-striking left-slip faults in northern Tibet are part of a passive bookshelf system (Fig. 3.6b) because they are bounded to the northwest by the left-slip Altyn Tagh fault (Fig. 3.1). An active left-slip bookshelf fault system (Fig. 3.6a) would require a right-slip bounding shear zone to drive clockwise panel rotation, whereas the passive system allows the panels to rotate in a clockwise fashion against a rigid boundary to the west, creating a left-slip shear zone. This simple model involving clockwise rotation across the region may explain why Tibet is bounded by a left-slip fault system to the northwest (i.e., the Altyn Tagh fault) and minor-to-insignificant right-slip faulting to the southeast (i.e., within the Longmen Shan) (Fig. 3.1), rather than the expected broad right-slip shear zones as predicted by the classic rigid-bookshelf model (England and Molnar, 1990).

The predicted velocity field from the passive bookshelf system (Equation [9]) can be compared to the GPS-derived velocity field across northern Tibet (Fig. 3.4). The eastern

boundary of northern Tibet does not have a significant north-striking strike-slip bounding fault like the western boundary (i.e., the Altyn Tagh fault); only minor right-slip faulting is observed in the Longmen Shan (Densmore et al., 2007; Yin, 2010b) (Fig. 3.1). Because of this, I infer that the N-S velocity due to clockwise rotation is matched by the northward translation velocity, so that  $v_{ro}$  is equal but opposite to  $v_t$  at  $x = 0$  (the eastern boundary) (Fig. 3.7b) in Equation (9). The N20°E velocity gradient plotted in Figure 3.4c shows a maximum velocity near the western boundary ( $x = -h$ ) of  $\sim 16$  mm/yr, which requires  $v_r$  and  $v_t$  of Equation (9) to equal  $\sim 8$  mm/yr. A northward translational velocity ( $v_t$ ) of 8 mm/yr is reasonable given that the northward GPS velocities just south of the Kunlun fault are 7-15 mm/yr (Zhang et al., 2004; Yin and Taylor, 2011). If I assume that the fixed width of the system  $h$  is 1400 km (Fig. 3.1), the N-S velocity field can be described by  $v = (-1.14 \times 10^{-8})x \text{ yr}^{-1}$  (Fig. 3.7b). The resulting shear strain rate and clockwise rotation rate are  $\dot{\epsilon}_{xy} = -1.81 \times 10^{-16} \text{ s}^{-1}$  and  $\dot{\omega} = 0.65 \text{ }^\circ/\text{Ma}$  respectively. These rates are comparable to the paleomagnetic, geologic, and geodetic data discussed above.

Since the boundary domains in the active or passive bookshelf system are relatively rigid, the bookshelf panels must be non-rigid to resolve the space issues that arise at the panel ends (Figs. 3.2 and 3.6) (e.g., Luyenduk et al., 1980; Onderdonk, 2005; Platt and Becker, 2013). The necessary fault-parallel stretching or shortening of the fault-bounded domains accommodates negligible slip at the ends of each rotating fault. The strike-slip faults in a non-rigid bookshelf system, bounded by deformable rather than rigid wallrock, are referred to as stretching faults (Means, 1989, 1990).

Unlike the models of either Onderdonk (2005) or Platt and Becker (2013), the bookshelf panels in the non-rigid passive bookshelf model do not have to either *all stretch* or *all shorten* to accommodate rotation in a deforming material. Instead, each quadrant of wallrock deforms

according to the kinematics of the bounding strike-slip faults, so that off-strike-slip-fault wallrock deformation accommodates negligible slip at the strike-slip faults tips (Fig. 3.5). An example of a possible interaction along the left-most boundary is shown in Figure 3.8. Given the small angle of clockwise rotation of the left-slip faults ( $\theta \ll 1^\circ$ ), the resulting left-lateral slip ( $d$ ) must be accommodated by fault-parallel stretching *and* shortening strain ( $\varepsilon_{xx}$ ) in the panels adjacent to the strike-slip fault (i.e., panels A and B in Fig. 3.8). Assuming that the resulting strain is homogenous throughout one-half of the bookshelf panel and affects both panels A and B by the same magnitude, this strain can be written as:

$$\varepsilon^A_{xx} = \frac{1}{2} \frac{d}{S} \quad (12a)$$

$$\varepsilon^B_{xx} = -\frac{1}{2} \frac{d}{S} \quad (12b)$$

where  $\varepsilon^A_{xx}$  and  $\varepsilon^B_{xx}$  are the extension strain in panel A and panel B, respectively,  $d$  is the left-lateral slip, and  $S$  is the half the length of the bookshelf panel ( $S = L/2$ ), all in the  $x$ -direction (Fig. 3.8). Because this left-slip ( $d$ ) is caused by clockwise rotation, I relate this strain to rotation rate, and derive the resulting fault-parallel strain rate:

$$\dot{\varepsilon}^A_{xx} = \frac{1}{2} \frac{W \tan(\Delta\theta)}{S \Delta t} \quad (13a)$$

$$\dot{\varepsilon}^B_{xx} = -\frac{1}{2} \frac{W \tan(\Delta\theta)}{S \Delta t} \quad (13b)$$

where  $W$  is the width of the bookshelf panel in the  $y$ -direction,  $\Delta\theta$  is the small angle of clockwise rotation of the left-slip faults over a short timescale ( $\Delta t$ ), and the other variables are the same as above. The corresponding velocity field may be written as

$$u^A_x = \frac{x}{2} \frac{W \tan(\Delta\theta)}{S \Delta t} + c \quad (14a)$$

$$u^B_x = -\frac{x}{2} \frac{W \tan(\Delta\theta)}{S \Delta t} + c \quad (14b)$$

where  $u_x^A$  and  $u_x^B$  are the velocity components in the  $x$ -direction in panels A and B respectively, and  $c$  is a constant of integration that may be dropped by setting the boundary condition of  $u_x = 0$  at  $x = 0$  (Fig. 3.8). Combining Equations (14) and (11) yields an expression for fault-parallel stretching rate ( $u_x$ ) as a function of  $v_{ro}$ :

$$u_x^A = \frac{xW}{2S} \tan^{-1} \frac{-2v_{ro}}{h} \quad (15a)$$

$$u_x^B = -\frac{xW}{2S} \tan^{-1} \frac{-2v_{ro}}{h}. \quad (15b)$$

Taking  $v_{ro}$  to be 8 mm/yr (as discussed above), the bookshelf panel between the Kunlun and Qinling faults to have a width of 150 km and length of 1400 km ( $S = 700$  km) (Fig. 3.1), and the width of the bookshelf system  $h$  as 1400 km, I arrive at fault-parallel stretching rates of  $\sim 1$  mm/yr. For the Kunlun fault, as an example, this should be accommodated by fault-parallel shortening in the Qimen Tagh and extension to the south in central Tibet at a rate of  $\sim 1$  mm/yr (Fig. 3.1).

### 3.4.3. Active bookshelf faulting: the Garlock fault in California

One example of an active bookshelf fault system may be the left-slip Garlock fault that is located adjacent to the San Andreas transform-plate boundary (Fig. 3.9). The  $\sim 150$ -km-long northeast-striking Garlock fault intersects the right-slip San Andreas fault in the west, along the northern edge of the Western Transverse Range. It divides the relatively high-relief Tehachapi-Sierra Nevada and Basin and Range domains in the north from the relatively flat Mojave domain in the south (e.g., Davis and Burchfiel, 1973; Guest et al., 2003) (Fig. 3.9a). Observed fault offset is  $\sim 50$  km across the central segment of this fault (Smith, 1962; Davis and Burchfiel, 1973). GPS analysis indicates a contemporary clockwise rotation rate of  $4.4 \pm 0.7$   $^{\circ}$ /Ma and a slip rate of  $\sim 6$  mm/yr (Platt and Becker, 2013) (Fig. 3.9b). Another geodetic model suggests that left-



lateral slip rate decreases from ~3 mm/yr along the central fault segment to ~1 mm/yr in the east (Meade and Hager, 2005).

There has been rigorous debate regarding the tectonic significance of the Garlock fault (e.g., Davis and Burchfiel, 1973; Guest et al., 2003; McGill et al., 2009), but here I suggest that the Garlock fault may be best explained as a non-rigid active bookshelf fault (e.g., Fig. 3.6a). The clockwise rotation of the fault (e.g., Platt and Becker, 2013) predicts an asymmetric strain distribution (e.g., Fig. 3.5a) with fault-parallel shortening in the northwest and southeast quadrants and fault-parallel stretching in the northeast and southwest quadrants. This distribution is observed. To the northwest, fault-parallel shortening is expressed as deformation in the Tehachapi Mountains, as well as a prominent westward bend of the San Andreas fault. To the southeast, the Garlock fault merges with the north-trending Avawatz Mountains (Fig. 3.9c). Late Cenozoic Garlock-fault-parallel shortening across this range has been documented (e.g., Chinn, 2013a, 2013b), although the magnitude of this deformation remains unknown. Fault-parallel extension occurs to the northeast of the Garlock fault, as part of the larger Basin and Range system (Fig. 3.9c). The required extension in the southwestern quadrant of the Garlock fault has not been firmly established, although the northwest-striking right-slip faults would be consistent with east-west extension. This region, just south the Tehachapi Mountains, is a broad Cenozoic basin, which may have formed partly due to Garlock-fault-parallel extension (e.g., Luyendyk et al., 1980).

As opposed to the passive bookshelf fault system of northern Tibet, the Garlock fault must be part of an active bookshelf fault system. Right-lateral shear is prevalent across the Pacific-North America plate boundary, and the clockwise rotation of the left-slip Garlock fault is

consistent with this shear sense (Fig. 3.9). In northern Tibet, clockwise rotation of left-slip faults is opposite that of the shear sense of the bounding left-lateral Altyn Tagh shear zone (Fig. 3.1).

Further interpretation of this fault system is not within the scope of this present work, but the Garlock fault may be an example of a non-rigid active bookshelf fault system. Several testable predictions emerge from this hypothesis: (1) Geodetic and geologic slip rates and offset magnitudes should decrease bidirectionally from the center of the Garlock fault. (2) The magnitude of Late Cenozoic shortening across the Avawatz Mountains and associated uplift should match with left-lateral offset along the eastern Garlock fault. (3) The magnitude and timing of extension and related basin formation in the southwest quadrant of the Garlock fault, just south of the Tehachepi Mountains, should be compatible with strike-slip offset. (4) The magnitude and rate of Garlock fault rotation should be consistent with the relative plate motion velocities between the Pacific and North American plates (e.g., can the  $\sim 4.5^\circ/\text{Ma}$  clockwise rotation rate of the Garlock fault be explained within the context of  $\sim 5$  cm/yr right-lateral shear along the western North America plate boundary?).

### **3.5. Discussion**

#### **3.5.1. Driving mechanism for clockwise rotation**

Applying the passive bookshelf fault model to northern Tibet requires clockwise rotation of the left-slip faults and fault-bounded wallrock relative to the relatively fixed Tarim and North China (i.e., the top, left, and right sides of the passive bookshelf fault system in Fig. 3.6b). This system can be driven by either rotation of the bottom boundary (i.e., rotation of central and southern Tibet) or basal drag beneath the system. In the simplest case, clockwise rotation of southern Tibet and/or the Himalaya relative to North China (Fig. 3.10a) can drive clockwise

rotation of northern Tibet. Due to the lack of paleomagnetic and GPS data across central and southern Tibet, this model is difficult to test with confidence (Figs. 3.1 and 3.4a). However, existing geologic data from central and southern Tibet suggest that the regions are actually experiencing counterclockwise rotation (e.g., Yin, 2006; Burgess et al., 2012), which is inconsistent with the model requirements.

Alternatively, rotation of northern Tibet could have been driven by an eastward decrease in gravitational potential energy (GPE) and GPE gradient in central Tibet (England and Molnar, 1997) (Fig. 3.10b). This GPE distribution may lead to faster spreading of the thickened lithosphere in the west than that in the east, causing clockwise rotation of northern Tibet. One potential problem is that this model would require north-south extension across central Tibet that is not observed. However, the spreading-induced extensional strain may be overwhelmed by India-indentation-induced shortening strain in the region. It is also possible that fault rotation in northern Tibet is driven by a toroidal asthenospheric flow (Fig. 3.10c) that develops as the Burma trench, which is located just south of the Eastern Himalayan Syntaxis, retreats westward. The roll-back of the Burma slab causes poloidal flow of the asthenosphere around the slab, which draws in a toroidal flow around its northern edge. This inference is consistent with the current knowledge of mantle seismic anisotropy in the region (e.g., León Soto et al., 2012).

### **3.5.2. Implications for the Cenozoic development of northern Tibet**

Recent work on the timing of structures in northern Tibet suggests a two-stage development of the region (Fig. 3.3b), with a change from thrust-dominated to strike-slip-dominated deformation at 20 to 15 Ma (e.g., Craddock et al., 2011; Duvall et al., 2013) due to a change in boundary conditions and stress regime (Yuan et al., 2013). As discussed by Clark

(2012), the average bulk strain rate (i.e.,  $\dot{\epsilon} = v/L$ ) across the Himalayan-Tibetan orogen has remained constant since the onset of collision ( $\dot{\epsilon} = \sim 7 \times 10^{-16} \text{ s}^{-1}$ ); deformation and narrowing of the orogen ( $L$ ) has been balanced by slowed plate convergence ( $v$ ) as a result of viscous mantle resistance. A constant strain for a viscous medium (i.e., the Tibetan-Eurasian lithosphere) equates to constant contractional stress acting on it, regardless of a shift in the geodynamics (e.g., crustal thickness, rheology, boundary conditions). The calculated present-day shear strain rates and clockwise rotation rates across northern Tibet are consistent with geologic and paleomagnetic rotation rates. This similarity suggests that strain rates have remained constant throughout the Cenozoic, which is inconsistent with the discrete two-stage deformation model for the development of northern Tibet (e.g., Yuan et al., 2013) that requires a change in boundary conditions. Alternatively, the non-rigid passive bookshelf model proposed in this study implies that coeval and kinematically linked thrust and strike-slip faulting could have formed under a constant stress regime.

The fundamental mode of Cenozoic deformation in northern Tibet appears to be protracted north-trending right-lateral simple shear (England and Molnar, 1990), nearly parallel to the northeast-striking Altyn Tagh fault, since the onset (or soon after) of the India-Eurasian collision at 60-55 Ma (e.g., Zhu et al., 2005; Green et al., 2008; Dupont-Nivet et al., 2010) (Fig. 3.11). Right-lateral shear strain was accommodated in the Eocene-Oligocene to early Miocene by distributed shortening and crustal-thickening in the Qimen Tagh, Qaidam Basin, and southern Qilian Shan thrust belts (Fig. 3.11a). An eastward decrease in north-south shortening strain was associated with the passive clockwise rotation of northern Tibet against the left-slip Altyn Tagh fault.

Crustal thickening led to a reorientation of the intermediate compressive stress orientation from horizontal to vertical by 20 to 15 Ma that shifted deformation to a mixed-mode of thrusting and left-slip faulting along preexisting weaknesses (i.e., Phanerozoic sutures) (Fig. 3.11b). The clockwise rotation and northward translation of the east-striking left-slip Haiyuan, Qinling, and Kunlun faults against the left-slip Altyn Tagh bounding fault zone in the northwest and the Longmen Shan in the southeast operated as passive bookshelf fault system. Combined northward translation and clockwise rotation of northern Tibet lead to minor observable right-slip shear along the eastern northeast-striking bounding faults (i.e., right-slip faulting within the thrust belt) (Figs. 3.6b and 3.11b). The rotating fault-bounded domains, surrounded by a relatively rigid medium (i.e., a strong Tarim and North China) (e.g., Molnar and Tapponnier, 1981), require fault-parallel deformation to resolve the space issues at the panel ends (Fig. 3.11c). Note that the Altyn Tagh fault is oblique to the regional shear direction, and this orientation results in more shortening in the west than the east as the left-slip faults rotate against rigid Tarim and the Altyn Tagh boundary shear zone. Wallrock deformation and subsequent fault stretching (Means, 1989) result in negligible fault slip at the ends of each east-striking left-slip fault.

Several testable predictions emerge from this proposed model. First, the east-striking left-slip faults should be relatively weak. The western and central sections of the faults strike at a high angle to the maximum compressive stress direction (Fig. 3.4b) which indicates that minimal shear stress is acting on the fault planes. The faults also initiated along sutures (Fig. 3.1) that are presumably zones of preexisting weaknesses. The orthogonal orientation of the strike-slip faults to the maximum compressive stress direction in the west allows for the development of thrust belts that obliquely merge with the left-slip faults, as opposed to the eastern thrust belts that

develop orthogonally to the strike-slip faults (Fig. 3.1). Second, the distinct two stages of deformation in northern Tibet (e.g., Yuan et al., 2013) may be apparent as a result of limited sampling and loose timing constraints. For example, I note that there are no direct age constraints for the initiation of the Haiyuan fault (Yuan et al., 2013) (Fig. 3.3b). The complex deformational patterns in northern Tibet make differentiating between thrust and strike-slip fault initiation difficult with current thermochronology techniques. Lastly, detailed studies of crustal strain can reveal if the fault-parallel shortening and extension in the off-fault regions equal offset on the strike-slip faults. There is currently little detailed structural data across the Qimen Tagh and Qilian Shan thrust belts (cf. Chapter 2) to convincingly test this hypothesis, and GPS stations are sparse in these regions (Fig. 3.4a).

An important implication of the non-rigid bookshelf-fault model is that the style and magnitude of Cenozoic deformation in northern Tibet vary considerably in the east-west direction. In order to understand processes of continental deformation and plateau construction, future geologic studies must establish along-strike variations of the structural framework along the left-slip faults to examine the relationship between discrete left-slip faulting and distributed off-fault deformation. It is clear that a single north-south cross section and its kinematic reconstruction across the northeastern margin of the Tibetan Plateau would not properly quantify the complex deformational processes of plateau formation.

### **3.5. Conclusions**

The Cenozoic tectonic development of northern Tibet is characterized by the clockwise rotation of three major east-striking left-slip faults. Similar rotation and shear strain rates from paleomagnetic, geologic, and geodetic datasets (e.g.,  $\dot{\epsilon}_{xy} = \sim 10^{-16} \text{ s}^{-1}$ ) suggest continuous

clockwise rotation of the region since the Eocene, which is consistent with a constant bulk strain rate across the Himalayan-Tibetan orogen since the onset of India-Eurasia collision (Clark, 2012). The proposed non-rigid passive bookshelf-fault model, which relates discrete left-slip faulting to distributed off-fault deformation during regional clockwise rotation, accounts for the rotation of major left-slip faults, bidirectional decrease in slip from the central segments of these faults, eastward-tapering northwest-trending thrust belts, and four-quadrant strain pattern in the wallrock of the strike-slip faults. This model quantifies the relationship between strike-slip faulting and off-fault deformation during processes of continental tectonics and highlights the complexity of Cenozoic continental deformation in northern Tibet.

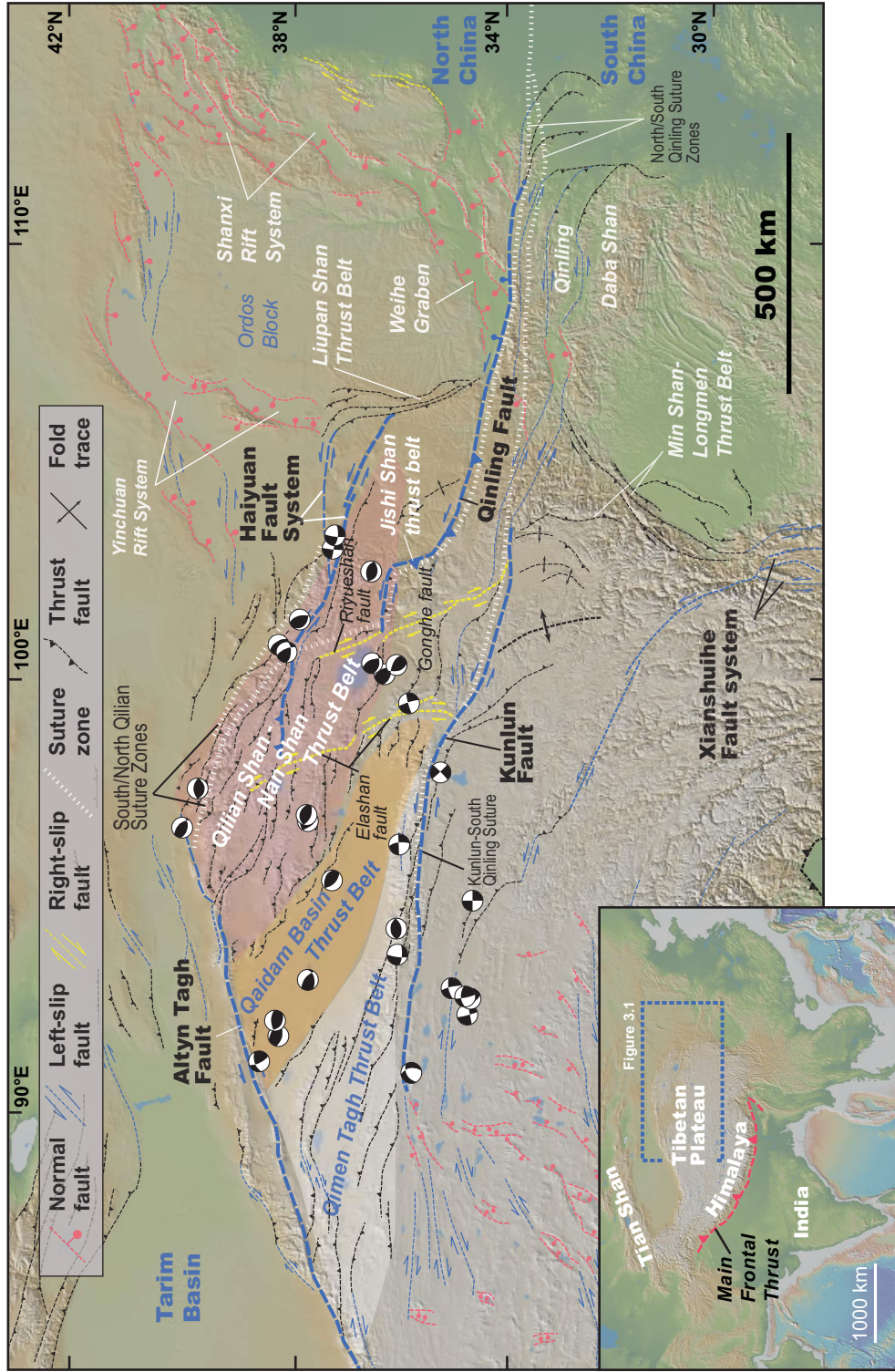


**Figure 3.1.** Color-shaded relief map showing Cenozoic faults related to the Indo-Asian collision zone after Yin et al. (2008a), Taylor and Yin (2009), and Zuza et al. (2016). Also shown are Harvard centroid moment tensor (CMT) earthquake focal mechanisms from 1 January 1977 to 1 January 2009 of events  $>M 5.5$ . Inset shows location of northern Tibet in the context of the Himalayan-Tibetan orogen. The digital topographic basemap is from GeoMapApp software (Ryan et al., 2009) available at <http://www.geomapp.org/>.



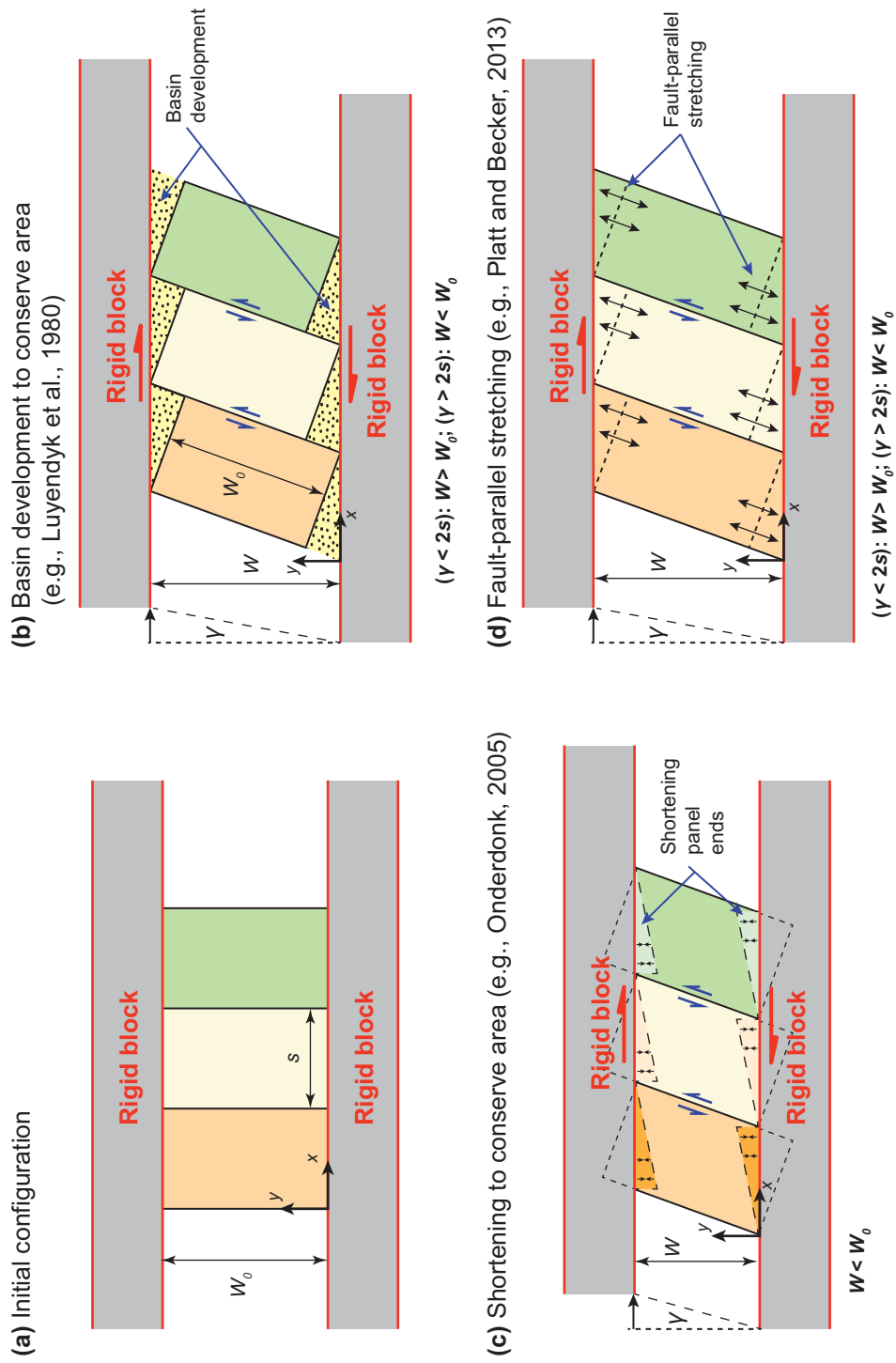


**Figure 3.2.** Conceptual models for the space issue that arises in a bookshelf fault system given an (a) initial configuration with three bookshelf panels bounded on the bottom and top with rigid but movable blocks. Three mechanisms have been proposed to conserve area at the ends of the panels, including (b) lithospheric-scale basin development (e.g., Luyendyk et al., 1980), (c) crustal shortening at the ends of the panels (e.g., Onderdonk, 2005), and (d) fault-parallel stretching throughout the panels (e.g., Platt and Becker, 2013). Note that in each case, the width of the system ( $W$ ) is not constant.

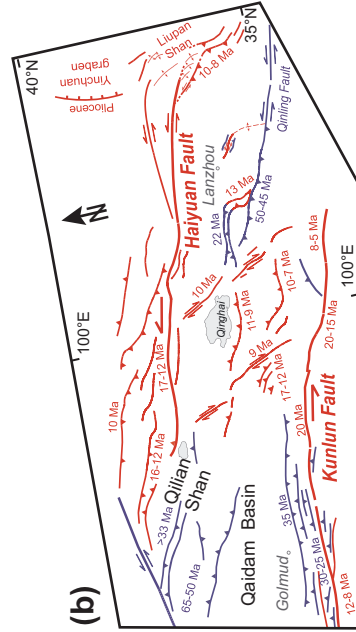
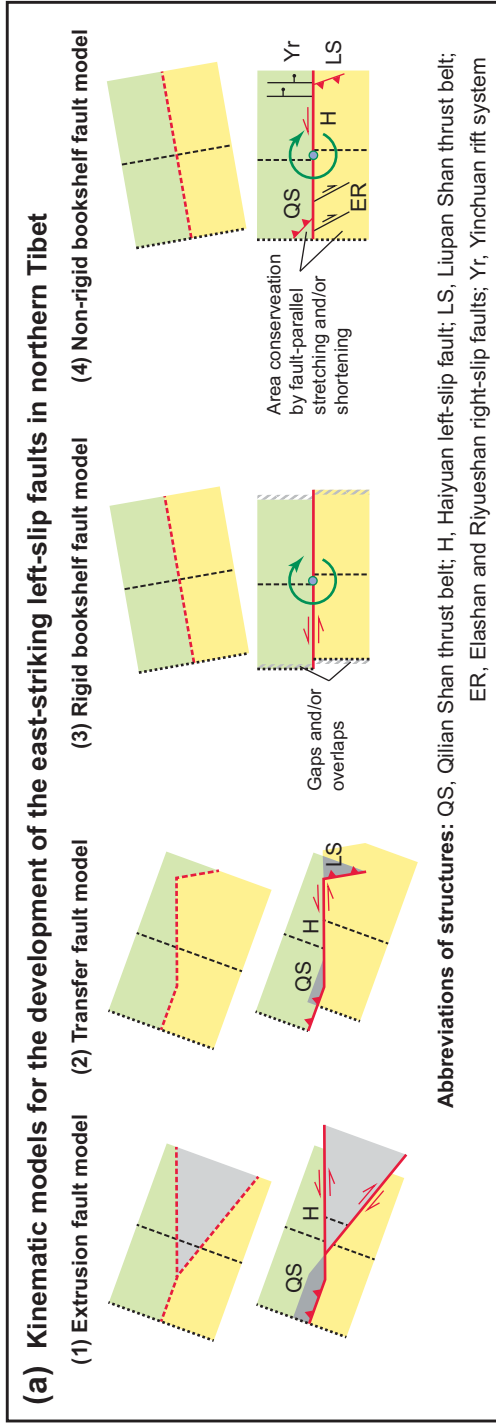


**Figure 3.3.** (a) Simplified sketches showing end-member models for the role of the east-striking left-slip faults (i.e., the Haiyuan, Qiling, and Kunlun faults) in the Cenozoic tectonic development of northern Tibet. Only one left-slip fault is shown in each scenario but the same model predictions apply to each of left-slip faults in northern Tibet. Annotations show, as an example, how predicted structures match the geology for Haiyuan fault and linked termination structures. The (1) extrusion fault model (e.g., Tapponnier et al., 1982) predicts the presence of a conjugate right-slip fault with a similar slip magnitude near the western end the fault, the (2) transfer fault model (e.g., Burchfiel et al., 1991; Duvall and Clark, 2010) requires a left-slip component across the termination thrusts, the (3) rigid bookshelf fault model (e.g., England and Molnar, 1990) predicts gaps and/or overlaps at the ends of the rigid blocks, and the (4) non-rigid bookshelf fault model predicts fault-parallel stretching and/or shortening to preserve mass at the panel ends (this study). (b) Ages of deformation in northern Tibet from numerous sources. Ages represent initiation of fault activity. Faults initiated in the Paleogene are in blue whereas faults initiated in the Neogene are red. Modified from Yuan et al. (2013).

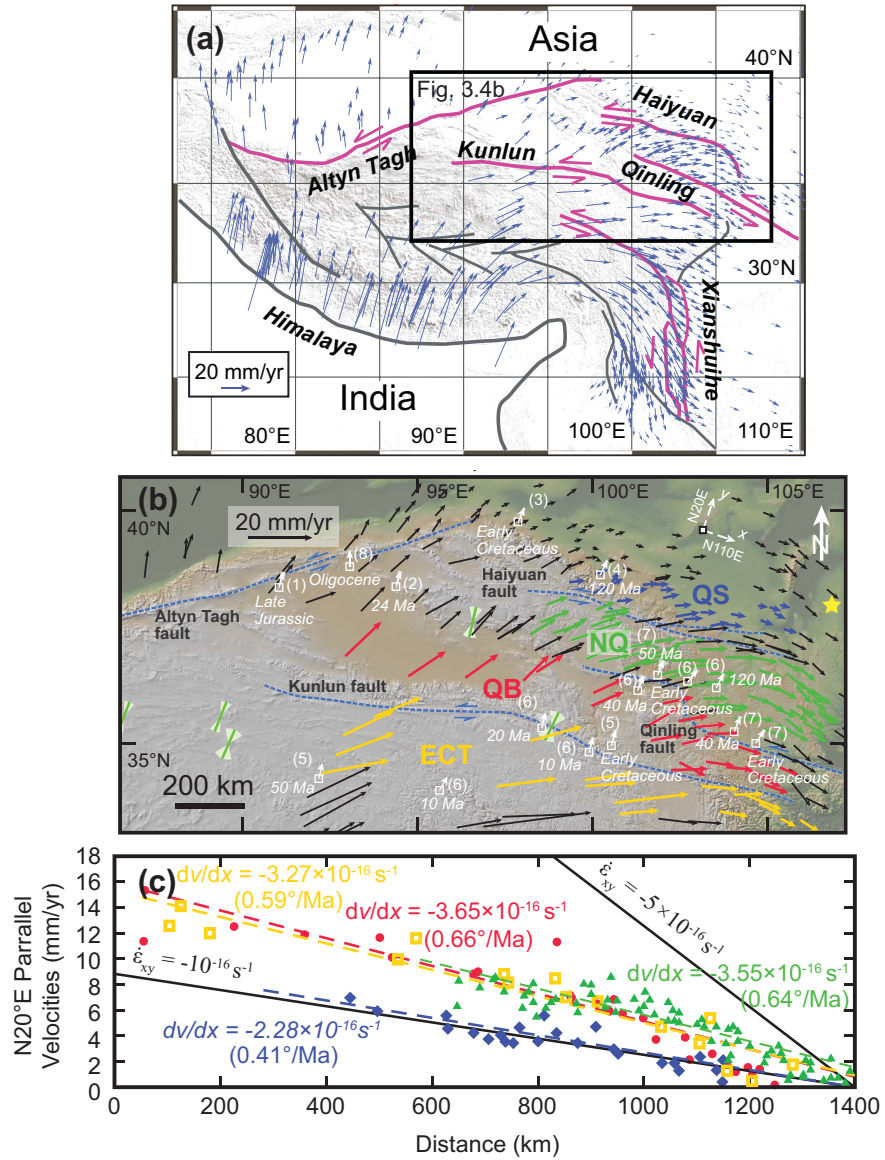
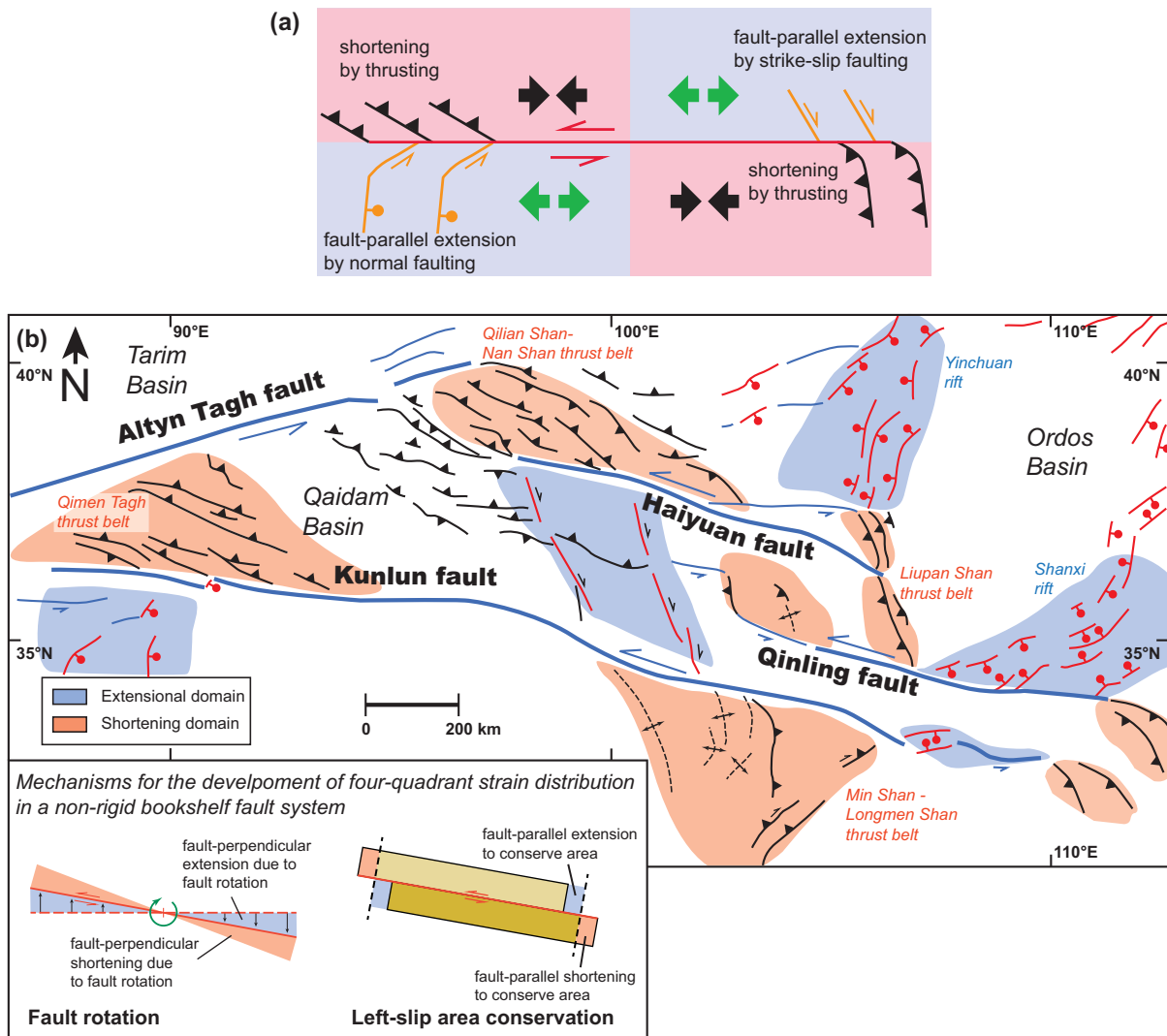
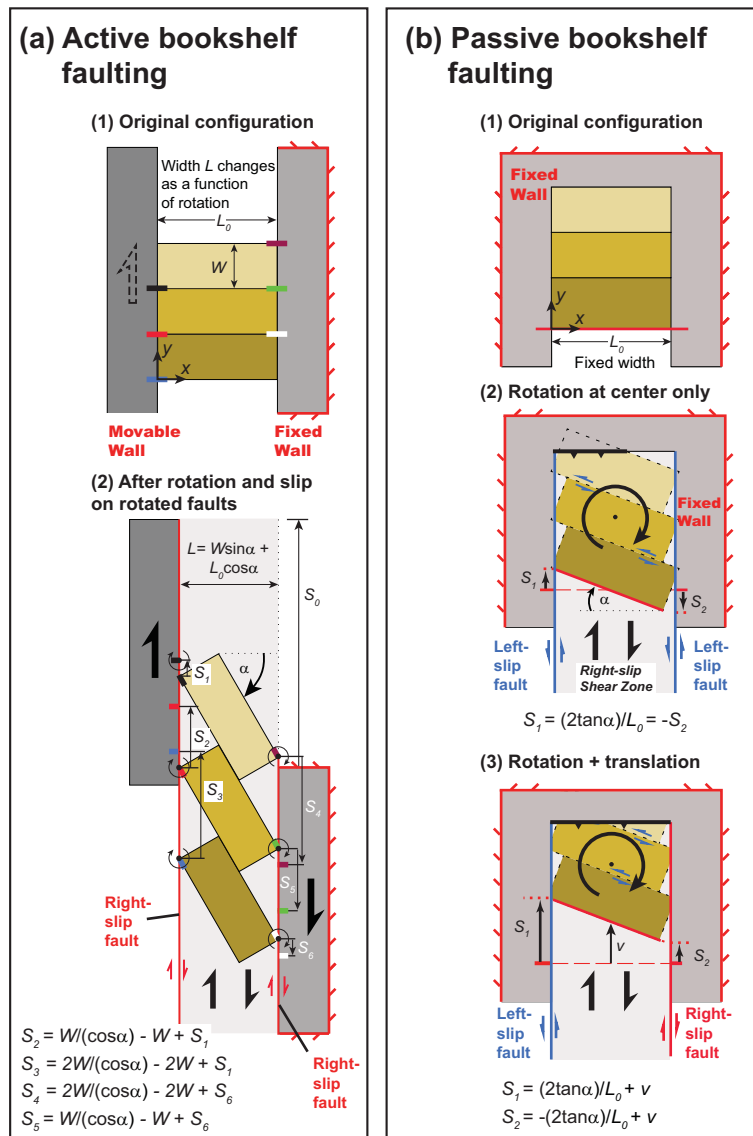


Figure 3.4. Full figure caption on next page.

**Figure 3.4 (continued).** (a) Global positioning system (GPS) velocity field across Tibet relative to stable Eurasia modified from Gan et al. (2007). Also shown is the location of Figure 3.4b. (b) GPS velocity field relative to stable Eurasia with data from Gan et al. (2007). Colored vectors represent stations from four distinct domains that are bounded by the left-slip Kunlun, Qinling, and Haiyuan faults, from south to north: East Central Tibet (ECT), Qaidam Basin (QB), North Qaidam (NQ), and Qilian Shan (QS). Paleomagnetic rotation magnitudes are shown with white arrows along with the lower age bound for the onset of rotation. The averaged maximum compressive stress directions from the World Stress Map are plotted as green lines (Heidbach et al., 2008). Gold star shows the reference location for analyses in Figure 3.4c. Also shown is the  $x$ - $y$  coordinate system, with the  $x$ -axis parallel to N110°E. Paleomagnetic rotation data are from (1) Halim et al. (2003), (2) Chen et al. (2002a), (3) Chen et al. (2002b), (4) Frost et al. (1995), (5) Halim et al. (1998), (6) Cogné et al. (1999), (7) Dupont-Nivet et al., (2004), and (8) Dupont-Nivet et al. (2002). (c) GPS velocity component in the N20°E direction perpendicular to the general strike of the left-slip Kunlun, Qinling, and Haiyuan faults in northern Tibet. The N20°E velocity components relative to a fixed point in the Tibetan Plateau foreland (i.e., gold star in Figure 3.4b) in each fault-bounded domain (color codes corresponding to those in Figure 3.4b) are projected onto a N110°E-trending line. Best-fit (blue, yellow and red dashed lines) velocity gradients are bounded by shear strain rates ( $\epsilon_{xy}$ ) of  $10^{-16} \text{ s}^{-1}$  and  $5 \times 10^{-16} \text{ s}^{-1}$  shown as thick black lines.



**Figure 3.5.** (a) Simplified diagram highlighting a possible four-quadrant deformation pattern with a strike-slip fault and its coeval termination structures. Note that fault-parallel extension can be accommodated by either normal or strike-slip faulting. (b) Sketch map highlighting the relationship between east-striking left-slip faults and off-fault wallrock deformation. The Haiyuan, Qinling, and Kunlun faults all display a four-quadrant strain distribution, with fault-parallel shortening in the northwest and southeast quadrants and fault-parallel extension in the southwest and northeast quadrants. Inset shows how the non-rigid bookshelf faulting can generate the observed four-quadrant strain distribution. Fault-perpendicular deformation accommodates clockwise rotation of the faults whereas fault-parallel deformation is required to resolve the “gap” and “overlap” issues that arise at the panel ends. Note that the specific strain asymmetry corresponds to a clockwise fault rotation direction.



**Figure 3.6.** (a) Conceptual model for the active bookshelf fault system (Freund, 1970) where shear is driven by drag along the boundary walls and the sense of shear of the bounding shear zones must be opposite of the slip between the bookshelf panels. (b) Conceptual model for a passive bookshelf fault system, where panels rotating about the center of the system are driven by a push from the bottom. The panels can both rotate and translate. Note that at some point between stages (2) and (3), the easternmost bounding fault transitions from left-slip to right slip, and at this point there is negligible strike-slip offset at this right-side boundary.

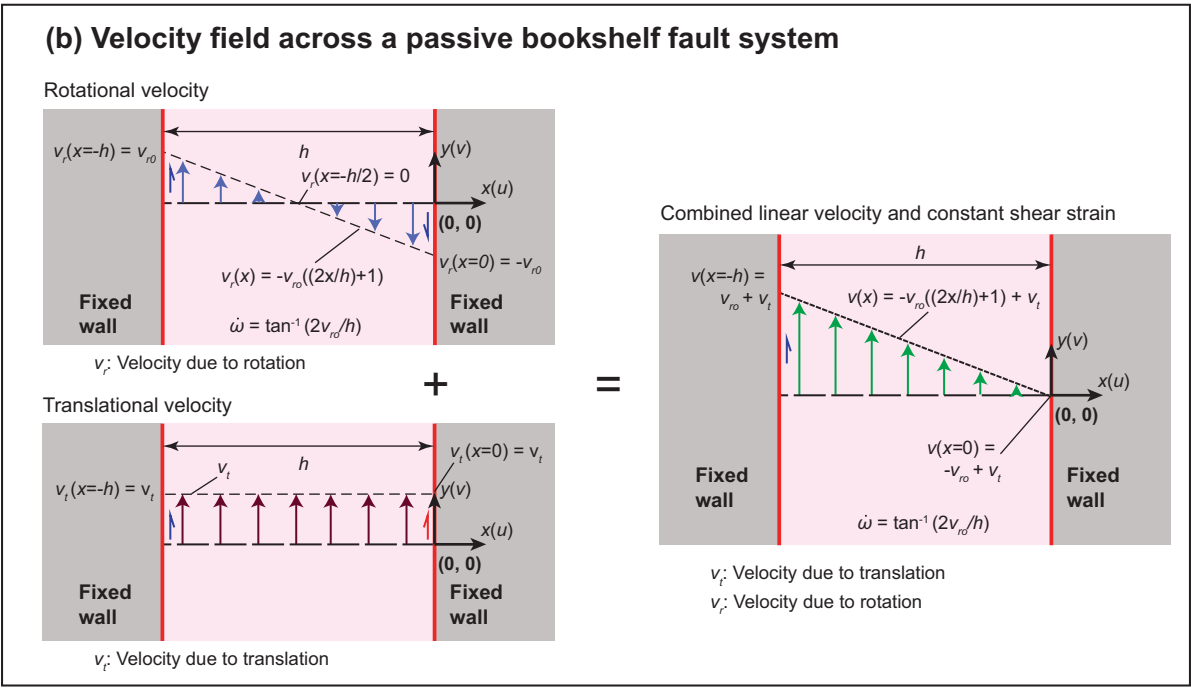
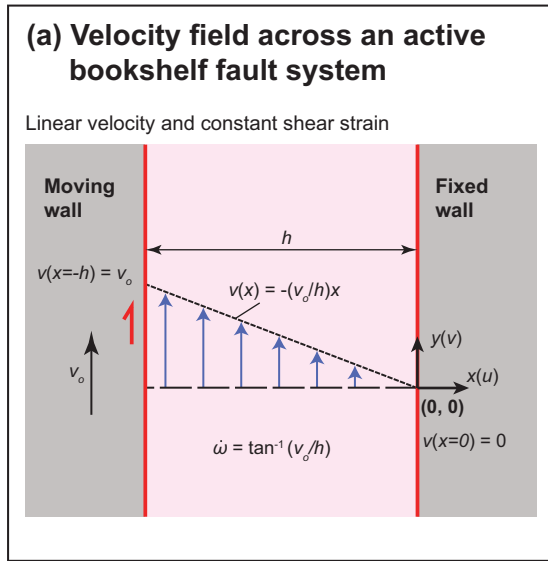


**Figure 3.7.** Velocity fields for the (a) active and (b) passive bookshelf fault systems. Note that the velocity field in the passive system involves the summation of translational ( $v_t$ ) and rotational ( $v_r$ ) velocities. See text for discussion.

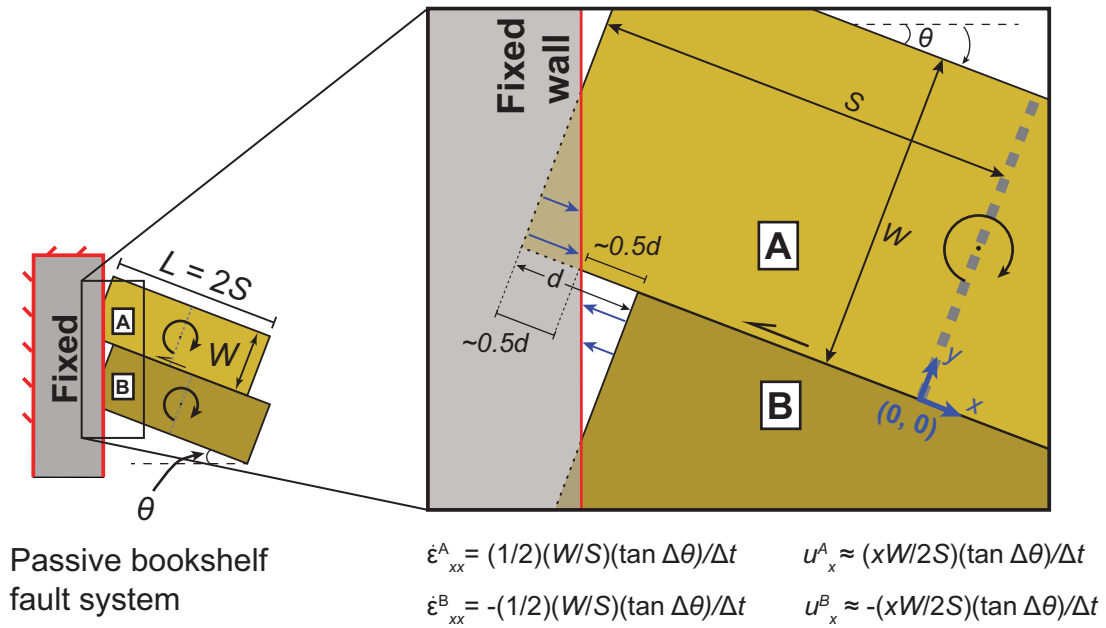


**Figure 3.8.** Kinematic model illustrating the required fault-parallel strain at the western end of one passive bookshelf fault. Given a rigid left-side boundary, left-lateral offset on the fault ( $d$ ) caused by clockwise fault rotation requires fault-parallel shortening and stretching strain ( $\epsilon_{xx}$ ), for panels A and B respectively, related to approximately one-half the fault slip divided by half the length of each panel,  $L$ :  $\epsilon_{xx}^A \approx 0.5 d/L$  and  $\epsilon_{xx}^B \approx -0.5 d/L$ . In this example, the angle of rotation,  $\theta$ , is very small, such that  $\tan\theta$  can be approximated as  $\theta$ . See text for discussion.



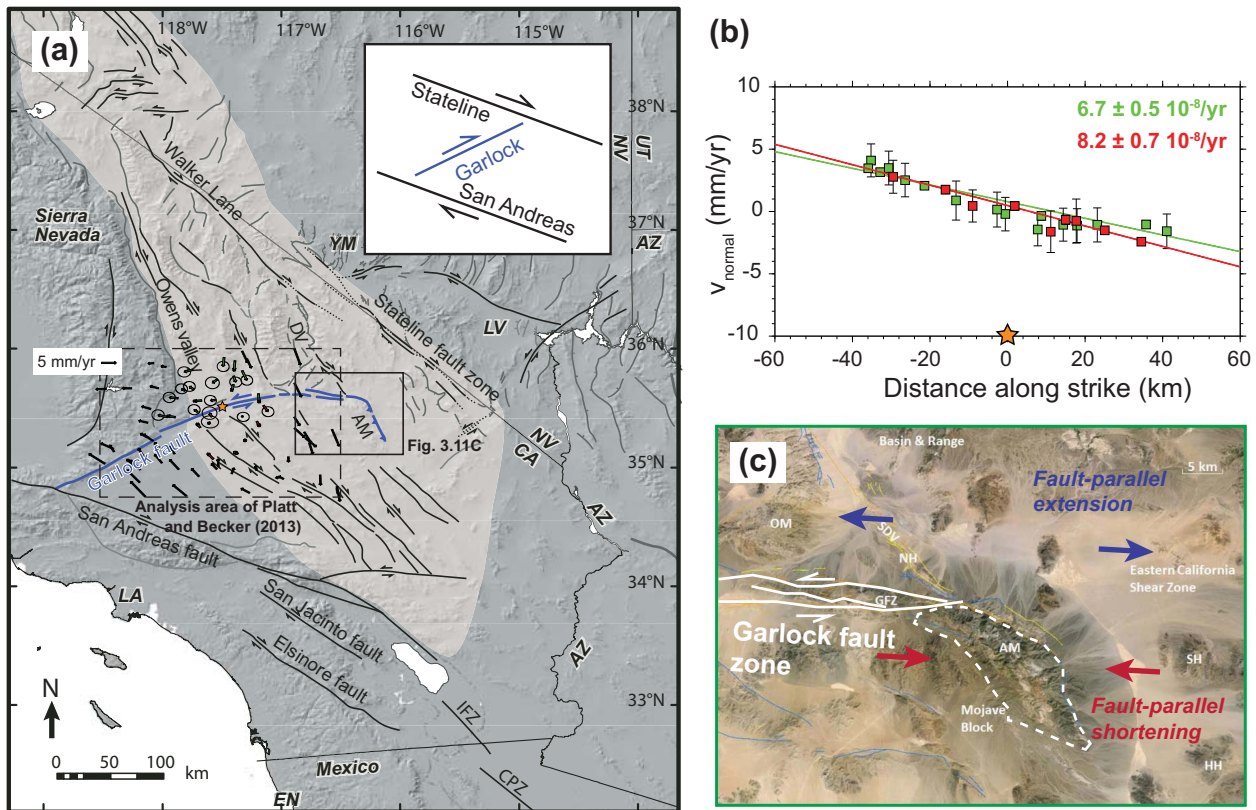


**Figure 3.9.** Active bookshelf faulting example of the Garlock fault in California. (a) Map of southern California, Nevada, and western Arizona highlighting major faults within the active Eastern California shear zone–Walker Lane fault system from Mahan et al. (2009). The Garlock fault is shown in blue. GPS vectors around the Garlock faults are from Platt and Becker (2013); the red and green vectors correspond to GPS stations to the south and north of the Garlock fault, respectively. The gold star shows the reference location for the analyses shown in Fig. 3.9b. Inset shows simplified fault geometries. AM—Avawatz Mountains; OV—Owens Valley; DV—Death Valley; YM—Yucca Mountain; LV—Las Vegas; EN—Ensenada; LA—Los Angeles; SJFZ—San Jacinto fault zone; IFZ—Imperial fault zone; CPZ—Cerro Prieto fault zone. (b) Garlock-fault-perpendicular velocities projected onto a line approximating the Garlock-fault trajectory. From Platt and Becker (2013). The best-fit velocity gradients correspond to the shear strain rate of the fault and surrounding rocks, which correspond to a rotation rate of  $4.0 \pm 0.7$  °/Ma. As in Figure 3.9a, the red and green data points correspond to GPS stations to the south and north of the Garlock fault, respectively. (c) Eastern termination structures of the Garlock fault showing fault-parallel extension in the Basin and Range province to the northeast and fault-perpendicular shortening in the Avawatz Mountains to the southeast. Google Earth image is from Chinn (2013b).

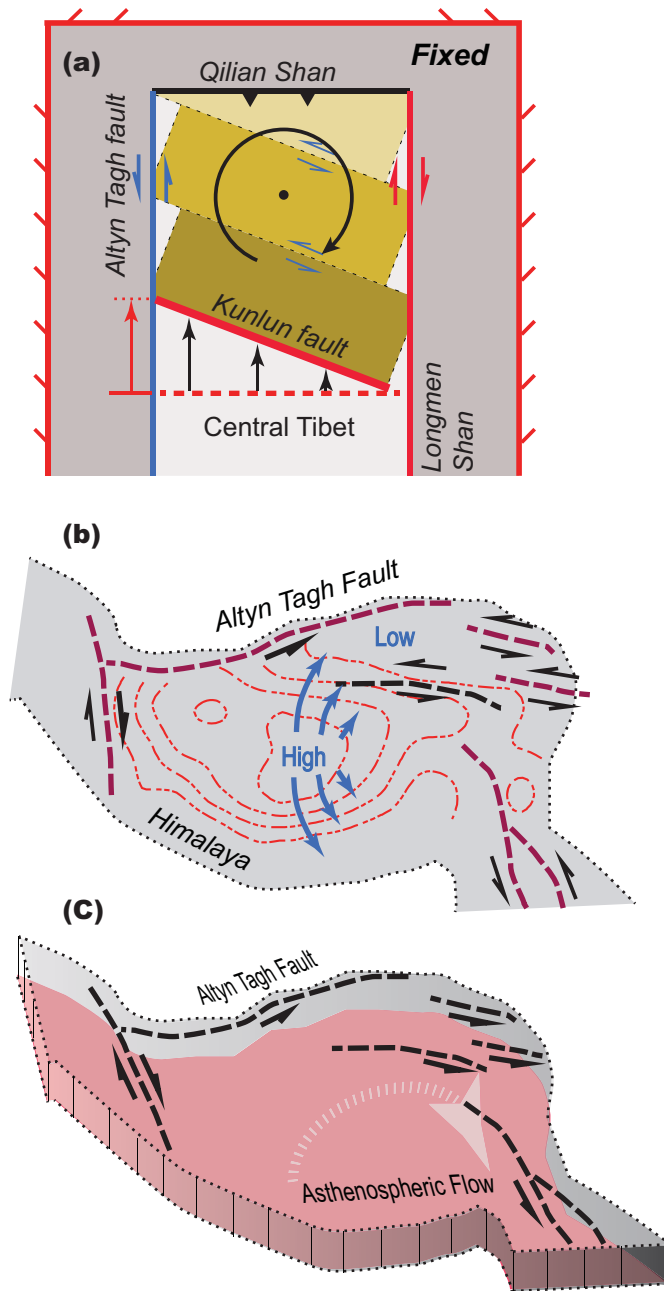


**Figure 3.10.** Passive bookshelf faulting in northern Tibet may be driven by (a) boundary-zone rotation to the south, (b) gravitational spreading of thick central Tibet lithosphere with the distribution of gravitational potential energy after England and Molnar (1997), or (c) a toroidal flow in the asthenosphere (e.g., León Soto et al., 2012). See text for further discussion.

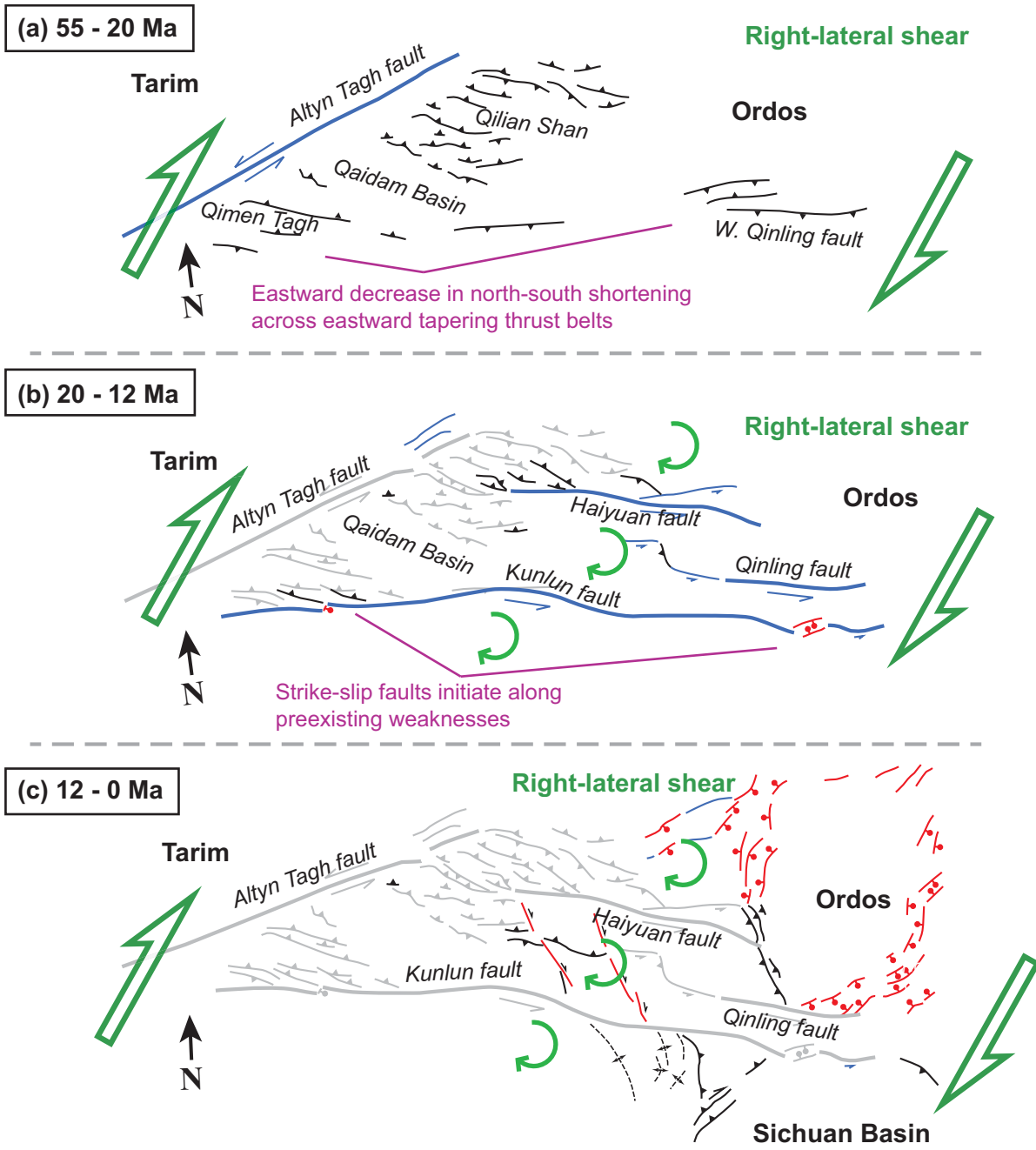


Figure 3.11. Full figure caption on next page.

**Figure 3.11 (continued).** Cenozoic tectonic evolution of northern Tibet, showing the timing of major fault initiation where grey structures are already active at given time interval. (a) Right-lateral shear, driven from the south, begins in the Eocene and is expressed by north-south shortening in the Qimen Tagh, North Qaidam, and southern Qilian Shan thrust belts. An eastward decrease in north-south shortening magnitude and thrust spacing indicates clockwise rotation of northern Tibet. (b) Progressive crustal thickening causes the initiation of the east-striking left-slip faults along preexisting weaknesses. Continued right-lateral shear drives clockwise rotation of these faults and their wallrock passively against the left-slip Atlyn Tagh bounding fault zone. (c) The left-slip faults in this passive bookshelf fault system develop a four-quadrant deformation pattern with domains of fault-parallel stretching and shortening. Age data from Craddock et al. (2011), Yuan et al. (2013), Duvall et al. (2013), and references therein.

### 3.6. References

- Avouac, J. P., and Tapponnier, P., 1993, Kinematic model of active deformation in central Asia: *Geophysical Research Letters*, v. 20, no. 10, p. 895-898.
- Burchfiel, B.C., Zhang, P. Wang, Y., Zhang, W., Song, F., Deng, Q., Molnar, P., and Royden, L., 1991, Geology of the Haiyuan fault zone, Ningxia Hui Autonomous Region, China, and its relation to the evolution of the northeastern margin of the Tibetan Plateau: *Tectonics*, v. 10, p. 1091-1110.
- Burchfiel, B.C., Chen, Z., Liu, Y., and Royden, L.H., 1995, Tectonics of the Longmen Shan and adjacent regions: *International Geology Review*, v. 37p. 661-735.
- Burgess, W.P., Yin, A., Dubey, C.S., Shen, Z.K., and Kelty, T. K., 2012, Holocene shortening across the Main Frontal Thrust zone in the eastern Himalaya: *Earth and Planetary Science Letters*, v. 357, p. 152-167.
- Cavalié, O., Lasserre, C., Doin, M. P., Peltzer, G., Sun, J., Xu, X., and Shen, Z. K., 2008, Measurement of interseismic strain across the Haiyuan fault (Gansu, China), by InSAR: *Earth and Planetary Science Letters*, v. 275, no. 3, p. 246-257.
- Chen, Y., Gilder, S., Halim, N., Cogné, J. P., Courtillot, V., 2002a, New paleomagnetic constraints on central Asian kinematics: Displacement along the Altyn Tagh fault and rotation of the Qaidam Basin: *Tectonics*, v. 21, no. 5, p. 6-1.
- Chen, Y., Wu, H., Courtillot, V., and Gilder, S., 2002b, Large N-S convergence at the northern edge of the Tibetan plateau? New Early Cretaceous paleomagnetic data from Hexi Corridor, NW China: *Earth and Planetary Science Letters*, v. 201, no. 2, p. 293-307.
- Cheng, F., Jolivet, M., Fu, S., Zhang, Q., Guan, S., Yu, X., and Guo, Z., 2014, Northward growth of the Qimen Tagh Range: A new model accounting for the Late Neogene strike-slip deformation of the SW Qaidam Basin: *Tectonophysics*, v. 632, p. 32-47.
- Cheng, F., Jolivet, M., Dupont-Nivet, G., Wang, L., Yu, X., and Guo, Z., 2015, Lateral extrusion along the Altyn Tagh Fault, Qilian Shan (NE Tibet): insight from a 3D crustal budget: *Terra Nova*, v. 27, no. 6, p. 416-425.
- Chinn, L. D., 2013a, Blind contractional faulting responsible for exhumation of the eastern Garlock fault zone, Avawatz Mountains, California: *GSA abstracts with programs*, v. 45, no. 7, p. 596.
- Chinn, L. D., 2013b, Low-Temperature Thermochronometry of the Avawatz Mountains; Implications for the Eastern Terminus and Inception of the Garlock Fault Zone [M.S. thesis]: University of Washington.
- Clark, M.K., 2012, Continental collision slowing due to viscous mantle lithosphere rather than topography: *Nature*, v. 483, no. 7387, p. 74-77.

- Clark, M.K., Farley, K.A., Zheng, D., Wang, Z., and Duvall, A.R., 2010, Early Cenozoic faulting of the northern Tibetan Plateau margin from apatite (U–Th)/He ages: *Earth and Planetary Science Letters*, v. 296, no. 1, p. 78-88.
- Cobbold, P.R., and Davy, P.H., 1988, Indentation tectonics in nature and experiment. 2. Central Asia: *Bull. Geol. Inst. Univ. Uppsala*, v. 14, p. 143-162.
- Cogné, J.P., Halim, N., Chen, Y., and Courtillot, V., 1999, Resolving the problem of shallow magnetizations of Tertiary age in Asia: insights from paleomagnetic data from the Qiangtang, Kunlun, and Qaidam blocks (Tibet, China), and a new hypothesis: *Journal of Geophysical Research: Solid Earth*, v. 104, no. B8, p.17715-17734.
- Craddock, W., Kirby, E., and Zhang, H., 2011, Late Miocene–Pliocene range growth in the interior of the northeastern Tibetan Plateau: *Lithosphere*, v. 3, no. 6, p. 420-438.
- Davis, G.A., and Burchfiel, B.C., 1973, Garlock fault: An intracontinental transform structure, southern California: *Geological Society of America Bulletin*, v. 84, no. 4, p. 1407-1422.
- Densmore, A.L., Ellis, M.A., Li, Y., Zhou, R., Hancock, G.S., and Richardson, N., 2007, Active tectonics of the Beichuan and Pengguan faults at the eastern margin of the Tibetan Plateau: *Tectonics*, v. 26, no. 4.
- Dupont-Nivet, G., Guo, Z., Butler, R.F., Jia, C., 2002, Discordant paleomagnetic direction in Miocene rocks from the central Tarim Basin: evidence for local deformation and inclination shallowing: *Earth and Planetary Science Letters*, v. 199, no. 3, p. 473-482.
- Dupont-Nivet, G., Horton, B.K., Butler, R.F., Wang, J., Zhou, J., and Waanders, G.L., 2004, Paleogene clockwise tectonic rotation of the Xining-Lanzhou region, northeastern Tibetan Plateau. *Journal of Geophysical Research*, v. 109, DOI: 10.1029/2003JB002620.
- Dupont-Nivet, G., Lippert, P.C., Van Hinsbergen, D.J., Meijers, M.J., and Kapp, P., 2010, Palaeolatitude and age of the Indo–Asia collision: palaeomagnetic constraints: *Geophysical Journal International*, v. 182, no. 3, p. 1189-1198.
- Duvall, A.R., and Clark, M.K., 2010, Dissipation of fast strike-slip faulting within and beyond northeastern Tibet: *Geology*, v. 38, p. 223-226.
- Duvall, A.R., Clark, M.K., Kirby, E., Farley, K.A., Craddock, W.H., Li, C., and Yuan, D.Y., 2013, Low-temperature thermochronometry along the Kunlun and Haiyuan faults, NE Tibetan Plateau: Evidence for kinematic change during late-stage orogenesis: *Tectonics*, 32(5), p. 1190-1211.
- England, P., and Houseman, G., 1986, Finite strain calculations of continental deformation: 2. Comparison with the India-Asia collision zone: *Journal of Geophysical Research: Solid Earth*, v. 91, no. B3, p. 3664-3676.
- England, P., and Molnar, P., 1990, Right-lateral shear and rotation as the explanation for strike-slip faulting in eastern Tibet: *Nature*, v. 344, p. 140-142.

- England, P., and Molnar, P., 1997, Active deformation of Asia: From kinematics to dynamics: *Science*, v. 278, p. 647-650.
- Freund, R., 1970, Rotation of strike slip faults in Sistan, southeast Iran: *Journal of Geology*, v. 78, p. 188-200.
- Frost, G.M., et al., 1995, Preliminary early Cretaceous paleomagnetic results from the Gansu Corridor, China: *Earth and Planetary Science Letters*, v. 129, no. 1, p. 217-232.
- Fu, B. and Awata, Y., 2007, Displacement and timing of left-lateral faulting in the Kunlun Fault Zone, northern Tibet, inferred from geologic and geomorphic features: *Journal of Asian Earth Sciences*, v. 29, p. 253-265.
- Fu, B., Awata, Y., Du, J., and He, W., 2005, Late Quaternary systematic stream offsets caused by repeated large seismic events along the Kunlun fault, northern Tibet: *Geomorphology*, v. 71, no. 3, p. 278-292.
- Gan, W., Zhang, P., Shen, Z.-K., Niu, Z., Wang, M., Wan, Y., Zhou, D., and Cheng, J., 2007, Present-day crustal motion within the Tibetan Plateau inferred from GPS measurements: *Journal of Geophysical Research*, v. 112, no. B8.
- Gao, R., Wang, H., Yin, A., Dong, S., Kuang, Z., Zuba, A. V., Li, W., and Xiong, X., 2013, Tectonic development of the northeastern Tibetan Plateau as constrained by high-resolution deep seismic-reflection data: *Lithosphere*, v. 5, no. 6, p. 555-574.
- Gaudemer, Y., Tapponnier, P., Meyer, B., Peltzer, G., Guo, S., Chen, Z., Dai, H., and Cifuentes, I., 1995, Partitioning of crustal slip between linked, active faults in the eastern Qilian Shan, and evidence for a major seismic gap, the 'Tianzhu gap', on the western Haiyuan Fault, Gansu (China): *Geophysical Journal International*, v. 120, p. 599-645.
- Godard, V., Pik, R., Lavé, J., Cattin, R., Tibari, B., De Sigoyer, J., Pubellier, M., and Zhu, J., 2009, Late Cenozoic evolution of the central Longmen Shan, eastern Tibet: insight from (U-Th)/He thermochronometry: *Tectonics*, v. 28, no. 5.
- Green, O.R., Searle, M.P., Corfield, R.I., and Corfield, R.M., 2008, Cretaceous-Tertiary carbonate platform evolution and the age of the India-Asia collision along the Ladakh Himalaya (Northwest India): *The Journal of Geology*, v. 116, no. 4, p. 331-353.
- Guest, B., Pavlis, T. L., Golding, H., and Serpa, L., 2003, Chasing the Garlock: A study of tectonic response to vertical axis rotation: *Geology*, v. 31, no. 6, p. 553-556.
- Halim, N., et al., 1998, New Cretaceous and Early Tertiary paleomagnetic results from Xining-Lanzhou basin, Kunlun and Qiangtang blocks, China: Implications on the geodynamic evolution of Asia. *Journal of Geophysical Research: Solid Earth*, v. 103, no. B9, p. 21025-21045.

- Halim, N., Chen, Y., and Cogné, J.P., 2003, A first palaeomagnetic study of Jurassic formations from the Qaidam basin, Northeastern Tibet, China—tectonic implications: *Geophysical Journal International*, v. 153, no. 1, p. 20-26.
- Harkins, N., and Kirby, E., 2008, Fluvial terrace riser degradation and determination of slip rates on strike - slip faults: An example from the Kunlun fault, China: *Geophysical Research Letters*, v. 35, no. 5.
- Harkins, N., Kirby, E., Shi, X., Wang, E., Burbank, D., and Chun, F., 2010, Millennial slip rates along the eastern Kunlun fault: Implications for the dynamics of intracontinental deformation in Asia: *Lithosphere*, v. 2, p. 247-266.
- Heidbach, O., Tingay, M., Barth, A., Reinecker, J., and Kurfeß, D., Müller, B., 2010, Global crustal stress pattern based on the World Stress Map database release 2008: *Tectonophysics*, v. 482, no. 1, p. 3-15.
- Hubbard, J. and Shaw, J. H., 2009, Uplift of the Longmen Shan and Tibetan plateau, and the 2008 Wenchuan (M= 7.9) earthquake: *Nature*, v. 458, no. 7235, p. 194-197.
- Jolivet, M., Brunel, M., Seward, D., Xu, Z., Yang, J., Malavieille, J., Roger, F., Leyreloup, A., Arnaud, N., and Wu, C., 2003, Neogene extension and volcanism in the Kunlun fault zone, northern Tibet: New constraints on the age of the Kunlun fault: *Tectonics*, v. 22, DOI: 10.1029/2002TC001428.
- Kidd, W.S., and Molnar, P., 1988, Quaternary and active faulting observed on the 1985 Academia Sinica--Royal society geotraverse of Tibet: *Philosophical Transactions of the Royal Society of London. Series A*, v. 327, 337-363.
- Kirby, E., Whipple, K. X., Burchfiel, B. C., Tang, W., Berger, G., Sun, Z., and Chen, Z., 2000, Neotectonics of the Min Shan, China: Implications for mechanisms driving Quaternary deformation along the eastern margin of the Tibetan Plateau: *Geological Society of America Bulletin*, v. 112, no. 3, p. 375-393.
- Kirby, E., Harkins, N., Wang, E., Shi, X., Fan, C., and Burbank, D., 2007, Slip rate gradients along the eastern Kunlun fault: *Tectonics*, v. 26, no. 2.
- Lasserre, C. et al., 1999, Postglacial left slip rate and past occurrence of M> 8 earthquakes on the western Haiyuan fault, Gansu, China: *Journal of Geophysical Research: Solid Earth*, v. 104, no. B8, p. 17633-17651.
- Lasserre, C., Gaudemer, Y., Tapponnier, P., Mériaux, A. S., Van der Woerd, J., Daoyang, Y., Ryerson, F. J., Finkel, R. C., and Caffee, M. W., 2002, Fast late Pleistocene slip rate on the Leng Long Ling segment of the Haiyuan fault, Qinghai, China: *Journal of Geophysical Research: Solid Earth*, v. 107, no. B11.
- Lease, R.O., Burbank, D.W., Zhang, H., Liu, J., and Yuan, D., 2012, Cenozoic shortening budget for the northeastern edge of the Tibetan Plateau: Is lower crustal flow necessary?: *Tectonics*, v. 31, no. 3.



- León Soto, G., Sandvol, E., Ni, J.F., Flesch, L., Hearn, T.M., Tilmann, F., Chen, J., and Brown, L.D., 2012, Significant and vertically coherent seismic anisotropy beneath eastern Tibet: *Journal of Geophysical Research: Solid Earth*, v. 117, no. B5.
- Li, C., Zhang, P., Yin, J., and Min, W., 2009, Late Quaternary left-lateral slip rate of the Haiyuan fault, northeastern margin of the Tibetan Plateau: *Tectonics*, v. 28.
- Li, H., et al., 2005, Slip rate on the Kunlun fault at Hongshui Gou, and recurrence time of great events comparable to the 14/11/2001, Mw ~7.9 Kokoxili earthquake, *Earth and Planetary Science Letters*, v. 237, p. 285-299.
- Luyendyk, B.P., Kamerling, M.J., and Terres, R., 1980, Geometric model for Neogene crustal rotations in southern California: *Geological Society of America Bulletin*, v. 91, no. 4, p. 211-217.
- McGill, S.F., Wells, S.G., Fortner, S.K., Kuzma, H.A., and McGill, J.D., 2009, Slip rate of the western Garlock fault, at Clark Wash, near Lone Tree Canyon, Mojave Desert, California: *Geological Society of America Bulletin*, v. 121, no. 3-4, p. 536-554.
- Meade, B.J., 2007, Present-day kinematics at the India-Asia collision zone: *Geology*, v. 35, no. 1, p. 81-84.
- Meade, B.J., and Hager, B.H., 2005, Block models of crustal motion in southern California constrained by GPS measurements: *Journal of Geophysical Research: Solid Earth*, v. 110, no. B3.
- Means, W.D., 1989, Stretching faults: *Geology*, v. 17, v. 10, p. 893-896.
- Means, W.D., 1990, One-dimensional kinematics of stretching faults: *Journal of Structural Geology*, v. 12, no. 2, p. 267-272.
- Mercier, J.L., Vergely, P., Zhang, Y.Q., Hou, M.J., Bellier, O., and Wang, Y.M., 2013, Structural records of the Late Cretaceous–Cenozoic extension in Eastern China and the kinematics of the Southern Tan-Lu and Qinling Fault Zone (Anhui and Shaanxi provinces, PR China): *Tectonophysics*, v. 582, p. 50-75.
- Meyer, B., Tapponnier, P., Bourjot, L., Métivier, F., Gaudemer, Y., Peltzer, G., Shunmin, G., and Zhitai, C., 1998, Crustal thickening in Gansu-Qinghai, lithospheric mantle subduction, and oblique, strike-slip controlled growth of the Tibet Plateau: *Geophysical Journal International*, v. 135, no. 1, p. 1–47, doi:10.1046/j.1365-246X.1998.00567.x.
- Mock, C., Arnaud, N. O., and Cantagrel, J. M., 1999, An early unroofing in northeastern Tibet? Constraints from  $^{40}\text{Ar}/^{39}\text{Ar}$  thermochronology on granitoids from the eastern Kunlun range (Qianghai, NW China): *Earth and Planetary Science Letters*, v. 171, no. 1, p. 107-122.
- Molnar, P., and Tapponnier, P., 1981, A possible dependence of tectonic strength on the age of the crust in Asia: *Earth and Planetary Science Letters*, v. 52, p. 107–114.

- Onderdonk, N.W, 2005, Structures that accommodated differential vertical axis rotation of the western Transverse Ranges, California: *Tectonics*, v. 24, no. 4.
- Peltzer, G. and Saucier, F., 1996, Present-day kinematics of Asia derived from geologic fault rates: *Journal of Geophysical Research: Solid Earth*, v. 101, no. B12, p. 27943-27956.
- Peltzer, G. and Tapponnier, P., 1988, Formation and evolution of strike - slip faults, rifts, and basins during the India - Asia collision: An experimental approach: *Journal of Geophysical Research: Solid Earth*, v. 93, no. B12, p. 15085-15117.
- Platt, J.P. and Becker, T. W., 2010, Where is the real transform boundary in California?: *Geochemistry, Geophysics, Geosystems*, v. 11, no. 6.
- Platt, J.P. and Becker, T. W., 2013, Kinematics of rotating panels of E–W faults in the San Andreas system: what can we tell from geodesy?: *Geophysical Journal International*, v. 194, no. 3, p. 1295-1301.
- Ramsay, J.G., and Huber, M.I., 1983, *The techniques of modern structural geology. Vol. 1. Strain Analysis*: Academic Press, London.
- Ratschbacher, L., Hacker, B.R., Calvert, A., Webb, L.E., Grimmer, J.C., McWilliams, M.O., Ireland, T., Dong, S., and Hu, J., Tectonics of the Qinling (Central China): tectonostratigraphy, geochronology, and deformation history: *Tectonophysics*, v. 366, p. 1-53.
- Reith, R.C., 2013, *Structural Geology of a Central Segment of the Qilian Shan-Nan Shan Thrust Belt: Implications for the Magnitude of Cenozoic Shortening in the Northeastern Tibetan Plateau [M.S. thesis]*: Los Angeles, University of California, 73 p.
- Ryan, W.B.F., Carbotte, S.M., Coplan, J.O., O'Hara, S., Melkonian, A., Arko, R., Weissel, R.A., Ferrini, V., Goodwillie, A. Nitsche, F., Bonczkowski, J., and Zemsky, R., 2009, Global Multi-Resolution Topography synthesis: *Geochemistry Geophysics Geosystems*, v. 10, no. 8.
- Savage, J.C., and Burford, R.O., 1973, Geodetic determination of relative plate motion in central California: *Journal of Geophysical Research*, v. 78, no. 5, p. 832-845.
- Smith, G.I., 1962, Large Lateral Displacement on Garlock Fault, California, as Measured from Offset Dike Swarm: *AAPG Bulletin*, v. 46, no. 1, p. 85-104.
- Sun, Z.M., Yang, Z.Y., Pei, J.L., Yang, T.S., and Wang, X.S., 2006, New Early Cretaceous paleomagnetic data from volcanic and red beds of the eastern Qaidam Block and its implications for tectonics of Central Asia: *Earth and Planetary Science Letters*, v. 243, p. 268-281.
- Tapponnier, P., Peltzer, G., Le Dain, A.Y., Armijo, R., and Cobbold, P., 1982, Propagating extrusion tectonics in Asia: new insights from simple experiments with plasticine: *Geology*, v. 10, no. 12, p. 611-616.

- Tapponnier, P., Xu, Z., Roger, F., Meyer, B., Arnaud, N., Wittlinger, G., and Yang, J., 2001, Oblique stepwise rise and growth of the Tibet Plateau: *Science*, v. 294, p. 1671-1677.
- Taylor, M., Yin, A., 2009, Active structures of the Himalayan-Tibetan orogen and their relationships to earthquake distribution, contemporary strain field, and Cenozoic volcanism: *Geosphere*, v. 5, p. 199-214.
- Thatcher, W., 2007, Microplate model for the present - day deformation of Tibet. *Journal of Geophysical Research: Solid Earth*, v. 112, no. B1.
- Van Der Woerd, J., Ryerson, F.J., Tapponnier, P., Gaudemer, Y., Finkel, R., Mériaux, A.S., Caffee, M., Guoguang, Z., and Qunlu, H., 1998, Holocene left-slip rate determined by cosmogenic surface dating on the Xidatan segment of the Kunlun fault (Qinghai, China): *Geology*, v. 26, no. 8, p. 695-698.
- Van Der Woerd, J., Ryerson, F.J., Tapponnier, P., Meriaux, A.S., Gaudemer, Y., Meyer, B., Finkel, R., Caffee, M., Guoguang, Z., and Zhiqin, X., 2000, Uniform slip-rate along the Kunlun Fault: Implications for seismic behaviour and large-scale tectonics: *Geophysical Research Letters*, v. 27, no. 16, p. 2353-2356.
- Van Der Woerd, J. et al., 2002, Uniform postglacial slip-rate along the central 600 km of the Kunlun Fault (Tibet), from <sup>26</sup>Al, <sup>10</sup>Be, and <sup>14</sup>C dating of riser offsets, and climatic origin of the regional morphology: *Geophysical Journal International*, v. 148, no. 3, p. 356-388.
- Van Hinsbergen, D. J., Kapp, P., Dupont - Nivet, G., Lippert, P. C., DeCelles, P. G., and Torsvik, T. H., 2011, Restoration of Cenozoic deformation in Asia and the size of Greater India: *Tectonics*, v. 30, no. 5.
- Wang, E. and Burchfiel, B.C, 2004, Late Cenozoic right-lateral movement along the Wenquan Fault and associated deformation: implications for the kinematic history of the Qaidam Basin, Northeastern Tibetan Plateau: *International Geology Review*, v. 46, no. 10, p. 861-879.
- Wang, C., Gao, R., Yin, A., Wang, H., Zhang, Y., Guo, T., Li, Q., and Li, Y., 2011, A mid-crustal strain-transfer model for continental deformation: A new perspective from high-resolution deep seismic-reflection profiling across NE Tibet: *Earth and Planetary Science Letters*, v. 306, no. 3, p. 279-288.
- Wang, E. et al., 2012, Two-phase growth of high topography in eastern Tibet during the Cenozoic: *Nature Geoscience*, v. 5, no. 9, p. 640-645.
- Weldon, R. and Humphreys, E., 1986, A kinematic model of southern California: *Tectonics*, v. 5, no. 1, p. 33-48.
- Wu, C., Yin, A., Zuza, A. V., Zhang, J., Liu, W., and Ding, L., 2016, Pre-Cenozoic Geologic History of the Central and Northern Tibetan Plateau and the Role of Wilson Cycles in Constructing the Tethyan Orogenic System: *Lithosphere*, in press.

- Yin, A., 2000, Mode of Cenozoic east-west extension in Tibet suggesting a common origin of rifts in Asia during the Indo-Asian collision. *Journal of Geophysical Research: Solid Earth*, v. 105, no. B9, p. 21745-21759.
- Yin, A., 2006, Cenozoic tectonic evolution of the Himalayan orogen as constrained by along strike variation of structural geometry, exhumation history, and foreland sedimentation: *Earth-Science Reviews*, v. 76, no. 1, p. 1-131.
- Yin, A., 2010a, Cenozoic tectonic evolution of Asia: A preliminary synthesis: *Tectonophysics*, v. 488, no. 1, p. 293-325.
- Yin, A., 2010b, A special issue on the great 12 May 2008 Wenchuan earthquake ( $M_w$ 7.9): Observations and unanswered questions: *Tectonophysics*, v. 491, p. 1-9.
- Yin, A., Dang, Y.-Q., Zhang, M., McRivette, M.W., Burgess, W.P., and Chen, X.-H., 2007, Cenozoic tectonic evolution of Qaidam Basin and its surrounding regions (part 2): Wedge tectonics in southern Qaidam Basin and the Eastern Kunlun Range, in Sears, J.W., Harms, T.A., and Evenchick, C.A., eds., *Whence the Mountains? Inquiries into the Evolution of Orogenic Systems: A Volume in Honor of Raymond A. Price*: Geological Society of America Special Paper 433, p. 369-390.
- Yin, A., Dang, Y.-Q., Wang, L.-C., Jiang, W.-M., Zhou, S.-P, Chen, X. -H., Gehrels, G.E., and McRivette, M.W., 2008a, Cenozoic tectonic evolution of Qaidam Basin and its surrounding regions (part 1): The southern Qilian Shan–Nan Shan thrust belt and northern Qaidam Basin: *Geological Society of America Bulletin*, v. 120, no. 7/8, p. 813–846, doi: 10.1130.B26180.1.
- Yin, A., Dang, Y.Q., Zhang, M., Chen, X.H., and McRivette, M.W., 2008b. Cenozoic tectonic evolution of the Qaidam basin and its surrounding regions (Part 3): Structural geology, sedimentation, and regional tectonic reconstruction. *Geological Society of America Bulletin*, v. 120, no. 7-8, p. 847-876.
- Yin, A., and Harrison, T.M., 2000, Geologic evolution of the Himalayan-Tibetan orogen: *Annual Review of Earth and Planetary Sciences*, v. 28, no. 1, p. 211-280.
- Yin, A. and Taylor, M.H., 2011, Mechanics of V-shaped conjugate strike-slip faults and the corresponding continuum mode of continental deformation: *Geological Society of America Bulletin*, v. 123, no. 9-10, p. 1798-1821.
- Yin, A., and Pappalardo, R.T., 2015, Gravitational spreading, bookshelf faulting, and tectonic evolution of the South Polar Terrain of Saturn’s moon Enceladus: *Icarus*, v. 260, p. 409-439.
- Yuan, W., Dong, J., Shicheng, W., and Carter, A., 2006, Apatite fission track evidence for Neogene uplift in the eastern Kunlun Mountains, northern Qinghai–Tibet Plateau, China: *Journal of Asian Earth Sciences*, v. 27, no. 6, p. 847-856.

- Yuan et al., 2013, The growth of northeastern Tibet and its relevance to large-scale continental geodynamics: A review of recent studies: *Tectonics*, v. 32, p. 1358-1370.
- Zhang, P. et al., 1991, Amount and style of late Cenozoic deformation in the Liupan Shan area, Ningxia Autonomous Region, China: *Tectonics*, v. 10, no. 6, p. 1111-1129.
- Zhang, Y.Q., Vergely, P., and Mercier, J., 1995, Active faulting in and along the Qinling Range (China) inferred from SPOT imagery analysis and extrusion tectonics of south China: *Tectonophysics*, v. 243, no. 1, p. 69-95.
- Zhang, Y.Q., Mercier, J. L., and Vergely, P., 1998, Extension in the graben systems around the Ordos (China), and its contribution to the extrusion tectonics of south China with respect to Gobi-Mongolia: *Tectonophysics*, v. 285, no. 1, p. 41-75.
- Zhang, P.Z. et al., 2004, Continuous deformation of the Tibetan Plateau from global positioning system data: *Geology*, v. 32, no. 9, p. 809-812.
- Zheng, D. et al., 2006, Rapid exhumation at~ 8 Ma on the Liupan Shan thrust fault from apatite fission-track thermochronology: Implications for growth of the northeastern Tibetan Plateau margin: *Earth and Planetary Science Letters*, v. 248, no. 1, p. 198-208.
- Zhu, B., Kidd, W.S.F., Rowley, D.B., Currie, B.S., and Shafique, N., 2005, Age of initiation of the India–Asia collision in the east-central Himalaya: *J. Geol.*, v. 113, p. 265–285.
- Zuza, A.V., Yin, A., 2013, Ductile bookshelf faulting: A new kinematic model for Cenozoic deformation in northern Tibet: *AGU Fall Meeting Abstracts*, v. 1, p. 2.
- Zuza, A.V., Yin, A., Li, Jianhua, 2014, Deciphering the coupled Paleozoic and Cenozoic tectonic history of the Qilian Shan, northeastern Tibetan Plateau: *AGU Fall Meeting Abstracts*, v.1 p. 4563.
- Zuza, A.V., Cheng, X., Yin, A., 2016, Testing models of Tibetan Plateau formation with Cenozoic shortening estimates across the Qilian Shan-Nan Shan thrust belt: *Geosphere*, v. 12, no. 2, p. 501-532.

**-Chapter 4-**

**Spacing and strength of active continental strike-slip faults**

## 4.1. Abstract

Parallel and evenly-spaced active strike-slip faults occur widely in nature across a diverse range of continental settings. Despite their common existence, the fundamental question of what controls fault spacing remains unanswered. In this chapter I present a mechanical model for the generation of parallel strike-slip faults that relates fault spacing to the following parameters: brittle-crust thickness, fault strength, crustal strength, and the crustal stress state. Scaled analogue experiments using dry sand, crushed walnut shells, and viscous putty were employed to test the key assumptions of the quantitative model. The physical models demonstrate that fault spacing is linearly proportional to brittle-layer thickness, both in experiments with only brittle materials and two-layer trials with dry sand overlying viscous putty. Although the  $S/h$  slope in the sand-putty experiments may be controlled by the (1) frictional interaction at the sand-putty interface and/or (2) effects of distributed basal loading caused by the viscous layer (i.e., a wider basal shear zone with the putty layer), I demonstrate that this first effect is most important in the analogue experiments. I apply this quantitative model to crustal-scale strike-slip faults using fault spacing and the seismogenic-zone thickness obtained from high-resolution earthquake-location data to estimate absolute fault friction of active strike-slip faults in Asia and along the San Andreas fault system in California. The average friction coefficient of strike-slip faults in the India-Asia collisional orogen is lower than that of faults in the San Andreas fault system. Weaker faults explain why deformation penetrates >3500 km into Asia from the Himalaya and why the interior of Asia is prone to large ( $M > 7.0$ ) devastating earthquakes along major strike-slip faults. This new approach of estimating absolute fault strength may be useful in future studies of continental deformation and earthquake mechanics.

## 4.2. Introduction

Parallel strike-slip faults occur widely in nature, from a few meters to >100s km in length and spacing (e.g., Segall and Pollard, 1983; Davy and Cobbold, 1988; Swanson, 1988; Martel and Pollard, 1989; Dickinson, 1996; Yin, 2010). Regularly spaced strike-slip faults are observed along plate transform boundaries (e.g., the San Andreas fault system; Fig. 4.1a) (e.g., Nur et al., 1986; Dickinson, 1996), across collisional orogens (e.g., the Himalayan-Tibetan orogen; Fig. 4.1b) (Molnar and Tapponnier, 1975; Taylor and Yin, 2009; Yin, 2010), in analogue experiments (e.g., Tchalenko, 1970; Freund, 1974; Naylor et al., 1986; Yin and Taylor, 2011), and on icy satellites (e.g., Yin et al., 2016). Irregularly spaced parallel strike-slip systems have also been documented, including the seismically active right-slip fault systems across northern China with fault spacing varying from ~100 km to ~500 km (e.g., Yin et al., 2015). The characteristic spacing of strike-slip faults, or lack thereof, inevitably reflects how the faults interact with one another and with the fault-bounded crust. Thus, this readily observed geometric parameter may be used to estimate fault strength and stress state across diverse tectonic settings on Earth and other planetary bodies. Despite being such a common feature in zones of lithospheric deformation, the mechanics of evenly-spaced active continental strike-slip faults has never been satisfactorily explained nor quantified.

In this contribution, I develop a stress-shadow model (e.g., Lachenbruch, 1961; Yin et al., 2016) that relates strike-slip-fault spacing to the brittle-crust thickness of the fault-hosting lithosphere, fault and crustal strength, and the regional stress. The model assumptions are tested and validated with scaled analogue experiments using dry sand, crushed walnut shells, and viscous putty. These models use a basal shear device to generate Riedel shears in dry granular materials. By experimenting with various thicknesses and viscosities of a putty layer beneath a



brittle layer, I also explore the effects of distributed versus localized basal shear on strike-slip fault spacing.

Strike-slip fault spacing is linearly proportional to brittle-layer thickness in both the analogue models and for crustal-scale faults. The application of this theoretical model using seismogenic zone thickness and fault spacing observations allows us to estimate the effective coefficient of fault friction ( $\overline{\mu_f}$ ) of strike-slip faults in actively deforming regions of on Earth. This method leads to the finding that the faults in the India-Asia collisional orogen are weaker ( $\overline{\mu_f} = \sim 0.10-0.20$ ) than faults in the San Andreas transform system ( $\overline{\mu_f} = \sim 0.15-0.21$ ) in California.

### **4.3. Generating parallel strike-slip faults**

#### *4.3.1. Existing models*

The following models have been proposed to account for the generation of parallel strike-slip faults: (1) reactivation of preexisting extensional joints in crystalline and/or other low-porosity rock (e.g., Segall and Pollard, 1983; Martel and Pollard, 1989), (2) deformation bands forming in high-porosity rocks (e.g., Aydin and Johnson, 1978; Fossen et al., 2007), and (3) viscoelastic models that predict strike-slip fault spacing based on the rheology contrasts of the upper and lower crust (Roy and Royden 2000a, 2000b).

The first two groups of models explain faulting in specific tectonic settings (e.g., previously normal-faulted rocks or deformation-band generation in porous sandstone) at small scales (i.e.,  $< \sim 1$  km), and they ultimately lack generality for crustal-scale deformation. It is unlikely that strike-slip faulting at a range of scales (from  $< 1$  mm to  $> 1000$ s km) across diverse lithologies (e.g., Fig. 4.1) is universally derived from the reactivation of preexisting regularly-

spaced structures. I note that strike-slip faulting in northern Tibet and certain regions of California may be respectively exploiting suture zones and older normal faults (e.g., Taylor and Yin, 2009; Dokka, 1989), but the majority of the faults in both settings actually crosscut preexisting fabrics (Fig. 4.1) (Dickinson, 1996; Yin and Taylor, 2001). The deformation band mechanism (Aydin and Johnson, 1978) leads to strain localization and strain hardening, which in turn can produce through-going faults. This process predicts sequential deformation and deactivation of individual faults, but does not explain coeval motion of parallel strike-slip faults that occur independent of the fault-hosting lithology.

The viscoelastic models of Roy and Royden (2000a; 2000b) examine the effects of rheologic stratification on strike-slip faulting. These studies show that fault spacing varies as a function of the strength of the upper crust and viscosity contrast between the upper and lower crusts. Two limitations hinder the applicability of these models to actual continent-scale strike-slip faults: (1) the depth-averaged shear stress is infinity at the fault surface in their dislocation model and (2) when one fault is active, the other faults remain locked (i.e., total welding of the other faults), which implies that the faults are created sequentially but not active simultaneously. This last point is at odds with many strike-slip fault systems on Earth (Fig. 4.1).

#### *4.3.2. Stress-shadow model for extensional joints*

My analysis of strike-slip fault spacing employs the stress-shadow model, which was originally developed to quantify the spacing of extensional joints (Lachenbruch, 1961). Rock under regional remote tensile stress,  $\sigma_n = \sigma_n^r$ , fractures if  $\sigma_n^r$  exceeds the tensile strength of the rock  $T$  (Fig. 4.2). The presence of a new fracture imposes a low stress boundary condition; for extensional joints, the normal stress on the fracture surface  $\sigma_n^c$  is assumed to drop to zero

(Pollard and Segall, 1987). This in turn casts a stress shadow within which tensile stress is below the tensile strength of the rock. This condition prohibits fractures from forming adjacent to the initial joint. Stress increases away from the fracture  $\sigma_n(x = 0) = \sigma_n^c = 0$  to the regional tensile stress  $\sigma_n(x = \infty) = \sigma_n^r$  (Fig. 4.2). The distance at which  $\sigma_n$  surpasses  $T$  defines the stress-shadow length,  $S$ , such that  $\sigma_n(x = S) = T$  (Fig. 4.2). New fractures can only be created immediately outside of the stress shadows, resulting in a characteristic joint spacing. The stress rise in the above scenario (Fig. 4.2) can be quantified by an analytical solution of the stress-distribution for mode-I opening cracks from linear elastic fracture mechanics (LEFM) (Lachenbruch, 1961; Pollard and Segall, 1987).

#### 4.3.3. Stress-shadow model for strike-slip faulting

The stress-shadow model for strike-slip faulting used in this study is based in part on a derivation presented by Yin et al. (2016), which examined strike-slip fault spacing on Enceladus (an icy satellite of Saturn) to infer its ice shell thickness. In both Yin et al. (2016) and this study, I (1) treat a strike-slip fault as a mode-III crack driven by a remote fault-parallel shear stress, (2) seek the fault-motion-parallel shear stress distribution (e.g., Pollard and Segall, 1987), (3) regard the deforming lithosphere as a plastic material governed by the Coulomb fracture criterion, and (4) assume that crustal strength resides in the brittle crust, consistent with the stress-guide concept (Lister and Davis, 1989) and the current understanding of continental lithosphere rheology (e.g., Jackson et al., 2008).

First, I assume that shear stress  $\sigma_{xz}$  satisfies the following boundary conditions (Fig. 4.3):

$$\sigma_{xz}(x = 0) = \overline{\sigma^f} \quad (1a)$$

$$\sigma_{xz}(x = \infty) = \sigma_s^r = \sigma^{bc} \quad (1b)$$

where  $x$  is the distance from the fault (Fig. 4.3),  $\overline{\sigma^f}$  is the vertically-averaged shear stress on the fault plane, and  $\sigma_s^r$  is the regional shear stress, which I denote as  $\sigma^{bc}$ . The boundary condition in equation (1a) is an important departure from the stress-shadow model for extensional jointing, as the magnitude of the shear stress on a strike-slip fault is not zero, but rather equals the vertically averaged shear stress of the fault plane,  $\overline{\sigma^f}$  (Fig. 4.3) (cf. Roy and Royden, 2000a, 2000b). The following solution for the shear stress distribution satisfies the boundary conditions in equations (1a) and (1b):

$$\sigma_{xz}(x) = \sigma^{bc} + (\sigma^{bc} - \overline{\sigma^f}) \left[ \frac{|x|^{n/m}}{(|x|^n + h^n)^{1/m}} - 1 \right] \quad (2)$$

where  $x$  is the distance from the fault,  $h$  is the depth of the fault equal to the brittle-crust thickness in the  $y$  direction,  $n > 0$ , and  $m > 0$  (Fig. 4.3). The above solution is not unique when it is constrained only by the boundary conditions. For example, the following solution also satisfies the boundary conditions shown in equations (1a) and (1b):

$$\sigma_{xz}(x) = \sigma^{bc} + (\sigma^{bc} - \overline{\sigma^f}) \left[ \frac{\tan^{-1}(x)}{(\frac{\pi}{2})} - 1 \right] \quad (3)$$

where  $\tan^{-1}(x = 0) = 0$  and  $\tan^{-1}(x = \infty) = \frac{\pi}{2}$ , thus allowing  $\sigma_{xz}(x = 0) = \overline{\sigma^f}$

and  $\sigma_{xz}(x = \infty) = \sigma^{bc}$ . However, as shown below, the solution in equation (2) permits a linear relationship between  $S$  and  $h$ , which is observed in the analogue experiments and continental strike-slip fault data (see below in sections 3 and 4), whereas equation (3) does not have this mathematical property.

Using equation (2), the length of the stress shadow  $S$  can be obtained by:

$$\sigma_{xz}(x = S) = \overline{Y} = \sigma^{bc} + (\sigma^{bc} - \overline{\sigma^f}) \left[ \frac{S^{n/m}}{(S^n + h^n)^{1/m}} - 1 \right] \quad (4)$$

where  $\bar{Y}$  is the vertically averaged shear fracture strength within the domain of strike-slip faulting (Fig. 4.3). Note that  $\bar{Y}$  is analogous to the tensile strength  $T$  in the extensional joint example discussed above.

When  $n = m = 2$ , equations (2) and (4) are similar to the LEFM solution for the stress distribution of a mode-III crack embedded in an elastic half space (Pollard and Segall, 1987). However, this solution is not ideal for continental strike-slip faults (e.g., Fig. 4.1) that cut through the entire brittle crust (e.g., Yin et al., 2016). Furthermore, a linear  $S$ - $h$  relationship (validated in sections 3 and 4) requires that  $n = m = 1$ , which allows simplification of equation (4) to the following relationship:

$$S = \frac{\bar{Y} - \bar{\sigma}^f}{\sigma^{bc} - \bar{Y}} h \quad (5)$$

Equation (5) demonstrates that fault spacing  $S$  is a function of the (i) brittle-crust thickness  $h$ , (ii) regional shear stress acting on the brittle crust  $\sigma^{bc}$ , (iii) shear fracture strength of the deforming brittle crust  $\bar{Y}$ , and (iv) shear stress on the fault surface  $\bar{\sigma}^f$ . Fault shear stress and crustal shear strength are pressure-, and therefore, depth-dependent, and their mean values can be obtained by assuming that the normal stresses acting on the fault planes are lithostatic. From this assumption, I determine:

$$\bar{\sigma}^f = \frac{1}{h} \int_0^h (C_1 + \bar{\mu}_f \rho g y) dy = C_1 + \frac{1}{2} \bar{\mu}_f \rho g h \quad (6)$$

and

$$\bar{Y} = \frac{1}{h} \int_0^h (C_0 + \bar{\mu}_\phi \rho g y) dy = C_0 + \frac{1}{2} \bar{\mu}_\phi \rho g h \quad (7)$$

where  $\rho$  is the density of the deforming layer,  $g$  is the gravitational acceleration,  $C_0$  and  $\bar{\mu}_\phi$  are the cohesive strength and the effective coefficient of internal friction for the crust next to the fault, respectively, and  $C_1$  and  $\bar{\mu}_f$  are the cohesive strength of the fault and the effective

coefficient of fault friction, respectively. The effective coefficient of internal (i.e., crustal) and fault friction are defined respectively as

$$\overline{\mu_\varphi} = (1 - \lambda_\varphi)\mu_\varphi \quad (8a)$$

$$\overline{\mu_f} = (1 - \lambda_f)\mu_f \quad (8b)$$

where  $\lambda_\varphi$  and  $\mu_\varphi$  are the pore-fluid-pressure ratio and coefficient of internal friction of the fault-bounded domains, respectively, and  $\lambda_f$  and  $\mu_f$  are the pore-fluid-pressure ratio and coefficient of fault friction, respectively.

Here I address the issue of quantifying the regional shear stress acting on the strike-slip faulting domains. First I assume that shear strength is linearly proportional to the brittle-crust thickness, and that the strike-slip faulting domains are bounded by stronger, thus thicker, but still deforming regions (Fig. 4.3). If strike-slip faulting does not occur within these adjacent regions, the regional shear stress must be below the shear fracture strength of these stronger and thicker domains. Therefore I can assume that the regional stress  $\sigma^{bc}$  equals the vertically averaged shear strength of the stronger but still deforming regions ( $\overline{Y^{BR}}$ ) bounding the strike-slip faulting domain (Fig. 4.3). That is

$$\sigma^{bc} = \overline{Y^{BR}} = \frac{1}{H} \int_0^H (C_2 + \overline{\mu_\varphi^{BR}} \rho g y) dy = C_2 + \frac{1}{2} \overline{\mu_\varphi^{BR}} \alpha \rho g h \quad (9)$$

where  $C_2$  and  $\overline{\mu_\varphi^{BR}}$  are the cohesive strength and effective coefficient of internal friction of the bounding regions, respectively,  $H$  is the brittle-layer thickness of bounding regions, and  $\alpha$  is a proxy for regional-stress magnitude defined as  $\alpha = H/h > 1$  (Fig. 4.3). Using  $\overline{Y}$ ,  $\overline{\sigma^f}$ , and  $\sigma^{bc}$  from equations (6), (7), and (9), and assuming  $\overline{\mu_\varphi^{BR}} = \overline{\mu_\varphi}$  and  $C_0 = C_2$ , I arrive at the following  $S$ - $h$  relationship:

$$S = \frac{(C_0 - C_1) + \frac{1}{2} \rho g h (\overline{\mu_\varphi} - \overline{\mu_f})}{\frac{1}{2} \rho g h \overline{\mu_\varphi} (\alpha - 1)} h \quad (10)$$

Because  $S$  is relatively insensitive to  $(C_0 - C_1)$  (Fig. 4.4a), I simplify to:

$$S = \frac{(\overline{\mu_\phi} - \overline{\mu_f})}{\overline{\mu_\phi}(\alpha - 1)} h \quad (11)$$

and

$$\overline{\mu_f} = \overline{\mu_\phi} \left[ 1 - \frac{s}{h} (\alpha - 1) \right] \quad (12)$$

Given that  $\overline{\mu_f} > 0$ , the following relationship must also hold:

$$\alpha \leq \left( \frac{h}{s} + 1 \right) \quad (13)$$

Equation (13) indicates that for the same brittle-crust thickness, wider fault spacing requires lower values of  $\alpha$ . This means that a larger stress magnitude and/or stress gradient (i.e., a larger  $\alpha$  value due to stronger bounding crust or weaker deforming crust) leads to more closely spaced strike-slip faulting because the stress rise is more rapid from  $\sigma_{xz}(x = 0) = \overline{\sigma^f}$  to  $\sigma_{xz}(x = S) = \overline{Y}$  (Figs. 4.3 and 4.4b). Fault strength  $\overline{\mu_f}$  also affects  $S$ ; larger values of  $\overline{\mu_f}$  leads to smaller fault spacing  $S$  (Fig. 4.4c).

#### 4.4. Analogue modeling

To test the above model assumptions and predictions, I conducted scaled analogue experiments using dry granular materials, which can simulate brittle-crust deformation (e.g., Davy and Cobbold, 1988). The experiments use a 12-cm-wide basal-sliding-plate device to generate two parallel shear zones in which Riedel shears form (see Yin and Taylor, 2011) (Fig. 4.5). The model boundary-wall dimensions (65 cm  $\times$  70 cm) are an order of magnitude larger than the width of the shear zones created in the experiments, which are typically  $\leq 6$  cm (Fig. 4.5a).

One set of experiments use a single layer of dry sand or crushed walnut shells to determine the relationship between brittle-layer thickness and fault spacing. The second set of experiments include a ductile putty layer underneath the frictional materials to examine the how a viscous layer beneath the brittle crust affects the relationship between fault spacing and brittle-layer thickness.

#### *4.4.1. Experimental materials*

Two different granular materials were used for the brittle layer—commercially available dry sand and crushed walnut shells (e.g., Hubbert, 1937, 1951; Davy and Cobbold, 1988; Cruz et al., 2008)—for two distinct reasons. First, they have different frictional properties, which allows for more rigorous testing of the analytical model predictions against the observed physical experiments. Second, the materials have different densities (i.e., 1670 vs. 790 kg/m<sup>3</sup> for sand and crushed walnut shells, respectively), which results in slightly different scaling relationships between the model and nature (see section 4.4.2).

The frictional properties of the experimental materials were determined with a Hubbert-type apparatus (Hubbert, 1951), which involves constructing a shear stress versus normal stress failure envelope for each of the experimental materials (e.g., Cruz et al., 2008). The shear stress that generates Riedel shear fractures is a function of the basal friction ( $\mu_b$ ) beneath the sand/crushed walnut shells (see section 4.4.4). Therefore I quantify  $\mu_b$  between the (1) granular materials and underlying basal-sliding plate covered by P100 sandpaper (~162  $\mu\text{m}$  grain size) and (2) dry sand and putty layer. This second interface consists of sand embedded in the putty, which creates a sticky sandpaper-like surface. The grain size distributions and measured



frictional properties of the granular materials are reported in Table 4.1 and Figure A.2. All of these procedures were repeated at least five times to generate statistical uncertainties.

Putty obtained from Isokinetics Inc. was used as the viscous layer underneath the brittle layer. An inclined plane experiment was conducted to determine the approximate viscosity of the putty. The strain rate of simple-shear flow of the putty with an overlying mass on an inclined surface can be used to calculate the viscosity following the relationship  $\tau = 2\eta\dot{\gamma}$ , where  $\tau$  is shear stress,  $\eta$  is viscosity, and  $\dot{\gamma}$  is shear strain rate. Note that because of this relationship, the experiments using different viscosity putties also incorporate the effects of variable strain rates. The simple-shear experiments yield viscosities of  $6.2 \times 10^3$  Pa s and  $9.5 \times 10^3$  Pa s for the two types of putties.

#### 4.4.2. Scaling considerations

Relating the analogue experiments to crustal-scale strike-slip faults requires dynamic and geometric scaling governed by the following relationships (Hubbert, 1937):

$$\frac{C^{model}}{C^{nature}} = \frac{\sigma_V^{model}}{\sigma_V^{nature}} = \frac{\rho^{model} \times l^{model} \times g^{model}}{\rho^{nature} \times l^{nature} \times g^{nature}} \quad (14)$$

where superscripts *model* and *nature* denote the model and crustal parameters and  $l$ ,  $\sigma_V$ ,  $\rho$ , and  $g$  are cohesive strength, vertical thickness, vertical stress, density, and the gravitational acceleration at the Earth's surface, respectively. As the densities of the model and crustal materials are of the same order of magnitude (e.g.,  $1670 \text{ kg/m}^3$  for sand versus  $2750\text{-}3100 \text{ kg/m}^3$  for rock), appropriate scaling depends primarily on the cohesive-strength ratio. The cohesive shear strength of rock varies greatly depending on rock type, ranging from 20 MPa to 110 MPa (Jaeger et al., 2009). The experimental materials have a cohesive strength ( $C^{model}$ ) of 40-60 Pa (Table 4.1), and rock cohesive strength ( $C^{nature}$ ) is 50 MPa, then I arrive at scaling relationships

of sand and crushed walnut shells of  $l_{sand}^{model} \approx \sim 1.7 \times 10^{-6} l^{nature}$  and  $l_{walnut}^{model} \approx \sim 3.5 \times 10^{-6} l^{nature}$  respectively, where the superscripts *sand* and *walnut* refer to each experimental material. Accordingly, 1 cm model thickness using sand represents ~6 km crustal thickness. The experiments, which use layer thicknesses of 1-6 cm for sand and 3-7 cm for crushed walnut shells, can simulate deformation of the crust with overlapping thicknesses of ~6-36 km and ~3-21 km for each material, respectively.

#### 4.4.3. Experimental procedure and results

The first set of experiments was run with dry granular materials (i.e., sand and crushed walnut shells) with thicknesses ranging from 1 cm to 7 cm. Trials run with thicknesses of <1 cm or >7 cm failed to produce observable shear fractures. Sandpaper was used for friction between the materials and the apparatus. In the second series of experiments, the viscous-putty layer was overlain by a sand layer. Both the viscosity and thickness of the putty were varied to observe their effects on fault spacing. Experiments were run with 7-mm- (Fig. 4.5c) and 13-mm-thick putty layers underneath a dry-sand layer with varying thicknesses (1 to 5 cm). Five trials were repeated for each experiment of varying thicknesses of granular materials. The perpendicular distance between the Riedel shears was measured and the results from all five runs were averaged; the calculated uncertainties are the standard deviation of my observations. Vertical-layer-thickness uncertainty is ~1 mm.

Results from both sets of experiments can be explained by a simple linear relationships between fault spacing ( $S$ ) and layer thickness ( $h$ ) (Figs. 4.5d and 4.5e). For the granular-material-only trials, the following linear relationships are observed:  $S/h = 0.68 \pm 0.1$  for sand and  $S/h = 0.82 \pm 0.2$  for crushed walnut shells (Fig. 4.5d).

The experiments with sand overlying a viscous-putty layer all show linear  $S/h$  relationships ranging from  $0.45 \pm 0.03$  to  $0.56 \pm 0.05$  (Fig. 4.5e). Although a linear regression fits the brittle-viscous experiments within the uncertainties, the observed  $S/h$  relationship in these trials appears to deviate slightly from the linear relationship (Fig. 4.5e). There is significant scatter of fault-spacing data for the thicker brittle layers (e.g., when  $h > \sim 3\text{-}4$  cm), which makes any further interpretation of this relationship ambiguous. One possibility is that larger variability of fault spacing arises when the fault spacing  $S$  and experiment-model length  $M$  ratio ( $S/M$ ) (Fig. 4.5a) becomes sufficiently high enough that compression and extension along experimental boundaries affect strike-slip fault generation and spacing.

#### 4.4.4. Analogue experiments and the stress-shadow model

The fault-parallel shear stress generated by basal shearing in the analogue experiments differs from the depth-dependent fault-parallel shear stress assumed in the analytical solutions (e.g., equation [11]). That is, the fault-parallel shear stress in the experiments depends on the basal coefficient of friction but is independent of the vertical axis. Because of this difference, the detailed formation processes of strike-slip faults in nature and in the experiments are slightly different, although the experimental results can be satisfactorily explained by the stress-shadow model detailed below. First, I obtain an expression for the “sidewall” shear stress ( $\sigma_{sidewall}$ ) on a plane perpendicular to the basal sliding plate and parallel to the sliding direction (see derivation in Auxiliary Text A.3):

$$\sigma_{sidewall} = \mu_b \rho g y \quad (15)$$

where  $\mu_b$  is the measured coefficient of friction of the experimental materials against the basal-sliding plate covered in sandpaper (Table 4.1), and  $y$  is the axis parallel to the basal-sliding plate

but orthogonal to the sliding direction. I set  $y = 0$  at the center of the basal-sliding plate (Figs. 4.5a and 4.5b). The relationship in equation (15) states that the sidewall shear stress depends on the coefficient of basal friction and the density of the experimental material; it increases with its distance from the central dividing line of the sliding plate.

Although  $\sigma_{sidewall} = \mu_b \rho g y$  goes to infinite as  $y \rightarrow \infty$ , its induced Riedel-shear-fracture parallel shear stress ( $\sigma_{fp}$ ) is finite. Evaluation of this value at  $y = d$ , which marks the edge of the Riedel shear zone (Fig. 4.5a), including a transformation of coordinates to the Riedel-shear-parallel orientation, leads to the following expression for the effective fault-parallel shear stress ( $\sigma_{fp}$ ):

$$\sigma_{fp} = \mu_b \rho g d \cos(2\theta) \quad (16)$$

where  $d$  is a distance measured along the  $y$ -axis (Fig. 4.5a) such that  $\sigma_{fp}(y = d)$  is greater than the yield strength of the experimental materials and  $\theta$  is the angle between the basal-shear direction and the Riedel shear orientation ( $\sim 16^\circ$  in the experiments) (Figs. 4.5b and 4.5c) (Jaeger et al., 2009; Auxiliary Text A.3).

#### 4.5. Continental strike-slip faults

The goal of this study is to use fault spacing to determine the mechanical properties of parallel strike-slip faults and fault-bounded crust in various continental settings. First I determine the average fault spacing of domains of strike-slip faulting in the India-Asia collisional orogen and along the San Andreas transform fault boundary in California (Fig. 4.1). Application of the stress-shadow model (i.e., equation [11]) to crustal-scale strike-slip faults requires knowledge of the brittle-crust thickness (i.e.,  $h$  in Fig. 4.3) and coefficient of internal friction ( $\overline{\mu_\phi}$ ). The latter parameter is well constrained from experimental rock mechanics (Jaeger et al., 2009). I estimate

brittle-crust thickness by identifying the seismogenic zone thickness ( $L$ ) using high-precision relocated earthquake data from Asia and California.

#### *4.5.1. Strike-slip faults in California and Asia*

Four domains of parallel strike-slip faults were investigated along the San Andreas system in California (e.g., Dickinson, 1996) and across the India-Asia collision zone (e.g., Yin, 2010) (Fig. 4.1). Spacing between the faults was measured perpendicular to the fault strike. The average and standard deviation for fault spacing within each domain are given in Table 4.2.

Strike-slip fault domains are observed on either side of the San Andreas fault (e.g., Dickinson, 1996) (Fig. 4.1a). In central California near San Francisco, four right-slip faults are parallel to the San Andreas fault (e.g., Savage and Lisowski, 1993), including the Hayward, Calaveras, and Greenville faults from west to east. These faults have an average fault spacing of  $33 \pm 3$  km (Fig. 4.1c). In southern California west of the San Andreas fault, nine north-striking right-slip faults extend from the Western Transverse Range in the north through the borderland region in the south. These faults have an average fault spacing of  $47 \pm 15$  km (Fig. 4.1c), and are the Ferrelo, San Clemente-San Isidro, Newport-Inglewood-Rose Canyon, Elsinore, and San Jacinto faults, from west to east (e.g., Dickinson, 1996). East of the San Andreas fault in southern California, the Eastern Transverse Range is comprised of six west-striking left-slip faults: Mammoth Wash-Black Eagle, Salton Creek-Aztec Mines Wash, Chiriaco, Smoke Tree Wash-Victory Pass, Blue Cut, and Pinto Mountain fault zones (e.g., Dickinson, 1996). These faults have an average spacing of  $20 \pm 8$  km (Fig. 4.1c). Also east of the San Andreas fault but north of the left-slip Pinto Mountain fault, there are eight north-striking right-slip faults in the Mojave domain (Fig. 4.1a) with an average spacing of  $16 \pm 2$  km (Fig. 4.1c). They are, from

west to east, the Helendale, Lockhard-Lenwood, Gravel Hills-Camp Rock, Blackwater-Calico, Pisgah-Bullion, Ludlow, Bristol Mountain, and Granite Mountain faults (Dokka and Travis, 1990).

Active intracontinental deformation in Asia is the combined result of continental collision in the south and oceanic subduction in the east (e.g., Yin, 2010). A series of active right-slip faults occur in central Asia (e.g., Yin, 2010) (Fig 4.1b). These faults, dispersed from the Caspian Sea in the southwest to the southern edge of Lake Baikal in the northeast, have an average fault spacing of  $407 \pm 99$  km (Fig. 4.1d). Three active east-striking left-slip faults, with an average fault spacing of  $178 \pm 53$  km (Fig. 4.1d), are present across the northern Tibetan Plateau (Fig. 4.1b): the Kunlun, Qinling, and Haiyuan faults (e.g., Taylor and Yin, 2009). The V-shaped conjugate strike-slip faults of central Tibet (Taylor and Yin, 2009; Yin and Taylor, 2011) consist of left-slip faults in the north that merge with right-slip faults to the south (Fig. 4.1b). The average spacing of these conjugate faults is  $92 \pm 24$  km (Fig. 4.1d). In Iran, parallel and active north-northwest-striking right-slip faults (Bachmanov et al., 2004) (Fig. 4.1b) have an average spacing of  $139 \pm 50$  km (Fig. 4.1d).

#### *4.5.2. Seismogenic zone thickness observations*

Relocated earthquake location data were compiled for California (Schaff and Waldhauser, 2005; Lin et al., 2007; Waldhauser and Schaff, 2008; Hauksson et al., 2012), Central Asia (Chu et al., 2009; Sloan et al., 2011), Tibet (Chu et al., 2009; Sloan et al., 2011), and Iran (Chu et al., 2009; Sloan et al., 2011; Maggi et al., 2000).

Compiled earthquake location data from central California encompasses events from 1984 to 2011 that were relocated by waveform cross correlation and double-difference methods

(Schaff and Waldhauser, 2005; Waldhauser and Schaff, 2008). Reported vertical depth errors are less than 0.7 km at 95% confidence. Earthquake events from 1981 to 2011 are compiled in the southern California earthquake database of Lin et al. (2007) and Hauksson et al. (2012). The relative and absolute vertical depth errors are reported to be less 0.1 km and 1.25 km, respectively, at 90% confidence. In Asia, teleseismically relocated earthquake-location data span events from 1977 to 1998 (Maggi et al., 2000), 1990 to 2005 (Chu et al., 2009), and 1965 to 2009 (Sloan et al., 2011). Reported vertical errors are  $< 1$  km (Chu et al., 2009) and  $< 4$  km (Maggi et al., 2000; Sloan et al., 2011).

The compiled earthquake events and their focal depths are plotted in Figure 4.6. I seek the base of the seismogenic zone, and ultimately the brittle-crust thickness, from each strike-slip fault domain (Fig. 4.1). Seismic events from the stronger bounding regions, where strike-slip faulting is not observed, were also examined (Fig. 4.6) to constrain  $\alpha$ . I avoid earthquakes at mantle depths whose occurrences may have been associated with continental subduction, especially near the Pamirs and Tian Shan (Burtmann and Molnar, 1993).

Events from each domain were projected onto a vertical plane perpendicular to the strike-slip faults (Fig. 4.6). Plots of earthquake depth versus horizontal distance along this perpendicular plane are shown in Figure A.5, for which the cutoff depth above which 95% (D95) and 90% (D90) seismicity was calculated (Table 4.2). This was done in several segments along each profile and their average value defines the seismogenic zone thickness (Fig. A.5). Specifically, I use segment length of 25 km for Californian faults and 500 to 1000 km for Asian faults (Fig. A.5). The longer segment length for Asian domains reflects the sparse seismic data.

These results show that average fault spacing in California and Asia (Fig. 4.1) is linearly proportional to the seismogenic zone thickness (Fig. 4.7a) (Table 4.2), with a steeper slope for the data from Asia and negative vertical-axis intercepts for both datasets.

## 4.6. Discussion

Observations from the analogue experiments and crustal-scale strike-slip faults reveal a fundamental observation that fault spacing ( $S$ ) is linearly proportional to brittle-layer thickness ( $h$ ). The physical models show this relationship to hold for experiments with solely frictional materials (Fig. 4.5d) and for two-layer experiments with a viscous layer underlying frictional materials (Fig. 4.5e).

### 4.6.1. Minimum and maximum thickness cutoffs for generating strike-slip faults

In the analogue experiments, strike-slip faults were only generated when the thickness of the frictional materials was between  $\sim 1$  and  $\sim 7$  cm (Fig. 4.5), which suggests that a minimum ( $h_0$ ) and maximum ( $h_{max}$ ) brittle-layer cutoff thicknesses exist for nucleating strike-slip faults. The regressions of continental  $S$  versus  $h$  yield negative vertical-axis intercepts for both the Asian and Californian datasets (Fig. 4.7a). The simplest explanation for these negative intercepts is that there is a minimum cutoff thickness for generating strike-slip faults. As previously discussed (section 4.4.4), the boundary conditions that drive strike-slip faulting in the analogue experiments are different from those assumed in the stress-shadow model derivation. Thus, the brittle-layer cutoff thickness values for each setting require different explanations.

In the stress-shadow model for crustal-scale strike-slip faulting, the regional shear stress ( $\sigma_s^r$ ) and shear fracture strength ( $\bar{Y}$ ) increase linearly with depth ( $h$ ). The two quantities also



have intercepts at the surface ( $h = 0$ ), with their values equal to  $C_0$  and  $C_2$  as defined in equations (7) and (9). Although  $C_0 = C_2$  is assumed in the stress-shadow derivation, their difference may explain the minimum cutoff value for the observed fault spacing in continental settings (Fig. 4.7a). Given that the regional shear stress ( $\sigma_s^r$ ) and shear fracture strength ( $\bar{Y}$ ) also have different slopes, these two lines must intersect in the  $\sigma_s^r$  and  $\bar{Y}$  vs.  $h$  plot (Fig. 4.8a). Thus, the portion of the shear stress curve below the strength curve defines the value for the minimum fault-spacing cutoff (i.e.,  $h_0$  in Fig. 4.8a). Although the above explanation may apply to crustal-scale strike-slip faults, it is clearly not applicable to the occurrence of strike-slip faults whose spacing is on the order of 10s to 100s m. These smaller scale faults are not controlled by the thickness of the brittle crust but rather local bedding thickness and/or reactivation of pre-existing fractures as commonly observed at outcrop scales (e.g., Aydin and Johnson, 1978; Segall and Pollard, 1983; Martel and Pollard, 1989).

In the analogue experiments, the effective fault-parallel shear stress ( $\sigma_{fp}$ ) is not depth-dependent (Fig. 4.8c). However, the vertically averaged shear fracture strength ( $\bar{Y}$ ) of the sand/crushed walnut shells in the experiments does vary with  $h$  (Fig. 4.8c). For lower brittle-layer thickness values ( $h < \sim 7$  cm),  $\sigma_{fp}$  is greater than  $\bar{Y}$  and parallel strike-slip faulting occurs (Fig. 4.8d). When  $h$  exceeds some critical thickness (i.e.,  $h_{max}$  in Fig. 4.8c), the shear fracture strength  $\bar{Y}$  surpasses the fault-parallel shear stress  $\sigma_{fp}$  (i.e.,  $\bar{Y} > \sigma_{fp}$ ), and Riedel-shear fracturing is suppressed (Fig. 4.8d).

The analogue experiments show that Riedel-shear fractures are not created when the brittle-layer thickness is  $< \sim 1$  cm for sand and  $< \sim 3$  cm for crushed walnut shells (Fig. 4.5d). The fact that this minimum thickness,  $h_{min}$ , varies for different density materials indicates that the vertical stress must play a controlling role in determining the condition that favors strike-slip

faulting. I tentatively suggest that the reduction of the sand/crushed walnut shell thickness leads to a switch of the principal stress directions, from  $\sigma_2$  being vertical for the strike-slip regime when  $h > h_{min}$  to  $\sigma_2$  being horizontal for dip-slip fault regime when  $h < h_{min}$ . I further interpret that the inferred dip-slip faulting was blind and concentrated immediately above the sliding-plate surface at the base of the experimental materials. This would have produced no observable surface deformation.

The intersection of the shear fracture strength and shear stress curves in Figure 4.8c can be used to further verify the stress-shadow model. At  $h = h_{max}$ ,  $\bar{Y} = \sigma_{fp}$  which requires

$$C_0 + \frac{1}{2}\mu_\phi\rho gh_{max} = \mu_b\rho gd \times \cos 2\theta \quad (18)$$

The maximum cutoff thickness for the sand and crushed walnut shell experiments were ~6 cm and ~7 cm respectively. By incorporating the frictional properties of the experimental materials (Table 4.1) into equation (18), I estimate  $d$ . For both the sand and crushed walnut shell experiments, the calculated  $d$  value is ~0.04 m. Figures 4.5b and 4.5c show that the boundaries of Riedel shear zones are 2-4 cm from basal-sliding plate center, which corroborates this result.

#### 4.6.2. Effects of a diffuse brittle-ductile transition and fault healing on brittle-crust thickness

The seismogenic zone thickness was previously assumed to directly equate to the brittle-crust thickness. The seismogenic zone ( $L$ ) likely consists of both a purely frictional-sliding layer ( $h_f$ ) and a transitional zone ( $h_{fv}$ ) of frictional sliding and viscous creeping (Fig. 4.4), such that  $L = h_f + h_{fv}$ . This diffuse brittle-ductile transition zone should have a maximum thickness of a few kilometers. Assuming that  $h_{fv}$  is relatively constant globally, a systematic overestimation of the brittle-crust thickness ( $h = h_f$ ) by several kilometers in both Asia and California (Fig. 4.7) would

affect the vertical-axis intercept of the  $S$ - $h$  linear regression but the  $S/h$  slope should remain the same.

In addition, the fault cohesive strength may be locally greater than the crustal cohesive strength (i.e.,  $C_I > C_0$ ) due to fault healing effects (e.g., Tenthorey and Cox, 2006). Given equation (10), this condition would lead to a negative vertical-axis intercept on a  $S$  versus  $h$  plot (e.g., Fig. 4.7a). This seems counterintuitive but may be applicable to Asia and California where penetrative fracturing, expressed by the widespread off-fault seismicity (e.g., Chu et al., 2009; Hauksson, 2011), may have reduced the cohesive strength of the deforming crust. That is, the actively forming fractures away from through-going faults are mostly isolated, creating dead pores that are less likely to be healed by chemical precipitation than the well-connected fracture networks in active fault zones after major rupture events (Tenthorey and Cox, 2006). Thus, the seismogenic thickness  $L$  may be written more completely as  $L = (h' + h_{FH}) + h_{fv}$ , where  $h'$  is the *effective brittle-crust thickness* and  $h_{FH}$  is the *pseudo brittle-crust thickness* induced by fault healing. Only if  $h_{FH} = h_{fv} = 0$  does the seismogenic thickness  $L$  equal the brittle-crust thickness  $h' = h$ . Because the effects of fault healing and a diffuse brittle-crust transition counteract each other, and any healing effects must be minor because the strike-slip faults are still active, I reasonably assume that  $L = h$  (Fig. 4.7a).

#### 4.6.3. Formation of irregularly-spaced strike-slip faults

Northeast-striking right-slip faults in northern China are irregularly spaced at intervals ranging from ~100 km in the west to > 500 km in the east (Yin et al., 2015). Equation (11) implies that irregularly spaced faults may be generated if the (a) strengths of the parallel faults are different, (b) fault-bounded crust has spatially varying shear strengths, and/or (c) thickness of

the fault-hosting layer varies in laterally. The seismogenic thickness across North China varies from ~20 km in the west to >30 km in the east (Wang et al., 2013), which correlates with closer fault spacing in the west (Yin et al., 2015). Alternatively, spatially varying crustal strength or fault strength may locally affect faulting in northern China.

Related to such heterogeneities, the role of preexisting weaknesses in controlling fault spacing should not be underestimated. Major fault systems will inevitably exploit preexisting weaknesses (e.g., Segall and Pollard, 1983; Martel and Pollard, 1989) but an overarching fundamental mechanism controls the observed even spacing of active crustal-scale strike-slip faults (Fig. 4.1). Although the strike-slip faults in northern Tibet parallel Phanerozoic sutures (Taylor and Yin, 2009) and some of the strike-slip faults in California exploit preexisting normal faults (Dokka, 1989), most of the parallel strike-slip faults discussed here crosscut the regional structural trend (Fig. 4.1).

#### *4.6.4. Role of the lower crust driving strike-slip faulting*

Regional shear stress  $\sigma^{bc}$  (or  $\overline{\sigma_s^r}$ ) is a key parameter that drives faulting in the stress-shadow model (Fig. 4.3). In the derivation for continental strike-slip faults, I assumed that  $\overline{\sigma_s^r}$  equals  $\overline{Y^{bc}}$  (Fig. 4.3). Alternatively,  $\overline{\sigma_s^r}$  may be driven by basal shear in a viscous lower crust (Roy and Royden, 2000a, 2000b), similar to the analogue experiments. However, the experiments demonstrate that neither the viscosity nor the thickness of an underlying viscous layer—parameters which are proportional and inversely proportional, respectively, to shear stress—significantly affect the spacing of brittle-layer faulting (Fig. 4.5e), which contrasts the viscoelastic models of Roy and Royden (2000a, 2000b). The relationships between the stress-shadow mechanism and basal stress (see section 4.4.4 and Auxiliary Text A.3) can explain this

observation. Equation (16) states that the fault-parallel shear stress ( $\sigma_{fp}$ ) is controlled by  $d$  and  $\mu_b$ . Basal shear of the viscous layer is expected to be relatively distributed, decreasing  $d$  and thus increasing the  $S/h$  slope, which is not observed (Fig. 4.5e). The coefficient of friction between the sand and underlying putty (i.e.,  $\mu_b$  of equation [16]) is 0.73, which is higher than for sand against sand paper (Table 4.1). The higher  $\mu_b$  for the sand-putty experiments should lead to a reduced  $S/h$  slope, which is observed in the sand-putty experiments (Fig. 4.5e). Furthermore, all else being equal, equation (16) predicts that given the measured  $\mu_b$  values for each set of experiments (Table 4.1), the sand-only experiments will have a  $S/h$  slope that is  $\sim 1.3$  times that of the sand-putty experiments. This slope difference is observed: the 0.68  $S/h$  slope for the sand-only experiments is  $\sim 1.2$ - $1.3$  times the  $\sim 1.52$  slope for the sand-putty experiments (Figs. 4.5d and 4.5e). These results suggest that the friction coefficient at viscous-brittle layer interface (i.e., the coupling between the two layers) affects the strike-slip fault spacing in the brittle layer more than the effects of distributed basal shear.

#### 4.6.5. Estimates of absolute fault friction from fault spacing and seismogenic zone thickness

The observed difference in  $S/h$  slope between Asia and California must reflect differences in how the faults interact with one another and with the fault-bounded crust. Based on equation (11) and assuming that the crustal internal coefficient of friction  $\overline{\mu_\phi}$  for both continents is the same, the steep  $S/h$  slope observed in Asia may result from (1) a lower magnitude of effective fault friction ( $\overline{\mu_f}$ ), (2) a higher magnitude regional shear stress, or (3) a combination of factors.

In California, the seismogenic thicknesses of the relatively stable Western Transverse and Central Valley-Sierra regions were compared with the  $L$  values of the adjacent deforming regions (Fig. 4.6) to estimates  $\alpha = H/h$  values of 1.05 to 1.2. Using regionally averaged  $\alpha = 1.1$

and  $\overline{\mu}_\phi = 0.24$  values, I find that the closely spaced faults in the eastern San Andreas fault system are stronger at  $\overline{\mu}_f = 0.18-0.22$  than the widely spaced faults in the western San Andreas fault system at  $\overline{\mu}_f = 0.15-0.18$  (Fig. 4.7b). Because of the sparser data in Asia, I was not able to resolve between the internal variation of seismogenic zone thickness in a single strike-slip domain ( $h$ ) and its difference from the seismogenic zone thickness of its bounding regions ( $H$ ). I take this to indicate  $\alpha = H/h \approx 1.0$ . Available earthquake data near the edges of the central Asia strike-slip domain yield an  $\alpha$  value of  $\sim 1.03$ . Using this value for all the strike-slip systems in Asia, I find their strength to be weaker ( $\overline{\mu}_f = \sim 0.10-0.20$ ) than the fault strength in the San Andreas system ( $\overline{\mu}_f = 0.15-0.21$ ) (Figs. 4.7b and 4.7c). The weak faults in Asia and relatively stronger faults in California are consistent with fault-strength studies (e.g., Bird and Kong, 1994; Vernant and Chéry, 2006; Fay and Humphreys, 2006; Humphreys and Coblenz, 2007; He and Chéry, 2008).

The San Andreas transform fault boundary and Asia both experience large strike-slip earthquakes (Figs. 4.1a and 4.1b). The relatively weak faults in Asia (Fig. 4.7c) may explain the long-puzzling observation that active deformation induced by the indentation of India extends  $\sim 3500$  km north of the Himalaya (Fig. 4.1b). Specifically, the weakest faults in Asia (i.e., in Central Asia and northern Tibet) (Fig. 4.7c) are also the furthest from the India-Asia collisional front, which permits intracontinental deformation to occur within the Asian interior. The slippery faults in Asia make them sensitive to minor changes in crustal stress magnitude, which explains why the Asian interior is prone to large ( $M > 7.0$ ) devastating strike-slip earthquakes (Fig. 4.1b). The weaker faults in both locations can be readily explained by their hosting crustal compositions containing friction-reducing clays and hydrated phyllosilicates (e.g., Collettini et al., 2009): central Asia is dominated by flysch complexes (e.g., Sengör et al., 1993) and the

western San Andreas system is dominated by mélangé and forearc materials (e.g., Dickinson, 1981).

Constraining fault strength is critical in modeling continental deformation (Bird and Kong, 1994) and earthquake mechanics (Console et al., 2015), and this work provides an additional method of estimating this critical parameter.

#### **4.7. Conclusions**

In this chapter I have shown that strike-slip fault spacing is linearly proportional to brittle-layer thickness in nature and scaled analogue experiments. Specifically, this relationship can be quantified as a function of brittle-crust thickness, fault strength, and regional stress state with a newly developed stress-shadow model. The application of this model using seismogenic zone thickness and fault spacing reveals that the closely spaced faults in the eastern San Andreas system are stronger than the widely spaced faults in the western San Andreas system. Furthermore, I have shown that the average friction coefficient of active strike-slip faults in the India-Asia collisional orogen is lower than that of faults in the San Andreas transform system.

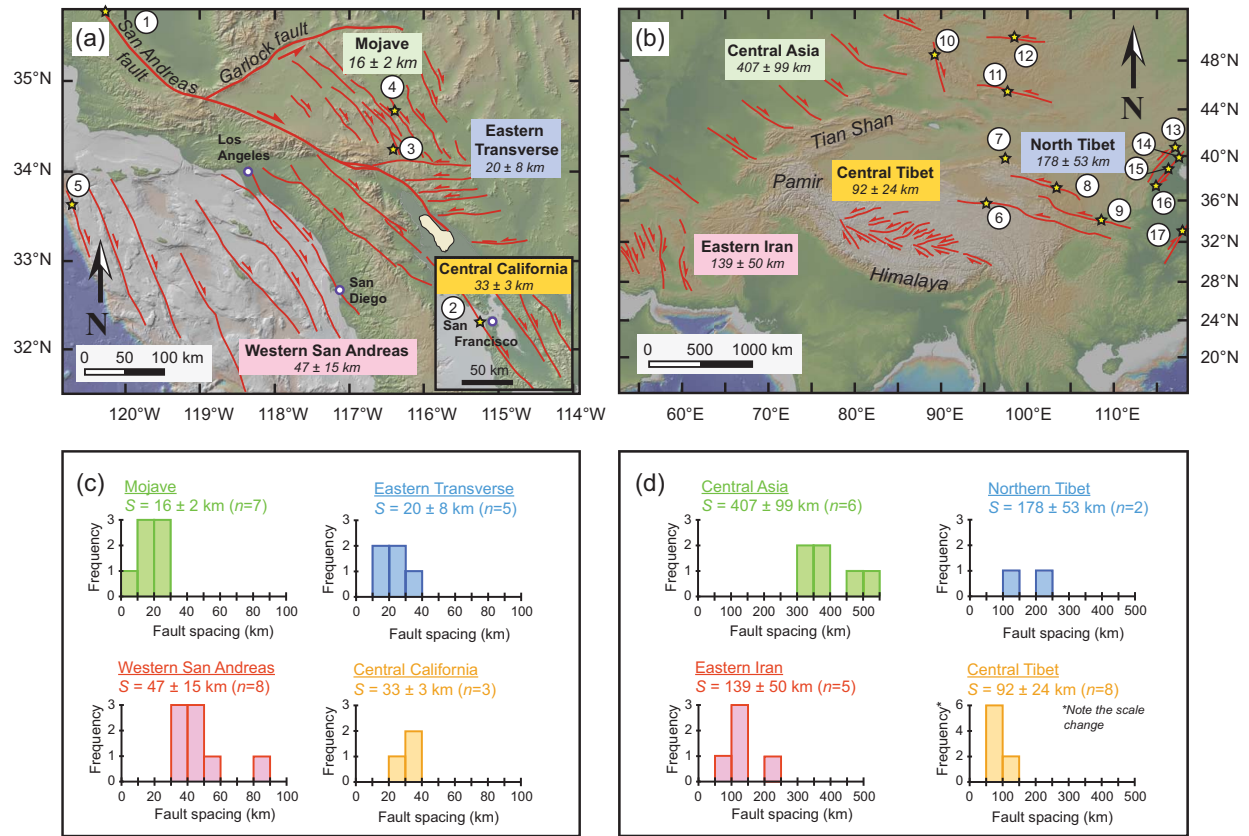


**Figure 4.1.** Evenly-spaced strike-slip domains in (a) California and (b) Asia and their average fault spacing. Inset in (a) shows parallel faults in central California. Histograms show fault spacing for each domain of strike-slip faulting in (c) California and (d) Asia. Locations (shown as yellow stars) and magnitudes of major intracontinental earthquakes along strike-slip faults in California and Asia: (1) 1857  $M = 7.9$  Fort Tejon earthquake, (2) 1906  $M = 7.8$  San Francisco earthquake, (3) 1992  $M = 7.3$  Landers earthquake, (4) 1999  $M = 7.1$  Hector Mine earthquake, (5) 1927  $M = 7.3$  Lompoc earthquake, (6) 2001  $M = 8.1$  Kunlun Pass earthquake, (7) 1932  $M = 7.6$  Changma earthquake, (8) 1920  $M = 7.8$  Haiyuan earthquake, (9) 1556  $M = 8.0$  Shaanxi earthquake, (10) 1931  $M = 8.0$  Fuyun earthquake, (11) 1957  $M = 8.1$  Gobi Altai earthquake, (12) 1905  $M = 8.4$  Bulnay earthquake, (13) 1679  $M = 8.0$  Sanhe-Pinggu earthquake, (14) 1976  $M = 7.8$  Tanshan earthquake, (16) 1966  $M = 7.2$  Xingtai earthquake, (16) 1830  $M = 7.5$  Cixian earthquake, and (17) 1668  $M = 8.0$  Tancheng earthquake.



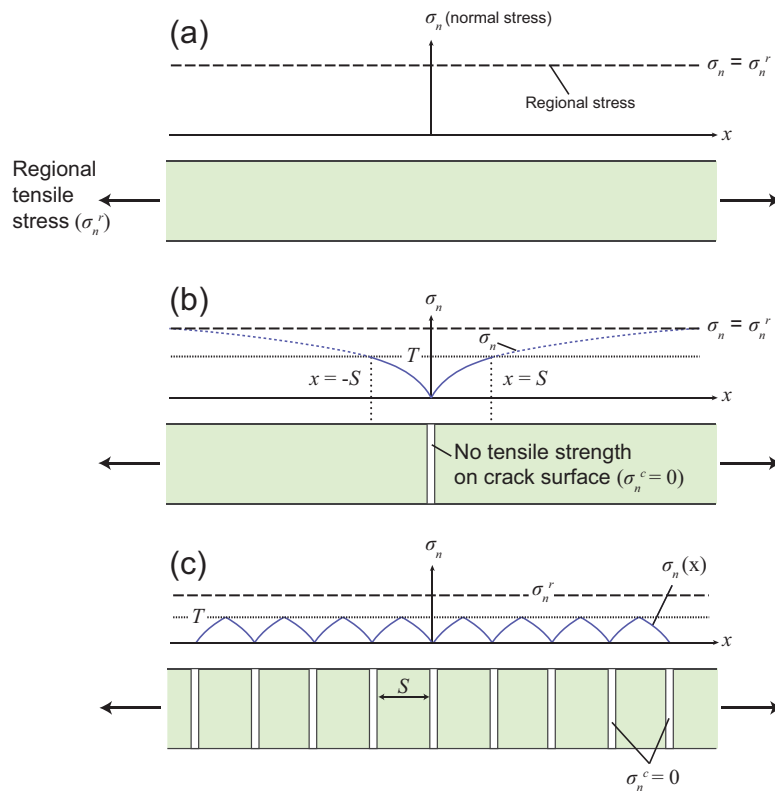


**Figure 4.2.** Conceptual model for the formation of evenly-spaced joints due to the stress shadow effect. (a) A layer under regional extension with a remote normal stress  $\sigma_n = \sigma_n^r$ . (b) The presence of a fracture causes a local stress reduction and the stress-shadow effect prevents fractures from forming within the strength shadow, with length  $S$ . (c) This effect causes fractures in the deforming region to be spaced by this critical distance  $S$ . Figure is modified from Yin et al. (2016).

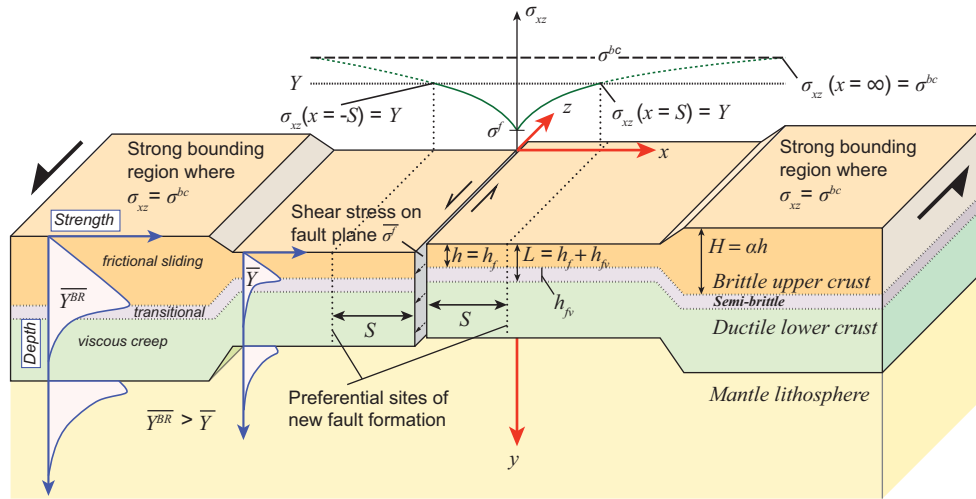


**Figure 4.3.** Model set up, model parameters, and boundary conditions for the formation of evenly-spaced strike-slip faults. Vertically uniform shear stress drives the formation of parallel strike-slip faults in a brittle layer. Off-fault shear stress  $\sigma_{xz}$  satisfies the boundary conditions of  $\sigma_{xz}(x=0) = \sigma^f$  and  $\sigma_{xz}(x=\infty) = \sigma^{bc}$ . Parameters in the model:  $\sigma^f$ , shear stress on the fault;  $\overline{\sigma^f}$ , vertically averaged shear strength of the fault;  $\sigma^{bc}$ , regional shear stress in the brittle crust;  $S$ , stress-shadow length equal to fault spacing;  $Y$  and  $\overline{Y}$ , shear fracture strength and vertically averaged shear fracture strength of the deforming strike-slip fault domain;  $\overline{Y}^{BR}$ , vertically averaged shear fracture strength of the stronger bounding region with a thickness  $H$ ;  $h$ , brittle-crust thickness in region of strike-slip faulting;  $L$ , seismogenic zone thickness that includes regimes of frictional sliding ( $h_f$ ) and transitional frictional sliding and viscous creep ( $h_{fv}$ );  $\alpha = H/h$ . Coordinate system and sign convention are shown with red arrows.

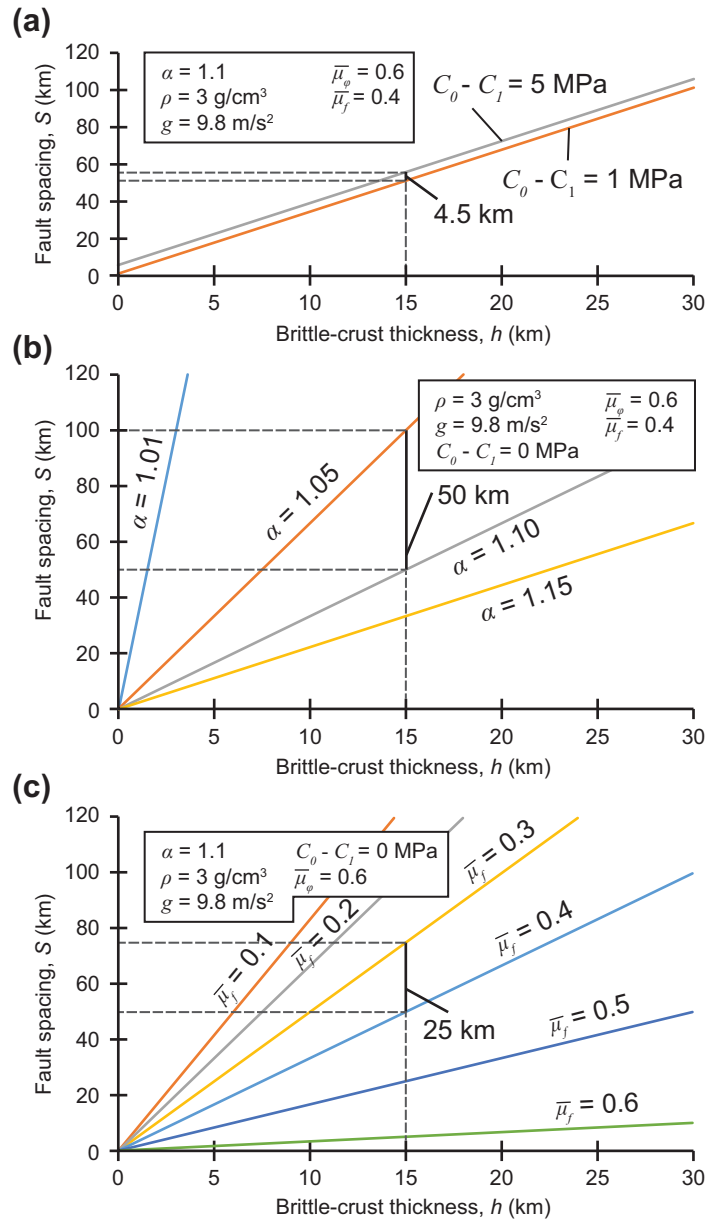


**Figure 4.4.** Effects of model parameters on the relationship between fault spacing and brittle-crust thickness as a function of (a) the difference between fault and crustal cohesive strengths  $C_0 - C_1$ , (b)  $\alpha$  values, and (c) the effective fault friction  $\bar{\mu}_f$ .

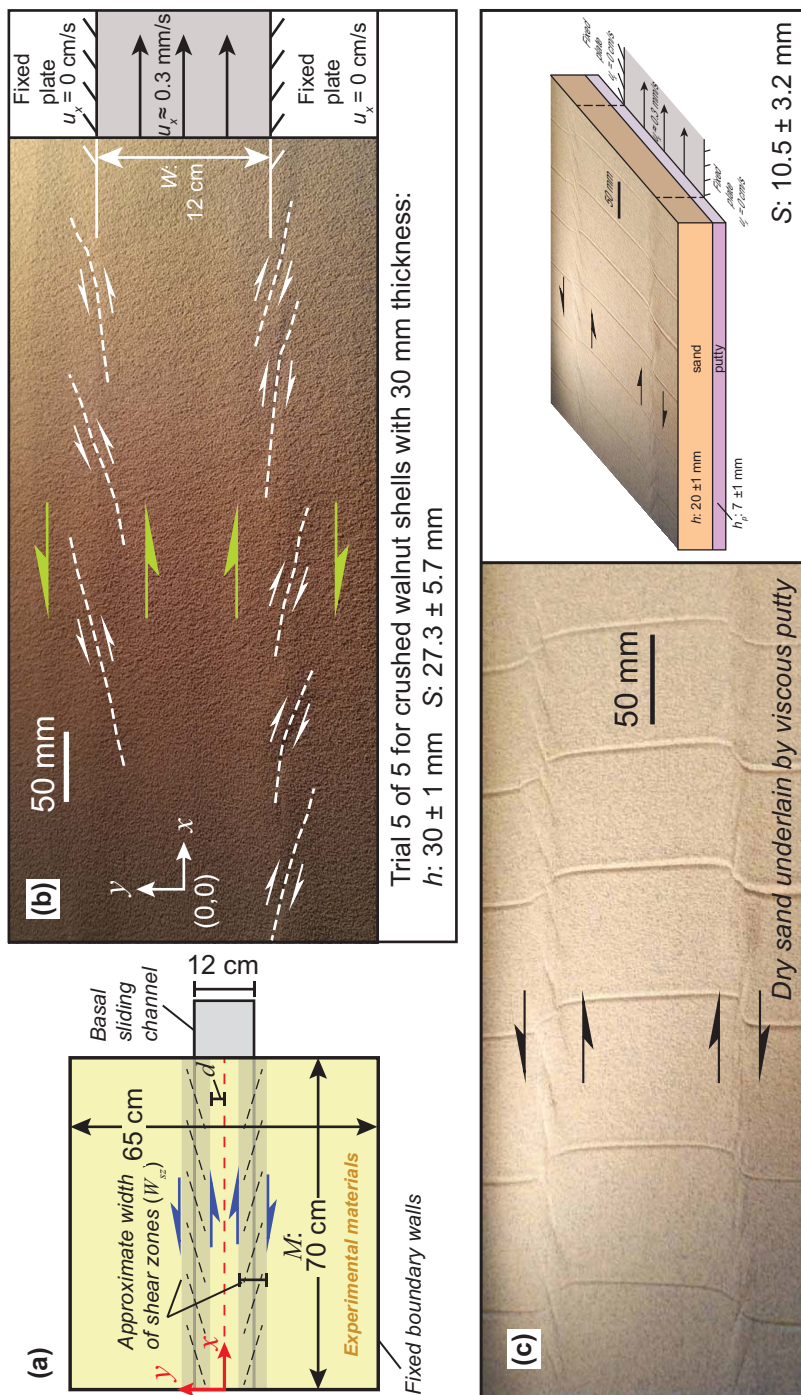
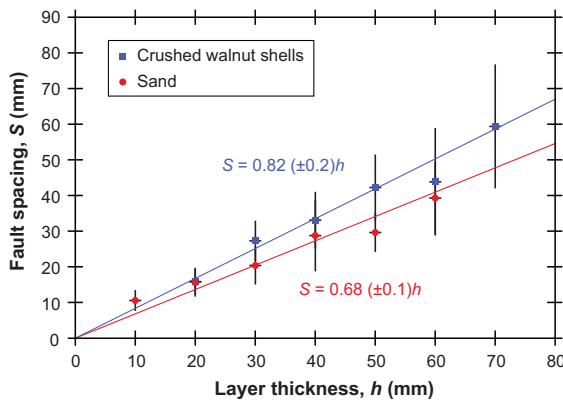
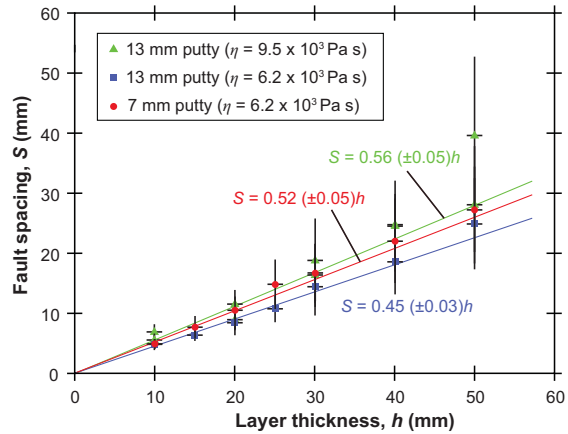


Figure 4.5. Full caption on following page.

(d) Dry granular materials



(e) Dry sand underlain by viscous putty



**Figure 4.5 (continued).** (a) Plan view of experimental setup with 12-cm-wide basal sliding plate that is used to create two parallel shear zones in which Riedel shears form. Note that the resulting shear zone has a length and width of  $M$  and  $W_{sz}$ , respectively. Also shown is the coordinate axis and  $d$ -value, which measures the distance from the center of the basal-sliding plate to the Riedel-shear zone (b) A representative experimental run showing the general apparatus setup and the resulting development of nearly evenly-spaced parallel Riedel shear fractures in two parallel distributed shear zones using crushed walnut shells ( $h = 30$  mm). The basal plate moved to the right in this image, which created left- and right-slip shear zones in the top and bottom of the image respectively. (c) Another representative experimental run with 7-mm-thick viscous putty ( $h_p$ ) overlain by dry sand ( $h = 20$  mm). The viscosity of the putty is  $6.2 \times 10^3$  Pa s. The basal plate in this image moved to the right. (d) Plot of fault spacing versus brittle layer thickness of sand and crushed walnut shells obtained from this study for all experimental runs. The best-fit linear regression is accomplished by forcing the lines through the origin. (e) Plot of fault spacing versus brittle layer thickness of sand underlain by viscous putty of different thicknesses and viscosities. The best-fit linear regression is accomplished by forcing the lines through the origin.

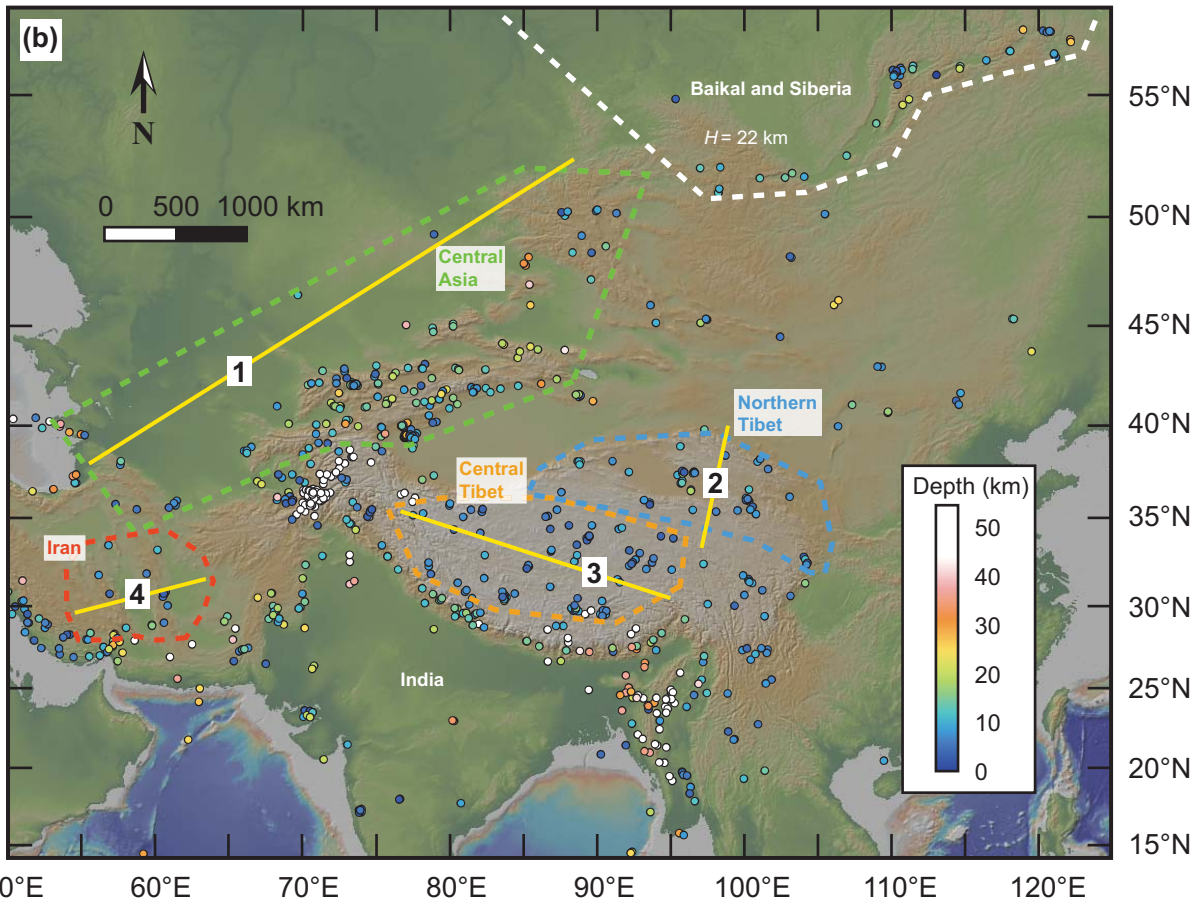
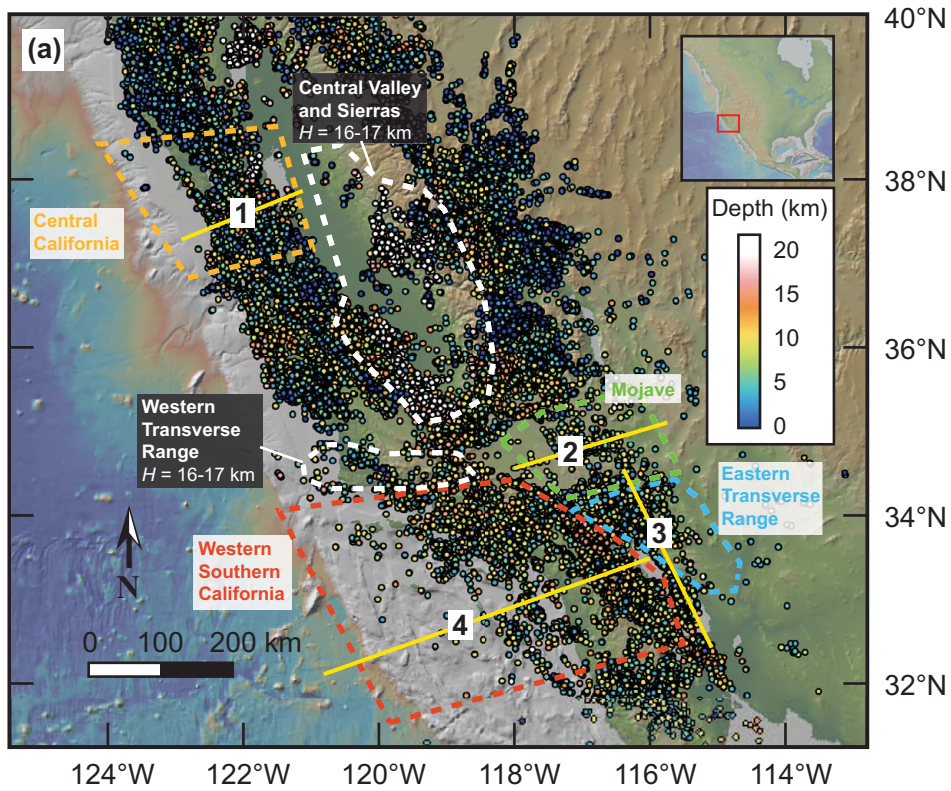
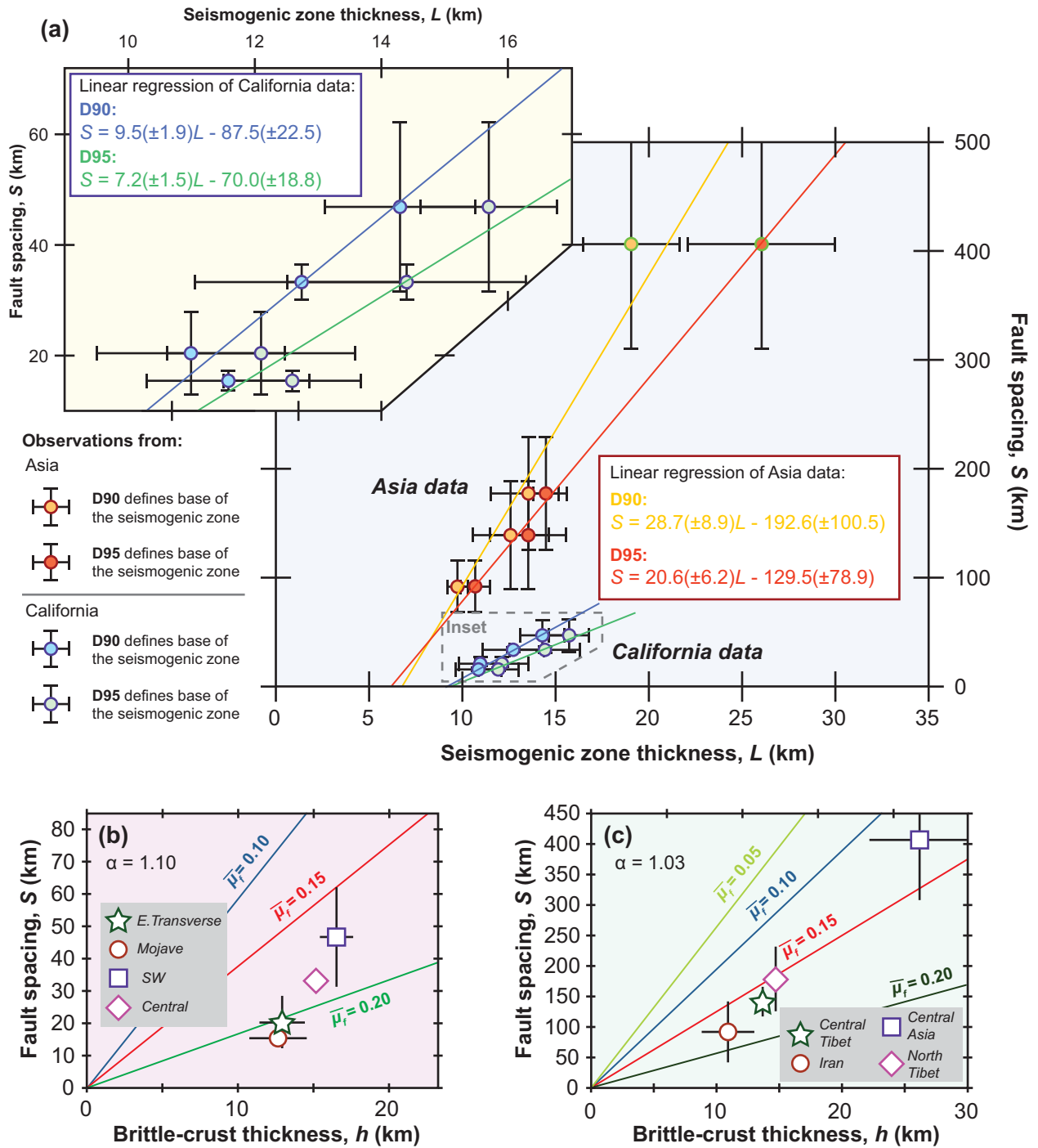


Figure 4.6. Full caption on following page.

**Figure 4.6 (continued).** Earthquake location data earthquake data from (a) California and (b) Asia. Domains of evenly-spaced strike-slip faults with characteristic fault spacing are outlined. Calculation of seismogenic zone thickness used the data outlined for each domain. The profile numbers correspond to those shown in Figure A3. Data from Maggi et al. (2000), Schaff and Waldhauser (2005), Lin et al. (2007), Waldhauser and Schaff (2008), Chu et al. (2009), Sloan et al. (2011), and Hauksson et al. (2012).



**Figure 4.7.** (a) Plot of seismogenic zone thickness (using both D90 and D95 values) versus fault spacing for Asia and California. The inset shows an enlarged plot of the California data. The best-fit linear regressions for the seismogenic zone thickness data using either the D90 or D95 data show similar slopes. Note the negative vertical and positive horizontal intercepts for the regression lines. (b-c) Relationship between fault spacing ( $S$ ) and brittle-crust thickness ( $h$ ) for given  $\alpha$  values. Plots for faults in (b) California use  $\alpha = 1.10$  and (c) Asia use  $\alpha = 1.10$ . Other parameters used in the plots are  $(\bar{\mu}_\phi) = 0.24$ ,  $\rho = 3 \text{ g/cm}^3$ , and  $(C_0 - C_1) = 0 \text{ MPa}$ .



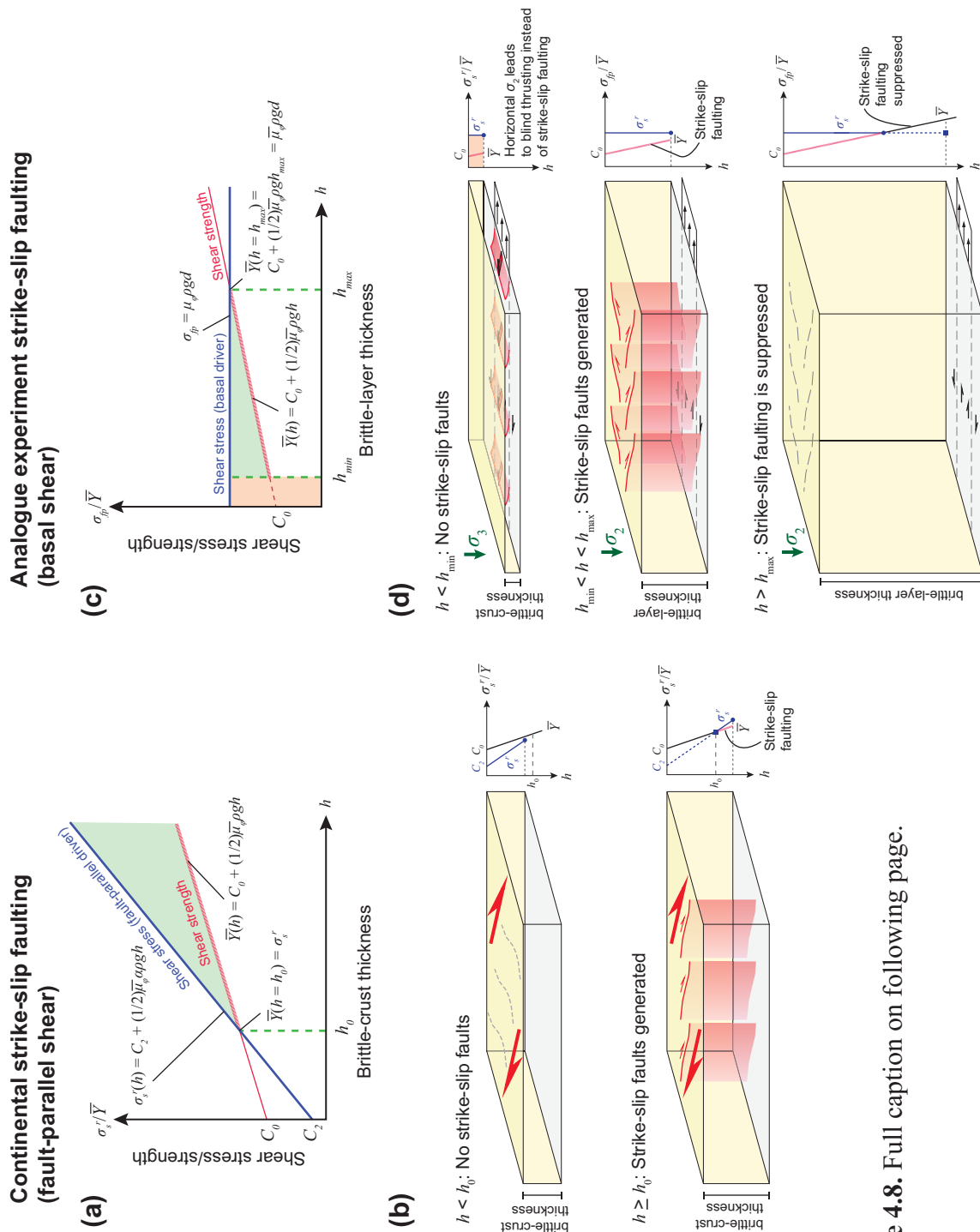


**Figure 4.8.** Full caption on following page.

**Figure 4.8 (continued).** (a) Conceptual plot of dimensionless shear stress/strength versus brittle-crust thickness showing the inferred minimum brittle-crust thickness ( $h_0$ ) cutoff for the formation of continental strike-slip faults. Strike-slip faults will only be generated when the regional shear stress  $\sigma_s^r$ , which is linearly proportional to  $h$ , exceeds the vertically integrated shear-fracture strength of the material ( $\bar{Y}$ ) at a critical brittle-crust thickness  $h_0$ . (b) Two scenarios for the continental strike-slip faulting that highlight the concepts in (a). When the brittle-crust is too thin ( $h < h_0$ ), the regional shear stress is not large enough to surpass the vertically averaged shear-fracture strength of the crust, and no strike-slip faults are formed. When the brittle-crust thickness is greater than the cutoff thickness, strike-slip faulting can occur. (c) Conceptual plot of dimensionless shear stress/strength versus brittle-crust thickness showing the minimum ( $h_{min}$ ) and maximum ( $h_{max}$ ) brittle-layer thickness cutoffs for strike-slip faulting in the analogue experiments. The depth-independent fault-parallel shear stress ( $\sigma_{fp}$ ) intersects the depth-dependent shear-fracture strength ( $\bar{Y}$ ) curve at a critical thickness  $h_{max}$ . Above this thickness value, strike-slip faulting is suppressed by the strength of the material. Below some threshold thickness  $h_{min}$ , strike-slip faults are also not formed. (d) Three scenarios for strike-slip faulting in the analogue experiments. When  $h$  is too low, there is a switch of the principal stress directions, from  $\sigma_2$  being vertical for the strike-slip regime when  $h > h_{min}$  to  $\sigma_2$  being horizontal for dip-slip fault regime when  $h < h_{min}$ , which results in blind thrusting and folding rather than strike-slip faulting. Additionally, when the brittle layer is too thick ( $h > h_{max}$ ), the vertically averaged shear strength ( $\bar{Y}$ ) of the brittle layer is greater than  $\sigma_{fp}$ , which suppresses strike-slip faulting. Strike-slip faulting does occur when  $h_{min} < h < h_{max}$ . Note that the green arrows indicates the principal stress orientation.

**Table 4.1. Physical and mechanical properties of experimental materials.**

| <b>Material</b>            | <b>Density<br/>(kg/m<sup>3</sup>)</b> | <b>Grain<br/>size (μm)</b> | <b>± σ</b> | <b>C<sub>0</sub> (Pa)</b> | <b>± σ</b> | <b>μ<sub>φ</sub></b> | <b>± σ</b> | <b>φ (°)</b> |
|----------------------------|---------------------------------------|----------------------------|------------|---------------------------|------------|----------------------|------------|--------------|
| Sand                       | 1670                                  | 220                        | 86         | 62.5                      | 10.5       | 0.50                 | 0.01       | 26.5         |
| Sand vs sandpaper          | -                                     | -                          | -          | 51.5                      | 40.5       | 0.53                 | 0.03       | 28.1         |
| Sand vs putty/sand         | -                                     | -                          | -          | -                         | -          | 0.73                 | 0.05       | 36.1         |
| Crushed walnut shells      | 790                                   | 332                        | 82         | 36.8                      | 10.2       | 0.40                 | 0.01       | 21.6         |
| Walnut shells vs sandpaper | -                                     | -                          | -          | 31.0                      | 29.0       | 0.51                 | 0.04       | 27.1         |

μ<sub>φ</sub>, Coefficient of friction  
φ, Angle of friction

**Table 4.2. Observed fault spacing and seismogenic zone thickness.**

|  | <b>D95 thickness<br/>(km)</b> | <b>± σ</b> | <b>D90 thickness<br/>(km)</b> | <b>± σ</b> | <b>Fault spacing<br/>(km)</b> | <b>± σ</b> |
|--|-------------------------------|------------|-------------------------------|------------|-------------------------------|------------|
| <i>California</i>  |                               |            |                               |            |                               |            |
| Central California   | 14.4                          | 1.9        | 12.8                          | 1.7        | 33 [ref. 1]                   | 3          |
| Western Southern California  | 15.7                          | 1.1        | 14.3                          | 1.2        | 47 [ref. 2]                   | 15         |
| Mojave   | 11.9                          | 1.1        | 10.9                          | 1.3        | 16 [ref. 3]                   | 2          |
| Eastern Transverse Range   | 12.1                          | 1.5        | 11.0                          | 1.2        | 20 [ref. 2]                   | 8          |
| <u>Best-fit linear regression of brittle-crust thickness vs. fault spacing for California</u>              |                               |            |                               |            |                               |            |
| <b>D95:</b> $S = 7.2 (\pm 1.5)L - 70.0 (\pm 18.8)$ <b>D90:</b> $S = 9.5 (\pm 1.9)L - 87.5 (\pm 22.5)$      |                               |            |                               |            |                               |            |
| <i>Asia</i>  |                               |            |                               |            |                               |            |
| Central Asia   | 26.0                          | 4.0        | 19.0                          | 2.6        | 407 [ref. 4]                  | 99         |
| Northern Tibet   | 14.5                          | 0.7        | 13.5                          | 2.1        | 178 [ref. 5]                  | 53         |
| Central Tibet  | 10.7                          | 0.8        | 9.7                           | 0.6        | 92 [ref. 6]                   | 24         |
| Iran   | 13.5                          | 2.1        | 12.5                          | 2.1        | 139 [ref. 7]                  | 50         |
| <u>Best-fit linear regression of brittle-crust thickness vs. fault spacing for Asia</u>                    |                               |            |                               |            |                               |            |
| <b>D95:</b> $S = 20.6 (\pm 6.2)L - 129.5 (\pm 78.9)$ <b>D90:</b> $S = 28.7 (\pm 8.9)L - 192.6 (\pm 100.5)$ |                               |            |                               |            |                               |            |

Sources: [ref. 1]: Savage and Lisowski (1993); [ref. 2]: Dickinson (1996); [ref. 3]: Dokka and Travis (1990); [ref. 4]: Yin (2010); [ref. 5]: Taylor and Yin (2009); [ref. 6]: Yin and Taylor (2011) [ref. 7]: Bachmanov et al., (2004).

#### 4.8. References

- Aydin, A., and Johnson, A. M., 1978, Development of faults as zones of deformation bands and as slip surfaces in sandstone: *Pure and Applied Geophysics*, v. 116, p. 931-942.
- Bird, P., and Kong, X., 1994, Computer simulations of California tectonics confirm very low strength of major faults: *Geological Society of America Bulletin*, v. 106, no. 2, p. 159-174.
- Burtman, V. S., and Molnar, P., 1993, Geological and geophysical evidence for deep subduction of continental crust beneath the Pamir: *Special Publication of the Geological Society of America*, v. 291, p. 1-76.
- Chu, R., Zhu, L., and Helmberger, D. V., 2009, Determination of earthquake focal depths and source time functions in central Asia using teleseismic P waveforms: *Geophysical Research Letters*, v. 36, no. 17.
- Collettini, C., Niemeijer, A., Viti, C., and Marone, C., 2009, Fault zone fabric and fault weakness: *Nature*, v. 462, no. 7275, p. 907-910.
- Console, R., Carluccio, R., Papadimitriou, E., and Karakostas, V., 2015, Synthetic earthquake catalogs simulating seismic activity in the Corinth Gulf, Greece, fault system: *Journal of Geophysical Research: Solid Earth*, v. 120, no. 1, p. 326-343.
- Cruz, L., Teyssier, C., Perg, L., Take, A., and Fayon, A., 2008, Deformation, exhumation, and topography of experimental doubly-vergent orogenic wedges subjected to asymmetric erosion: *Journal of Structural Geology*, v. 30, no. 1, p. 98-115.
- Davy, P., and Cobbold, P. R., 1988, Indentation tectonics in nature and experiment. 1. Experiments scaled for gravity: *Bulletin of the Geological Institutions of Uppsala*, v. 14, p. 129-141.
- Dickinson, W. R., 1981, Plate tectonic evolution of the southern Cordillera. Relations of tectonics to ore deposits in the southern Cordillera: *Arizona Geological Society Digest*, v. 14, p. 113-135.
- Dickinson, W. R., 1996, Kinematics of transrotational tectonism in the California Transverse Ranges and its contribution to cumulative slip along the San Andreas transform fault system: *Geological Society of America Special Paper*, v. 305, p. 1-46.
- Dokka, R. K., 1989, The Mojave extensional belt of southern California: *Tectonics*, v. 8, no. 2, p. 363-390.
- Dokka, R. K. and Travis, C. J., 1990, Late Cenozoic strike-slip faulting in the Mojave desert, California: *Tectonics*, v. 9, p. 311-340.
- Fay, N., and Humphreys, E., 2006, Dynamics of the Salton block: Absolute fault strength and crust-mantle coupling in Southern California: *Geology*, v. 34, no. 4, p. 261-264.

- Fossen, H., Schultz, R. A., Shipton, Z. K., and Mair, K., 2007, Deformation bands in sandstone: a review: *Journal of the Geological Society*, v. 164, no. 4, p. 755-769.
- Freund, R., 1974, Kinematics of transform and transcurrent faults: *Tectonophysics*, v. 21, no. 1, p. 93-134.
- Hauksson, E., Yang, W., and Shearer, P. M., 2012, Waveform relocated earthquake catalog for southern California (1981 to June 2011): *Bulletin of the Seismological Society of America*, v. 102, no. 5, p. 2239-2244.
- He, J., and Chéry, J., 2008, Slip rates of the Altyn Tagh, Kunlun and Karakorum faults (Tibet) from 3D mechanical modeling: *Earth and Planetary Science Letters*, v. 274, no. 1, p. 50-58.
- Hubbert, M. K., 1937, Theory of scale models as applied to the study of geologic structures: *Geological Society of America Bulletin*, v. 48, no. 10, p. 1459-1520.
- Hubbert, M. K., 1951, Mechanical basis for certain familiar geologic structures: *Geological Society of America Bulletin*, v. 62, no. 4, p. 355-372.
- Humphreys, E. D., and Coblenz, D. D., 2007, North American dynamics and western US tectonics: *Reviews of Geophysics*, v. 45, no. 3.
- Jackson, J., McKenzie, D., Priestley, K., and Emmerson, B., 2008, New views on the structure and rheology of the lithosphere: *Journal of the Geological Society*, v. 165, no. 2, p. 453-465.
- Jaeger, J. C., Cook, N. G., and Zimmerman, R., 2009, *Fundamentals of rock mechanics*: John Wiley & Sons.
- Lachenbruch, A. H., 1961, Depth and spacing of tension cracks: *Journal of Geophysical Research*, v. 66, no. 12, p. 4273-4292.
- Lin, G., Shearer, P. M., and Hauksson, E., 2007, Applying a three-dimensional velocity model, waveform cross correlation, and cluster analysis to locate southern California seismicity from 1981 to 2005: *Journal of Geophysical Research: Solid Earth*, v. 112, no. B12.
- Lister, G. S., and Davis, G. A., 1989, f: *Journal of Structural Geology*, v. 11, no. 1, p. 65-94.
- Maggi, A., Jackson, J. A., Priestley, K., and Baker, C. A., 2000, A reassessment of focal depth distributions in southern Iran, the Tien Shan and northern India: do earthquakes really occur in the continental mantle?: *Geophysical Journal International*, v. 143, p. 629-661.
- Martel, S. J., and Pollard, D. D., 1989, Mechanics of slip and fracture along small faults and simple strike-slip fault zones in granitic rock: *Journal of Geophysical Research: Solid Earth*, v. 94, no. B7, p. 9417-9428.

- Molnar, P., and Tapponnier, P., 1975, Cenozoic tectonics of Asia: effects of a continental collision: *Science*, v. 189, no. 4201, p. 419-426.
- Naylor, M. A., Mandl, G. T., and Supesteijn, C. H. K., 1986, Fault geometries in basement-induced wrench faulting under different initial stress states: *Journal of Structural Geology*, v. 8, no. 7, p. 737-752.
- Nur, A., Ron, H., and Scotti, O., 1986, Fault mechanics and the kinematics of block rotations: *Geology*, v. 14, no. 9, p. 746-749.
- Pollard, D. D., and Segall, P., 1987, Theoretical displacements and stresses near fractures in rock: with applications to faults, joints, veins, dikes, and solution surfaces: *Fracture mechanics of rock*, v. 277, no. 349, p. 277-349.
- Roy, M., and Royden, L. H., 2000a, Crustal rheology and faulting at strike-slip plate boundaries: 1. An analytic model: *Journal of Geophysical Research: Solid Earth*, v. 105, no. B3, p. 5583-5597.
- Roy, M., and Royden, L. H., 2000b, Crustal rheology and faulting at strike-slip plate boundaries: 2. Effects of lower crustal flow: *Journal of Geophysical Research: Solid Earth*, v. 105, no. B3, p. 5599-5613.
- Savage, J. C., and Lisowski, M., 1993, Inferred depth of creep on the Hayward fault, central California: *Journal of Geophysical Research: Solid Earth*, v. 98, no. B1, p. 787-793.
- Schaff, D. P., and Waldhauser, F., 2005, Waveform cross-correlation-based differential travel-time measurements at the Northern California Seismic Network: *Bulletin of the Seismological Society of America*, v. 95, no. 6, p. 2446-2461.
- Segall, P., and Pollard, D. D., 1983, Nucleation and growth of strike slip faults in granite: *Journal of Geophysical Research: Solid Earth*, v. 88, no. B1, p. 555-568.
- Sengör, A. M. C., Natal'in, B. A., and Burtman, V. S., 1993, Evolution of the Altiid tectonic collage and Palaeozoic crustal growth in Eurasia: *Nature*, v. 364, p. 299-307.
- Sibson, R. H., 1982, Fault zone models, heat flow, and the depth distribution of earthquakes in the continental crust of the United States: *Bulletin of the Seismological Society of America*, v. 72, no. 1, p. 151-163.
- Sloan, R. A., Jackson, J. A., McKenzie, D., and Priestley, K., 2011, Earthquake depth distributions in central Asia, and their relations with lithosphere thickness, shortening and extension: *Geophysical Journal International*, v. 185, no. 1, p. 1-29.
- Swanson, M. T., 1988, Pseudotachylite-bearing strike-slip duplex structures in the Fort Foster Brittle Zone, S. Maine: *Journal of Structural Geology*, v. 10, no. 8, p. 813-828.

- Taylor, M., and Yin, A., 2009, Active structures of the Himalayan-Tibetan orogen and their relationships to earthquake distribution, contemporary strain field, and Cenozoic volcanism: *Geosphere*, v. 5, no. 3, p. 199-214.
- Tchalenko, J. S., 1970, Similarities between shear zones of different magnitudes: *Geological Society of America Bulletin*, v. 81, no. 6, 1625-1640.
- Tenthorey, E., and Cox, S. F., 2006, Cohesive strengthening of fault zones during the interseismic period: An experimental study: *Journal of Geophysical Research: Solid Earth*, v. 111, no. B9.
- Vernant, P., and Chery, J., 2006, Low fault friction in Iran implies localized deformation for the Arabia–Eurasia collision zone: *Earth and Planetary Science Letters*, v. 246, no. 3, p. 197-206.
- Waldhauser, F., and Schaff, D. P., 2008, Large-scale relocation of two decades of Northern California seismicity using cross-correlation and double-difference methods: *Journal of Geophysical Research: Solid Earth*, v. 113, no. B8.
- Wang, J., Dapeng, Z. and Yao, Z., 2013, Crustal and uppermost mantle structure and seismotectonics of North China Craton: *Tectonophysics*, v. 582, p. 177-187.
- Yin, A., 2010, Cenozoic tectonic evolution of Asia: A preliminary synthesis: *Tectonophysics*, v. 488, no. 1, p. 293-325.
- Yin, A., and Taylor, M. H., 2011, Mechanics of V-shaped conjugate strike-slip faults and the corresponding continuum mode of continental deformation: *Geological Society of America Bulletin*, v. 123, no. 9-10, p. 1798-1821.
- Yin, A., Yu, X., Shen, Z. K., and Liu-Zeng, J., 2015, A possible seismic gap and high earthquake hazard in the North China Basin: *Geology*, v. 43, no. 1, p. 19-22.
- Yin, A., Zuza, A. V., and Pappalardo, R. T., 2016, Mechanics of evenly spaced strike-slip faults and its implications for the formation of tiger-stripe fractures on Saturn's moon Enceladus: *Icarus*, v. 266, p. 204-216.



**-Chapter 5-**

**Pre-Mesozoic tectonic evolution of the Qilian Shan**

## 5.1. Abstract

The Qilian Shan of northern Tibet exposes a record of the early Paleozoic convergence and collision between the Kunlun-Qaidam continent and North China craton. In the central Qilian Shan ophiolite complexes, passive continental margin sequences, and strongly deformed forearc strata are juxtaposed against arc plutonic/volcanic rocks and ductilely deformed basement rocks as a result of the early Paleozoic Qilian orogen. To better constrain the evolution of the Qilian orogen and the resulting closure of the Qilian Ocean, I conducted an integrated investigation involving detailed geologic mapping across the central Qilian Shan, U-Th-Pb zircon and monazite geochronology, whole-rock geochemistry of igneous rocks, thermobarometry of the metamorphosed basement rocks, and synthesis of existing datasets across northern Tibet. The central Qilian Shan experienced two phases of arc magmatism at ~960-870 Ma and ~475-445 Ma that were each immediately followed by periods of continental collision. Given the magmatic, metamorphic, and regional geologic history, I propose the following tectonic model for the Proterozoic through Paleozoic history of northern Tibet. (1) Early Neoproterozoic subduction accommodates the convergence and collision between the South Tarim-Qaidam and North Tarim-North China continents. (2) Late Neoproterozoic rifting partially separates a peninsular Qaidam continent from the southern margin of the Tarim-North China craton and opens the Qilian Ocean as an embayed marginal sea; this separation broadly follows the trace of the early Neoproterozoic suture zone. (3) South-dipping subduction along the northern margin of the Kunlun-Qaidam continent initiates in the Cambrian, first developing as the Yushigou supra-subduction zone (SSZ) ophiolite (which links along strike with the Aoyougou and Dongcaohe SSZ ophiolites) and then transitioning into the continental Qilian arc. (4) South-dipping subduction, arc magmatism, and the convergence between Qaidam and North

China continued throughout the Ordovician, with a trench-parallel intra-arc strike-slip fault system that is presently represented by the high-grade metamorphic rocks that display a pervasive right-lateral shear sense. (5) The closure of the Qilian Ocean occurred following the counter-clockwise rotation of the peninsular Qaidam continent toward North China, which is supported by the right-lateral kinematics of the intra-arc strike-slip fault and the westward tapering map-view geometry of Silurian flysch-basin strata. Continental collision at ~445-440 Ma leads to widespread plutonism across the Qilian Shan and is recorded as the youngest population of monazite ages observed in this study (~450-420 Ma). This tectonic model implies the parallel closure of two oceans along the trace of Qilian suture zone since ~1.0 Ga. In addition, the Qilian Ocean was not the Proto- or Paleo-Tethys (i.e., the earliest through-going ocean separating Gondwana from Laurasia) as suggested by earlier studies, but rather represented a smaller marginal sea along the southern margin of the Laurasian continent. Lastly, Cenozoic deformation that results from India-Asia convergence is focused along these sites of repeated ocean closure. The major Cenozoic left-slip faults parallel these sutures, and Cenozoic shortening and continental underthrusting may have been assisted by the preexisting arc-subduction-mélange channels.

## **5.2. Introduction**

The Paleo-Asian and Tethyan oceanic domains are separated by the so-called “Intermediate Units” of Şengör and Natal’in (1996), which consist of the Tarim and North China cratons in northern Tibet (Fig. 5.1). The tectonic evolution of the southern and northern margins of these cratons is key to the accretionary history of the Eurasian continent (Şengör and Natal’in, 1996; Heubeck, 2001). The Tian Shan-Yin Shan and Solonker-Jilin-Yanji suture zones (Fig.

5.1), along the north of Tarim and North China, record the closure of the Paleo-Asian Ocean at the end of the Paleozoic (e.g., Xiao et al., 2003, 2004; Charvet et al., 2007; Windley et al., 2007). It is traditionally believed that the southern margin of the Intermediate Units experienced two distinct periods of ocean closure: (1) the early Paleozoic closure of the Qilian Ocean along the Qilian-Qinling suture zone and (2) the late Paleozoic-Mesozoic closure of the Paleo-Tethys (or the Neo-Kunlun Ocean of Wu et al., 2016) along the Kunlun-Dabie suture zone (Fig. 5.1B) (e.g., Yin and Nie, 1993; Yin et al., 2007a; Xiao et al., 2009; Song et al., 2013, 2014; cf. Wu et al., 2016). However, the Proterozoic and Paleozoic tectonic history of this southern margin is particularly enigmatic because in addition to ocean-closure-related arc-continent and continent-continent collisional events, the region was modified by later deformation including Mesozoic extension and Cenozoic intracontinental deformation (Yin and Harrison, 2000; Chen et al., 2003; Cowgill et al., 2003; Yin, 2010). Specifically, whether the Qilian Ocean is the oldest oceanic domain separating Gondwana from Laurasia (i.e., the Proto- or Paleo-Tethys; e.g., Hou et al., 2006; Gehrels et al., 2011; Stampfli et al., 2013) or an embayed marginal sea along southern Laurasia (Guo et al., 2005; Zuza and Yin, 2014) depends on how and when the ocean was opened and closed.

The Cenozoic Qilian Shan-Nan Shan and North Qaidam thrust belts (see Chapter 2) (Fig. 5.2) presently expose the Qilian suture(s), Qilian orogen, the southern margin of the North China craton, and the northern Kunlun-Qaidam microcontinent (Fig. 5.1B). The abundance of ophiolite-bearing *mélange* and blueschist assemblages in the Qilian Shan led early workers to suggest that this region represents the site of the closed Qilian Ocean (Wang and Liu, 1976; Xiao et al., 1978). More recent research has shown that this ocean opened in the Neoproterozoic and closed during the early Paleozoic Qilian orogen (e.g., Yin and Harrison, 2000; Gehrels et al.,

2003a, 2003b, 2011; Yin et al., 2007a; Xiao et al., 2009; Song et al., 2013, 2014; Wu et al., 2016). The timing, subduction polarity, and nature of the Qilian arc and Qilian orogen, which accommodated the closure of the Qilian Ocean, remain poorly constrained.

In this chapter I provide new insights into the tectonic evolution of the Qilian Ocean, Qilian orogen, and southern margin of the North China craton, which impacts reconstructions of Neoproterozoic and Paleozoic Earth (e.g., Heubeck, 2001; Stampfli and Borel, 2002; Li et al., 2008; Wu et al., 2016). I conducted an integrated investigation of the central Qilian Shan that involved detailed geologic mapping, U-Th-Pb zircon and monazite geochronology, whole-rock geochemistry, thermobarometry, and synthesis of existing datasets across northern Tibet. This research leads to a new reconstruction of the Proterozoic-Paleozoic development of northern Tibet that involves the parallel closure of two oceans along the Qilian suture zone since ~1.0 Ga.

### **5.3. Deformation history of northern Tibet**

The early Paleozoic Qilian orogen is comprised, generally from north to south, of the mélange-ophiolite complex of the Qilian suture(s), the Ordovician-Silurian arc belt, and the intra-arc North Qaidam ultra-high pressure (UHP) metamorphic belt (Yin and Harrison, 2000; Yin et al., 2007a; Menold et al., 2009; Song et al., 2013, 2014) (Figs 5.1B and 5.2). The original configuration of the combined Qilian orogen and North Qaidam UHP metamorphic belt has been modified by Mesozoic extension and Cenozoic intracontinental deformation associated with the India-Asia collision (Vincent and Allen, 1999; Yin and Harrison, 2000; Chen et al., 2003; Gehrels et al., 2003a, 2003b), yet existing models of the Qilian orogen rarely consider the effects of this later deformation (e.g., Mattinson et al., 2007; Xiao et al., 2009; Song et al., 2013, 2014;

cf. Yin et al., 2007a). Below I briefly outline the important Phanerozoic tectonic events that affected northern Tibet.

### **5.3.1. Cenozoic deformation**

As discussed in Chapters 2 and 3, the eastward-tapering Cenozoic Qilian Shan-Nan Shan thrust belt defines the northeastern margin of the Tibetan Plateau (Fig. 5.2). The thrust belt links with the left-slip Haiyuan fault to the east and is bounded to the west by the left-slip Altyn Tagh fault (Fig. 5.2) (Burchfiel et al., 1989; Meyer et al., 1998). The thrust belt is thick skinned and most thrusts are northeast-dipping, with the exception of the southwest-dipping North Qilian Shan frontal thrust system. Cenozoic shortening juxtaposes Precambrian-Paleozoic basement rocks against late Paleozoic through Cenozoic strata (Meyer et al., 1998; Wang and Burchfiel, 2004; Yin et al., 2007a; Zheng et al., 2010). As a result, restoration of this deformation is required to observe the pre-Cenozoic regional configuration.

Cenozoic shortening across the Qaidam Basin, North Qaidam, and Qilian Shan-Nan Shan thrust belts is 250-350 km (Yin et al., 2007b, 2008a, 2008b; Zuza et al., 2016; Chapter 2). Because fault offset and slip rate along the Haiyuan fault is negligible (< 10 of km) at its western termination (Zuza and Yin, 2016; Chapter 3), east-west translation and modification of the Paleozoic structures is minimal. However, the left-slip Altyn Tagh fault truncates the surface traces of the Qilian orogen and suture (Fig. 5.2). Paleozoic UHP and suture zone rocks in the Altyn Tagh Range correlate with those in North Qaidam and the Qilian Shan, which indicates ~450 km of left-lateral offset on the Altyn Tagh fault (Sobel and Arnaud, 1999; Yang et al., 2001; Zhang et al., 2001).

### 5.3.2. Mesozoic extension

Mesozoic regional extension may have affected much of northern Tibet, including the Altyn Tagh Range, Qaidam Basin, Qilian Shan-Nan Shan, and Hexi Corridor, from southwest to northeast, respectively (Fig. 5.2) (Huo and Tan, 1995; Vincent and Allen, 1999; Chen et al., 2003; Yin et al., 2008a, 2008b). This extension is expressed by the development of extensive Jurassic and Cretaceous extensional and transtensional basins (Vincent and Allen, 1999; Chen et al., 2003; Yin et al., 2008a, 2008b). Because of the limited exposure of Mesozoic rocks and structures, the magnitude of this extension is unconstrained. However, early Paleozoic muscovite  $^{40}\text{Ar}/^{39}\text{Ar}$  ages from the footwall of Cretaceous normal faults indicate that magnitude of Cretaceous normal faulting was small ( $< \sim 10$  km) (Chen et al., 2003).

### 5.3.3. Paleozoic tectonics

The early Paleozoic Qilian orogen is the most dominant Paleozoic feature in the Qilian Shan, and it records the closure of the Qilian Ocean(s) as the Qaidam-Kunlun continent collided against the southern margin of the Tarim-North China cratons (Yin and Nie, 1996; Sengör and Natal'in, 1996; Sobel and Arnaud, 1999; Yin and Harrison, 2000; Gehrels et al., 2003a, 2003b; Yin et al., 2007a; Xiao et al., 2009; Song et al., 2013, 2014). The Qilian orogen is composed of flysch, arc-type assemblages, ophiolites, and low- to high-grade metamorphic rocks. Several important first-order problems regarding the development of the Qilian orogen remain unresolved (Fig. 5.3; Table 5.1). (1) How many arcs and what type of arcs (i.e., oceanic or continental) were involved in orogeny (e.g., Xiao et al., 2009; Yang et al., 2009, 2012; Song et al., 2013)? (2) Was the subduction polarity north- and/or south-dipping (e.g., Sobel and Arnaud, 1999; Yin and Harrison, 2000; Gehrels et al., 2003a, 2003b; Yin et al., 2007a; Xiao et al., 2009;

Yang et al., 2009, 2012; Yan et al., 2010; Gehrels et al., 2011; Song et al., 2013)? (3) When did collision occur (e.g., Liu et al., 2006; Qi, 2003; Tung et al., 2007; Lin et al., 2010)? Lastly, when was the final closure of the Qilian ocean (i.e., Devonian or Silurian) (e.g., Xiao et al., 2009; Yang et al., 2012)?

Despite these uncertainties, the following is known about the Qilian orogen. (1) An open ocean(s) existed from ~550 to 448 Ma as evidenced by the distribution of ophiolite fragments (Smith et al., 2006; Xiang et al., 2007; Tseng et al., 2007; Zhang et al., 2007; Xia and Song, 2010; Song et al., 2013). (2) Arc magmatism, subduction, and collision occurred from ~516 Ma to ~400 Ma as evidenced by the distribution of arc-related and syn-collisional plutons (Qian et al., 1998; Cowgill et al., 2003; Gehrels et al., 2003a; Su et al., 2004; Wu et al., 2004, 2006, 2010; Hu et al., 2005; Liu et al., 2006; Quan et al., 2006; He et al., 2007; Tseng et al., 2009; Dang et al., 2011; Xia et al., 2012; Xiao et al., 2012; Xiong et al., 2012; Song et al., 2013; Wu et al., 2016). (3) Geochronology ages for metamorphism across the Qilian Shan range from 489-684 Ma (U-Pb zircon rim ages from Song et al., 2006; Zhang et al., 2007) to 490-470 Ma (Th-Pb in-situ monazite ages from this study). Two distinct pulses of metamorphism are observed in the North Qaidam UHP rocks: the first from 490-460 Ma and the second from 440-420 Ma (Mattinson et al., 2006; Menold et al., 2009, 2016; Song et al., 2014). (4) Finally, high pressure blueschist is exposed in the northern Qilian Shan, and cooling ages range from 454-442 Ma ( $^{39}\text{Ar}/^{40}\text{Ar}$  white mica ages of Liu et al., 2006) to 415-413 Ma ( $^{39}\text{Ar}/^{40}\text{Ar}$  glaucophane ages of Lin et al., 2010).

In the central Qilian Shan, the boundary between the Qilian arc complex and the North China craton is expressed as a ductile right-slip shear zone in high-grade metamorphic rocks (Qi, 2003) juxtaposed against a low-grade metamorphosed mafic to ultramafic mélangé, Ordovician



forearc strata, and ophiolite complexes. Silurian flysch deposits in have been attributed to both a back-arc (Song et al., 2013) and fore-arc setting (Yan et al., 2007, 2010). Based on similar lithological assemblages, the Qilian orogen and suture(s) probably connect with the Qinling orogen to the southeast (e.g., Xu et al., 2008; Tseng et al., 2009; Dong et al., 2011; Wu et al., 2016), forming a >1000 km long early Paleozoic orogenic belt (Figs. 5.1 and 5.2).

#### **5.4. Regional geologic setting of the Qilian Shan**

The primary elements of the early Paleozoic Qilian orogen include, from north to south, the (1) southern margin of the North China craton, including Neoproterozoic passive margin strata along this margin, (2) the North Qilian suture, which is a belt of discontinuously exposed ophiolitic material that locally experienced blueschist-facies metamorphism, (3) the South Qilian suture, which is a belt of variably exposed ophiolite fragments that do not record high-grade metamorphism, (4) a wide zone of arc volcanic and plutonic rocks associated with the Qilian arc, which respectively overly and intrude amphibolite-grade metamorphic rocks, (5) the North Qaidam ultra-high pressure (UHP) metamorphic belt with associate ophiolite complex, and (6) the Kunlun-Qaidam Precambrian microcontinent (e.g., Yin et al., 2007a; Xiao et al., 2009; Song et al., 2013, 2014; Wu et al., 2016).

##### **5.4.1. Geology of the Qilian Shan**

The southern margin of the North China craton consists of Paleoproterozoic (~2.3-1.8 Ga) basement with a Mesoproterozoic cover sequence (Xiu et al., 2002; Tung et al., 2007; Gong et al., 2011; Wan et al., 2013). Some of the oldest intrusions have ~2.3 Ga magmatic zircon ages and ~2.85 zircon Hf model ages, which are similar to ages in the Kunlun-Qaidam continent and

thus the two continents may have shared a common Proterozoic history (Dan et al., 2012). The Neoproterozoic opening of the Paleo-Asian and Qilian Oceans along the northern and southern margins of the North China craton, respectively (Fig. 5.1), is evidenced by widespread passive margin sequences and ~825-600 Ma bimodal volcanic and intrusive rocks (Li et al., 2005; Tseng et al., 2006, 2007; Xu et al., 2015).

The discontinuously exposed North Qilian suture zone (Fig. 5.2) consists of ophiolite complexes, high-pressure metamorphic rocks including lawsonite-bearing eclogite, volcanic arc rocks, a westward-tapering Silurian flysch basin, and dispersed Devonian molasse (e.g., Pan et al., 2004; Song et al., 2007, 2013; Zhang et al., 2007; Xiao et al., 2009). The high-pressure blueschist rocks yield  $^{40}\text{Ar}/^{39}\text{Ar}$  cooling ages that range from 454-442 Ma (white mica ages of Liu et al., 2006) to 415-413 Ma (glaucofan ages of Lin et al., 2010). Ophiolite suites along this suture zone, which consist of gabbro, pillow basalt, diabase dikes, mafic rocks, and serpentized peridotite, are exposed at the Jiugequan, Biandukou, and Laohushan localities. Zircon ages from gabbroic rocks or diabase dikes range from ~510 to 470 Ma, numerous inherited zircon grains in a single sample (Xia and Song, 2010; Lin et al., 2010; Song et al., 2013). The significant zircon inheritance coupled with a depleted mantle geochemical signatures suggests that the ophiolites are supra-subduction zone (SSZ)-type ophiolites (e.g., Shervais, 2001; Wakabayashi et al., 2010; Xia et al., 2012).

The South Qilian suture zone (Fig. 5.2B) consists of suites of serpentinite, altered ultramafic rocks, gabbro, pillow basalt, and mélangé with marl and chert that are exposed at the Aoyougou, Yushigou, Dongcaohe, and Yongdeng localities, from northwest to southeast respectively (e.g., Yang et al., 2002; Shi et al., 2004; Tseng et al., 2007; Song et al., 2013). Magmatic zircons from gabbroic samples yield a range of ages from 550 to 490 Ma (Yang et al.,

2002; Shi et al., 2004; Tseng et al., 2007; Song et al., 2013). This zircon inheritance is further evidence that these ophiolites may be SSZ-type ophiolites. Note that the North and South Qilian sutures may not be separate suture zones that record separate ocean closure events. Both “belts” consist of sporadic outcrops of ophiolite fragments that are discontinuously exposed throughout the Qilian Shan (Yin and Harrison, 2000; Song et al., 2013) (Fig. 5.2B), and their exposure is directly controlled by Cenozoic thrusting. The surface traces of both suture zones are also truncated to the northwest against the left-slip Altyn Tagh fault (e.g., Sobel and Arnaud, 1999; Cowgill et al., 2003). The South Qilian suture appears to link to the southeast with the North Qinling suture zone (Fig. 5.2) (Yin and Nie, 1996; Tseng et al., 2009).

The Kunlun-Qaidam basement of the Qilian Shan varies from west to east. In the west, Mesoproterozoic cratonal and/or passive margin strata, intruded by ~960-900 Ma plutons (Gehrels et al., 2003a, 2003b; Wu et al., 2016; this study), are juxtaposed against an eclogite-bearing metamorphic complex with 775-930 Ma magmatic zircons (Tseng et al., 2006; Xue et al., 2009; Tung et al., 2007) and paragneiss with > 880 Ma detrital zircon grains (Tung et al., 2007). In the eastern Qilian Shan, Paleoproterozoic crystalline rocks are intruded by 1190–750 Ma plutons and overlain by a Neoproterozoic-Cambrian shelf sequence (Guo et al., 1999; Wan et al., 2001, 2003; Wang et al., 2007; Tung et al., 2007). Volcanic arc plutons with ages of 516-440 Ma are found throughout the Qilian Shan (Qian et al., 1998; Cowgill et al., 2003; Gehrels et al., 2003a; Su et al., 2004; Wu et al., 2004, 2006, 2010; Hu et al., 2005; Liu et al., 2006; Quan et al., 2006; He et al., 2007; Tseng et al., 2009; Dang et al., 2011; Xia et al., 2012; Xiao et al., 2012; Xiong et al., 2012; Tung et al., 2012; Song et al., 2013; Wu et al., 2016; this study). Silurian syn-collisional plutons are also dispersed throughout the Qilian Shan (e.g., the ~424 Ma Jinfosi pluton dated by Wu et al., 2010).

### 5.4.2. Geology of the North Qaidam metamorphic belt

The northwest-trending early Paleozoic North Qaidam metamorphic belt is located along the northeastern margin of Qaidam Basin (Fig. 5.2). The metamorphic rocks, which locally experienced ultra-high pressure (UHP) metamorphism, are exposed in the Lüliang Shan, Xitie Shan, and Dulan localities (Mattinson et al., 2007; Yin et al., 2007a; Menold et al., 2009, 2016; Song et al., 2014). This belt is truncated to the northwest by the Altyn Tagh fault, and is apparently offset ~450 km left-laterally to a position in the Altyn Tagh Range (Fig. 5.2). Metamorphic rocks at Jianggelesayi and Bashiwake of the Altyn Tagh Range are correlative to those in the North Qaidam UHP metamorphic belt (Mattinson et al., 2007; Zhang et al., 2001; Yang et al., 2001; Yin and Harrison, 2000). Both metamorphic belts consist of orthogneiss, paragneiss, and marble, with lenses of eclogite and ultramafic to mafic rocks.

Most of metamorphic rocks in North Qaidam, including the eclogite blocks and ophiolitic rocks, experienced (epidote-)amphibolite facies metamorphism (Menold et al., 2009). The eclogite-bearing rocks experienced UHP metamorphism followed by later amphibolite overprinting, but the ophiolite rocks do not show signs of metamorphism greater than epidote-amphibolite facies (Menold et al., 2009). Because the ophiolite and UHP rocks are tightly folded together and their contacts are often transposed, the two units were probably juxtaposed in the middle- to lower-crust (Yin et al., 2007a; Menold et al., 2009). It is important to note that that all of the pre-Devonian metamorphic rocks in the North Qaidam metamorphic belt are bounded by north-dipping Cenozoic thrust faults, and that the exposure of the epidote-amphibolite facies and UHP metamorphic rocks is controlled by Cenozoic deformation (Yin et al., 2007a). This fact is important for my tectonic model of the Qilian Shan (see section 5.10).

### 5.4.3. Tectonic models for the Qilian orogen

Numerous tectonic models have been proposed to account for the geologic observations described above. Although the work presented in this chapter is focused on the central Qilian Shan, any viable model must also account for the geologic history of the Altyn Tagh Range, Kunlun, Qaidam Basin, North Qaidam, and the North China craton (Figs. 5.1 and 5.2). This includes eclogite and ultra-high pressure (UHP) metamorphism of continental and oceanic material exposed in the Altyn Tagh Range and North Qaidam (Sobel and Arnaud, 1999; Zhang et al., 2005; Yin et al., 2007a; Menold et al., 2009; Song et al., 2014), early Paleozoic arc-related granitoids throughout northern Tibet, Cambrian-aged ophiolites including supra-subduction zone (SSZ) ophiolites (Song et al., 2013), ophiolitic mélangé dispersed throughout the Qilian Shan, and early Paleozoic blueschist and eclogite in the northern Qilian Shan and Altyn Tagh Range (e.g., Wu et al., 1993; Liu et al., 2006; Song et al., 2006, 2007; Zhang et al., 2007; Xiao et al., 2009).

The end-member models proposed for the Qilian arc and orogen (e.g., Mattinson et al., 2007; Yin et al., 2007a) primarily differ in the number of arcs involved, what the arc(s) was constructed upon (i.e., oceanic or continental crust), subduction polarity, timing of collision, and the processes responsible for UHP metamorphism and UHP rock exhumation (Fig. 5.3; Table 5.1). For example, a single south-dipping arc would require the arc plutons to intrude the Qaidam microcontinent to the south of the main Qilian suture and accretionary wedge (e.g., Sobel and Arnaud, 1999; Gehrels et al., 2003a, 2003b), whereas northward subduction would require the arc to develop north of the main suture within the North China craton (Song et al., 2006, 2013, 2014) (Fig. 5.3). The north-dipping-subduction model implies that the UHP metamorphic rocks were brought to UHP-depths at the subduction zone and were exhumed 100s of km to the south

through the Qaidam lithosphere (e.g., Song et al., 2006, 2014) (Fig. 5.3A). This model also cannot account for early Paleozoic magmatism within the Qaidam continent, south of the Qilian suture trace(s).

## **5.5. Geologic mapping of the central Qilian Shan**

Geologic mapping was conducted in the central Qilian Shan, near the town of Yanglong (~38.5°N, ~98.5°E) (Figs. 5.2), along the Shule, Tuo Lai, and Heihe Rivers. Details of this mapping, including a detailed lithostratigraphic column, are presented in Chapter 2. A simplified geologic map of the Tuo Lai Nan Shan and Tuo Lai Shan, focused on the tectonostratigraphic units, is given in Figures 5.5, whereas a regional-scale geologic map of the central Qilian Sha is provided in Figure 5.6. Full-size geologic maps are attached as a supplementary file (Supplementary Files 1 and 2).

### **5.5.1. Proterozoic and Paleozoic map units**

The important geologic relationships observed in the central Qilian Shan can be summarized in a simplified tectonostratigraphic column (Fig. 5.4). This column also integrates U-Pb zircon and Th-Pb monazite dating (see section 5.6), detrital zircon ages (Y. Zhang, C. Wu, A. Yin, L. Ding, and A. Zuza, unpublished data), whole-rock geochemistry data (see section 5.7), and thermobarometry analysis (see section 5.8). General stratigraphic age assignments are from Pan et al. (2004), Gansu Geological Bureau (1989), Qinghai BGMR (1991), Zhiyi and Dean (1996), our unpublished detrital zircon data, and my own observations.

The metamorphosed basement rocks consist of gneiss, schist, foliated amphibolite, quartzite, and local phyllite, marble, and slate. These rocks have been interpreted as a

Proterozoic passive margin sequence (Gehrels et al., 2003a, 2003b). The youngest age population from our detrital zircon analysis has a weighted mean age of  $\sim 1.27 \pm 0.05$  Ga (Fig. 5.4B), which supports a Mesoproterozoic age for the protolith. Foliated granitoid rocks also intrude the metamorphic unit. Foliations are all generally near vertical and northwest striking, and stretching lineations generally have a northwest trend and are subhorizontal (Fig. 5.5C). Kinematic indicators, including S-C fabric and mantled porphyroclasts (e.g.,  $\sigma$ - and  $\delta$ -clasts), suggest right-lateral shear of this entire unit (Figs. 5.6 and 6.7A-6.7C). Because the different metamorphic units (e.g., schist, amphibolite, and foliated granitoid) all have parallel foliations and stretching lineations (Fig. 5.5C), it is likely that the same deformational event affected the units together.

The dating of the foliated granitoid by zircon geochronology is discussed in section 5.6, and the interpreted crystallization ages range from 961 Ma to 868 Ma. This confirms that the schist and gneiss protoliths are older than Neoproterozoic in age, and requires that regional deformation affected all of these units after the intrusion of the youngest granitoid at  $\sim 860$  Ma.

The oldest sedimentary strata exposed in the central Qilian Shan consist of massive-bedded limestone and dolostone (mostly marble) interbedded with low-grade metamorphosed basalt and volcanoclastic layers (Fig. 5.4A). The carbonate rocks have a distinct massive blue/grey or orange appearance. The regional geologic map (Pan et al., 2004) give this unit a Changchengian age (i.e., Paleo- or Mesoproterozoic) on the basis of an older regional geologic survey (Gansu Geological Bureau, 1989). However, I assign a Neoproterozoic age based on recent geochronology studies on the widespread basalt that is interbedded with carbonate strata (Mao et al., 1998; Xia et al., 1999), including new 600-580 Ma ages for these basalts (Xu et al.,

2015). Compared to the higher-grade Mesoproterozoic gneiss and schist unit, the relatively low-grade deformation observed in these rocks corroborates a Neoproterozoic age.

An ophiolite complex known as the Yushigou ophiolite suite (Shi et al., 2004; Hou et al., 2006; Song et al., 2013) is exposed in the northern portion of the mapping area (Figs. 5.5 and 5.8). This complex is variably composed of mélangé and fragments of an incipient oceanic arc. The unit is strongly deformed and original lithologic contacts are highly sheared. There are ultramafic to mafic rocks, pillow basalts, and limestone and quartzite-sandstone knockers with chert. In addition, there are outcrops of massive plagioclase-pyroxene gabbro. The unit has been assigned a Cambrian age based on reported fossils (Xiao et al., 1978) and geochronology studies (Shi et al., 2004; Song et al., 2013). Cross-cutting diabase dikes yield U-Pb ages that span 550-500 Ma (discussed in section 5.6) (see also Song et al., 2013), and because of the prevalence of inherited zircon ages, I suggest that the Yushigou ophiolite may have formed in a supra-subduction zone (SSZ) setting (Shervais, 2001; Wakabayashi et al., 2010) (see section 5.6 for further discussion). Taken together, this unit represents part of the South Qilian suture (Fig. 5.2), which connects along strike with the Aoyougou ophiolite (Zhang et al., 2001; Xiang et al., 2007) to the northwest and the Dongcaohe ophiolite (Tseng et al., 2007) to the southeast.

Early Paleozoic rocks consist of deformed sandstone, siltstone, thinly-bedded limestone, and volcanoclastic rocks that are intruded by Ordovician arc plutons (Fig. 5.4A). The sedimentary strata are interpreted to represent forearc to foreland basin deposits (Xiao et al., 2009; Zhiyi and Dean, 1996). Both the basement rocks and early Paleozoic strata are intruded by early Paleozoic plutons. The dating of these bodies via U-Pb zircon geochronology is discussed in section 5.6, and their interpreted crystallization ages range from 474 Ma to 445 Ma. The oldest



plutons (~474 Ma) are foliated, with foliations parallel to the other metamorphosed rocks, whereas the younger granitoids (~450-455 Ma) are undeformed.

Taken together, the early Paleozoic and Proterozoic rocks represent the Qilian orogen. Following early Paleozoic orogeny, the Qilian basement rocks are unconformably overlain by post-orogenic cover sequences of parallel and conformable Carboniferous through Triassic strata (Fig. 5.4). The middle- to late-Paleozoic time represents a relatively quiescent time in northern Tibet, until subduction of the Paleo-Tethys and Paleo-Asian Oceans initiates to the south and north respectively (e.g., Wu et al., 2016; see Chapter 6).

### **5.5.2. Field relationships**

Detailed field relationships focused on the Cenozoic tectonic evolution of the mapping areas are described in Chapter 2. Here, I describe geologic features that are related to the Proterozoic and Paleozoic history of the Qilian Shan.

The Proterozoic basement unit has strongly developed foliations and stretching lineations. These fabrics are inferred to have developed in the early Paleozoic as a result of the Qilian arc and subsequent Qilian orogen. Foliations are defined by mica layering in the mica  $\pm$  garnet schist rocks, gneissic banding with relatively mafic (biotite and amphibole) and felsic (plagioclase and quartz) layers, plagioclase layering in foliated garnet amphibolite rocks, or weak-to-strong mineral alignment (mostly mica and/or amphibole grains) in the foliated granitoid rocks. Stretching lineations are observed within the foliation surface and stretched quartz or plagioclase is most evident in many outcrops.

Because this metamorphic unit has been affected by later deformation (e.g., Cenozoic folding and thrust faulting), it is possible that these foliation and lineation attitudes were

modified from their early Paleozoic configuration. For example, the near vertical foliations and subhorizontal lineations could have originally been part of a major early Paleozoic thrust fault with lineations that parallel the dip of the foliations. To constrain their original orientation, as in Chapter 2, I restore the foliation and lineation attitudes back to their pre-Carboniferous state by rotating the data so that Carboniferous strata are horizontal (Fig. 5.5C). The average foliation attitude and lineation plunge-trend observations from the corrected pre-Carboniferous datasets are 126/84°SW and 12/119, respectively (Fig. 5.5C). Mantled porphyroclasts (e.g.,  $\sigma$ - and  $\delta$ -clasts) and an S-C fabric indicate right-lateral shear (Figs. 5.7A-5.7C) across the entire central metamorphic unit (Fig. 5.6). This data suggests that the sheared basement rocks were part of an early Paleozoic right-slip strike-slip shear zone (Fig. 5.6).

The Cambrian ophiolite (i.e., fragments of the Yushigou ophiolite) and *mélange* units (Fig. 5.8) are only juxtaposed against the Neoproterozoic marble unit (Figs. 5.6 and 5.7), and where observed, the Neoproterozoic unit is always structural beneath the ophiolite suite. Although this tectonic contact may have been reactivated in the Cenozoic, this relationship suggests that the Neoproterozoic strata were originally thrust beneath the obducted ophiolite suite during the Qilian orogen.

Early Paleozoic slightly deformed to undeformed plutonic rocks are common throughout the mapping area (Fig. 5.5). Outcrops range in size from 10s to 1s of square kilometers. These granitoids, which range in composition alkali feldspar granite to quartz monzonite, intrude basement rocks and early Paleozoic strata. Furthermore, these plutons intrude the contact between the Ordovician and Proterozoic basement units (Fig. 5.5), which requires this contact to be pre-Ordovician. The plutons also intrude the northern schist unit in the Tuo Lai Shan (Fig. 5.5), which presently have no independent age constraints. This requires the schist to be similar

to the Proterozoic schist in the Tuo Lai Nan Shan (Fig. 5.5). It is important to note that the Ordovician plutons do not intrude Neoproterozoic rocks that are inferred to be part of North China's passive continental margin.

Carboniferous strata unconformably overly these plutonic rocks, Proterozoic rocks, and early Paleozoic strata (Fig. 5.5). This unconformity indicates that following the Qilian orogen, all of these rocks were at or near the surface, at least locally. I also use this unconformity surface as a marker horizon for cross-section restoration (see Chapter 2).

## **5.6. Geochronology**

### **5.6.1. U-Pb zircon geochronology**

#### **5.6.1.1. Methods**

Zircon grains were separated using standard crushing and density methods, including heavy liquid and magnetic separation, at UCLA and the Institute of Geomechanics, Chinese Academy of Geological Sciences (CAGS) in Beijing. Grains were mounted in 1" epoxy rounds along with zircon standards, and the mount was polished to 0.25  $\mu\text{m}$  and coated with  $\sim 100 \text{ \AA}$  of gold using a sputter-coater. Prior to analysis, zircon grains were observed by a cathodoluminescence (CL) detector on a JEOL SuperProbe scanning electron microscope (SEM) to document their internal structure and guide analysis locations (Fig. A.6).

U-Pb single shot analyses on zircon were acquired on two separate ion microprobe instruments, depending on the sample: analyses were performed either on the Sensitive High Resolution Ion Microprobe (SHRIMP) - II at the Beijing SHRIMP center, Institute of Geology, Chinese Academy of Geological Sciences (CAGS) in Beijing following the procedures of Williams (1998), or on a CAMECA IMS-270 secondary ion mass spectrometer (SIMS) at UCLA

using the analytical procedures of Quidelleur et al. (1997). Each instrument used different zircon standards. The interelement fractionation between U, Th, and Pb during analysis were corrected by using a linear calibration curve of  $^{206}\text{Pb}/\text{U}$  RSF (relative sensitivity factor) versus  $\text{UO}/\text{U}$  for the following zircon standards: TEM (zircon from the Middledale Gabbroic Diorite in eastern Australia:  $416.75 \pm 0.24\text{Ma}$ ; Black et al., 2003) and AS3 (zircon from the Duluth Complex:  $1099.1 \pm 0.5\text{ Ma}$ ; Paces and Miller, 1993; Schmitz et al., 2003) at CAGS and UCLA, respectively. The absolute concentrations of U, Th, and Pb were calibrated using the following zircon standards: SL 13 (Sri Lankan zircon:  $572.1 \pm 0.4\text{ Ma}$ ; Claoué-Long et al., 1995) and Harvard 91500 (i.e., a Canadian zircon:  $1065\text{ Ma}$ ; Wiedenbeck et al., 1995) at CAGS and UCLA, respectively. Analyses were made using an 8-15 nA O<sup>-</sup> primary beam focused to a spot of  $\sim 20\text{ }\mu\text{m}$  diameter. To enhance the secondary ionization of Pb<sup>+</sup> and increase the measured Pb isotope intensity, the sample chamber was flooded with oxygen at a pressure of  $\sim 3 \times 10^{-5}$  torr. The isotopic ratios were corrected for common Pb with a  $^{204}\text{Pb}$  correction from the model of Stacey and Kramers (1975). Data was reduced and processed via the in-house ZIPS 3.0.4 program developed by Chris Coath. Concordia plots and ages were obtained using Isoplot/Ex 4.15 (Ludwig, 2003).

The primary goal of U-Pb zircon analysis was to interpret a crystallization age of the igneous samples. To this end, I analyzed 15-25 grains from each sample (Fig. A.6) and examined the resulting age distribution of concordant analyses for each sample. If multiple age populations existed, the weighted mean age of the youngest population of zircon ages was interpreted as the crystallization age. Additional criteria for excluding specific analyses are given along with the full isotopic information in Table A.7. Most of the analyzed zircon grains are early Paleozoic in

age and I report their  $^{206}\text{Pb}/^{238}\text{U}$  ages. For samples that yield Neoproterozoic ages (i.e., 1000-541 Ma), their  $^{206}\text{Pb}/^{207}\text{Pb}$  ages are reported.

#### **5.6.1.2. Sample description and results**

Thirteen samples were analyzed, including six slightly deformed to undeformed samples from the early Paleozoic Qilian arc, two mafic dike samples from the ophiolite complex, one tonalitic dike sample that crosscuts Ordovician rocks, and four foliated granitoid samples from the metamorphic basement (Table 5.2). All of the samples were collected from the mapping area (Fig. 5.5B; Supplemental Fig. 2), with the exception of one that was collected from a large pluton ~300 km to the east of the mapping area (Table 5.2; Fig. 5.2).

Individual spot locations can be found in Figure A.6, and the detailed isotopic results can be found in Table A.7. Concordia diagrams showing the results of single shot zircon analyses and relative probability plots of the ages for each sample are shown in Figure 5.9. The interpreted crystallization age for the igneous samples is summarized in Table 5.2.

All of the undeformed and some of the deformed plutonic bodies exposed throughout the central Qilian Shan (e.g., Figs. 5.5 and 5.6) are inferred to be early Paleozoic in age (Pan et al., 2004). I dated six granitoid samples to constrain the timing of local magmatism (Table 5.2). Two samples were collected from a large undeformed alkali feldspar granite body in the Tuo Lai Nan Shan that intrudes the foliated Proterozoic gneiss (Fig. 5.5B; Supplemental Fig. 2). Sample AZ 07-17-13 (4) was collected on the southern flank of the range. Fifteen zircons were analyzed and U-Pb ages range from 314 Ma to 680 Ma (Fig. 5.9B). The weighted average of twelve concordant analyses is  $449 \pm 13$  Ma (MSWD = 0.99). The other analyses were excluded because of discordance or low radiogenic Pb. Sample RR 05-03-12 (6) was collected ~6.5 km northeast

of the previous sample. Twenty-five grains were analyzed, yielding ages that range from 451 Ma to 510 Ma (Fig. 5.9D). Twenty-two grains define the youngest age population and the weighted mean of these ages is  $457 \pm 2$  Ma (MSWD = 3.5). This same plutonic body was previously assigned a K-Ar age of  $345 \pm 17$  Ma in a regional 1:200,000 geologic map (Qinghai BGMR, 1991).

Sample AZ 04-30-12 (11) is from an undeformed syenogranite located along the northeastern bank of the Tuo Lai River in the Tuo Lai Shan (Fig. 5.5B; Supplemental Fig. 2). The pluton intrudes the Proterozoic metamorphic unit, including a strongly foliated granitoid, and is unconformably overlain by Carboniferous strata. Ordovician metasedimentary rocks are thrust over the pluton ~500 m to the northeast of the sample location. Twenty-five zircons were analyzed yielding twenty-two concordant ages that range from 441 Ma to 522 Ma (Fig. 5.9C). The four older grains are interpreted to be inherited and the weighted mean of the younger population of nineteen analyses is  $450 \pm 1$  Ma (MSWD = 0.92).

Sample AZ 05-04-12 (7) is part of a granite sill that intrudes the medium- to low-grade metamorphosed unit in the Tuo Lai Shan (Fig. 5.5B; Supplemental Fig. 2). Twenty-five grains were analyzed and all yielded concordant ages ranging 420 Ma to 511 Ma (Fig. 5.9E). Two ages are distinctly younger (~418 Ma), which may have resulted from Pb loss during a younger metamorphic event, and one population of ages is distinctly older, possibly due to older zircon-grain inheritance. The weighted mean of the average population of nineteen ages is  $474 \pm 3$  (MSWD = 3.4), which I interpret as the best estimate of a crystallization age. Sample RR 05-05-12 (5) is from a NE-SW oriented undeformed quartz monzonite dike (Fig. 5.5B; Supplemental Fig. 2) that crosscuts the foliations of a Proterozoic gneiss (Fig. 5.7F). I analyzed nineteen zircons; eighteen analyses gave concordant U-Pb ages that range from 435 Ma to 520 Ma (Fig.

5.9A). The oldest grains are interpreted to be inherited. The weighted mean of the youngest population ( $n = 17$ ) yields an age of  $445 \pm 3$  Ma (MSWD = 0.38), which is interpreted as the crystallization age of this granite dike.

Sample AZ 09-14-14 (8) was collected from a granite pluton located ~300 km to the east of the main mapping area (Fig. 5.2). The large pluton is exposed in a restraining bend of the left-slip Haiyuan fault. Nine grains were analyzed; one was normally discordant and one was reversely discordant (Fig. 5.9M). The remaining seven grains yield concordant ages that range from 438 Ma to 508 Ma. The weighted mean age of these concordant ages is  $462 \pm 14$  Ma (MSWD = 1.2).

Two medium-grained diabase bodies that intrude the internally deformed ophiolite complex were dated: AZ 05-06-12 (2) and AZ 05-03-12 (11). I analyzed twenty-five zircons from each sample. Sample AZ 05-06-2012 (2) yielded twenty five concordant ages that ranged from 511 Ma to 566 Ma (Fig. 5.9F). I interpret the weighted mean of youngest population of twenty analyses to best represent the crystallization age, which yields a mean age of  $521 \pm 2$  Ma (MSWD = 1.3). Analysis of zircon grains from sample AZ 05-03-2012 (11) yielded twenty concordant yet diverse ages, ranging from an U-Pb age of 501 Ma to a Pb-Pb age of ~1670 Ma (Fig. 11G), which suggests significant zircon inheritance. Several distinct age populations are observed. I excluded the oldest populations and take the weighted mean of the middle populations of ages ( $n = 15$ ) to represent the crystallization age of the diabase:  $541 \pm 6$  Ma (MSWD = 10.1). I interpret that the youngest set of ages is possibly the result of Pb loss as fluid infiltration and mineral modification may have occurred within the highly deformed and altered ophiolite complex. Alternatively, these young 511-501 Ma ages may reflect later pulsed intrusion or slow cooling.

The two previously discussed samples are part of Yushigou ophiolite suite (e.g., Hou et al., 2006; Song et al., 2013). Whole-rock geochemical analysis of pillow basalts in the Yushigou ophiolite complex indicates that they are tholeiitic (Hou et al., 2006; Song et al., 2013). Although I do not further constrain the petrogenesis of these intrusive rocks via geochemical analysis, the prevalence of inherited zircon ages in both samples suggests that these mafic intrusions are not related to mid-ocean ridge basalt (MORB) and do not represent oceanic lithosphere. Unpublished zircon ages from gabbro samples in this complex yield concordant ages ranging from 566 Ma to 530 Ma (Song et al., 2013), and similar inherited zircon ages are also observed in the Dongcaohe and Jiugequan ophiolite suites (Xia and Song, 2010; Xia et al., 2012; Song et al., 2013). In light of these observations, I suggest that the Yushigou ophiolite may have formed in a supra-subduction zone (SSZ) setting (Shervais, 2001; Wakabayashi et al., 2010) and these zircon ages may record the period of subduction initiation (e.g., Stern, 2004). Similar conclusions have been made regarding the Jiugequan ophiolite complex that is exposed ~25 km to the north (Xia and Song, 2010).

The high-grade metamorphic unit is intruded by several large foliated granitoid bodies (Fig. 5.5B). Granitoid foliations (Figs. 5.7A-5.7C), ranging from weakly foliated to mylonitized, are parallel to foliations of the high-grade gneiss, schist, and amphibolite rocks which they intrude (e.g., Fig. 5.5C). The original crystallization age of this plutonic body places an upper bound on the protolith age of the metamorphic unit. Two samples were collected from a mylonitized granitoid (quartz diorite to granodiorite) along the southern bank of the Tuo Lai River in the Tuo Lai Nan Shan: AZ 05-01-12 (1) and AY 09-21-11 (4) (Fig. 5.5B). The mylonitized granite has near-vertical NW-SE-striking foliations and subhorizontal stretching lineations, which are parallel to structures found throughout the Tuo Lai Nan Shan metamorphic



belt (Fig. 5.5). Mantled porphyroclasts (e.g.,  $\sigma$ - and  $\delta$ -clasts) and an S-C fabric indicate right-lateral shear (Figs. 5.7A-5.7C). Twenty-five zircons were analyzed from sample AZ 05-01-12 (1) and one was normally discordant (Fig. 5.9K). The remaining analyses yield Pb-Pb ages that range from 941 Ma to 1016 Ma, with a majority of the ages clustering at ~960 Ma. The weighted mean Pb-Pb age of twenty-four grains is  $961 \pm 12$  Ma (MSWD = 2.4). Seventeen grains were analyzed from sample AY 09-21-2011 (4), and all of the ages were concordant (Fig. 5.9I). Individual Pb-Pb zircon ages range from 884 Ma to 948 Ma, and the weighted mean age is  $905 \pm 7$  Ma (MSWD = 1.3). Across the Tuo Lai River, 3 km to the northeast, the basement granitoid is only weakly foliated (Fig. 5.5). Sample AZ 09-24-2013 (9) was collected from this weakly foliated granitoid (Fig. 5.5) and eight zircons were analyzed, yielding a range of Pb-Pb zircon ages from 891 Ma to 949 Ma (Fig. 11L). The weighted mean age of all of the analyses is  $921 \pm 10$  Ma (MSWD = 1.8).

A similar body of strongly foliated granitoid outcrops ~20 km to the east in the Tuo Lai Shan. Twenty-five zircons were analyzed from sample RR 05-04-2012 (2), which was collected from this unit (Fig. 5.5), yielding a wide range of ages (Fig. 5.9H). The youngest grain has a U-Pb age of  $655 \pm 6$  Ma and a distinctly low Th/U ratio (0.04) (Table 2.2), which may be related to multiple zircon growth episodes or Pb loss during a later metamorphic event. By excluding both this youngest age and the significantly older, presumably inherited ages (~1.2-1.0 Ga), I obtain a weighted mean Pb-Pb age from nineteen grains of  $868 \pm 16$  Ma (MSWD = 0.79). These ~850-950 Ma Neoproterozoic ages for the foliated granitoid rocks indicate that the protolith for the paragneiss and paraschist units must be older than ~0.85 Ga because the plutons intrude these metasedimentary rocks.

Sample AZ 04-30-2012 (4) is from an east-west-trending leucocratic tonalite dike that intrudes the Ordovician metasedimentary rock. Sixteen zircons were analyzed and only six provided concordant ages, ranging from ~1.9 Ga to ~0.9 Ga (Fig. 5.9J). Although no meaningful crystallization age can be determined, two concordant age clusters yield weighted Pb-Pb mean ages of  $1837 \pm 18$  Ma ( $n = 2$ ) and  $912 \pm 21$  Ma ( $n = 3$ ), which likely reflects inheritance of wall-rock zircons of the Proterozoic basement. Two best-fit discordia lines intercept concordia at ~0.9 Ga: the first discordia line has a lower-intercept age of  $916 \pm 70$  Ma and probably represents older inherited grains that fell off concordia as a result of Pb loss or metamorphic mineral overgrowth at ~0.9 Ga, whereas the second has an upper-intercept age of  $915 \pm 69$  Ma that may represent an original crystallization event at ~0.9 Ga grains with subsequent Pb loss that causes younger ages to fall off concordia (Fig. 5.9J). These observations are consistent with the dike intruding through Proterozoic basement rocks.

### **5.6.2. In-situ Th-Pb monazite geochronology**

To constrain the age of metamorphism, I conducted in-situ Th-Pb dating of monazite. Monazite grains appear in metasedimentary rocks near the garnet isograd (Smith and Barreiro, 1990). Monazite dating can be complicated by the fact that monazite is a relatively reactive phase that readily grows new age domains during progressive or repeated metamorphism (e.g., Foster et al., 2000; Catlos et al., 2002; Pyle and Spear, 2003; Pyle et al., 2005; Kohn et al., 2005; Rasmussen and Muhling, 2007; Bosse et al., 2009). In-situ dating allows for determination of the relationship between monazite grains and the tectonic fabric (Harrison et al., 1995), and when monazite grains are included in porphyroblasts (e.g., garnet or staurolite), they are shielded from Pb loss and/or dissolution during retrograde metamorphism (Montel et al., 2000; Kohn et al.,

2005; Gasser et al., 2012). Thus, the ages of included grains should represent the timing of peak metamorphism (Harrison et al., 1997) and matrix ages may or may not equal these ages (Catlos et al., 2002). Combination of the interpreted monazites ages with estimated pressure-temperature ( $P$ - $T$ ) conditions (e.g., Spear, 1993) allows for the metamorphic evolution of the rock to be constrained (i.e., the  $P$ - $T$ - $t$  path).

#### **5.6.2.1. Methods**

Monazite grains are too small (~5-50  $\mu\text{m}$ ) to be clearly identified on an optical microscope (e.g., Fig. 10). Doubly polished thin sections were examined first with a petrographic microscope to determine the metamorphic textures. Samples with synkinematic garnet growth were targeted because the age of a monazite included in garnet likely constrains the timing of when rock passed through the garnet isograd (Smith and Barreiro, 1990). Next, the thin sections were examined with a scanning electron microscope (SEM) in backscatter mode (Scherrer et al., 2000) (Fig. 5.10). Monazite grains were observed in the matrix and included in garnet. They appear brighter than most other phases in the thin sections. Grains included in garnet were very small (<15-20  $\mu\text{m}$  in diameter) whereas matrix grains were larger (50-15  $\mu\text{m}$  in diameter). Their identity was qualitatively confirmed with the energy-dispersive X-ray spectroscopy (EDX) on the SEM. Chosen monazite grains were photographed at 50 $\times$ , 100 $\times$ , and 250 $\times$ . The grains were relocated on a reflected-light microscope and photographed at 10 $\times$  and 20 $\times$  to aid identification on the microprobe optics.

The thin sections were cut and mounted in 1" epoxy rounds along with monazite standards, and the mount was polished to 0.25  $\mu\text{m}$  and coated with ~100  $\text{\AA}$  of gold using a sputter-coater. Grains were dated in-situ, following the procedure of Harrison et al. (1995, 1999)

and Catlos et al. (2002) on the CAMECA IMS-270 secondary ion mass spectrometer (SIMS) at UCLA. A 10-15 nA O<sup>-</sup> beam was focused to a diameter of 15-20 μm.

The interelement fractionation between U, Th, and Pb during analysis were corrected by using a linear calibration curve Pb/Th versus ThO<sub>2</sub>/Th for the monazite standards. Two monazite standards were used during two separate analytical sessions; the first session used monazite standard 44069 and the second used monazite standards 44069 and 554. Monazite standard 44069 is from the Wilmington Complex of the northeastern United States (Aleinikoff et al., 2006). The standard has a thermal ionization mass spectrometry (TIMS) age of  $424.9 \pm 0.4$  Ma and a sensitive high resolution ion microprobe (SHRIMP) age of  $426 \pm 3$  Ma (Aleinikoff et al., 2006). Monazite standard 554 is from a peraluminous granodiorite from Santa Catalina Mountains in Arizona (Force, 1997). The standard has a TIMS age of  $45.3 \pm 1.4$  Ma (measured by M. Tatsumoto, as cited in Harrison et al., 1999).

#### **5.6.2.2. Sample description and results**

Two garnet-mica schist samples were selected for in situ monazite geochronology: AY 09-21-11 (2) and AZ 04-18-12 (4) (see Fig. 5.5B for sample locations). Both samples are composed garnet, biotite, white mica, minor chlorite, quartz, and plagioclase with minor amounts of spinel, rutile, tourmaline, zircon, and monazite. The inclusion trail patterns in many of the garnet grains indicate synkinematic growth (Fig. 5.10). Observed matrix monazite grains are relatively large (50-15 μm in diameter) whereas grains included in garnet are very small (<15-20 μm in diameter). Many grains (~100) were identified and documented, but only twenty-three were analyzed, including six grains that were included in garnet and seventeen that were found in the matrix.

Isotopic data and monazite age results can be found in Table 5.3. Both samples yield similar and overlapping Th-Pb ages populations for both included-in-garnet and matrix monazites. Although the apparent Th-Pb monazite ages can be biased by varying Th content in the unknown analysis as compared to the standard-grain analyses (Stern and Berman, 2001), the ages show no correlation between Th or U concentrations. In addition, the U-Th-Pb systematics are concordant on a plot of  $^{208}\text{Pb}^*/^{206}\text{Pb}^*$  vs  $^{248}\text{ThO}/^{254}\text{UO}$  (plot not shown) (e.g., Harrison et al., 1995). All of the in-situ Th-Pb monazite ages range from 421 Ma to 772 Ma (Table 5.3). The oldest age analysis has very large uncertainties ( $772 \pm 131$  Ma), but this same sample yields a concordant U-Pb age of  $401 \pm 80$  Ma (Table 5.3). For this analysis only, I use the U-Pb age, and therefore the modified monazite-age range of the entire population is 421 Ma to 576 Ma (Fig. 5.11).

Monazite age populations from both the matrix and those included in garnet overlap within error (Fig. 5.11A). The weighted mean age of included and matrix monazite grains is  $498 \pm 19$  Ma (MSWD = 1.6) and  $477 \pm 5$  Ma (MSWD = 4.3), respectively. Because of their overlapping age populations, the weighted mean age of all analyses,  $479 \pm 9$  Ma (MSWD = 3.5) (Fig. 5.11A) may best represent the age of peak metamorphism. However, the high MSWD values suggests that either the analytical errors are too small or that the monazite ages are recording multiple age populations. Given that individual analysis uncertainties are ~5-10%, it is probable that the monazite analyses are recording multiple age populations.

Examination of normalized probability density plots of the monazite ages—divided into groups of included-in-garnet grains, matrix grains, and the total population (Fig. 5.11B)—reveals three distinct age populations. The lack of a correlation between age and Th or U concentrations suggests that these differences in apparent age are not due to monazite-grain composition

variation (e.g., Stern and Berman, 2001). Included-in-garnet grain ages are all older than ~455 Ma and they show two age peaks at ~475 Ma and ~535 Ma. The oldest age peak correlates with a subtle age population in the matrix monazite analyses that broadly spans ~550-530 Ma. The weighted mean age of all monazite-grain analyses in this population is  $538 \pm 20$  Ma (MSWD = 0.5) (Fig. 5.11B). These grains may represent the first generation of monazite growth, possibly associated with the initial subduction and arc activity within the Qilian arc. The youngest age population of the included-in-garnet monazite grains correlates to a similar age population in the matrix-monazite grains. This ~490-470 Ma signature is the largest age population of all of the analyses. The weighted mean age of this population is  $478 \pm 5$  Ma (MSWD = 1.3) (Fig. 5.11B). Because these monazite grains are included in garnet, they have been shielded from reactions with other phases, Pb loss, and overgrowth (e.g., DeWolf et al., 1993; Foster et al., 2000; Catlos et al., 2002). I interpret the  $478 \pm 5$  Ma age to best represent the age of peak prograde metamorphism and synkinematic garnet growth. Note that the  $478 \pm 5$  Ma age overlaps with the overall weighted mean age of all analyses,  $479 \pm 9$  Ma (MSWD = 3.5).

Lastly, there is a small population of younger ages from the matrix-monazite grains at ~440 Ma (Fig. 5.11B). The weighted mean age of this population is  $437 \pm 17$  Ma (MSWD = 0.34). These younger matrix-monazite ages may either represent late-stage monazite overgrowth or Pb loss during fluid infiltration. This age range coincides with arc magmatism, igneous intrusion, and/or the collision age of the Qilian orogen. An undeformed ~445 Ma dike crosscutting the foliation of the metamorphic complex (Figs. 5. 7F and 5.11) indicates that ductile shearing and prograde metamorphism was complete by this time, at least locally. This suggests that the youngest monazite age population (i.e., ~437 Ma) may not represent any prograde growth, but rather late-stage Pb loss or pluton intrusion and monazite overgrowth. Note

that this youngest age population overlaps within error with some of the youngest zircon ages (see section 5.6.1); for example, sample AZ 05-04-12 (7) has two zircons with a U-Pb age cluster of ~420 Ma.

## **5.7. Whole-rock geochemistry**

Major and trace element geochemistry were obtained from plutonic bodies, to determine their source and tectonic setting, and from metamorphic rocks for constrain their bulk composition for pseudosection analysis (see section 5.8). The geochemical composition of the metamorphic rocks also constrains their provenance and tectonic setting. Three samples were analyzed by Inductively Coupled Plasma-Optical Emission Spectrometry (ICP-OES) and Inductively Coupled Plasma-Mass Spectrometry (ICP-MS) at Activation Laboratories in Ontario, Canada, whereas the other samples were analyzed by X-ray fluorescence (XRF) at Pomona College.

### **5.7.1. Methods**

Samples were crushed and powdered to <75  $\mu\text{m}$  (i.e., 200 mesh) for bulk whole-rock geochemical analysis. Three plutonic samples [RR 05-03-2012 (6), AZ 04-30-2012 (11), and AZ 07-17-2013 (4)] were sent for analysis to Activation Laboratories Ltd. (Actlabs) in Ancaster, Ontario, Canada. Powders were dissolved via a lithium metaborate/tetraborate fusion technique. Major- and minor-element abundances and loss on ignition (LOI) values were measured by Inductively Coupled Plasma-Optical Emission Spectrometry (ICP-OES) with a detection limit of ~0.01%. ICP-OES was also used to analyze the trace elements Sc, Be, V, Sr, Y, Zr, and Ba at a detection limit of 1 to 5 ppm. Other trace elements were analyzed by Inductively Coupled

Plasma-Mass Spectrometry (ICP-MS) with a detection limit of 0.05 to 5 ppm for most elements, except for Cr, Ni, Cu, and Zn, which have detection limits of 10 to 30 ppm.

The remaining geochemical analyses were performed by X-ray fluorescence (XRF) at Pomona College following the methods of Johnson et al. (1999). Representative powdered samples and flux (i.e., dilithium tetraborate,  $\text{Li}_2\text{B}_4\text{O}_7$ ) were mixed at a 2:1 ratio, around 3.5 grams powder to 7.0 grams flux. The mixture was fused to a glass bead in a graphite crucible at 1000°C for 10 minutes, reground, and fused a second time. The bead was then polished on diamond laps, and analyzed. The Pomona Lab analyzes major and minor, and selected trace elements (V, Cr, Ni, Rb, Sr, Y, Zr, Nb, Ba, La, Ce, Nd, Cu, Pb, Zn, Th, U, Ga) on the same fused bead using a 3.0 kW Panalytical Axios WD-XRF equipped with PE, LiF 200, LiF 220, GE, and PX1 crystals. Concentrations are determined using reference calibration curves defined by fifty-five certified reference materials that span a range of natural igneous, metamorphic, and sedimentary rock compositions. Initial LOI values were determined during the first analysis for each sample.

Ideally, the summation of major- and trace-element oxide abundances and the LOI percent should be equal ~100%. The totals for all analyses range from 98.31% to 100.4% (Table 5.4), which suggests that these results are reliable. For sample comparison and classification, all measured major- and trace-element oxide abundances were normalized so that their sum equals 100% without including LOI values (not shown in Table 5.4). Trace element data presented in Table 5.4 has also been normalized.



### 5.7.2. Results and discussion

Discussion of the analyzed samples is divided among four groups of samples: the (1) plutonic rocks that are inferred to represent the early Paleozoic Qilian arc (i.e., RR 05-03-12 [6], AZ 04-30-12 [11], and AZ 07-17-13 [4]), (2) diabase dike and serpentinite samples (i.e., AZ 05-05-12 [7] and AZ 05-03-12 [13]), (3) ~0.9 Ga foliated granitoid samples (see section 5.6 for the geochronology), and (4) metamorphic samples (i.e., garnet amphibolite, garnet-mica schist, and gneiss rocks).

#### *Early Paleozoic granitoid samples*

Samples RR 05-03-12 (6), AZ 04-30-12 (11), and AZ 07-17-13 (4), collected from three separate undeformed granitoid bodies, are classified as alkali feldspar granite, granite (syenogranite), and alkali feldspar granite respectively, based on their normative quartz-alkali feldspar-plagioclase mineralogy (see Fig. 5.5B for sample locations). All of these samples are felsic ( $\text{SiO}_2$  63-75 wt%) and highly peraluminous ( $\text{Al}_2\text{O}_3/[\text{Na}_2\text{O} + \text{CaO} + \text{K}_2\text{O}] > 1.30$ ) (Table 5.4). Based on their weight percentage of silica and alkaline elements ( $\text{SiO}_2$  versus  $\text{Na}_2\text{O} + \text{K}_2\text{O}$ ), their classifications span quartz monzonite to granite (Table 5.4). The samples are all calc-alkaline (Fig. 5.12A). On the granite classification diagrams of Pearce (1984), samples plot mostly in the volcanic-arc field, with minor overlap on the syn-collisional and within-plate boundaries (Fig. 5.12B).

All three samples display steep rare earth element (REE) ( $\text{La}/\text{Yb} > 15$ ) patterns (Fig. 5.13), and sample AZ 07-17-13 (4) (i.e., the alkali feldspar granite) has the highest light REE enrichment ( $\text{La}/\text{Yb}$  42). This LREE enrichment suggests continental crustal melt source. Samples are characterized by negative Ba, Nb, P, and Ti anomalies, which is indicative of an

arc/subduction setting for the original melt. Two samples show weak negative Eu anomalies, indicating minor involvement of plagioclase in fractional melting, whereas sample AZ 04-30-12 (11) displays no Eu anomaly (Fig. 5.13). Taken together, the geochemical data indicate that the undeformed plutons in our field area are likely sourced from melted continental crust in a volcanic-arc setting.

#### *Diabase and serpentinite samples*

The diabase dike sample AZ 05-05-12 (7) is mafic (SiO<sub>2</sub> 48 wt% and MgO 8 wt%) and follows a subalkaline/tholeiitic trend (Na<sub>2</sub>O + K<sub>2</sub>O 2.1 wt %) (Table 5.4). More rigorous geochemical analysis of similar diabase and pillow basalt samples led Song et al. (2013) to suggest they were formed in a supra-subduction zone (SSZ) environment.

The serpentinite sample AZ 05-03-12 (13) has a high LOI content (15.2 wt%), and therefore only its normalized geochemistry is discussed (not shown in Table 5.4). The ultramafic rock (normalized SiO<sub>2</sub> 39 wt% and MgO 47 wt%) rock has a high Mg# value (i.e.,  $\text{MgO}/[\text{MgO} + \text{Fe}_2\text{O}_3] \times 100$ ) of 79 and contains very low TiO<sub>2</sub> (0.01 wt%) and alkalinity (Na<sub>2</sub>O + K<sub>2</sub>O values below the detection limit) (Table 5.4). The concentrations of Cr (4684 ppm) and Ni (2076 ppm) are very high. According to the classification scheme of Jensen (1976), this sample is an ultramafic komatiite (due to its high MgO values), whereas in the classification scheme of Winchester and Floyd (1977), it plots in the basanite/nephelinite field ( $\text{Nb}/\text{Y} > 2-3$  and  $\text{SiO} > 45$ ). Overall, the geochemistry of this serpentinite sample indicates that it represents altered ultramafic rock that is part of the Yushigou ophiolite complex.

### *Foliated granitoid samples*

The foliated granitoid samples are felsic ( $\text{SiO}_2 \sim 72 \text{ wt\%}$ ) and highly peraluminous ( $\text{Al}_2\text{O}_3/[\text{Na}_2\text{O} + \text{CaO} + \text{K}_2\text{O}] > 1.58$ ) (Table 5.4). The normative quartz-alkali feldspar-plagioclase mineralogy of samples AZ 07-21-13 (7) and AY 09-21-11 (3) classifies them as alkali feldspar granite and quartz diorite respectively. Based on their weight percentage of silica and alkaline elements ( $\text{SiO}_2$  versus  $\text{Na}_2\text{O} + \text{K}_2\text{O}$ ), they are classified as granite (Table 5.4). Both samples are calc-alkaline (Fig. 5.12A). On the classification diagrams of Pearce (1984), both samples plot in the volcanic-arc and joint volcanic arc-syn collisional granite fields (Fig. 5.12B). The samples display relatively flat (La/Yb 5-10) REE patterns (Fig. 5.13), characterized by negative Ba, Nb, P, and Ti anomalies, which is indicative of an arc/subduction setting for the melt. Sample AZ 07-21-13 (7) shows a negative Eu anomaly, indicating involvement of plagioclase in fractional melting, whereas sample AY 09-21-11 (3) has no Eu anomaly, which is consistent with their respective mineralogies. These granitoids were likely generated in a volcanic-arc setting, although more thorough geochemical analysis is required to draw more substantive conclusions.

### *Metamorphic samples*

The primary purpose of obtaining whole-rock geochemical data of the metamorphic samples is for thermobarometry analysis (see section 5.8). However, the bulk geochemical data can also constrain the protolith of the metamorphic samples. The gneiss samples RR 05-05-12 (8) and AZ 04-18-12 (4) are rather different. The first sample is felsic ( $\text{SiO}_2 \text{ 73 wt\%}$ ), highly peraluminous ( $\text{Al}_2\text{O}_3/[\text{Na}_2\text{O} + \text{CaO} + \text{K}_2\text{O}] = 1.7$ ) (Table 5.4), and plots along a calc-alkaline trend (Fig. 5.12A). The sample plots within the volcanic-arc field on a granite classification

diagram of Pearce (1984) (Fig. 5.12B) and displays a somewhat flat REE pattern ( $\text{La/Yb} > 6$ ) (Fig. 5.13). The second gneiss sample [i.e., AZ 04-18-12 (4)] has an intermediate composition ( $\text{SiO}_2$  54 wt%) (Table 5.4). In metamorphic rock classification diagrams, both samples plot in the sedimentary-rock-protolith field (Fig. 5.14A) (Garrels and MacKenzie, 1971). The relatively high  $\text{SiO}_2$  and  $\text{K}_2\text{O}$  wt% cause sample RR 05-05-12 (8) to plot as an arkosic sandstone deposited along a passive continental margin setting (Figs. 5.14B and 5.14C) (Roser and Korsch, 1986; Herron, 1988). The more intermediate sample AZ 04-18-12 (4) plots as an iron-rich shale deposited along an active margin (Figs. 5.14B and 5.14C) (Roser and Korsch, 1986; Herron, 1988). However, according to the classification of Werner (1987), gneiss sample RR 05-05-12 (8) plots in the igneous protolith field ( $\text{P}_2\text{O}_5/\text{TiO}_2$  0.45 and  $\text{MgO}/\text{CaO}$  0.44) (not shown). These two samples experienced amphibolite-grade metamorphism (see section 5.8), which obscures the nature of the protoliths, and further interpretation is beyond the scope of this study.

The two garnet-mica schist samples AZ 04-18-12 (4b) and AY 09-21-11 (2) both plot along the pelite trend in a  $\text{K}_2\text{O}/\text{Al}_2\text{O}_3$  versus  $\text{Na}_2\text{O}/\text{Al}_2\text{O}_3$  diagram (Garrels and MacKenzie, 1971) (Fig. 5.14A). Additionally, protolith classification diagrams indicate that the sedimentary protoliths may have been deposited in an active continental margin (Figs. 5.14B and 5.14C) (Roser and Korsch, 1986; Herron, 1988).

The three garnet amphibolite samples are compositionally similar to gabbro ( $\text{SiO}_2$  50-53 wt%) and they follow a subalkaline/tholeiitic trend ( $\text{Na}_2\text{O} + \text{K}_2\text{O} < 2.7$  wt %) (Table 5.4; Fig. 5.12A). In a  $\text{K}_2\text{O}/\text{Al}_2\text{O}_3$  versus  $\text{Na}_2\text{O}/\text{Al}_2\text{O}_3$  diagram, the samples plot in the field of a mafic igneous rock protolith (Garrels and MacKenzie, 1971) (Fig. 5.14A). The protoliths of these garnet amphibolites were likely mafic dikes intruding an upper-crustal sedimentary sequence.

## 5.8. Thermobarometry

To determine the metamorphic conditions of the high-grade rocks in the central Qilian Shan, thermobarometric studies were conducted on representative garnet-mica schist, garnet amphibolite, and garnet-bearing gneiss samples. These samples are either part of, or grade into, the right-slip ductile shear zone that is exposed throughout the mapping area (Fig. 5.5). The goal in constraining the pressure-temperature ( $P$ - $T$ ) histories of these representative samples is to address two questions: (1) is there any significant variation in metamorphic grade that may indicate that present rock exposures are part of a tilted section of the Qilian orogen, and (2) broadly, what part of the Qilian orogen and arc do these rocks represent? Map relationships indicate that these metamorphic rocks were intruded by early Paleozoic arc granites (Fig. 5.5), and thus they should represent part of the country rock of the Qilian arc.

### 5.8.1. Methods

Two thermobarometric techniques were employed to investigate the  $P$ - $T$  conditions experienced by the metamorphic rocks of the central Qilian Shan: the average  $P$ - $T$  mode of THERMOCALC 3.37 (Holland and Powell, 1998) and pseudosection construction using the *Perple\_X* 09 software (Connolly, 2005). These quantitative techniques were preceded by petrographic and electron microprobe examination of thin sections from the garnet-mica schist, garnet amphibolite, and garnet-bearing gneiss samples. Thin sections of selected samples were examined through petrographic microscope to characterize the representative mineral assemblages and to assess which phases grew together in equilibrium. Next, doubly-polished thin sections were carbon coated and analyzed on the JEOL JXA-8200 electron microprobe at UCLA. X-ray compositional maps of Ca, Na, Mg, Mn, and K were made for selected garnet

porphyroblasts using an accelerating voltage of 15 kV and a current of ~100 nA with 5-10  $\mu\text{m}$  pixels and a dwell time of 30 ms per pixel (Fig. 5.15). These maps were used to assess compositional zoning patterns, as well as to aid in mineral identification, especially for the garnet inclusions. Analytical traverses were made across the garnet to quantitatively identify zonation patterns, particularly in samples that have undergone retrogression (Fig. 5.15). For these traverses and individual mineral analysis, a  $<1 \mu\text{m}$  spot size was used with a 15 kV accelerating voltage and a current of 10 nA for all phases except Ca-rich plagioclase and the micas, which required a 5  $\mu\text{m}$  spot size. Calibrations were performed periodically using natural and synthetic standards. The JEOL software applied a ZAF correction.

*P-T* estimates were determined from the chemical data using the average P-T mode of THERMOCALC 3.37 (Holland and Powell, 1998), with the most up-to-date internally-consistent thermodynamic dataset (i.e., dataset 62: Holland and Powell, 2011). The program uses the chemical composition data of mineral phases that are apparently in equilibrium to determine the intersection between exchange reaction geothermometers (e.g., garnet-biotite and garnet-hornblende; Hodges and Spear, 1982; Graham and Powell, 1984; Bhattacharya et al., 1992) and net transfer geobarometers (e.g., garnet-plagioclase-muscovite-biotite, garnet-plagioclase-hornblende-quartz, and garnet-plagioclase-rutile-ilmenite-quartz; Bohlen and Liotta, 1986; Kohn and Spear, 1989, 1990; Dale et al., 2000) equilibria. The activity coefficients for each phase were calculated with the AX program (Tim Holland: <http://www.esc.cam.ac.uk/research/researchgroups/holland/ax>). Additional geothermometers, including the fluid-independent Ti-in-biotite calibration of Henry et al. (2005) and the hornblende-plagioclase geothermometer of Holland and Blundy (1994), were used to provide additional temperature constraints. Amphibole phases were classified using the Excel

spreadsheet of Locock (2014) following the latest nomenclature and classification of the International Mineralogical Association (IMA) published by Hawthorne et al. (2012). The program also estimates iron allocation between  $\text{Fe}^{2+}$  and  $\text{Fe}^{3+}$ .

The  $P$ - $T$  conditions experienced by the rock samples were further constrained by pseudosection construction using the Gibbs free energy minimization software Perple\_X 09 (Connolly, 2009). Pseudosections allow for sample-specific bulk compositions to be used to calculate the equilibrium relationships between coexisting phases. Bulk compositions for samples of interest were determined by whole-rock XRF analysis (see section 5.7), and total Fe was input as FeO. All sections were constructed in the MnNCKFMASH( $\pm$ O) system. For the metapelite samples, the following solution models were used: TiBio(WPH) (White et al., 2007), Mica(CHA) (Coggon and Holland, 2002), Gt(HP) (Holland et al., 1998), Chl(HP) (Holland et al., 1998), Pl(h) (Newton et al., 1980), and sometimes Kf (Waldbaum and Thompson, 1968). For the garnet amphibolite samples, the following solution models were employed: Gt(HP) (Holland et al., 1998), Amph(DPW) (Dale et al., 2005), Mica(CHA) (Coggon and Holland, 2002), TiBio(WPH) (White et al., 2007), and Pl(h) (Newton et al., 1980). Lastly, for the garnet-bearing gneiss sample, the following solution models were used: Gt(HP) (Holland et al., 1998), TiBio(WPH) (White et al., 2007), Mica(CHA) (Coggon and Holland, 2002), Kf (Waldbaum and Thompson, 1968), and Pl(h) (Newton et al., 1980). All samples were assumed to be water saturated ( $a_{\text{H}_2\text{O}} = 1$ ) and have  $\text{SiO}_2$  in excess. Garnet isopleths for grossular, almandine, pyrope, and spessartine were calculated using the werami subroutine of Perple\_X 09 and plotted to track the sample in  $P$ - $T$  space.

### 5.8.2. Sample description and mineral composition

Sample locations are shown in Figure 5.5B. The representative phase compositions for all of the samples are listed in Auxiliary Table A.8.

#### *AY 09-21-11 (1A): garnet-mica schist*

Sample AY 09-21-2011 (1A) was collected from a garnet-mica schist outcrop just south of the Tuo Lai River. The metapelite has Fe-rich garnet porphyroblasts ( $X_{Mg} = 0.08-0.11$ ). Foliation is defined by biotite ( $X_{Mg} = 0.45$ , Ti = 0.09-0.07 apfu), white mica ( $X_{Mg} = 0.46-0.39$ , Si = 3.02-2.99 apfu), and minor chlorite ( $X_{Mg} = 0.48$ , Fe = 2.32 apfu). Additional present minerals include quartz, minor plagioclase (An<sub>18-20</sub>), spinel, rutile, and tourmaline. Garnet exhibits prograde growth zoning compositions that range between 79-70% almadine, 16-8% grossular, 10-3% spessartine, and 8-4% pyrope (Fig. 5.15). Quartz is almost completely recrystallized: grain boundary migration has become the dominant mechanism with minor subgrain rotation crystallization, suggesting peak temperatures of ~500-550°C (Hirth and Tullis, 1992). Garnet inclusions include zircon, magnetite, and minor monazite. The prograde growth zoning in the garnet suggests peak temperatures of less than 650°C.

#### *AY 09-21-11 (2): garnet-mica schist*

Sample AY 09-21-11 (2) was collected from a garnet-mica schist outcrop that is laterally continuous with the rocks of sample AY 09-21-11 (1A) (Fig. 5.5). The schist is composed of garnet, biotite, white mica, minor chlorite, quartz, and plagioclase with minor amounts of spinel, rutile, tourmaline, zircon, and monazite. Monazites from this sample were dated via in-situ techniques (see section 5.6.2) and the whole-rock geochemistry of the rock was determined by



XRF (see section 5.7). This sample is assumed to be similar to AY 09-21-11 (1A), and the constructed pseudosection from sample AY 09-21-11 (2) was compared against the phase compositions of AY 09-21-11 (1A) (see section 5.8.4).

*AZ 04-18-12 (4b): garnet-mica schist*

Sample AZ 04-18-12 (4b) was collected from an outcrop of garnet-mica schist in the Proterozoic gneiss unit along the southern flank of the Tuo Lai Nan Shan (Fig. 5.5). Within this same outcrop was a lense of amphibolite gneiss from which sample AZ 04-18-12 (4) was collected. The metapelite sample AZ 04-18-12 (4b) has Fe-rich garnet porphyroblasts ( $X_{Mg} = 0.13-0.15$ ). Foliation is defined by biotite ( $X_{Mg} = 0.40$ , Ti = 0.16 apfu), white mica (not analyzed), and minor chlorite (not analyzed). Additional present minerals include quartz, plagioclase feldspar, and alkali feldspar. Garnet exhibits relatively flat compositional zoning with Mn enrichment at the rims (Fig. 5.15), which may indicate diffusional zoning at temperatures greater than 600°C and subsequent retrogression. Quartz has been fully recrystallized and with lobate, interfingering grain boundaries that indicate peak temperatures > 500°C (Hirth and Tullis, 1992). Garnet compositions range between 75-72% almadine, ~4% grossular, 13-12% spessartine, and 13-11% pyrope (Table A.8).

*AZ 04-18-12 (4): garnet-epidote amphibolite gneiss*

Sample AZ 04-18-2012 (4) was collected adjacent to sample AZ 04-18-12 (4b) from a lense of epidote-amphibolite gneiss (Fig. 5.5). The gneiss has Fe-rich garnet porphyroblasts ( $X_{Mg} = 0.07-0.09$ ), and foliation is defined by bands of calcic amphibole ( $Ca_B \geq 1.50$ ) and plagioclase ( $An_{79-82}$ ). Amphibole are classified as Fe-hornblende ( $X_{Mg} = \sim 0.45$ ,  $[Na+K]_A < 0.50$ ) and Fe-

pargasite ( $X_{Mg} = \sim 0.45$ ,  $[Na+K]_A \geq 0.50$ ,  $Si < 6.5$  apfu) (Fig. 5.16) (Leake et al., 2004). In the mafic foliation bands, plagioclase is very minor and clinozoisite is common. Additional phases include quartz, biotite, magnetite, and ilmenite. Amphibole hosts inclusions of zircon. Titanite and rutile are not observed. Garnet grains exhibit flat diffusional zoning profiles with minor Mn enrichment near the rims, which may indicate late retrograde metamorphism (Fig. 5.15).

*AY 09-21-11 (6): Garnet amphibolite*

This sample was collected from an outcrop of foliated garnet amphibolite in the Tuo Lai River valley (Fig. 5.5). At this outcrop, amphibolite is interlayered with garnet-mica schist rocks. In thin section, this sample has a granofelsic texture with nearly equant hornblende grains, which suggests that this sample experienced contact metamorphism. This sample has Fe-rich garnet porphyroblasts ( $X_{Mg} = 0.15$ ), and foliation is defined by bands of calcic amphibole ( $Ca_B \geq 1.50$ ) and plagioclase ( $An_{60-30}$ ). Amphibole are classified as Mg-hornblende ( $X_{Mg} = >0.5$ ,  $[Na+K]_A < 0.50$ ) and edenite-pargasite ( $X_{Mg} = >0.5$ ,  $[Na+K]_A \geq 0.50$ ) (Fig. 5.16) (Leake et al., 2004). Quartz is also present. Garnet compositions show very minor prograde growth zoning, but they are relatively flat compared to other samples (Fig. 5.15). Garnet compositions range from 59-56% almandine, 33-29% grossular, 3-1% spessartine, and 12-8% pyrope (Fig. 5.15). Because of the observed zoning profiles (Fig. 5.15), the sample likely experienced peak conditions at or greater than  $\sim 600^\circ C$ .

*RR 05-05-12 (12): garnet amphibolite*

Sample RR 05-05-2012 (12) was collected from a lense of foliated garnet amphibolite (Fig. 5.5). In thin section, the rock displays a nearly granofelsic texture with equant mineral

grains that suggests the sample experienced minor contact metamorphism. The sample consists of calcic amphiboles ( $Ca_B > 1.50$ )—classified as Mg-hornblende ( $X_{Mg} > 0.50$ ,  $[Na+K]_A < 0.50$ ), edenite ( $X_{Mg} > 0.50$ ,  $[Na+K]_A \geq 0.50$ ), and pargasite ( $X_{Mg} > 0.50$ ,  $[Na+K]_A \geq 0.50$ ,  $Si > 6.5$  apfu) (Fig 5.16) (Leake et al., 2004)—plagioclase ( $An_{54-41}$ ), quartz, minor ilmenite, and garnet ( $X_{Mg} = 0.18-0.12$ ) with diffusional zoning compositions that range between 60-55% almadine, 33-30% grossular, 6-1% spessartine, and 11-6% pyrope (Fig. 5.15). Quartz, amphibole, and garnet host fluid and solid inclusions. Garnets display prograde Mn-growth zoning (Fig. 5.15), suggesting peak temperatures of less than 650°C. There are only minor compositional deflections at the rims, which indicates that the sample experienced minor retrogression.

*AZ 07-21-13 (5): Garnet amphibolite*

Sample AZ 07-21-13 (5), collected along the northern bank of the Shule River valley (Fig. 5.5), was part of a large outcrop of vertically foliated schist, quartzite, and amphibolite. Foliation is defined by plagioclase ( $An_{33-22}$ ) and calcic amphibole ( $Ca_B > 1.50$ ), and there are also Fe-rich garnet porphyroblasts ( $X_{Mg} = 0.06-0.04$ ). Amphibole are classified as Fe-hornblende ( $X_{Mg} < 0.50$ ,  $[Na+K]_A < 0.50$ ), and Fe-edenite-pargasite ( $X_{Mg} < 0.50$ ,  $[Na+K]_A \geq 0.50$ ,  $Si > 6.0$  apfu) (Fig 5.16) (Leake et al., 2004). Garnet compositions show minor prograde growth zoning, especially for Fe and Mn, however the overall compositional profile is relatively flat (Fig 5.15). Garnet compositions range from 62-55% almadine, 31-26% grossular, 13-7% spessartine, and 4-3% pyrope.

*RR 05-05-2012 (8): quartzofeldspathic mylonitic gneiss*

Sample RR 05-05-2012 (8) is a quartzofeldspathic mylonitic gneiss, collected from the near the Tuo Lai Nan Shan range crest (Fig. 5.5), that exhibits well-defined stretching lineations. Observed phases include potassium feldspar ( $Or_{96-92}$ ), plagioclase feldspar ( $An_{27-12}$ ), biotite ( $X_{Mg} = 0.28$ ,  $Ti = 0.18$  apfu), white mica ( $X_{Mg} = 0.35$ ,  $Si = 3.0$  apfu), ilmenite, and garnet ( $X_{Mg} = 0.10-0.04$ ) with flat diffusional zoning compositions that range between 76-70% almandine, 5-4% grossular, 20-10% spessartine, and 8-5% pyrope. Quartz has been fully recrystallized and with lobate, interfingering grain boundaries that indicate peak temperatures  $> 500^{\circ}C$ . Small garnet inclusions include quartz, plagioclase, zircon, and monazite. There is little to no compositional zoning in the garnets and there are minor deflections at the garnet rims (Fig 5.15), indicating diffusional zoning at temperatures greater than  $600^{\circ}C$  and late-stage retrogression.

### **5.8.3. THERMOCALC *P-T* histories**

Effective and accurate use the average *P-T* mode of THERMOCALC 3.37 (Holland and Powell, 1998) requires that the mineral phases of interest are in equilibrium, which was initially verified by petrological examination. However, this task is complicated by the fact that minerals may have experienced prograde and retrograde growth during metamorphism that can cause single mineral grains to exhibit significant compositional variation, particularly the plagioclase, garnet, biotite, and amphibole phases (e.g., Figs 5.15 and 5.16). In these cases, I examined the compositional variation within each phase to determine what compositions are representative of interest were recording peak, early, or late stages of metamorphism. For example, reverse zoning of Ca in plagioclase (i.e., Ca increases toward the rim), suggests that rim analyses are more representative of peak metamorphic conditions. Conversely, low-Ca plagioclase cores may

represent early stages of metamorphism and/or relict pre-metamorphic grains. Similarly, increasing Ti in biotite generally corresponds to increasing metamorphic grade (e.g., Henry et al., 2005). For garnet, peak conditions may be best represented by spots with lowest Mn (spessartine) and highest Fe (almandine) (Fig. 5.15), whereas early metamorphic conditions are found in the cores with highest Ca (grossular) and lowest Mn (spessartine). Calculated  $P$ - $T$  data for all analyzed samples are shown in Table 5.5 and the representative electron-microprobe analyses are given in Table A.8.

The metapelite sample AY 09-21-11 (1A) experienced peak metamorphic temperatures of  $552 \pm 35^\circ\text{C}$  and pressures of  $7.2 \pm 1.2$  kbar ( $\sim 26$  km) (Fig. 5.17). This range overlaps the  $569 \pm 24^\circ\text{C}$  estimates found using the Ti-in-bt geothermometer of Henry et al. (2005) (Table 5.5). Preliminary data from another metapelite sample, AZ 04-18-12 (4b), shows that it experienced higher peak temperatures of  $625 \pm 23^\circ\text{C}$ . This higher temperature estimates overlaps peak  $P$ - $T$  estimates of adjacent sample AZ 04-18-12 (4), a garnet-epidote amphibolite gneiss, which experienced peak metamorphic temperatures of  $615 \pm 47^\circ\text{C}$  and pressures with high uncertainties of  $8.1 \pm 2.7$  kbar ( $\sim 29 \pm 9.5$  km) (Fig. 5.17).

The quartofeldspathic gneiss sample RR 05-05-12 (8) experienced temperatures and pressures of  $725 \pm 85^\circ\text{C}$  and  $6.8 \pm 1.0$  kbar ( $\sim 24$  km) respectively (Fig. 5.17). The Ti-in-bt geothermometer of Henry et al. (2005) yields a peak temperature estimate of  $678 \pm 24^\circ\text{C}$ , which corroborates the THERMOCALC results (Table 5.5). Garnet-amphibolite sample AY 09-21-11 (6) shows signs of early- and late-stage metamorphism. Estimates using garnet-core and early-stage amphibole analyses suggest early metamorphic conditions of  $614 \pm 49^\circ\text{C}$  and  $7.2 \pm 0.9$  kbar ( $\sim 26$  km) (Fig. 5.17). Peak metamorphic conditions involved temperatures of  $725 \pm 53^\circ\text{C}$  and pressures of  $7.9 \pm 0.9$  kbar ( $\sim 28$  km) (Fig. 5.17). This nearly isobaric increase in temperature

correlates with the granofelsic texture of this sample; it likely experience contact metamorphism, possibly caused by the intrusion of nearby plutons.

Another garnet amphibolite sample, AZ 07-21-13 (5), shows a large range of peak temperature estimates, and overall, this sample has large uncertainties for its  $P$ - $T$  estimates:  $576 \pm 88^\circ\text{C}$  and  $5.4 \pm 1.6$  kbar ( $\sim 19$  km) (Fig. 5.17). Garnet amphibolite sample RR 05-05-12 (12) shows the effects of early, peak, and late-retrograde metamorphic conditions. Although the uncertainties are large on the  $P$ - $T$  estimates for each of these stages, due to the limited analyses per stage, the THERMOCALC analyses show clockwise  $P$ - $T$  path (Fig. 5.17B). Estimated early, peak, and late-retrograde conditions are  $650 \pm 100^\circ\text{C}$  and  $7.0 \pm 1.7$  kbar ( $\sim 25$  km),  $791 \pm 110^\circ\text{C}$  and  $8.9 \pm 1.7$  kbar ( $\sim 31$  km), and  $662 \pm 95^\circ\text{C}$  and  $6.2 \pm 1.6$  kbar ( $\sim 22$  km) respectively (Fig. 5.17B). The weighted average of all of these overlapping measurements is  $696 \pm 41^\circ\text{C}$  and  $7.3 \pm 0.8$  kbar ( $\sim 26$  km) (Fig. 5.17B)

Taken together, all of the THERMOCALC estimates suggest that the metamorphic basement units experienced amphibolite to epidote-amphibolite grade metamorphism (Fig 5.17). Despite some large uncertainties, most of the samples recorded pressures of 6 to 8 kbar (22-28 km depth). The temperature range recorded by these rocks is very large, from  $\sim 500^\circ\text{C}$  to  $> \sim 700^\circ\text{C}$ . Evidence from petrographic analysis and garnet-composition traverses corroborate the higher temperatures experienced by some of these samples. For example, all of the samples that yield temperature estimates above  $\sim 600^\circ\text{C}$  have diffusional zoning compositions in the garnet phases and recrystallized quartz grains. Given that the peak pressures are similar for all samples, these higher temperatures suggest nearly isobaric heating. One possibility is that localized pluton intrusion led to the observed temperature increase experienced by some samples, but this would

imply very deep (e.g., ~25 km) magma/pluton intrusion. Further constraints on the  $P$ - $T$  conditions are provided in the pseudosection analysis below.

#### 5.8.4. Pseudosection $P$ - $T$ histories

Calculated pseudosections for garnet-mica schist samples AY 09-21-11 (2) and AZ 04-18-12 (4b), amphibolite gneiss sample AZ 04-18-12 (4), garnet amphibolite sample RR 05-05-12 (12), and gneiss sample RR 05-05-12 (8) are shown in Figure 5.18, along with the modeled bulk sample composition. When relevant, additional  $P$ - $T$  constraints are plotted along with pseudosections, including THERMOCALC estimates from section 5.8.3., to better constrain the metamorphic conditions.

The pseudosection for garnet-mica schist sample AY 09-21-11 (2) (Fig. 5.18A), which was collected in the same rock unit as sample AY 09-21-11 (1A), shows that the garnet stability fields exist above ~490°C. Garnet composition isopleths for pyrope and grossular are also plotted to track garnet-composition evolution. The observed mineral assemblage of grt-bt-ms-chl-pl-ru is located at approximately 480°C and 5.4kbar (location 3 of Fig. 5.18A). However, plagioclase is minor and appears to be an early relict phase. I interpret that plagioclase is unstable with the observed peak mineral assemblages, and that these conditions occurred across the plagioclase-out equilibria line at higher temperatures and pressures (locations 2 and 3 of Fig. 5.18A). The sample has not crossed the chlorite-out equilibria line because chlorite is a major phase. The garnet isopleths for peak conditions (~0.10 pyrope and ~0.12 grossular) intersect within this stability field at ~521°C and ~6.6 kbar. The THERMOCALC average  $P$ - $T$  estimate for sample AY 09-21-11 (1A) also overlaps the grt-bt-ms-chl-ru stability field (Fig. 5.18A), and the best

estimate for the peak metamorphic conditions of these two samples is the  $P$ - $T$  space within this overlap:  $530 \pm 10^\circ\text{C}$  and  $7.2 \pm 0.7$  kbar ( $\sim 26$  km) (location 1 of Fig. 5.18A).

The pseudosection RR 05-05-12 (12) has a large stability field for the observed stable mineral assemblage grt-bt-amph-pl-ilm (Fig. 5.18B). The intersection of garnet isopleths for pyrope and grossular track a prograde metamorphism from  $\sim 600^\circ\text{C}$  and  $\sim 6.5$  kbar (23 km) to peak conditions at  $\sim 725^\circ\text{C}$  and  $\sim 7.6$  kbar (27 km) (Fig. 5.18B). This prograde metamorphism range overlaps with the THERMOCALC results (see inset of Figure 5.18B). The 0.50  $X_{\text{Mg}}$  isopleth for amphibole also constrains the temperature range to near  $\sim 650^\circ\text{C}$  at pressures  $>4$  kbar (Fig. 5.18B). Spinel is not an observed stable phase in this sample, which further constrains the possible  $P$ - $T$  conditions.

The pseudosection for gneiss sample RR 05-05-12 (8) has a large stability field for the observed mineral assemblages of grt-pl-kfs-bt-ms-ilm (Fig. 5.18C). The THERMOCALC average  $P$ - $T$  estimate also overlaps this stability field (Fig. 5.18C). By tracking peak and late-retrograde garnet isopleths for pyrope and grossular—i.e.,  $\sim 0.05$  grs and  $\sim 0.08$  prp to  $\sim 0.05$  grs and  $\sim 0.05$  prp, respectively (locations 2 and 3 in Fig. 5.18C respectively)—I observe the peak and retrograde  $P$ - $T$  history of this sample. Because the peak pseudosection- and THERMOCALC-modeled conditions do not overlap, there is some uncertainty regarding the peak pressure conditions (i.e., from  $\sim 7$  kbar to  $\sim 5$  kbar). Thus, peak conditions can only be loosely constrained at  $\sim 700^\circ\text{C}$  and  $\sim 6 \pm 1.5$  kbar ( $\sim 21$  km). Late metamorphic conditions recorded by the garnet rims indicate retrograde conditions of  $630^\circ\text{C}$  and  $\sim 3.1$  kbar ( $\sim 11$  km) (location 3 in Fig. 5.18C).

Together, the three samples discussed above [i.e., AY 09-21-11 (2), RR 05-05-12 (12), and RR 05-05-12 (8)] are evenly spaced along the northern slope of the Tuo Lai Nan Shan (Fig. 5.5B). No major Cenozoic faults are observed between the samples, and therefore they may have



recorded similar metamorphic conditions and stages during early Paleozoic deformation. Samples AY 09-21-11 (2) and RR 05-05-12 (12) record prograde metamorphism from ~550-500°C and ~5.5 kbar to ~700-600°C and ~7kbar (Fig. 5.18C). Sample RR 05-05-12 (12) records higher temperatures (>~700°C), which may be related to the numerous early Paleozoic plutons that intrude the central and southern part of the Tuo Lai Nan Shan range (Fig. 5.5). The gneiss sample RR 05-05-12 (8) records similar peak conditions as RR 05-05-12 (12) (Fig. 5.18C). This sample also shows retrogression conditions to 630 °C and ~3.1 kbar (Fig. 5.18C). These three samples reveal an overall clockwise *P-T* path, which is corroborated by the THERMOCALC estimates for RR 05-05-12 (12) that also show this clockwise path, although the uncertainties are large (Fig. 5.17B).

The remaining pseudosections were constructed for samples collected along the southern flank of the Tuo Lai Na Shan range. Amphibole gneiss sample AZ 04-18-12 (4) consists of stable clinozoisite and minor plagioclase. Minor O<sub>2</sub> (0.02 wt %) was added the modeled bulk-composition input for this sample to account for the prevalence of oxides, opaque minerals (e.g., magnetite and ilmenite), and clinozoisite-epidote, which is required to generate Fe<sub>2</sub>O<sub>3</sub> from FeO in the Perple\_X software (Fig. 5.18D) (e.g., Massonne, 2012). The constructed pseudosection for this sample has a relatively small stability field for the clinozoisite and plagioclase phases (e.g., near location 2 in Fig. 5.18D). Garnet composition isopleths for pyrope, grossular, and almandine (Fig. 5.15) intersect within this stability field at peak- and late-stage metamorphic conditions of ~660°C and ~7.0 kbar (~25 km) and ~630°C and ~6.3 kbar (~ 23 km) respectively (Fig. 5.18D). The transition from 12% pyrope to 9-10% pyrope at the garnet rims most dominantly controls this modeled drop in metamorphic conditions. However, given uncertainties in pseudosection construction, these differences are not significant, and thus I suggest that the

modeled pseudosection more generally yields peak metamorphic conditions of 670-620°C and 7.1-6.0 kbar. These estimated conditions have slightly higher temperatures and lower pressures than the THERMOCALC results (Fig. 5.18D), and given that plagioclase is a minor phase, it is likely that the sample should plot closer to the plagioclase-out equilibria line (i.e., lower temperature) in  $P$ - $T$  space (Fig. 5.18D).

An additional  $P$ - $T$  constraint for sample AZ 04-18-12 (4) was provided by the TZARS equilibria barometer of Kapp et al. (2009) (see inset of Fig. 5.18E). The TZARS equilibrium lines for two different activity ratios of rutile and titanite (i.e.,  $a_{\text{ru}}/a_{\text{tn}} = 0.42$  and  $a_{\text{ru}}/a_{\text{tn}} = 0.89$ ), are plotted given the calculated activities of clinozoisite ( $a_{\text{cz}} = 0.7$ ) and anorthite ( $a_{\text{an}} = 0.85$ ). Along these equilibrium lines clinozoisite and anorthite feldspar should coexist, and in this sample plagioclase is minor and clinozoisite is common. Kapp et al. (2009) prefer an  $a_{\text{ru}}/a_{\text{tn}}$  activity of 0.42 when both rutile and titanite are absent from this sample, and thus this TZARS equilibria line represents a useful geobarometer for this sample (see inset of Fig. 5.18E). The geothermometer estimates and TZARS geobarometer intersect at slightly higher pressures and lower temperatures than the modeled pseudosection results, and provide my preferred peak  $P$ - $T$  estimate of ~620°C and 7.5 kbar.

The pseudosection for garnet-mica schist sample AZ 04-18-12 (4b), which was collected adjacent to sample AZ 04-18-12 (4b) (Fig. 5.5B), indicates that the stability field for stable alkali feldspar and muscovite is relatively narrow (Fig. 5.19A). The intersection of peak-garnet isopleths for grossular and pyrope yield metamorphic conditions of ~700°C and ~5 kbar (~18 km) (Fig. 5.18D), which is slightly higher than the temperature estimates of  $625 \pm 23^\circ\text{C}$  from the Ti-in-bt geothermometer of Henry et al. (2005).

Samples AZ 04-18-12 (4b) and AZ 04-18-12 (4) are from the same outcrop and should record the same metamorphic conditions. The garnet-mica schist sample AZ 04-18-12 (4b) records lower pressures yet higher temperatures and may represent late-stage metamorphic conditions during retrograde metamorphism and nearby pluton intrusion (see inset of Fig. 5.18E). The prevalence of chlorite in this sample corroborates this assertion.

### **5.9. Deformation history of the central Qilian Shan**

Here I outline the major deformational events that affected northern Tibet and the central Qilian Shan, along with insights provided by the geochronological and thermobarometric analyses presented in this chapter (e.g., Fig. 5.19). Early Neoproterozoic (i.e., ~1.0-0.9 Ga) plutonism evidenced by granitoid and gneiss rocks throughout northern Tibet (Fig. 5.1B) was followed by regional metamorphism. Leucogranites and metamorphic zircon rims have been reported with ages of ~0.9-0.85 Ga in the Tian Shan, Tarim, and Qilian Shan (Gehrels et al., 2003b; Zhu et al., 2011; Kröner et al., 2013; Wang et al., 2014). This age signature is associated with the inferred collision between North and South Tarim along the Tarim suture (Guo et al., 2005).

In the late Neoproterozoic, rifting led to the opening of the Qilian Ocean (e.g., Song et al., 2013). Cambrian-aged ophiolites are found throughout the Qilian Shan, and many are SSZ-type with zircon ages ranging from 540-500 Ma (Xia and Song, 2010; Song et al., 2013; this study). Continental volcanic arc magmatism began by at least ~520 Ma and arc-related plutons have ages that range from ~520 Ma to 440 Ma (e.g., Dang et al., 2011; Xia et al., 2012; Xiao et al., 2012; Song et al., 2013; Wu et al., 2016). SSZ-ophiolite formation and subduction initiation corresponds to the oldest monazite ages obtained in this study (i.e.,  $538 \pm 20$  Ma) (Fig. 5.11). I

interpret that this earliest population of monazite ages is related to the development of the middle to late Cambrian Qilian arc. Furthermore, the development of an Andean-type active margin lead to crustal thickening and the early-stage *P-T* conditions recorded by some of the metamorphic sample (Figs. 5.17 and 5.18).

Locally, in my study area in the central Qilian Shan, the earliest recorded magmatism occurred at ~475 Ma (Table 5.2), which overlaps with the main population of included-in-garnet monazite ages at ~485-475 Ma (Fig. 5.11). Peak prograde metamorphism at this time and right-slip shearing was operating at depths of 25-20 km (Fig. 5.19), as indicated by peak metamorphic conditions (Figs. 5.17-5.18). Ductile shearing of these rocks ceased by ~445 Ma, when the foliated metamorphic rocks are crosscut by an undeformed granitoid dike with a U-Pb age of  $445 \pm 3$  Ma (Figs. 5.7F and 5.11; Table 5.2). The depth of dike emplacement was not determined, but I infer that the basement rocks and intruding dike were at depths of 10-15 km at ~445 Ma because (1) many arc plutons are intrude at depths of  $< \sim 15$  km (e.g., Petford et al., 2000; Putnam et al., 2015) and (2) the lowest-grade *P-T* signature recorded in the metamorphic rocks corresponds to these depths (Figs. 5.17-5.19).

Intrusions with ages ranging from 450 to 440 Ma are widespread throughout the Qilian Shan. Such extensive plutonism may correspond with continental collision between North China and Tarim (Wu et al., 2016), although this cannot be directly confirmed in my study area. This late-stage pulse of magmatism also corresponds to matrix monazite ages in the analyzed metapelite samples (Fig. 5.11).

Prior to and during continental collision in the Qilian orogen, there is deposition of Silurian turbidite sequences to the north and south of the central Qilian Shan. These strata were likely deposited in back-arc and forearc-to-foreland basins as the Qilian arc transitioned to a

collisional orogen. They were strongly deformed during the protracted continental collision. This collision brought basement rocks toward the surface, and Silurian strata and Devonian terrestrial sediments were deposited unconformably over the exposed basement rocks.

Widespread and laterally continuous Carboniferous shallow marine deposition indicates that much of the Qilian Shan was at or just below sea level at this time (Fig. 5.19). Nearly uninterrupted shallow marine sedimentation continued into the Triassic. The sedimentary facies does not vary significantly in the Carboniferous-Triassic sections, which requires either subsidence of the Qilian Shan or global sea level rise to accommodate the deposition of these strata.

Jurassic extension brought these rocks toward the surface, and Jurassic strata were deposited in a marginal marine to swamp setting. Extensive Jurassic-aged coal deposits are widespread across the Qilian Shan. Regional extension continued into the Cretaceous, subaerial sedimentation requires that the Qilian Shan was above sea level at this time (Fig. 5.19). Terrestrial late Oligocene to Miocene deposits record the initiation of shortening across the central Qilian Shan

## **5.10. Discussion**

### **5.10.1. Lateral extent of the Qilian suture**

Based on similar lithological assemblages and geologic histories, it has been argued that the Qilian orogen and suture(s) were laterally continuous with the Qinling suture to the southeast (e.g., Xu et al., 2008; Tseng et al., 2009; Dong et al., 2011; Wu et al., 2016) (Fig. 5.2), forming a >1000 km long early Paleozoic orogenic belt. However, the northwestern termination of this orogen and suture is not known. Three geometrically plausible models exist for its continuation:

(1) it may continue into Tarim and be currently covered by Mesozoic-Cenozoic sediments, (2) it may veer to the south of Tarim and be overprinted by the Western Kunlun and Pamir thrust belts, although evidence for this suture in the Altyn Tagh Range suggests that the suture cannot be that far to the southwest, or (3) the Kunlun-Qaidam continent may have only partially separated from Tarim and the abrupt western termination of the Qilian suture represents the western extent of the Qilian Ocean. An additional model suggested that the Qilian suture connected to the northwest to the Beishan suture (Zhou and Graham, 1996d), although this idea has been abandoned because the Beishan suture has more recently been related to the Central Asian Orogenic System and the closure of the Paleo-Asian Ocean (e.g., Xiao et al., 2010; Guo et al., 2011; Cleven et al., 2015).

The Precambrian basement of Kunlun-Qaidam is similar to that of Tarim-North China (Hu et al., 2000; Gehrels et al., 2003b; Tung et al. 2007; Long et al. 2010; Zhao et al. 2012; Wu et al., 2016), which indicates that these two continents may have been contiguous prior to Neoproterozoic rifting. In addition, no Phanerozoic sutures or amalgamation structures have been reported between Qaidam and Tarim (Fig. 5.1), which further bolsters their Precambrian connection.

Some researchers argue that the Kunlun-Qaidam continent was connected to the South China craton based on correlative ~950-900 Ma granites. This age signature is not a unique signature among Precambrian continents, as similar-aged plutons are found within North China, Tarim, the Tian Shan, and the CAOS microcontinents (e.g., ; Han et al., 2011; Rojas-Agramonte et al., 2011; Ma et al., 2012).

### 5.10.2. Nature of the Qilian arc

In many of the reconstructions of the Qilian orogen and suture zone, the exposures of discontinuous of UHP metamorphic rocks, ophiolite and mélangé complexes, arc plutons, and blueschist rocks (Fig. 5.2) have been used as evidence to suggest that the Qilian orogen resulted from the collision of multiple arcs along multiple sutures in the early Paleozoic (Li et al., 1978; Hsü et al., 1995; Yin and Nie, 1996; Yin and Harrison, 2000; Xiao et al., 2009; Gehrels et al., 2011; Song et al., 2013, 2014) (Table 5.1). However, the effects of Ordovician arc construction, protracted Silurian-Devonian continental collision, Mesozoic extension, and Cenozoic intracontinental deformation must have modified the original geological configuration.

Any viable model for the Qilian arc must explain the following key observations (Fig. 5.3; Table 5.1): (1) northward younging magmatism across northern Tibet (e.g., Zuza et al., 2015; Wu et al., 2016), (2) Cambrian SSZ-type ophiolite and mélangé material dispersed throughout the Qilian Shan, (3) the spatial and temporal overlap between arc magmatism and UHP metamorphism in North Qaidam (e.g., Yin et al., 2007), and (4) high-pressure blueschist rocks exposed in the northeastern Qilian Shan (e.g., Song et al., 2013) (Figs 5.1 and 5.2). The temporal and spatial distribution of arc plutons could fit with any of the Qilian arc models except the north-dipping subduction model because no Ordovician plutons intrude the North China craton (Fig. 5.3; Table 5.1). Given that most of the ophiolite complexes are SSZ-type ophiolites (e.g., Meng et al., 2010; Xia and Song, 2010; Song et al., 2013; this study), these rocks may have been variably obducted onto the continental arc and/or underthrust beneath the Qaidam continent. This suggests the ophiolite fragments were initially scattered throughout the Qaidam continent even before Qilian orogen-related collision, which means that the bidirectional or

multiple-arc models are not required to account for the extensive ophiolite-mélange distribution across the Qilian Shan (Fig. 5.3).

In light of the above considerations, I suggest that a single south-dipping subduction system operated along the northern margin of the Qaidam continent. The distribution of Cambrian ophiolites and strata throughout the Qilian Shan may be the result of complex mélange/ophiolite obduction or ophiolite underthrusting. For example, the Mesozoic Cordilleran arc involved both complicated SSZ ophiolite obduction of the coast-range ophiolite (e.g., Wakabayashi et al., 2010) and significant mélange underthrusting/underplating as far east as the Rand-schist outcrops (e.g., Grove et al., 2003). Across the Qilian Shan, the wide belt of arc plutons that generally young to the north-northeast (e.g., Zuza et al., 2015; Wu et al., 2016) can be explained by northward rollback of the Qilian oceanic slab. This also explains why Ordovician arc plutons intrude older forearc sediments (Fig. 5.5). The blueschist rocks in the northeast Qilian Shan were generated in this subduction system and their early and/or Silurian cooling ages either record peak metamorphism or exhumation, respectively (Liu et al., 2006; Lin et al., 2010). This configuration is further discussed below in the tectonic model presented in section 5.10.3.

### **5.10.3. Mesoproterozoic-Paleozoic tectonic evolution of northern Tibet**

Here I present a self-consistent tectonic model for the Mesoproterozoic to Paleozoic tectonic evolution of northern Tibet that conforms to our present understanding of the Qilian Shan (Fig. 5.20). In the Mesoproterozoic, cratonal shelf or passive margin strata are deposited along the southern margin of the linked North Tarim-North China craton (Fig. 5.20A). This margin faces the Tarim (or Paleo-Qilian) Ocean, and the sediments consist of ~1.8 Ga and ~1.45



Ga detrital zircon grains derived from the North China craton (i.e., sample AY 09-21-11 [1] in Fig. 5.4B) (see also Gehrels et al., 2003a). At ~1.0 Ga, north-dipping subduction along the southern margin of the North Tarim-North China continent accommodates the convergence of the continuous South Tarim-Qaidam continent and the closure of the Tarim Ocean (Fig. 5.20B) (e.g., Guo et al., 2005). The 1.0-0.9 Ga granitoid belt that outcrops throughout Qaidam, the Qilian Shan, the Altyn Tagh Range, Tarim, and Tian Shan (Fig. 5.1B) is evidence for the existence of the Tarim Ocean and Tarim arc (Fig. 5.20B). This subduction system generated blueschist rocks that are presently exposed near Aksu in Tarim (e.g., Liou et al., 1996; Zhu et al., 2011). The inferred suture associated with the collision of the South Tarim-Qaidam and North Tarim-North China continents is exposed at Aksu and partially parallels and overlaps with the Qilian and Qinling sutures to the southeast (e.g., Guo et al., 2005; Wu et al., 2016).

In the late Neoproterozoic, rifting of this joined continent and the opening of the Paleo-Asian, Qilian, and Tethys Oceans initiated at variable times (Fig. 5.20C). The earliest rifting event was associated with the ~825 Ma Jinchuan ultramafic intrusion (Li et al., 2005), the deposition of the Hanmushan Group passive margin strata, and the opening of the Paleo-Asian Ocean to the north of the North China craton (Fig. 5.20C). Bimodal volcanism from ~775 to 600 Ma was associated with the opening of the Qilian Ocean and the deposition of the passive margin Baiyangguo/Daliugou Group (Tseng et al., 2006, 2007; Xu et al., 2015) (Fig. 5.20C). This rifting occurred subparallel to the early Neoproterozoic Tarim suture zone. Because there is no observed Phanerozoic suture or amalgamation structures between Qaidam and Tarim, I infer that these continents remained connected during the opening of the Qilian Ocean. The Qaidam continent may have rotated away from North China as a peninsula that led to the opening of a westward-tapering Qilian Ocean. This interpretation also suggests the Qilian Ocean was a relatively small

sea and not a thoroughgoing ocean separating Laurasia and Gondwana (cf. Stampfli and Borel, 2002).

In the Cambrian, the Qilian Ocean reached its maximum extent and subduction initiated along the southern bounds of this ocean. During nascent arc formation, the Qilian SSZ ophiolites were generated (~540-500 Ma) to the north of the Qaidam continent (Fig. 5.20D). Inherited zircon ages during this time record a complex process of recycling and influence of underlying and adjacent continental crust. Continental subduction begins in the early Ordovician as Qilian oceanic lithosphere dips to the south beneath the Qaidam continent. The Qilian SSZ ophiolite obducted onto Qaidam and was also simultaneously underthrust beneath the continent (e.g., Grove et al., 2003) (Fig. 5.20D). These dispersed ophiolites are observed throughout the present-day Qilian Shan and North Qaidam.

In the Ordovician, volcanic arc magmatism began as the Qilian Ocean was subducted beneath the Qaidam continent (Fig. 5.20E). Ordovician strata were deposited in back-arc and forearc settings, to the south and north of the Qilian arc respectively. During this time, fragments of the Qaidam continent were brought to UHP depths via the subduction channel (e.g., Yin et al., 2007; Menold et al., 2016). The UHP rocks were later exhumed to the middle crust via either diapiric flow or subduction-channel flow (e.g., Mattinson et al., 2007; Yin et al., 2007a; Menold et al., 2016), where they were juxtaposed against amphibolite-grade SSZ ophiolite rocks (Menold et al., 2016). A trench-parallel intra-arc right-slip strike-slip fault developed within the Qilian arc, which is evidenced by the right-lateral shear zone that is exposed in the central Qilian Shan (Fig. 5.6). Ages from monazite grains included in garnet indicate that this shear zone was operating at ~480 Ma (Fig. 5.11). I envision that this strike-slip fault was similar to the present-day Sumatra strike-slip fault (e.g., Diament et al., 1992). The kinematics of the Qilian strike-slip

fault suggests right-lateral obliquity during the subduction of the Qilian Ocean (Fig. 5.20E), which is consistent with clockwise closure of the Qilian Ocean.

Northward slab rollback at the south-dipping Qilian arc-subduction can explain three key observations (Fig. 5.20F). First, the northeastward-younging trend of arc magmatism throughout the Qilian Shan (e.g., Zusa et al., 2015; Wu et al., 2016). Second, the observation that late Ordovician arc plutons intrude Ordovician forearc strata (Fig. 5.5). Finally, this event helps to explain how ophiolite fragments and UHP rocks are positioned within and behind the Qilian arc. The arc simply propagated northeast over these features (Fig. 5.20F).

By ~445-440 Ma, the Tarim-North China cratons collided with the Qaidam continent (Fig. 5.20F). The timing of collision is not well constrained, but diffuse ~445-440 Ma plutonism is followed by relatively little magmatism (e.g., Wu et al., 2016). Also, the youngest pulse of monazite ages corresponds to this time period (Fig. 5.11). Silurian strata have been classified as flysch deposits that transition to Devonian molasse rocks. During this collision, North China's passive margin strata is juxtaposed against the accretionary wedge, mélangé rocks, and ophiolite complex of the Qilian arc (Figs. 5.5 and 5.20F).

This protracted history of two major ocean-closure events in the Neoproterozoic and early Paleozoic was reactivated in the Cenozoic by focused strike-slip and thrust faulting. The major left-slip faults of northern Tibet parallel Phanerozoic sutures (Taylor and Yin, 2009; see Chapter 3), and the Haiyuan fault parallels the surface trace of the Qilian-Qinling suture zone (Fig. 5.2). In addition, the Neoproterozoic north-dipping and early Paleozoic south-dipping subduction zones suggested in this work would provide subduction-mélangé channels to focus Cenozoic shortening in northern Tibet. This may help explain why significant crustal shortening

across the Qilian Shan occurs nearly 1500 km to the north the Himalayan collisional front (Fig. 5.2).

### **5.11. Conclusions**

The Qilian Shan, North Qaidam, and Qaidam Basin of northern Tibet experienced two major arc/collisional events in the Neoproterozoic and early Paleozoic. Through an integrated investigation of the magmatic and deformational history of the central Qilian Shan, together with existing work across northern Tibet, I have developed a coherent tectonic model that describes the evolution of the southern margins of the continuous Tarim-North China craton from ~1.0 Ga to the present. (1) Early Neoproterozoic subduction accommodates the convergence and collision between South Tarim-Qaidam and North Tarim-North China continents. (2) Late Neoproterozoic rifting partially separates a peninsular Qaidam from North China and opens the Qilian Ocean as an embayed marginal sea; this separation broadly follows the trace of the early Neoproterozoic suture zone. (3) South-dipping subduction along the northern margin of the Kunlun-Qaidam continent initiates in the Cambrian, which leads to the formation of the Yushigou supra-subduction zone (SSZ) ophiolite (which links along strike with the SSZ Aoyougou and Dongcaohe ophiolites) and the formation of the Qilian arc. (4) Subduction, arc magmatism, and the convergence between Qaidam and North China continued throughout the Ordovician, with a trench-parallel intra-arc strike-slip fault system that is presently represented by the high-grade metamorphic rocks with a pervasive right-lateral shear sense. (5) The closure of the Qilian Ocean occurred following the counter-clockwise rotation of a peninsular Qaidam continent toward North China, which is supported by the right-lateral kinematics of the intra-arc strike-slip fault and the westward tapering map-view geometry of Silurian flysch basins; continental collision

occurred at ~445-440 Ma, which lead to widespread plutonism across the Qilian Shan and is recorded as the youngest population of monazite ages.

This tectonic model implies the parallel closure of two oceans along the Qilian suture zone since ~1.0 Ga. In addition, the Qilian Ocean was not the Proto-Tethys (i.e., the earliest through-going ocean separating Gondwana from Laurasia) as suggested by earlier studies, but rather represented a smaller marginal sea along the southern margin of the Laurasian continent. Lastly, Cenozoic deformation that results from India-Asia convergence is focused along these sites of repeated ocean closure. The major left-slip faults parallel these sutures, and Cenozoic shortening and continental underthrusting may have been assisted by the subduction-mélange channels.

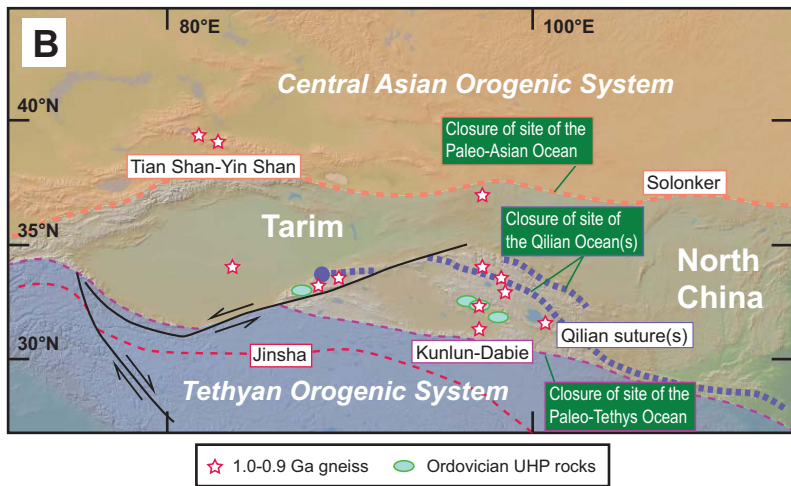
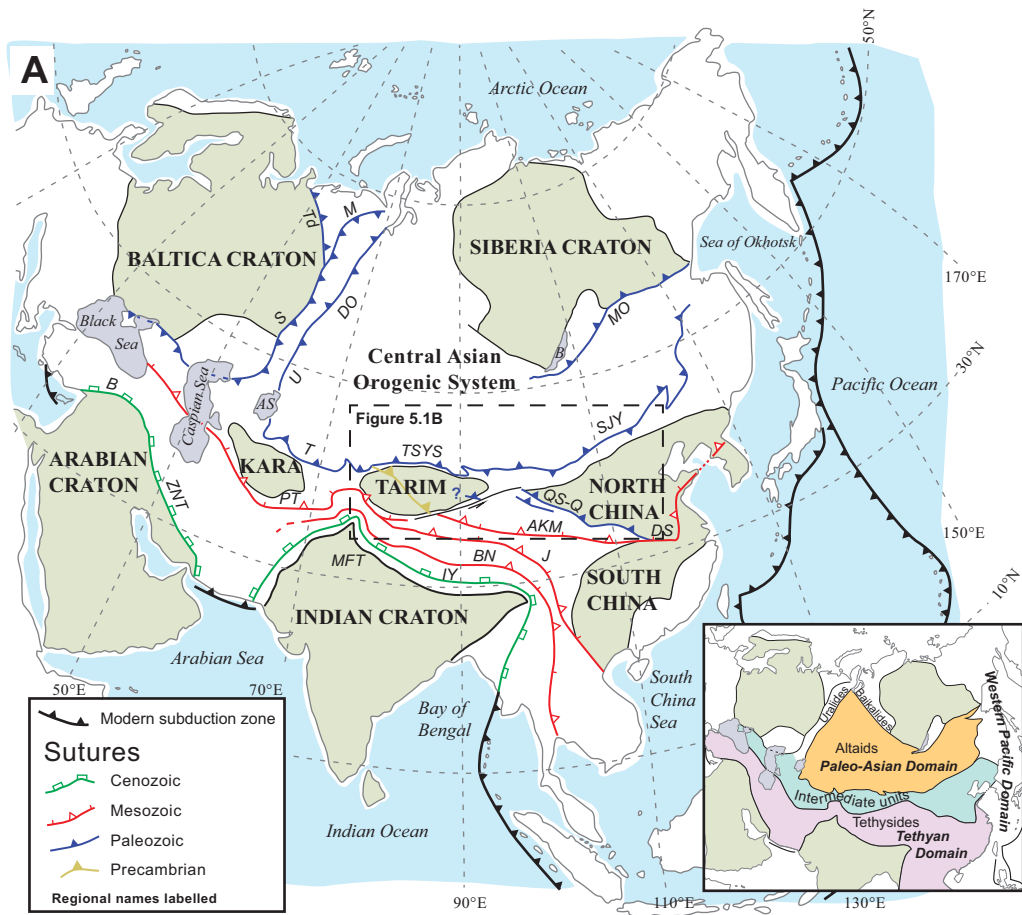
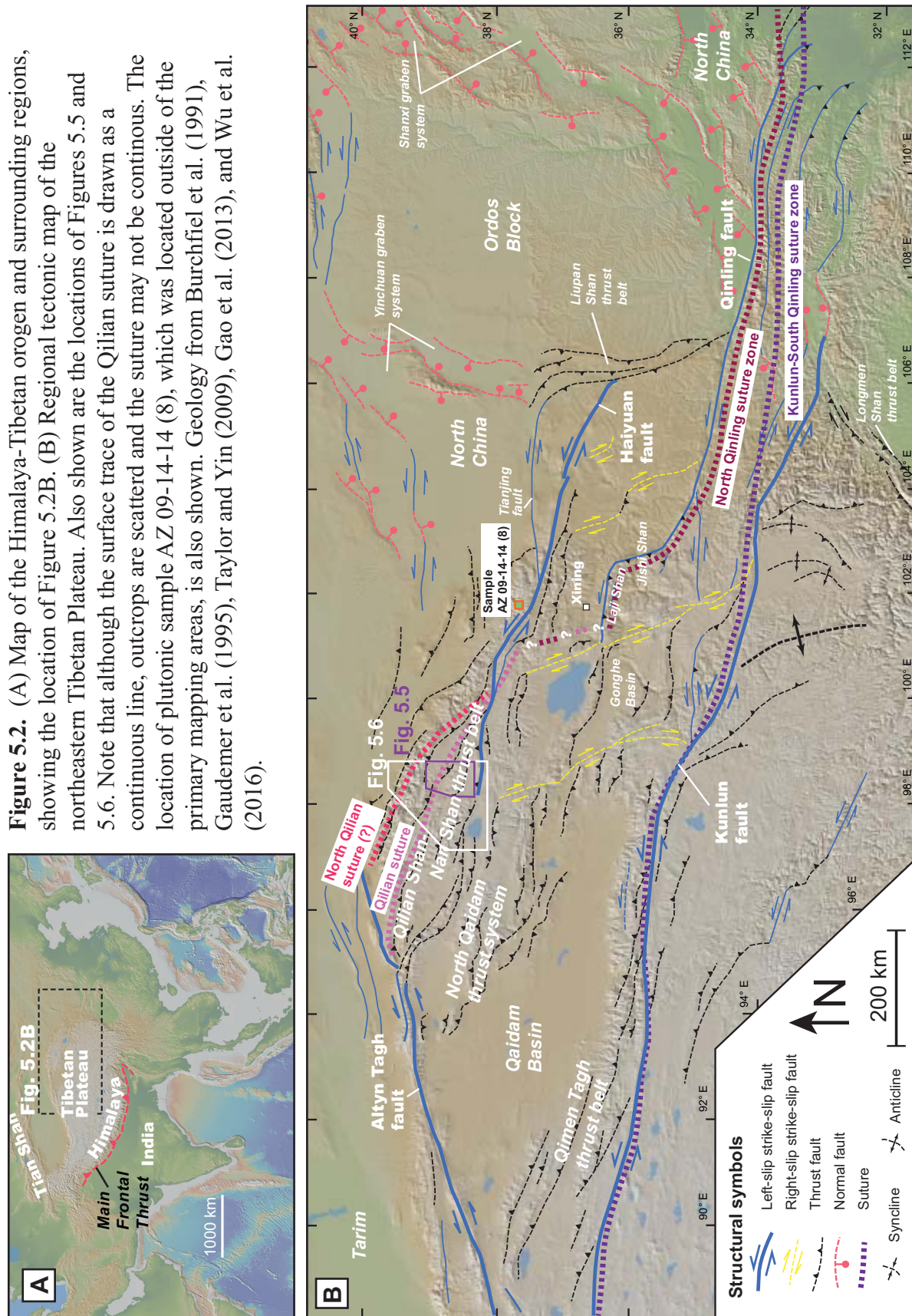


Figure 5.1. Complete figure caption on following page.

**Figure 5.1 (continued).** (A) Simplified tectonic map of Asia showing cratons, sutures, and modern subduction zones. Teeth on are on over-riding plate. For simplicity, the structures and sutures within the Central Asian Orogenic System are omitted. Pre-Neoproterozoic sutures within cratons are not shown. Inset map shows major tectonic division and oceanic domains. Also shown is the location of Figure 5.1.B. AS—Aral Sea, B—Lake Baikal, Kara—Karakum Craton, MFT—Main Frontal Thrust. Labelled sutures: AKM—Anyimaqen-Kunlun-Muztagh, B—Bitlis, BN—Bangong- Nujiang, DO—Denisov-Oktyabrsk, DS—Dabie Shan, J—Jinsha, M—Magnitogorsk, MO—Mongol-Okhotsk, PT—Paleo-Tethys, S—Sakmara, SJY—Solonker-Jilin-Yanji, TSYS—Tian Shan-Ying Shan, T—Turketsan, Td—Timanide, U—Ural, QS-Q—Qilian Shan-Qinling, ZNT—Zagros-Neo-Tethys. After Yin and Nie (1996), Şengör and Natal'in (1996), Natal'in and Şengör (2005), Xiao et al. (2010), and Zheng et al. (2013). (B) Tectonic divisions of the Intermediate Units of Şengör and Natal'in (1996), the Central Asian Orogen System, and the Tethys Orogenic System. Note that the Paleo-Asian and Tethyan Oceans closed on either side of the Tarim-North China cratons. Boxed text indicates the major suture names. Also shown are the locations of intraplate ultra-high pressure (UHP) metamorphic rocks and 1.0-0.9 Ga gneiss. Figure after Yin and Nie (1996), Yin and Harrison (2000), and Wu et al. (2016).

**Figure 5.2.** (A) Map of the Himalaya-Tibetan orogen and surrounding regions, showing the location of Figure 5.2B. (B) Regional tectonic map of the northeastern Tibetan Plateau. Also shown are the locations of Figures 5.5 and 5.6. Note that although the surface trace of the Qilian suture is drawn as a continuous line, outcrops are scattered and the suture may not be continuous. The location of plutonic sample AZ 09-14-14 (8), which was located outside of the primary mapping areas, is also shown. Geology from Burchfiel et al. (1991), Gaudemer et al. (1995), Taylor and Yin (2009), Gao et al. (2013), and Wu et al. (2016).





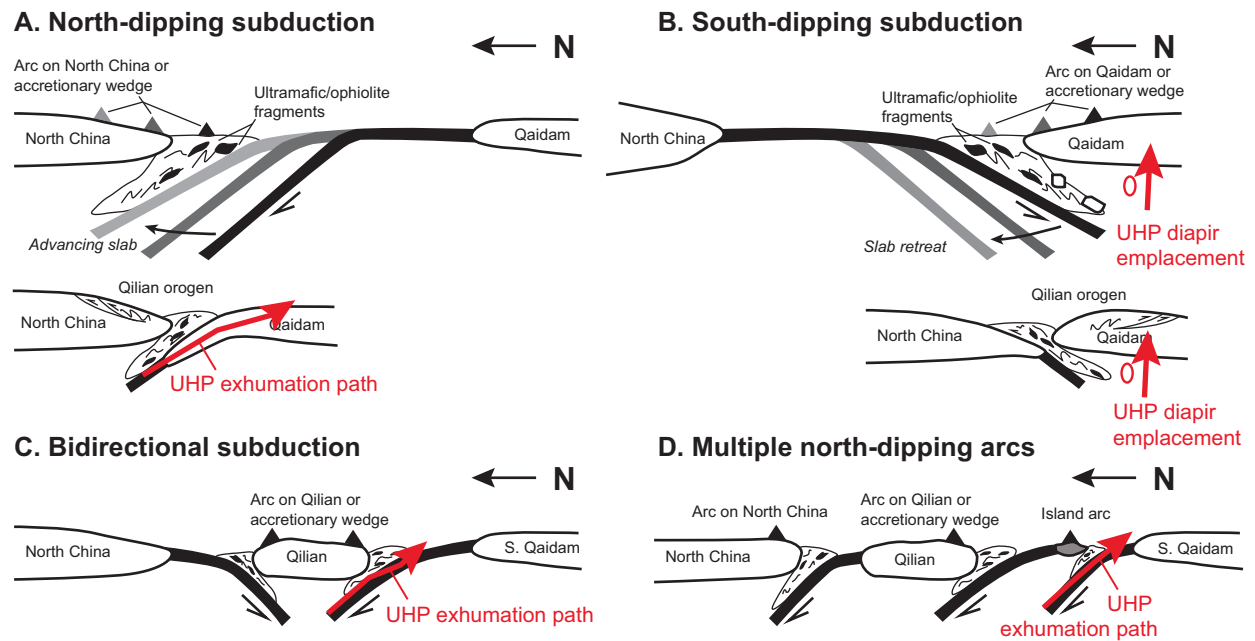


**Figure 5.3.** Major tectonic models for the development of the early Paleozoic Qilian orogen, including the implied UHP rock exhumation paths. (A) The north-dipping subduction model requires the Qilian arc to have been constructed primarily on the North China craton with northward-migrating arc magmatism caused by subduction-slab shallowing. (B) The south-dipping subduction model requires the Qilian arc to develop along the northern margin of the Qaidam microcontinent, and northward arc migration was caused by slab steepening and rollback. (C) The bidirectional subduction model requires the Qilian arcs to develop within the Qilian microcontinent. In this scenario, two suture zones should have developed, including separate collisional orogens and forearc basins. (D) The multiple north-dipping arc model requires several arc belts, suture zones, and collisional events. The arcs may have developed on the North China craton, Qilian microcontinent (or North Qaidam), accretionary wedges, and/or oceanic lithosphere. See text and Table 5.1 for further discussion and references.

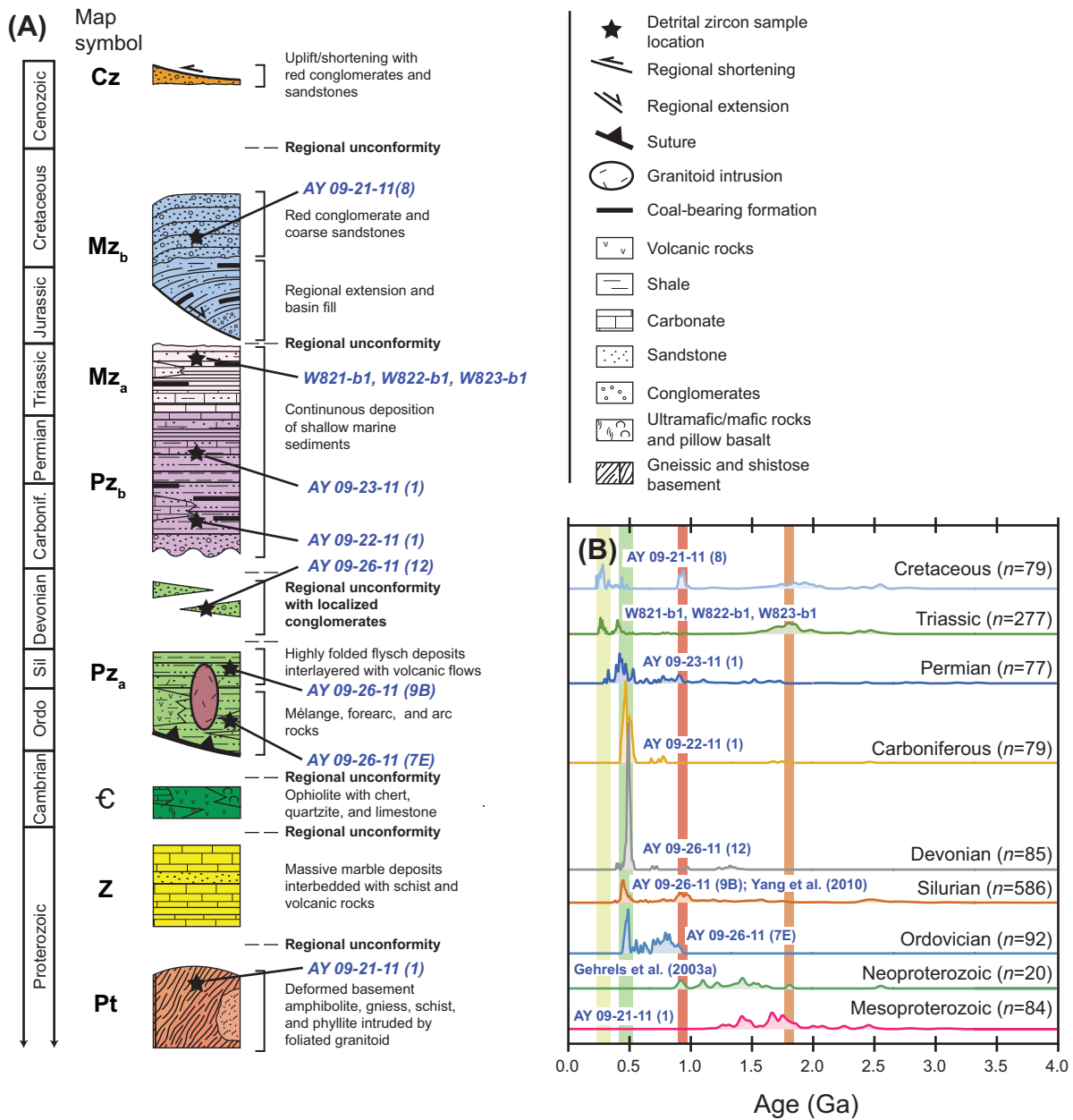


**Figure 5.4.** (A) Tectonostratigraphy of the central Qilian Shan. (B) Detrital zircon age spectra of the major tectonic units. Data from unpublished ages obtained by Y. Zhang, C. Wu, A. Yin, L. Ding, and A. Zuzva, and published sources including Gehrels et al. (2003a) and Yang et al. (2010).

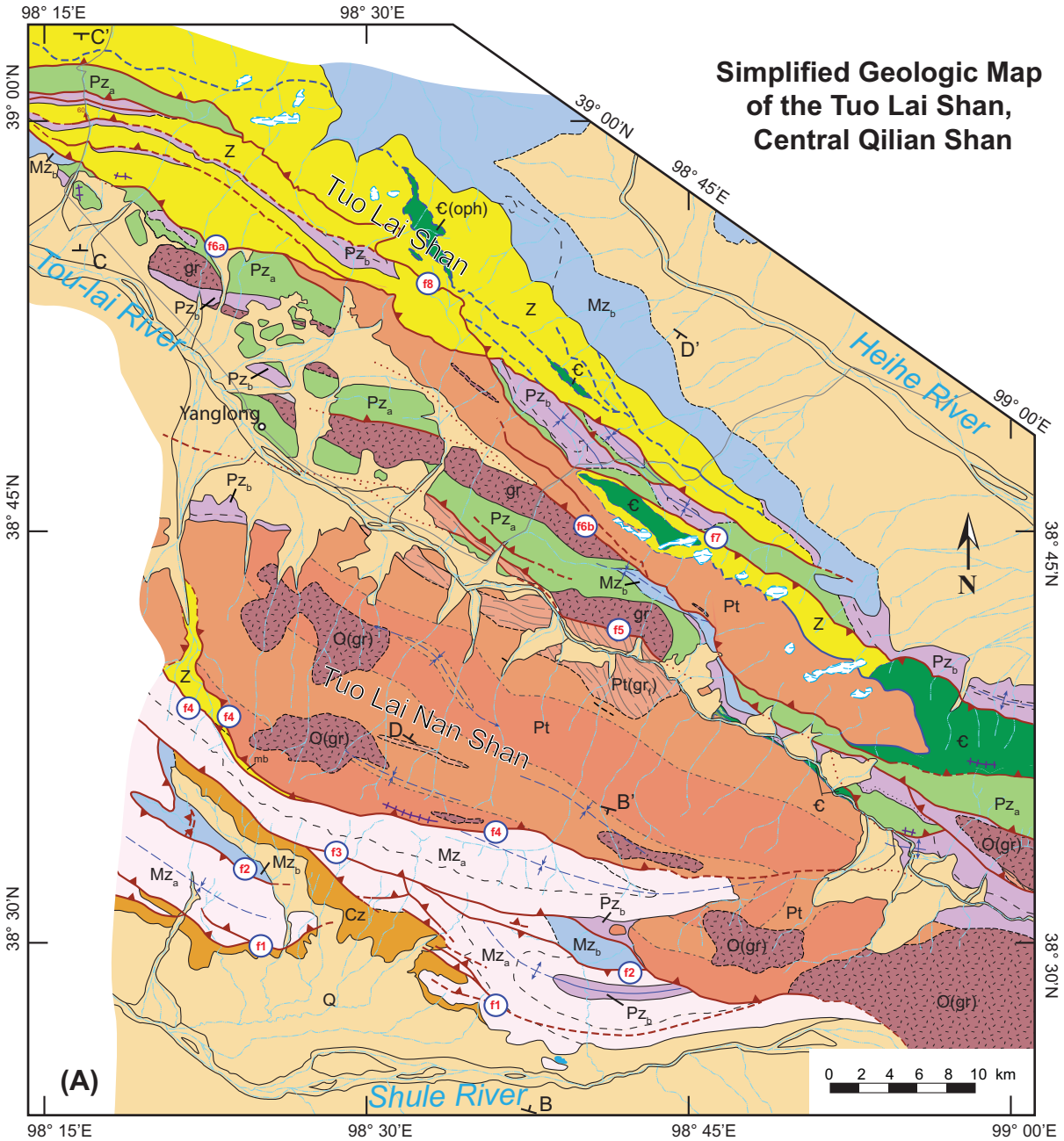
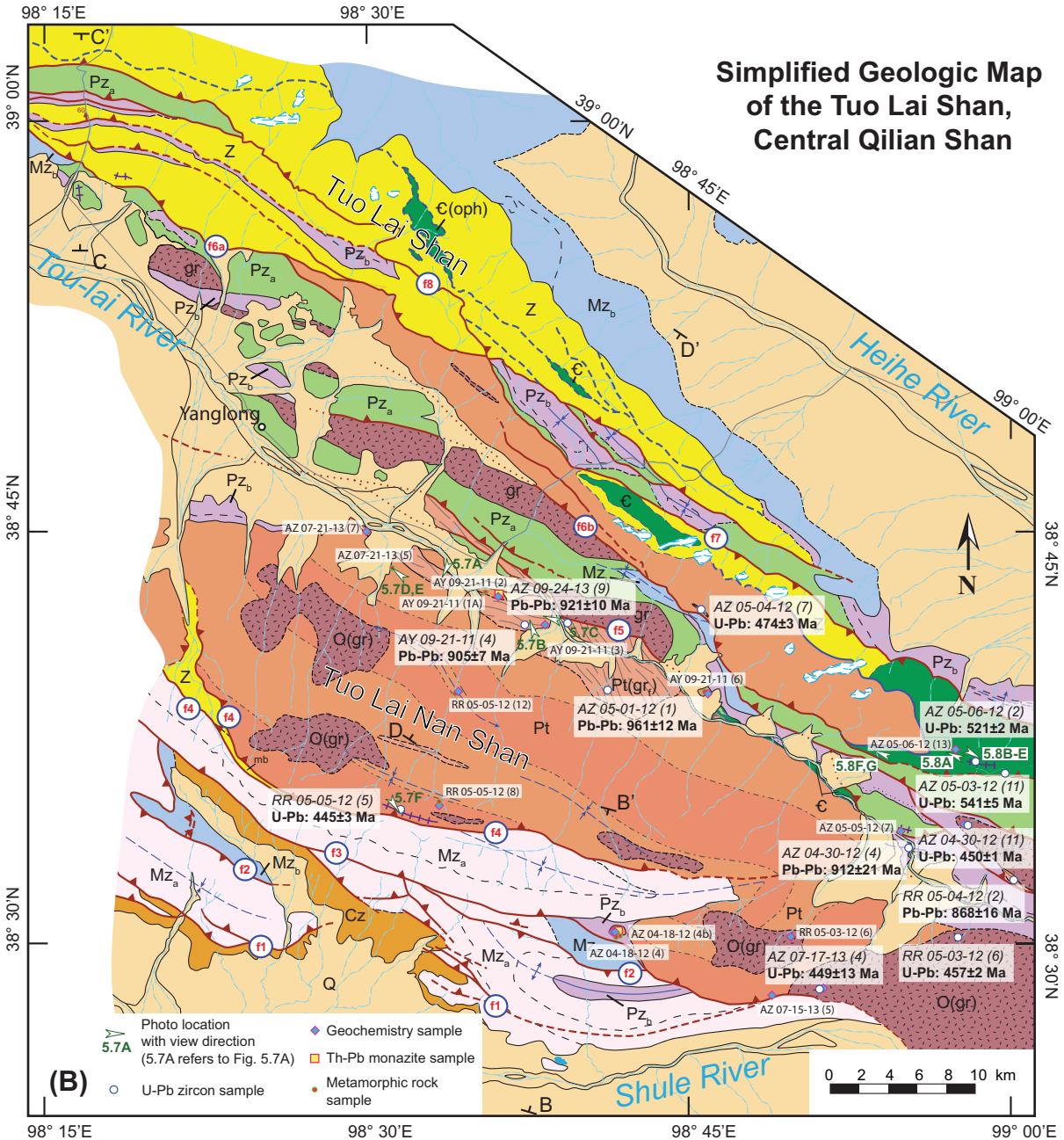


**Figure 5.5.** (A) Simplified geologic map of the Tuo Lai Nan Shan and Tuo Lai Shan in the central Qilian Shan. Note that analyzed samples are omitted for map clarity. For explanation of the geologic symbols, see Figure 2.8 or Supplementary Figure 2.



**Map units**



- Q, Quaternary fluvial and alluvial sediments
- Cz, Cenozoic fluvial sediments
- Mz<sub>b</sub>, Upper Mesozoic terrestrial deposits
- Mz<sub>a</sub>, Lower Mesozoic shallow marine rocks
- Pz<sub>a</sub>, Upper Paleozoic shallow marine rocks

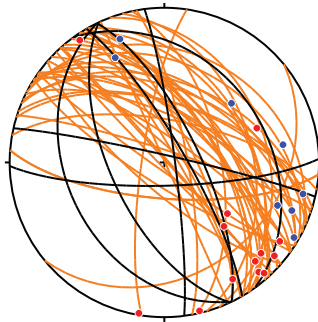
- Pz<sub>b</sub>, Lower Paleozoic mélangé, forearc, and arc rocks
- C, Cambrian ophiolitic complex
- Z, Neoproterozoic marble and schist
- Pt, Proterozoic schist and gneiss
- O(gr), Ordovician granitoid
- Pt(gr), Proterozoic foliated granitoid

**Figure 5.5 (continued).** (B) Simplified geologic map of the Tuo Lai Nan Shan and Tuo Lai Shan in the central Qilian Shan showing analyzed samples. Note that the map is the same as A, except that sample and field photograph locations are indicated. For explanation of the geologic symbols, see Figure 2.8 or Supplementary Figure 2.

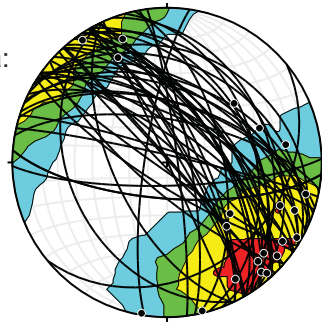
**(C) Unfolded pre-Carboniferous structural data**

Stretching lineation ( · )  
and foliation ( / ) data from:

-  North of f4
-  South of f4



All data:



Mean lineation: 12/119

Mean foliation: 126/84SW

**Figure 5.5 (continued).** (C) Unfolded structural data (i.e., foliation and lineation attitudes) from the metamorphic basement units that represent the pre-Carboniferous state.

## Regional geologic map of the Central Qilian Shan-Nan Shan thrust belt

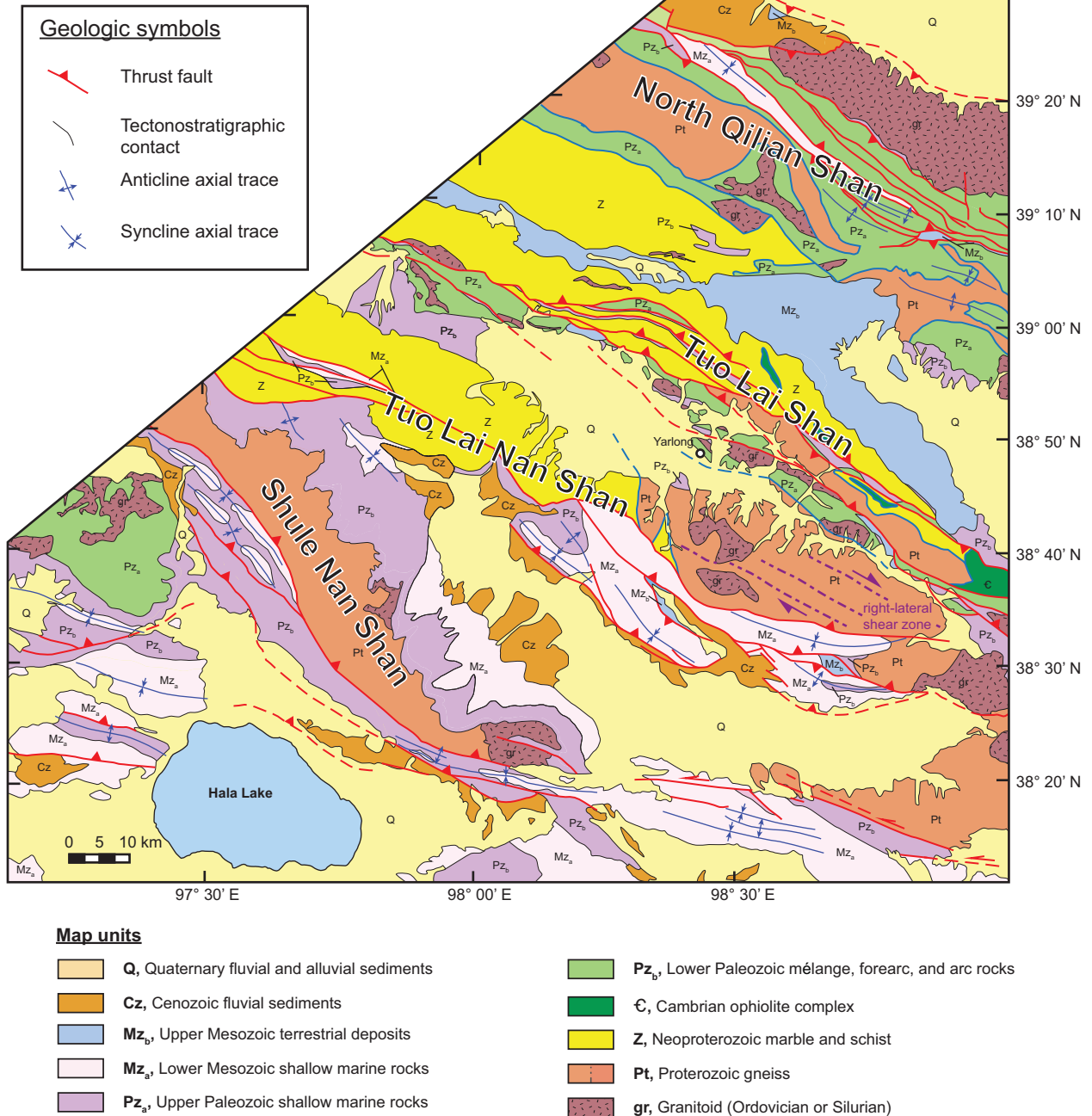


**Figure 5.6.** Regional geologic map of the central Qilian Shan-Nan Shan thrust belt based on Gansu Geological Bureau (1989), Qinghai BGMR (1991), Pan et al. (2004), and my own geologic mapping and structural interpretations. The map units are from a simplified tectonostratigraphic scheme presented in Figure 5.4A. Location is shown in Figure 5.2B.

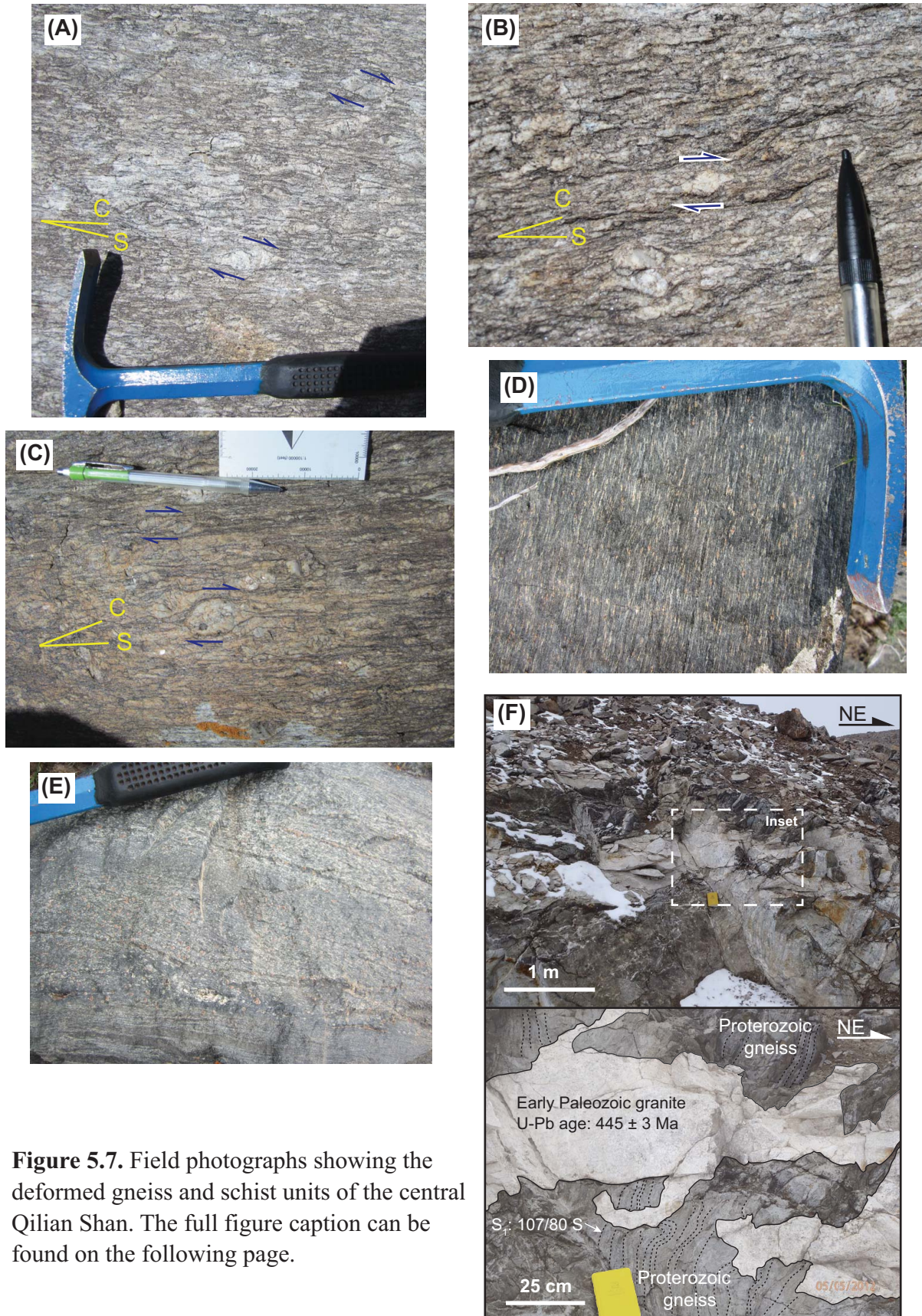


**Figure 5.7.** Field photographs showing the deformed gneiss and schist units of the central Qilian Shan. The full figure caption can be found on the following page.

**Figure 5.7 (continued).** Field photographs showing outcrops from the deformed gneiss and schist units of the central Qilian Shan. (A-C) Foliated granitoid rocks, often mylonitized, showing a right-lateral shear sense. Rocks have a near-vertical northwest-striking foliation. (D-E) Strongly foliated garnet amphibolite rocks. Rocks have a near-vertical northwest-striking foliation. Note the plagioclase coronas rimming the garnet grains. Shear sense in these rocks is also right-lateral. (F) An undeformed early Paleozoic granitoid dike crosscuts the Proterozoic gneiss. The apparent U-Pb zircon crystallization age of the dike constrains the maximum age of metamorphism of the gneiss.



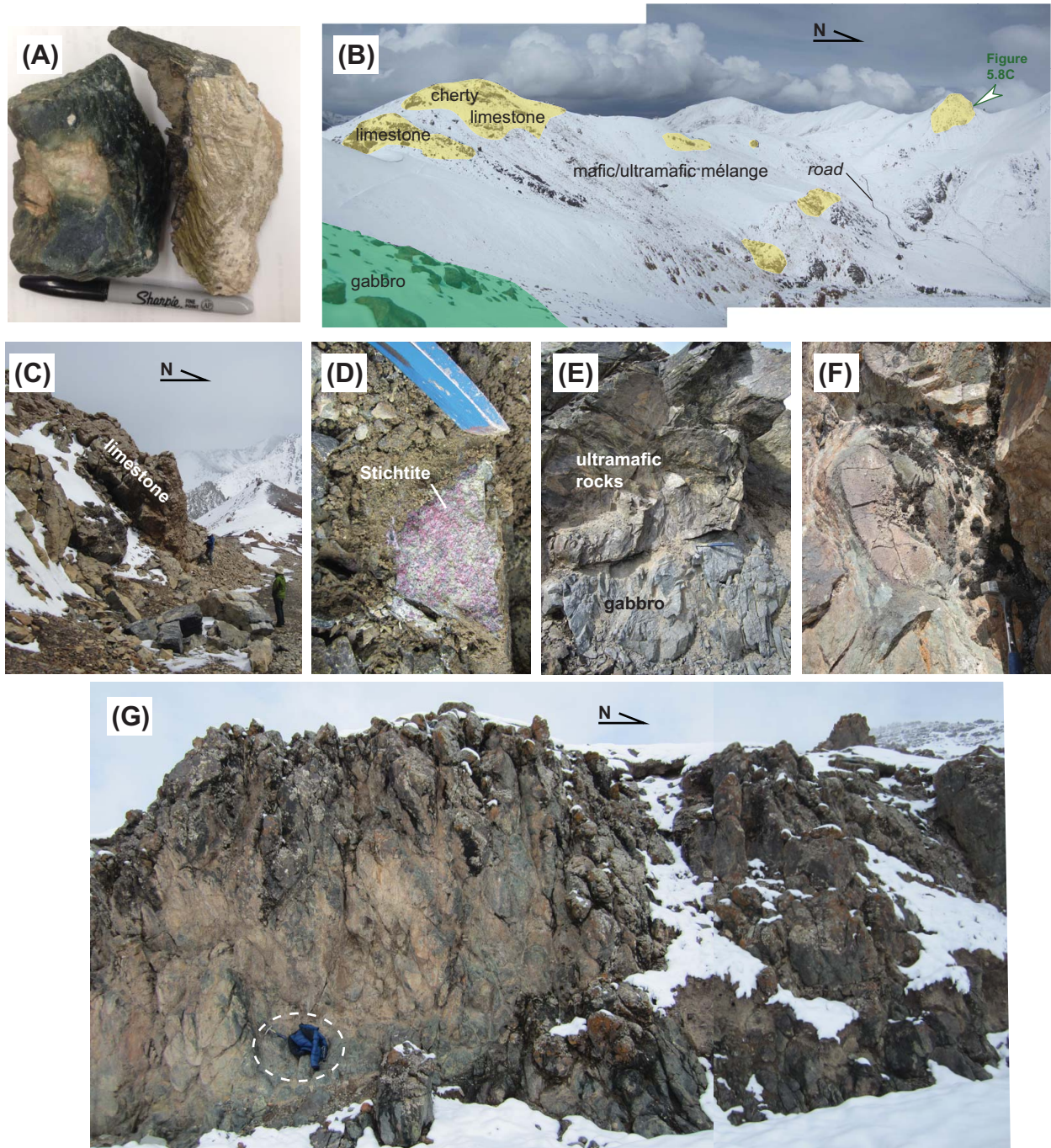


**Figure 5.8.** Field photographs from the ophiolitic mélangé complex of the central Qilian Shan. (A) Serpentinite samples with light-green colored asbestos veins. (B) View of cherty-sandy “knockers” in mélangé material. Sketched outlines highlight approximate location, size, and position of “knockers” within the mélangé. (C) Outcrop view of limestone “knocker” within mélangé. Location of outcrop is indicated in B. (D) Stichite from a vein within the ultramafic complex. Hammer adze for scale. (E) Massive plagioclase-pyroxene gabbro (bottom) in fault contact with ultramafic rocks (top). Note that the hammer, for scale, is near the fault surface. (F) Close-up view of pillow basalt, with a rock hammer for scale. (G) Outcrop of pillow basalts. Note the circled jacket and rock hammer for scale.

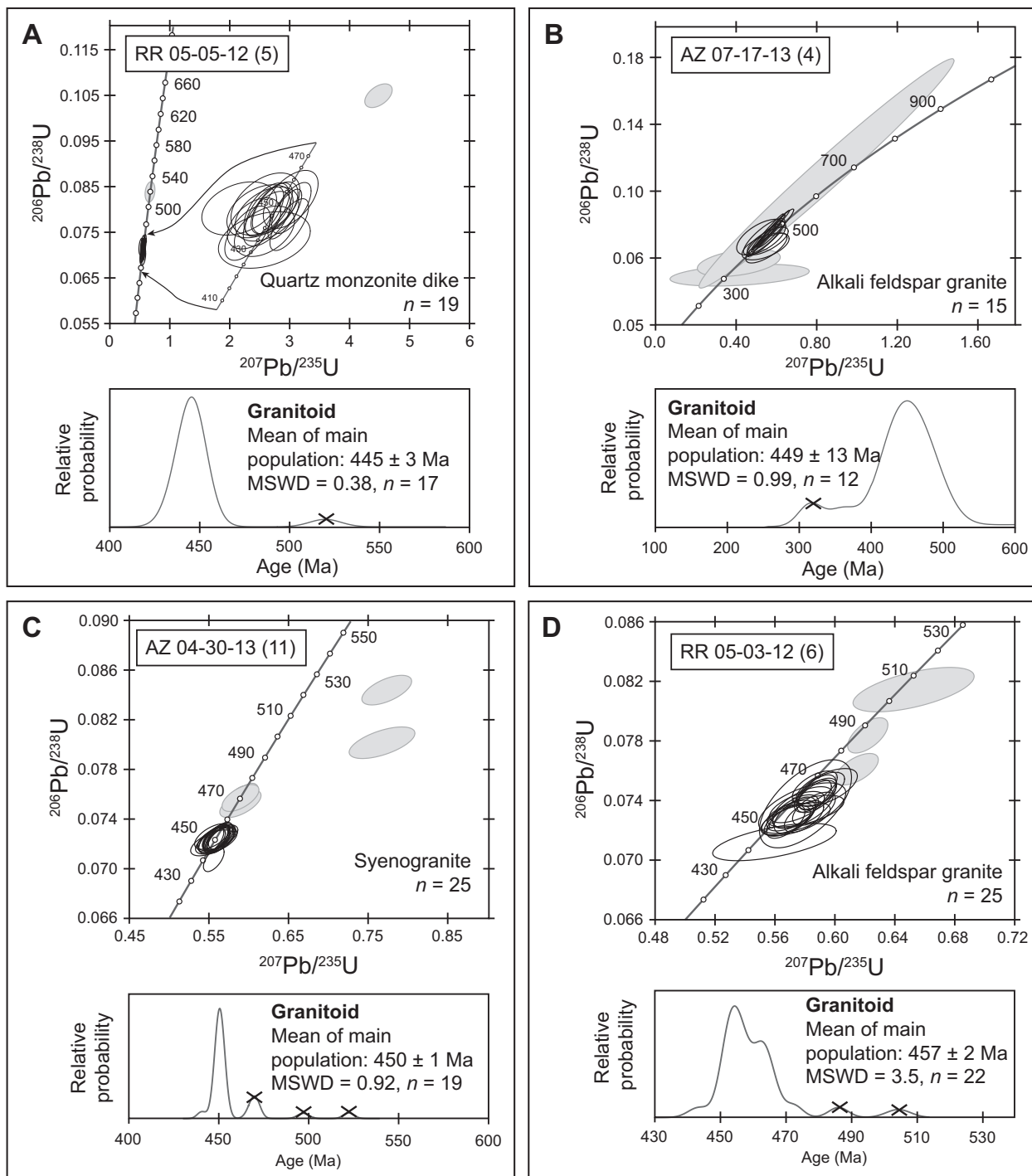


Figure 5.9 (continued). Complete figure caption can be found on page following I-L.

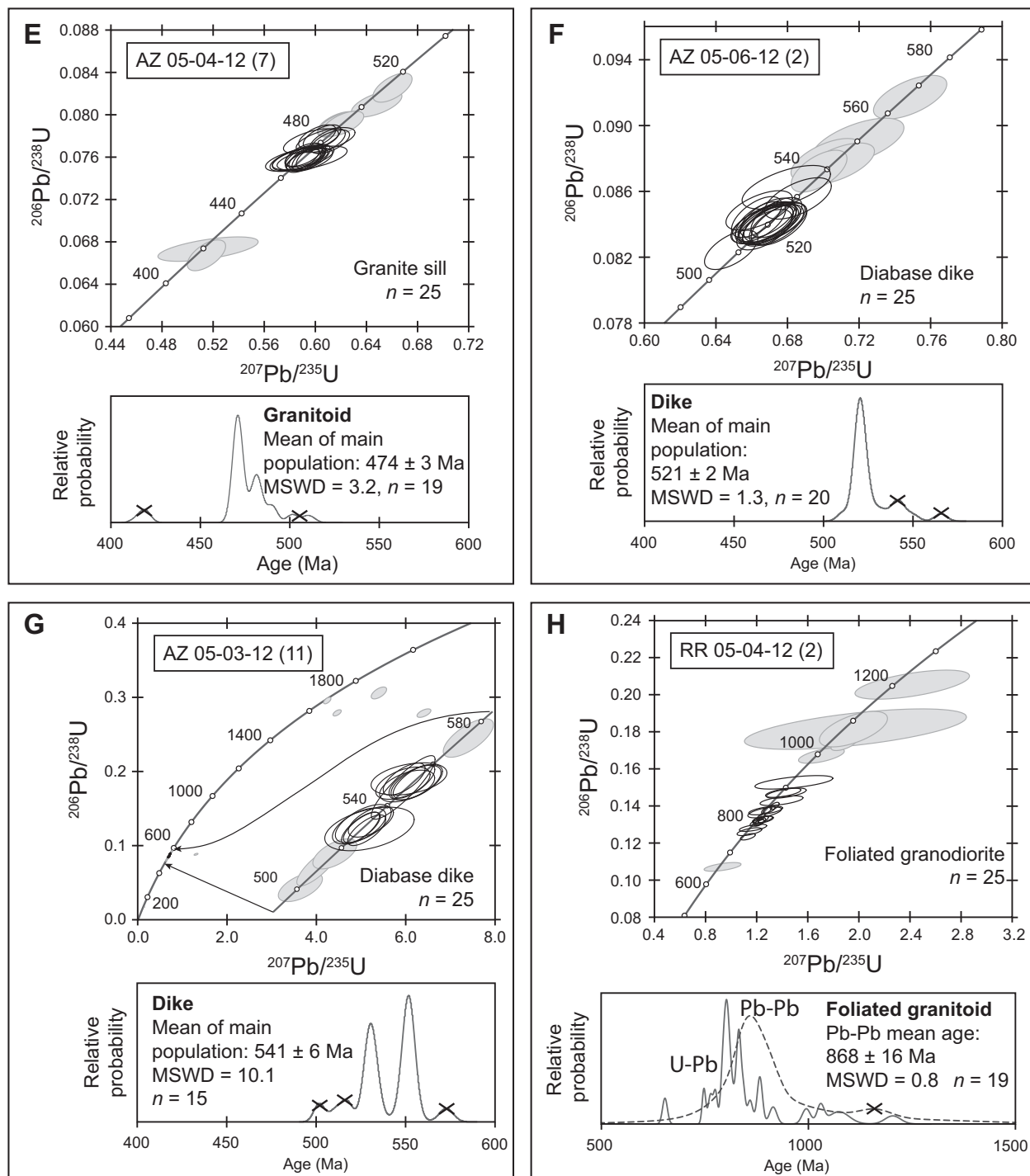


Figure 5.9 (continued). Complete figure caption can be found on page following I-L.

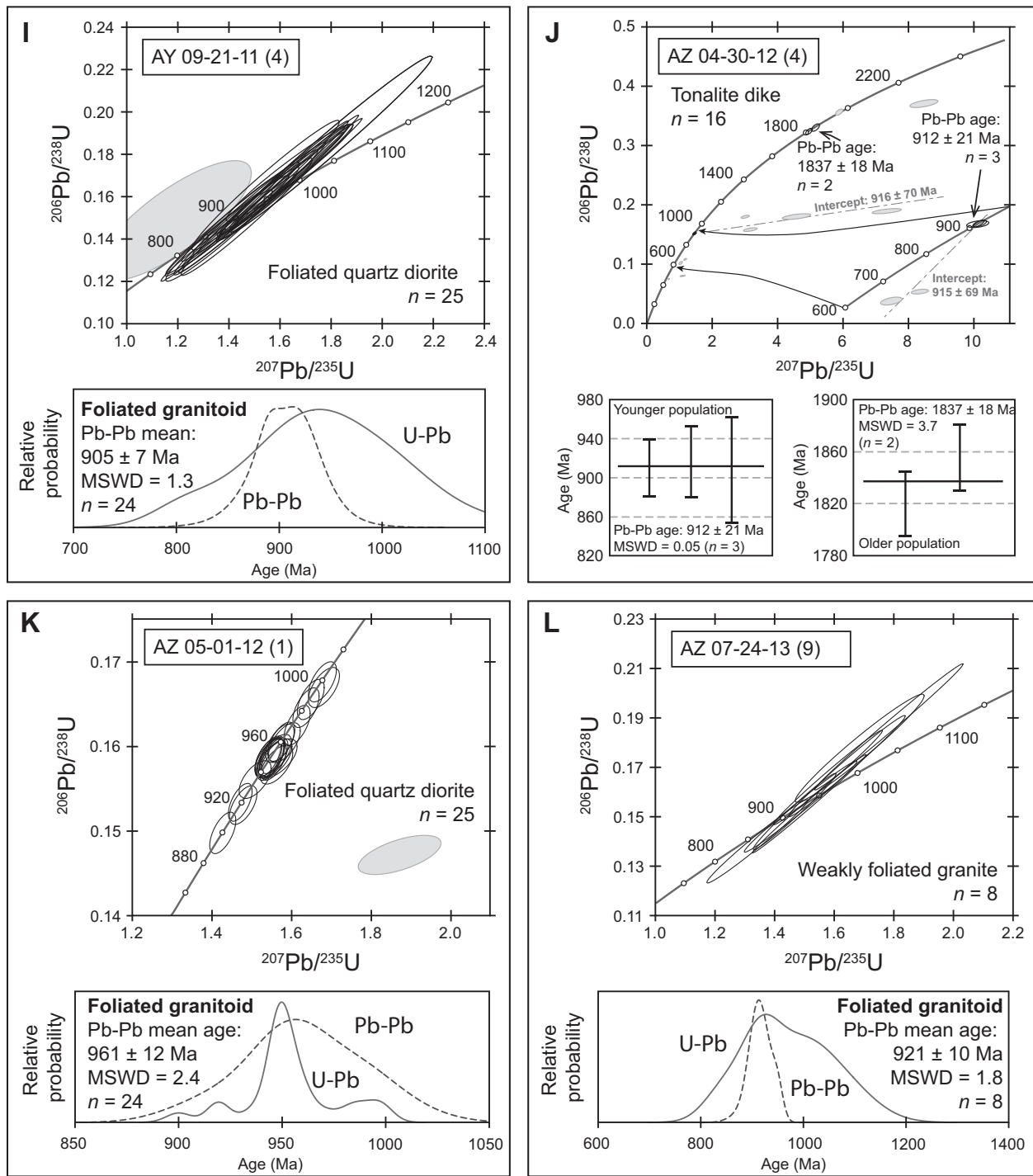
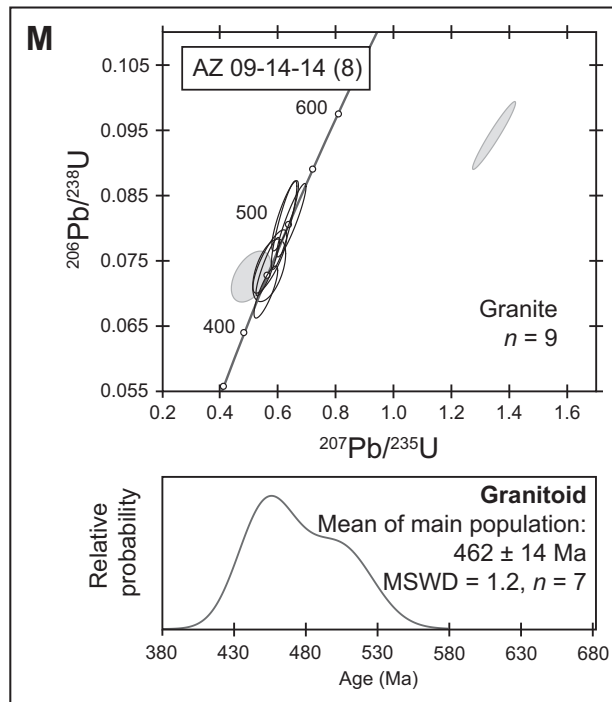
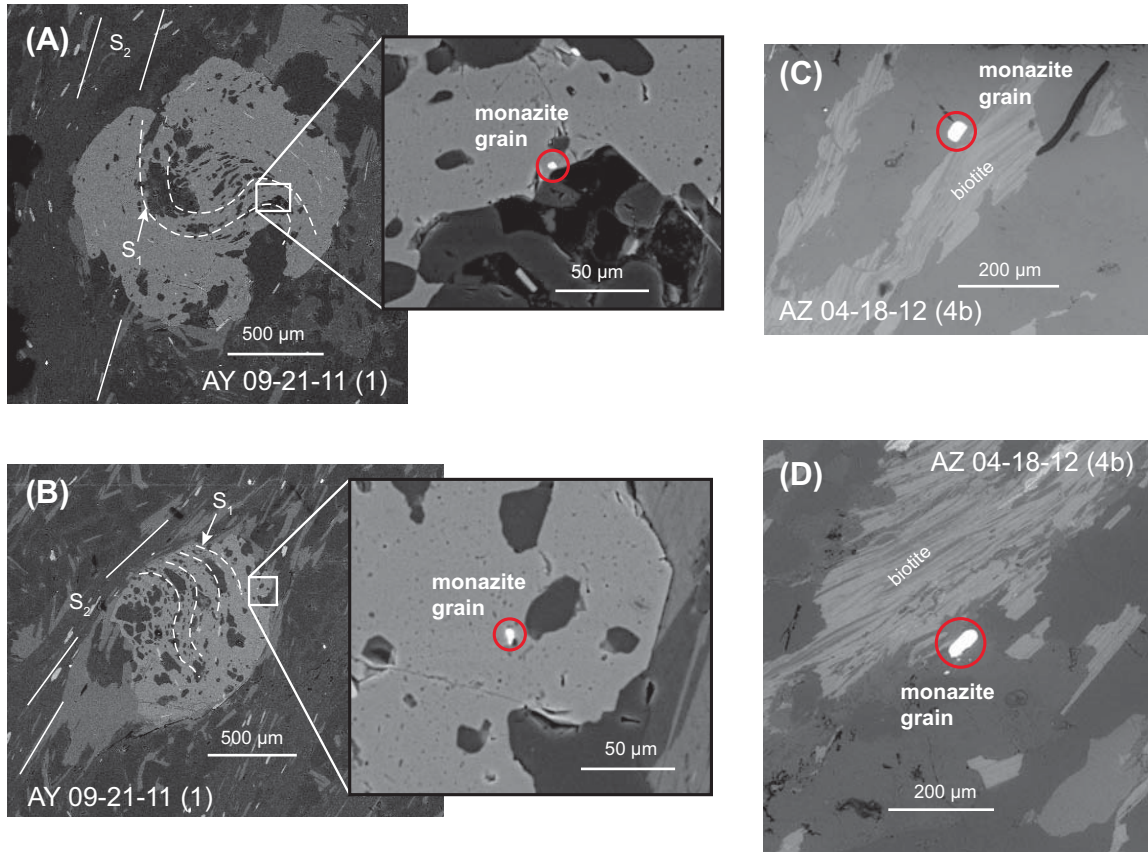


Figure 5.9 (continued). Complete figure caption on following page.



**Figure 5.9 (continued).** U-Pb concordia diagrams showing results of single shot zircon analyses and relative probability plots of zircon ages for each sample. Error ellipses are  $2\sigma$  and grey shaded ellipses show individual analyses that were excluded from weighted mean calculations. Only concordant ages are plotted in probability distributions and crossed out peaks were not included in weighted mean calculation. All weighted mean ages are U-Pb ages (unless specified) at the 95% confidence level. See text for further discussion of rationale and Figure 5.6 for sample locations. Note that tonalitic dike analysis shown in (J) shows a scattered spread of ages; calculated weighted mean ages of two age clusters provides age constraints on the basement that the dike intrudes. Plots were created with Isoplot 4.1 of Ludwig (2003).



**Figure 5.10.** Scanning electron microscope (SEM) image of a representative garnet and monazite grains from the garnet-mica schist samples that were targeted for in situ Th-Pb monazite dating. (A-B) Synkinematic garnet with an included monazite grain. (C-D) Matrix monazite grains. Note the size difference between matrix and included-in-garnet monazite grains.

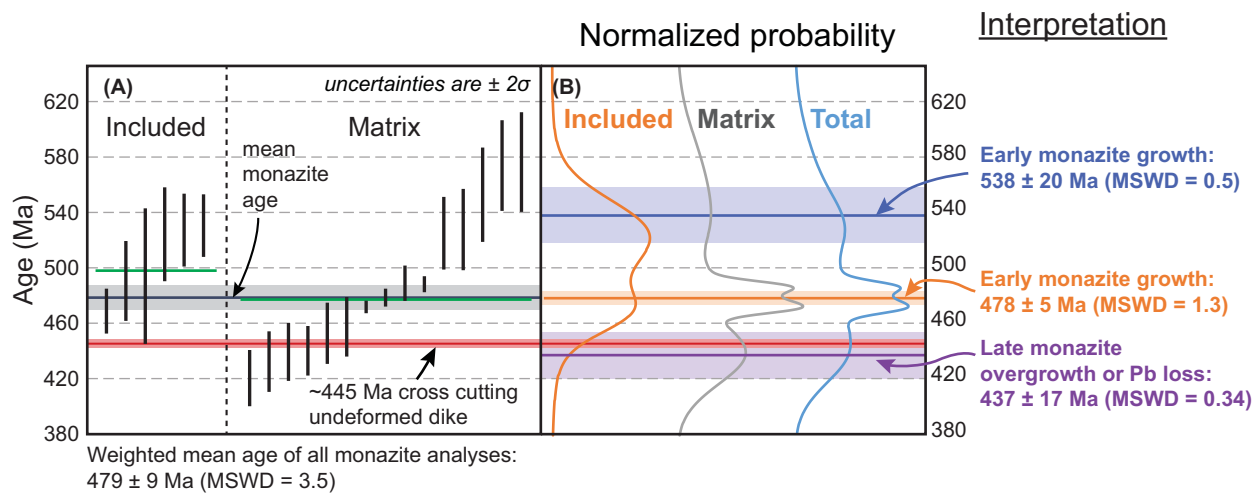


**Figure 5.11.** In-situ Pb-Th monazite dating results from metapelite samples. (A) Weighted mean ages of the entire population, the included-in-garnet grains, and the matrix grains. Also shown is the apparent U-Pb zircon crystallization age of the dike that cross cuts the foliation of the metamorphic complex. (B) Normalized probability density plot of the monazite ages of the included-in-garnet grains, matrix grains, and the total population. Interpretations of the three significant age populations are indicated.

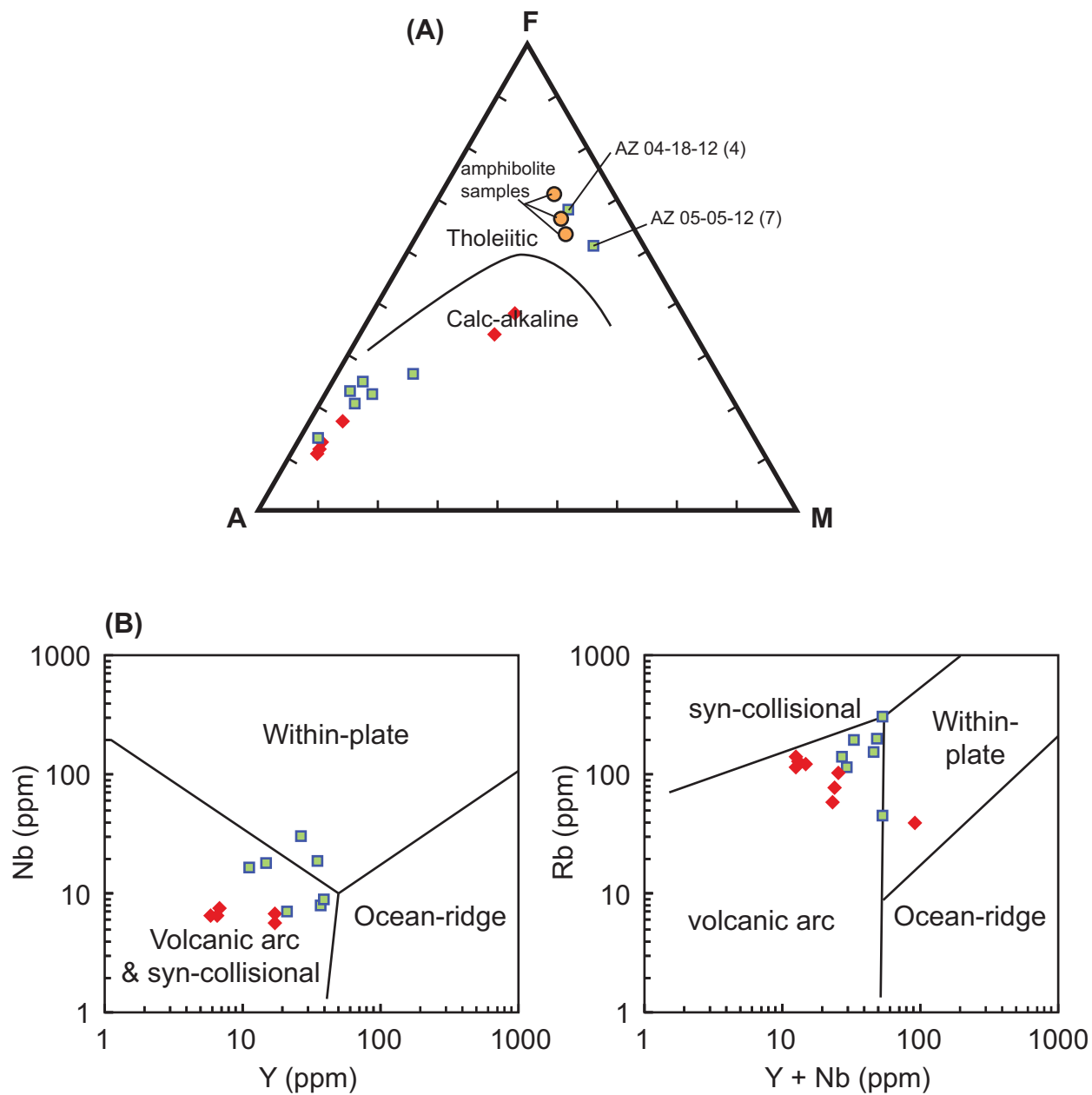


**Figure 5.12.** (A) AFM diagram for granitoid samples; A = K<sub>2</sub>O + Na<sub>2</sub>O; F = Fe<sub>2</sub>O<sub>3</sub> + FeO; M = MgO. Curve for calc-alkaline and tholeiitic division is from Kuno (1968). Only samples that fall outside of the dominant calc-alkaline trend are labelled. (B) Geochemical discrimination diagrams for granites after Pearce et al. (1984). Red diamonds from Zhang et al. (2006) and the rest are from this study.



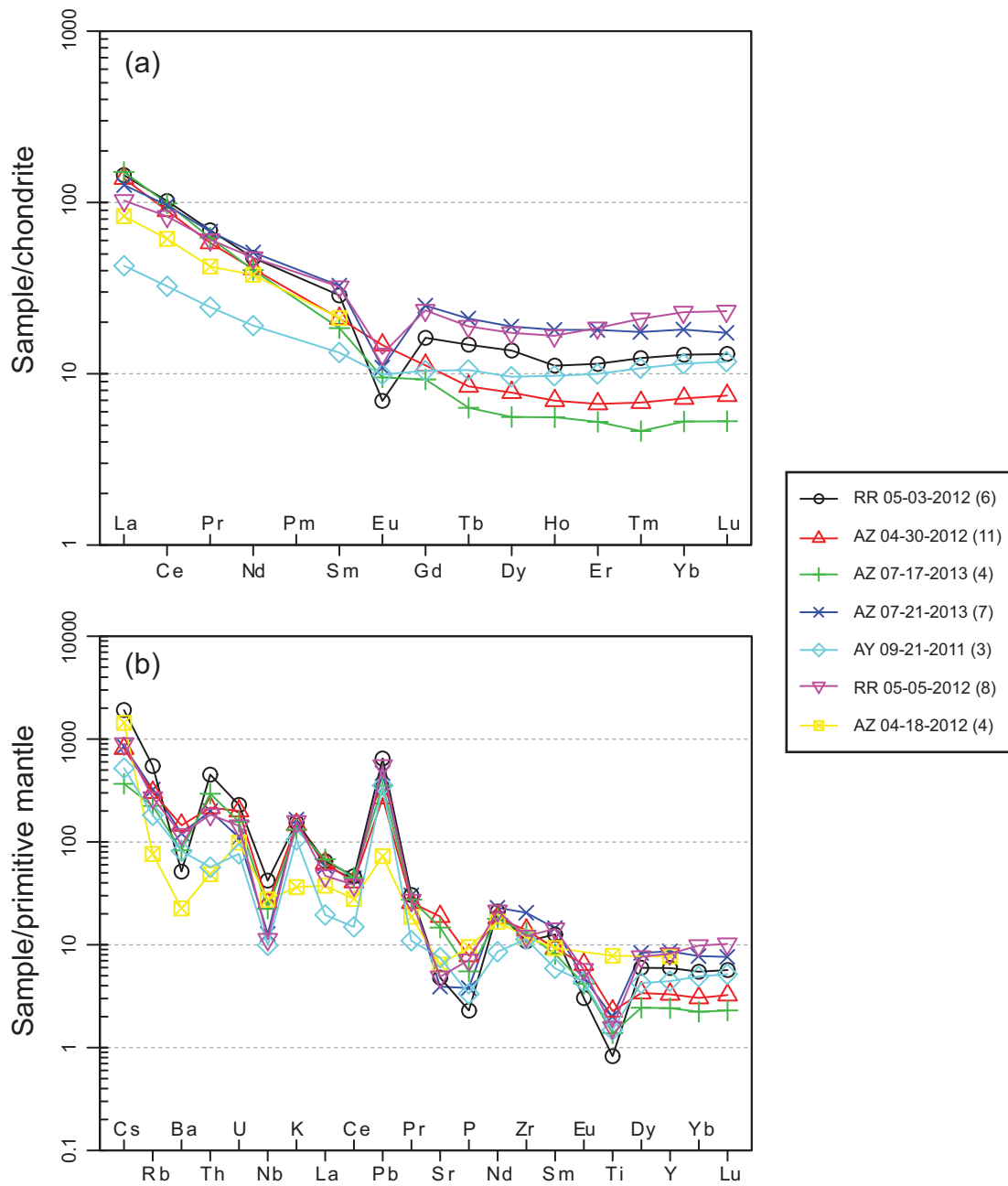


**Figure 5.13.** Trace element geochemistry. (A) Rare earth element plot normalized to chondrite of Boynton (1984). (B) Trace element plot normalized to primitive mantle values of Sun and McDonough (1989).

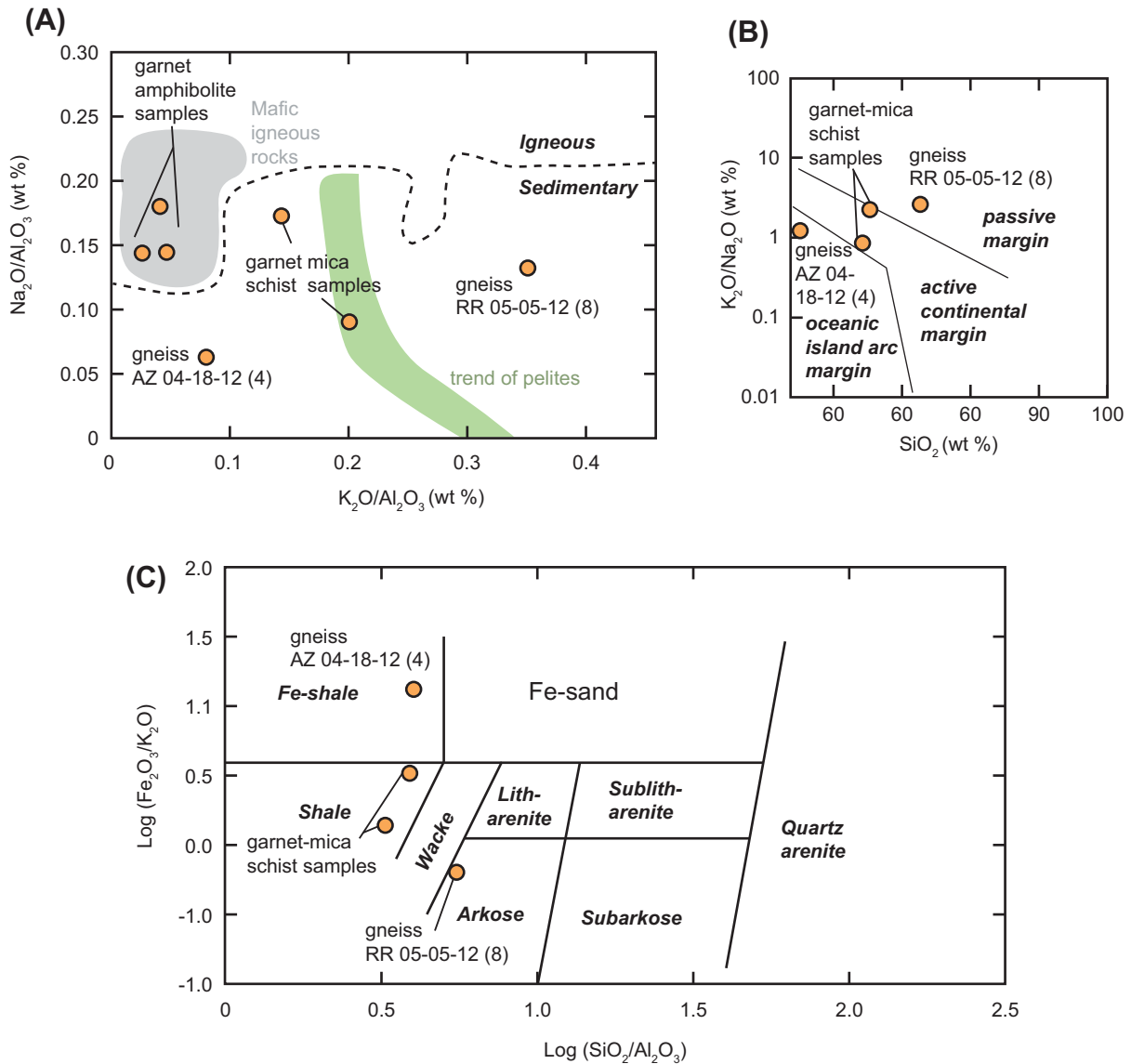
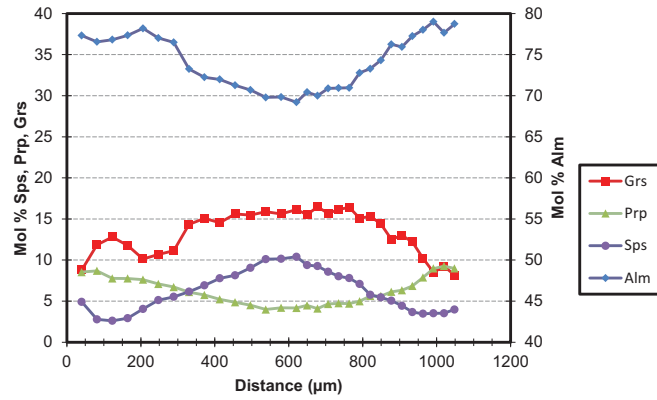
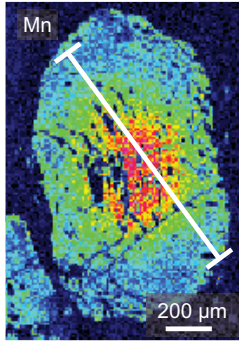
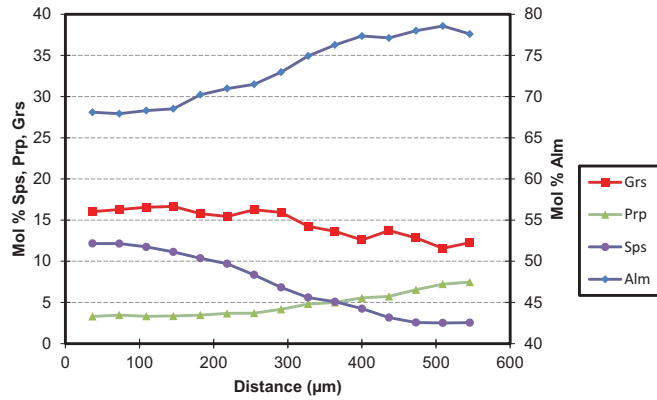
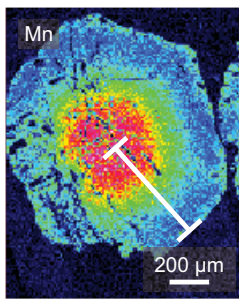


**Figure 5.14.** Geochemical discrimination diagrams for the metamorphic rock samples. (A)  $\text{K}_2\text{O}/\text{Al}_2\text{O}_3$  versus  $\text{Na}_2\text{O}/\text{Al}_2\text{O}_3$  from Garrels and MacKenzie (1971). The thick dashed line is the lower limited for most igneous rock compositions. (B) Depositional tectonic setting discrimination diagram from Roser and Korsch (1986). (C) SandClass system for geochemical classification of terrigenous sands and shales from Herron (1988).

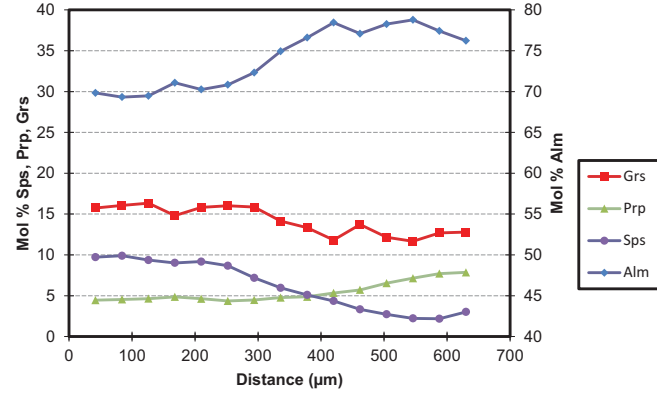
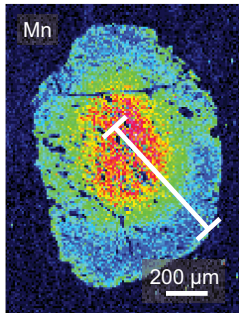
AY 09-21-11 (1A), gt2



AY 09-21-11 (1A), gt3



AY 09-21-11 (1A), gt4



AY 09-21-11 (1A), gt5

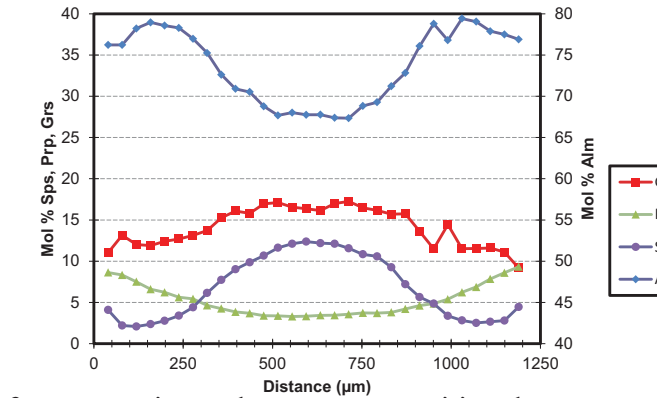
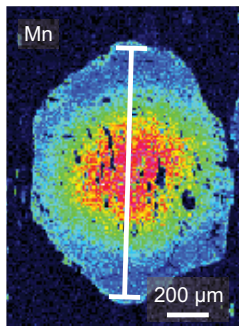
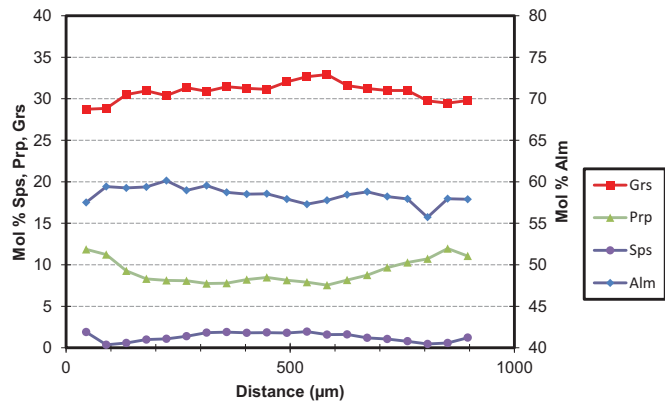
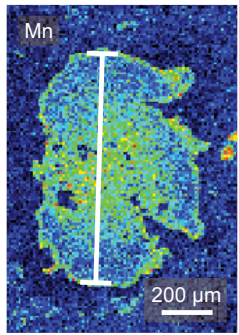
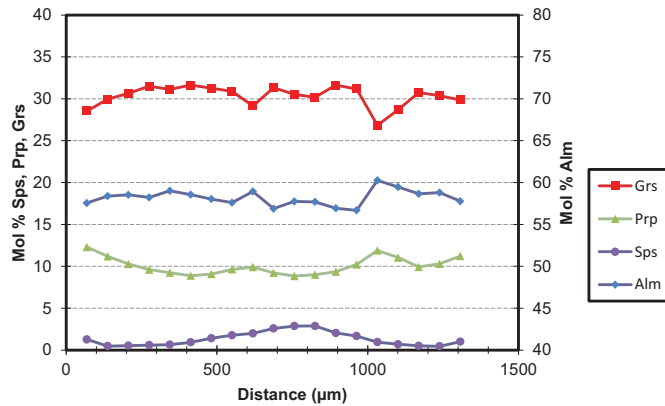
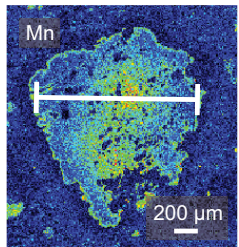


**Figure 5.15.** Mn concentration maps of garnet grains and garnet compositional traverses. Grs—grossular, Prp—pyrope, Sps—spessartine, Alm—almadine.

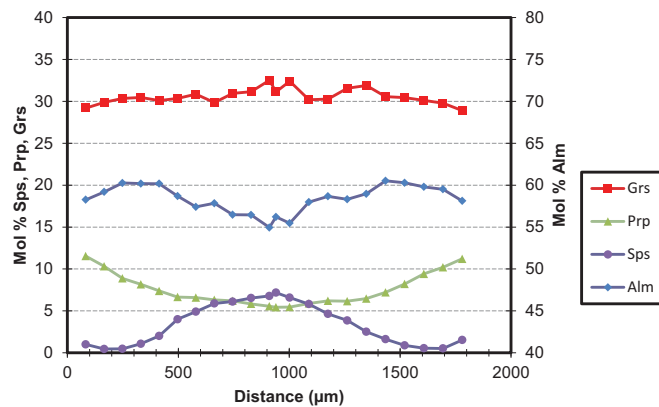
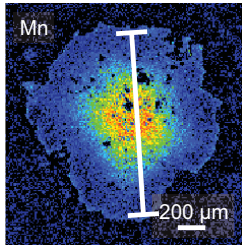
AY 09-21-11 (6A), gt2



AY 09-21-11 (6A), gt4



RR 05-05-12 (12), gt 1



RR 05-05-12 (12), gt 4

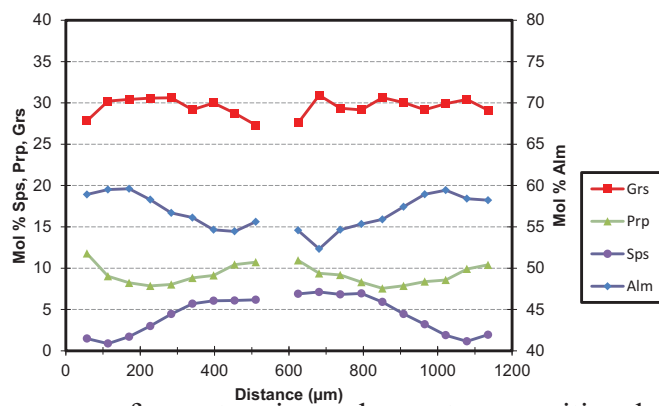
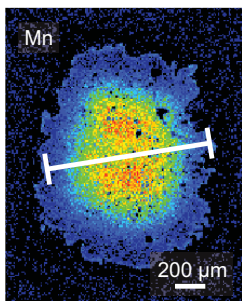
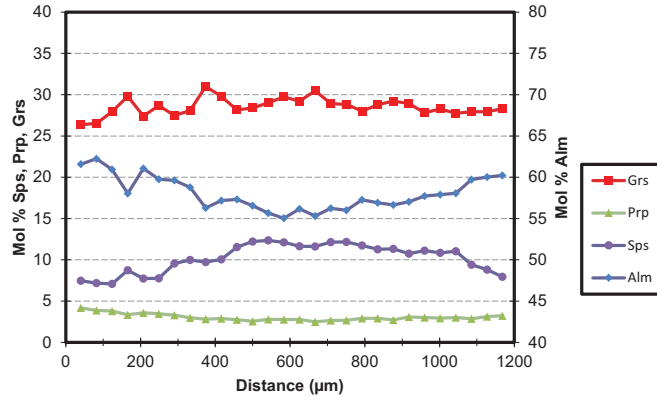
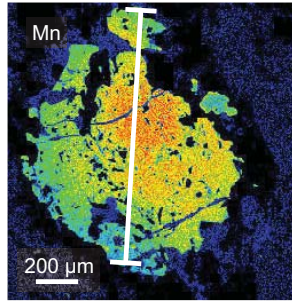
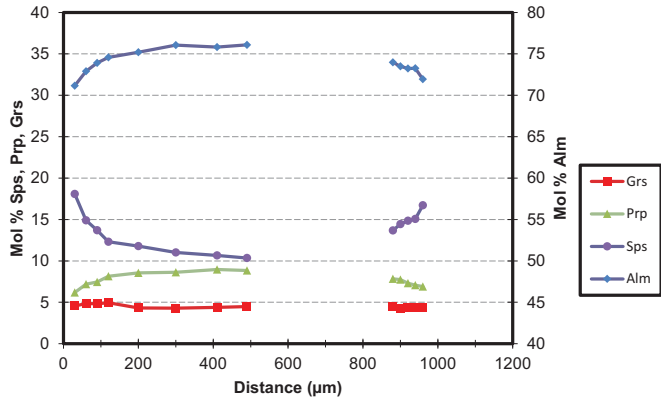
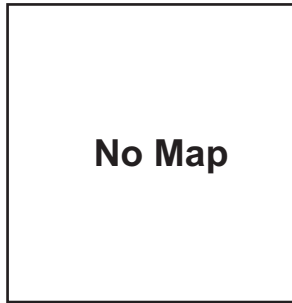


**Figure 5.15 (continued).** Mn concentration maps of garnet grains and garnet compositional traverses. Grs—grossular, Prp—pyrope, Sps—spessartine, Alm—almadine.

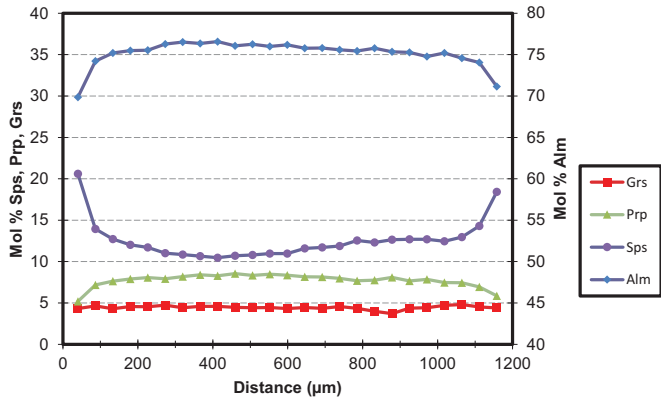
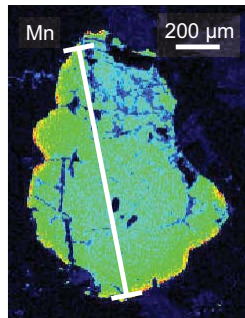
AZ 07-21-13 (5), gt 1



RR 05-05-12 (8), gt1



RR 05-05-12 (8), gt2



RR 05-05-12 (8), gt3

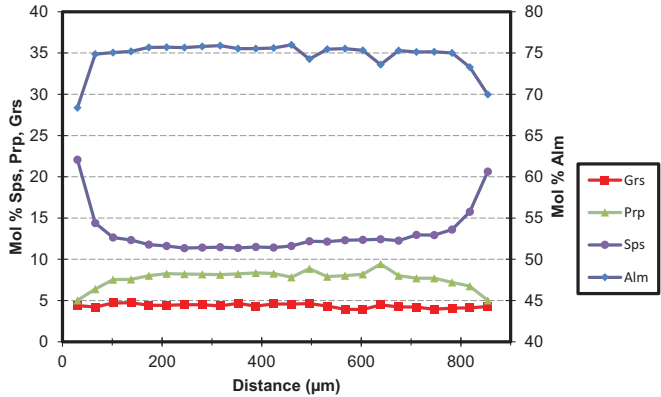
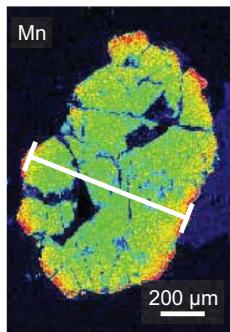
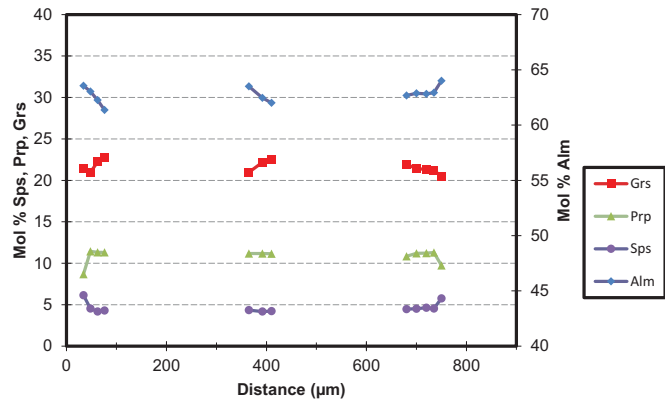
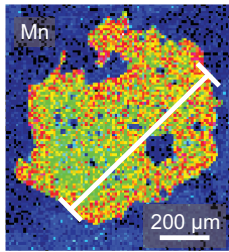
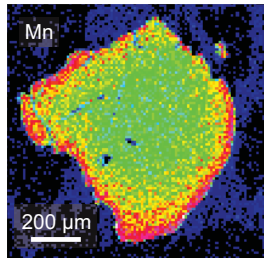


**Figure 5.15 (continued).** Mn concentration maps of garnet grains and garnet compositional traverses. Grs—grossular, Prp—pyrope, Sps—spessartine, Alm—almadine.

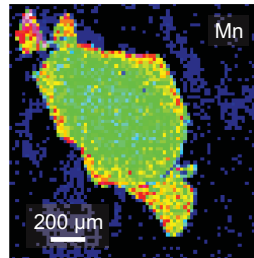
AZ 04-18-12 (4), gt1



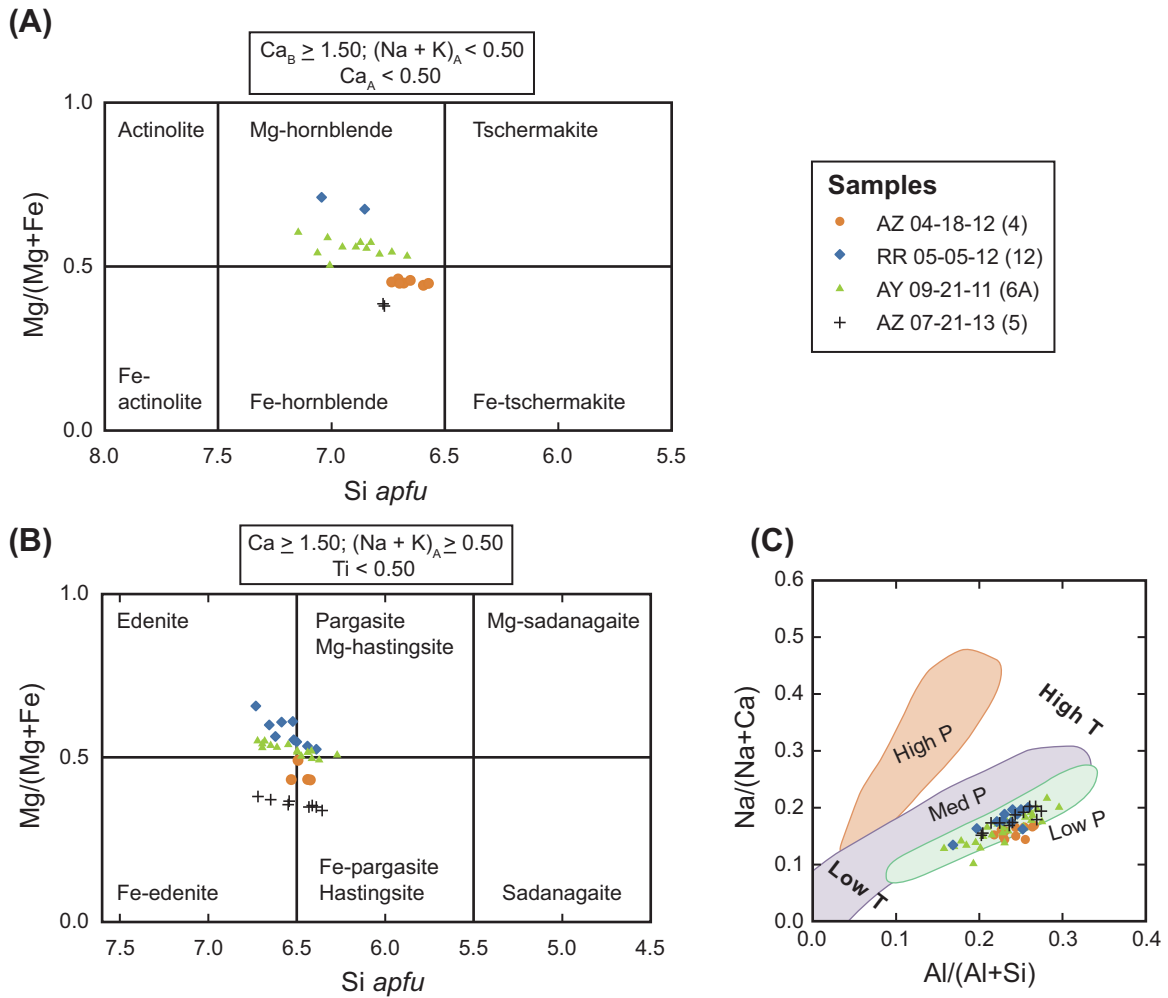
AZ 04-18-12 (4b), gt1



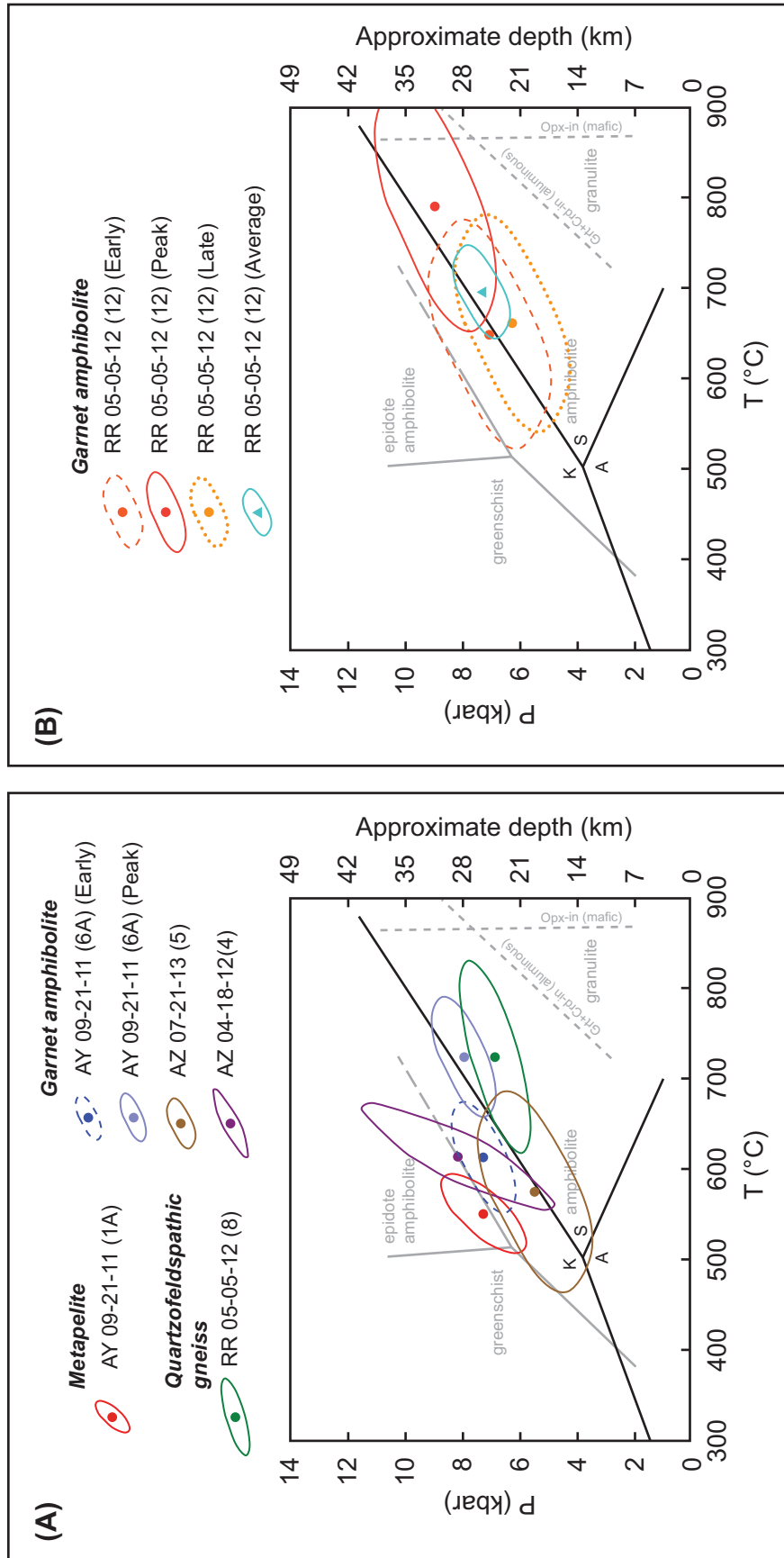
AZ 04-18-12 (4b), gt2



**Figure 5.15 (continued).** Mn concentration maps of garnet grains and garnet compositional traverses. Grs—grossular, Prp—pyrope, Sps—spessartine, Alm—almandine.

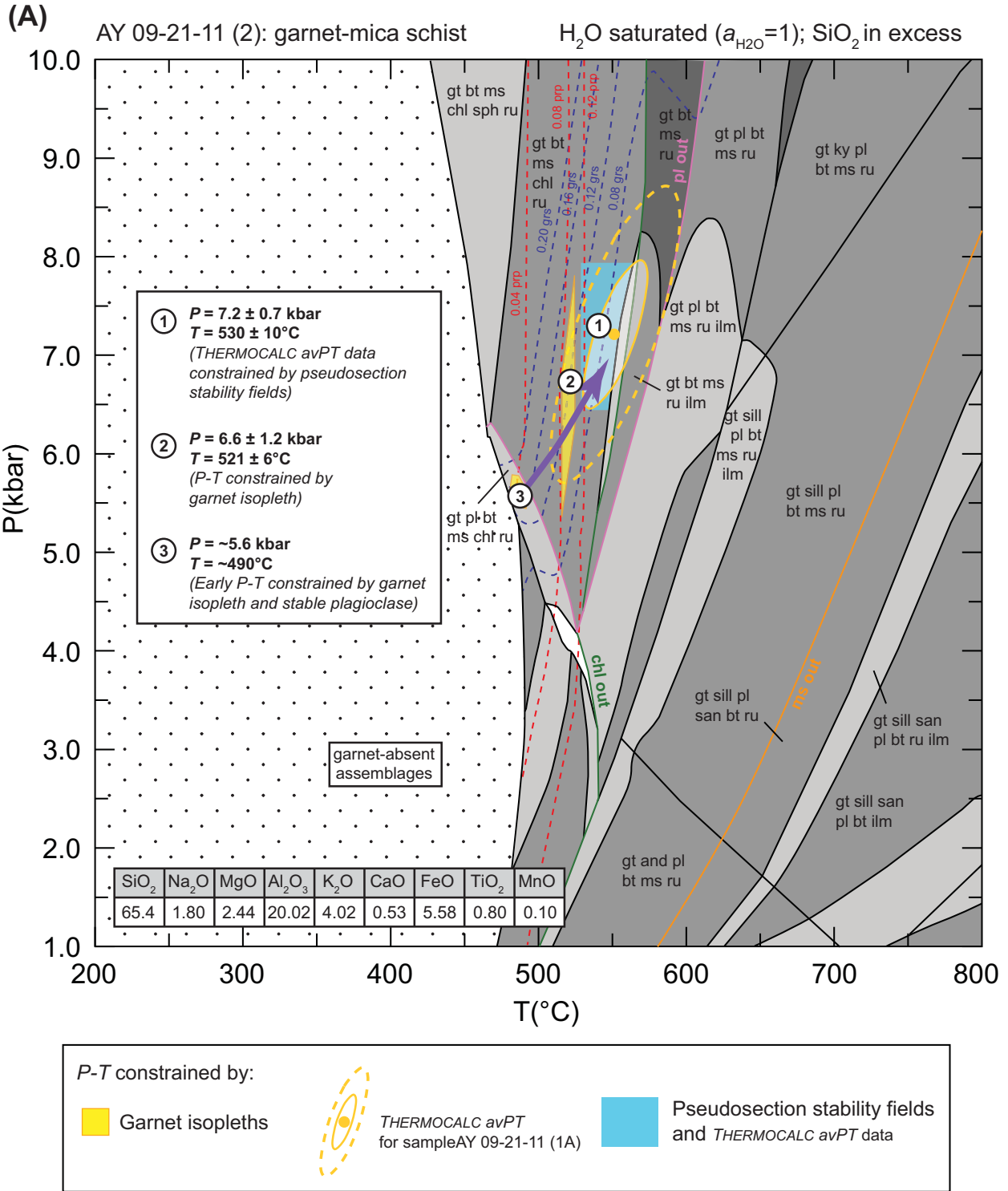


**Figure 5.16.** Amphibole classification diagrams for (A) calcic amphiboles with low A-site occupancy and (B) calcic amphiboles with high A-site occupancy. (B) Plot of Na# versus Al# for amphibole samples. Compositional ranges of amphiboles from high-, medium-, and low-pressure (P) facies series are from Laird and Albee (1981). Points are all plotted as single electron-microprobe spot analyses.

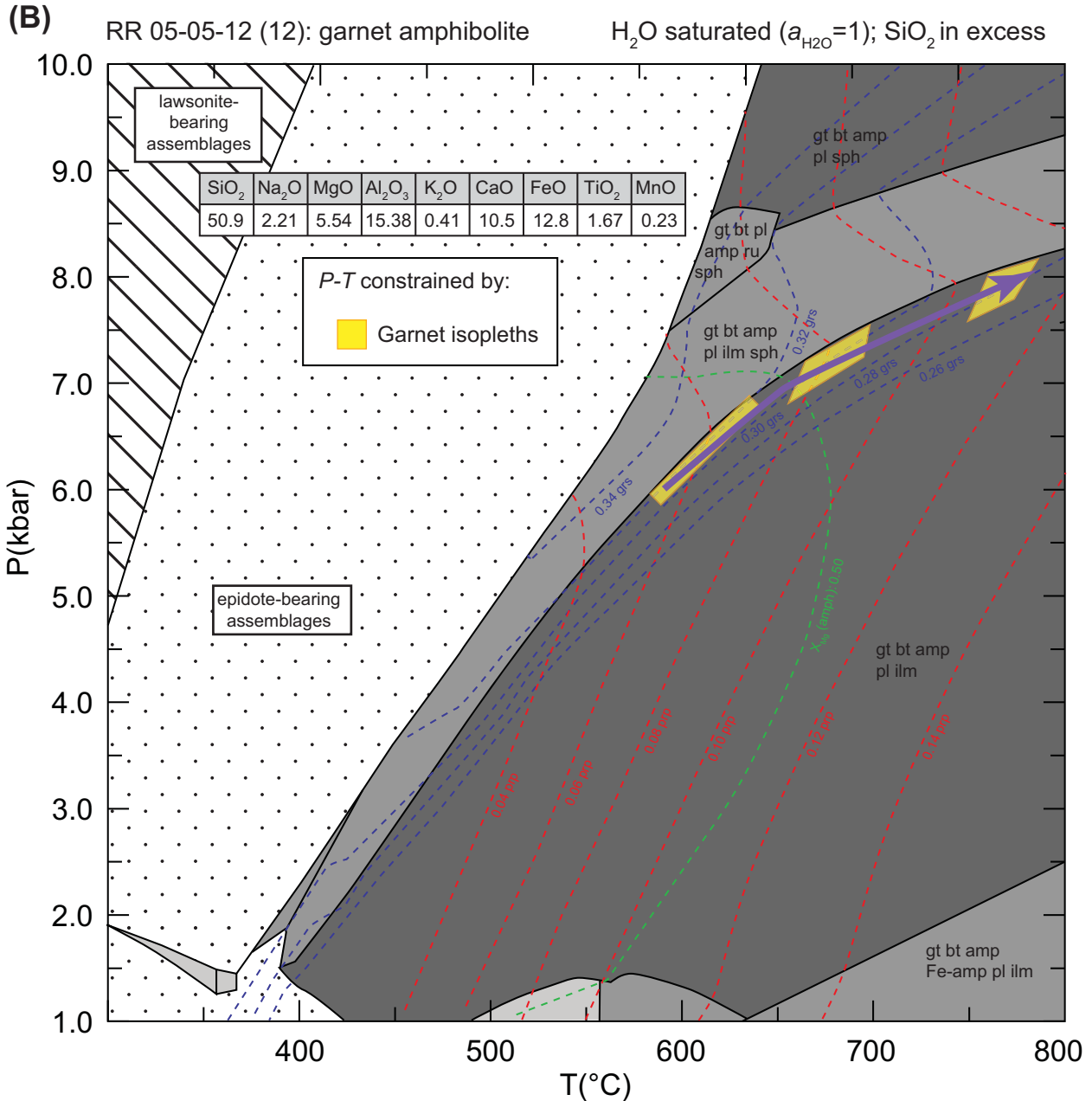


**Figure 5.17.** Thermobarometry results, plotted as  $2\sigma$  error ellipses for each sample. (A) and (B) are the same plots with different samples; (B) shows early, peak, and late  $P$ - $T$  estimates for a garnet amphibolite sample. Also shown is the overall weighted average of all these estimates. Aluminosilicate triple junction, greenschist-amphibolite-epidote amphibolite stability field (Evans, 1990), and granulite stability field (Pattison et al., 2003) shown for reference. Approximate depth scale assumes a crustal density of  $2850 \text{ kg/m}^3$ . A—andalusite; K—kyanite; S—sillimanite.

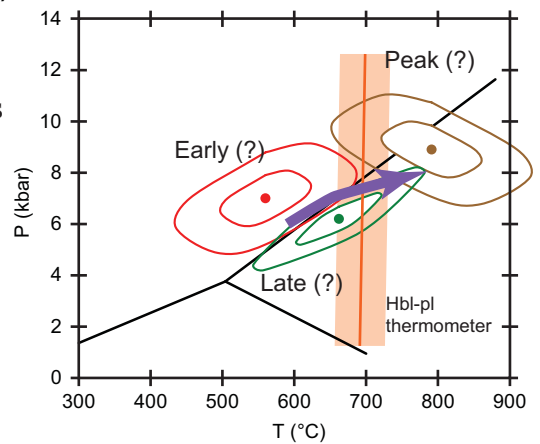




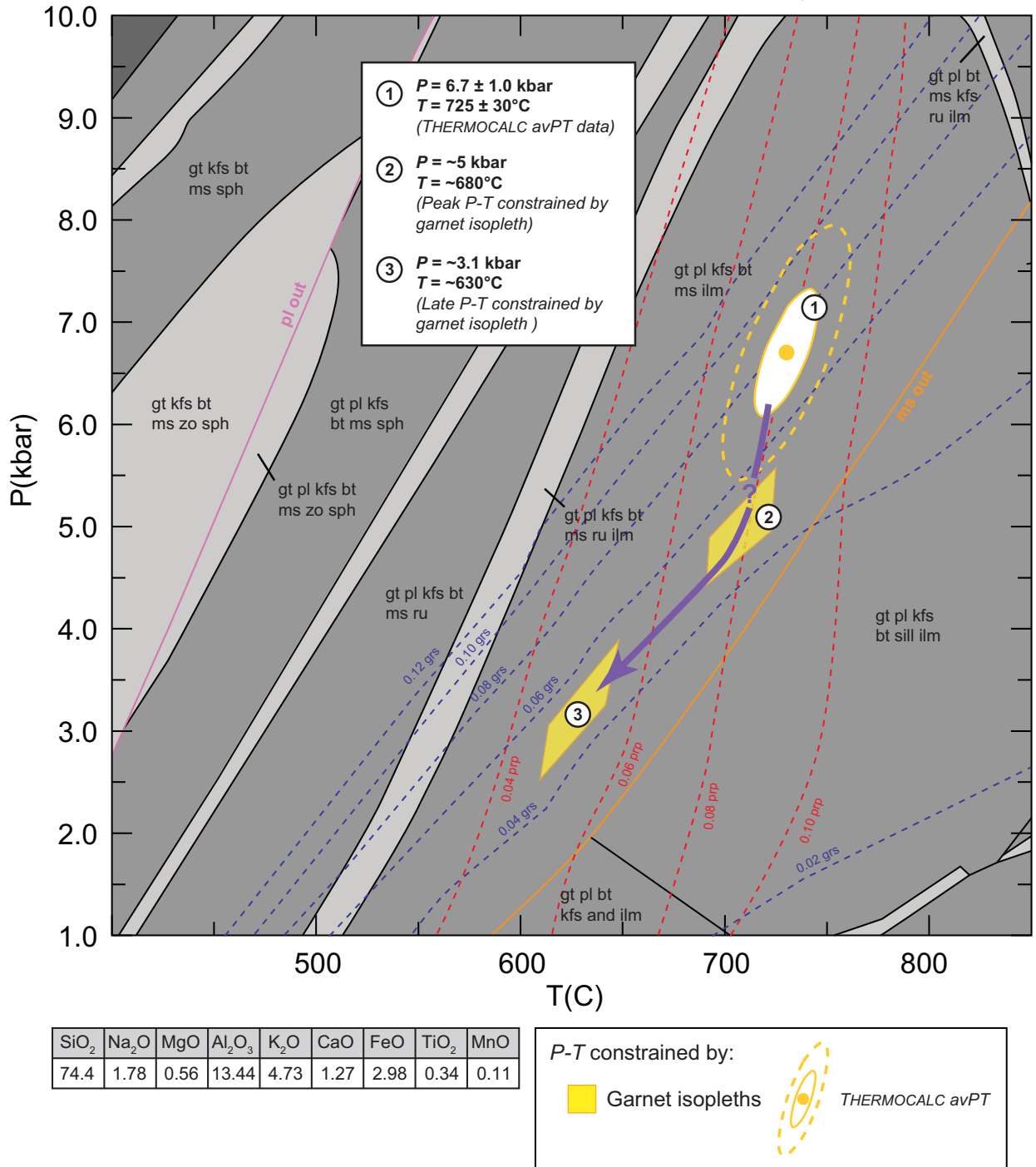
**Figure 5.18.** Pseudosections and *P-T* plots for selected samples. (A) Pseudosection for garnet-mica schist sample AY 09-21-11 (2). The garnet compositions are from adjacent sample AY 09-21-11 (1A). Relict plagioclase may be from an early stage of metamorphism, or alternatively, it may have formed during late-stage retrogression. gt—garnet; and—andalusite; sill—sillimanite; ky—kyanite; pl—plagioclase; san—k-feldspar; ms—muscovite; bt—biotite; chl—chlorite; ru—rutile; sph—sphene; ilm—ilmenite.



**Figure 5.18 (continued).** Pseudosections and *P-T* plots for selected samples. (B) Pseudosection for garnet amphibolite sample RR 05-05-12 (12). Garnet isopleths may track prograde metamorphism. The absence of sphere in the sample is an upper bound on the *P-T* conditions. Inset shows range of *THERMOCALC* *avPT* results (at  $1\sigma$  and  $2\sigma$ ) and Hbl-Pl thermometer constraints overlain by the pseudosection constraints (purple arrow). gt—garnet; bt—biotite; amp—amphibole; Fe-amp—Fe-amphibole; pl—plagioclase; sph—sphene; ilm—ilmenite; ru—rutile.

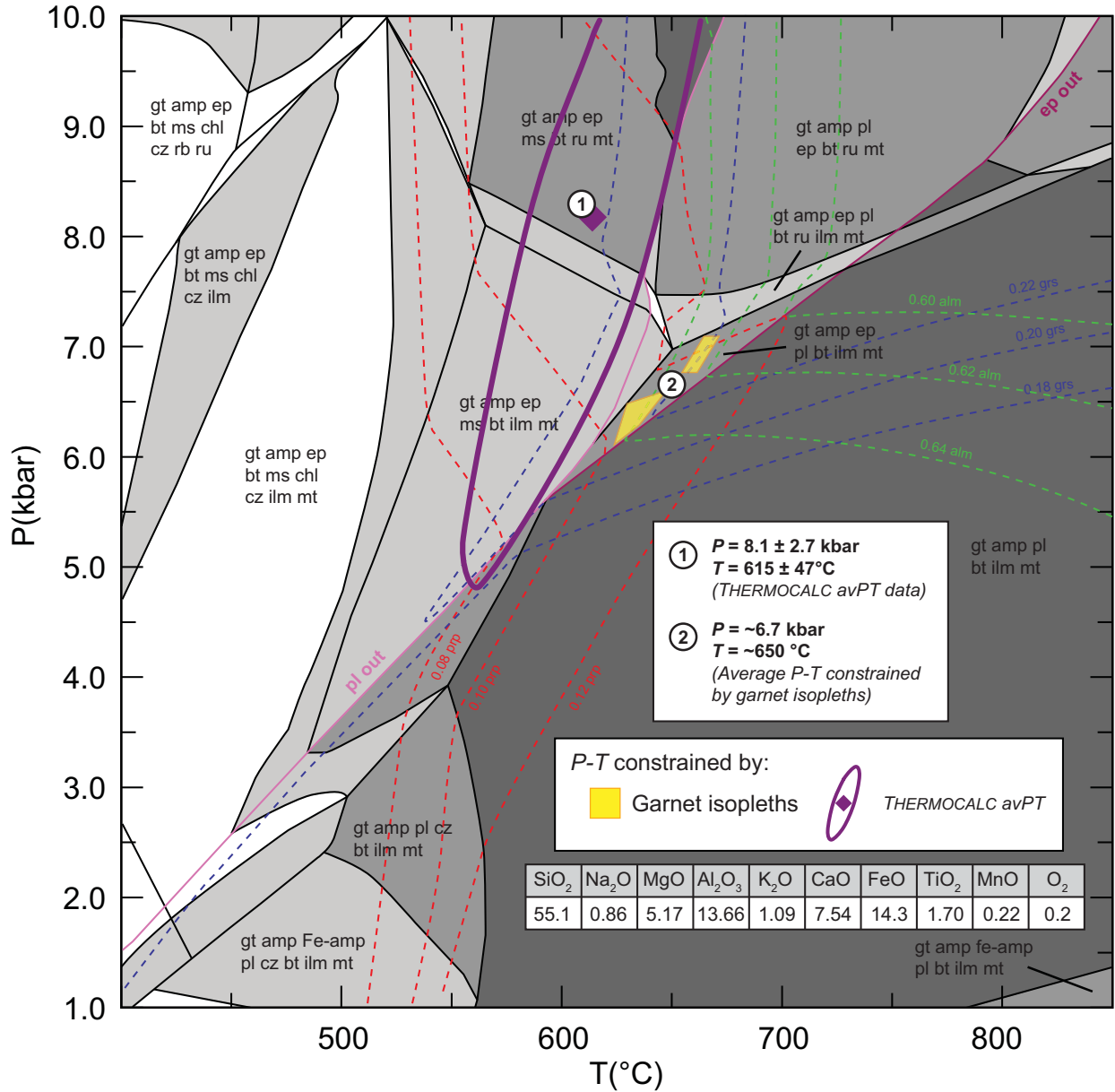


(C) RR 05-05-12 (8): quartzofeldspathic gneiss H<sub>2</sub>O saturated (a<sub>H<sub>2</sub>O</sub>=1); SiO<sub>2</sub> in excess

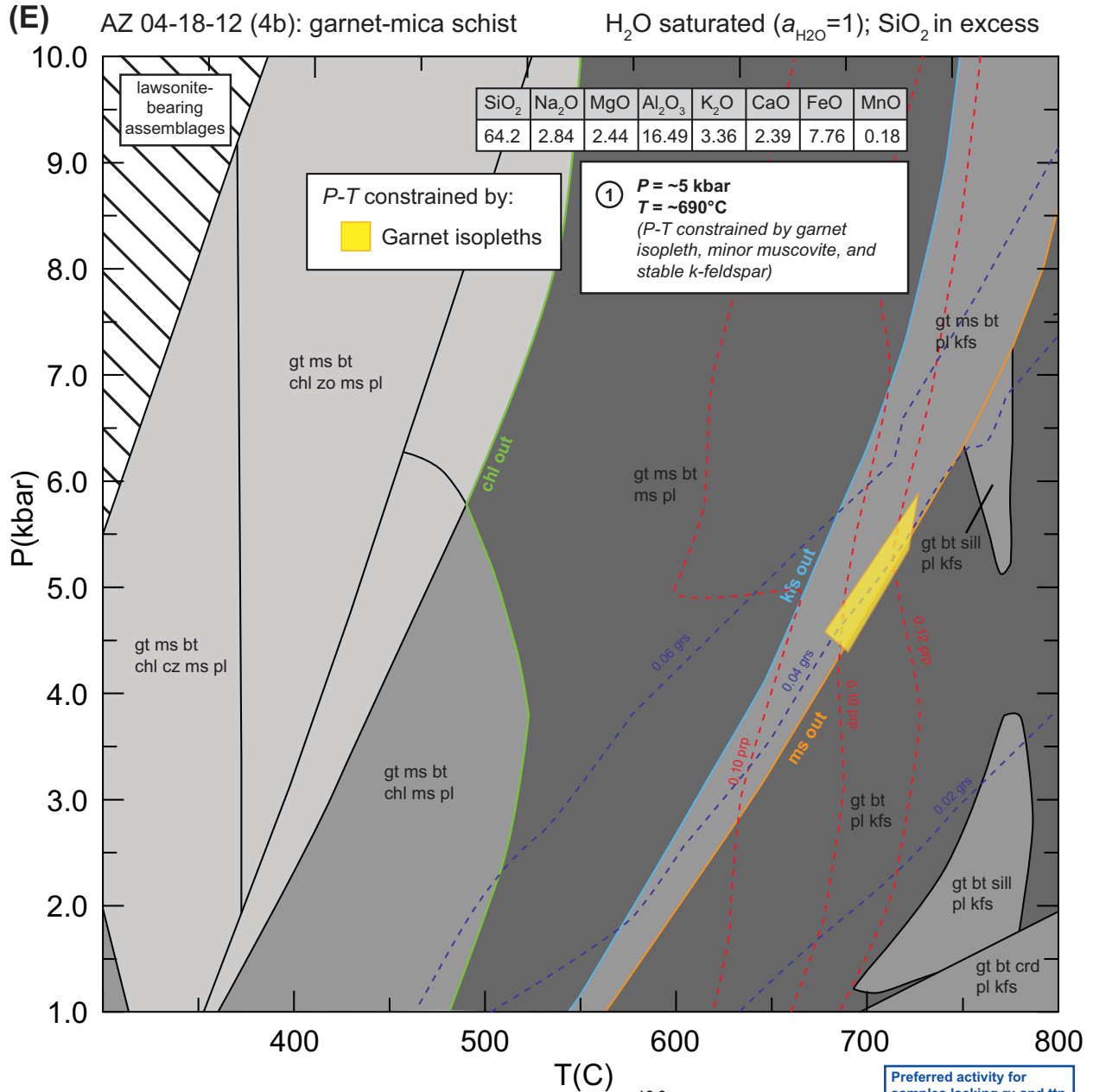


**Figure 5.18 (continued).** Pseudosections and P-T plots for selected samples. (C) Pseudosection for gneiss sample RR 05-05-12 (8). The THERMOCALC avPT and peak garnet isopleth intersection do not overlap, and thus peak conditions are only loosely constrained to ~700°C and ~6 ± 1.5 kbar. Late-stage garnet compositions show retrograde conditions at ~630°C and ~3.1 kbar. gt—garnet; pl—plagioclase; kfs—K-feldspar; ms—muscovite; bt—biotite; sill—sillimanite; and—andalusite; zo—zoisite; sph—sphene; ilm—ilmenite; ru—rutile.

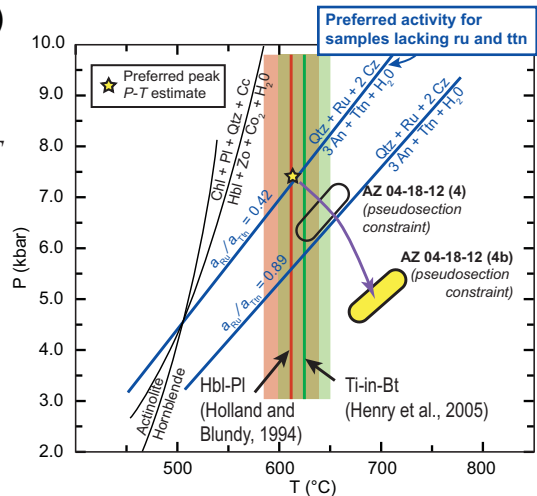
(D) AZ 04-18-12 (4): epidote-amphibolite gneiss H<sub>2</sub>O saturated ( $a_{\text{H}_2\text{O}}=1$ ); SiO<sub>2</sub> in excess



**Figure 5.18 (continued).** Pseudosections and P-T plots for selected samples. (D) Pseudosection for amphibolite gneiss AZ 04-18-12 (4). gt— garnet; amp— amphibole; Fe-amp—Fe-amphibole; pl—plagioclase; bt—biotite; ms—muscovite; chl—chlorite; ep—epidote; cz—clinozoisite; ilm—ilmenite; mt—magnetite; ru—rutile.



**Figure 5.18 (continued).** Pseudosections and *P-T* plots for selected samples. (E) Pseudosection for garnet-mica schist RR 05-05-12 (4b). Inset shows *P-T* estimates from this pseudosection, AZ 04-18-12 (4), two geothermometers (Holland and Blundy, 1994; Henry et al., 2005), reaction curves from Plyusniina (1982) (blue) and Kapp et al. (2009) (black), and possible *P-T* path (purple line). gt—garnet; pl—plagioclase; bt—biotite; ms—muscovite; chl—chlorite; cz—clinozoisite; zo—zoisite; ttn—titanite; kfs—k-feldspar; sill—sillimanite; crd—cordierite.



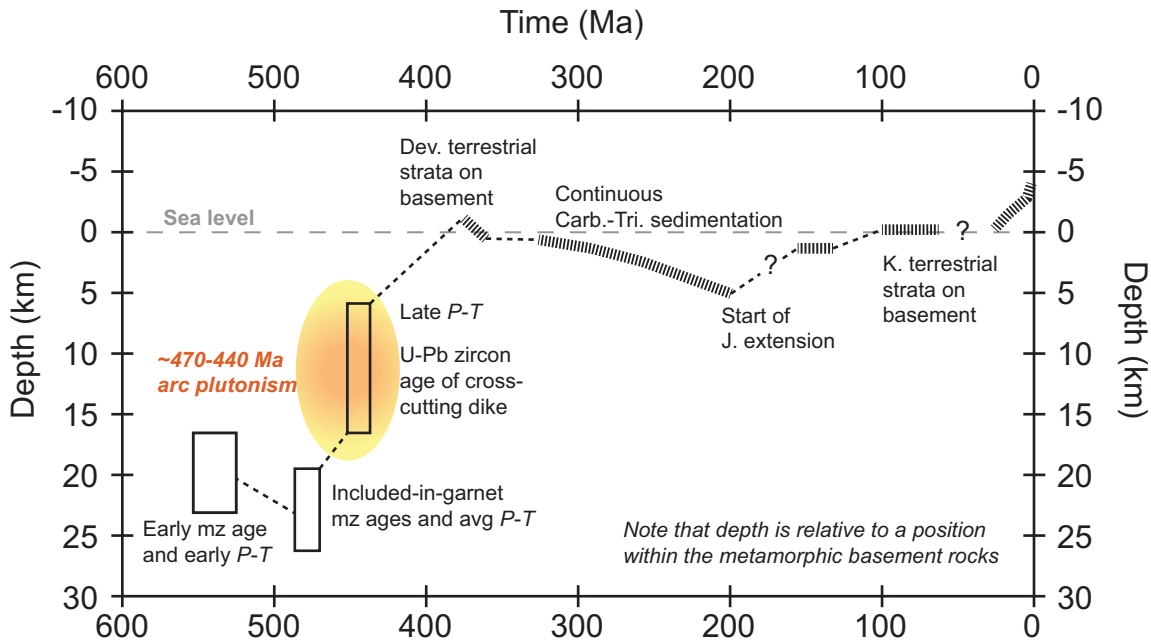


**Figure 5.19.** Estimated depth history for the metamorphic basement rocks of the central Qilian Shan from the Neoproterozoic to the present. The oldest population of monazite ages (~540 Ma) may correspond to the earliest stage *P-T* estimates. Subduction and arc magmatism thickened the continent, resulting in peak *P-T* conditions and the main population of included-in-garnet monazite ages (~480 Ma). Magmatism continues throughout the Silurian, and late *P-T* conditions record shallow crustal depths, possibly as a result of erosion. Metamorphic foliations are truncated by undeformed granite at ~445 Ma. Devonian molasse is unconformably deposited on basement rocks, which requires that the basement rocks were exhumed to near the surface by this time. Continuous shallow marine to lacustrine Carboniferous-Triassic sedimentation suggests that these rocks remained near the Earth's surface. Jurassic and Cretaceous extension lead to progressively shallower to terrestrial sedimentation, and Cenozoic deposits are entirely terrestrial during intracontinental shortening. mz—monazite; avg—average; Dev.—Devonian; Carb.—Carboniferous; Tri.—Triassic; J—Jurassic; K.—Cretaceous.

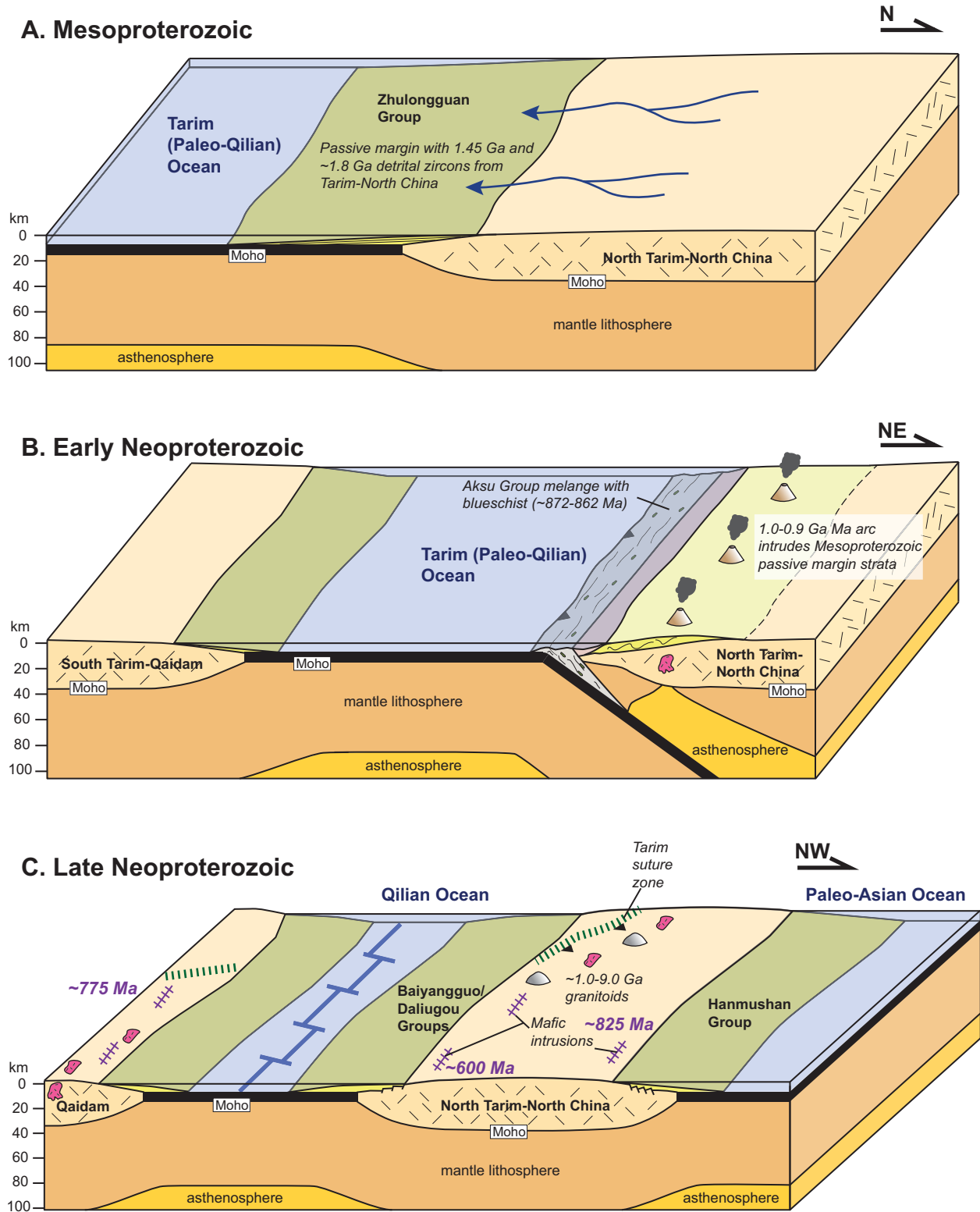


**Figure 5.20.** Block models of the tectonic evolution of north Tibet and the Qilian Shan from the Mesoproterozoic through Devonian. Full caption on page following panel (G).

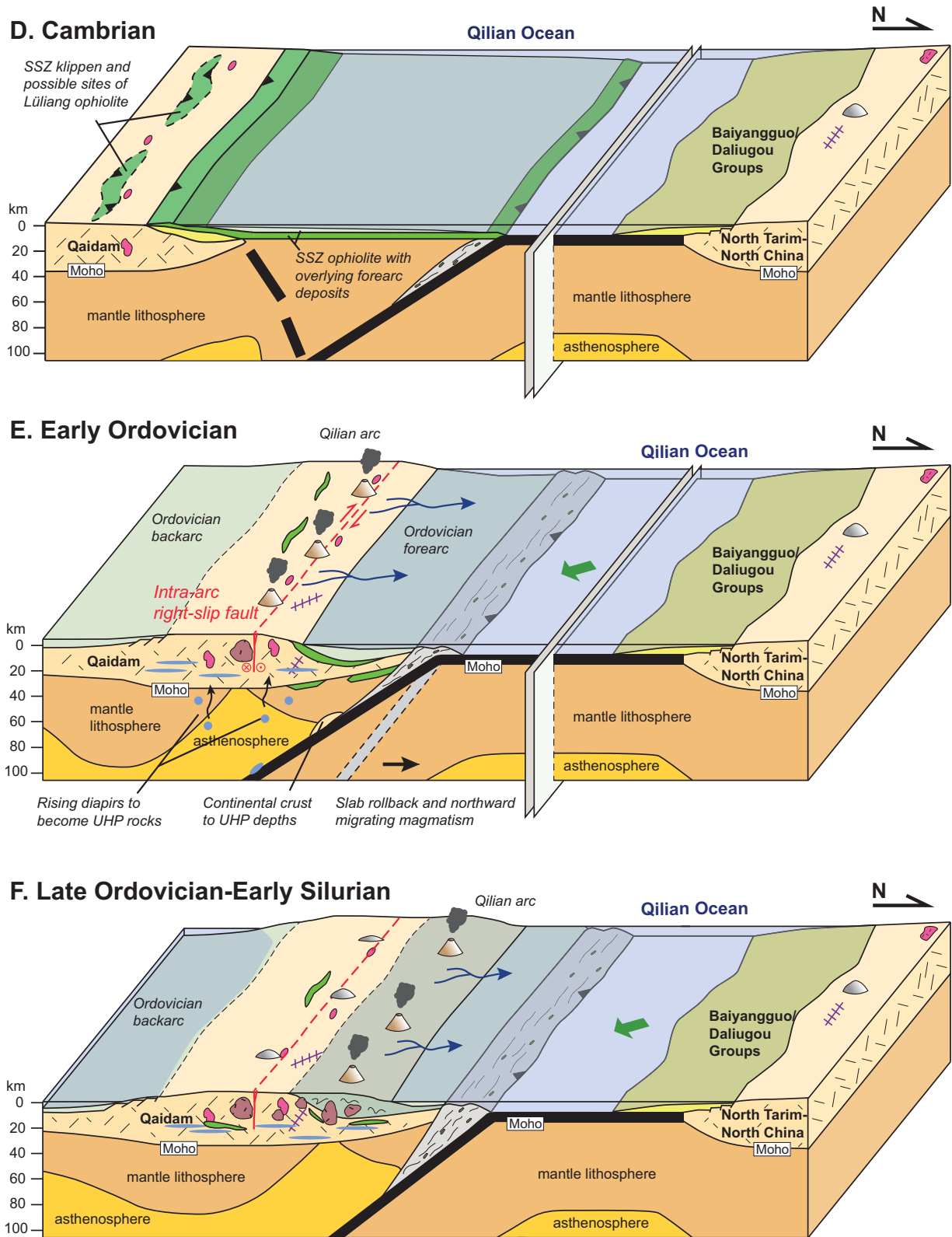


**Figure 5.20 (continued).** Block models of the tectonic evolution of north Tibet and the Qilian Shan from the Mesoproterozoic through Devonian. Full caption on page following panel (G).



### G. Silurian-Devonian

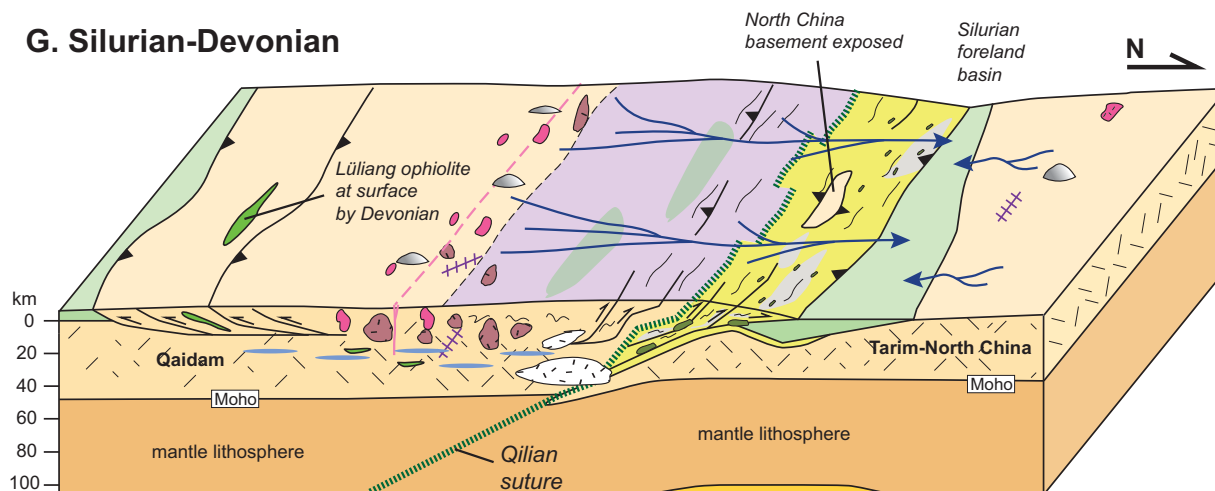


**Figure 5.20 (continued).** Block models of the tectonic evolution of north Tibet and the Qilian Shan from the Mesoproterozoic through Devonian. Note that the scale is relatively and changes between panels. (A) In the Mesoproterozoic, cratonal and/or passive margin deposits along the southern margin of a combined North Tarim-North China continent possess ~1.45 and ~1.8 Ga detrital zircons. (B) Early Neoproterozoic north-dipping subduction leads to the development of the Tarim arc (with ~1.0-0.9 Ga magmatism) which accommodates the convergence of the South Tarim-Qaidam and North Tarim-North China continents. (C) Late Neoproterozoic rifting leads to the opening of the Qilian and Paleo-Asian Oceans. Bimodal volcanism (~830-600 Ma) occurs throughout Qaidam, Tarim, and North China. (D) Cambrian-aged supra-subduction zone (SSZ) ophiolites are generated in an incipient arc setting, as south-dipping subduction initiates just north of Qaidam's northern margin. The SSZ ophiolites are obducted onto Qaidam and underthrust beneath the continent. (E) Continental arc magmatism initiates in earnest in the Ordovician, along with a trench-parallel intra-arc right-lateral strike-slip fault. Continental crust is brought to UHP depths along the subduction channel, and returned to mid-crustal levels by via diapiric flow or subduction channel flow. (F) Slab rollback causes the northward migrating arc to develop on older Ordovician and Cambrian strata. (G) Collision between Qaidam and North China occurs at ~440 Ma and is associated with a magmatic pulse at this time. Syn- and post-orogenic magmatism is diffuse but widespread. Continued convergence variably exposes ophiolites and basement rocks to surface by the Devonian.

**Table 5.1. Tectonic model predictions for the early Paleozoic Qilian arc and orogen**

|                                    | Predictions   |  |   |   | Key References                                       |   |  |
|------------------------------------|---|--|---|---|--|---|--|
|                                    | <i>Spatial relationship between arc plutons and suture(s)</i> | <i>Arc basement</i>                            | <i>Explanation for wide and complex mélange/ophiolite belt</i>                        | <i>Northward younging of magmatism</i>                  |  | <i>Dextral shear zone in Qaidam at ~475 Ma</i>  | <i>Explanation for North Qaidam UHP rocks</i>  |
| <b>North-dipping subduction</b>    | Plutons north of suture                                       | North China craton or accretionary material    | Paleozoic continental deformation and Mesozoic/Cenozoic reorganization of main suture | Subduction-slab shallowing                              | Unrelated to Qilian arc                              | Subduction of Qaidam microcontinent and intracontinental channel flow exhumation during collision | Yang et al. (2001), Song et al. (2005, 2006, 2013, 2014)   |
| <b>South-dipping subduction</b>    | Plutons south of main suture                                  | Qaidam microcontinent or accretionary material | Paleozoic continental deformation and Mesozoic/Cenozoic reorganization of main suture | Subduction-slab steepening and slab rollback            | Intra-arc strike-slip fault                          | Subduction of North China craton and diapir emplacement near arc during and after arc magmatism   | Sobel and Arnaud (1999), Gehrels et al. (2003a,b), Yin et al. (2007a)                                |
| <b>Bidirectional subduction</b>    | Sutures on surrounding arc belts to the north and south       | Qilian microcontinent or oceanic lithosphere   | Two Paleozoic collisions and subsequent later modification                            | Earlier initiation of southern north-dipping subduction | Intra-arc strike-slip fault and/or collision related | Subduction southern Qaidam and channel flow exhumation along North Qaidam suture                  | Xiao et al. (2009)*  |
| <b>Multiple north-dipping arcs</b> | Distinct belts of sutures and plutons                         | Microcontinent and/or oceanic lithosphere      | Several Paleozoic collisions and subsequent modification                              | Arcs initiated and progressed at various times          | Intra-arc strike-slip fault and/or collision related | Variable subduction of microcontinents and cratons  | Li et al. (1978), Hsü et al. (1995), Yin and Nie (1996), Yang et al. (2002), Yin and Harrison (2000) |

**Note: These hypotheses and predictions are based on the assumption that Mesozoic and Cenozoic deformation are constrained and restored. \*This work also envisions multiple oceanic arcs, but is most concerned with bidirectional subduction beneath the Qaidam microcontinent.**

**Table 5.2. Summary of zircon geochronology results**

| Sample                       | Rock type                 | Latitude      | Longitude      | Elevation (m) | Interpreted age (Ma)        | MSWD         | n            |
|------------------------------|---------------------------|---------------|----------------|---------------|-----------------------------|--------------|--------------|
| RR 05-05-12 (5)              | Quartz monzonite dike     | 38° 34.698' N | 98° 31.760' E  | 4584          | <b>445 ± 3</b>              | <b>0.38</b>  | 17 out of 19 |
| AZ 07-17-13 (4)              | Alkali feldspar granite   | 38° 28.546' N | 98° 49.882' E  | 4290          | <b>449 ± 13</b>             | <b>0.99</b>  | 12 out of 15 |
| AZ 04-30-12 (11)             | Syenogranite              | 38° 34.473' N | 98° 58.035' E  | 3911          | <b>450 ± 1</b>              | <b>0.92</b>  | 19 out of 25 |
| RR 05-03-12 (6)              | Alkali feldspar granite   | 38° 29.415' N | 98° 54.218' E  | 3982          | <b>457 ± 2</b>              | <b>3.5</b>   | 22 out of 25 |
| AZ 09-14-14 (8) <sup>1</sup> | Granite                   | 37° 37.658' N | 101° 49.904' E | 3198          | <b>462 ± 14</b>             | <b>1.2</b>   | 7 out of 9   |
| AZ 05-04-12 (7)              | Granite                   | 38° 41.752' N | 98° 45.627' E  | 3850          | <b>474 ± 3</b>              | <b>3.2</b>   | 19 out of 25 |
| AZ 05-06-12 (2)              | Diabase dike              | 38° 36.800' N | 98° 58.482' E  | 4509          | <b>521 ± 2</b>              | <b>1.3</b>   | 20 out of 25 |
| AZ 05-03-12 (11)             | Diabase dike              | 38° 36.640' N | 98° 59.398' E  | 4442          | <b>541 ± 6</b>              | <b>10.1</b>  | 15 out of 25 |
| RR 05-04-12 (2)              | Foliated granitoid        | 38° 32.708' N | 99° 00.082' E  | 4060          | <b>868 ± 16<sup>2</sup></b> | <b>0.79</b>  | 19 out of 25 |
| AY 09-21-11 (4)              | Foliated granitoid        | 38° 41.418' N | 98° 37.762' E  | 3551          | <b>905 ± 7<sup>2</sup></b>  | <b>1.3</b>   | 24 out of 25 |
| AZ 04-30-12 (4) <sup>3</sup> | Tonalitic dike            | 38° 33.522' N | 98° 55.447' E  | 3778          | <b>912 ± 21<sup>2</sup></b> | <b>0.053</b> | 3 out of 16  |
| AZ 07-24-13 (9)              | Weakly foliated granitoid | 38° 42.472' N | 98° 38.763' E  | 3554          | <b>921 ± 10<sup>2</sup></b> | <b>1.8</b>   | 8 out of 8   |
| AZ 05-01-12 (1)              | Foliated granitoid        | 38° 39.452' N | 98° 41.372' E  | 3624          | <b>961 ± 12<sup>2</sup></b> | <b>2.4</b>   | 24 out of 25 |

<sup>1</sup>Sample collected outside of mapping area<sup>2</sup>Pb-Pb age (all others are U-Pb ages)<sup>3</sup>Range of ages picked up by intrusion; interpreted age is a well-defined age population

**Table 5.3. Monazite isotopic data for central Qilian Shan samples**

| Spot  | mz loc. <sup>1</sup> | <sup>208</sup> Pb/ <sup>232</sup> Th |            | Age (Ma)                             |            | <sup>206</sup> Pb/ <sup>238</sup> U | 1 $\sigma$ | <sup>206</sup> Pb* (%) | <sup>208</sup> Pb*/ <sup>232</sup> Th | 1 $\sigma$ | Isotopic ratios                      |                                      | 1 $\sigma$ | <sup>207</sup> Pb*/ <sup>206</sup> Pb | ThO <sub>2</sub> /Th |
|---|----------------------|--------------------------------------|------------|--------------------------------------|------------|-------------------------------------|------------|------------------------|---------------------------------------|------------|--------------------------------------|--------------------------------------|------------|---------------------------------------|----------------------|
|   |                      | <sup>208</sup> Pb/ <sup>232</sup> Th | 1 $\sigma$ | <sup>206</sup> Pb*/ <sup>238</sup> U | 1 $\sigma$ |                                     |            |                        |                                       |            | <sup>206</sup> Pb*/ <sup>238</sup> U | <sup>207</sup> Pb*/ <sup>235</sup> U |            |                                       |                      |
| 16m3_1                                      | m                    | 433.9                                | 20.2       | 400.2                                | 41.3       | 99.4                                | 0.02170    | 0.00102                | 0.00681                               | 0.4822     | 0.0513                               | 0.05460                              | 0.000606   | 0.00681                               | 2.56                 |
| 1m1_1                                       | m                    | 526.7                                | 24.4       | 543.7                                | 63.7       | 97.8                                | 0.02640    | 0.00124                | 0.01070                               | 0.7055     | 0.0875                               | 0.05815                              | 0.001190   | 0.01070                               | 2.54                 |
| 1am1_2                                      | m                    | 529.2                                | 27.3       | 553.8                                | 76.0       | 97.8                                | 0.02653    | 0.00139                | 0.01280                               | 0.7251     | 0.1070                               | 0.05863                              | 0.001810   | 0.01280                               | 2.39                 |
| 3m1_3                                       | m                    | 422.0                                | 19.0       | 373.1                                | 35.4       | 97.4                                | 0.02110    | 0.00096                | 0.00581                               | 0.4781     | 0.0489                               | 0.05819                              | 0.001670   | 0.00581                               | 2.60                 |
| 5g1_4                                       | g                    | 532.1                                | 20.9       | 525.7                                | 48.3       | 97.1                                | 0.02667    | 0.00106                | 0.00814                               | 0.6415     | 0.0702                               | 0.05476                              | 0.002710   | 0.00814                               | 2.93                 |
| 7m1_7                                       | m                    | 575.5                                | 30.7       | 589.5                                | 84.1       | 98.6                                | 0.02888    | 0.00156                | 0.01430                               | 0.7412     | 0.1110                               | 0.05614                              | 0.000734   | 0.01430                               | 2.35                 |
| 10g2_3                                      | g                    | 526.0                                | 31.7       | 535.8                                | 93.2       | 95.9                                | 0.02636    | 0.00161                | 0.01570                               | 0.6988     | 0.1590                               | 0.05848                              | 0.007710   | 0.01570                               | 2.23                 |
| 12g2_4                                      | g                    | 567.8                                | 33.8       | 685.9                                | 81.4       | 76.9                                | 0.02849    | 0.00172                | 0.01400                               | 0.8445     | 0.3350                               | 0.05456                              | 0.019400   | 0.01400                               | 2.34                 |
| 9m2_6                                       | m                    | 577.9                                | 35.3       | 612.4                                | 102        | 98.2                                | 0.02900    | 0.00180                | 0.01740                               | 0.7970     | 0.1400                               | 0.05801                              | 0.001070   | 0.01740                               | 2.19                 |
| 8m2_9                                       | m                    | 554.5                                | 33.1       | 564.0                                | 87.7       | 97.6                                | 0.02781    | 0.00168                | 0.01480                               | 0.6903     | 0.1140                               | 0.05475                              | 0.001500   | 0.01480                               | 2.22                 |
| 20g3_12                                     | g                    | 528.9                                | 24.3       | 443.5                                | 48.6       | 96.5                                | 0.02651    | 0.00123                | 0.00807                               | 0.5678     | 0.0686                               | 0.05782                              | 0.002330   | 0.00807                               | 2.57                 |
| 22m3_13                                     | m                    | 441.4                                | 16.3       | 461.7                                | 44.5       | 98.7                                | 0.02208    | 0.00082                | 0.00742                               | 0.5602     | 0.0562                               | 0.05472                              | 0.000544   | 0.00742                               | 2.92                 |
| 21m3_14                                     | m                    | 774.5                                | 126.0      | 400.9                                | 79.7       | 99.1                                | 0.03906    | 0.00650                | 0.01320                               | 0.4894     | 0.1010                               | 0.05532                              | 0.000961   | 0.01320                               | 1.50                 |
| 25m3_15                                     | m                    | 458.9                                | 19.6       | 448.4                                | 46.0       | 97.7                                | 0.02296    | 0.00099                | 0.00765                               | 0.5572     | 0.0604                               | 0.05610                              | 0.001070   | 0.00765                               | 2.67                 |
| 26g3_16                                     | g                    | 492.1                                | 27.1       | 276.3                                | 34.9       | 95.9                                | 0.02464    | 0.00137                | 0.00565                               | 0.3264     | 0.0430                               | 0.05406                              | 0.001150   | 0.00565                               | 2.31                 |
| 26ag3_18                                    | g                    | 495.8                                | 47.9       | 313.3                                | 53.0       | 94.4                                | 0.02483    | 0.00243                | 0.00863                               | 0.3902     | 0.0689                               | 0.05683                              | 0.001720   | 0.00863                               | 1.79                 |
| 24m3_19                                     | m                    | 454.4                                | 20.4       | 398.7                                | 39.4       | 99.1                                | 0.02273    | 0.00103                | 0.00650                               | 0.4858     | 0.0498                               | 0.05522                              | 0.000692   | 0.00650                               | 2.59                 |
| <b>Calibration: 0.096x - 11.234(±0.727)</b> |                      |                                      |            |                                      |            |                                     |            |                        |                                       |            |                                      |                                      |            |                                       |                      |
| 11g1_0                                      | g                    | 469.1                                | 15.2       |                                      |            | 95.7                                | 0.02348    | 0.000772               |                                       |            |                                      |                                      |            |                                       | 0.45                 |
| 3m1_1                                       | m                    | 489.2                                | 12.0       |                                      |            | 93.7                                | 0.02450    | 0.000610               |                                       |            |                                      |                                      |            |                                       | 0.40                 |
| 15m1_2                                      | m                    | 488.4                                | 5.0        |                                      |            | 98.8                                | 0.02446    | 0.000253               |                                       |            |                                      |                                      |            |                                       | 0.33                 |
| 4m1_3                                       | m                    | 472.0                                | 3.8        |                                      |            | 99.7                                | 0.02363    | 0.000191               |                                       |            |                                      |                                      |            |                                       | 0.39                 |
| 10m2_0                                      | m                    | 439.8                                | 19.9       |                                      |            | 87.3                                | 0.02200    | 0.001010               |                                       |            |                                      |                                      |            |                                       | 0.38                 |
| 23m2_1                                      | m                    | 479.0                                | 5.5        |                                      |            | 99.8                                | 0.02398    | 0.000280               |                                       |            |                                      |                                      |            |                                       | 0.38                 |

<sup>1</sup>Monazite location: matrix (m) or included in garnet (g)

**Table 5.4. Whole-rock geochemistry data**

|            |                                      |                                     |                                     |                                      |                                      |                                    |
|------------|--------------------------------------|-------------------------------------|-------------------------------------|--------------------------------------|--------------------------------------|------------------------------------|
| Sample:    | RR 05-03-<br>12 (6)                  | AZ 04-30-<br>12 (11)                | AZ 07-17-<br>13 (4)                 | AZ 05-05-<br>12 (7)                  | AZ 07-21-<br>13 (7)                  | AY 09-21-<br>11 (3)                |
| Rock type: | Alkali<br>feldspar<br>granite        | Syenogranite                        | Alkali<br>feldspar<br>granite       | Diabase                              | Foliated K-<br>feldspar<br>granite   | Foliated<br>granitoid              |
| Location:  | 38.49025° N<br>98.90364° E<br>3982 m | 38.5745° N<br>98.96725° E<br>3911 m | 38.4758° N<br>98.83137° E<br>4290 m | 38.56992° N<br>98.91741° E<br>3827 m | 38.75413° N<br>98.49783° E<br>3441 m | 38.697° N<br>98.64175° E<br>3540 m |

*Major and minor elements (wt %)*

|                                |       |       |       |       |       |       |
|--------------------------------|-------|-------|-------|-------|-------|-------|
| SiO <sub>2</sub>               | 75.45 | 62.72 | 70.55 | 46.16 | 71.08 | 69.34 |
| Al <sub>2</sub> O <sub>3</sub> | 13.18 | 14.04 | 14.14 | 13.50 | 13.37 | 15.01 |
| Fe <sub>2</sub> O <sub>3</sub> | 1.69  | 4.37  | 2.85  | 14.24 | 3.01  | 2.59  |
| MnO                            | 0.05  | 0.07  | 0.05  | 0.24  | 0.03  | 0.05  |
| MgO                            | 0.34  | 1.93  | 0.73  | 7.69  | 0.47  | 0.84  |
| CaO                            | 0.80  | 3.17  | 1.15  | 10.56 | 1.68  | 2.72  |
| Na <sub>2</sub> O              | 3.24  | 3.13  | 3.80  | 1.94  | 2.54  | 3.18  |
| K <sub>2</sub> O               | 4.65  | 4.42  | 3.97  | 0.12  | 4.82  | 3.06  |
| TiO <sub>2</sub>               | 0.18  | 0.49  | 0.30  | 1.55  | 0.42  | 0.31  |
| P <sub>2</sub> O <sub>5</sub>  | 0.05  | 0.17  | 0.12  | 0.12  | 0.08  | 0.07  |
| LOI <sup>@</sup>               | 0.78  | 3.81  | 0.87  | 3.76  | 2.35  | 2.69  |
| Total <sup>#</sup>             | 100.4 | 98.31 | 98.51 | 99.88 | 99.85 | 99.86 |

*Trace elements (ppm)*

|    |       |       |       |     |       |       |
|----|-------|-------|-------|-----|-------|-------|
| Sc | 4     | 10    | 4     | 55  | 7     | 9     |
| Be | 5     | 2     | 3     | -   | -     | -     |
| V  | 11    | 88    | 24    | 408 | 31    | 45    |
| Cr | 40    | 50    | 40    | 254 | 50    | 70    |
| Co | 2     | 10    | 4     | 73  | 5     | 5     |
| Ni | < 20  | < 20  | < 20  | 136 | < 20  | < 20  |
| Cu | < 10  | < 10  | 20    | 105 | < 10  | < 10  |
| Zn | 30    | 40    | 50    | 147 | 50.0  | 50.0  |
| Ga | 18    | 14    | 17    | 17  | 18.0  | 19.0  |
| Ge | 2     | 2     | 2     | -   | 2     | 2     |
| As | < 5   | 6     | < 5   | 8   | 14    | 7     |
| Rb | 347   | 192   | 142   | 4   | 204   | 115   |
| Sr | 101   | 397   | 310   | 196 | 82    | 157   |
| Y  | 27    | 15    | 11    | 29  | 39    | 20    |
| Zr | 121   | 155   | 145   | 93  | 228   | 126   |
| Nb | 30    | 18    | 16    | 16  | 9     | 7     |
| Mo | < 2   | < 2   | < 2   | 3   | 0     | 3     |
| Ag | 1     | 1.2   | 1.2   | -   | 0.5   | < 0.5 |
| In | < 0.2 | < 0.2 | < 0.2 | -   | < 0.2 | < 0.2 |
| Sn | 10    | 1     | 3     | -   | 3.0   | 3.0   |
| Sb | 0.6   | 6.2   | 3.4   | -   | 0.7   | 0.6   |
| Cs | 15.1  | 6.4   | 2.9   | 1.0 | 6.7   | 4.1   |
| Ba | 360   | 1014  | 579   | 37  | 839   | 566   |
| La | 44.7  | 42.8  | 46.7  | 0   | 39.4  | 13.3  |
| Ce | 82.5  | 72.4  | 79.8  | 19  | 78.2  | 26.3  |
| Pr | 8.41  | 7.09  | 7.59  | 2   | 8.3   | 3.0   |

**Table 5.4. Whole-rock geochemistry data (continued)**

| Sample:    | RR 05-03-<br>12 (6)                  | AZ 04-30-<br>12 (11)                | AZ 07-17-<br>13 (4)                 | AZ 05-05-<br>12 (7)                  | AZ 07-21-<br>13 (7)                       | AY 09-21-<br>11 (3)                |
|------------|--------------------------------------|-------------------------------------|-------------------------------------|--------------------------------------|---|------------------------------------|
| Rock type: | Alkali<br>feldspar<br>granite        | Syenogranite                        | Alkali<br>feldspar<br>granite       | Diabase                              | Foliated<br>alkali<br>feldspar<br>granite | Foliated<br>granitoid              |
| Location:  | 38.49025° N<br>98.90364° E<br>3982 m | 38.5745° N<br>98.96725° E<br>3911 m | 38.4758° N<br>98.83137° E<br>4290 m | 38.56992° N<br>98.91741° E<br>3827 m | 38.75413° N<br>98.49783° E<br>3441 m      | 38.697° N<br>98.64175° E<br>3540 m |
| Nd         | 29                                   | 25                                  | 24                                  | 17                                   | 31  | 12                                 |
| Sm         | 6                                    | 4                                   | 4                                   | 4                                    | 6   | 3                                  |
| Eu         | 0.5                                  | 1.1                                 | 0.7                                 | -                                    | 0.8                                       | 0.7                                |
| Gd         | 4.2                                  | 2.9                                 | 2.4                                 | -                                    | 6.5                                       | 2.7                                |
| Tb         | 0.7                                  | 0.4                                 | 0.3                                 | -                                    | 1.0                                       | 0.5                                |
| Dy         | 4.4                                  | 2.5                                 | 1.8                                 | -                                    | 6.1                                       | 3.1                                |
| Ho         | 0.8                                  | 0.5                                 | 0.4                                 | -                                    | 1.3                                       | 0.7                                |
| Er         | 2.4                                  | 1.4                                 | 1.1                                 | -                                    | 3.8                                       | 2.1                                |
| Tm         | 0.4                                  | 0.22                                | 0.15                                | -                                    | 0.6                                       | 0.4                                |
| Yb         | 2.7                                  | 1.5                                 | 1.1                                 | -                                    | 3.8                                       | 2.4                                |
| Lu         | 0.4                                  | 0.24                                | 0.17                                | -                                    | 0.6                                       | 0.4                                |
| Hf         | 3.4                                  | 3.6                                 | 3                                   | 2.1                                  | 6.1                                       | 3.4                                |
| Ta         | 3.7                                  | 1.2                                 | 1.1                                 | 7.3                                  | 1.0                                       | 0.9                                |
| W          | < 1                                  | 3                                   | 4                                   | -                                    | -   | -                                  |
| Tl         | 2.2                                  | 0.9                                 | 0.9                                 | -                                    | 1.4                                       | 0.8                                |
| Pb         | 46                                   | 19                                  | 25                                  | 5.2                                  | 33.0                                      | 25.0                               |
| Bi         | < 0.4                                | < 0.4                               | < 0.4                               | -                                    | < 0.4                                     | 0.4                                |
| Th         | 38.4                                 | 18.3                                | 25                                  | 1.0                                  | 16.9                                      | 4.8                                |
| U          | 4.8                                  | 4.2                                 | 3.3                                 | 7.3                                  | 2.3                                       | 1.6                                |
| S          | -                                    | -                                   | -                                   | < dl                                 | < dl                                      | 90.4                               |
| Ti*        | 1073                                 | 2944                                | 1793                                | 9648                                 | 2577                                      | 1910                               |
| K*         | 38600                                | 36693                               | 32957                               | 1034                                 | 40951                                     | 26105                              |
| P*         | 218                                  | 742                                 | 524                                 | 544                                  | 358                                       | 314                                |

**Table 5.4. Whole-rock geochemistry data (continued)**

| Sample:                                | RR 05-05-<br>12 (8)                 | AZ 05-03-<br>12 (13)                 | AZ 04-18-<br>12 (4)                 | AZ 07-15-<br>13 (5)                | AZ 04-18-<br>12 (4b)                | AY 09-21-<br>11 (2)                 |
|--|-------------------------------------|--------------------------------------|-------------------------------------|------------------------------------|-------------------------------------|-------------------------------------|
| Rock type:                             | Mylonitic gneiss                    | Serpentinite                         | Gneiss                              | Garnet amphibolite                 | Garnet mica schist                  | Garnet mica schist                  |
| Location:                              | 38.58889° N<br>98.5402° E<br>4215 m | 38.60758° N<br>98.99772° E<br>4360 m | 38.50647° N<br>98.6993° E<br>4314 m | 38.4625° N<br>98.8036° E<br>4170 m | 38.5065° N<br>98.69933° E<br>4314 m | 38.7131° N<br>98.60619° E<br>3516 m |
| <i>Major and minor elements (wt %)</i> |                                     |                                      |                                     |                                    |                                     |                                     |
| SiO <sub>2</sub>                       | 72.62                               | 33.28                                | 53.37                               | 48.1                               | 61.76                               | 63.43                               |
| Al <sub>2</sub> O <sub>3</sub>         | 13.11                               | 0.91                                 | 13.24                               | 11.42                              | 15.86                               | 19.42                               |
| Fe <sub>2</sub> O <sub>3</sub>         | 2.91                                | 10.57                                | 13.89                               | 17.37                              | 7.46                                | 5.41                                |
| MnO                                    | 0.11                                | 0.07                                 | 0.21                                | 0.26                               | 0.17                                | 0.10                                |
| MgO                                    | 0.55                                | 39.36                                | 5.01                                | 4.93                               | 2.35                                | 1.41                                |
| CaO                                    | 1.24                                | 0.03                                 | 7.31                                | 9.15                               | 2.30                                | 0.51                                |
| Na <sub>2</sub> O                      | 1.74                                | 0.00                                 | 0.83                                | 2.06                               | 2.73                                | 1.75                                |
| K <sub>2</sub> O                       | 4.61                                | 0.00                                 | 1.06                                | 0.47                               | 2.27                                | 3.90                                |
| TiO <sub>2</sub>                       | 0.33                                | 0.01                                 | 1.64                                | 2.52                               | 0.97                                | 0.78                                |
| P <sub>2</sub> O <sub>5</sub>          | 0.15                                | 0.00                                 | 0.20                                | 0.24                               | 0.06                                | 0.06                                |
| LOI <sup>@</sup>                       | 2.44                                | 15.24                                | 3.07                                | 3.31                               | 3.92                                | 3.09                                |
| Total <sup>#</sup>                     | 99.81                               | 99.47                                | 99.83                               | 99.93                              | 99.85                               | 99.86                               |
| <i>Trace elements (ppm)</i>            |                                     |                                      |                                     |                                    |                                     |                                     |
| Sc                                     | 10                                  | 4                                    | 40                                  | 47                                 | 20                                  | 17                                  |
| Be                                     | -                                   | -                                    | -                                   | -                                  | -                                   | -                                   |
| V                                      | 44                                  | 22                                   | 352                                 | 451                                | 123                                 | 116                                 |
| Cr                                     | 70                                  | 4684                                 | 105                                 | 27                                 | 118                                 | 92                                  |
| Co                                     | 5                                   | 185                                  | 55                                  | 77                                 | 37                                  | 4                                   |
| Ni                                     | 5                                   | 2076                                 | 28                                  | 328                                | 27                                  | 29                                  |
| Cu                                     | 37                                  | 27                                   | 122                                 | 147                                | 88                                  | 34                                  |
| Zn                                     | 50                                  | 122                                  | 108                                 | 105                                | 47                                  | 88                                  |
| Ga                                     | 17                                  | 1                                    | 20                                  | 21                                 | 22                                  | 24                                  |
| Ge                                     | 2                                   | -                                    | -                                   | -                                  | -                                   | -                                   |
| As                                     | < 5                                 | 0                                    | 7                                   | 2                                  | 5                                   | 5                                   |
| Rb                                     | 170                                 | 0                                    | 49                                  | 18                                 | 143                                 | 185                                 |
| Sr                                     | 102                                 | 0                                    | 135                                 | 123                                | 151                                 | 102                                 |
| Y                                      | 37                                  | 2                                    | 35                                  | 52                                 | 41                                  | 35                                  |
| Zr                                     | 135                                 | 13                                   | 133                                 | 182                                | 258                                 | 174                                 |
| Nb                                     | 8                                   | 9                                    | 20                                  | 24                                 | 23                                  | 18                                  |
| Mo                                     | 3                                   | 2                                    | 2                                   | 0                                  | 2                                   | 1                                   |
| Ag                                     | < 0.5                               | -                                    | -                                   | -                                  | -                                   | -                                   |
| In                                     | < 0.2                               | -                                    | -                                   | -                                  | -                                   | -                                   |
| Sn                                     | 3.0                                 | -                                    | -                                   | -                                  | -                                   | -                                   |
| Sb                                     | 0.8                                 | -                                    | -                                   | -                                  | -                                   | -                                   |
| Cs                                     | 7.1                                 | 2.4                                  | 11.3                                | 0.0                                | 11.4                                | 15.5                                |
| Ba                                     | 822.0                               | 0.0                                  | 157.8                               | 95.1                               | 525.2                               | 707.3                               |
| La                                     | 32.0                                | 0.0                                  | 25.8                                | 11.4                               | 44.7                                | 55.7                                |
| Ce                                     | 67.4                                | 0.0                                  | 49.5                                | 34.1                               | 115.4                               | 113.4                               |
| Pr                                     | 7.4                                 | 3.5                                  | 5.2                                 | 3.1                                | 13.5                                | 12.4                                |

**Table 5.4. Whole-rock geochemistry data (continued)**

| Sample:    | RR 05-05-<br>12 (8)                 | AZ 05-03-<br>12 (13)                 | AZ 04-18-<br>12 (4)                 | AZ 07-15-<br>13 (5)                | AZ 04-18-<br>12 (4b)                | AY 09-21-<br>11 (2)                 |
|------------|-------------------------------------|--------------------------------------|-------------------------------------|------------------------------------|-------------------------------------|-------------------------------------|
| Rock type: | Mylonitic gneiss                    | Serpentinite                         | Gneiss                              | Garnet amphibolite                 | Garnet mica schist                  | Garnet mica schist                  |
| Location:  | 38.58889° N<br>98.5402° E<br>4215 m | 38.60758° N<br>98.99772° E<br>4360 m | 38.50647° N<br>98.6993° E<br>4314 m | 38.4625° N<br>98.8036° E<br>4170 m | 38.5065° N<br>98.69933° E<br>4314 m | 38.7131° N<br>98.60619° E<br>3516 m |
| Nd         | 28                                  | 13                                   | 23                                  | 19                                 | 51                                  | 45                                  |
| Sm         | 6                                   | 1                                    | 4                                   | 5                                  | 8                                   | 8                                   |
| Eu         | 1                                   | -                                    | -                                   | -                                  | -                                   | -                                   |
| Gd         | 6                                   | -                                    | -                                   | -                                  | -                                   | -                                   |
| Tb         | 1                                   | -                                    | -                                   | -                                  | -                                   | -                                   |
| Dy         | 6                                   | -                                    | -                                   | -                                  | -                                   | -                                   |
| Ho         | 1                                   | -                                    | -                                   | -                                  | -                                   | -                                   |
| Er         | 4                                   | -                                    | -                                   | -                                  | -                                   | -                                   |
| Tm         | 1                                   | -                                    | -                                   | -                                  | -                                   | -                                   |
| Yb         | 5                                   | -                                    | -                                   | -                                  | -                                   | -                                   |
| Lu         | 1                                   | -                                    | -                                   | -                                  | -                                   | -                                   |
| Hf         | 4                                   | 0                                    | 3                                   | 2                                  | 6                                   | 6                                   |
| Ta         | 1                                   | 0                                    | 0                                   | 0                                  | 0                                   | 1                                   |
| W          | -                                   | -                                    | -                                   | -                                  | -                                   | -                                   |
| Tl         | 1                                   | -                                    | -                                   | -                                  | -                                   | -                                   |
| Pb         | 39                                  | 0                                    | 5                                   | 0                                  | 30                                  | 37                                  |
| Bi         | < 0.4                               | -                                    | -                                   | -                                  | -                                   | -                                   |
| Th         | 16                                  | 0                                    | 4.1                                 | 00                                 | 18                                  | 23                                  |
| U          | 3                                   | 0                                    | 2.1                                 | 3                                  | 3                                   | 6                                   |
| S          | 238                                 | 712                                  | 232                                 | 64                                 | < dl                                | < dl                                |
| Ti*        | 2028                                | 71                                   | 10142                               | 15618                              | 6047                                | 4821                                |
| K*         | 39228                               | 0                                    | 9078                                | 4034                               | 19598                               | 33381                               |
| P*         | 671                                 | 0                                    | 900                                 | 1083                               | 272                                 | 270                                 |



**Table 5.4. Whole-rock geochemistry data (continued)**

|               |                                      |                                      |
|---------------|--------------------------------------|--------------------------------------|
| Sample:       | RR 05-05-<br>12 (12)                 | AY 09-21-<br>11 (6)                  |
| Rock<br>type: | Garnet<br>amphibolite                | Garnet<br>amphibolite                |
| Location:     | 38.66430° N<br>98.56219° E<br>3725 m | 38.65617° N<br>98.76244° E<br>3693 m |

*Major and minor elements (wt %)*

|                                |       |       |
|--------------------------------|-------|-------|
| SiO <sub>2</sub>               | 49.76 | 52.1  |
| Al <sub>2</sub> O <sub>3</sub> | 1.63  | 1.59  |
| Fe <sub>2</sub> O <sub>3</sub> | 15.02 | 12.63 |
| MnO                            | 12.49 | 14.39 |
| MgO                            | 0.22  | 0.24  |
| CaO                            | 5.41  | 5.19  |
| Na <sub>2</sub> O              | 10.26 | 9.03  |
| K <sub>2</sub> O               | 2.16  | 1.82  |
| TiO <sub>2</sub>               | 0.40  | 0.59  |
| P <sub>2</sub> O <sub>5</sub>  | 0.15  | 0.16  |
| LOI <sup>@</sup>               | 2.41  | 2.17  |
| Total <sup>#</sup>             | 99.91 | 99.91 |

*Trace elements (ppm)*

|    |     |     |
|----|-----|-----|
| Sc | 44  | 43  |
| Be | -   | -   |
| V  | 343 | 372 |
| Cr | 82  | 39  |
| Co | 72  | 73  |
| Ni | 176 | 127 |
| Cu | 108 | 118 |
| Zn | 34  | 118 |
| Ga | 20  | 18  |
| Ge | -   | -   |
| As | 9   | 13  |
| Rb | 17  | 20  |
| Sr | 190 | 132 |
| Y  | 37  | 37  |
| Zr | 126 | 131 |
| Nb | 16  | 18  |
| Mo | 0   | 0   |
| Ag | -   | -   |
| In | -   | -   |
| Sn | -   | -   |
| Sb | -   | -   |
| Cs | 4   | 0   |
| Ba | 75  | 104 |
| La | 22  | 17  |
| Ce | 34  | 39  |
| Pr | 2   | 1   |

**Table 5.4. Whole-rock geochemistry data (continued)**

| Sample:       | RR 05-05-<br>12 (12)                 | AY 09-21-<br>11 (6)                  |
|---------------|--------------------------------------|--------------------------------------|
| Rock<br>type: | Garnet<br>amphibolite                | Garnet<br>amphibolite                |
| Location:     | 38.66430° N<br>98.56219° E<br>3725 m | 38.65617° N<br>98.76244° E<br>3693 m |
| Nd            | 14                                   | 10                                   |
| Sm            | 4                                    | 6                                    |
| Eu            | -                                    | -                                    |
| Gd            | -                                    | -                                    |
| Tb            | -                                    | -                                    |
| Dy            | -                                    | -                                    |
| Ho            | -                                    | -                                    |
| Er            | -                                    | -                                    |
| Tm            | -                                    | -                                    |
| Yb            | -                                    | -                                    |
| Lu            | -                                    | -                                    |
| Hf            | 4                                    | 3                                    |
| Ta            | 0                                    | 0                                    |
| W             | -                                    | -                                    |
| Tl            | -                                    | -                                    |
| Pb            | 5                                    | 7                                    |
| Bi            | -                                    | -                                    |
| Th            | 0                                    | 2                                    |
| U             | 3                                    | 5                                    |
| S             | < dl                                 | < dl                                 |
| Ti*           | 10004                                | 9736                                 |
| K*            | 3400                                 | 5003                                 |
| P*            | 670                                  | 713                                  |

"< dl" Below lower detection limit

-- Not measured or below detection limit

\*Calculated from oxide wt %

@ Loss on ignition (LOI) values

# Summed major-element oxide abundances, including LOI values

Trace element concentrations have been normalized

**Table 5.5. P-T data from THERMOCALC for selected metamorphic rocks**

| Sample   | Location <sup>&amp;</sup>                            | Minerals                         | T (°C) | S.D. | P (kbar) | S.D.  | Corr <sup>@</sup> |       |
|--|--|----------------------------------|--------|------|----------|-------|-------------------|-------|
| AY 09-21-11 (1A)<br><i>Garnet-mica schist</i>                                | grt3b_p  | Grt Bt Ms Pl                     | 490    | 83   | 7.4      | 1.4   | 0.813             |       |
|  |  | Grt Bt Ms Pl                     | 591    | 80   | 8.3      | 1.3   | 0.729             |       |
|  | grt3a_p  | Grt Bt Ms Pl                     | 531    | 90   | 7.8      | 1.5   | 0.757             |       |
|  |  | Grt Chl Ms Pl H <sub>2</sub> O*  | 555    | 19   | 6.2      | 1.0   | 0.595             |       |
|  | grt4_p   | Grt Bt Ms Pl                     | 450    | 153  | 7.0      | 2.6   | 0.865             |       |
|  | grt5_p   | Ti-in-Bt <sup>l</sup>            | 569    | 24   | -        | -     | -                 |       |
| <i>Weighted average (95% confidence)<sup>%</sup></i>                         |  |                                  | 552    | 35   | 7.2      | 1.2   | 0.724             |       |
| *X <sub>H<sub>2</sub>O</sub> =0.68; no water gives 561±72°C and 5.1±1.1 kbar |  |                                  |        |      |          |       |                   |       |
| AZ 04-18-12 (4b)<br><i>Garnet-mica schist</i>                                | grt1_p   | Grt Bt                           | 589    | 23   | -        | -     |                   |       |
|  |  | Grt Bt                           | 674    | 23   | -        | -     |                   |       |
|  | grt4_p   | Ti-in-Bt <sup>l</sup>            | 572    | 24   | -        | -     |                   |       |
|  |  | Ti-in-Bt <sup>l</sup>            | 662    | 24   | -        | -     |                   |       |
|  | <i>Weighted average (95% confidence)</i>             |                                  |        | 625  | 23       |       |                   |       |
| RR 05-05-12 (8)<br><i>Quartzofeldspathic gneiss</i>                          | grt1_p   | Grt Bt Ms Pl H <sub>2</sub> O    | 714    | 27   | 6.1      | 1.1   | 0.722             |       |
|  |  | Ti-in-Bt <sup>l</sup>            | 730    | 29   | 6.5      | 1.1   | 0.727             |       |
|  |  | Ti-in-Bt <sup>l</sup>            | 692    | 24   | -        | -     | -                 |       |
|  |  | Ti-in-Bt <sup>l</sup>            | 748    | 29   | 7.4      | 1.1   | 0.716             |       |
|  | grt2_p   | Grt Bt Ms Pl Kf H <sub>2</sub> O | 733    | 28   | 6.7      | 1.1   | 0.722             |       |
|  |  | Ti-in-Bt <sup>l</sup>            | 678    | 24   | -        | -     | -                 |       |
|  | grt3_p   | Grt Bt Ms Pl Kf H <sub>2</sub> O | 728    | 27   | 7        | 1.1   | 0.726             |       |
|  | <i>Weighted average (95% confidence)<sup>%</sup></i> |                                  |        | 725  | 85       | 6.8   | 1.0               | 0.723 |
| AY 09-21-11 (6A)<br><i>Garnet amphibolite</i>                                | grt1_p   | Grt Pl Qtz Hbl                   | 748    | 93   | 7.8      | 1.5   | 0.607             |       |
|  |  | Grt Pl Qtz Hbl                   | 872    | 101  | 9.8      | 1.6   | 0.725             |       |
|  |  | Grt Pl Qtz Hbl                   | 685    | 73   | 7.6      | 1.2   | 0.635             |       |
|  | grt2_p   | Grt Pl Qtz Hbl                   | 664    | 89   | 7.2      | 1.5   | 0.698             |       |
|  |  | Grt Pl Qtz Hbl                   | 699    | 72   | 7.9      | 1.2   | 0.635             |       |
|  |  | Grt Pl Qtz Hbl                   | 738    | 80   | 8.1      | 1.3   | 0.645             |       |
|  |  | Grt Pl Qtz Hbl                   | 638    | 65   | 6.4      | 1.0   | 0.585             |       |
|  | grt4_p   | Grt Pl Qtz Hbl                   | 799    | 90   | 9        | 1.4   | 0.673             |       |
|  |  | Grt Pl Qtz Hbl                   | 838    | 95   | 9.7      | 1.5   | 0.689             |       |
|  | <i>Weighted average (95% confidence)</i>             |                                  |        | 725  | 53       | 7.9   | 0.9               | 0.655 |
|  | grt1_c   | Grt Pl Qtz Hbl                   | 635    | 68   | 6.7      | 1.2   | 0.664             |       |
|  |  | Grt Pl Qtz Hbl                   | 638    | 69   | 6.7      | 1.2   | 0.659             |       |
|  | grt2_c   | Grt Pl Qtz Hbl                   | 591    | 63   | 6.8      | 1.1   | 0.670             |       |
|  |  | Grt Pl Qtz Hbl                   | 634    | 68   | 6.5      | 1.1   | 0.641             |       |
|  | grt4_c   | Grt Pl Qtz Hbl                   | 601    | 64   | 7.6      | 1.2   | 0.672             |       |
|  |  | Grt Pl Qtz Hbl                   | 601    | 64   | 8.2      | 1.3   | 0.671             |       |
| Grt Pl Qtz Hbl   |  | 607                              | 65     | 7.9  | 1.2      | 0.675 |                   |       |
| <i>Weighted average (95% confidence)</i>                                     |  |                                  | 614    | 49   | 7.2      | 0.9   | 0.665             |       |

**Table 5.5. P-T data from THERMOCALC for selected metamorphic rocks (continued)**

| Sample                                   | Location   | Minerals            | T (°C) | S.D. | P (kbar) | S.D. | Corr  |
|--|--|---------------------|--------|------|----------|------|-------|
| RR 05-05-12 (12)                         |  |                     | 629    | 135  | 6.7      | 2.2  | 0.555 |
| <i>Garnet amphibolite</i>                | grt1_c   | Grt Pl Qtz Hbl      | 613    | 161  | 6        | 2.6  | 0.515 |
|  |  |                     | 605    | 157  | 6.3      | 2.6  | 0.531 |
|  | grt4_c   | Grt Pl Qtz Hbl      | 669    | 67   | 7.3      | 1.1  | 0.540 |
|  | <i>Weighted average (95% confidence)</i>             |                     | 650    | 100  | 7        | 1.7  | 0.535 |
|  | grt1_p   | Grt Pl Qtz Hbl      | 772    | 91   | 9        | 1.5  | 0.683 |
|  |  |                     | 825    | 96   | 10.1     | 1.6  | 0.644 |
|  | grt4_p   | Grt Pl Qtz Hbl      | 788    | 138  | 7.8      | 2.1  | 0.591 |
|  |  |                     | 772    | 123  | 7.9      | 1.9  | 0.589 |
|  | grt1   | Hbl-Pl <sup>2</sup> | 695    | 35   | -        | -    | -     |
|  | <i>Weighted average (95% confidence)<sup>%</sup></i> |                     | 791    | 110  | 8.9      | 1.7  | 0.627 |
|  | grt1_r   | Grt Pl Qtz Hbl      | 667    | 68   | 6.3      | 1.1  | 0.558 |
|  | grt4_r   | Grt Pl Qtz Hbl      | 658    | 67   | 6        | 1.1  | 0.550 |
|  | <i>Weighted average (95% confidence)</i>             |                     | 662    | 95   | 6.2      | 1.6  | 0.554 |
|  | <i>Overall weighted average (95% confidence)</i>     |                     | 696    | 41   | 7.3      | 0.8  | 0.575 |
| <hr/>                                    |  |                     |        |      |          |      |       |
| AZ 07-21-13 (5)                          | grt1_c   |                     | 574    | 102  | 4.6      | 1.8  | 0.590 |
| <i>Garnet amphibolite</i>                | grt1_p   | Grt Pl Qtz Hbl      | 574    | 71   | 5.2      | 1.3  | 0.587 |
|  |  |                     | 578    | 68   | 6.1      | 1.3  | 0.573 |
|  | <i>Weighted average (95% confidence)</i>             |                     | 576    | 88   | 5.4      | 1.6  | 0.583 |
| <hr/>                                    |  |                     |        |      |          |      |       |
| AZ 04-18-12 (4)                          | grtb1_p  | Hbl-Pl <sup>2</sup> | 611    | 24   | -        | -    |       |
| <i>Garnet-epidote amphibolite gneiss</i> | grt1a_p  | Grt Pl Qtz Hbl Ep   | 686    | 133  | 8.2      | 1.9  | 0.867 |
|  |  |                     | 683    | 145  | 8.1      | 2.0  | 0.873 |
|  | <i>Weighted average (95% confidence)</i>             |                     | 615    | 47   | 8.1      | 2.7  | 0.870 |

<sup>%</sup> Average of THERMOCALC data only

<sup>@</sup> Corr is correlation coefficient from THERMOCALC

<sup>&</sup> Location within the thin section (e.g., the specific garnet grain); r is retrogressed rim, p is inferred peak-metamorphism position based on garnet compositional zoning, and c is early metamorphism recorded in the core of the garnet grain

<sup>1</sup> Ti-in-biotite geothermometer of Henry et al. (2005)

<sup>2</sup> Geothermometer for coexisting hornblende and plagioclase of Holland and Blundy (1994)

## 5.12. References

- Aleinikoff, J. N., Schenck, W. S., Plank, M. O., Srogi, L., Fanning, C. M., Kamo, S. L., and Bosbyshell, H., 2006, Deciphering igneous and metamorphic events in high-grade rocks of the Wilmington Complex, Delaware: Morphology, cathodoluminescence and backscattered electron zoning, and SHRIMP U-Pb geochronology of zircon and monazite: *Geological Society of America Bulletin*, v. 118, no. 1-2, p. 39-64.
- Bhattacharya, A., Mohanty, L., Maji, A., Sen, S. K., and Raith, M., 1992, Non-ideal mixing in the phlogopite-annite binary: constraints from experimental data on Mg-Fe partitioning and a reformulation of the biotite-garnet thermometer: *Contributions to Mineralogy and Petrology*, v. 111, p. 87-93.
- Black, L. P., Kamo, S. L., Allen, C. M., Aleinikoff, J. N., Davis, D. W., Korsch, R. J., and Foudoulis, C., 2003, TEMORA 1: a new zircon standard for Phanerozoic U-Pb geochronology: *Chemical Geology*, v. 200, p. 155-170.
- Bohlen, S. R., and Liotta, J. J., 1986, A barometer for garnet amphibolites and garnet granulites: *Journal of Petrology*, v. 27, no. 5, p. 1025-1034.
- Bosse, V., et al., 2009, Fluid-induced disturbance of the monazite Th-Pb chronometer: in situ dating and element mapping in pegmatites from the Rhodope (Greece, Bulgaria): *Chemical geology*, v. 261, no. 3, p. 286-302.
- Boynton, W. V., 1984, Cosmochemistry of the rare earth elements: Meteorite studies, in Henderson, P., ed., *Rare Earth Element Geochemistry*: Amsterdam, Netherlands, Elsevier, p. 63-114.
- Burchfiel, B. C., Quidong, D., Molnar, P., Royden, L., Yipeng, W., Peizhen, Z., and Weiqi, Z., 1989, Intracrustal detachment within zones of continental deformation: *Geology*, v. 17, no. 8, p. 748-752.
- Catlos, E. J., Gilley, L. D., and Harrison, T. M., 2002, Interpretation of monazite ages obtained via in situ analysis: *Chemical Geology*, v. 188, no. 3, p. 193-215.
- Charvet, J., Shu, L. S., and Laurent-Charvet, S., 2007, Paleozoic structural and geodynamic evolution of eastern Tianshan (NW China): welding of the Tarim and Junggar plates: *Episodes*, v. 30, no. 3, p. 162-186.
- Chen, X., Yin, A., Gehrels, G. E., Cowgill, E. S., Grove, M., Harrison, T. M., and Wang, X. F., 2003, Two phases of Mesozoic north-south extension in the eastern Altyn Tagh range, northern Tibetan Plateau: *Tectonics*, v. 22, no. 5.
- Claoué-Long, J. C., Compton, W., Roberts, J., and Fanning, C. M., 1995, Two Carboniferous ages: a comparison of SHRIMP zircon dating with conventional zircon ages and  $^{40}\text{Ar}/^{39}\text{Ar}$  analysis: *SEPM special publication*, p. 3-21.

- Cleven, N. R., Lin, S., and Xiao, W., 2015, The Hongliuhe fold-and-thrust belt: Evidence of terminal collision and suture-reactivation after the Early Permian in the Beishan orogenic collage, Northwest China: *Gondwana Research*, v. 27, no. 2, p. 796-810.
- Coggon, R., and Holland, T. J. B., 2002, Mixing properties of phengitic micas and revised garnet-phengite thermobarometers: *Journal of Metamorphic Geology*, v. 20, no. 7, p. 683-696.
- Connolly, J. A. D., 2005, Computation of phase equilibria by linear programming: A tool for geodynamic modeling and its application to subduction zone decarbonation: *Earth and Planetary Science Letters*, v. 236, p. 524-541.
- Cowgill, E., Yin, A., Harrison, T. M., and Xiao-Feng, W., 2003, Reconstruction of the Altyn Tagh fault based on U-Pb geochronology: Role of back thrusts, mantle sutures, and heterogeneous crustal strength in forming the Tibetan Plateau: *Journal of Geophysical Research: Solid Earth*, v. 108, no. B7.
- Dale, J., Holland, T., and Powell, R., 2000, Hornblende–garnet–plagioclase thermobarometry: a natural assemblage calibration of the thermodynamics of hornblende: *Contributions to Mineralogy and Petrology*, v. 140, no. 3, p. 353-362.
- Dan, W., Li, X. H., Guo, J., Liu, Y., and Wang, X. C., 2012, Paleoproterozoic evolution of the eastern Alxa Block, westernmost North China: evidence from in situ zircon U-Pb dating and Hf–O isotopes: *Gondwana Research*, v. 21, no. 4, p. 838-864.
- Dang, J., 2011, Geochemical characteristics and tectonic implications of Jinfosi granite in north Qilian: *Gansu Geology*, v. 20, p. 40-44 (in Chinese with English abstract).
- Diamant, M., et al., 1992, Mentawai fault zone off Sumatra: A new key to the geodynamics of western Indonesia: *Geology*, v. 20, no. 3, p. 259-262.
- Dong, Y., Zhang, G., Neubauer, F., Liu, X., Genser, J., and Hauzenberger, C., 2011, Tectonic evolution of the Qinling orogen, China: review and synthesis: *Journal of Asian Earth Sciences*, v. 41, no. 3, p. 213-237.
- Evans, B.W., 1990, Phase relations of epidote-blueschists: *Lithos*, v. 25, no. 1, p. 3-23.
- Force, E. R., 1997, Geology and mineral resources of the Santa Catalina Mountains, southeastern Arizona. *Monographs in Mineral Science*, vol. 1: Tuscon, AZ, Center for Mineral Resources, 135 p.
- Foster, G., Kinny, P., Vance, D., Prince, C., and Harris, N., 2000, The significance of monazite U–Th–Pb age data in metamorphic assemblages; a combined study of monazite and garnet chronometry: *Earth and Planetary Science Letters*, v. 181, no. 3, p. 327-340.
- Gansu Geological Bureau, 1989, Regional geology of Gansu Province: Beijing, Geological Publishing House, 692 p. (in Chinese).

- Garrels, L. M., and MacKenzie, F. T., 1971, *Evolution of Sedimentary Rocks*: New York, W. W. Norton and Co., 397 p.
- Gasser, D., Bruand, E., Rubatto, D., and Stüwe, K., 2012, The behaviour of monazite from greenschist facies phyllites to anatectic gneisses: an example from the Chugach Metamorphic Complex, southern Alaska: *Lithos*, v. 134, p. 108-122.
- Gehrels, G. E., Yin, A., and Wang, X.F., 2003a, Detrital zircon geochronology of the northeastern Tibet: *Geological Society of America Bulletin*, v. 115, p. 881-896.
- Gehrels, G. E., Yin, A., and Wang, X. F., 2003b, Magmatic history of the Altyn Tagh, Nan Shan, and Qilian Shan region of western China: *Journal of Geophysical Research*, v. 108.
- Gehrels, G., et al., 2011, Detrital zircon geochronology of pre-Tertiary strata in the Tibetan-Himalayan orogen: *Tectonics*, v. 30, no. 5.
- Gong, J. H., Zhang, J. X., and Yu, S. Y., 2011, The origin of Longshoushan Group and associated rocks in the southern part of the Alxa block: constraint from LA-ICP-MS U-Pb zircon dating: *Acta Petrologica et Mineralogica*, v. 30, no. 5, p. 795-818.
- Graham, C. M., and Powell, R., 1984, A garnet–hornblende geothermometer: calibration, testing, and application to the Pelona Schist, Southern California: *Journal of Metamorphic Geology*, v. 2, p. 13-21.
- Grove, M., Jacobson, C. E., Barth, A. P., and Vucic, A., 2003, Temporal and spatial trends of Late Cretaceous-early Tertiary underplating of Pelona and related schist beneath southern California and southwestern Arizona: *Tectonic evolution of northwestern Mexico and the southwestern USA*, v. 374.
- Guo, Z. J., Yin, A., Robinson, A., and Jia, C. Z., 2005, Geochronology and geochemistry of deep-drill-core samples from the basement of the central Tarim basin: *Journal of Asian Earth Sciences*, v. 25, no. 1, p. 45-56.
- Guo, Q. Q., Xiao, W. J., Windley, B. F., Mao, Q. G., Han, C. M., Qu, J. F., Ao, S. J., Li, J. L., Song, D. F., and Yong, Y., 2011, Provenance and tectonic settings of Permian turbidites from the Beishan Mountains, NW China: Implications for the Late Paleozoic accretionary tectonics of the southern Altaids: *Journal of Asian Earth Sciences*, v. 49, p. 54-68.
- Han, G., Liu, Y., Neubauer, F., Genser, J., Li, W., Zhao, Y., and Liang, C., 2011, Origin of terranes in the eastern Central Asian Orogenic Belt, NE China: U–Pb ages of detrital zircons from Ordovician–Devonian sandstones, North Da Xing'an Mts: *Tectonophysics*, v. 511, no. 3, p. 109-124.
- Harrison, T. M., McKeegan, K. D., and LeFort, P., 1995, Detection of inherited monazite in the Manaslu leucogranite by  $^{208}\text{Pb}/^{232}\text{Th}$  ion microprobe dating: crystallization age and tectonic implications: *Earth and Planetary Science Letters*, v. 133, no. 3, p. 271-282.

- Harrison, T. M., Grove, M., and Lovera, O. M., 1997, New insights into the origin of two contrasting Himalayan granite belts. *Geology* v. 25, p. 899-902.
- Harrison, T. M., Grove, M., McKeegan, K. D., Coath, C. D., Lovera, O. M., and Le Fort, P., 1999, Origin and episodic emplacement of the Manaslu Intrusive Complex, central Himalaya: *Journal of Petrology*, v. 40, p. 3-19.
- Hawthorne, F. C., Oberti, R., Harlow, G. E., Maresch, W. V., Martin, R. F., Schumacher, J. C., and Welch, M. D., 2012, Nomenclature of the amphibole supergroup: *American Mineralogist*, v. 97, no. 11-12, p. 2031-2048.
- Hawthorne, F. C., Oberti, R., Harlow, G. E., Maresch, W. V., Martin, R. F., Schumacher, J. C., and Welch, M. D., 2012, Nomenclature of the amphibole supergroup: *American Mineralogist*, v. 97, no. 11-12, p. 2031-2048.
- He, S. P., Wang, H. L., Chen, J. L., Xu, X. Y., Zhang, H. F., Ren, G. M., and Yu, J. Y., 2007, LA-ICP-MS U-Pb zircon geochronology of basic dikes within Maxianshan rock group in the central Qilian orogenic belt and its tectonic implications: *Journal of China University of Geosciences*, v. 18, p. 19-29.
- Henry, D. J., Guidotti, C. V., and Thomson, J. A., 2005, The Ti-saturation surface for low-to-medium pressure metapelitic biotites: Implications for geothermometry and Ti-substitution mechanisms: *American Mineralogist*, v. 90, no. 2-3, p. 316-328.
- Herron, M. M., 1988, Geochemical classification of terrigenous sands and shales from core or log data: *Journal of Sedimentary Research*, v. 58, no. 5.
- Heubeck, C., 2001, Assembly of central Asia during the middle and late Paleozoic, in *Paleozoic and Mesozoic Tectonic Evolution of Central Asia: From Continental Assembly to Intracontinental Deformation*, Hendrix, M.S., and Davis, G.A. (eds): Geological Society of America Memoir 194, p. 1-22.
- Hirth, G., and Tullis, J., 1992, Dislocation creep regimes in quartz aggregates: *Journal of Structural Geology*, v. 14, no. 2, p. 145-159.
- Hodges, K. V., and Spear, F. S., 1982, Geothermometry, geobarometry garnet closure temperatures and the Al<sub>2</sub>SiO<sub>5</sub> triple point, Mt. Moosilauke: *NH Trans.-Am. Geophys. Union*, v. 62, no. 45.
- Holland, T., and Blundy, J., 1994, Non-ideal interactions in calcic amphiboles and their bearing on amphibole-plagioclase thermometry: *Contributions to mineralogy and petrology*, v. 116, no. 4, p. 433-447.
- Holland, T. J. B., and Powell, R., 2011, An improved and extended internally consistent thermodynamic dataset for phases of petrological interest, involving a new equation of state for solids: *Journal of Metamorphic Geology*, v. 29, no. 3, p. 333-383.



- Holland, T., and Powell, R., 1998, An internally consistent thermodynamic dataset for phases of petrological interest: *Journal of Metamorphic Geology*, v. 16, p. 309.
- Hou, Q., Zhao, Z., Zhang, H., Zhang, B., and Chen, Y., 2006, Indian Ocean-MORB-type isotopic signature of Yushigou ophiolite in North Qilian Mountains and its implications: *Science in China Series D*, v. 49, no. 6, p. 561-572.
- Hsü, K. J., Guitang, P., and Sengör, A. M. C., 1995, Tectonic evolution of the Tibetan Plateau: a working hypothesis based on the archipelago model of orogenesis: *International Geology Review*, v. 37, no. 6, p. 473-508.
- Hu, A., Jahn, B.M., Zhang, G., Chen, Y., and Zhang, Q., 2000, Crustal evolution and Phanerozoic crustal growth in northern Xinjiang: Nd isotopic evidence. Part I. Isotopic characterization of basement rocks: *Tectonophysics*, v. 328, no. 1, p. 15-51.
- Hu, N.G., Xu, A.D., and Yang, J.X., 2005, Characteristics and tectonic environment of Zhigoumen pluton in Longshoushan area: *Journal of Earth Sciences and Environment*, v. 27, p. 5-11 (in Chinese with English abstract).
- Huo, Y. L., and Tan, S. D., 1995, Exploration case history and petroleum geology in Jiuquan continental basin: Beijing, China, Petroleum Industry Press, 211 p.
- Jensen, L.S., 1976, A new cation plot for classifying subalkalic volcanic rocks: Ontario Geological Survey Miscellaneous Paper, v. 66.
- Johnson, D. M., Hooper, P. R., and Conrey, R. M., 1999, XRF analysis of rocks and minerals for major and trace elements on a single low dilution Li-tetraborate fused bead: *Advances in X-ray Analysis*, v. 41, p. 843-867.
- Kohn, M. J., Wieland, M. S., Parkinson, C. D., and Upreti, B. N., 2005, Five generations of monazite in Langtang gneisses: implications for chronology of the Himalayan metamorphic core: *Journal of Metamorphic Geology*, v. 23, no. 5, p. 399-406.
- Kapp, P., Manning, C. E., and Tropper, P., 2009, Phase-equilibrium constraints on titanite and rutile activities in mafic epidote amphibolites and geobarometry using titanite–rutile equilibria: *Journal of Metamorphic Geology*, v. 27, no. 7, p. 509-521.
- Kohn, M. J., and Spear, F. S., 1989, Empirical calibration of geobarometers for the assemblage garnet+ plagioclase+ quartz: *American Mineralogist*, v. 74, no. 1-2, p. 77-84.
- Kohn, M. J., and Spear, F. S., 1990, Two new geobarometers for garnet amphibolites, with applications to southeastern Vermont: *American Mineralogist*, v. 75, no. 1-2, p. 89-96.
- Kröner, A., et al., 2013, Mesoproterozoic (Grenville-age) terranes in the Kyrgyz North Tianshan: zircon ages and Nd–Hf isotopic constraints on the origin and evolution of basement blocks in the southern Central Asian Orogen: *Gondwana Research*, v. 23, no. 1, p. 272-295.

- Kuno, H., 1968, Differentiation of basaltic magma, in Hess, H.H., and Poldervaart, A.A., eds., *The Poldervaart Treatise on Rocks of Basaltic Composition*, 2: New York, Interscience, p. 623-688.
- Laird, J., and Albee, A.L., 1981, Pressure, temperature, and time indicators in mafic schist; their application to reconstructing the polymetamorphic history of Vermont: *American Journal of Science*, v. 281, no. 2, p. 127-175.
- Leake, B. E., et al., 2004, Nomenclature of amphiboles: additions and revisions to the International Mineralogical Association's amphibole nomenclature: *Mineralogical Magazine*, v. 68, n. 1, p. 209-215
- Li, C. Y., Liu, Y. W., Zhu, B. C., Feng, Y. M., and Wu, H. Q., 1978, Structural evolutions of Qinling and Qilian: Beijing, Geological Publishing House (in Chinese with English abstract).
- Li, Z. X., et al., 2008, Assembly, configuration, and break-up history of Rodinia: a synthesis: *Precambrian research*, v. 160, no. 1, p. 179-210.
- Li, X. H., Su, L., Chung, S. L., Li, Z. X., Liu, Y., Song, B., and Liu, D. Y., 2005, Formation of the Jinchuan ultramafic intrusion and the world's third largest Ni-Cu sulfide deposit: Associated with the ~825 Ma south China mantle plume?. *Geochemistry, Geophysics, Geosystems*: v. 6, no. 11.
- Lin, Y. H., Zhang, L.F., Ji, J.Q., and Song, S.G., 2010,  $^{40}\text{Ar}/^{39}\text{Ar}$  age of Jiugequan lawsonite blueschists in northern Qilian Mountains and its petrologic significance: *Chinese Science Bulletin*, v. 55, p. 2021-2027.
- Liou, J. G., Graham, S. A., Maruyama, S., and Zhang, R. Y., 1996, Characteristics and tectonic significance of the Late Proterozoic Aksu blueschists and diabasic dikes, Northwest Xinjiang, China: *International Geology Review*, v. 38, no. 3, p. 228-244.
- Liu, Y. J., Neubauer, F., Genser, J., Takasu, A., Ge, X. H., and Handler, R., 2006,  $^{40}\text{Ar}/^{39}\text{Ar}$  ages of blueschist facies pelitic schists from Qingshuigou in the Northern Qilian Mountains, western China: *Island Arc*, v. 15, no. 1, p. 187-198.
- Locock, A. J., 2014, An Excel spreadsheet to classify chemical analyses of amphiboles following the IMA 2012 recommendations: *Computers & Geosciences*, v. 62, p. 1-11.
- Long, X., et al., 2010, Archean crustal evolution of the northern Tarim craton, NW China: Zircon U-Pb and Hf isotopic constraints: *Precambrian Research*, v. 180, no. 3, p. 272-284.
- Ludwig, K. R., 2003, User's manual for Isoplot 3.00: a geochronological toolkit for Microsoft Excel: Berkeley Geochronology Center: Special Publication, no. 4.
- Ma, X., Shu, L., Santosh, M., and Li, J., 2012, Detrital zircon U-Pb geochronology and Hf isotope data from Central Tianshan suggesting a link with the Tarim Block: implications on Proterozoic supercontinent history: *Precambrian Research*, v. 206, p. 1-16.

- Mao, J., Zhang, Z., Yang, J., Song, B., Wu, M., and Zuo, G., 1998, Single-zircon dating of Precambrian strata in the west sector of the northern Qilian Mountains and its geological significance: *Chinese Science Bulletin*, v. 43, no. 15, p. 1289-1294.
- Massonne, H. J., 2012, Formation of amphibole and clinozoisite–epidote in eclogite owing to fluid infiltration during exhumation in a subduction channel: *Journal of Petrology*, v. 53, no. 10, p. 1969-1998.
- Mattinson, C. G., Wooden, J. L., Liou, J. G., Bird, D. K., and Wu, C. L., 2006, Age and duration of eclogite-facies metamorphism, North Qaidam HP/UHP terrane, western China: *American Journal of Science*, v. 306, no. 9, p. 683-711.
- Mattinson, C. G., Menold, C. A., Zhang, J. X., and Bird, D. K., 2007, High-and ultrahigh-pressure metamorphism in the North Qaidam and South Altyn Terranes, western China: *International Geology Review*, v. 49, no. 11, p. 969-995.
- Meng, F. C., Zhang, J. X., Ker, C. M., and Li, J. P., 2010, Constraints on the evolution of the North Qilian ocean basin: MOR-type and SSZ-type ophiolites from Dachadaban: *Acta Petrologica et Mineralogica*, v. 29, no. 5, p. 453-466.
- Menold, C. A., Manning, C. E., Yin, A., Tropper, P., Chen, X. H., and Wang, X. F., 2009, Metamorphic evolution, mineral chemistry and thermobarometry of orthogneiss hosting ultrahigh-pressure eclogites in the North Qaidam metamorphic belt, Western China: *Journal of Asian Earth Sciences*, v. 35, no. 3, p. 273-284.
- Menold, C. A., Grove, M., Manning, C. E., Yin, A., Young, E. D., and Ziegler, K., 2016, Argon and Oxygen Isotopic Evidence for Pervasive Metasomatism during Ultrahigh-Pressure Continental Subduction: *EPSL*, in press.
- Meyer, B., Tapponnier, P., Bourjot, L., Métivier, F., Gaudemer, Y., Peltzer, G., Shunmin, G., and Zhitai, C., 1998, Crustal thickening in Gansu-Qinghai, lithospheric mantle subduction, and oblique, strike-slip controlled growth of the Tibet Plateau: *Geophysical Journal International*, v. 135, p. 1-47.
- Montel, J. M., Kornprobst, J., and Vielzeuf, D., 2000, Preservation of old U-Th-Pb ages in shielded monazite: example from the Beni Bousera Hercynian kinzigites (Morocco): *Journal of Metamorphic Geology*, v. 18, no. 3, p. 335-342.
- Newton, R. C., and Perkins, D. I. I., 1982, Thermodynamic calibration of geobarometers based on the assemblages garnet-plagioclase-orthopyroxene (clinopyroxene)-quartz: *American Mineralogist*, v. 67, no. 3-4, p. 203-222.
- Paces, J. B., and Miller, J. D., 1993, Precise U-Pb ages of Duluth complex and related mafic intrusions, northeastern Minnesota: Geochronological insights to physical, petrogenetic, paleomagnetic, and tectonomagmatic processes associated with the 1.1 Ga midcontinent rift system: *Journal of Geophysical Research: Solid Earth*, v. 98, no. B8, p. 13997-14013.

- Pan, G., Ding, J., Yao, D., and Wang, L., 2004, Geological map of Qinghai-Xiang (Tibet) plateau and adjacent areas (1:1,500,000): Chengdu Institute of Geology and Mineral Resources, China Geological Survey, Chengdu Cartographic Publishing House, Chengdu, China.
- Pattison, D.R., Chacko, T., Farquhar, J., and McFarlane, C.R., 2003, Temperatures of granulite-facies metamorphism: constraints from experimental phase equilibria and thermobarometry corrected for retrograde exchange: *Journal of Petrology*, v. 44, no. 5, p. 867-900.
- Pearce, J. A., Harris, N. B., and Tindle, A. G., 1984, Trace element discrimination diagrams for the tectonic interpretation of granitic rocks: *Journal of Petrology*, v. 25, no 4, p. 956-983.
- Petford, N., Cruden, A. R., McCaffrey, K. J. W., and Vigneresse, J. L., 2000, Granite magma formation, transport and emplacement in the Earth's crust: *Nature*, v. 408, no. 6813, p. 669-673.
- Plyusnina, L. P., 1982, Geothermometry and geobarometry of plagioclase-hornblende bearing assemblages: *Contributions to Mineralogy and Petrology*, v. 80, no. 2, p. 140-146.
- Putnam, R., Glazner, A. F., Coleman, D. S., Kylander-Clark, A. R., Pavelsky, T., and Abbot, M. I., 2015, Plutonism in three dimensions: Field and geochemical relations on the southeast face of El Capitan, Yosemite National Park, California: *Geosphere*, v. 11, no. 4.
- Pyle, J.M., and Spear, F.S., 2003, Four generations of accessory-phase growth in low pressure migmatites from SW New Hampshire: *The American Mineralogist*, v. 88, p. 338–351.
- Pyle, J. M., Spear, F. S., Wark, D. A., Daniel, C. G., and Storm, L. C. (2005). Contributions to precision and accuracy of monazite microprobe ages: *American Mineralogist*, v. 90, no. 4, p. 547-577.
- Qian, Q., Wang, Y.M., Li, H.M., Jia, X.Q., Han, S., and Zhang, Q., 1998, Geochemical characteristics and genesis of diorites from Laohushan, Gansu Province: *Yanshi Xuebao*, v. 14, p. 520–528 (in Chinese with English abstract).
- Qinghai BGMR (Qinghai Bureau of Geology and Mineral Resources), 1991, Regional geology of Qinghai Province: Beijing, China, Geological Publishing House (in Chinese with English abstract).
- Quan, S., Jia, Q., Guo, Z., and Wang, W., 2006. Basic characteristics of granitoids related to tungsten mineralization in the Qilian mountain: *Mineral Deposits*, v. 25, p. 143-146 (in Chinese).
- Quidelleur, X., Grove, M., Lovera, O.M., Harrison, T.M., Yin, A., and Ryerson, F.J., 1997, The thermal evolution and slip history of the Renbu Zedong Thrust, southeastern Tibet: *Journal of Geophysical Research*, v. 102, p. 2659-2679.

- Rasmussen, B., and Muhling, J.R., 2007, Monazite begets monazite: evidence for dissolution of detrital monazite and reprecipitation of syntectonic monazite during low grade regional metamorphism: *Contributions to Mineralogy and Petrology*, v. 154, p. 675-689.
- Rojas-Agramonte, Y., et al., 2011, Detrital and xenocrystic zircon ages from Neoproterozoic to Palaeozoic arc terranes of Mongolia: significance for the origin of crustal fragments in the Central Asian Orogenic Belt: *Gondwana Research*, v. 19, no. 3, p. 751-763.
- Roser, B. P., and Korsch, R. J., 1986, Determination of tectonic setting of sandstone-mudstone suites using content and ratio: *The Journal of Geology*, p. 635-650.
- Scherrer, N. C., Engi, M., Gnos, E., Jakob, V. and Leichti, A., 2000, Monazite analyses: from sample preparation to microprobe age dating and REE quantification: *Schweizerische Mineralogische und Petrographische Mitteilungen*, v. 80, p. 93-105.
- Schmitz, M. D., Bowring, S. A., and Ireland, T. R., 2003, Evaluation of Duluth Complex anorthositic series (AS3) zircon as a U-Pb geochronological standard: New high-precision isotope dilution thermal ionization mass spectrometry results: *Geochimica et Cosmochimica Acta*, v. 67, no. 19, p. 3665-3672.
- Sengör, A. M. C., and Natal'in, B. A., 1996, Paleotectonics of Asia: Fragments of a synthesis, in Yin, A., and Harrison, T. M., eds., *The tectonics of Asia*: New York, NY, Cambridge University Press, p. 486-640.
- Shervais, J. W., 2001, Birth, death, and resurrection: The life cycle of suprasubduction zone ophiolites: *Geochemistry, Geophysics, Geosystems*, v. 2, no. 1.
- Shi, R. D., Yang, J. S., and Wu, C. L., 2004, First SHRIMP dating for the formation of the late Sinian Yushigou ophiolite North Qilian Mountains: *Acta Geologica Sinica*, v. 78, p. 649-657 (in Chinese with English abstract).
- Smith, H. A., and Barreiro, B., 1990, Monazite U-Pb dating of staurolite grade metamorphism in pelitic schists: *Contributions to Mineralogy and Petrology*, v. 105, no. 5, p. 602-615.
- Smith, A. D., 2006, The geochemistry and age of ophiolitic strata of the Xinglongshan Group: Implications for the amalgamation of the Central Qilian belt: *Journal of Asian Earth Sciences*, v. 28, p. 133-142.
- Sobel, E. R., and Arnaud, N., 1999, A possible middle Paleozoic suture in the Altyn Tagh, NW China: *Tectonics*, v. 18, no. 1, p. 64-74.
- Song, S. G., Zhang, L. F., Niu, Y., Wei, C. J., Liou, J. G., and Shu, G. M., 2007, Eclogite and carpholite-bearing metasedimentary rocks in the North Qilian suture zone, NW China: implications for Early Palaeozoic cold oceanic subduction and water transport into mantle: *Journal of Metamorphic Geology*, v. 25, no. 5, p. 547-563.

- Song, S., Zhang, L., Niu, Y., Su, L., Song, B., and Liu, D., 2006, Evolution from oceanic subduction to continental collision: a case study from the Northern Tibetan Plateau based on geochemical and geochronological data: *Journal of Petrology*, v. 47, no. 3, p. 435-455.
- Song, S., Niu, Y., Su, L., and Xia, X., 2013, Tectonics of the North Qilian orogen, NW China: *Gondwana Research*, v. 23, no. 4, p. 1378-1401.
- Song, S., Niu, Y., Su, L., Zhang, C., and Zhang, L., 2014, Continental orogenesis from ocean subduction, continent collision/subduction, to orogen collapse, and orogen recycling: The example of the North Qaidam UHPM belt, NW China: *Earth-Science Reviews*, v. 129, p. 59-84.
- Spear, F. S., 1993, *Metamorphic phase equilibria and pressure-temperature-time paths*: Mineralogical Society of America Monograph, 799 p.
- Stacey, J. T., and Kramers, J. D., 1975, Approximation of terrestrial lead isotope evolution by a two-stage model: *Earth and Planetary Science Letters*, v. 26, no. 2, p. 207-221.
- Stampfli, G. M., and Borel, G. D., 2002, A plate tectonic model for the Paleozoic and Mesozoic constrained by dynamic plate boundaries and restored synthetic oceanic isochrones: *Earth and Planetary Science Letters*, v. 196, no. 1, p. 17-33.
- Stampfli, G. M., Hochard, C., V  rard, C., and Wilhem, C., 2013, The formation of Pangea: *Tectonophysics*, v. 593, p. 1-19.
- Stern, R. J., 2004, Subduction initiation: spontaneous and induced: *Earth and Planetary Science Letters*, v. 226, no. 3, p. 275-292.
- Stern, R. A., and Berman, R. G., 2001, Monazite U–Pb and Th–Pb geochronology by ion microprobe, with an application to in situ dating of an Archean metasedimentary rock: *Chemical Geology*, v. 172, no. 1, p. 113-130.
- Su, J. P., Zhang, X. H., Hu, N. G., Fu, G. M., and Zhang, H. F., 2004, Geochemical characteristics and genesis of adakite-like granites at Yema Nanshan in the western segment of the Central Qilian Mountains: *Chinese Geology*, v. 31, no. 1, p. 365-371 (in Chinese with English abstract).
- Sun, S. S., and McDonough, W. F., 1989, *Chemical and isotopic systematics of oceanic basalts: implications for mantle composition and processes*: Geological Society London, Special Publications, v. 42, no. 1, p. 313-345.
- Thompson, J. B., and Waldbaum, D. R., 1968, Mixing properties of sanidine crystalline solutions. I. Calculations based on ion-exchange data: *American Mineralogist*, v. 53, no. 11-1.
- Tseng, C. Y., Yang, H. Y., Yusheng, W., Dunyi, L., Wen, D. J., Lin, T. C., and Tung, K. A., 2006, Finding of Neoproterozoic (~775 Ma) magmatism recorded in metamorphic

- complexes from the North Qilian orogen: Evidence from SHRIMP zircon U-Pb dating: Chinese Science Bulletin, v. 51, no. 8, p. 963-970.
- Tseng, C.Y., Yang, H. J., Yang, H.Y., Liu, D., Tsai, C.L., Wu, H., and Zuo, G., 2007, The Dongcaohe ophiolite from the North Qilian Mountains: a fossil oceanic crust of the Paleozoic Qilian ocean: Chinese Science Bulletin, v. 52, no. 17, p. 2390-2401.
- Tseng, C. Y., Yang, H. J., Yang, H. Y., Liu, D., Wu, C., Cheng, C.K., Chen, C.H., and Ker, C. M., 2009, Continuity of the North Qilian and North Qinling orogenic belts, Central Orogenic System of China: evidence from newly discovered Paleozoic adakitic rocks; Gondwana Research, v. 16, no. 2, p. 285-293.
- Tung, K., Yang, H., Liu, D., Zhang, J., Tseng, C., and Wan, Y., 2007, SHRIMP U-Pb geochronology of the detrital zircons from the Longshoushan Group and its tectonic significance: Chinese Science Bulletin, v. 52, no. 10, p. 1414-1425.
- Vincent, S. J., and Allen, M. B., 1999, Evolution of the Minle and Chaoshui Basins, China: Implications for Mesozoic strike-slip basin formation in Central Asia: Geological Society of America Bulletin, v. 111, no. 5, p. 725-742.
- Wakabayashi, J., Ghatak, A., and Basu, A. R., 2010, Suprasubduction-zone ophiolite generation, emplacement, and initiation of subduction: A perspective from geochemistry, metamorphism, geochronology, and regional geology: Geological Society of America Bulletin, v. 122, no. 9-10, p. 1548-1568.
- Waldbaum, D. R., and Thompson, J. B., 1968, Mixing properties of sanidine crystalline solutions. 2. Calculations based on volume data: American Mineralogist, v. 53.
- Wan, Y., Xu, Z., Yang, J., and Zhang, J., 2001, Ages and Compositions of the Precambrian High-grade Basement of the Qilian Terrane and Its Adjacent Areas: Acta Geologica Sinica (English Edition), v. 75, p. 375-384.
- Wan, Y., Xu, Z., Yang, J., and Zhang, J., 2003, The Precambrian high-grade basement of the Qilian terrane and neighboring areas: its ages and compositions: Acta Geoscientia Sinica, v. 24, p. 319-324 (in Chinese with English abstract).
- Wan, Y., et al., 2013, Is the Ordos block Archean or Paleoproterozoic in age? Implications for the Precambrian evolution of the North China Craton: American Journal of Science, v. 313, no. 7, p. 683-711.
- Wang, E., and Burchfiel, B. C., 2004, Late Cenozoic right-lateral movement along the Wenquan fault and associated deformation: implications for the kinematic history of the Qaidam Basin, northeastern Tibetan Plateau: International Geology Review, v. 46, no. 10, p. 861-879.
- Wang, Q., and Liu, X. Y., 1976, The ancient oceanic crust and its tectonic implications, North Qilian Mountains, China: Scientia Geologica Sinica, no. 1, p. 42-55 (in Chinese with English abstract).

- Wang, B., Liu, H., Shu, L., Jahn, B. M., Chung, S. L., Zhai, Y., and Liu, D., 2014, Early Neoproterozoic crustal evolution in northern Yili Block: insights from migmatite, orthogneiss and leucogranite of the Wenquan metamorphic complex in the NW Chinese Tianshan: *Precambrian Research*, v. 242, p. 58-81.
- Werner, C. D., 1987, Saxonian granulites-igneous or lithogenous. A contribution to the geochemical diagnosis of the original rocks in high-metamorphic complexes: Contribution to the geology of the Saxonian granulite massif (Sächsisches Granulitgebirge), v. 133, p. 221-250.
- White R. W., Powell, R., Holland, T. J. B., 2007, Progress relating to calculation of partial melting equilibria for metapelites: *Journal of Metamorphic Geology*, v. 25, p. 511-27.
- Wiedenbeck, M. A. P. C., et al., 1995, Three natural zircon standards for U-Th-Pb, Lu-Hf, trace element and REE analyses: *Geostandards newsletter*, v. 19, no. 1, p. 1-23.
- Williams, I. S., 1998, U-Th-Pb geochronology by ion microprobe, in. McKibben, M.A., Shanks, W. C., Ridley, W. I., eds., *Applications of microanalytical techniques to understanding mineralizing processes: Reviews in Economic Geology*, v. 7, p. 1-35.
- Winchester, J. A., and Floyd, P. A., 1977, Geochemical discrimination of different magma series and their differentiation products using immobile elements: *Chemical geology*, v. 20, p. 325-343.
- Windley, B. F., Alexeiev, D., Xiao, W., Kröner, A., and Badarch, G., 2007, Tectonic models for accretion of the Central Asian Orogenic Belt: *Journal of the Geological Society*, v. 164, no. 1, p. 31-47.
- Wu, H., Feng, Y. and Song, S., 1993, Metamorphism and deformation of blueschist belts and their tectonic implications, North Qilian Mountains, China: *Journal of Metamorphic Geology*, v. 11, p. 523-536
- Wu, C. L., Yang, J.S., Yang, H.Y., Wooden, J.L., Shi, R.D., Chen, S.Y., and Zheng, Q.G., 2004, Two types of I-type granite dating and geological significance from North Qilian, NW China: *Acta Petrologica Sinica*, v. 20, no. 3, p. 425-432 (in Chinese with English abstract).
- Wu, C. L., Yao, S. Z., Zeng, L. S., et al., 2006, Double subduction of the Early Paleozoic North Qilian oceanic plate: evidence from granites in the central segment of North Qilian, NW China: *Geology in China*, v. 33, no. 6, p. 1197-1208 (in Chinese with English abstract).
- Wu, C. L., Xu, X.Y., Gao, Q.M., Li, X. M., Lei, M., Gao, Y. H., Frost, R. ., and Wooden, J. L., 2010, Early Palaeozoic granitoid magmatism and tectonic evolution in North Qilian, NW China: *Acta Petrologica Sinica*, v. 26, p. 1027-1044 (in Chinese with English abstract).
- Wu, C., Yin, A., Zusa, A. V., Zhang, J., Liu, W., and Ding, L., 2016, Pre-Cenozoic geologic history of the central and northern Tibetan Plateau and the role of Wilson cycles in constructing the Tethyan orogenic system: *Lithosphere*, in press.



- Xia, X., and Song, S., 2010, Forming age and tectono-petrogenises of the Jiugequan ophiolite in the North Qilian Mountain, NW China: *Chinese Science Bulletin*, v. 55, no. 18, p. 1899-1907. Xia et al., 1999
- Xia, X., Song, S., and Niu, Y., 2012, Tholeiite–Boninite terrane in the North Qilian suture zone: Implications for subduction initiation and back-arc basin development: *Chemical Geology*, v. 328, p. 259-277.
- Xiang, Z. Q., Lu, S. N., Li, H. K., Li, H. M., Song, B., and Zheng, J. K., 2007, SHRIMP U–Pb zircon age of gabbro in Aoyougou in the western segment of the North Qilian Mountains, China and its geological implications: *Geological Bulletin of China*, v. 26, p.1686-1691.
- Xiao, X. C., Chen, G.M., and Zhu, Z.Z., 1978, A preliminary study on the tectonics ancient ophiolites in the Qilian Mountain, northwest China: *Acta Geologica Sinica*, v. 4, p. 279-295 (in Chinese with English abstract).
- Xiao, W., Windley, B. F., Hao, J., and Zhai, M., 2003, Accretion leading to collision and the Permian Solonker suture, Inner Mongolia, China: termination of the central Asian orogenic belt: *Tectonics*, v. 22, no. 6.
- Xiao, W., Zhang, L. C., Qin, K. Z., Sun, S. and Li, J. L., 2004, Paleozoic accretionary and collisional tectonics of the eastern Tianshan (China): implications for the continental growth of Central Asia: *American Journal of Science*, v. 304, p. 370-395.
- Xiao, W., Windley, B. F., Yong, Y., Yan, Z., Yuan, C., Liu, C., and Li, J., 2009, Early Paleozoic to Devonian multiple-accretionary model for the Qilian Shan, NW China: *Journal of Asian Earth Sciences*, v. 35, no. 3, p. 323-333.
- Xiao, W., Huang, B., Han, C., Sun, S., and Li, J., 2010, A review of the western part of the Altaids: a key to understanding the architecture of accretionary orogens: *Gondwana Research*, v. 18, no. 2, p. 253-273.;
- Xiao, W., Li, S., Santosh, M., and Jahn, B. M., 2012, Orogenic belts in Central Asia: correlations and connections: *Journal of Asian Earth Sciences*, v. 49, p. 1-6.
- Xiong, Z., Zhang, H., and Zhang, J., 2012, Petrogenesis and tectonic implications of the Maozangsi and Huangyanghe granitic intrusions in Lenglongling area, the eastern part of North Qilian Mountain, NW China: *Earth Science Frontiers*, v. 19, p. 214-227.
- Xiu, Q. Y., Lu, S. N., Yu, H. F., and Yang, C. L., 2002, The isotopic age evidence for main Longshoushan Group contributing to Palaeoproterozoic: *Progress in Precambrian Research*, v. 25, no. 2, p. 93-96.
- Xu, X., He, S., Wang, H., Zhang, e., Chen, J., Sun, J., 2008. Tectonic framework of north Qinlian mountain and north Qilian mountain conjuction area in early Paleozoic: a study of the evidence from strata and tectonic-magmatic events: *Northwestern Geology*, v. 41, p. 1-21 (in Chinese with English abstract).

- Xu, X., Song, S., Su, L., Li, Z., Niu, Y., and Allen, M. B., 2015, The 600–580Ma continental rift basalts in North Qilian Shan, northwest China: Links between the Qilian-Qaidam block and SE Australia, and the reconstruction of East Gondwana: *Precambrian Research*, v. 257, p. 47-64.
- Yan, Z., Xiao, W., Wang, Z., and Li, J., 2007, Integrated analyses constraining the provenance of sandstones, mudstones, and conglomerates, a case study: the Laojunshan conglomerate, Qilian orogen, northwest China: *Canadian Journal of Earth Sciences*, v. 44, no. 7, p. 961-986.
- Yan, Z., Xiao, W. J., Windley, B. F., Wang, Z. Q., and Li, J. L., 2010, Silurian clastic sediments in the North Qilian Shan, NW China: Chemical and isotopic constraints on their forearc provenance with implications for the Paleozoic evolution of the Tibetan Plateau: *Sedimentary Geology*, v. 231, no. 3, p. 98-114.
- Yang, J. S., Xu, Z.Q., Zhang, J.X., Chu, C.Y., Zhang, R., and Liou, J.G., 2001, Tectonic significance of early Paleozoic high-pressure rocks in Altun-Qaidam-Qilian Mountains, northwest China, in Hendrix, M.S., and Davis, G.A., eds., *Paleozoic and Mesozoic Tectonic Evolution of Central Asia: From Continental Assembly to Intracontinental Deformation: Geological Society of America Memoir*, v. 194, p. 151-170.
- Yang, J. H., Du, Y.S., Cawood, P. A., and Xu, Y. J., 2009, Silurian collisional suturing onto the southern margin of the North Craton: Detrital zircon geochronology constraints from the Qilian orogen: *Sedimentary Geology*, v. 220, p. 95-104.
- Yang, J. H., Du, Y., Cawood, P. A., and Xu, Y., 2012, Modal and geochemical composition of the Lower Silurian clastic rocks in North Qilian, NW China: Implications for provenance, chemical weathering, and tectonic setting: *Journal of Sedimentology*, v. 82, p. 92-103.
- Yang, J., Xu, Z., Zhang, J., Song, S., Wu, C., Shi, R., Li, H., and Brunel, M., 2002, Early Paleozoic North Qaidam UHP metamorphic belt on the north-eastern Tibetan plateau and a paired subduction model: *Terra Nova*, v. 14, no. 5, p. 397-404.
- Yin, A., and Harrison, T. M., 2000, Geologic evolution of the Himalayan-Tibetan orogen: *Annual Review of Earth and Planetary Sciences*, v. 28, no. 1, p. 211-280.
- Yin, A., and Nie, S., 1993, An indentation model for the North and South China collision and the development of the Tan-Lu and Honam fault systems, eastern Asia: *Tectonics*, v. 12, no. 4, p. 801-813.
- Yin, A., and Nie, S. Y., 1996, A Phanerozoic palinspastic reconstruction of China and its neighboring regions, in Yin, A., and Harrison, T.M., eds., *The Tectonic Evolution of Asia: New York, Cambridge University Press*, p. 442-485.
- Yin, A., Manning, C. E., Lovera, O., Menold, C. A., Chen, X. H., and Gehrels, G. E., 2007a, Early Paleozoic tectonic and thermomechanical evolution of ultrahigh-pressure (UHP) metamorphic rocks in the northern Tibetan Plateau, northwest China: *International Geology Review*, v. 49, p. 681-716.

- Yin, A., Dang, Y. Q., Zhang, M., McRivette, M. W., Burgess, W. P., and Chen, X. H., 2007b, Cenozoic tectonic evolution of Qaidam Basin and its surrounding regions (part 2): Wedge tectonics in southern Qaidam Basin and the Eastern Kunlun Range, in Sears, J.W., Harms, T.A., and Evenchick, C.A., eds., *Whence the Mountains? Inquiries into the Evolution of Orogenic Systems: A Volume in Honor of Raymond A. Price*: Geological Society of America Special Paper, v. 433, p. 369-390.
- Yin, A., Dang, Y. Q., Wang, L. C., Jiang, W. M., Zhou, S. P., Chen, X. H., Gehrels, G. E., and McRivette, M. W., 2008a, Cenozoic tectonic evolution of Qaidam Basin and its surrounding regions (Part 1): The southern Qilian Shan–Nan Shan thrust belt and northern Qaidam Basin: *Geological Society of America Bulletin*, v. 120, p. 813-846.
- Yin, A., Dang, Y. Q., Zhang, M., Chen, X. H., and McRivette, M. W., 2008b, Cenozoic tectonic evolution of the Qaidam Basin and its surrounding regions (Part 3): Structural geology, sedimentation, and regional tectonic reconstruction: *Geological Society of America Bulletin*, v. 120, p. 847-876.
- Zhang, X. T., Yang, S.D., and Yang, Z. J., 2005, *Introduction to Regional Geology of Qinghai Province-Explanatory Notes of Geological Map of Qinghai Province in 1:1,000,000*: Beijing, Geological Publishing House, 158 p. (in Chinese with English abstract).
- Zhang, J., Zhang, Z., Xu, Z., Yang, J., and Cui, J., 2001, Petrology and geochronology of eclogites from the western segment of the Altyn Tagh, northwestern China: *Lithos*, v. 56, no. 2, p. 187-206.
- Zhang, J. X., Meng, F. C., Wan, Y. S., 2007, A cold Early Palaeozoic subduction zone in the North Qilian Mountains, NW China: petrological and U–Pb geochronological constraints: *Journal of Metamorphic Geology*, v. 25, p. 285-304.
- Zhao, G. C., Wilde, S. A., Guo, J. H., Cawood, P. A., Sun, M., and Li, X. P., 2010, Single zircon grains record two Paleoproterozoic collisional events in the North China Craton: *Precambrian Research*, v. 177, p. 266–276.
- Zheng, D., Clark, M. K., Zhang, P., Zheng, W., and Farley, K. A., 2010, Erosion, fault initiation and topographic growth of the North Qilian Shan (northern Tibetan Plateau): *Geosphere*, v. 6, p. 937-941.
- Zhiyi, Z., and Dean, W. T., 1996, *Phanerozoic geology of northwest China*: Beijing, China, Science Press, 316 p.
- Zhou, D., and Graham, S. A., 1996, Extrusion of the Altyn Tagh wedge: A kinematic model for the Altyn Tagh fault and palinspastic reconstruction of northern China: *Geology*, v. 24, no. 5, p. 427-430.
- Zhu, W., et al., 2011, Neoproterozoic tectonic evolution of the Precambrian Aksu blueschist terrane, northwestern Tarim, China: insights from LA-ICP-MS zircon U–Pb ages and geochemical data: *Precambrian Research*, v. 185, no. 3, p. 215-230.

- Zuza, A. V., and Yin, A., 2014, Initial and boundary conditions for the evolution of the Central Asian orogenic system (CAOS): The Balkatach hypothesis: Geological Society of America Abstracts with Programs, v. 46, no. 6, p. 789.
- Zuza, A. V., Yin, A., and Wu, C., 2015, The Neoproterozoic-Paleozoic tectonic history of the Qilian Shan and its control on the development of the Tibetan Plateau's northern margin: GSA Abstracts with programs, v. 47, no. 7, p. 38.
- Zuza, A. V., and Yin, A., 2016, Continental deformation accommodated by non-rigid passive bookshelf faulting: An example from the Cenozoic tectonic development of northern Tibet: Tectonophysics, v. 677-678, p. 226-240.
- Zuza, A. V., Cheng, X., and Yin, A., 2016, Testing models of Tibetan Plateau formation with Cenozoic shortening estimates across the Qilian Shan–Nan Shan thrust belt. Geosphere, v. 12, no. 2, p. 501-532.

**-Chapter 6-**

**The tectonic history of central Asia: The Balkatach hypothesis and a new model for the evolution of the Paleo-Pacific, Tethyan, and Paleo-Asian Oceans**

## 6.1. Abstract

The Phanerozoic history of the Paleo-Asian, Tethyan, and Pacific oceanic domains is key to unraveling the tectonic evolution and development of the Eurasian continent. The validity of existing models that account for the growth and closure of the Paleo-Asian and Tethyan Oceans critically depends on the assumed initial configuration and relative positions of the Precambrian cratons that separate the two oceanic domains, including the North China, Tarim, Karakum, Turan, and Baltica cratons. Existing studies largely neglect the Phanerozoic tectonic modification of these Precambrian cratons (e.g., the effects of India-Eurasia convergence and post-Rodinia rifting). In this chapter, I systematically restore these effects and evaluate the tectonic relationships of these important cratons to test the hypothesis that Baltica, Turan, Karakum, Tarim, and North China were linked as a single continental strip, with variable along-strike widths, in the Neoproterozoic. Because most of the tectonic boundaries currently separating these cratons postdate the closure of the Paleo-Asian and Tethyan Oceans, I am able to establish a > 6000 km-long Neoproterozoic continental strip referred to here as Balkatach (i.e., after the **Baltica-Karakum-Tarim-China** connection). By focusing on the regional geologic history of the margins of a continuous Balkatach continent, I propose the following tectonic model for development and evolution of the Paleo-Asian, Tethyan, and Pacific Oceans and the protracted growth of the Eurasia continent. (1) The early Neoproterozoic collision of the combined Baltica-Turan-Karakum-South Tarim continents with the linked North Tarim-North China cratons led to the formation of a coherent Balkatach continent. (2) Rifting along Balkatach's margins in the late Neoproterozoic lead to the opening of the Tethyan Ocean and unified Paleo-Asian-Pacific Oceans, and released numerous Balkatach-derived microcontinents within the Paleo-Asian Ocean. (3) These rifted microcontinents acted as nuclei for subduction to

develop within the Paleo-Asian Ocean during the evolution of the Central Asian Orogenic System (CAOS), which assisted the closure of the Paleo-Asian Ocean. The subduction of this ocean within an archipelago arc system accommodated the oroclinal bending of Balkatach around the CAOS. (4) Initial collision of central Balkatach and the CAOS in the mid-Carboniferous was followed by a bi-directional propagation of suturing to the northwest and east, in present-day coordinates. (5) The complete closure of the Paleo-Asian Ocean in the Permian was accompanied by a magmatic flare up, which may have been related to the avalanche of the subducted oceanic slabs of the Paleo-Asian Ocean across the 660 km phase boundary in the mantle. (6) The closure of the Paleo-Tethys, against the southern margin of Balkatach, proceeded diachronously, from west to east, in the Triassic-Jurassic.

## **6.2. Introduction**

Eurasia, the largest and youngest continent on Earth, was assembled mostly through the Neoproterozoic to the present over a time span of ~1.0 Ga (Scotese and McKerrow, 1990). The three major oceanic domains of Eurasia—the Paleo-Asian, Tethyan, and Pacific Oceans—represent three large Phanerozoic oceans that were intimately related with the assembly and evolution of the Eurasian continent (Fig. 6.1) (e.g., Zonenshain et al., 1990; Yin and Nie, 1996; Şengör and Natal'in, 1996; Heubeck, 2001; Badarch et al., 2002; Stampfli and Borel, 2002; Sone and Metcalf, 2008; Biske and Seltmann, 2010; Gehrels et al., 2011). Decades of research have generated a wealth of geologic data, yet the processes responsible for the opening and closing of these major ocean systems remain debated. For example, researchers have variably attributed the evolution of the Paleo-Asian Ocean to (1) lateral expansion of juvenile continental crust via protracted trench retreat and strike-slip duplexing of a long-lived continental-margin arc derived

from Siberia or Baltica (Şengör et al., 1993; Yakubchuk, 2002), (2) accretion of multiple intra-oceanic and/or continental-margin arcs onto the continents bounding the Paleo-Asian oceans (i.e., the multi-arc model) (e.g., Zonenshain et al., 1990; Hsü and Chen, 1999; Filippova et al., 2001; Badarch et al., 2002; Windley et al., 2007; Xiao et al., 2008), and (3) redistribution and entrapment of pre-existing microcontinents within the Paleo-Asian oceans (e.g., Kröner et al., 2013). Similarly, the provenance of tectonic continents/terrane in the Tethyan orogenic system is also enigmatic: were they derived from (1) the northern margin of Gondwana (Stampfli et al., 2013), (2) the southern margin of Laurasia (at least partially) (Şengör et al., 1993; Yakubchuk, 2002), or (3) a continent located within the Paleozoic-early Mesozoic Tethyan oceans (Şengör, 1984)?

Although past research has focused on the evolution of the Central Asian and Tethyan orogens, relatively little attention has been paid to the tectonic history and role of the cratonic units that lie between these two orogenic systems, including the Baltica, Karakum, Turan, Tarim, and North China cratons. This may be attributed to (1) poor exposure of bedrock in the region (e.g., Turan, Karakum, and Tarim are extensively covered by Mesozoic-Cenozoic sand-desert deposits) and (2) significant tectonic modification that occurred during and after the closure of the Paleo-Asian and Tethyan oceans throughout the Phanerozoic. The lack of studies on these “intermediate units” of Şengör and Natal’ in (1996) (Fig. 6.1) has limited our ability to use a process-based approach to reconstruct the tectonic history of the Paleo-Asian and Tethyan orogenic systems in Asia.

In this chapter, I first thoroughly review the geology of the Precambrian cratons that separate the Paleo-Asian and Tethyan oceanic domains, which includes their mutual tectonic relationships and their deformational history during and after they became individual tectonic



entities. Most of the tectonic boundaries currently separating these cratons postdate the closure of the Paleo-Asian and Tethyan Oceans, and thus I systematically restore the geometry of these cratons from their present-day configuration through the Phanerozoic and into the Proterozoic. By removing the tectonic distortion effects on the shape of the cratons, I ultimately show that Baltica, Karakum, Turan, Tarim, and North China were once linked continuously in the Neoproterozoic as a ~6,000-km-long continental strip. I herein refer to this contiguous strip of Precambrian continental lithosphere as Balkatach (named after the **Baltica-Karakum-Tarim-China** connection of traditionally-defined Precambrian cratons).

The proposed Balkatach hypothesis has implications for the boundary conditions of the development of the three major Phanerozoic Oceans, and affects reconstructions of the Proterozoic-Phanerozoic tectonic evolution of Asia. Furthermore, the newly established Neoproterozoic continuity of this long continental strip provides new constraints on global supercontinent reconstructions (i.e., Columbia and Rodinia) (e.g., Li et al., 2008; Santosh, 2010). I show how the rifting of this continent during the breakup of Rodinia opened the twin Paleo-Asian and Pacific Oceans. This rifting event also provided a source for the Central Asian microcontinents (Fig. 6.2), which subsequently acted as nucleation points for subduction and destruction of the Paleo-Asian Ocean as part of the Central Asian Orogenic System (CAOS) (e.g., Briggs et al., 2007). Initial collision of central Balkatach and the CAOS in the mid-Carboniferous was followed by bi-directional suturing and “double zipper” closure of the Paleo-Asian Ocean. On the other hand, closure of the Paleo-Tethys Ocean along the southern margin of Balkatach was diachronous, proceeding from west to east in the Triassic-Jurassic. My model fits the Wilson-cycle evolution of the southern margin of Asia (Wu et al., 2016) into a global tectonic setting.

### **6.3. Methods and regional tectonic analysis**

Paleogeographic reconstructions rely on multiple lines of evidence, including sea floor, paleomagnetic, geologic, geochronological, paleontological, conjugate margin, and geophysical datasets (e.g., Meert, 2014). Although Mesozoic and younger reconstructions can often use reliable seafloor magnetic anomaly data, paleomagnetic poles, and apparent polar wander paths (APW), the lack or limitation of these quantitative tools in the Paleozoic and Precambrian requires a careful integration of other geologic methods.

#### **6.3.1. Data handling**

This review takes into account decades of existing work in central Asia, including a compilation of geochronologic, sedimentary, stratigraphic, paleomagnetic, biostratigraphic, and structural datasets, which were integrated with existing paleogeographic maps and geodynamical models. Data was organized for each of the geologically significant tectonic domains (e.g., Baltica, Karakum, Turan, Tarim, and North China) (Fig. 6.2) and specific attention was given to the accretion/collision histories along the margins of these domains. Events affecting the margins of the cratons are displayed in Figure 6.3, including collisional orogens, arc magmatism, and passive margin sedimentation. Although I attempt to conform to all existing geologic datasets, the weight of each geologic data point varies significantly depending on its integration into coherent geologic processes. When contrasting structural models can explain the geologic observations, the simplest, globally consistent reconstruction was chosen. As discussed below, I do not infer structures or geologic features (e.g., sutures, transform faults, rift events) without direct observational basis for such. Because of the non-uniqueness regarding the above data, I take an iterative, process-based approach to develop our paleogeographic reconstruction, so that

each step can proceed forwards and backwards in time and be explained by established geologic processes.

The reconstruction presented here uses the updated geologic timescale of the Chinese Geological Survey (2014). In this timescale, Phanerozoic Periods are similar to the timescale of Gradstein et al. (2012), which is often used for North American geology. However, Proterozoic era subdivisions in the Chinese literature (e.g., Wang et al., 2013) are different (Table 6.1). The Mesoproterozoic is divided into the Changcheng Period (1.8-1.6 Ga), Jixian Period (1.6-1.4 Ga), and a currently-unnamed period (1.4-1.0 Ga). The Neoproterozoic is divided into the Qingbaikou (1000-780 Ma), Nanhua (780-635 Ma), and Sinian (635-541 Ma) Periods. The Nanhua Period is broadly correlative to the Cryogenian (Gradstein et al., 2012), and is further subdivided into the Lower (730-725 Ma), Middle (725-660 Ma), and Upper Nanhua (660-635 Ma) Periods

The reconstruction and kinematic tectonic model were developed using the using the Gplates software ([www.gplate.org](http://www.gplate.org)) (Boyden et al., 2010). Eurasian continents were first digitized as undeformable polygons using their present-day shape or estimated geologic boundaries (Fig. 6.2) (Ren et al., 2013). Deformable regions were constructed with separate lines that demarcate the geologic boundaries; motion of these lines with respect to time allowed for the restoration of the deformed area along the margins of these polygons, following observed geologic constraints. When applicable, structural information, including the magnitude, timing, and style of deformation, was used to provide a context for the other geological datasets, and when possible, known deformation was restored.

### 6.3.2. Assembly of tectonic domains

The recognition and interpretation of suture zones (Dewey, 1977) is critical in evaluating the evolution of the continents. A suture refers to a zone along which the collision of two preexisting pieces of lithosphere and the destruction of an interlying oceanic lithosphere has occurred (e.g., Burke et al., 1976; Şengör and Natal'in, 1996). Implicit in this definition, the convergence and amalgamation of two continents requires:

- (1) A subduction zone that consumes the interlying oceanic lithosphere, possibly with a subduction-accretion complex.
- (2) A calc-alkaline volcanic-plutonic belt that results from the subduction of oceanic lithosphere.
- (3) A collisional orogen—complete with an accretionary wedge-mélange zone, foreland basin, fold-and-thrust belt, and Barrovian metamorphic core—that results from the docking of two continents.
- (4) A regional unconformity and/or a transition to terrestrial sedimentation due uplift associated with this collision.

Every verified Phanerozoic continent-continent and arc-continent collision consists of these features (e.g., Taiwan, Himalaya-Tibet, Uralides, Laramide). It has been demonstrated that the presence of oceanic material alone is not enough to demarcate a unique suture that juxtaposes distinct pieces of lithosphere (e.g., Yin, 2002; Kapp et al., 2003; Yin et al., 2007a) and the tectonic setting must be fully realized. If the package of the aforementioned suture features is missing, an amalgamation of two distinct continental lithospheres *cannot be inferred* without an adequate alternative explanation. As an example, which I discuss in more detail below, there is no geologic evidence for a Phanerozoic collision between Karakum, Tarim, and North China. In

light of this, the simplest explanation is best. Thus, I may infer that these continents were contiguous by the start of the Phanerozoic or must propose an alternative model.

Large-scale transform faults and intracontinental shear zones can reposition continental lithosphere without the direct closure of an ocean (e.g., the Cenozoic translation of southeast Asia and the San Andreas Fault in the western United States) although all of these present-day examples are related to nearby subduction-collision tectonics. Without direct evidence for such structures, they should not be inferred. Although the primary prediction for Şengör et al. (1993)'s strike-slip duplication of the Kipchak arc within the Central Asian Orogenic System is numerous lithospheric-scale strike-slip faults, faults that were previously inferred to be strike-slip faults have more recently been interpreted as thrust faults (Briggs et al., 2007, 2009; cf. Şengör et al., 2014). Of course, the plate tectonics cycle may be nonuniformitarian and a different process may have operated in the Proterozoic (Kröner, 1983), although recent work has revealed the importance of Archean and Proterozoic plate tectonics with subduction of oceanic lithosphere (Cawood et al., 2006).

### **6.3.3. Tectonic modification of Precambrian cratons**

An important issue for Proterozoic tectonic reconstructions is the effect of later Neoproterozoic-Phanerozoic tectonic modification on the original shape and configuration of Precambrian cratons. These effects include post-Rodinia rifting and drifting of microcontinents and intracontinental deformation as induced by continental collision and ocean-closure orogenies, which are particularly significant in modifying the Neoproterozoic shape of the North China, Tarim, and Karakum cratons (Fig. 6.2). The shape and position of the North China craton in popular Rodinia reconstructions (Zhang et al., 2006b; Pei et al., 2006; Whitmeyer et al., 2007;

Li et al., 2008; Chen et al., 2013) provides a striking example of this oversight. North China is placed outside of the inferred Rodinia supercontinent and its shape is limited to the current geographically defined northern China, north of the Qinling-Dabie orogenic belt (Fig. 6.1). Three fundamental issues exist with this configuration: (1) North China was much larger in the Precambrian, stretching as far west (in present coordinates) as Karakum or Baltica (Fig. 6.2) (Yin and Nie, 1996; Heubeck, 2001) (this issue is further discussed in this chapter), (2) Phanerozoic deformation (e.g., arc-continent accretionary and collisional events in the Paleozoic across central Asia and large-scale intracontinental deformation associated with the India-Asia collision) (Şengör and Natalin, 1996; Yin, 2010) significantly modified the original shape of the craton, and (3) Paleoproterozoic and Mesoproterozoic structures are inexplicably truncated by Neoproterozoic rifts and passive margins (Zonenshain et al., 1990; Guo et al., 2005; Zhao et al., 2005; Kusky et al., 2007), which requires the North China craton to fit into a larger continental assemblage prior to this time.

#### **6.3.4. Paleomagnetic considerations**

Although many reconstructions consider paleomagnetism as the principle line of evidence for assessing the paleogeographic location of Precambrian continents (e.g., Li et al., 2008; Evans, 2009; Meert, 2014), the goal of this work is to focus on geologic relationships. Issues of ambiguous hemisphere polarity, unconstrained latitude, poor temporal resolution, and rigid-block approximation make paleomagnetic analysis an invalid primary approach to reconstructing the internally-deformed units of central Asia back into the Proterozoic. Future work may improve the spatial and temporal resolution of paleopoles and may lead to better constrained paleopositions. Regardless, my reconstruction and continental configuration are fit

within existing paleomagnetic datasets (Table 6.2). Ultimately, there are too few reliable paleomagnetic poles for the continents within Balkatach to draw significant quantitative conclusions.

#### **6.4. Geology of the major pre-Mesozoic tectonic domains of central Asia**

The assembly of present-day central Asia has progressed through the Proterozoic and Phanerozoic as an amalgamation of numerous cratons, continental blocks, island-arc fragments, and accretionary complexes (e.g., Şengör et al., 1993; Yin and Nie, 1996; Şengör and Natal'in, 1996). Şengör and Natal'in (1996) divided Central Asia into the Altaids (or Central Asian Orogenic System, CAOS) (e.g., Briggs et al., 2007, 2009; Kelty et al., 2008) and the Tethysides, in the north and south respectively, with “intermediate units” occupying the space between (Fig. 6.1). These units are surrounded by three large Phanerozoic oceans: the Paleozoic Paleo-Asian to the north, Tethyan to the south, and present-day Pacific Oceans to the east (Fig. 6.1) (Stampfli, 2000; Zheng et al., 2013). This spatial division is also a temporal one, as the “intermediate units” docked with Eurasia after the predominantly Paleozoic assembly of the CAOS but prior their collision with the Mesozoic Tethysides.

Below I outline the regional geologic framework of each of the “intermediate units” while focusing on (1) the Precambrian and Paleozoic assemblage history of the basement and (2) the later tectonic modification of each unit throughout the Phanerozoic. I only provide cursory discussion of Mesozoic and Cenozoic events, as this most-recent time period is substantially covered in the literature (e.g., Molnar and Tapponnier, 1975; Tapponnier et al., 1982; Hendrix et al., 1992; Yin and Harrison, 2000; Yin, 2010; van Hinsbergen et al., 2011). The following review begins the Central Asian Orogenic System (CAOS)—because many of the other continent

descriptions reference this region—continues with the western margin of Baltica in western Asia and progresses eastward to the North China craton (Figs. 6.1 and 6.2).

#### **6.4.1. The Central Asian Orogenic System (CAOS)**

The Central Asian Orogenic System (CAOS) (Briggs et al., 2007, 2009; Kelty et al., 2008)—also referred to as the Altaids (Suess, 1901; Şengör et al., 1993; Şengör and Natal'in, 1996; Xiao et al., 2008, 2009a, 2009b, 2010), the Central Asia Foldbelt (Zonenshain et al., 1990; Filippova et al., 2001), and the Central Asian Orogenic Belt (e.g., Mossakovsky et al., 1993; Jahn et al., 2002; Xiao et al., 2003; Windley et al., 2007)—is the largest Phanerozoic accretionary orogen on Earth. This immense collage is bounded to the north and south by the Siberia and North China-Tarim cratons, respectively, and extends from the Urals and Baltica in the west to the Pacific Ocean in the east (Figs. 6.1 and 6.2). Most models for the development of the CAOS involve a complicated and long-lived arc-continent collisional process that involves the successive amalgamation of Precambrian microcontinents and island-arcs that began at ~1.0 Ga (Khain et al., 2002) and concluded by the Late Permian (e.g., Filippova et al., 2001; Windley et al., 2007; Xiao et al., 2003).

The various tectonic reconstructions of the CAOS can be summarized by two distinct models: (1) duplication and expansion of single long-lived arc (Şengör et al., 1993; Yakubchuk, 2002) or (2) multiple microcontinents and arcs within the Paleo-Asian Ocean (Zonenshain et al., 1990; Filippova et al., 2001; Badarch et al., 2002). The first model requires Siberia and Baltica to be linked in the Neoproterozoic and the Precambrian basement rocks within the CAOS to be derived from Siberia or Baltica to the north (present-day coordinates), whereas the second



requires Neoproterozoic Baltica and Siberia to be separate and that the CAOS microcontinents are predominately derived from Gondwana or Tarim.

Some of these major Archean to Proterozoic microcontinents within the CAOS include, from west to east, the Kazakhstan, Tian Shan, Tuva-Mongol, Baydaric (Dzabkhan), Erguna, Xing'an, and Songliao (Fig. 6.2), as well as other less substantiated fragments (e.g., Avdeev, 1984; Windley et al., 2007; Demoux et al., 2009). These microcontinents may have been derived from Siberia, Tarim, North China, or the northern margin of Gondwana (e.g., Zonenshain et al., 1990; Kheraskova et al., 2003, 2010; Khain et al., 2003; Li et al., 2006; de Jong et al., 2006; Dobretsov and Buslov, 2007; Zhou et al., 2009; Levashova et al., 2010, 2011; Han et al., 2011; Meert et al., 2011; Zhou et al., 2011). Kazakhstan is often considered to be a large conglomeration of several microcontinents that developed toward the end of the CAOS's activity (Zonenshain et al., 1990; Flipova et al., 2001; Windley et al., 2007). Modeling the collision of Baltica, Tarim, and Karakum against a single Kazakhstan is a useful simplifying assumption in global reconstructions (e.g., Ziegler, 1989; Flipova et al., 2001; Windley et al., 2007; Xiao et al., 2015).

Similarities between many of the microcontinents include (1) Archean-Mesoproterozoic basement, (2) regional metamorphism at ~1.85-1.80 Ga, (3) magmatic activity at ~950 Ma, (4) rift features from 790-750 Ma, and (5) the development of circumscribing passive margins by the Cambrian. Detrital zircon ages shown in Figure 6.4 (Han et al., 2011; Rojas-Agramonte et al., 2011) highlight similar age signatures between the microcontinents. The oldest exposed rocks of Lesser Karatau block of Kazakhstan (Levashova et al., 2011) consist of Paleoproterozoic flysch (Sovetov et al., 1990). The Tuva-Mongol microcontinent consists of several Archean-Paleoproterozoic granulite-grade terranes covered by lower-grade Mesoproterozoic to Cambrian

schist, marble, and quartzite cover (Badarch et al., 2002). The oldest gneiss in this collage has a whole-rock Rb-Sr isochron age of  $3153 \pm 57$  Ma (Aktanov et al., 1992), and basement rocks have U-Pb zircon ages of 2650 to 2364 Ma (Kotov et al., 1995; Kozakov et al., 1999). Granulite-grade metamorphism, as determined U-Pb zircon rim ages, occurred at  $1839.8 \pm 0.6$  Ma (Kröner et al., 2001). The Baydaric microcontinent, to the south of the Tuva-Mongol microcontinent, consists of tonalitic gneiss with a U-Pb zircon age of  $2646 \pm 45$  (Kozakov et al., 1993) overlain by Paleoproterozoic metasedimentary rock. This basement is intruded by Paleoproterozoic granite (Kotov et al., 1995) and the region experienced granulite-facies metamorphism at 1850-1800 Ma (Khain et al., 2003). The microcontinents to the east within China (e.g., Erguna, Xing'an, and Songliao) are made up of younger Mesoproterozoic to Paleozoic basement (e.g., Han et al., 2011).

Qingbaikou magmatism and metamorphism (970-910 Ma) is observed in many of the CAOS microcontinents (Fig. 6.4). Subsequently, Nanhua-age (late Neoproterozoic) bimodal volcanism (e.g., Zonenshain et al., 1990; Kuzmichev et al., 2005) and passive margin deposition (e.g., Markova, 1982; Alexeiev et al., 2000; Cook et al., 2002) occurred on all of the microcontinents and are inferred to be rift related (Fig. 6.5) (e.g., Meert et al., 2011; Rojas-Agramonte et al., 2011). The microcontinents are presently surrounded by Neoproterozoic to Early Cambrian ophiolites, ophiolite mélanges, and/or shelf carbonates, which suggests that they were surrounded by an open ocean at this time (i.e., the Paleo-Asian Ocean) (Ren et al., 1999; Khain et al., 2003; Demoux et al., 2009). Nanhua-aged (Cryogenian-Ediacaran) glacial tillite-bearing deposits have been documented in the Dzabkhan terrane (Lindsay et al., 1996; Macdonald et al., 2009; Meert et al., 2011) (Fig. 6.5). Many of the microcontinents with early Paleozoic passive margin cover were juxtaposed by subduction-accretion processes, as

evidenced by the intervening Paleozoic accretionary complexes, subduction-related volcanics, and flysch deposits.

Detrital zircon age distributions reveal significant age populations at ~2.5 Ga, 1.85-1.8 Ga, 970-910 Ma, and 790-750 Ma that are common to all of microcontinents (Fig. 6.4). The peaks at ~2.5 Ga correspond to a global period of continental growth at the end of the Archean (Kröner et al., 2005; Condie et al., 2009; Yao et al., 2011). The 1.85-1.80 Ga and 970-910 Ma (Qingbaikou-age) peaks may have correlations with other Asian continents (e.g., Tarim, Qilian-Qaidam, and South China) (Ling et al., 2003; Gehrels et al., 2003a, 2003b; Wang et al., 2006; Li et al., 2009; Tung et al., 2013), and the Nanhua ages correspond to the rifting of these microcontinents (Fig. 6.5).

A Precambrian link between Tarim and Central Tian Shan has been proposed based on stratigraphy and additional detrital zircon age data (Fig. 6.4) (Shu et al., 2011; Gao et al., 1998; Charvet et al., 2007; Lei et al., 2011; Meert et al., 2011; Ma et al., 2011, 2012) (cf. Hu et al., 2000; Liu et al., 2004; Xiao et al., 2013). Granitic orthogneisses in the Tian Shan yield U-Pb zircon ages of 948-919 Ma (Qingbaikou-age) (Chen et al., 2009; Hu et al., 2010), which may be correlative to Tarim and the Qilian-Qaidam-Kunlun regions, as discussed below.

#### **6.4.2. Baltica**

The 3000-km-wide Baltica craton is typically defined with its core as the East European platform (e.g., Zonenshain et al., 1990; Filippova et al., 2001), which consists of a collage of Precambrian basement (i.e., the Fennoscandia, Sarmatia and Volgo-Uralia blocks) (Bogdanova et al., 2008), and its surrounding Neoproterozoic-Phanerozoic margins (e.g., Torsvik et al., 1996), including the Uralide and Caledonian orogens. The craton was affixed to Laurentia once in the

Neoproterozoic as part of Rodinia (e.g., Hartz and Torsvik, 2002; Li et al., 2008; Pease et al., 2008) and also in the Paleozoic as part of Laurussia (e.g., Ziegler, 1989; Cocks and Torsvik, 2011).

An in-depth review of this craton is not within the scope of this chapter (see Bogdanova et al., 2008 and references therein), and subsequent focus will be solely on the eastern margin of Baltica, which has been suggested to extend to the southeast to the Scythian domain and underneath the Peri-Caspian Basin (Pease et al., 2008). Geology in much of this region is exposed as a result of the late Paleozoic-early Mesozoic Uralide orogen, which records the collision between Baltica, Siberia, and Kazakhstan.

The 2000-km-long Uralides consist of several longitudinal terranes that run parallel to the eastern margin of Baltica. These tectonic domains are variably divided, from west to east, as the (1) undeformed foreland basin, (2) foreland fold and thrust belt, (3) Tagil-Magnitogorsk Zone, and (4) East Uralian Zone (Maslov et al., 1997; Puchkov, 2009, 2013; Brown et al., 2011). These zones record Paleozoic subduction, arc magmatism, island arc amalgamation, and the final collision of Baltica with Siberia and Kazakhstan. Preexisting structures within the Precambrian basement are at a high angle to these tectonics domains. A NW-SE structural trend within Archean and Proterozoic rocks is comprised of several basement highs and lows, including the Mid-Russian aulacogen, Perm-Bashkir Arch, Kaltasin (or Kama-Belsk) Aulacogen, Tatar Arch, Sernovodsk-Abdulino Aulacogen, and Orenburg Arch, from north to south (Bogdanova et al., 2008; Brown et al., 2011). The aulacogens are filled with up to 15 km of Proterozoic sediments that record ~200 Ma of variably interrupted intracontinental rifting during the Qingbaikou Period (Maslov et al., 1997; Brown et al., 1999).

Early Mesoproterozoic rifting led to initial formation of these aulacogens and the entire region remained an east facing passive margin on the western margin of the Proto-Urals Ocean (present coordinates) (Mossakovsky et al., 1998; Kheraskova et al., 2001). Throughout the Neoproterozoic, accretion-deformational events affected this eastern margin as several (?) terranes and/or continents collided against eastern Baltica (e.g., Brown et al., 1996, Glasmacher et al., 2001); these events are poorly-constrained as they were later overprinted by late Neoproterozoic-Early Paleozoic rifting and later Uralide deformation (Fig. 6.6) (Brown et al., 1996). Most workers suggest that one or two terranes (e.g., the Bashkirian terrane) accreted to the region to form the Proto-Ural orogen prior to Timanian orogen along the north-northeastern margin at 615-575 Ma (Puchkov, 1997; Glasmacher et al., 1999). As the geologic relationships of these features are not well understood, it is also possible that these accreted terranes were part of a larger continent that later rifted from Baltica in the latest Neoproterozoic to Early Proterozoic.

Sinian-Cambrian rifting (Khain, 1985) and associated bimodal volcanism (e.g., Abdullin et al., 1977; Zonenshain et al., 1984) led to the opening of the Ural Ocean by the early Ordovician (Zonenshain et al., 1984; Burtman et al., 2000). Ophiolites with ages of 670 Ma and 580 Ma (Khain et al., 1999; Scarrow et al., 2001; Remizov and Pease, 2004) (Fig. 6.6) have been reported in this region and may represent oceanic crust that obducted during the later Uralide orogen. Early Paleozoic sediments along this margin are typical shelf-passive margin sequences.

The northern margin of Baltica was affected by the late Neoproterozoic-early Cambrian Timanide orogen, when the inferred continent Arctida (Zonenshain et al., 1990) collided with Baltica (e.g., Gee and Pease, 2004; Gee et al., 2006; Kuznetsov et al., 2007, 2009, 2010). The

Cambrian collision is predated by calc-alkaline magmatism in the Bolshezemel domain of Arctica (i.e., the Bolshezemel arc), with ages ranging from 700 Ma to 560 Ma.

Baltica's eastern margin along the Ural Ocean remained passive, with the exception of several poorly understood arc accretion events (Fig. 6.6). The Tagil and Magnitogorsk oceanic arcs collided with the eastern margin of Baltica in the Devonian and Carboniferous, respectively (Fig. 6.6) (e.g., Herrington et al., 2002; Brown et al., 2006, 2011). In the Late Carboniferous, the Ural Ocean began to subduct underneath Kazakhstan to the east (Bea et al., 2002); thick andesitic volcanic deposits in the Balkash area of Kazakhstan (Dercourt et al., 2000) record the initiation of subduction magmatism as part of the Valerianovsky arc (Fig. 6.6). This subduction system accommodated the convergence of Kazakhstan and Baltica, which led collision and closure of the Ural Ocean at ~320 Ma (Artyushkov and Baer, 1983; Ronov et al., 1984; Zonenshain et al., 1984) (Fig. 6.3). This collision was diachronous (Zonenshain et al., 1984; Ronov et al., 1984), initiating by ~320 Ma in the south (Puchkov, 2000) and propagating northward to the Novaya Zemlya foreland basin by ~280 Ma (Heafford, 1988). Syn-collisional granite ages also young northward, from 305-290 Ma in the south to ~265 Ma in the central Urals (Fig. 6.6) (Fershtater et al., 2007; Fershtater, 2013). An extensive, west-migrating foreland basin developed in the Late Carboniferous and persisted through the Early Permian (Nikishin et al., 1996; Proust et al., 1998; Chuvachov and Crasquin-Soleau, 2000), and Permian flysch transitioned to late Permian-early Triassic molasses and continental deposits. The Taimyr fold belt to the north records the collision of Baltica with Siberia during the same time (Vernikovsky, 1997; Torsvik and Andersen, 2002), and it is possible that this subduction system connected to the North American Cordilleran arc-trench system (e.g., Zonenshain et al., 1987; Miller et al., 2011).

### 6.4.3. Turan

The Turan Platform lies east-northeast of the Caspian Sea and stretches from the CAOS in the north to the Kopet Dagh or Alborz Mountains in the south (Fig. 6.2) (Alavi, 1991; Thomas et al., 1999a; Natal'in and Şengör, 2005). The pre-Mesozoic basement in this region is known as the Turan domain (Thomas et al., 1999a), where the Turan platform demarcates the extent of Mesozoic-Cenozoic sedimentary cover. The limited basement exposure in this region has led to inconsistencies in the literature regarding the tectonic boundaries and geologic context of the domain. The Karakum craton is to the east-southeast and Scythian domain is to the west, and some have suggested that the Turan and Scythian domains were connected throughout the Paleozoic (e.g., Natal'in and Şengör, 2005). However, as described below, I suggest that the two domains were separate (e.g., Brunet et al., 1999; Volozh et al., 2003). The divide between these units is poorly exposed and is often arbitrarily set geographically as the Caspian Sea, rather than geologically (e.g., a suture or transform zone), although structures appear to connect through the Caspian Sea (Fig. 6.7).

For the purposes of this synthesis, I suggest that the Permian ophiolites in the Alborz Range (Alavi, 1991), and related outcrops along strike that are associated with the closure of the Paleo-Tethys, demarcate the southern margin of both the Turan and Scythian domains. Although a Paleozoic connection between Scythian and Turan domains is still debated, a meaningful divide between the two domains is the northwest-trending Karpinsky Swell and Mangyshlak-Ustyurt foldbelt that stretch to the Kopet Dagh Mountains in the southeast (e.g., Zonenshain et al., 1990; Volozh et al., 2003) (Fig. 6.7). This division is corroborated by a strong fabric of northwest-trending magnetic and gravity anomalies (e.g., Volvovsky et al., 1966; Litvinova, 2000) and documented late Paleozoic thrust faults (Volozh et al., 1999). Following this

demarcation, the Turan domain stretches from the CAOS in the north-northeast to the Mangyshlak-Ustyurt foldbelt in the southwest (Fig. 6.7). No collision/convergence structures between the Turan domain and Karakum to the southeast have been observed.

Turan was partially covered by the Turkestan Ocean (part of the Paleo-Asian Ocean) in the northeast for much of the Paleozoic, and is covered by regionally extensive late Silurian to Devonian carbonate rocks (Zonenshain et al., 1990; Kurenkov and Aristov, 1995; Garzanti and Gaetani, 2002). Northward subduction of the Turkestan Ocean underneath the CAOS (specifically Kazakhstan and its associated microcontinents) led to its eventual closure in the Late Carboniferous (Fig. 6.3) (e.g., Zonenshain et al., 1990; Filippova et al., 2001). Devonian extension recorded in the Karpinsky Swell (Volozh et al., 1999) was followed by north-northeastward subduction of the Paleo-Tethys under the Turan domain. Associated arc magmatism began in the Carboniferous and continued into the Mesozoic (Garzanti and Gaetani, 2002), and a back-arc basin developed in the Triassic (Gaetani et al., 1998; Thomas et al., 1999a). This subduction accommodated the collision of Turan and Iran-Lut to the south, which may have been linked with the Scythian domain, as part of the Late Triassic Eo-Cimmerian orogen in northern Iran (Zanchi et al., 2009). This collision may be expressed in the Mangyshlak-Ustyurt foldbelt (Fig. 6.7). Deformed Permian-Triassic flysch in the Mangyshlak anticlinorium are unconformably overlain by Jurassic shallow-marine sandstone (Marcinowski et al., 1996; Ulmishek, 2001). In the Kopet Dag Mountains to the southeast, strongly deformed Permian volcanic and sedimentary strata are intruded by 207-180 Ma leucogranites (Belov, 1981). Additionally, 227-200 Ma K-Ar ages from greenschist rocks have been documented (Lemaire et al., 1997). A regional unconformity in the latest Triassic (Saidi et al., 1997) is followed by Jurassic deltaic strata that record the unroofing of this orogen (Garzanti and Gaetani,



2002). Cretaceous carbonates covered the region as part of an interior seaway across the Baltica craton (Marcinowski et al., 1996; Baraboshkin et al., 2003). The Jurassic-Tertiary deposits to the north of the Mangyshlak-Ustyurt foldbelt are important oil reservoirs of the Ushyurt Basin (e.g., Ulmishek, 2001).

#### **6.4.4. Karakum**

Karakum is covered by thick Mesozoic-Cenozoic sediments, but Cenozoic deformation in the southwestern Tian Shan thrust belt locally exposes basement rocks in the Baisun and Garm massifs of eastern Karakum (Burtman, 1976; Biske, 1996). The oldest rocks are gneisses, migmatites, and amphibolites with Pb isochron ages of 3.0-2.6 Ga (Budanov, 1993), which are covered by Proterozoic schist and marble. This Precambrian basement experienced rifting and diffuse alkali and tholeiitic basaltic magmatism in the Neoproterozoic (Volkova and Budanov, 1999; Bakirov and Maksumova, 2001; Biske and Seltmann, 2010). Meta-basalt exposed in the Garm massif (Volkova and Budanov, 1999) have Pb isochron ages of 745 to 583 Ma (Baratov et al., 1983). The northern and southern margins of Karakum experienced relatively uninterrupted Neoproterozoic-Cambrian to early Carboniferous marine transgression (Biske and Seltmann, 2010). Ordovician volcanic rocks in southern Karakum (Mukhin et al., 1991; Dalimov et al., 1993) suggest a south-facing arc system may have developed along this margin in the early Paleozoic. Ordovician-Silurian seamounts and mid-oceanic ridge basalt (MORB) (Volkova and Budnov, 1999) corroborate this assertion, and may have been part of the Paleo-Tethys Ocean.

Along the northern margin of Karakum, early Carboniferous ophiolitic fragments of the Hissar suture (Portnyagin, 1974; Burtman, 1976, 2006) are thought to represent oceanic lithosphere of the Turkestan Ocean (part of the larger Paleo-Asian Ocean) to the north.

Carboniferous to Permian arc-related plutons are found throughout Karakum (Brookfield, 2000; Konopelko et al., 2007; Seltmann et al., 2011). Carboniferous volcanic arc rocks, including lightly metamorphosed rhyolite, dacite, and andesite, and synorogenic clastic sediments, rest unconformably on oceanic lithosphere, and represent a transition from a passive to an active margin with south-dipping subduction of Turkestan Ocean (part of the Paleo-Asian Ocean) at this time (Zonenshan et al., 1990; Brookfield, 2000). This subduction system accommodated the convergence of Kazakhstan and the eventual closure of the Paleo-Asian Ocean (Chen et al., 1999; Charvet et al., 2007). Collision of Karakum with Kazakhstan began at ~320 Ma and the intervening Turkestan Ocean was completely closed by 295-290 Ma (Biske and Seltmann, 2010) (Fig. 6.3). Northward subduction of the Paleo-Tethys Ocean initiated during this collision, which explains the presence of seamount and oceanic lithosphere that accreted onto the southern margin of Karakum. The absence of Permian strata indicate that the region was above sea level for most of this time (Cook et al., 1994). Mesozoic northward subduction of the Paleo-Tethys may have stretched from Turan to Qinling as part of the Silk Road Arc (Natal'in and Şengör, 2005). Early Cimmerian deformation affected the southern margin as Iran-Lut collided with Karakum by the end of the Triassic (Saidi et al., 1997; Zanchi et al., 2009).

#### **6.4.5. Tarim**

Although Tarim Basin's very thick (>15 km) Cenozoic sedimentary cover obscures much of the basement, the earliest studies along the margins of the basin recognized cratonic basement underlying these younger sediments (Fig. 6.8A) (e.g., Argand, 1924; Norin, 1937, 1946). The Precambrian geology of Tarim is inferred from bedrock outcrops along the basins' margins (i.e., Quruqtagh, Altyn Tagh, Dunhuang, and Tieklik uplifts) and substantial subsurface data (i.e.,

well, seismic reflection, seismic refraction, gravity, and magnetic studies). Archean orthogneiss, tonalite–trondhjemite–granodiorite (TTG) gneiss, and amphibolite enclaves are found in the Quruqtagh, Altyn Tagh Range, and Tieklik regions (Fig. 6.8A). U-Pb zircon ages from these suites indicate a long-lived period of crustal growth at ~2.8-2.55 Ga (Lu, 1992; Mei et al., 1998; Lu and Yuan, 2003; Lu et al., 2006). The oldest ages come from the Altyn Tagh Range, where xenocrystic zircons have U-Pb ages of ~3.6 Ga (Lu et al., 2008).

Paleoproterozoic metapelites unconformably overlie Archean basement (Gao et al., 1993), and early Paleoproterozoic magmatism occurred throughout Tarim, with observed ages ranging from 2.45-2.35 Ga (Lu, 2002; Lu and Yuan, 2003; Lu et al., 2006, 2008). Granitoids with zircon ages of ~1.94-1.93 intrude the Quruqtagh region (Ge et al., 2015), and subsequently North Tarim experienced amphibolite- to granulite-facies metamorphism at 1.92-1.91 Ga as documented by U-Pb zircon ages of metamorphic zircons or zircon rims (Lu et al., 2006, 2008; Ge et al., 2015). The timing of these magmatic and metamorphic events is similar to that of the ~1.95 Ga Khondalite orogen in North China (e.g., Zhao et al., 2005; Santosh et al., 2006, 2007; Zhao, 2009). The presence of ~1.85 Ga mafic dikes (Lu et al., 2008) and ~1.77 Ga rapakivi-type granite and mafic dike swarms (Xiao et al., 2003; Lu et al., 2006) suggests an extensional setting at this time (Lu et al., 2006).

The Mesoproterozoic Ailiankate Group of southern Tarim consists of calc-alkaline basalt, andesite, and rhyolite, and is inferred to represent an accreted island arc (Guo et al., 2004). Although outcrop exposure is poor, this island-arc collisional event contrasts the geologic history of North Tarim, where a thick Mesoproterozoic basal conglomerate unconformably overlies Paleoproterozoic rocks, and is subsequently stratigraphically overlain by siliciclastic garnet

schist and marble (Wang et al., 2004). North Tarim is inferred to have been an undisturbed passive margin throughout most of the Mesoproterozoic.

High-pressure, low-temperature glaucophane-muscovite blueschist near Aksu and chlorite-rich greenschist near Wushi (Liou et al., 1989; Nakajima et al., 1990; Turner, 2010), both in northwest Tarim (Fig. 6.8A) may represent a relic subduction system between the North and South Tarim craton (Guo et al., 1999, 2005). Dating efforts of the blueschist yield a range of ages, including K-Ar glaucophane ages of  $718 \pm 22$  Ma and  $710 \pm 21$  Ma, Rb-Sr phengite ages of  $698 \pm 26$  Ma and  $714 \pm 24$  Ma (Nakajima et al., 1990), and  $^{40}\text{Ar}/^{39}\text{Ar}$  phengite ages of  $\sim 750$  Ma (Yong et al., 2013). However, these ages must be questioned because undeformed crosscutting dikes have an older U-Pb zircon age of  $807 \pm 12$  Ma (unpublished data in Chen et al., 2004). In addition, unpublished  $^{40}\text{Ar}/^{39}\text{Ar}$  ages from glaucophane show peak metamorphism occurring at 872-862 Ma (e.g., Chen et al., 2004). Many of these thermochronometric ages may have been reset by later heating because, as discussed below, the Tarim continent experienced long-lived and extensive bimodal volcanism from  $\sim 870$  Ma to  $\sim 630$  Ma.

The interlying ocean involved in the Aksu suture is evidenced by the occurrence of metabasalts, which have an enriched mid-ocean ridge basalt (E-MORB) protoliths with a Sm-Nd isochron age of  $890 \pm 23$  Ma (Zheng et al., 2010). Prior to the collision of North and South Tarim, a subduction system must have facilitated the convergence of these two blocks. This system may have generated the Qingbaiku-aged granitoids (970-910 Ma) northeast of this inferred suture (Fig. 6.8A) in the Altyn Tagh Range (Cowgill et al., 2003; Gehrels et al., 2003a), the Qilian Shan (Gehrels et al., 2003a; Tung et al., 2007, 2013; Wu et al., 2016), and the Qinling (Chen et al., 2006) which suggests that this subduction zone was part of a northeast-dipping Tarim arc. This arc would have stretched from Tarim through the Qaidam and Qilian Shan to

present-day Qinling (Fig. 6.8B) (see Chapter 5; Wu et al., 2016). Although no Precambrian suture has been reported in Qaidam, the Qilian Shan, or Qinling, Neoproterozoic rifting (discussed below) or extensive Cenozoic basin deposits may obscure such findings (Fig. 6.8B). It is also possible that the ophiolite, eclogite, and mélangé exposures found in the Altyn Tagh Range, North Qaidam, and the Qilian Shan (e.g., Sobel and Arnaud, 1999; Xiao et al., 2009c; Song et al., 2013, 2014) may contain fragments of this Precambrian suture, which have been mistakenly grouped with the early Paleozoic Qilian suture.

Following these early Neoproterozoic events, the area experienced regional rifting and the development of extensive passive margins (Turner, 2010). Evidence for Neoproterozoic rift activity along Tarim's northern and southern margins includes mafic dike intrusions, alkaline plutonism, bimodal volcanism, rift basin development, and passive margin sedimentation (Fig. 6.5). In northern Tarim, two or three distinct pulses of rift-related magmatic and/or plume activity occurred at 830-800 Ma, 790-740 Ma, and 650-630 Ma (e.g., Zhang et al., 2007; Lu et al., 2008; Zhu et al., 2008; Shu et al., 2011) (e.g., Fig. 6.4), which are generally associated with the opening of the Paleo-Asian Ocean. The 830-800 Ma plutons in northern Tarim may either be related to an initial phase of rift-development (Lu et al., 2008; Zhu et al., 2008) or arc subduction and collision along the Tarim arc (e.g., Fig. 6.8), but the lack of geochemical analysis and observed bimodal volcanism makes this assertion uncertain. The second distinct pulse of magmatic activity, from 790 to 740 Ma, was accompanied by bimodal volcanism and has been related to rifting (Lu et al., 2002, Guo et al., 2005, Xu et al., 2005, Zhang et al., 2006a). The 650-630 Ma Korla dikes indicate that rift-related magmatism continued into the Upper Nanhua (~Ediacaran) (Zhu et al., 2008; Zheng et al., 2010). This latest stage of volcanism (Xu et al.,

2009; Xu et al., 2013) may be related to the opening of the more minor Qilian Ocean to the southeast (e.g., Xu et al., 2015).

In southern Tarim, specifically in the Tiekelik region, bimodal volcanism and rift-basin development at 900-870 Ma (Wang et al., 2015a, 2015b) indicates that rifting along Tarim's southern margin initiated earlier than in the north. This requires rifting to immediately follow collision along the Tarim suture. This event is associated with the opening of the (Paleo-)Tethys Ocean.

Following the rifting along Tarim's margins, the region is overlain by thick successions of latest Neoproterozoic to Cambrian passive continental margin deposits (Jia, 1997; Zhang et al., 2000; Jia et al., 2004; Huang et al., 2005; Xu et al., 2005; Biske and Seltmann, 2010; Turner, 2010; Shu et al., 2011) (Fig. 6.5). The northern margin remained a passive continental shelf throughout much the Paleozoic (Graham et al., 1993; Carroll et al., 1995, 2001), but two regional unconformities truncate the sedimentary record. The first occurred in the early Paleozoic, where Silurian-Devonian siliciclastic strata, sourced from the southeast, unconformably overlie Ordovician rocks (Carroll et al., 2001). Overlying Carboniferous strata are separated from Silurian-Devonian rocks by a sharp angular unconformity (Lin et al., 2014). These unconformity pulses and siliciclastic sediments are related to the Qilian orogen to the southeast, as the Qaidam continent collided with the southern margin of Tarim and North China. The thick deposits of Carboniferous through Lower Permian strata are truncated by a major angular unconformity (Carroll et al., 2001). This event is related to the collision of the Tian Shan and CAOS microcontinents along the northern margin of Tarim, and the closure of the Paleo-Asian Ocean.

Late Paleozoic-Mesozoic arc magmatism observed along the southern margin of Tarim in the Western Kunlun Range (Cowgill et al., 2003; Xiao et al., 2005) is related to northward

subduction of the Paleo-Tethys Ocean and arc development along the southern margin of Tarim. This magmatic arc represents the westward continuation of the Paleozoic-Mesozoic Kunlun magmatic arc that is located to southeast in Eastern Kunlun Range of the Qilian-Qaidam-Kunlun continent (Jiang et al., 1992; Cowgill et al., 2003; Wu et al., 2016).

#### **6.4.6. The Qilian-Qaidam-Kunlun (Qinling-Dabie) continent and orogens**

The Qilian-Qaidam-Kunlun (QQK) continent, which represents the northern margin of the Tibetan Plateau, experienced progressive subduction, arc-magmatism, and orogeny throughout the Paleozoic and Mesozoic (see Chapter 5) (e.g., Yin et al., 2007a, 2008; Xiao et al., 2009c; Gehrels et al., 2011; Song et al., 2013, 2014; Wu et al., 2016), as evidenced by the widespread exposure of ophiolitic mélangé (Wang and Liu, 1976, 1981; Xiao et al., 1978; Feng and He, 1995), ultra-high pressure (UHP) rocks (Yin et al., 2007a; Menold et al., 2009; Song et al., 2014), blueschist rocks (Xiao et al., 1974; Liu et al., 2006; Lin et al., 2010), and plutons (Gehrels et al., 2003a, 2003b, 2011; Wu et al., 2016). The Qilian Shan-Nan Shan, North Qaidam, and Kunlun-Qimen Tagh thrust belts bound the Qaidam Basin to the north and south respectively.

The heterogeneous basement consists of Mesoproterozoic passive-margin strata in the west and Archean to Proterozoic crystalline rocks to the east (e.g., Qinghai BGMR, 1991; Guo et al., 1999; Gehrels et al., 2003b; Pan et al., 2004). The Quanji Massif, the most well studied Precambrian basement in the Qilian Shan (Lu, 2002; Wan et al., 2006; Wang et al., 2008; Gong et al., 2012), consists of medium- to high-grade metamorphic rocks of the Delingha, Dakendaban, and Wandonggou Groups unconformably overlain by Neoproterozoic strata (Qinghai BGMR, 1991). The Delingha Group is composed of Paleoproterozoic granitic gneiss

with zircon ages of 2.39-2.37 Ga (Lu, 2002; Lu et al., 2006, 2008). The granite protoliths are interpreted to have formed in a rift setting, possibly related to the breakup of the Kenorland supercontinent (e.g., Gong et al., 2012). The Dakendaban Group was deposited after ~2.47 Ga but before ~2.43 Ga, based on a detrital zircon analyses and a cross-cutting pegmatite (Wang et al., 2008), whereas the Wandonggou Group was deposited between 2.24 and 1.95 Ga (Huang et al., 2011). The complex underwent amphibolite facies metamorphism at ~1.95-1.93 (Hao et al., 2004; Wang et al., 2008; Chen et al., 2009) and was subsequently intruded by 1.83 Ga mafic dikes (Liao et al., 2014) and ~1.8 rapakivi granite (Lu et al., 2006; Chen et al., 2012). Mesoproterozoic meta-sedimentary rocks are poorly understood (Lu et al., 2006) and are overlain by the tillite-bearing siliciclastic- and carbonate-dominated QuANJI Group (Shen et al., 2010; Wang et al., 2013) (Fig. 6.5).

The Qilian Shan, Qaidam, and Kunlun regions were intruded by 970-910 Ma plutons, which suggests that the region was contiguous by the start of the Neoproterozoic (Fig. 6.9A) (Gehrels et al., 2003b; Tung et al., 2013; Wu et al., 2016). Similar-aged plutons have been documented in the Altyn Tagh Range, Tarim, and the Tian Shan (Cowgill et al., 2003; Gehrels et al., 2003b; Lu et al., 2008; He et al., 2014). As previously discussed, these ~970-910 Ma plutons to the west and southeast (i.e., Tarim and the Altyn Tagh Range to the west, and Qinling to the southeast), suggest the existence of a south-facing Proterozoic subduction zone that stretched from Tarim to Qinling (e.g., Guo et al., 2005; Tseng et al., 2009a). The ~1.0-0.9 Ga plutons and zircon signature within Proterozoic strata of QJK (Fig. 6.4) may correlate with either the Tarim-North China (Gehrels et al., 2003a, 2011) or South China cratons (Tung et al., 2013).

The occurrence of 790–750 Ma intrusions in the Qilian Shan has been attributed to the rifting of the Qilian-Qaidam continent from another continent (North or South China) and the



opening of the Qilian Ocean (Tseng et al., 2006; Song et al., 2013; Wu et al., 2016).

Alternatively, the ~600 Ma basalt interbedded with thick marble rocks in the Qiqing Group may indicate later rifting and opening of the Qilian Ocean (Xu et al., 2015) (Fig. 6.5). The region was subsequently overlain by Neoproterozoic passive margin deposits (e.g., Guo et al., 1999; Wan et al., 2001, 2003a; Cowgill et al., 2003; Gehrels et al., 2003a, 2003b). If QJK was indeed derived from Tarim or North China, the Qilian Ocean is distinct from the proto-Tethys (or any Tethyan Ocean) (cf. Gehrels et al., 2011) because the Tethyan oceanic domain (Fig. 6.1) was originally defined as the ocean between Laurasia and Gondwana (Sengör, 1984), whereas the Qilian Ocean opened with the rifting of QJK from Tarim-North China.

The collision between Qilian-Qaidam, interlying arc(s), and the Tarim-North China craton is expressed as the early Paleozoic Qilian orogen (Yin and Nie, 1996; Sengör and Natal'in, 1996; Sobel and Arnaud, 1999; Yin and Harrison, 2000; Gehrels et al., 2003a, 2003b; Yin et al., 2007a; Xiao et al., 2009c; Song et al., 2013). The Qilian orogen is composed of flysch sequences, arc-type assemblages, ophiolites, and low- to high-grade metamorphic rocks.

Unresolved first-order problems regarding the Qilian orogen include: (1) how many arcs and what type of arcs (i.e., oceanic or continental) were involved in orogeny (e.g., Xiao et al., 2009c; Yang et al., 2009, 2012a; Song et al., 2013)? (2) was the subduction north- and/or south-dipping (e.g., Sobel and Arnaud, 1999; Yin and Harrison, 2000; Gehrels et al., 2003a, 2003b; Yin et al., 2007a; Xiao et al., 2009c; J. Yang et al., 2009, 2012a; Yan et al., 2010; Gehrels et al., 2011; Song et al., 2013, 2014)? (3) when did collision and closure of the Qilian Ocean occur (e.g., Liu et al., 2006; Qi, 2003; Tung et al., 2007; Xiao et al., 2009c; Lin et al., 2010)?

Regardless of the above uncertainties, the following is known about the Qilian orogen. An open ocean(s) existed from at least 550 Ma to 448 Ma, as evidenced by the widespread

distribution of ophiolite fragments (Shi et al., 2004; Smith, 2006; Xiang et al., 2007; Tseng et al., 2007; Zhang et al., 2007; Xia and Song, 2010; Song et al., 2013). Widespread arc-related plutons indicate that a major subduction system initiated by ~515 Ma and continued throughout the Ordovician; younger accretion -related magmatism may have persisted until 345 Ma (Qinghai BGMR, 1991; Qian et al., 1998; Cowgill et al., 2003; Gehrels et al., 2003a; Su et al., 2004; Wu et al., 2004, 2006, 2010; Hu et al., 2005; Liu et al., 2006; Quan et al., 2006; He et al., 2007; Tseng et al., 2009; Xiong et al., 2012; Song et al., 2013). The youngest major pulse of magmatism at ~445 Ma (e.g., Wu et al., 2016), ~454-442 Ma  $^{39}\text{Ar}/^{40}\text{Ar}$  mica cooling ages (Liu et al., 2006), and Silurian foreland basin deposits (Yan et al., 2007, 2010) suggest that collision between Qaidam and North China probably occurred at ~445-440 Ma. Silurian cooling ages and ~400 Ma zircon rim growth are consistent with intracontinental deformation due to collision at this time (Qi, 200; Lin et al., 2010).

Based on similar lithological assemblages and geologic histories, the Qilian orogen and suture(s) likely connect with the Qinling orogen (Fig. 6.1) to the southeast (e.g., Xu et al., 2008; Tseng et al., 2009; Dong et al., 2011; Wu et al., 2016), forming a >1000 km long Early Paleozoic orogenic belt. The western termination of this orogen and suture is not known, and three geometrically plausible models exist for its westward continuation (Fig. 6.9): (1) it may continue into Tarim and be currently covered by Mesozoic-Cenozoic sediments, (2) it may veer to the south of Tarim and be overprinted by the Western Kunlun and Pamir thrust belts, although evidence for this suture in the Altyn Tagh Range suggests that the suture cannot be that far to the southwest, or (3) the Qilian-Qaidam-Kunlun block may have only partially separated from Balkatach and the abrupt western termination of the Qilian suture represents the western extent of the Qilian Ocean. An additional model suggested that the Qilian suture connected to the

northwest to the Beishan suture (Zhou and Graham, 1996a), although this idea has mostly been abandoned because the Beishan suture has been related to the CAOS and the closure of the Paleo-Asian Ocean (e.g., Xiao et al., 2010; Guo et al., 2011; Cleven et al., 2015). Each model has implications for the nature of the Qilian-Qaidam-Kunlun continent, including its size, geometry, origin, and tectonic relationships between constituent blocks (Fig. 6.9C). For example, the first model requires the southern portion of Tarim to have linked with QQK in the Precambrian and that an early Paleozoic suture runs across Tarim. The second model is the only one that predicts QQK to be an individual entity surrounded entirely by oceans, and therefore presently surrounded by suture zones, whereas the third model requires a Precambrian linkage between QQK and Tarim.

Northward subduction of the Paleo-Tethys led to the development of the Kunlun magmatic arc along the southern margin of Tarim and Kunlun-Qaidam, which initiated by the Devonian (Li et al., 1991; Jiang et al., 1992; Wang et al., 1993; Wu et al., 2016) and accommodated the northward convergence of the Qiantang terrane and the South China craton. The Songpan-Ganzi flysch basin developed to the west as the North and South China cratons collided (Yin and Nie, 1993; Nie et al., 1994; Zhou and Graham, 1996b; Enkelmann et al., 2007; Pullen et al., 2008). Final closure of the Paleo-Tethys occurred by the latest Triassic (Fig. 6.3), which is demarcated by the Jinsha and Anyimaqen-Kunlun-Muztagh suture zones (Fig. 6.1).

#### **6.4.7. North China**

The wedge-shaped North China craton, also referred to as the Sino-Korean craton or platform, is bounded to the west-southwest by the early Paleozoic Qilian-Qinling orogen, to the north by the late Paleozoic Central Asian Orogenic System (CAOS), and to the south by the

Mesozoic Qinling-Dabie Shan orogen (Figs. 6.1 and 6.2). The craton is traditionally divided into two major Archean-Proterozoic blocks (i.e., the Eastern and Western Blocks) separated by the ~1500-km-long north-trending Paleoproterozoic (?) Trans-North China Orogen (TNCO) (e.g., Zhao et al., 1998, 2005, 2012; Trap et al., 2012) (Fig. 6.10A), which is also referred to as the Central Orogenic Belt (e.g., Kusky and Li, 2003; Kusky et al., 2007). Following this division, the Eastern Block is made up of the Langrim and Lonngang Blocks that joined along the Paleoproterozoic Liao-Liao-Ji orogen (e.g., Zhao et al., 2005; Tam et al., 2011), which contains 3.8-2.6 Ga gneiss and greenstone belts overlain by 2.6-2.5 Ga metasedimentary cover. The Western Block consists of the Ordos Block and Yinshan Block, which coalesced at ~1.92 Ga during the Khondalite orogen (e.g., Zhao et al., 2005; Santosh et al., 2006, 2007; Zhao, 2009).

The tectonic framework and timing of the collision between the Western and Eastern Blocks (Fig. 6.10A) has long been debated and two competing hypotheses have emerged. The primary difference between the two groups of models is the collisional age: ~1.85 Ga (e.g., Kröner et al., 2005a, 2005b, 2006; Zhang et al., 2007; Zhao et al., 1998, 1999, 2000a, 2005b, 2001a, 2001b, 2004b, 2005, 2007, 2010, 2012; Faure et al., 2007; Trap et al., 2007, 2008, 2009a, 2001b, 2011, 2012; Xiao et al., 2011; Zhao and Cawoord, 2012) or ~2.5 Ga (Li et al., 2000a, 2000b; Kusky and Li, 2003; Polat et al., 2005, 2006; Li and Kusky, 2007; Kusky et al., 2007; Kusky and Santosh, 2009; Kusky, 2011). However, it is becoming increasingly clear that both the 2.5 and 1.85 Ga events involved widespread intracontinental deformation that were not restricted to such narrow linear belts (e.g., Kusky and Li, 2003). Instead, the present-day exposure of these orogens is probably related to later tectonics. For example, the apparently north-trending TNCO is primarily exposed along Mesozoic-Cenozoic rift shoulders that are bounded by thick rift basins (e.g., Davis et al., 1996, 2001; Graham et al., 2012). Research on

Paleoproterozoic orogens in North America is undergoing a similar renaissance; orogens that were once considered narrow deformational belts are increasingly being reinterpreted as parts of broader zones of intracontinental deformation (e.g., Vervoort et al., 2016). I do not attempt to further interpret the Archean-early Proterozoic North China orogens, and for the purpose of my reconstruction, I assume that the North China craton was established by ~1.8 Ga.

Following the latest Paleoproterozoic event, near continuous Mesoproterozoic-Neoproterozoic sedimentation is observed in the Jixian County region of North China. The strata can be divided into four distinct successions—the Changcheng (1.8-1.6 Ga), Jixian (1.6-1.4 Ga), and Qingbaikou (1.4-0.85 Ga) Groups (Wan et al., 2011; Sun et al., 2012) (Table 6.1) (Fig. 6.10B)—although two more distinct groups may exist from 1.4 to 1.0 Ga (H. Li et al., 2013). A Changchengian rift event is evidenced by the Yan-Liao aulacogen, continental margin rift deposits (Figure 6.10B), and anorthosite-rapakivi granite (Li et al., 2000; Yang et al., 2005). Within the in Yan-Liao aulacogen, the oldest Changcheng Group deposits (i.e., ~1.8 Ga zircon ages of Wan et al., 2003b) unconformably overlie Paleoproterozoic orthogneiss, transitioning upward from conglomerate and sandstones at the base to shale and dolomite (Cheng et al., 1981). Jixian-aged sediments consist of ~4.5 km thick deposits of dolomite, minor limestone, mudstones, and shale deposited in an active (?) rift basin (Hebei BGMR, 1989; Wan et al., 2011; Ying et al., 2011). The Qingbaikou Group unconformably overlies the Jixian sections and consists of <500 m of predominantly siliciclastic rocks (Ying et al., 2011).

There are no Sinian (i.e., middle to late Neoproterozoic: 850-550 Ma) deposits in the Jixian region of North China, and only minor sections in the Hu-Huai and Lushan-Ruyang regions (Zhang et al., 2006b) to the south and the Liaodong Peninsula (Chang, 1980) to the east have reported strata of this age. These purported late Neoproterozoic deposits were determined

by biostratigraphy, regional correlations, and old isotopic dating techniques, with some formations dated to be out of stratigraphic order (Zhang et al., 2006b); more modern techniques (e.g., detrital zircon ages or cross cutting igneous rock ages) are needed to verify these findings. The general absence of Sinian strata is problematic as there is no regional geologic record of several important events that may have affected the region, including the breakup of the Rodinia supercontinent (e.g., Li et al., 2008) or possible global (?) Neoproterozoic glaciations (e.g., Hoffman et al., 1998; Allen et al., 2008; Li et al., 2013). The lack of Neoproterozoic rift deposits along the northern margin of North China has been used as evidence against the craton's involvement in Rodinia, but these deposits may have also been eroded away.

Neoproterozoic rift-related ultramafic or bimodal intrusions and volcanic rocks are documented along the southern margin of the North China craton, including the ~825 Ma Jinchuan intrusion (Li et al., 2005), the 1.0-0.84 Ga Qin'an dikes (Liu et al., 2012), and the ~830 Ma Luanchuan gabbros (Wang et al., 2011b). These ages correlate with rift-related rocks in southern Qaidam (Fig. 6.5).

Early Cambrian rocks unconformably overlie the uppermost section of Qingbaikou Group rocks in the Jixian region (i.e., the Jing'eryu Formation) (Ying et al., 2011; Sun et al., 2012). Widespread Cambrian shelf limestones (Meng et al., 1997; Myrow et al., 2015) indicate that North China was surrounded to the north and south by open oceans (i.e., the Paleo-Asian and Paleo-Tethys Oceans respectively). Some researchers suggest that North China and Tarim were linked to the northern margin of Gondwana in the Cambrian (McKenzie et al., 2011; Myrow et al., 2015; Han et al., 2016). However, this configuration is impossible as it does not allow for the collision of Qilian-Qaidam with the southern margin of North China in the Silurian. In the reconstruction of Han et al. (2016), the Paleo-Tethys is predicted to open in the same

location that the Qilian-Qinling collisional orogen is inferred to have occurred. In addition, a Cambrian linkage along North China's southern margin requires an additional unidentified pre-Mesozoic rifting event to create space for the collision of Songpan-Ganzi-South China with North China (Yin and Nie, 1993; cf. Han et al., 2016). On the other hand, passive margin sedimentation along the southern margin of the Eastern Kunlun range may have been related to the opening of the Paleo-Tethys (Neo-Kunlun) Oceans (Wu et al., 2016).

Collision between South China and North China (Yin and Nie, 1993; Zhang, 1997; Hacker et al., 2004, 2006; Wu et al., 2016) (Fig. 6.1) began in the latest Permian and concluded in the Triassic (Zhao and Coe, 1987; Ratschbacher et al., 2003; Hacker et al., 2006), and is demarcated by the Qinling-Dabie suture. Erosion of this orogen may have deposited thick clastic sediments in the Songpan-Ganzi remnant ocean basin (Zhou and Graham, 1996b; Enkelmann et al., 2007; Pullen et al., 2008). North China's northern margin remained quiescent until the Carboniferous-Permian initiation of south-directed subduction of the Paleo-Asian Ocean, which eventually led to a late Permian to Early Triassic collision against the CAOS that continued into the Jurassic (Xiao et al., 2003, 2009; Eizenhöfer et al., 2014).

## **6.5. Systematic restoration of central Asia and evidence for the Neoproterozoic Balkatach continent**

Here I describe my tectonic restoration of central Asia from the present through the Phanerozoic to the Proterozoic. Emphasis is placed on providing evidence for the Neoproterozoic Balkatach at its maximum extent at ~870 Ma, when the Western and Eastern Domains collided along the Tarim suture (Fig. 6.8). I systematically restore the significant *intracontinental deformation* and *tectonic calving* of microcontinents that have distorted this

Precambrian continent.

This restoration is based on the most up-to-date Geological Map of Asia (Ren et al., 2013). The reconstructions presented here (Fig. 6.11) makes no attempt to restore the polar region distortion, but the final restored shape files were produced by undefining polygons using GPlates software ([www.gplates.org](http://www.gplates.org)) (Boyden et al., 2010). Polar distortion effects are not significant because the general trend of the Balkatach is east-west. I start by restoring the most recent tectonic events that affected the geometry of Asia (i.e., Cenozoic deformation) and progress to older events in the Mesoproterozoic (Fig. 6.11). Reconstruction information is presented based on present-day geographic location, moving from west to east (i.e., Baltica to eastern China).

### **6.5.1. Late Mesozoic-Cenozoic intracontinental deformation**

First I restore intracontinental deformation associated with the Cenozoic India-Asia collision, which initiated at ~55 Ma (e.g., Le Fort, 1996; Zhu et al., 2005; Green et al., 2008; Dupont-Nivet et al., 2010a; Najman et al., 2010; Wang et al., 2011a), and the Mesozoic-Cenozoic development of the western Pacific subduction system (Figs. 6.1 and 6.11A).

#### *The Tian Shan, Pamirs, and Kopet Dagh*

Cenozoic crustal shortening across in the ~2,000-km-long east-trending Tian Shan thrust belt decreases from ~200 km in the west to almost zero in the east (Avouac et al., 1993; Yin et al., 1998), consistent with the westward increase of the width of the belt. The Pamir and Western Kunlun Shan accommodate southward continental subduction of Tarim (Cowgill et al., 2003) to depths of greater than 100 km (Burtman and Molnar, 1993). Crustal shortening of ~100 km has been estimated by balanced cross-section construction in the Western Kunlun Shan (Cowgill,



2001) and isostatic equilibrium calculations (Lyon-Caen and Molnar, 1984). The Kopet Dagh range is thrust to the northeast over the Turan Domain (Jackson and McKenzie, 1984; Thomas et al., 1999b) with crustal shortening estimates of ~70-75 km (Lyberis et al., 1998). I restore this deformation by assuming that the pre-Cenozoic sutures on both sides of the Pamirs were oriented as straight traces along great circles in the east-west direction (present coordinates) prior to the India-Asia collision. In order to accommodate the restoration of Cenozoic deformation in the westernmost Tian Shan (Avouac et al., 1993), the Pamir Mountains (Burtman and Molnar, 1993), and the western Kunlun Shan (Cowgill et al., 2003), the Tarim craton must extend westward and its geology can be traced through Tajikistan to the Karakum craton (e.g., Biske and Seltmann, 2010). Seismic-reflection profiles across the Junggar basin to the north (Song, 2006; Yang et al., 2012b) also suggest that post-Permian crustal shortening of at least 10s km may have occurred.

The Neoproterozoic connection between Tarim, Karakum, Turan, and Baltica is largely speculative due to >90 % Mesozoic-Cenozoic cover, but the available geologic datasets (Figs. 6.3, 6.4, 6.5, 6.7 and 6.8) are consistent with these blocks sharing a common Phanerozoic history.

#### *The Altyn Tagh, Qaidam, and Qilian Shan*

Cenozoic left-lateral motion along the Alytn Tagh fault was restored ~400 km based on offset piercing-point estimates by Yin and Harrison (2000), Yang et al. (2001), Gehrels et al. (2003b), and Cowgill et al. (2003). This restoration places the Paleoproterozoic basement of Dunhuang (Zong et al., 2012) alongside similar-aged basement in the North China craton (Zhang et al. 2012, 2013; cf. Long et al., 2014). In addition, geologic mapping (Yin et al., 2008; Reith,

2013; see Chapter 2), analysis of seismic reflection profiles (Gao et al., 2013; Wang et al., 2014; Zuza et al., 2016), and geodetic data (Duvall and Clark, 2010; Zuza and Yin, 2016) reveals a Cenozoic strain gradient across the North Qaidam and Qilian Shan-Nan Shan thrust belts, from ~50% in the west to 25% in east, which is restored in this reconstruction (Fig. 5.11A). Little work has been done in the Qimen Tagh thrust belt, but I assume that the strain magnitude in this region is similar to the Qaidam region (Yin et al., 2007b).

The Haiyuan and Kunlun strike-slip faults, and their terminal thrust belts to the east (i.e., the Liupan Shan and Longmen Shan thrust belts), are prominent features on the Tibetan Plateau today, but their contribution to modifying the pre-existing geology is minimal (Zuza and Yin, 2016; see Chapter 3). Offsets on the Kunlun fault vary from ~100 km in the west to <10 km in the east (Van der Woerd et al., 2000, 2002; Fu et al., 2005; Kirby et al., 2007), and offsets along the Haiyuan fault vary from ~90 km in the west to <15 km in the east (Burchfiel et al., 1991; Ding et al., 2004; Gaudemer et al., 1995). Based on my present understanding (Zuza and Yin, 2016), these faults result from crustal block rotation, and as they both parallel Phanerozoic sutures, they are not responsible for obscuring or distorting any earlier tectonic event or geometry.

#### *North China and eastern Asia*

From the Late Jurassic to the Tertiary, widespread extension has affected much of eastern Asia (e.g., Mongolia, northeast China, and the western Pacific) as the western Pacific trench system migrated eastward (e.g., Traynor and Sladen, 1995; Ren et al., 2002; Yin, 2010). Subduction rollback, postorogenic collapse, and regional extension began soon after 120 Ma (Davis et al., 1996, 2001; Graham et al., 2012), which is expressed by the formation of northeast-

to north-northeast-trending rift (or transtensional) basins with synrift volcanic rocks (Traynor and Sladen, 1995; Deng et al., 1999; S. Zhang et al., 2014) and marginal sea basins in the western Pacific. Extensional detachment faults have exposed mid-crustal rocks throughout eastern Asia (Zheng et al., 1991; Davis et al., 1996; Webb et al., 1999; Davis et al., 2001; G. Zhu et al., 2012). Based on the widespread exposure of mid-crustal rocks and rift basins, I assume that a total magnitude of 100% extensional strain affected the Huabei-Korea-Japan domain (see Yin, 2010) since ~120 Ma (Davis et al., 2001); I restore approximately 550 km of extension during this time (Fig. 6.11A).

### **6.5.2. Late Paleozoic-Mesozoic intracontinental deformation and ocean closure**

As the Paleo-Asian Ocean closed against Balkatach in the Late Paleozoic (Fig. 6.3), the northern passive margin rocks of Balkatach were deformed. In the Uralides, an unknown magnitude of the eastern passive margin of Baltica subducted beneath Kazakhstan (Brown et al., 2011); similar events occurred along the Tian Shan-Ying Shan and Solonker-Jilin-Yanji sutures (Fig. 6.1). The northern continental margin of the Tarim basin may have subducted below a Devonian arc (Charvet et al., 2011), making its original size larger than it is exposed today. Restoration of these margins is highly speculative, and thus I only restore 10s of km to the margins that show signs of continental subduction (i.e., the Uralides and the Tian Shan) (Fig. 6.11A).

The magnitude of deformation associated with the closure of the Paleo-Tethys along the southern margin of Balkatach is also poorly understood. I do not restore any shortening associated with the collision of the Qiangtang terrane and South China with Balkatach, but acknowledge that shortening along these margins may be on the order of 100s of km.

### 6.5.3. Neoproterozoic rifting and Paleozoic orogeny

As discussed above, restoration of Cenozoic intracontinental deformation shows that Tarim and North China were contiguous prior to the Mesozoic, and the late Paleozoic Kunlun arc suggests that Qilian-Qaidam-Kunlun and Tarim were linked at this time, which requires North China to also be linked with QQK. The belt of ~1.0-0.9 Ga granites found in Tarim and QQK further supports their Neoproterozoic linkage (e.g., Figs. 6.8 and 6.9).

The abundant Neoproterozoic rift and Cambrian passive margin deposits found along a majority of Balkatach's margins suggest that the continent was involved in the global-scale breakup of the Rodinia supercontinent (Fig. 6.5). Rifting was followed by several Paleozoic orogens as separate microcontinents collided against Balkatach, including the Qilian-Qinling, Tagil, and Magnitogorsk microcontinents and arcs. Coevally, several microcontinents were involved in the initiation and evolution of the CAOS throughout the Paleozoic. This major transition from rifting to collisional orogeny fundamentally depends on whether the colliding microcontinents are exotic or genetically related to Balkatach. In the first scenario, Neoproterozoic rifting must allow for the conjugate continents and microcontinents to travel far enough away from Balkatach to allow for exotic blocks to collide against its margins in the Paleozoic. This is envisioned in the reconstruction by Stampfli and Borel (2002), where following Neoproterozoic rifting, Gondwana-derived ribbons of continental crust crossed the Paleo-Tethys and collided with the southern margin of Balkatach and Laurasia (e.g., the Hunia and Galatia continents; see also von Raumer and Stampfli, 2008; Stampfli et al., 2011, 2013).

An alternative model is that Neoproterozoic rifting may have caused several large continents to separate and drift away from Balkatach, but some microcontinents broke off (partially and/or completely) to remain nearby within the Paleo-Asian and Tethyan Oceans. It is

these continents that collided against Balkatach in the Paleozoic and also served as nuclei for the initiation of the CAOS. Below I provide evidence and rationale for this second model.

#### **6.5.4. The origin of Qaidam-Qilian-Kunlun and CAOS microcontinents**

The early Paleozoic Qilian suture indicates that a late Neoproterozoic-early Paleozoic Ocean separated North China and QQK, but as previously discussed, there is no documented suture that divides QQK from Tarim (Fig. 6.9). The additional observation that Qaidam Precambrian basement is similar to the basement of Tarim-North China (e.g., Gehrels et al., 2003b; Wu et al., 2016) suggests that QQK was originally part of Tarim-North China and only a continental strip partially rifted from the North China margin in the Neoproterozoic (scenario 3 in Fig. 6.9C). Other researchers argue that QQK was derived from the South China craton based on correlative ~950-900 Ma granites, but it clear that this is not a unique signature among Precambrian crustal continents, as similar-aged plutons are found within North China, Tarim, the Tian Shan, and the CAOS microcontinents (Fig. 6.4).

As previously discussed, there is evidence that the Precambrian Tian Shan microcontinent was derived from Tarim. Several workers have also suggested the connection between some of the Mongolian CAOS microcontinents and Tarim-North China (e.g., Rojas-Agramonte et al., 2011; Levashova et al., 2011) on the basis of detrital zircon age distributions. Examination of the pre-800 Ma detrital zircon age distribution reveals that similar age peaks at ~2.5 Ga, 1.85-1.8 Ga, ~970-910 Ma, and 790-750 Ma (Fig. 6.4). The northeastern Gondwana margin also shares similar age peaks (Fig. 6.4) and a Gondwana origin for these microcontinents cannot be ruled out, but I follow the suggestion of Rojas-Agramonte et al. (2011) and favor a Tarim origin. Similarly, Han et al. (2011) suggested that the Erguna-Xing'an-Songliao

microcontinents in northern China were derived from Tarim on the basis of U-Pb detrital zircon ages (Fig. 6.4).

### **6.5.5. Paleomagnetic data**

The apparent polar wander (APW) paths from paleomagnetic poles are often used to develop and test plate-tectonic reconstructions. The goal of this study is to focus on the geologic histories and relationships of each continent to assess its paleogeographic location. However, preliminary paleomagnetic analysis presented in Figure 6.12 and Table 6.2 was used to constrain the tectonic reconstruction presented in section 6.6 and to test its viability. Ultimately, there are too few reliable paleomagnetic poles for the Balkatach continents to draw significant quantitative conclusions, but this high-quality paleomagnetic data places important paleolatitude bounds.

The connections between the CAOS microcontinents and Tarim-North China discussed above in section 6.5.5 are supported by paleomagnetic data. The estimated Precambrian paleolatitude of the Karatau and Baydaric microcontinents (Fig. 6.2) is similar to North China and Tarim but not Siberia at 805-770 Ma (Fig. 6.12) (Levashova et al., 2010, 2011). The apparent separation of Baltica and Tarim-North China at ~550 Ma and ~750 Ma (Fig. 6.12) can be explained by the elongate geometry of Balkatach. The ~25° separation corresponds to a distance of ~2800 km on Earth's surface, and given that Balkatach has a length of 4000-5000 km, this paleolatitude data may reveal that the continent may have had a north-trending orientation. Any apparent separation may be the result of the distance between paleomagnetic sample sites. In fact, these datasets may provide insights into the orientation of this long continent; the continent was oriented mostly N-S at ~750 Ma but rotated to W-E at the start of

the Cambrian. Further examination of paleomagnetic datasets and apparent polar wander paths in the context of the Balkatach hypothesis is necessary to interpret any of these observations.

## **6.6. Tectonic evolution of Balkatach**

I now retro-deform central Asia, with emphasis on the evolution of Balkatach, from the Proterozoic to the present. Here I provide 11 time slices from the Mesoproterozoic (~late Jixian) to the present in Figures 6.13-6.15 and 6.17, with higher spatial and temporal resolution progressing through time. Note that this reconstruction focuses more heavily on the eastern segment of Balkatach (i.e., east of Tarim), which is due to the scarcity of geologic data in west. Although there are numerous localized reconstructions that focus on one (or several) specific region(s) (e.g., Tarim, the Qilian orogen, North China, and the CAOS) (Filippova et al., 2001; Biske and Seltmann, 2010; Zhao and Zhai, 2013; Song et al., 2013, 2014; Xiao et al., 2013), none show how all of these regions relate and evolve through time and space. This model is first-order attempt at constraining the evolution of Balkatach and its constituent cratons, and adheres to our current knowledge of later tectonic modification. Quantitative paleopositions are not given for the Mesoproterozoic time, but are for later reconstructions. The evolution of the CAOS is largely after Filippova et al. (2001), with considerations of Windley et al. (2007) and Xiao et al. (2013).

### **6.6.1. Paleoproterozoic**

#### *Eastern Balkatach (North Tarim and North China)*

By the Paleoproterozoic, Archean crustal fragments consisting of orthogneiss, TTG gneiss, metamorphosed supracrustal rocks, and greenstone belts as old as 3.8 Ga were

amalgamated into the North China craton. The Neoproterozoic crust of North Tarim formed separately from North China (Long et al., 2010, 2014), although I postulate that they joined by the Paleoproterozoic as no later collisional events are observed (cf. Yuan and Yang, 2013). At the Paleoproterozoic start of this reconstruction, North Tarim and North China are together.

#### *Western Balkatach (Baltica, Turan, Karakum, and South Tarim)*

The collision and amalgamation of Samatia, Fennoscandia, and Volgo-Uralia of Baltica was complete by ~1.8 Ga (Bogdanova et al., 2006; Shchipansky et al., 2007). Turan, Karakum, and South Tarim were also connected to a unified Baltica craton.

#### **6.6.2. Mesoproterozoic (Fig. 6.13)**

Intracratonic rifting and aulacogen formation affected both the western and eastern domains Balkatach throughout the Mesoproterozoic, which suggests that other unknown continents were affixed to their respective margins prior to continental breakup. The eastern margin of Western Balkatach (i.e., the Ural-side) and southern margin of Eastern Balkatach witnessed a transition to passive margins, suggesting that these margins separated from their conjugate continents, although it is unclear if Balkatach entirely separated from other continents at this time.

#### **6.6.3. Neoproterozoic (Fig. 6.14)**

Subduction of the Tarim-Proto Urals Ocean underneath the East Balkatach led to the development of the 970-910 Ma Tarim arc, which stretched from the Qinling-Qilian-Qaidam-Kunlun regions through Tarim into an unknown continent. This subduction system



accommodated the convergence of the West and East Balkatach, which collided along the Tarim suture (e.g., Guo et al., 2005) by ~870 Ma, at which point Balkatach reached its full extent. The combined Songpan-Ganzi and South China cratons collided against the southern margin (present-day coordinates) of Balkatach at a similar time (Wu et al., 2016), although this collision must have occurred prior to the initiation of bimodal volcanism documented in southern Tarim at ~900 Ma (e.g., Wang et al., 2015a, 2015b).

Immediately after and/or during the collision of West and East Balkatach, rifting commenced along the continent's northern and southern margins. Several aulacogens developed obliquely to the inferred continental margins: in the east the Helan and Manjiaer aulacogens formed on either side of Balkatach (Lin et al., 1995, 2014) and in the west syn-rift sedimentation was more diffuse and several Mesoproterozoic aulacogens were reactivated as rift basins (e.g. Kaltasin and Sernovodsk-Abdulino Aulacogens in Baltica). Rifting of Balkatach from an unknown continent to the north and the Songpan-Ganzi-South China continent to the south (Wu et al., 2016) respectively opened the Paleo-Asian Ocean at ~800 Ma and the Paleo-Tethys Ocean (Paleo-Kunlun Ocean) at ~830 Ma.

The rifting process was complex and relatively long-lived, leading to protracted rift-related volcanism and volcanic passive margin development. The warmed lithosphere ultimately led to tectonic calving (e.g., Müller et al., 2001) (discussed further in section 6.7.2) of the CAOS microcontinents and the partial incomplete opening of the Qilian Ocean from 750-650 Ma. These rift events may be analogous to the continental fragments that rifted from northern Australia in the Mesozoic-Cenozoic (e.g., Hall, 2011; Metcalfe, 2011).

#### **6.6.4. Early-Middle Paleozoic (Fig. 6.15)**

The Paleo-Asian Ocean persisted throughout the Paleozoic, and may have been divided into up to four interconnected oceans by the Kazakhshtan continent. In this reconstruction, I follow the archipelago models of Filippova et al. (2001), and envision Balkatach wrapping around these accretionary arcs (e.g., Abrajevitch et al., 2008; Xiao and Santosh, 2014).

Much of the northern and southern margins of Balkatach, bounding the Paleo-Asian and Paleo-Tethys Oceans respectively, remained passive throughout most of the Paleozoic (Fig. 6.5), although western Balkatach experienced two arc-continent collision events as the Tagil and Magnitogorsk arcs collided with the proto-Urals in Devonian-Early Carboniferous. The closure of the Qilian Ocean in the earliest Silurian occurred during the Qilian-Qinling orogen. This collision progressed from west to east, consistent with the closure of a peninsular QQK rotating counter-clockwise. The north-dipping Paleo-Kunlun arc was constructed on the southern margin of Qaidam and may have stretched as far west as Karakum. Intra-arc extension led to the deposition of several Devonian basins in the Karakum and Kunlun regions.

Middle Carboniferous collision of central Western Balkatach with Kazakstan occurred during the southern Uralide orogen. Following collision, bi-directional suturing propagated northward (relative to the strike of the Urals), as Balkatach wrapped around the CAOS toward Siberia, and eastward, as the Paleo-Asian Ocean was consumed along the Solonker-Jilin-Yanji suture (Figs. 6.3, 6.15C, and 6.16).

#### **6.6.5. Late Paleozoic (Fig. 6.16)**

The bidirectional closure of the Paleo-Asian Ocean continued along the northern margin of Balkatach into the late Paleozoic (Fig. 6.3), and by ~300 Ma the Pacific Ocean was separated

from the Paleo-Asian Ocean (Fig. 6.15C). The complete closure of the Paleo-Asian Ocean in the Permian was accompanied by a widespread magmatic flare-up, which may have been related to the avalanche of subducted oceanic slabs of the Paleo-Asian Ocean across the 660 km phase boundary in the mantle (e.g., Schubert and Tackley, 1995; Cina, 2011) (Fig. 6.16). There was an enormous amount of oceanic crust that subducted in the CAOS and the closure of the Paleo-Asian Ocean. If these slabs stagnated at the 660 km phase transition (Schubert and Tackley, 1995) before simultaneously breaking through this phase-transition boundary, there would be a significant amount of asthenospheric upwelling that could melt the metasomatized lithospheric mantle and trigger widespread Permian magmatism across central Asia (Fig. 6.16).

#### **6.6.6. Mesozoic-Cenozoic (Fig. 6.17)**

Collision between Balkatach and the CAOS continued from central Balkatach (i.e., Karakum and Turan) eastward, with continued northward subduction under the CAOS (e.g., Kazakshstan and other microcontinents). This led to the progressive destruction of the Turkestan, Asiatic, and Solonker Ocean—parts of the Paleo-Asian Oceans—which are demarcated by the Denisov-Oktyabrsk, Turkestan, and Solonker-Jilin-Yanji sutures (Fig. 6.1). Collision and ocean closure was completed by the Triassic.

Northward subduction of the Paleo-Tethys under the southern margin of Balkatach continued in the Permian, as expressed by a Permian-Triassic Kunlun-Yidun-Earlangping-Qinling magmatic arcs, which accommodated the convergence of the South China craton and numerous other terranes (e.g., Qiangtang and Lhasa). Collision between South China and eastern Balkatach (i.e., North China) began in the latest Permian and concluded by the Triassic, and is demarcated by the Qinling-Dabie suture. The Paleo-Tethys was concurrently subducting to the

south under the Qiangtang-Indochina terranes, which collided with Baltica and South China in the late Triassic and led to the cessation of arc magmatism in the Kunlun arc (e.g., Wu et al., 2016). By the Late Triassic, the Lhasa block to the south, collided with the Qiangtang terrane along the Bangong-Nujiang suture following the closure of the Meso-Tethys (Yin et al., 1994; Murphy et al., 1997). The Middle Cretaceous initiation of northward subduction of the Neo-Tethys under Lhasa accommodated convergence of India toward Asia, which led to the formation of an Andean arc and the development of the Gangdese batholith (Allégre et al., 1984, Harrison et al., 1992). The Indus-Yarlung suture zone separates Lhasa from the Himalaya and demarcates the destruction of the Neo-Tethys.

Intracontinental deformation that resulted from the collision between India and Asia at ~55 Ma (e.g., Le Fort, 1996; Zhu et al., 2005; Green et al., 2008; Dupont-Nivet et al., 2010a; Najman et al., 2010; Wang et al., 2011a) modified the existing configuration of Asia. In addition to the Himalayan orogen, crustal shortening occurred in the Tian Shan, West Kunlun, Qimen Tagh, North Qaidam, and Qilian Shan-Nan Shan thrust belts. Continental subduction in the Pamirs and strike-slip offset along the Altyn Tagh fault obscured many of the pre-Cenozoic structures. Eastward extension of Asia along the western margin of the Pacific Ocean also continued at this time.

## **6.7. Discussion**

The above reconstruction conforms to existing geological observations, but in doing so, it raises the following questions:

- (1) What continents were affixed to the margins of Baltica in the Proterozoic? This long cratonal strip, with Archean and Proterozoic structures inexplicably truncated by

Neoproterozoic passive margin successions, must have fit into a larger continental assemblage prior to this time (cf. Li et al., 2008).

- (2) Where does the Precambrian Tarim arc (i.e., 1.0-0.9 Ga granitoids and gneiss) and suture extend to the north and south of Tarim (Fig. 6.14)? It is not likely that this arc could have laterally terminated within Tarim, and so there should be evidence of its continuation on another continent that was rifted away from Balkatach in the Neoproterozoic.
- (3) Although this chapter is focused specifically on the tectonic evolution of central Asian, Baltica's proposed connection within Balkatach has implications for the development of both Rodinia and Laurasia. In most reconstructions, Baltica collided with Laurentia twice since the Neoproterozoic (e.g., Ziegler, 1989; Scotese and McKerrow, 1990). My proposed Baltica-Balkatach connection represents a fundamental difference from the model of Şengör et al. (1993), where pre-Uralide and Baykalide subduction system (i.e., the Urals and southern Siberia) were connected at the end of the Neoproterozoic. Instead, the northern margin of Balkatach may have linked with the North American Cordilleran arc-trench system (e.g., Zonenshain et al., 1987; Miller et al., 2011).

### **6.7.1 Neoproterozoic Balkatach in Rodinia**

Balkatach must be reconsidered in the context of the supercontinents Columbia and Rodinia. For example, in the popular Rodinia reconstruction of Li et al. (2008), the North China, Tarim, and Baltica cratons are positioned separately along the outskirts of the supercontinent, even though Proterozoic structures truncated by rift-features along their margins (e.g., aulacogens and transitions to passive margin sequences) require their involvement in a larger continental assemblage. For reconstructions of Columbia, North China is often connected with

India on the basis of linking the Trans-North China Orogen with the Central Indian tectonic zone (Zhao et al., 2003, 2004). This connection may still be valid, but should be pursued further considering the dimensions of Eastern Baltica in the Proterozoic (e.g., North Tarm to North China, with several CAOS microcontinents) (Figs. 6.13-6.14). The long, relatively thin aspect ratio of Baltica readily allows for continents to be affixed to either side. I envision that the continent may serve as an alternative “missing link” between already postulated connections (e.g., Li et al., 1995).

The well documented truncation of Archean and Paleoproterozoic structures in western Laurentia (e.g., Taltson-Buffalo Head, Vulcan, and Great Falls Tectonic Zones) by a thick Neoproterozoic succession of miogeoclinal sediments led early workers to develop the hypothesis that a Precambrian continent had to have rifted away (e.g., Stewart, 1972, 1976; Burchfiel and Davis, 1972; Monger et al., 1972; Sears and Price, 1978). A similar situation exists for Baltica yet paleogeographic reconstructions of Baltica's constituent cratons, especially North China and Tarim, do not consider this issue.

One possibility is that the proposed Baltica continent was affixed to the western margin of Laurentia in the Proterozoic (Zuza and Yin, 2013, 2014), with Siberia positioned to the north of Laurentia following Rainbird et al. (1998) (e.g., Evans and Mitchell, 2011; Ernst et al., 2016). The ~6000-km length of Baltica is equivalent to the north-south length of western Laurentia from the northern tip of Alaska to the southern tip of the Gulf of California. This hypothesis is based on the following lines of observations:

- (1) *Proterozoic subduction and collision*: The ~1.85 Ga Trans-North China Orogen and Great Falls Tectonic Zone of western Laurentia (e.g., Goreman et al., 2002; Ross et al., 2002; Mueller et al., 2002; Foster et al., 2006) have similar arc-subduction-collision

histories that accommodated the convergence of Archean blocks. The exposed Paleoproterozoic basement in Karakum and Turan would link with the 1.9-1.85 Ga Fort Simpson belt (Ross et al., 2002) in western Canada.

(2) *Mesoproterozoic strata*: The Belt-Purcell Supergroup spatially and temporally correlates with Jixian deposits in North China (Hebei BGMR, 1989; Ross et al., 1992; Ross and Villeneuve, 2003; Zhai et al., 2015); both groups are thick (i.e., >10 km), and consist of carbonate and mudrocks deposited in active margin-bounded rift troughs. In addition, the Belt-Purcell rocks possess 1610-1500 Ma zircons that are rare in western Laurentia; it has long been postulated that a separate continent must provide a western source for these zircon grains (Ross et al., 1992; Ross and Villeneuve, 2003). North China has rapakivi granites with this age signature (e.g., Zhang et al., 2007).

(3) *Neoproterozoic rift histories*: Rifting and the development of a Neoproterozoic-Cambrian passive margin sequences occurred along the northern margin of Baltica and the western margin of Laurentia (e.g., Lund et al., 2010; Levashova et al., 2010, 2011; Meert et al., 2011; Shu et al., 2011, Han et al., 2011; Balgord et al., 2013). Additionally, similar-age (i.e., ~710 Ma, ~655 Ma, and ~630 Ma) diamictites have been reported in in the Windermere Group of North America (Lund et al., 2003; Balgord et al., 2013), Qurutagh Group of Tarim (Xu et al., 2005; Shu et al., 2011), and Central Asian microcontinents (Levashova et al., 2011; Meert et al., 2011).

### **6.7.2. Tectonic calving and CAOS microcontinent formation**

A central component of my reconstruction is that the microcontinents in the CAOS and the QJK continent are both genetically linked with the margins of Baltica. This implies that

these continents detached from Baltica during Neoproterozoic rifting. This detachment was either partial, like for the peninsular Kunlun-Qaidam continent, or entire, like for the CAOS microcontinents. However, in both cases, the continents remain near to the Baltica continent following rifting and collide with it in Paleozoic. These rifted microcontinents may be analogous to the continental fragments that rifted from northern Australia in the Mesozoic-Cenozoic (e.g., Hill and Hall, 2003; Hall, 2011; Metcalfe, 2011). I envision that these rifted microcontinents are the result of “tectonic calving” during rift development, akin to glacial calving.

An issue with microcontinent development during regional rifting is that extension should be isolated to the developing mid-ocean, which has a relatively low yield strength compared to the continental crust (Bodine et al., 1981). A rheological weakness must develop to concentrate rifting away from a nearby mid-ocean ridge and allow a microcontinent to separate from the rest of the continental lithosphere. Increasing the temperature of the lithosphere may be one mechanism to generate this weakness (Müller et al., 2001). For Baltica, especially around Tarim, there are three lines of evidence that suggest there was a warmed lithosphere in the Neoproterozoic: (1) subduction, arc-magmatism from ~970-910 Ma, and collision by ~870 Ma along the Tarim suture would have led to elevated heat flow; (2) long-lived magmatism (i.e., from 840 to 680 Ma) (e.g., Shu et al., 2011) predates, accompanies, and follows the main stages of rifting; and (3) there is evidence for a Neoproterozoic plume beneath Tarim (e.g., Li et al., 2003; Lu et al., 2008; Long et al., 2011).

Continental break-up involving a hotter lithosphere is generally associated with the development of a volcanic passive margin, or volcanic rift margins (Gernigon et al., 2004; Geoffrey, 2005). If distinct segments of Baltica's rifted margins involved volcanic passive



margin development, the associated large volume of warmer, weaker continental crust would allow extension and mid-ocean spreading to jump among zones of weakness. During the rifting of several large continents, smaller continental fragments could also rift away but they would remain nearby as local spreading centers shutoff and spreading eventually concentrates within a single and central mid-ocean ridge. Proterozoic volcanic passive margins have not been well identified or studied, and geophysical data would be needed to verify the presence of characteristic thick igneous layers in the lower crust or continent-ward dipping normal faults.

## **6.8. Conclusions**

By removing the tectonic-distortion effects in central Asia caused by intracontinental deformation and rifting events, I have shown that a continuous continent once stretched from the North China craton to Baltica in the west. I refer to this continent as **Balkatach** based on the linkage between the **Baltica**, **Karakum**, **Tarim**, and North **China** cratons. This continent, and the relative motion of its western and eastern arms (in present-day coordinates) in the Paleozoic, played an important role in the tectonic evolution of Asia. Neoproterozoic rifting along **Balkatach's** margins led to the opening of Paleo-Asian, Pacific, and Tethyan Oceans. Archipelago development and subduction within the Paleo-Asian Ocean accommodated the oroclinal bending of **Balkatach** around this ocean. The initial collision of central **Balkatach** and the CAOS in the mid-Carboniferous was followed by bi-directional suturing and “double zipper” closure of the Paleo-Asian Ocean by the Permian. The closure of the Paleo-Tethys Ocean along **Balkatach's** southern margin proceeded diachronously from west to east, during the Permian-Triassic.

The restored ~6000-km-long Balkatach continent must fit in Neoproterozoic Earth and Rodinia reconstructions. This tectonic reconstruction presented here is at odds with current Neoproterozoic models that place each of Balkatach's constituent continents separately along the outskirts of the Rodina supercontinent (e.g., Li et al., 2008). I tentatively propose that Balkatach was affixed to the western margin of Laurentia in the Proterozoic, with Siberia positioned to the north of Laurentia following Rainbird et al. (1998). More work is needed to test this hypothesis.

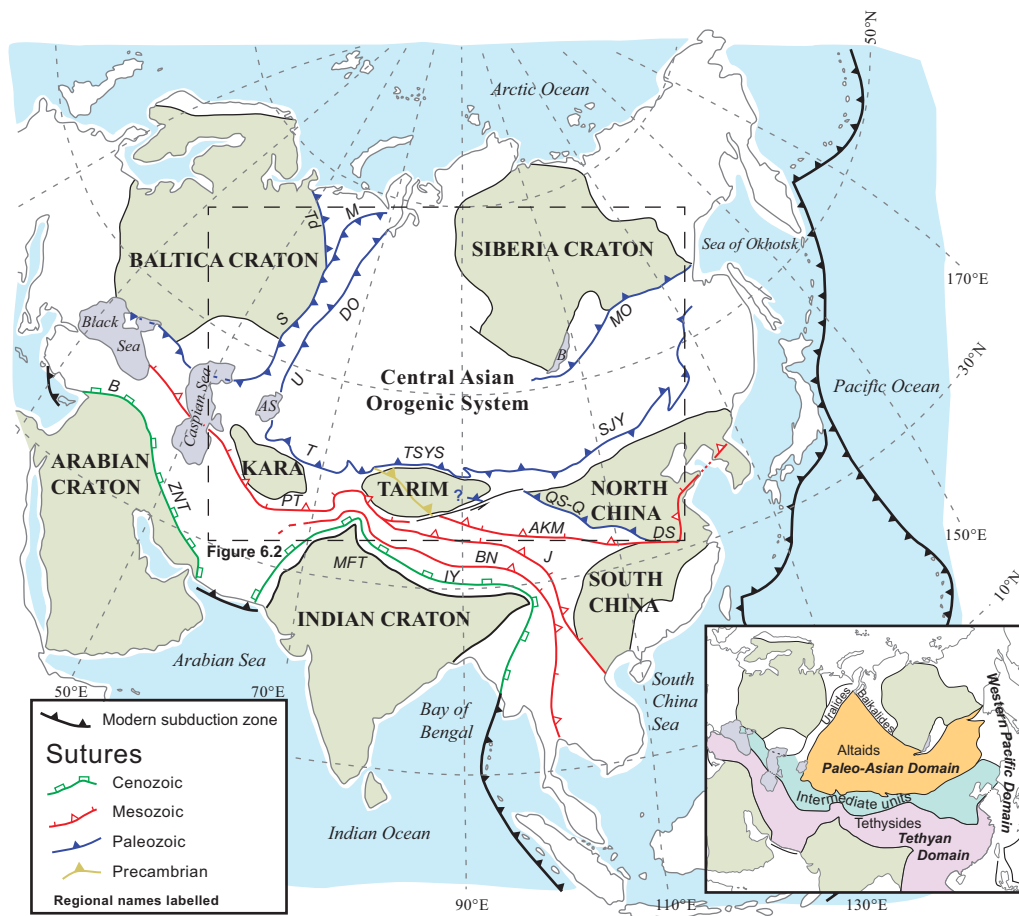


**Figure 6.1.** Simplified tectonic map of Asia showing cratons, sutures, and modern subduction zones. Teeth on are on over-riding plate. For simplicity, the structures and sutures within the Central Asian Orogenic System are omitted. Pre-Neoproterozoic sutures within cratons are not shown. Inset map shows major tectonic division and oceanic domains. Also shown is the location of Figure 6.2. AS—Aral Sea, B—Lake Baikal, Kara—Karakum Craton, MFT—Main Frontal Thrust. Labelled sutures: AKM—Anyimaqen-Kunlun-Muztagh, B—Bitlis, BN—Bangong-Nujiang, DO—Denisov-Oktyabrsk, DS—Dabie Shan, J—Jinsha, M—Magnitogorsk, MO—Mongol-Okhotsk, PT—Paleo-Tethys, S—Sakmara, SJY—Solonker-Jilin-Yanji, TSYS—Tian Shan-Ying Shan, T—Turketsan, Td—Timanide, U—Ural, QS-Q—Qilian Shan-Qinling, ZNT—Zagros-Neo-Tethys. After Yin and Nie (1996), Şengör and Natal'in (1996), Natal'in and Şengör (2005), Xiao et al. (2010), and Zheng et al. (2013).

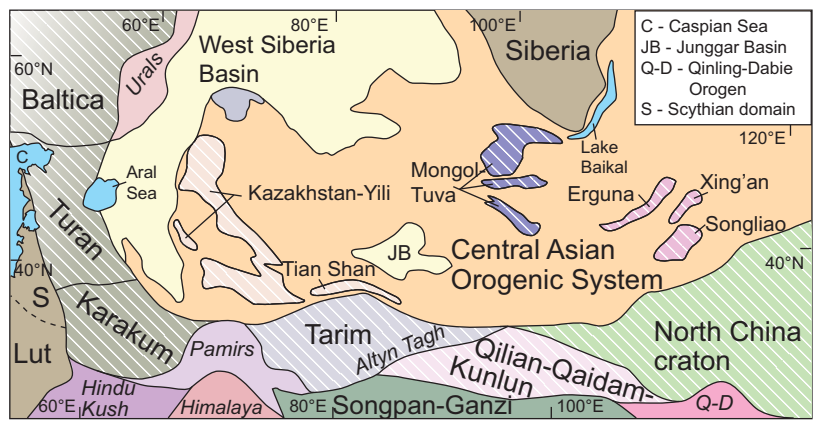


**Figure 6.2.** Simplified tectonic map of Central Asia showing the terranes and cratons of the proposed Balkatach continent (shown with white stripes). See Figure 6.1 for location.

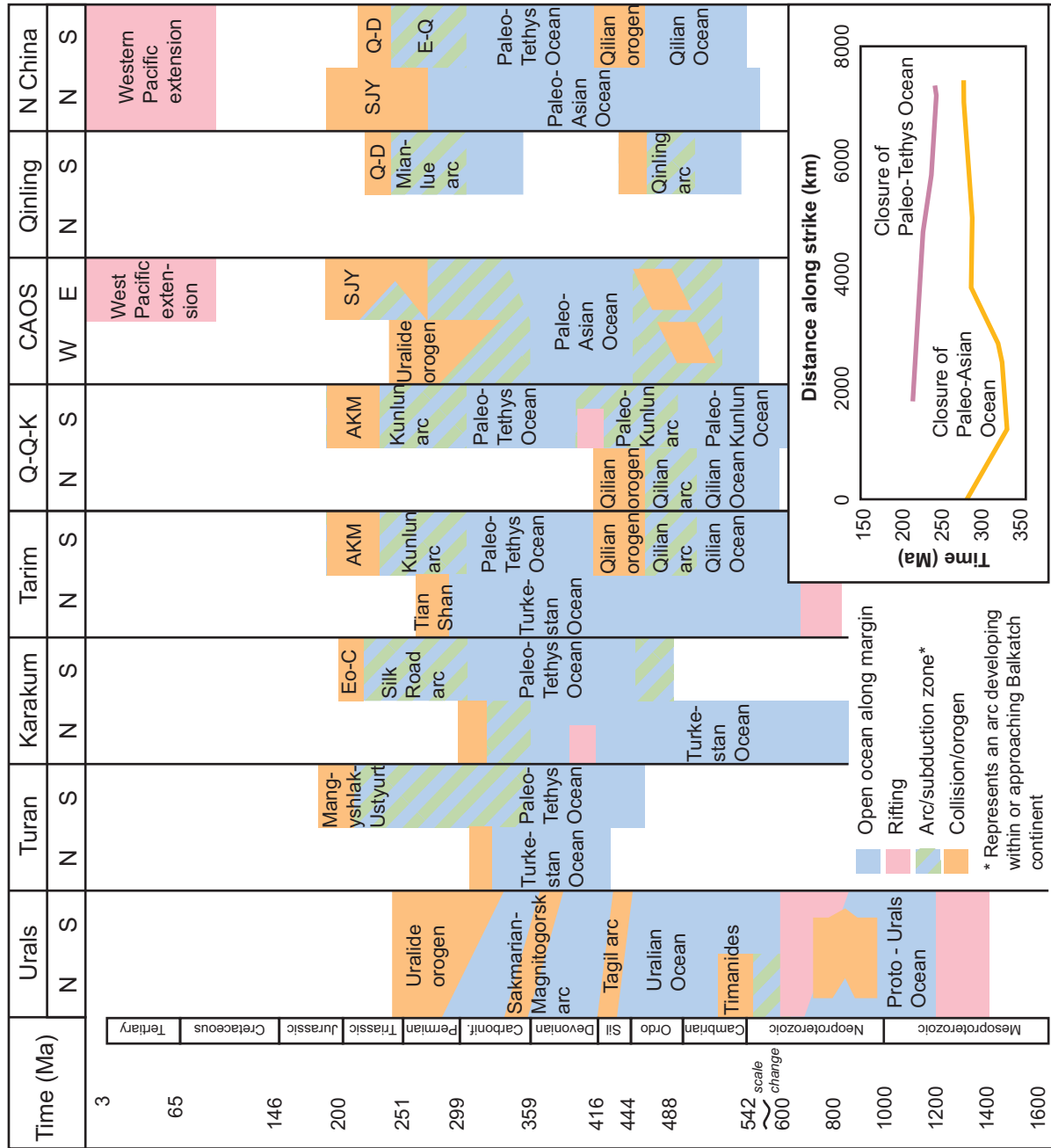
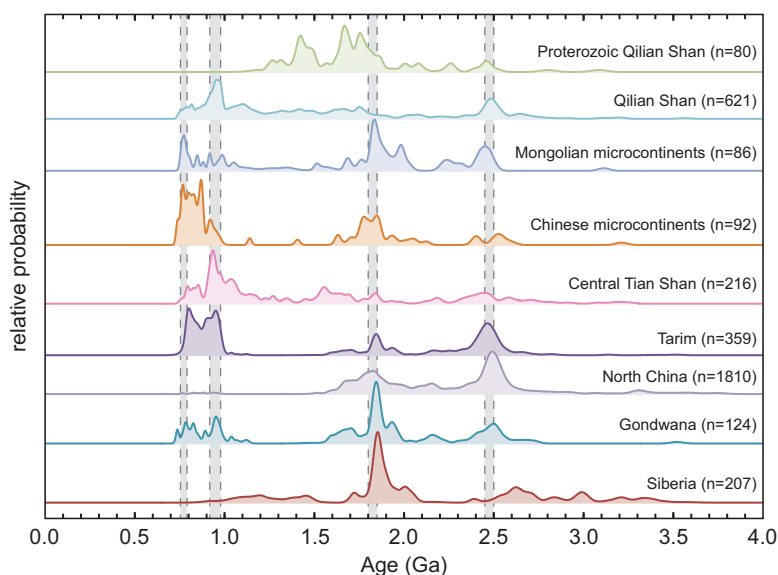
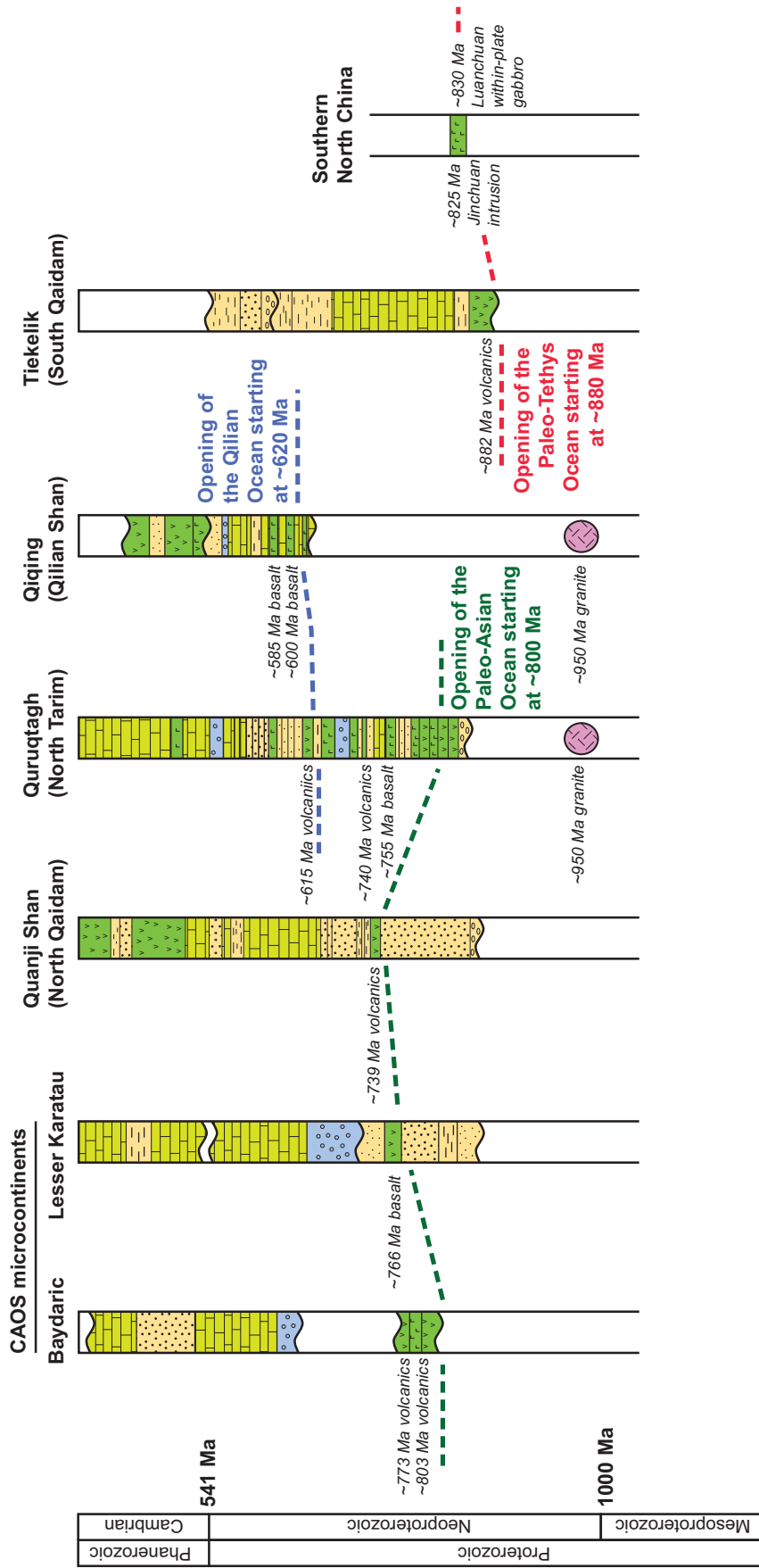


Figure 6.3. Complete caption on following page.

**Figure 6.3 (continued).** Tectonic correlation chart displaying major tectonic events along the northern (N) and southern (S) margins of the constituent cratons of Balkatach. Inset shows approximate closure time of the Paleo-Asian and Tethyan Oceans, to the north and south of Balkatach respectively, which are based on the earliest collisional ages observed in the geologic record. Abbreviations: AKM--Anyimaqen-Kunlun-Muztagh, CAOS--Central Asian Orogenic System, E-Q--Erlangping-Qinling arc, Eo-C--Eo-Cimmerian, Q-D--Qinling-Dabie Shan orogen, Q-Q-K--Qilian-Qaidam-Kunlun, and SJY--Solonker-Jilin-Yanji. Sources are discussed in text.



**Figure 6.4.** Normalized probability plot of zircon ages older than 775 Ma from the Qilian Shan, Mongolian and Chinese microcontinents, Tarim, North China, northeast Gondwana, and southern Siberia. U-Pb ages were used for zircons younger than 1000 Ma and Pb-Pb ages were used for older zircons. Grey shaded zones denote prominent age peaks around 790-760 Ma, 970-910 Ma, 1850-1800 Ma, and 2500-2450 Ma, which correspond to widespread tectonic events as discussed in the text. Chinese microcontinent ages from Han et al. (2011) and Mongolian microcontinent data from Rojas-Agramonte et al. (2011). Qilian Shan data is a compilation of our own unpublished work and Xu et al. (2010). Tarim, North China, and southern Siberia data compiled by Rojas-Agramonte et al. (2011). Northeast Gondwana data compiled by Squire et al. (2006).



**Figure 6.5.** Neoproterozoic tectonostatigraphic sections for key locations along the margins of Baltica showing the opening of the Paleo-Tethys, Paleo-Asian, and Qilian Oceans. Sections from the CAOS microcontinents, Tarim, the Qilian Shan, North Qaidam, and southern North China. Stratigraphy was compiled from Gehrels et al. (2003b), Li et al. (2005), Xu et al. (2009), Wang et al. (2011b), Levashova et al. (2010, 2011), Shu et al. (2011), Xu et al. (2013), Xu et al. (2015), and Wang et al., (2015a, 2015b).



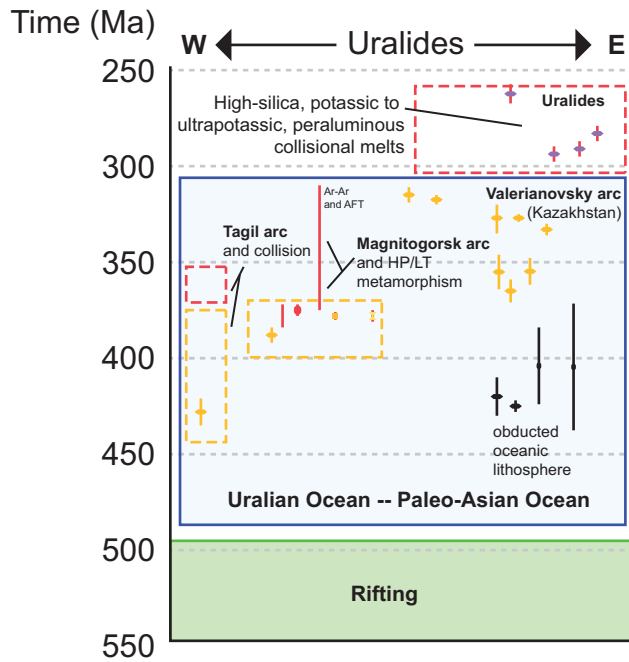


**Figure 6.6.** Timing of major Paleozoic events relative to west-east position in the Urals, based on geochronology, thermochronology, and sedimentological studies. Dashed boxes are timing constraints from the sedimentary record. Primary data sources include Bea et al. (1997, 2002), Fershtater et al. (1997, 2007), Savelieva et al. (2002), and Fershtater (2013).

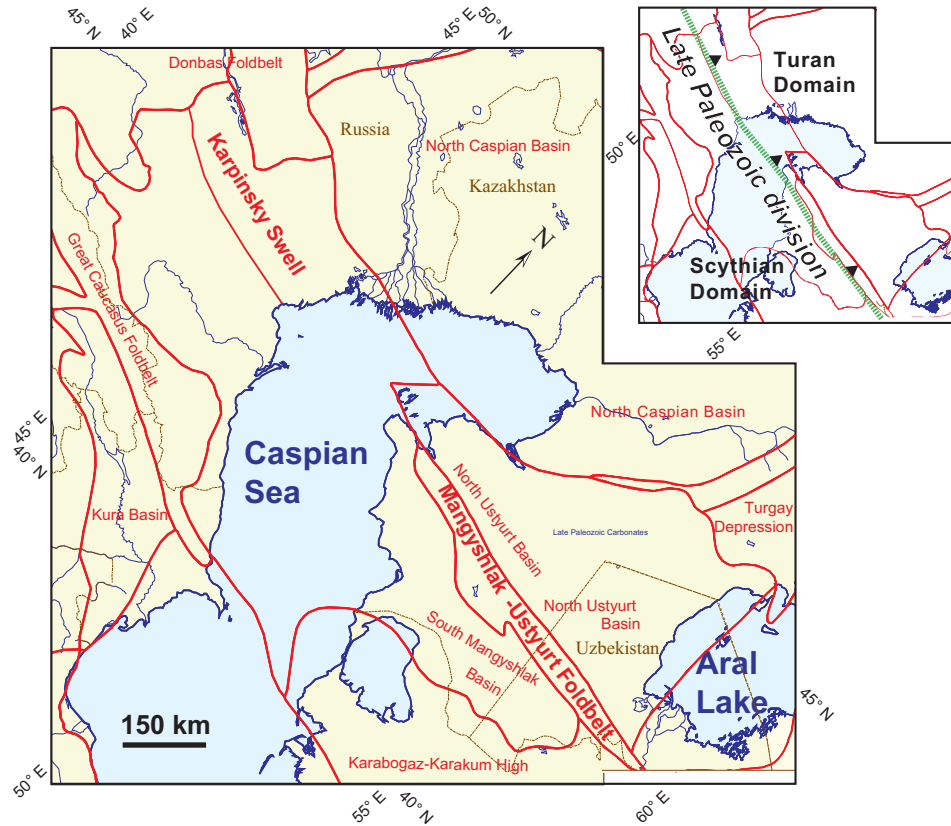


**Figure 6.7.** Tectonic units of the Caspian Sea region. Red lines are major tectonic boundaries. Inset shows simplified tectonic map with inferred division between the Scythian and Turan domains, outboard of the Karpinsky Swell and Mangyshlak-Ustyurt foldbelt. Modified from Ulmishek (2001a, 2001b).

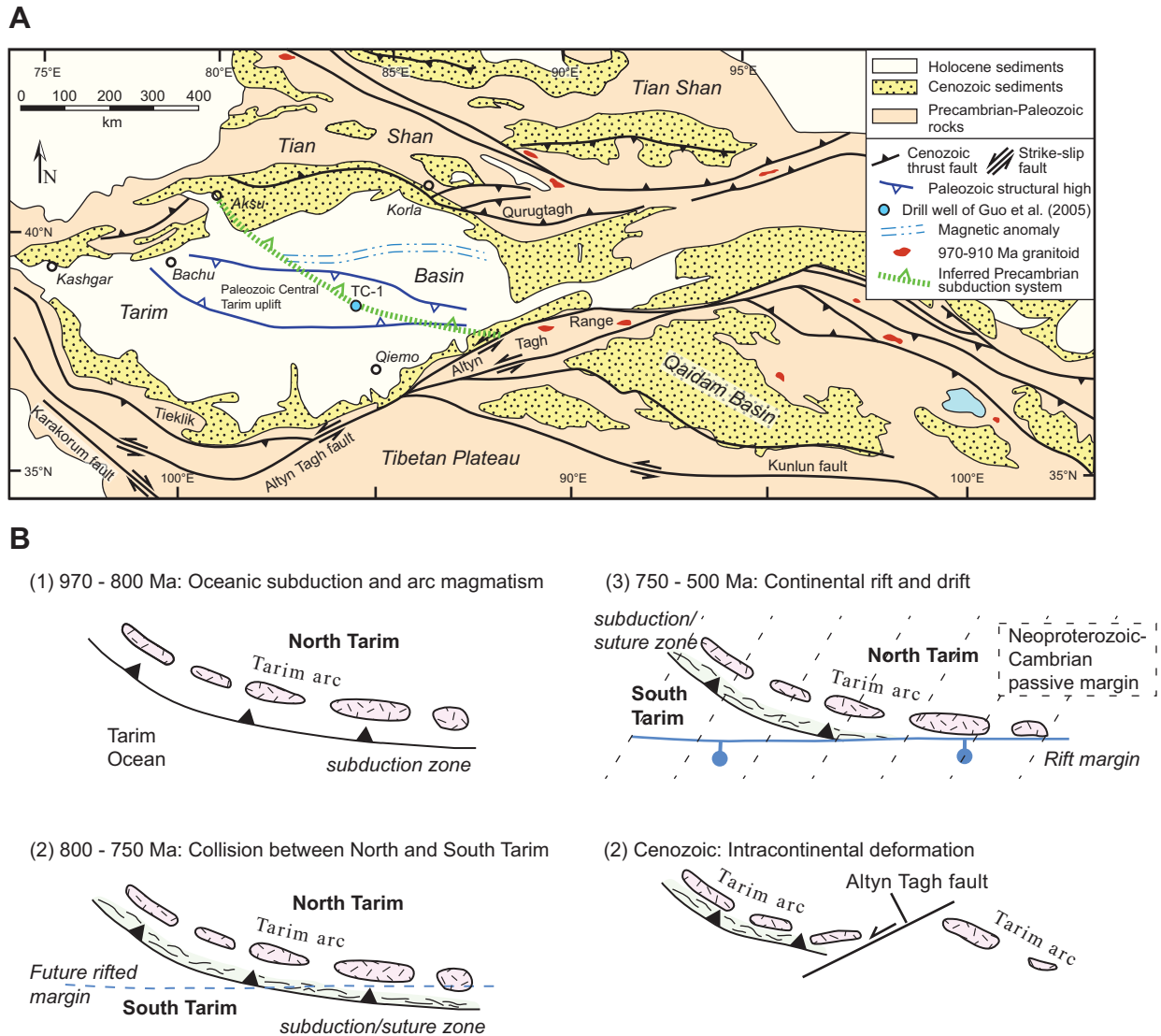


**Figure 6.8.** (A) Simplified tectonic map of the Tarim Basin, Qaidam Basin, Qilian Shan, and surrounding areas (after Guo et al., 2005). Also shown is the inferred Precambrian subduction system of Guo et al. (2005) and the location of Central Tarim Geologic Survey Well (TC-1). Note the truncated magnetic anomaly and locations of reported 970-910 Ma granitoids (Cowgill et al., 2003; Gehrels et al., 2003a; Wu et al., 2016; Chapter 5). (B) Tectonic evolution of the central Tarim basin and its surrounding regions as proposed by Guo et al. (2005): (1) Northward subduction under North Tarim formed the Precambrian Tarim arc, which led to the formation of 970-910 Ma granitoids and a blueschist belt along the subduction zone; (2) closure of the interlying ocean basin led to a collision between North and South Tarim; (3) Neoproterozoic rifting and continental breakup was followed by the deposition of passive continental margin sequences over Tarim and surrounding regions; and (4) most recent Cenozoic deformation further modified the geometry of inferred Precambrian arc.

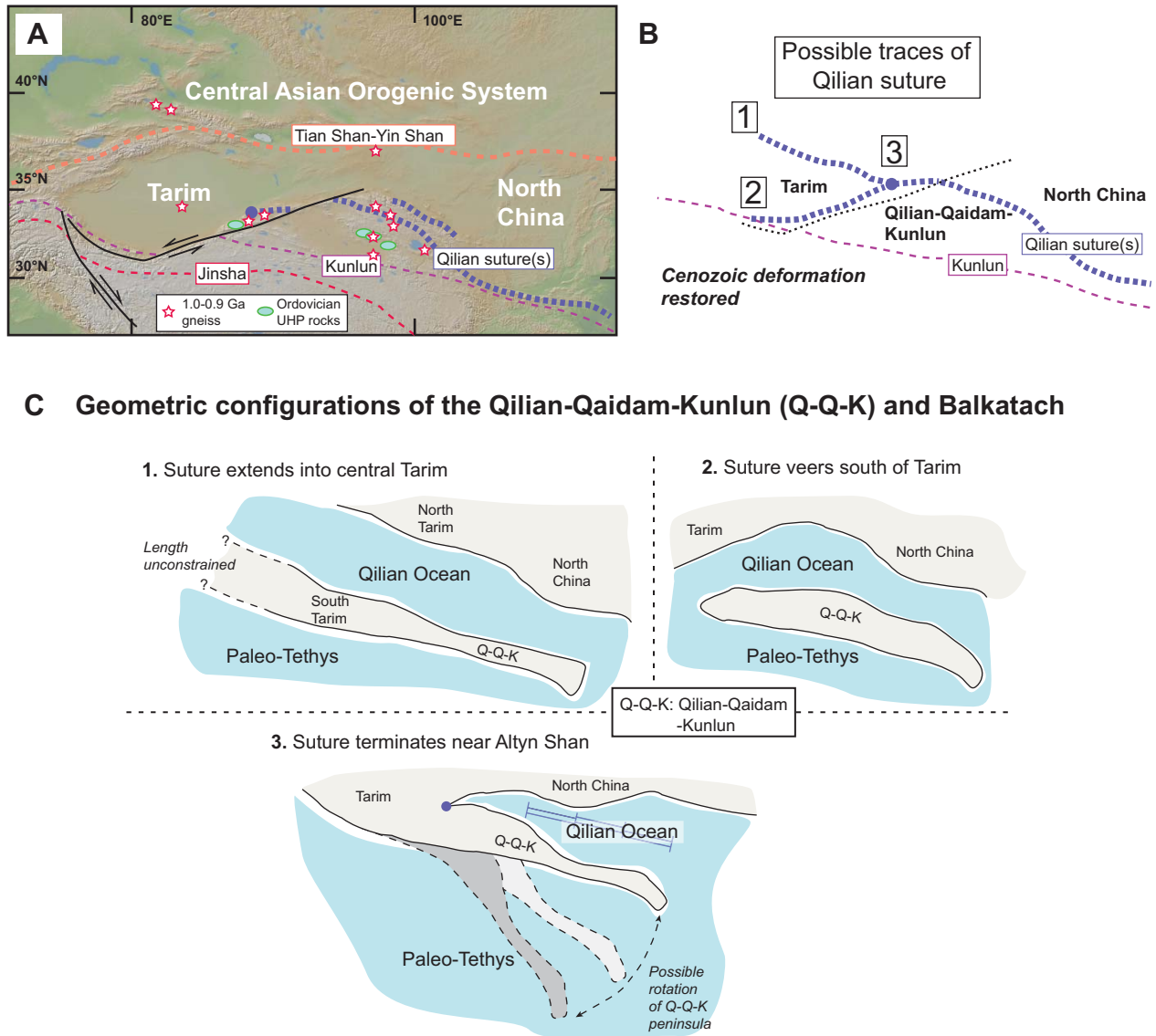


**Figure 6.9.** (A) Present-day configuration of the Jinsha, Kunlun, Qilian, and Tian Shan-Yin Shan suture zones, from south to north respectively. Note that the Qilian suture is offset by the Altyn Tagh fault. (B) Restored position of the Kunlun and Qilian sutures, after the removal of the effects of Cenozoic shortening and offset along the left-slip Altyn Tagh fault. (C) Three possible geometric configurations of the Qilian-Qaidam-Kunlun (Q-Q-K) continent and Balkatch given the restored surface trace of the Qilian suture as shown in Figure 6.9B.

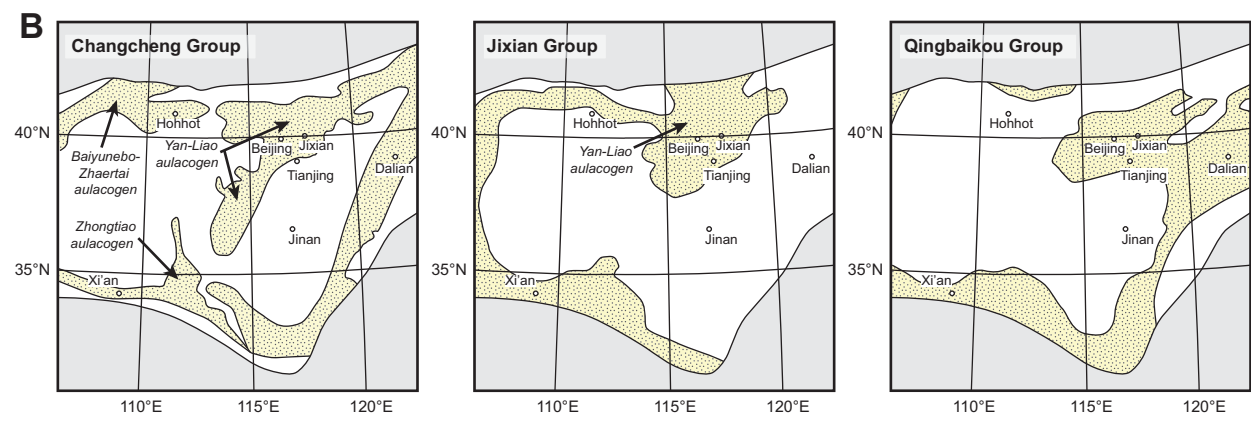
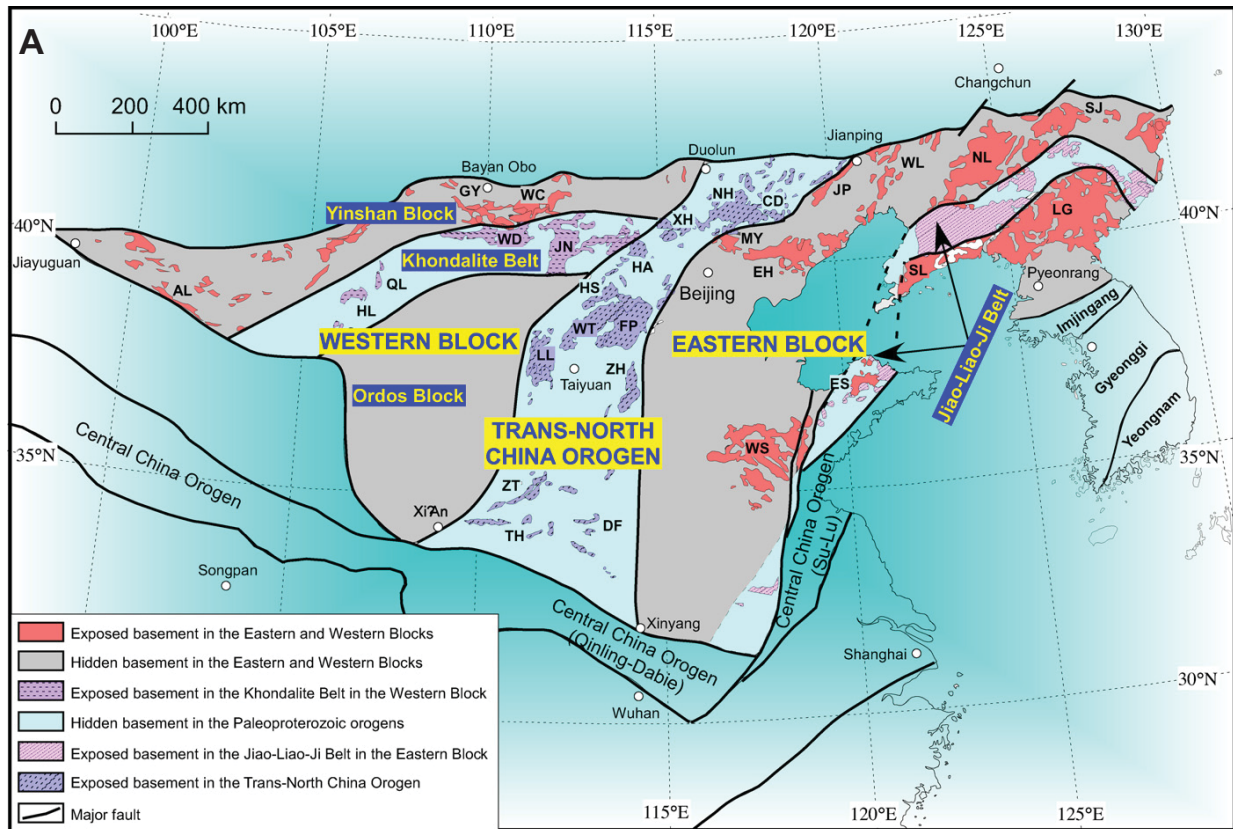


**Figure 6.10.** (A) Tectonic domains of the North China craton. Abbreviated metamorphic complexes: CD—Chengde; DF—Dengfeng; EH—Eastern Hebei; ES—Eastern Shandong; FP—Fuping; GY—Guyang; HA—Huai’an; HL—Helanshan; HS—Hengshan; JN—Jining; LG—Langrim; LL—Lüliang; MY—Miyun; NH—Northern Hebei; NL—Northern Liaoning; QL—Qianlishan; SJ—Southern Jilin; SL—Southern Liaoning; TH—Taihua; WD—Wulashan-Daqingshan; WL—Western Liaoning; WS—Western Shandong; WT—Wutai; XH—Xuanhua; ZH—Zanhuang; and ZT—Zhongtiao. From Zhao et al. (2005, 2012). (B) Sketch maps showing the distribution of the Proterozoic Changcheng, Jixian, and Qingbaikou Groups within the North China craton. There are no significant Sinan deposits in North China. Compiled from Wang et al. (1985), Lu et al. (2002), Wan et al. (2003b), and Meng et al. (2011). Note that intracontinental deformation and other later tectonic modification have not been restored in neither (A) nor (B).

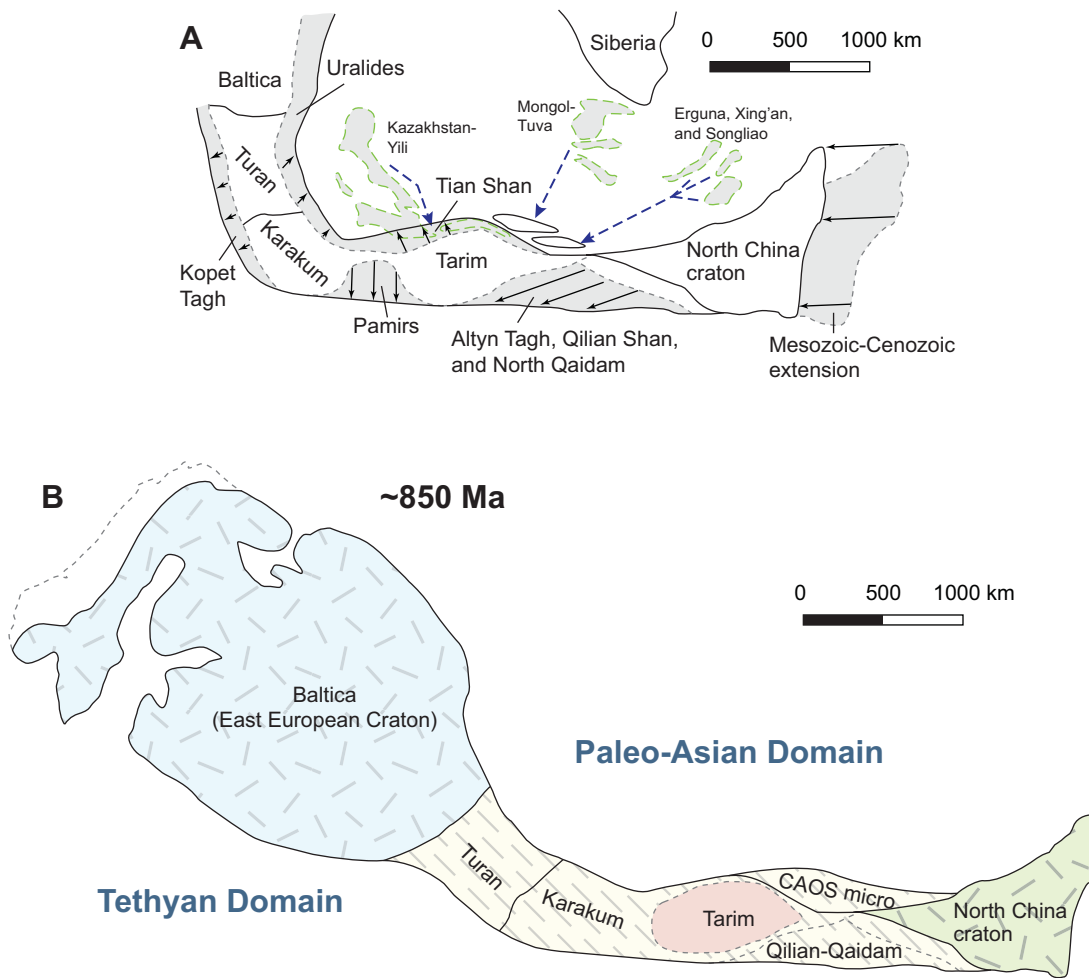


**Figure 6.11.** Schematic restoration of Balkatach based on the geologic map of Asia of Ren et al. (2013). (A) Mesozoic and Cenozoic deformation are restored. Note that the Kazakhstan-Yili microcontinents are reconstructed within the restored Tian Shan thrust belt. (B) Paleogeographic reconstruction of a continuous Balkatach continent in the Neoproterozoic. CAOS micro—Central Asian Orogenic System microcontinent.

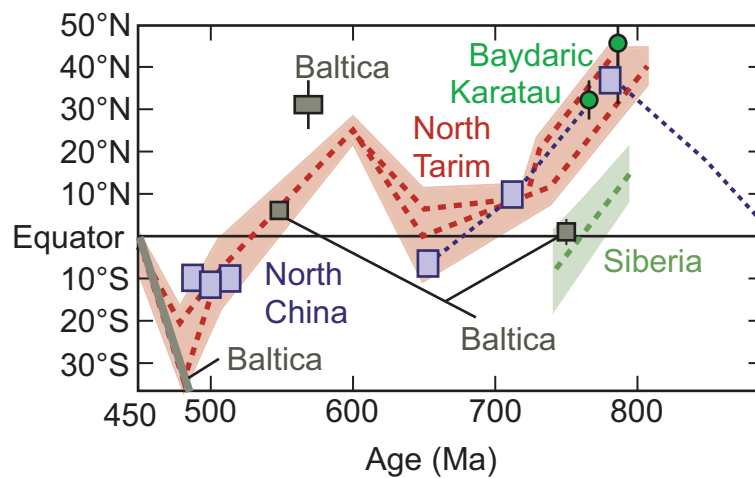


**Figure 6.12.** Paleomagnetically determined paleolatitude versus age for North China, Tarim, and, Baltica, and Siberia. Also shown are two CAOS microcontinents: Baydaric and Lesser Karatau. Note that the hemisphere polarity is ambiguous. Error bars or envelopes are shown, except when not provided or when the error is smaller than the symbol used. Age error in all studies is indiscernible in this figure. See Table 6.2 for sources used in this compilation.

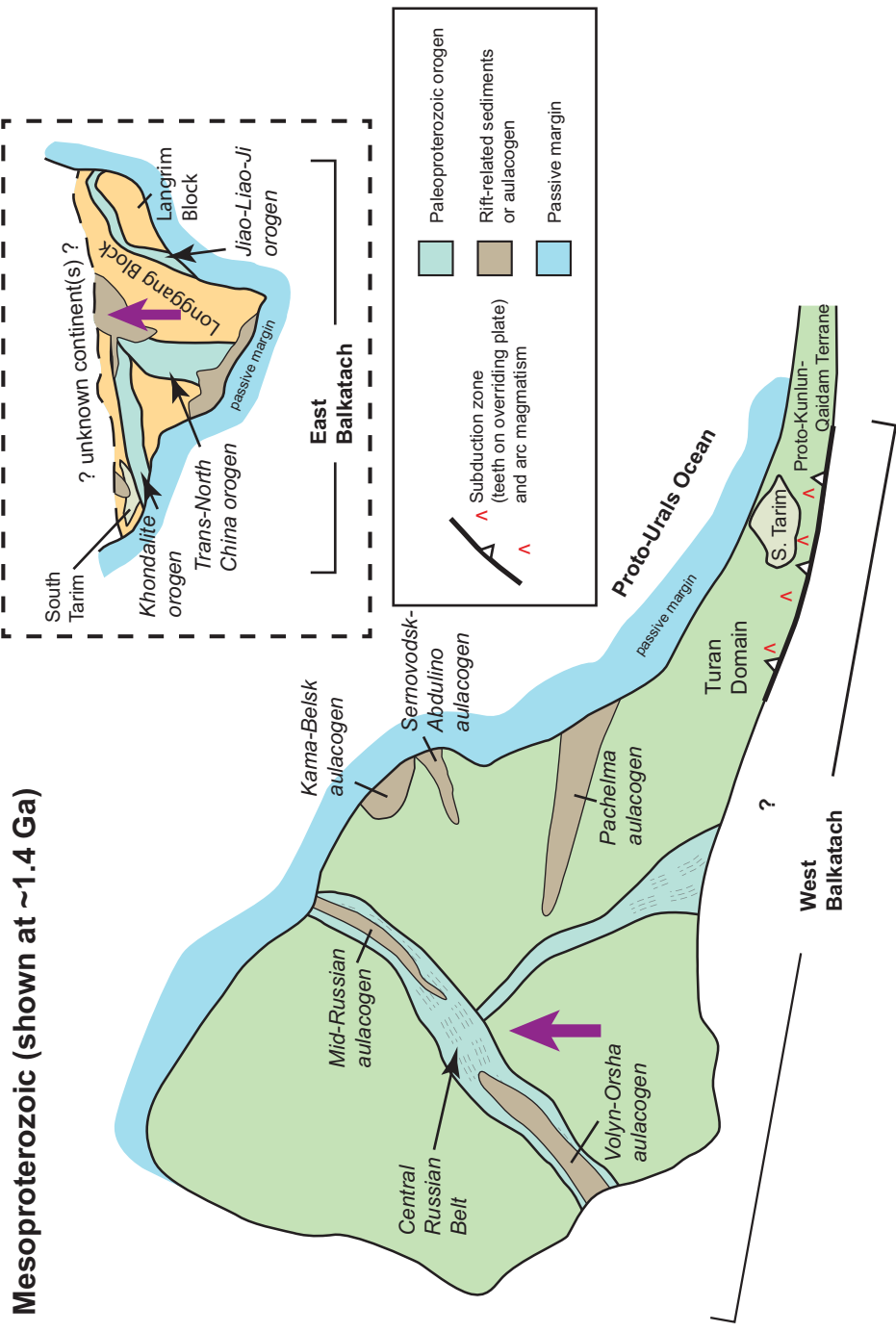


**Figure 6.13.** Paleoproterozoic configuration of the Western and Eastern Domains of the proposed Balkatach continent. For reference, purple arrow points to the north, in present-day coordinates, of each continent. Note that although the Paleoproterozoic orogens are drawn on each continent as linear belts, they may actually involve more widely distributed deformation throughout each continent. Also note that I infer that deformation associated with the Khondalite orogen in North China extends to North Tarim (e.g., Santosh et al., 2006, 2007; Ge et al., 2015).



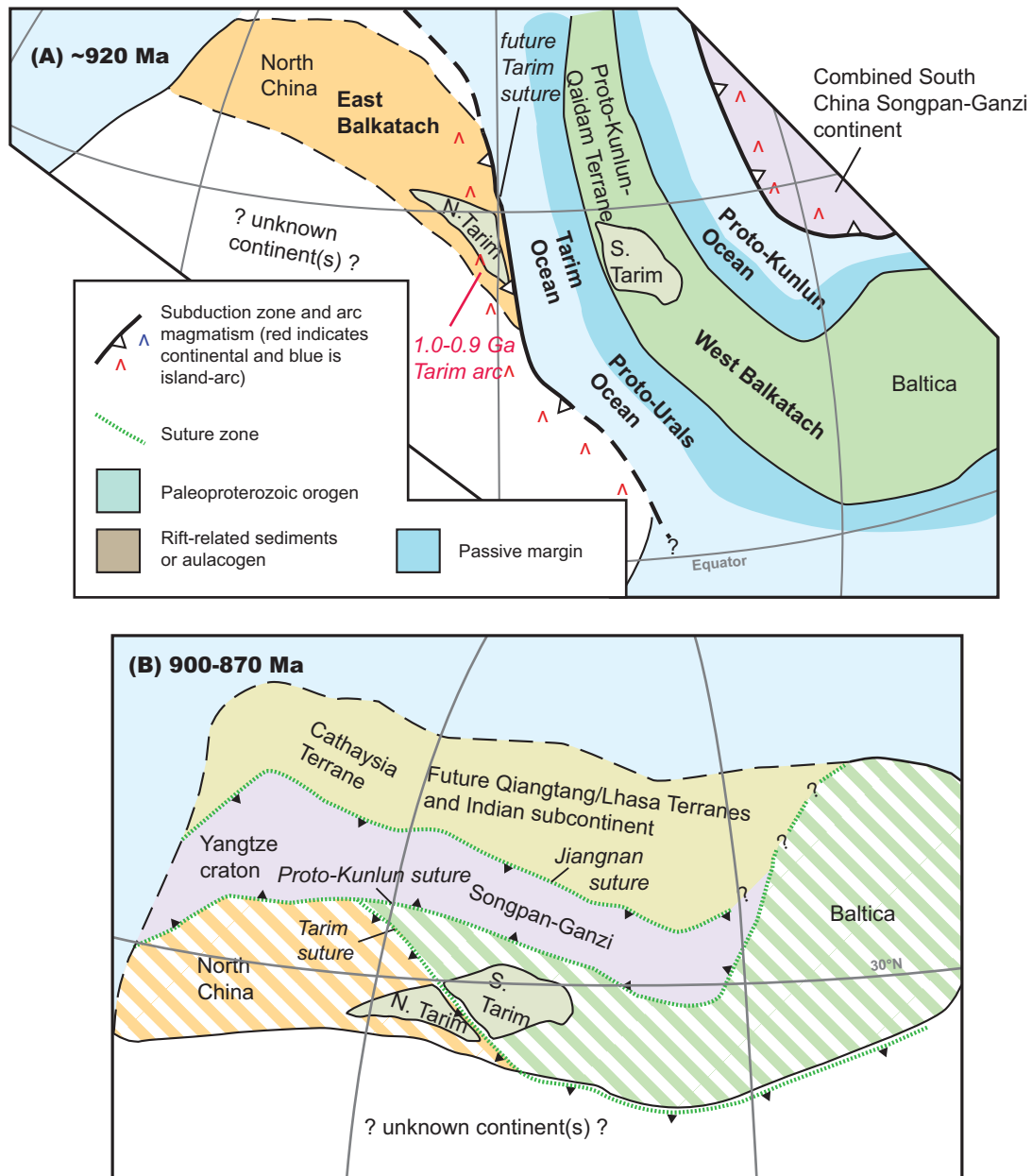


**Figure 6.14.** Neoproterozoic-Early Cambrian tectonic evolution of Balkatach. (A) Convergence of Eastern and Western Balkatach is accommodated by the ~1.0-0.9 Ga Tarim arc. Eastern Balkatach is connected to an unknown continent to the southwest during this time. The combined South China-Songpan-Ganzi continent approaches the northern margin of Balkatach (Wu et al., 2016). 3D globe projection and latitude/longitude lines are in 30° intervals.

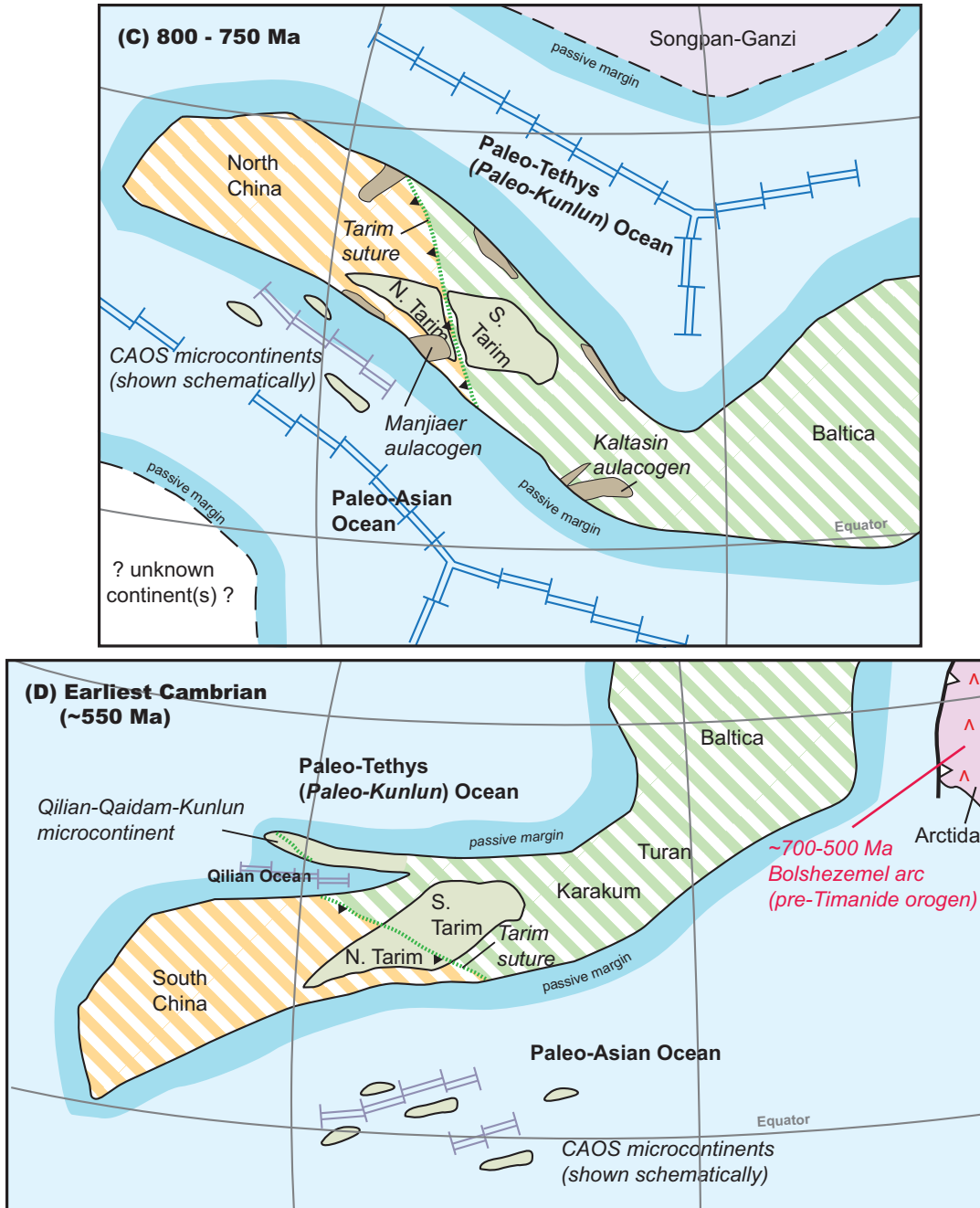


**Figure 6.14 (continued).** (B) By ~870 Ma, the Balkatach continent reaches its maximum extent. The future Qiangtang, Lhasa, and Indian subcontinent terranes are affixes along the northern margin of the Songpan-Ganzi terrane (Wu et al., 2016). (C) Rifting along the southwestern and northeastern margins of the Baltatach continent leads to the opening of the Paleo-Asian and Paleo-Tethys Oceans respectively. The CAOS microcontinents are dispersed throughout the Paleo-Asian Ocean. (D) Late-stage rifting causes the Qilian-Qaidam-Kunlun microcontinent to separate from the North China-Tarim, causing the peninsular opening of the Qilian Ocean in the late Neoproterozoic-early Cambrian. The Bolshezemel arc accommodates the convergence of the Arctida continent with the eastern margin of Baltatach (Kuznetsov et al., 2010). 3D globe projection and latitude/longitude lines are in 30° intervals.

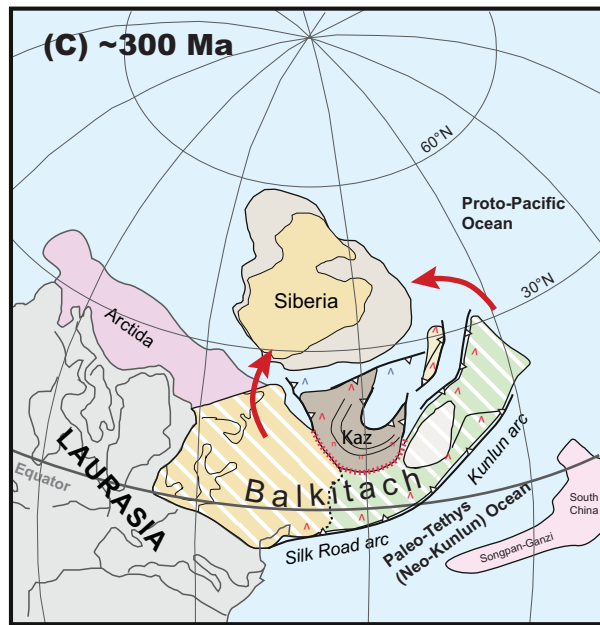
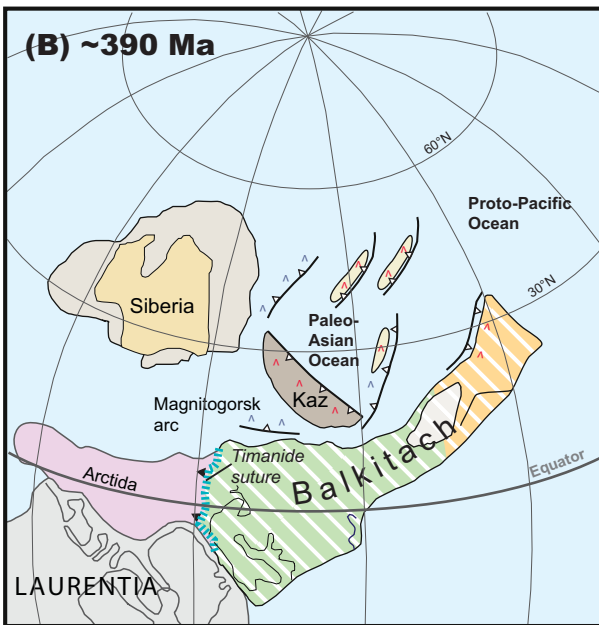
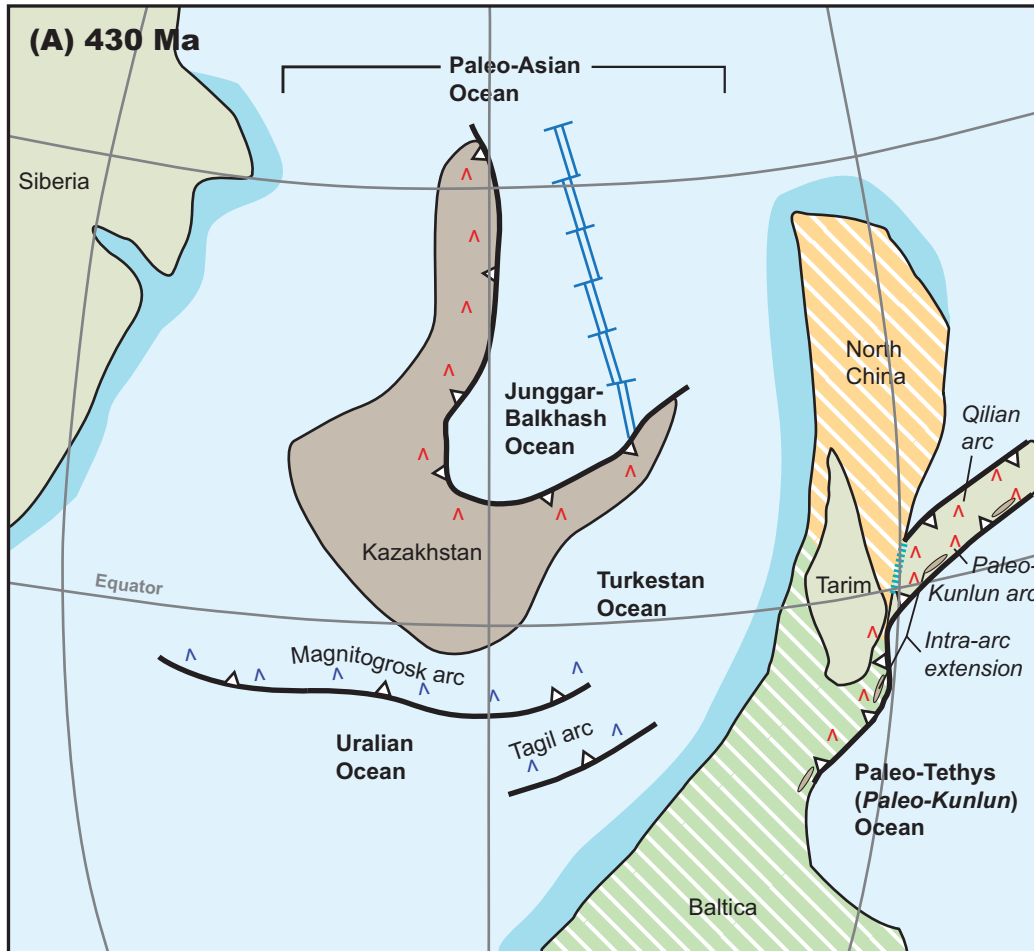
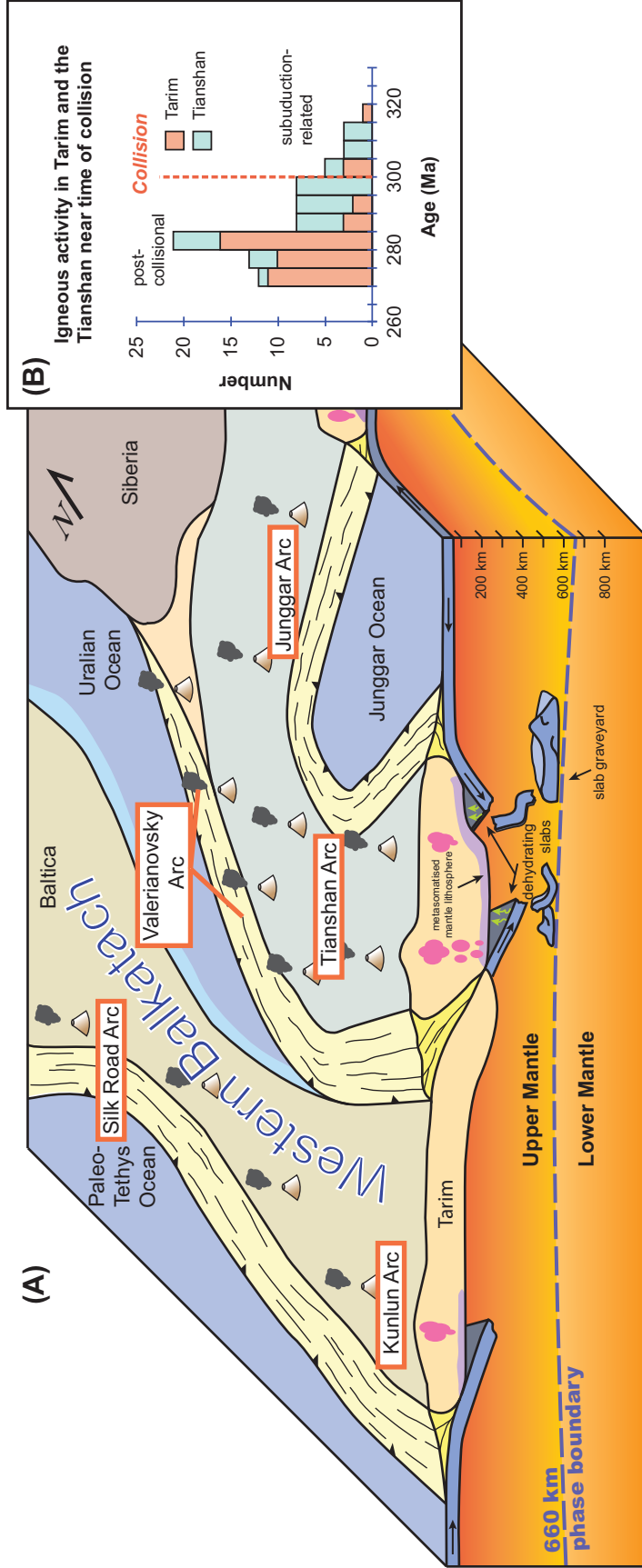


Figure 6.15. Full caption on following page.

**Figure 6.15 (continued).** Paleozoic tectonic evolution of Balkatach and the Paleo-Asian Ocean domain. (A) Subduction of the Paleo-Asian Ocean within the Central Asian Orogenic System causes Balkatach to wrap around the Paleo-Asian ocean. (B) Continued closure of the Paleo-Asian Ocean accommodates Balktach's convergence with the Kazakhstan microcontinent conglomeration. (C) Collision between Balkatach and Kazakhstan in. This figure is modified from Philippova et al. (2001), Abrajevitch et al. (2008), and Xiao and Santosh (2014). 3D globe projection and latitude/longitude lines are in 30° intervals.



**Figure 6.16.** The Kazakhstan orocline and the destruction of the Paleo-Asian Ocean. The large volume of subducted slabs may have collected near the 660-km phase transition, and their eventual sinking across this boundary triggered significant asthenospheric upwelling and the observed Permian magmatic flareup (e.g., Cina, 2011). (B) Histogram of observed granitoid ages in the Tian Shan and Tarim regions, in the area depicted in (A) (modified after Biske and Seltmann, 2010; Xiao et al., 2013). Note the large amount of igneous activity following the closure of the Paleo-Asian Ocean. Data sources include Mikolaichuk et al. (1997), Kiselev (1999), Zhang et al. (2007), Konopelko et al. (2008), Apayarov (2010), Glorie et al. (2010), Tian et al. (2010), Yu et al. (2010), Zhang et al., (2010), Qin et al. (2011), Seltmann et al. (2011), Zhang et al., (2012), and Zhang et al. (2013).

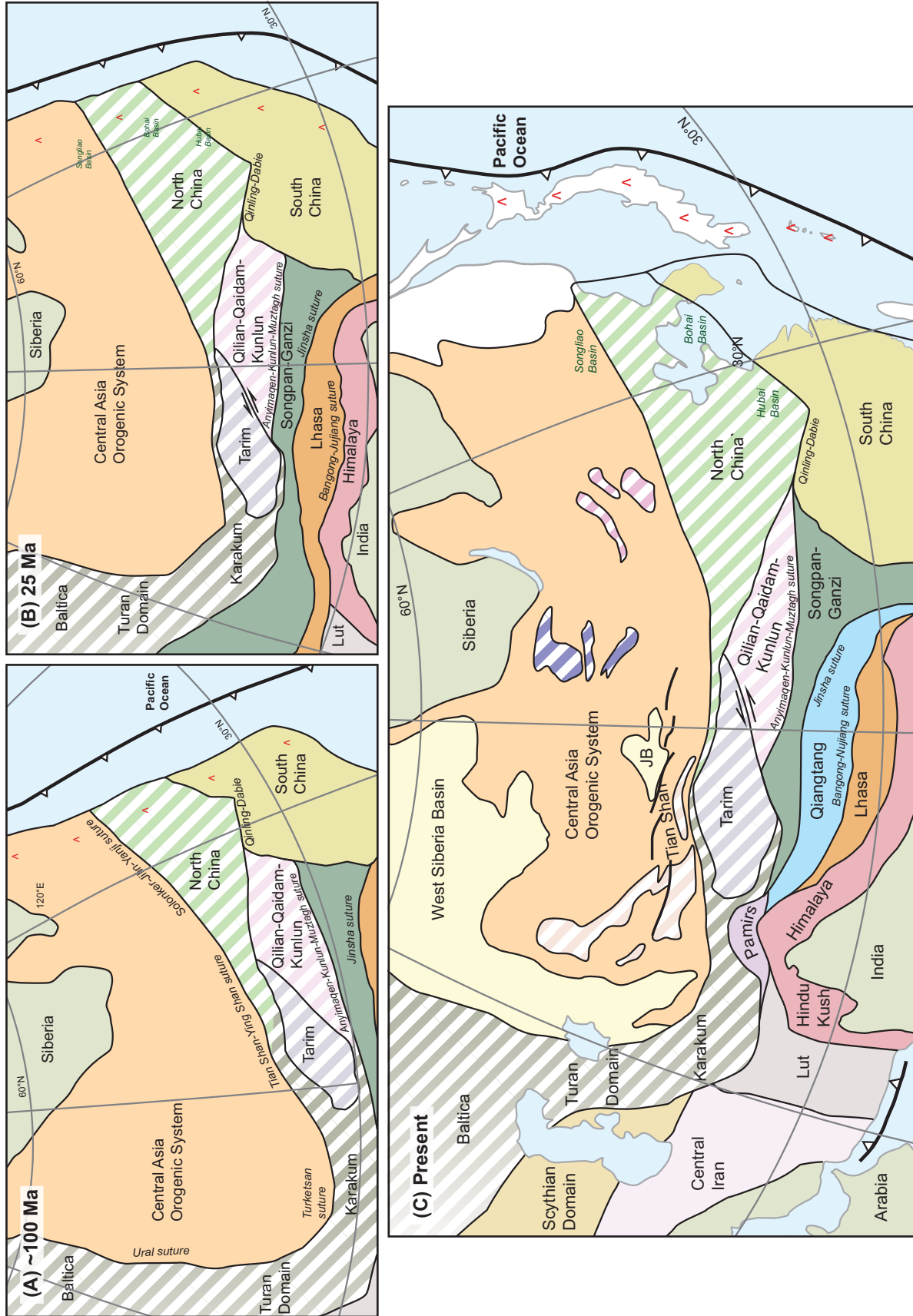


Figure 6.17. Full figure caption on following page.

**Figure 6.17.** (A) Middle Cretaceous and (B, C) Cenozoic evolution of Central Asia as restored in this reconstruction. Note that the colors of the tectonic units are changed from Figures 6.13-6.15 to match those in Figure 6.2. 3D globe projection and latitude/longitude lines are in 30° intervals. Proposed Balkatach continent is shown with white stripes.

**Table 6.1. Proterozoic timescale commonly used in the Chinese literature following Chinese Geological Survey (2014)**

| Eon              | Era             | Period (Chinese) | Subd.             | Approximate GTS2012 Period | Age (Ma)   |      |
|------------------|-----------------|------------------|-------------------|----------------------------|------------|------|
| Proterozoic      | Neoproterozoic  | Sinian           |                   |                            |            |      |
|                  |                 |                  | Upper Nanhua      | ~Ediacaran                 | 635        |      |
|                  |                 |                  | Middle Nanhua     | ~Cryogenian                | 660        |      |
|                  |                 |                  | Lower Nanhua      | ~Tonian                    | 725        |      |
|                  |                 |                  |                   |                            | 780        |      |
|                  | Mesoproterozoic |                  | Qingbaikou        |                            | ~Stenian   |      |
|                  |                 |                  | Currently unnamed |                            | ~Ectasian  | 1000 |
|                  |                 |                  | Jixian            |                            | Calymmian  | 1400 |
|                  |                 |                  | Changcheng        |                            | Statherian | 1600 |
|                  |                 |                  |                   |                            | 1800       |      |
| Paleoproterozoic |                 |                  |                   | 2500                       |            |      |



**Table 6.2. Selected paleomagnetic poles and paleolatitudes for Central Asian continents.**

| Rock unit                          | Age (Ma)   | Pole  |       | $A_{95}$ (°) | Paleolatitude (°) | Reference               |
|------------------------------------|------------|-------|-------|--------------|-------------------|-------------------------|
|                                    |            | (°N)  | (°E)  |              |                   |                         |
| <b><i>North China</i></b>          |            |       |       |              |                   |                         |
| Fengfeng/Pingliang Formations      | 480        | 37.4  | 324.3 | 8.5          | -10               | Huang et al. (1999)     |
| Changshan/Gushan Formations        | 500        | 31.7  | 329.6 | 5.1          | -13               | Huang et al. (1999)     |
| Zhangxia/ Xuzhuang Formations      | 520        | 37.0  | 326.7 | 5.5          | -10               | Huang et al. (1999)     |
| Dongjia Formation                  | 650        | -60.8 | 97.4  | 6.7          | 10                | Zhang et al. (2006)     |
| Huaibi Group                       | 700        | -42.9 | 107.0 | 5.7          | 8                 | Zhang et al. (2006)     |
| Nanfen Formation                   | 800 to 780 | -16.5 | 121.1 | 11.1         | 35                | Zhang et al. (2006)     |
| Wangshan Formation                 | 890        | 52.6  | 330.0 | 5.3          | 0 to 5            | Fu et al. (2015)        |
| Jingeryu Formation                 | 950        | -41.0 | 44.8  | 11.3         | 10                | Zhang et al. (2006)     |
| <b><i>North Tarim</i></b>          |            |       |       |              |                   |                         |
| Sugetbrak/Chigebrek Formations     | 600        | 19.1  | 149.7 | 9.3          | 27                | Zhang et al. (2007)     |
| Qiaoenbrak Formation               | 730        | 30.4  | 246.1 | 11.0         | 6.3 ± 39          | Wen et al. (2013)       |
| Baiyixi Formation                  | 740        | 17    | 194   | 4            | 6                 | Huang et al. (2005)     |
| Wushi Formation                    | 800 to 590 | -55   | 53    | 7.9          | 8 ± 6             | Li et al. (1991)        |
| Aksu dikes                         | 807 ± 12   | 19    | 128   | 6            | 43                | Chen et al. (2004)      |
| <b><i>CAOS microcontinents</i></b> |            |       |       |              |                   |                         |
| Baydaric                           | 805 to 770 | -     | -     | -            | 47 ± 14           | Levashova et al. (2010) |
| Karatau                            | 766 ± 7    | -     | -     | -            | 34.2 ± 5.3        | Levashova et al. (2011) |
| <b><i>Siberia</i></b>              |            |       |       |              |                   |                         |
| Karagas Series                     | 850-740    | -12   | 97    | 10           | 22 to 8           | Metelkin et al. (2005)  |
| Nersinsky Complex                  | 740        | -37   | 122   | 11           | 2 to -19          | Metelkin et al. (2005)  |
| <b><i>Baltica</i></b>              |            |       |       |              |                   |                         |
| Zigan Formation                    | 550        | -15.4 | 107.7 | 4.3          | 7.8 ± 2.5         | Levashova et al. (2013) |
| Average*                           | 560 to 550 | -     | -     | -            | 30-40             | From Meert (2014)       |
| Kildinskaya Formation              | 750        | -26   | 13    | 7.2          | ~0                | Torsvik et al. (1995)   |

\*Average paleolatitude from numerous datasets.

## 6.9. References

- Abdullin, A.A., Avdeev, A.B. and Seitov, N.S., 1977, Tectonics of the Sakmara and Or-Ilek Zones in Mugodjars: Almaty, Nauka, 241 p. (in Russian).
- Aktanov, V.I., Dorinna, N.A., Posokhov, V.F., Sklyarov, E.B., and Skopintsev, 1992, On the age and structure of the Gargan massif (south eastern Sayan) - Conference on structural analysis of crystalline complex: Abstract, Irkutsk, p. 89-90 (in Russian).
- Alavi, M., 1991, Sedimentary and structural characteristics of the Paleo-Tethys remnants in northeastern Iran: Geological Society of America Bulletin, v. 103, no. 8, p. 983-992.
- Alexeiev, D.V., Cook, H.E., Mikolaichuk, A.V. and Djenchuraeva, A.V., 2000, Upper Devonian through Lower Permian carbonates in the Middle Tian-Shan of Kyrgyzstan: new data on the evolution of passive margin carbonate platforms of the Kazakhstania paleocontinent, *in* Permo-Carboniferous Carbonate Platforms and Reefs, SEPM/IAS Convention, El Paso, TX, Program and Abstracts, v. 19.
- Allegre, C. et al., 1984, Structure and evolution of the Himalaya-Tibet orogenic belt: Nature, v. 207, p. 17-22.
- Allen, P.A., and Etienne, J.L., 2008, Sedimentary challenge to snowball Earth: Nature, v. 1, no. 12, p. 817-825.
- Andersson, U.B., Sjostrom, H., Hogdahl, K., and Eklund, O., 2004, The Transscandinavian igneous belt, evolutionary models: Special Paper-Geological Survey of Finland, v. 37, no. 104.
- Argand, E., 1924, La tectonique de l'Asie, *in* Congrès Géologique International, Comptes Rendus de la XII<sup>e</sup> Session: Liege, Vaillant-Carmanne.
- Artyushkov, E.V., and Baer, M.A., 1983, Mechanism of continental crust subsidence in fold belts: the Urals, Appalachians and Scandinavian Caledonides: Tectonophysics, v. 100, no. 1-3, p. 5-42.
- Avdeev, A.V., 1984, Ophiolite zones and geological history of the Kazakhstan territory: a mobilistic approach: Sovetskaya Geology, p. 63-72 (in Russian).
- Avouac, J.P., Tapponnier, P., Bai, M., You, H., and Wang, G., 1993, Active thrusting and folding along the northern Tien Shan and late Cenozoic rotation of the Tarim relative to Dzungaria and Kazakhstan: Journal of Geophysical Research: Solid Earth, v. 98, no. B4, p. 6755-6804.
- Badarch, G., Cunningham, W.D., and Windley, B.F., 2002, A new terrane subdivision for Mongolia: implications for the Phanerozoic crustal growth of Central Asia: Journal of Asian Earth Sciences, v. 21, no. 1, p. 87-110.

- Bakirov, A. B., and Maksumova, R. A., 2001, Geodynamic evolution of the Tien Shan lithosphere: *Russian Geology and Geophysics*, v. 42, no. 10, p. 1359-1366.
- Balgord, E., Yonkee, W., Link, P.K., and Fanning, C.M., 2013, Stratigraphic, geochronologic, and geochemical record of the Cryogenian Perry Canyon Formation, northern Utah: Implications for Rodinia rifting and snowball Earth: *Geological Society of America Bulletin*, v. 125, no. 9-10, p. 1442-1467.
- Baraboshkin, E.Y., Alekseev, A.S., and Kopaeovich, L.F., 2003, Cretaceous palaeogeography of the north-eastern Peri-Tethys: *Palaeogeography, Palaeoclimatology, Palaeoecology*, v. 196, no. 1, p. 177-208.
- Baratov, R.B., Lutkov, V.S., Minaev, V.E., Starshinin, D.A., Fedorov, G.B., 1983, Volcanism and lithosphere composition of the Katarmai-Jagnobsky glaucophane-greenschist belt (South Tianshan) *Dok: Akad. Nauk SSSR* v. 273, p. 958-964, (in Russian).
- Bea, F., Fershtater, G., Montero, P., Smirnov, V., and Zin'kova, E., 1997, Generation and evolution of subduction-related batholiths from the central Urals: constraints on the PT history of the Uralian orogen: *Tectonophysics*, v. 276, no. 1, p. 103-116.
- Bea, F., Fershtater, G. B., and Montero, P., 2002, Granitoids of the Uralides: implications for the evolution of the orogen. *Mountain Building in the Uralides: Pangea to the Present*, p. 211-232.
- Belov, A.A., 1981, Tectonic Development of the Alpine Fold Area in the Paleozoic: Moscow, USSR (in Russian).
- Biske, Y.S., 1996, Paleozoic Structure and History of Southern Tian-Shan: Leningrad University, Leningrad, 187 p.
- Biske, Y.S., and Seltmann, R., 2010, Paleozoic Tian-Shan as a transitional region between the Rheic and Urals-Turkestan oceans: *Gondwana Research*, v. 17, p. 602-613.
- Bodine, J. H., Steckler, M. S., and Watts, A. B., 1981, Observations of flexure and the rheology of the oceanic lithosphere: *Journal of Geophysical Research: Solid Earth*, v. 86, no. B5, p. 3695-3707.
- Bogdanova, S. et al., 2006, EUROBRIDGE: new insight into the geodynamic evolution of the East European Craton: *Geological Society, London, Memoirs*, v. 32, no. 1, p. 599-625.
- Bogdanova, S.V., Bingen, B., Gorbatshev, R., Kheraskova, T.N., Kozlov, V.I., Puchkov, V.N., and Volozh, Y.A., 2008, The East European Craton (Baltica) before and during the assembly of Rodinia: *Precambrian Research*, v. 160, no. 1, p. 23-45.
- Boyden, J.R., Müller, R.D., Gurnis, M., Torsvik, T.H., Clark, J., Turner, M., Ivey-Law, H., Watson, R., and Cannon, J., 2010, Next-generation plate tectonic reconstructions using GPlates, *in Geoinformatics*, eds, R. Keller and C. Baru: Cambridge, U.K., Cambridge University Press, p. 96-113.

- Briggs, S.M., Yin, A., Manning, C. E., Chen, Z.L., and Wang, X.F., 2009, Tectonic development of the southern Chinese Altai Range as determined by structural geology, thermobarometry,  $^{40}\text{Ar}/^{39}\text{Ar}$  thermochronology, and Th/Pb ion-microprobe monazite geochronology: Geological Society of America Bulletin, v. 121, no. 9-10, p. 1381-1393.
- Briggs, S.M., Yin, A., Manning, C.E., Chen, Z.L., Wang, X.F., and Grove, M., 2007, Late Paleozoic tectonic history of the Ertix Fault in the Chinese Altai and its implications for the development of the Central Asian Orogenic System: Geological Society of America Bulletin, v. 119, no. 7-8, p. 944-960.
- Brookfield, M.E., 2000, Geological development and Phanerozoic crustal accretion in the western segment of the southern Tien Shan (Kyrgyzstan, Uzbekistan and Tajikistan): Tectonophysics, v. 328, no. 1, p. 1-14.
- Brown, D., Alvarez-Marron, J., Perez-Estaun, A., Puchkov, V., and Ayala, C., 1999, Basement influence on foreland thrust and fold belt development: an example from the southern Urals: Tectonophysics, v. 308, no. 4, p. 459-472.
- Brown, D., Herrington, R.J., and Alvarez-Marron, J., 2011, Processes of Arc–Continent Collision in the Uralides, *in* Arc-Continent Collision: Berlin, Germany, Springer p. 311-340.
- Brown, D., Spadea, P., Puchkov, V., Alvarez-Marron, J., Herrington, R., Willner, A.P., Hetzel, R., Gorozhanina, Y., and Juhlin, C., 2006, Arc–continent collision in the Southern Urals: Earth-Science Reviews, v. 79, no. 3, p. 261-287.
- Brunet, M.F., Volozh, Y.A., Antipov, M.P., and Lobkovsky, L.I., 1999, The geodynamic evolution of the Precaspian Basin (Kazakhstan) along a north–south section: Tectonophysics, v. 313, no. 1, p. 85-106.
- Budanov, V.I., 1993, Metamagmatic complexes of the Garm block (Tianshan): Izvestia Akademia Nauk Respublica Tajikistanya. Otd. Nauk Zemle, v. 3, p. 32-49 (in Russian).
- Burchfiel, B.C. and Davis, G.A., 1972, Structural framework and evolution of the southern part of the Cordilleran orogen, western United States: American Journal of Science, v. 272, no. 2, p. 97-118.
- Burchfiel, B.C. et al., 1991, Geology of the Haiyuan fault zone, Ningxia-Hui Autonomous Region, China, and its relation to the evolution of the northeastern margin of the Tibetan Plateau: Tectonics, v. 10, no. 6, p. 1091-1110.
- Burke, K., Dewey, J.F., and Kidd, W.S.F., 1976, Precambrian paleomagnetic results compatible with contemporary operation of the Wilson cycle: Tectonophysics, v. 33, p. 287–299.
- Burtman, V.S., 1976, Structural evolution of Paleozoic fold systems: Nauka.
- Burtman, V.S., 2006, The Tien Shan Early Paleozoic tectonics and geodynamics: Russian Journal of Earth Sciences, v. 8, no. 3, p. 1-23.

- Burtman, V.S., and Molnar, P.H., 1993, Geological and geophysical evidence for deep subduction of continental crust beneath the Pamir: Boulder, Colorado, Geological Society of America Special Paper 281, 76 p.
- Burtman, V.S., Gurarii, G.Z., Dvorova, A.V., Kuznetsov, N.B., and Shipunov, S.V., 2000, The Uralian Paleoocean in the Devonian (as inferred from Paleomagnetic data): *Geotectonics*, v. 34, no. 5, p. 397-406.
- Carroll, A.R., Graham, S.A., Chang, E.Z., and McKnight, C., 2001, Sinian through Permian tectonostratigraphic evolution of the northwestern Tarim basin, China: *Memoirs-Geological Society of America*, p. 47-70.
- Carroll, A.R., Graham, S.A., Hendrix, M.S., Ying, D., and Zhou, D., 1995, Late Paleozoic tectonic amalgamation of northwestern China: sedimentary record of the northern Tarim, northwestern Turpan, and southern Junggar basins: *Geological Society of America Bulletin*, v. 107, no. 5, p. 571-594.
- Cawood, P.A., Kroner, A., and Pisarevsky, S., 2006, Precambrian plate tectonics: criteria and evidence: *GSA Today*, v. 16, no. 7.
- Chang, S.Q. (1980). Subdivision and correlation of late Precambrian of southern Liaodong Peninsula: Sinian Suberathem in China, Tianjin Science and Technology Press, Tianjin, p. 266-287.
- Charvet, J., Shu, L., Laurent-Charvet, S., Wang, B., Faure, M., Cluzel, D., Yan, C., and De Jong, K., 2011, Palaeozoic tectonic evolution of the Tianshan belt, NW China: *Science China Earth Sciences*, v. 54, p. 166-184.
- Charvet, J., Shu, L.S., and Laurent-Charvet, S., 2007. Paleozoic structural and geodynamic evolution of eastern Tianshan (NW China): welding of the Tarim and Junggar plates: *Episodes*, v. 30, p. 162–185.
- Chen, C.M., Lu, H.F., Jia, D., Cai, D.S., and Wu, S.M., 1999, Closing history of the southern Tianshan oceanic basin, western China: an oblique collisional orogeny: *Tectonophysics*, v. 302, p. 23–40.
- Chen, L., Huang, B., Yi, Z., Zhao, J., and Yan, Y., 2013, Paleomagnetism of ca. 1.35 Ga sills in northern North China Craton and implications for paleogeographic reconstruction of the Mesoproterozoic supercontinent: *Precambrian Research*, v. 228, p. 36-47.
- Chen, N.S., Zhang, L., Sun, M., Wang, Q., and Kusky, T.M. 2012, U–Pb and Hf isotopic compositions of detrital zircons from the paragneisses of the QuANJI Massif, NW China: implications for its early tectonic evolutionary history: *Journal of Asian Earth Sciences*, v. 54, p. 110-130.
- Chen, X.Y., Wang, Y.J., Sun, L.H., and Fan, W.M., 2009, Zircon SHRIMP U-Pb dating of the granitic gneisses from Bingdaban and Laerdundaban (Tianshan Orogen) and their

- geological significances: *Geochemica*, v. 38, no. 5, p. 424-431 (in Chinese with English abstract).
- Chen, Y., Xu, B., Zhan, S., and Li, Y., 2004, First mid-Neoproterozoic paleomagnetic results from the Tarim Basin (NW China) and their geodynamic implications: *Precambrian Research*, v. 133, no. 3, p. 271-281.
- Chen, Z., Lu, S., Li, H., Li, H., Xiang, Z., Zhou, H., and Song, B., 2006, Constraining the role of the Qinling orogen in the assembly and break-up of Rodinia: Tectonic implications for Neoproterozoic granite occurrences: *Journal of Asian Earth Sciences*, v. 28, no. 1, p. 99-115.
- Cheng J., Zhang, H., Xing, Y., and Ma, G., 1981, On the Upper Precambrian (Sinian Suberathem) in China: *Precambrian Research*, v. 15, p. 207-228.
- Chinese Geological Survey, 2014, *Geologic Time Units in China*: Geological Publishing House, Beijing.
- Chuvashov, B. I., and Crasquin-Soleau, S., 2000, Palaeogeography and palaeotectonic of the jointing area between the Eastern European Basin and the Tethys Basin during Late Carboniferous (Moscovian) and Early Permian (Asselian and Artinskian): *Mémoires du Muséum national d'histoire naturelle*, v. 182, p. 203-237.
- Cina, S. E., 2011, *Evolution of the Central Asian Orogenic System and Himalayan-Tibetan Orogen: Constraints from U-Th-Pb Geochronology, Thermobarometry, and Geochemistry* [Ph.D. dissertation]: University of California, Los Angeles, 374 p.
- Cleven, N.R., Lin, S., and Xiao, W., 2015, The Hongliuhe fold-and-thrust belt: Evidence of terminal collision and suture-reactivation after the Early Permian in the Beishan orogenic collage, Northwest China: *Gondwana Research*, v. 27, no. 2, p. 796-810.
- Cocks, L.R.M., and Torsvik, T.H., 2011, The Palaeozoic geography of Laurentia and western Laurussia: a stable craton with mobile margins: *Earth-Science Reviews*, v. 106, no. 1, p. 1-51.
- Condie, K.C., Belousova, E., Griffin, W.L., and Sircombe, K.N., 2009, Granitoid events in space and time: constraints from igneous and detrital zircon age spectra: *Gondwana Research*, v. 15, no. 3, p. 228-242.
- Cook, H.E., 2002, Devonian and Carboniferous carbonate platform facies in the Bolshoi Karatau, Southern Kazakhstan: outcrop analogs for coeval carbonate oil and gas fields in the North Caspian Basin, Western Kazakhstan.
- Cook, H.E., Zhemchuzhnikov, V.G., Buvtyshkin, V.M., Golub, L.Y., Gatovsky, Y.A., and Zorin, A.Y., 1994, Devonian and Carboniferous passive-margin carbonate platform of Southern Kazakhstan: summary of depositional and stratigraphic models to assist in the exploration and production of coeval giant carbonate platform oil and gas fields in the North Caspian

- Basin, Western Kazakhstan: Canadian Society of Petroleum Geology, Memoire, v. 17, p. 363-381.
- Cowgill, E., 2003, Reconstruction of the Altyn Tagh fault based on U-Pb geochronology: Role of back thrusts, mantle sutures, and heterogeneous crustal strength in forming the Tibetan Plateau: *Journal of Geophysical Research*, v. 108.
- Cowgill, E.S., 2001, Tectonic evolution of the Altyn Tagh-Western Kunlun fault system, northwestern China [PhD thesis]: Los Angeles, University of California, 311 p.
- Dalimov, T.N., Ganiyev, I.N., Shpotova, L.V., Kadyrov, M.H., 1993. Geodynamics of Tian-Shan. University, Tashkent, 206 p. (In Russian).
- Davis, G.A., Qian, X., Zheng, Y., Yu, H., Wang, C., Tong, H.M., Gehrels, G.E., Shafiquallah, M., and Fryxell, J.E., 1996, Mesozoic deformation and plutonism in the Yunmeng Shan: A Chinese metamorphic core complex north of Beijing, China, *in* Yin, A., and Harrison, T.M., eds., *The tectonic evolution of Asia*: Cambridge, Cambridge University Press, p. 253-280.
- Davis, G.A., Yadong, Z., Cong, W., Darby, B.J., Changhou, Z., and Gehrels, G., 2001, Mesozoic tectonic evolution of the Yanshan fold and thrust belt, with emphasis on Hebei and Liaoning provinces, northern China, *in* Hendrix, M.S., and Davis, G.A., eds., *Paleozoic and Mesozoic tectonic evolution of central Asia: From continental assembly to intracontinental deformation*: Boulder: Geological Society of America Memoir 194, p. 171-198.
- De Jong, K., Xiao, W., Windley, B.F., Masago, H., and Lo, C.H., 2006, Ordovician  $^{40}\text{Ar}/^{39}\text{Ar}$  phengite ages from the blueschist-facies Ondor Sum subduction-accretion complex (Inner Mongolia) and implications for the early Paleozoic history of continental blocks in China and adjacent areas: *American journal of Science*, v. 306, no. 10, p. 799-845.
- Demoux, A., Kröner, A., Badarch, G., Jian, P., Tomurhuu, D., and Wingate, M.T., 2009, Zircon ages from the Baydrag block and the Bayankhongor ophiolite zone: Time constraints on late Neoproterozoic to Cambrian subduction-and accretion-related magmatism in central Mongolia: *The Journal of Geology*, v. 117, no. 4, p. 377-397.
- Deng, J., Mo, X., Zhao, H., Luo, Z., and Zhao, G., 1999, Yanshanian magma-tectonic-metallogenic belt in east China of circum-Pacific domain (I): Igneous rocks and orogenic processes: *China University of Geosciences Journal*, v. 10, p. 21-24 (in Chinese with English abstract).
- Dercourt, J., Gaetani, M., Vrielynck, B., Barrier, E., Biju-Duval, B., Brunet, M.F., Cadet, J.P., Crasquin, S., and Sandulescu, M., 2000, Atlas Peri-Tethys, Palaeogeographical maps. CCGM/CCMW, Paris, 24 maps and explanatory notes, I-XX, 269 p.
- Dewey, J.F., 1977, Suture zone complexities: a review: *Tectonophysics*, v. 40, no. 1, p. 53-67.
- Ding, G., Chen, J., Tian, Q., Shen, X., Xing, C., and Wei, K., 2004, Active faults and magnitudes of left-lateral displacement along the northern margin of the Tibetan Plateau: *Tectonophysics*, v. 380, no. 3, p. 243-260.

- Dobretsov, N.L., and Buslov, M.M., 2007, Late Cambrian-Ordovician tectonics and geodynamics of Central Asia: *Russian Geology and Geophysics*, v. 48, no. 1, p. 71-82.
- Dong, Y., Zhang, G., Neubauer, F., Liu, X., Genser, J., and Hauzenberger, C., 2011, Tectonic evolution of the Qinling orogen, China: review and synthesis: *Journal of Asian Earth Sciences*, v. 41, no. 3, p. 213-237.
- Dupont-Nivet, G., Lippert, P. C., Van Hinsbergen, D. J., Meijers, M. J., and Kapp, P., 2010, Palaeolatitude and age of the Indo-Asia collision: palaeomagnetic constraints: *Geophysical Journal International*, v. 182, no. 3, p. 1189-1198.
- Duvall, A.R., and Clark, C.K., 2010, Dissipation of fast strike-slip faulting within and beyond northeastern Tibet: *Geology*, v. 38, no. 3, p. 223-226.
- Eizenhöfer, P.R., Zhao, G., Zhang, J., and Sun, M., 2014, Final closure of the Paleo-Asian Ocean along the Solonker Suture Zone: Constraints from geochronological and geochemical data of Permian volcanic and sedimentary rocks: *Tectonics*, v. 33, no. 4, p. 441-463.
- Enkelmann, E., Weislogel, A., Ratschbacher, L., Eide, E., Renno, A., and Wooden, J., 2007,. How was the Triassic Songpan-Ganzi basin filled? A provenance study: *Tectonics*, v. 26, no. 4.
- Ernst, R.E., et al., 2016, Long-lived connection between southern Siberia and northern Laurentia in the Proterozoic: *Nature geoscience*, in press.
- Evans, D.A., 2009, The palaeomagnetically viable, long-lived and all-inclusive Rodinia supercontinent reconstruction: *Geological Society, London, Special Publications*, v. 327, no. 1, p. 371-404.
- Evans, D.A., and Mitchell, R.N., 2011, Assembly and breakup of the core of Paleoproterozoic–Mesoproterozoic supercontinent Nuna: *Geology*, v. 39, no. 5, p. 443-446.
- Faure, M., Trap, P., Lin, W., Monié, P., and Bruguier, O., 2007, Polyorogenic evolution of the Paleoproterozoic Trans-North China Belt, new insights from the in Lüliangshan-Hengshan-Wutaishan and Fuping massifs: *Episodes*, v. 30, no. 2, p. 95-106.
- Feng, Y.M., and He, S.P., 1995, Research for geology and geochemistry of several ophiolites in the North Qilian Mountains, China: *Geological Review*, v. 40, p. 252-264.
- Fershtater, G.B., 2013, The main features of the Uralian Paleozoic magmatism and the epioceanic nature of the orogen: *Mineralogy and Petrology*, v. 107, no. 1, p. 39-52.
- Fershtater, G.B., Krasnobaev, A.A., Bea, F., Montero, P., and Borodina, N.S., 2007, Geodynamic settings and history of the Paleozoic intrusive magmatism of the central and southern Urals: results of zircon dating: *Geotectonics*, v. 41, no. 6, p. 465-486.



- Fershtater, G.B., Krasnobaev, A.A., Bea, F., Montero, P., Borodina, N.S., 2007, Geodynamic setting and history of the Paleozoic intrusive magmatism of the Central and Southern Urals: results of zircon dating: *Geotectonics*, v. 41, p. 465–486.
- Filippova, I.B., Bush, V.A., and Didenko, A.N., 2001, Middle Paleozoic subduction belts: the leading factor in the formation of the Central Asian fold-and-thrust belt: *Russian Journal of Earth Sciences*, v. 3, p. 405-426.
- Foster, D.A., Mueller, P.A., Mogk, D.W., Wooden, J.L., and Vogl, J.J., 2006, Proterozoic evolution of the western margin of the Wyoming craton: Implications for the tectonic and magmatic evolution of the northern Rocky Mountains: *Canadian Journal of Earth Sciences*, v. 43, p. 1601–1619.
- Fu, B., Awata, Y., Du, J., and He, W., 2005, Late Quaternary systematic stream offsets caused by repeated large seismic events along the Kunlun fault, northern Tibet: *Geomorphology*, v. 71, no. 3, p. 278-292.
- Fu, X. et al., 2015, New paleomagnetic results from the Huaibei Group and Neoproterozoic mafic sills in the North China Craton and their paleogeographic implications: *Precambrian Research*, v. 269, p. 90-106.
- Gaetani, M., Balini, M., Vuks, V.J., Gavrilova, V.A., Garzanti, E., Nicora, A., Erba, E., Cariou, E., Cecca, F., Premoli, I.S., Petrizzo, M.R., Cirilli, S., and Palliani, R.B., 1998, The Mesozoic of the Mangyshlak (west Kazakhstan): *Mémoires du Muséum national d'histoire naturelle*, v. 179, p. 35-74.
- Gao, J., Li, M., Xiao, X., Tang, Y., and He, G., 1998, Paleozoic tectonic evolution of the Tianshan Orogen, northwestern China: *Tectonophysics*, v. 287, no. 1, p. 213-231.
- Gao, R., Wang, H., Yin, A., Dong, S., Kuang, Z., Zuza, A.V., Li, W., and Xiong, X., 2013, Tectonic development of the northeastern Tibetan Plateau as constrained by high-resolution deep seismic-reflection data: *Lithosphere*, v. 5, no. 6, p. 555-574.
- Gao, Z.J., Chen, J.B., Lu, S.N., Peng, C.W., Qin, Z.Y., 1993, The Precambrian Geology in Northern Xinjiang: *Precambrian Geology* 6, 1-171 p. (in Chinese).
- Gao, Z.J., Chen, J.L., Lu, S.N., Peng, C.W., and Qin, Z.Y., 1993, The Precambrian metamorphic Rocks, *in* The Precambrian Geology, No. 6 (in Chinese with English abstract).
- Garzanti, E., and Gaetani, M., 2002, Unroofing history of Late Paleozoic magmatic arcs within the “Turan plate”(Tuarkyr, Turkmenistan): *Sedimentary Geology*, v. 151, no. 1, p. 67-87.
- Gaudemer, Y. et al., 1995, Partitioning of crustal slip between linked, active faults in the eastern Qilian Shan, and evidence for a major seismic gap, the ‘Tianzhu gap’, on the western Haiyuan Fault, Gansu (China): *Geophysical Journal International*, v. 120, no. 3, p. 599-645.
- Ge, R., Zhu, W., Wilde, S.A., He, J., and Cui, X., 2015, Synchronous crustal growth and reworking recorded in late Paleoproterozoic granitoids in the northern Tarim craton: *In situ*

- zircon U-Pb-Hf-O isotopic and geochemical constraints and tectonic implications: Geological Society of America Bulletin, v. 127, no. 5-6, p. 781-803.
- Gee, D.G., and Pease, V., 2004, The Neoproterozoic Timanide Orogen of eastern Baltica: introduction: Geological Society London Memoirs, v. 30, no.1, p. 1-3.
- Gee, D.G., Bogolepova, O.K., and Lorenz, H., 2006, The Timanide, Caledonide and Uralide orogens in the Eurasian high Arctic, and relationships to the palaeo-continent Laurentia, Baltica and Siberia: Geological Society London Memoirs, v. 32, no. 1, p. 507-520.
- Gehrels, G. et al., 2011, Detrital zircon geochronology of pre-Tertiary strata in the Tibetan-Himalayan orogen: Tectonics, v. 30, no. 5.
- Gehrels, G.E., Yin, A., and Wang, X.-F., 2003a, Detrital-zircon geochronology of the northeastern Tibetan plateau: Geological Society of America Bulletin, v. 115, p. 881-896.
- Gehrels, G.E., Yin, A., and Wang, X.-F., 2003b, Magmatic history of the northeastern Tibetan Plateau: Journal of Geophysical Research, v. 108, p. 2423.
- Geoffroy, L., 2005, Volcanic passive margins: Comptes Rendus Geoscience, v. 337, no. 16, p. 1395-1408.
- Gernigon, L., Ringenbach, J. C., Planke, S., and Le Gall, B., 2004, Deep structures and breakup along volcanic rifted margins: insights from integrated studies along the outer Vøring Basin (Norway): Marine and Petroleum Geology, v. 21, no. 3, p. 363-372.
- Glasmacher, U.A., Bauer, W., Giese, U., Reynolds, P., Kober, B., Puchkov, V., Stroink, L., Alekseyev, A., and Willner, A.P., 2001, The metamorphic complex of Beloretzk, SW Urals, Russia—a terrane with a polyphase Meso- to Neoproterozoic thermo-dynamic evolution: Precambrian Research, v. 110, p. 185-213.
- Glasmacher, U.A., Reynolds, P., Alekseyev, A.A., Puchkov, V.N., Taylor, K., Gorozhanin, V., and Walter, R., 1999,  $^{40}\text{Ar}/^{39}\text{Ar}$  thermochronology west of the Main Uralian fault, southern Urals, Russia: Geologische Rundschau, v. 87, no. 4, p. 515-525.
- Gong, S., Chen, N., Wang, Q., Kusky, T.M., Wang, L., Zhang, L., Ba, J., and Liao, F., 2012, Early Paleoproterozoic magmatism in the Quanji Massif, northeastern margin of the Qinghai-Tibet Plateau and its tectonic significance: LA-ICPMS U-Pb zircon geochronology and geochemistry: Gondwana Research, v. 21, no. 1, p. 152-166.
- Gorman, A.R. et al., 2002, Deep Probe: imaging the roots of western North America: Canadian Journal of Earth Sciences, v. 39, no. 3, p. 375-398.
- Graham, S.A., Cope, T., Johnson, C.L., and Ritts, B., 2012, Sedimentary basins of the late Mesozoic extensional domain of China and Mongolia, *in* Roberts, D.G. and Bally, A.W., eds, Phanerozoic Rift Systems and Sedimentary Basins: Elsevier, Amsterdam, The Netherlands, p. 443-461.

- Graham, S.A., Hendrix, M.S., Hendrix, M.S., Wang, L.B., and Carroll, A.R., 1993. Collisional successor basins of western China: impact of tectonic inheritance on sand composition: *Geological Society of America Bulletin*, v. 105, p. 323–344.
- Green, O.R., Searle, M.P., Corfield, R.I., and Corfield, R.M., 2008, Cretaceous-Tertiary carbonate platform evolution and the age of the India-Asia collision along the Ladakh Himalaya (Northwest India): *The Journal of Geology*, v. 116, no. 4, p. 331-353.
- Guo, K.Y., Zhang, C.L., Shen, J.L., Ye, H., Wang, A. G., and Li, C., 2004, Chemistry of Statherian volcanic rocks in the western Kunlun Mountains: *Geological Bulletin of China*, v. 23, p. 130-135 (in Chinese).
- Guo, Q.Q., Xiao, W.J., Windley, B.F., Mao, Q.G., Han, C.M., Qu, J.F., Ao, S.J., Li, J.L., Song, D.F., and Yong, Y., 2011. Provenance and tectonic settings of Permian turbidites from the Beishan Mountains, NW China: Implications for the Late Paleozoic accretionary tectonics of the southern Altaids: *Journal of Asian Earth Sciences*, v. 49, p. 54-68.
- Guo, Z.-J., Yin, A., Robinson, A., and Jia, C.-Z., 2005, Geochronology and geochemistry of deep-drill-core samples from the basement of the central Tarim basin: *Journal of Asian Earth Sciences*, v. 25, p. 45–56.
- Guo, Z.-J., Zhang, Z., and Wang, J., 1999, Sm-Nd isochron age of ophiolite along northern margin of Altun Tagh Mountain and its tectonic significance: *Chinese Science Bulletin*, v. 44, n. 5, p. 456-458.
- Hacker, B.R., Ratschbacher, L., and Liou, J.G., 2004, Subduction, collision, and exhumation in the Qinling-Dabie orogen: *Geological Society [London] Special Publication 226*, p. 157–175.
- Hacker, B.R., Wallis, S.R., Ratschbacher, L., Grove, M., and Gehrels, G., 2006, High-temperature geochronology constraints on the tectonic history and architecture of the ultrahigh-pressure Dabie-Sulu orogen: *Tectonics*, v. 25, TC5006, doi: 10.1029/2005TC001937.
- Hall, R., 2011, Australia–SE Asia collision: plate tectonics and crustal flow: *Geological Society, London, Special Publications*, v. 355, no. 1, p. 75-109.
- Han, G., Liu, Y., Neubauer, F., Genser, J., Li, W., Zhao, Y., and Liang, C., 2011, Origin of terranes in the eastern Central Asian Orogenic Belt, NE China: U–Pb ages of detrital zircons from Ordovician–Devonian sandstones, North Da Xing’an Mts.: *Tectonophysics*, v. 511, p. 109–124.
- Han, Y., Zhao, G., Cawood, P. A., Sun, M., Eizenhöfer, P.R., Hou, W., Zhang, X., and Liu, Q., 2016, Tarim and North China cratons linked to northern Gondwana through switching accretionary tectonics and collisional orogenesis: *Geology*, v. 44, no. 2, p. 95-98.

- Hao, G.J., Lu, S.N., Xin, H.T., Wang, H.C., and Yuan, G.B., 2004. The constitution and importance geological events of Pre-Devonian in the Dulan, Qinghai: *Journal of Jilin University*, v. 34, p. 495–501 (in Chinese with English abstract).
- Harrison, T.M., Copeland, P., Kidd, W.S.F., and Yin, A., 1992, Raising Tibet: *Science*, v, 255, no. 5052, p. 1663-1670.
- Hartz, E.H., and Torsvik, T.H., 2002, Baltica upside down: a new plate tectonic model for Rodinia and the Iapetus Ocean: *Geology*, v. 30, no. 3, p. 255-258.
- He, S., Wang, H., Chen, J., Xu, X., Zhang, H., Ren, G., and Yu, J., 2007, LA-ICP-MS U-Pb zircon geochronology of basic dikes within Maxianshan rock group in the central Qilian orogenic belt and its tectonic implications: *Journal of China University of Geosciences*, v. 18, no. 1, p. 19-29.
- He, Z.Y., Zhang, Z.M., Zong, K.Q., Xiang, H., Chen, X.J., and Xia, M.J., 2014, Zircon U–Pb and Hf isotopic studies of the Xingxingxia Complex from Eastern Tianshan (NW China): significance to the reconstruction and tectonics of the southern Central Asian Orogenic Belt: *Lithos*, v. 190, p. 485-499.
- Heafford, A.P., 1988, Carboniferous through Triassic stratigraphy of the Barents Shelf, *in* Hardland, W.B., and Dowdeswell, E.K. (eds.), *Geological Evolution of the Barents Shelf Region*, Graham and Trotman, London, p. 89-108.
- Hebei Bureau of Geology and Mineral Resources (Hebei BGMR), 1967, Geological map of the Zhangjiakou area: Beijing, Geological Publishing House, scale 1:200 000.
- Hendrix, M.S., Graham, S.A., Carroll, A.R., Sobel, E.R., McKnight, C.L., Schulein, B.J., and Wang, Z., 1992, Sedimentary record and climatic implications of recurrent deformation in the Tian Shan: Evidence from Mesozoic strata of the north Tarim, south Junggar, and Turpan basins, northwest China: *Geological Society of America Bulletin*, v. 104, no. 1, p. 53-79.
- Herrington, R.J., Armstrong, R.N., Zaykov, V.V., Maslennikov, V.V., Tessalina, S.G., Orgeval, J.J., and Taylor, R.N.A., 2002, Massive sulfide deposits in the South Urals: geological setting within the framework of the Uralide Orogen: *Mountain Building in the Uralides: Pangea to the Present*, p. 155-182.
- Heubeck, C., 2001, Assembly of central Asia during the middle and late Paleozoic, *in* *Paleozoic and Mesozoic Tectonic Evolution of Central Asia: From Continental Assembly to Intracontinental Deformation*, Hendrix, M.S., and Davis, G.A. (eds): *Geological Society of America Memoir* 194, p. 1-22.
- Hill, K.C., and Hall, R., 2003, Mesozoic-Cenozoic evolution of Australia's New Guinea margin in a west Pacific context: *Geological Society of America Special Papers*, v. 372, p. 265-290.
- Hoffman, P.F., Kaufman, A.J., Halverson, G.P., and Schrag, D.P., 1998, A Neoproterozoic snowball earth: *Science*, v. 281, no. 5381, p. 1342-1346.

- House, Beijing, 125 pp. Lu, S., and Yuan, G., 2003, Geochronology of early Precambrian magmatic activities in Aketasdhtage, east Altyn tagh: *Acta Geologica Sinica*, v. 77, p. 61–68 (in Chinese).
- Hsü, K.J., and Chen, H., 1999, *Geological Atlas of China*: Amsterdam, Elsevier, 262 p.
- Hu, A., Jahn, B.M., Zhang, G., Chen, Y., and Zhang, Q., 2000, Crustal evolution and Phanerozoic crustal growth in northern Xinjiang: Nd isotopic evidence. Part I. Isotopic characterization of basement rocks: *Tectonophysics*, v. 328, no. 1, p. 15-51.
- Hu, A.Q., Wei, G.J., Jahn, B.M., Zhang, J.B., Deng, W.F., and Chen, L.L., 2010, Formation of the 0.9 Ga Neoproterozoic granitoids in the Tianshan Orogen, NW China: constraints from the SHRIMP zircon age determination and its tectonic significance: *Geochimica*, v. 39, no. 3, p. 197–212 (in Chinese with English abstract).
- Huang, B., Xu, B., Zhang, C., Li, Y.A., and Zhu, R., 2005, Paleomagnetism of the Baiyisi volcanic rocks (ca. 740Ma) of Tarim, Northwest China: a continental fragment of Neoproterozoic Western Australia?: *Precambrian Research*, v. 142, no. 3, p. 83-92.
- Huang, B., Yang, Z., Otofujii, Y.I., and Zhu, R., 1999, Early Paleozoic paleomagnetic poles from the western part of the North China Block and their implications: *Tectonophysics*, v. 308, no. 3, p. 377-402.
- Huang, W., Zhang, L., Ba, J., Liao, F.X., and Chen, N.S., 2011. Detrital Zircon U-Pb Dating for K-Feldspar Leptynite Constrains the Age of Dakendaban Group: *Geological Bulletin of China*, v. 30, no. 9: p. 1353-1359 (in Chinese with English Abstract).
- Jackson, J., and McKenzie, D., 1984, Active tectonics of the Alpine—Himalayan Belt between western Turkey and Pakistan: *Geophysical Journal International*, v. 77, no. 1, p. 185-264.
- Jahn, B.M., Windley, B., Natal'in, B., and Dobretsov, N., 2004, Phanerozoic continental growth in Central Asia: *Journal of Asian Earth Sciences*, v. 23, no. 5, p. 599-603.
- Jia, C.Z., 1997, *Tectonic characteristics and petroleum, Tarim basin, China*, Petroleum Industry Press, Beijing.
- Jia, C.Z., Zhang, S.B., Wu, S.Z., 2004, *Stratigraphy of the Tarim Basin and Adjacent Area*: Science Press, 450 p. (in Chinese).
- Jiang, C.F., Yang, J.S., Feng, B.G., Zhu, Z.Z., Zhao, M., Chai, Y.C., Shi, X.D., Wang, H.D., and Ha, J.Q., 1992, Opening Closing Tectonics of Kunlun Mountains. *Geological Memoirs*: Geological Publishing House, Beijing, 224 p (in Chinese with English abstract).
- Kapp, P., Murphy, M. A., Yin, A., Harrison, T. M., Ding, L., and Guo, J., 2003, Mesozoic and Cenozoic tectonic evolution of the Shiquanhe area of western Tibet: *Tectonics*, v. 22, no. 4.
- Kelty, T.K., Yin, A., Dash, B., Gehrels, G E., and Ribeiro, A.E., 2008, Detrital-zircon geochronology of Paleozoic sedimentary rocks in the Hangay–Hentey basin, north-central

- Mongolia: implications for the tectonic evolution of the Mongol–Okhotsk Ocean in central Asia: *Tectonophysics*, v. 451, no. 1, p. 290-311.
- Khain, E.V., Bibikova, E.V., Degtyarev, K.E., Gibsher, A.S., Didenko, A.N., Klochko, A.A., Rytsk, E.Y., Salnikova, E.B., and Fedotova, A.A., 1999, The Palaeo-Asian ocean in the Neoproterozoic and early Palaeozoic: new radiometric data: *in* Kozakov, I.K. (ed.), *Geological History of the Proterozoic Marginal Palaeo-Oceanic Structures of Northern Eurasia*. Tema Publishing House, St. Petersburg, p. 175–181 (in Russian).
- Khain, E.V., Bibikova, E.V., Salnikova, E.B., Kröner, A., Gibsher, A.S., Didenko, A.N., Degtyarev, K.E., and Fedotova, A.A., 2003, The Palaeo-Asian ocean in the Neoproterozoic and early Palaeozoic: new geochronologic data and palaeotectonic reconstructions: *Precambrian Research*, v. 122, no 1, p. 329-358.
- Khain, V.E., 1985, *Geology of the USSR*: Berlin: Gebruder Borntraeger.
- Kheraskova, T.N., Bush, V.A., Didenko, A.N., and Samygin, S.G., 2010, Breakup of Rodinia and early stages of evolution of the Paleasian ocean: *Geotectonics*, v. 44, no. 1, p. 3-24.
- Kheraskova, T.N., Didenko, A.N., Bush, V.A., and Volozh, Y.A., 2003, The Vendian–Early Paleozoic history of the continental margin of eastern Paleogondwana, Paleasian ocean, and Central Asian foldbelt: *Russian Journal of Earth Sciences*, v. 5, no. 3, p. 165-184.
- Kheraskova, T.N., Voloj, YuA., and Andreeva, N.K., 2001. New data about structure and sedimentation of Riphey–Early Vendian within Central-Russian system of aulocagens. *Geological Vestnik of Central Russian region* 1, 10–22 (in Russian).
- Kirby, E., Harkins, N., Wang, E., Shi, X., Fan, C., and Burbank, D., 2007, Slip rate gradients along the eastern Kunlun fault: *Tectonics*, v. 26, no. 2.
- Konopelko, D., Biske, G., Seltmann, R., Eklund, O., and Belyatsky, B., 2007, Hercynian post-collisional A-type granites of the Kokshaal Range, southern Tien Shan, Kyrgyzstan: *Lithos*, v. 97, no. 1, p. 140-160.
- Kotov, A.B., Kozakov, I.K., Bibikova, E.V., Salnikova, E.B., Kirnozova, T.I., and Kovach, V.P., 1995, Duration of regional metamorphic episodes in areas of polycyclic endogenic processes: a U–Pb geochronological study: *Petrology*, v. 3, p. 567–575.
- Kozakov, I.K., Bibikova, E.V., Neymark, L.A., and Kirnozova, T.I., 1993, The Baydaric block, *in* Rudnik, B.A., Sokolov, Y.M., and Filatova, L.I. (eds.), *The Early Precambrian of the Central Asian Fold Belt*. St. Petersburg, Nauka, p. 118–137.
- Kozakov, I.K., Kotov, A.B., Salnikova, Y.B., Bibikova, Y.V., Kovach, V.P., Kirnozova, T.I., Berezhnaya, N.G., and Lykhin, D.A., 1999, Metamorphic age of crystalline complexes of Tuvino-Mongolian Massif. U–Pb geochronology of granitoids: *Petrologiya*, v. 7, p. 174-190.

- Kröner, A. et al., 2013, Mesoproterozoic (Grenville-age) terranes in the Kyrgyz North Tianshan: zircon ages and Nd–Hf isotopic constraints on the origin and evolution of basement blocks in the southern Central Asian Orogen: *Gondwana Research*, v. 23, no. 1, p. 272-295.
- Kröner, A., Wilde, S., O'Brien, P.J., and Li, J.H., 2001, The Hengshan and Wutai complexes of northern China: lower and upper crustal domains of a late Archean to Paleoproterozoic magmatic arc and significance for the evolution of the North China Craton *in* Cassidy, K.F., Dunphy, J.M., and Van Kranendonk, M.J. (eds.): *Fourth International Archean Symposium*, Perth, Australia, Extended Abstracts, AGSO—Geoscience Record, p. 327.
- Kröner, A., Wilde, S.A., Li, J.H., and Wang, K.Y., 2005a, Age and evolution of a late Archean to Paleoproterozoic upper to lower crustal section in the Wutaishan/Hengshan/Fuping terrain of northern China: *Journal of Asian Earth Sciences*, v. 24, no. 5, p. 577-595.
- Kröner, A., Wilde, S.A., O'Brien, P.J., Li, J.H., Passchier, C.W., Walte, N.P., and Liu, D.Y., 2013b, Field relationships, geochemistry, zircon ages and evolution of a late Archean to Palaeoproterozoic lower crustal section in the Hengshan Terrain of northern China: *Acta Geologica Sinica*, v. 79, no. 5, p. 605-629.
- Kröner, A., Wilde, S.A., Zhao, G.C., O'Brien, P.J., Sun, M., Liu, D.Y., Wan, Y.S., Liu, S.W., and Guo, J.H., 2006, Zircon geochronology and metamorphic evolution of mafic dykes in the Hengshan Complex of northern China: evidence for late Palaeoproterozoic extension and subsequent high-pressure metamorphism in the North China Craton: *Precambrian research*, v. 146, no. 1, p. 45-67.
- Kurenkov, S.A., and Aristov, V.A., 1995, On the time of formation of the Turkestan paleocean crust: *Geotectonics*, v. 29, no. 6, p.469-477.
- Kusky, T.M., 2011, Geophysical and geological tests of tectonic models of the North China Craton: *Gondwana Research*, v. 20, p. 20, 26–35.
- Kusky, T.M., and Li, J., 2003, Paleoproterozoic tectonic evolution of the North China Craton: *Journal of Asian Earth Sciences*, v. 22, no. 4, p. 383-397.
- Kusky, T.M., and Santosh, M., 2009, The Columbia connection in North China, in, Reddy, S.M., Mazumder, R., Evans, D., Collins, A.S., eds., *Paleoproterozoic Supercontinents and Global Evolution: Geological Society of London Special Publication*, v. 323, p. 49–71.
- Kusky, T.M., Li, J.H., and Santosh, M., 2007, The Paleoproterozoic North Hebei Orogen: North China Craton's Collisional Suture with the Columbia Supercontinent: *Gondwana Research*, v. 12, p. 4-28.
- Kuzmichev, A., Kröner, A., Hegner, E., Duniy, L., and Yusheng, W., 2005, The Shishkhid ophiolite, northern Mongolia: a key to the reconstruction of a Neoproterozoic island-arc system in central Asia: *Precambrian Research*, v. 138, no. 1, p. 125-150.
- Kuznetsov, N.B., Natapov, L.M., Belousova, E.A., Griffin, W.L., and O'Reilly, S.Y., 2009, First isotopic data on detrital zircons from the Engane-Pe Uplift (western Polar Urals):

- Implications for the primary tectonic position of the Pre-Uralides-Timanides: *Doklady Earth Sciences*, v. 426, no. 1, p. 567-573).
- Kuznetsov, N.B., Natapov, L.M., Belousova, E.A., O'Reilly, S.Y., and Griffin, W.L., 2010, Geochronological, geochemical and isotopic study of detrital zircon suites from late Neoproterozoic clastic strata along the NE margin of the East European Craton: implications for plate tectonic models: *Gondwana Research*, v. 17, no. 2, p. 583-601.
- Kuznetsov, N.B., Soboleva, A.A., Udoratina, O.V., Hertseva, M.V., and Andreichev, V.L., 2007, Pre-Ordovician tectonic evolution and volcano-plutonic associations of the Timanides and northern Pre-Uralides, northeast part of the East European Craton: *Gondwana Research*, v. 12, no. 3, p. 305-323.
- Le Fort, P., 1996, Evolution of the Himalaya: *World and Regional Geology*, v. 1, no. 8, p. 95-109.
- Lei, R.X., Wu, C. Z., Gu, L.X., Zhang, Z.Z., Chi, G.X., and Jiang, Y.H., 2011, Zircon U-Pb chronology and Hf isotope of the Xingxingxia granodiorite from the Central Tianshan zone (NW China): implications for the tectonic evolution of the southern Altaids: *Gondwana Research*, v. 20, no. 2, p. 582-593.
- Lemaire, M.M., Westphal, M., Gurevitch, E.L., Nazarov, K., Feinberg, H., and Pozzi, J.P., 1997, How far between Iran and Eurasia was the Turan plate during Triassic-Jurassic times? : *Geologie en Mijnbouw* v. 76, p. 73- 82.
- Levashova, N.M., Bazhenov, M.L., Meert, J.G., Kuznetsov, N.B., Golovanova, I.V., Danukalov, K.N., and Fedorova, N.M., 2013, Paleogeography of Baltica in the Ediacaran: Paleomagnetic and geochronological data from the clastic Zigan Formation, South Urals: *Precambrian Research*, v. 236, p. 16-30.
- Levashova, N.M., Kalugin, V.M., Gibsher, A.S., Yff, J., Ryabinin, A.B., Meert, J.G., and Malone, S.J., 2010, The origin of the Baydaric microcontinent, Mongolia: Constraints from paleomagnetism and geochronology: *Tectonophysics*, v. 485, p. 306-320.
- Levashova, N.M., Meert, J.G., Gibsher, A.S., Grice, W.C., and Bazhenov, M.L., 2011, The origin of microcontinents in the Central Asian Orogenic Belt: Constraints from paleomagnetism and geochronology: *Precambrian Research*, v. 185, p. 37-54.
- Li, H., Lu, S., Su, W., Xiang, Z., Zhou, H., and Zhang, Y., 2013, Recent advances in the study of the Mesoproterozoic geochronology in the North China Craton: *Journal of Asian Earth Sciences*, v. 72, p. 216-227.
- Li, J., and Kusky, T., 2007, A late Archean foreland fold and thrust belt in the North China Craton: implications for early collisional tectonics: *Gondwana Research*, v. 12, no. 1, p. 47-66.



- Li, J.H., Kroner, A., Qian, X.L., and O'Brien, P., 2000a, Tectonic Evolution of an Early Precambrian High-Pressure Granulite Belt in the North China Craton: *Acta Geologica Sinica*, v. 74, p. 246-258.
- Li, J.H., Kröner, A., Qian, X.L., O'Brien, P., 2000, Tectonic Evolution of an Early Precambrian High-Pressure Granulite Belt in the North China Craton: *Acta Geologica Sinica*, v. 74, p. 246-258.
- Li, J.H., Qian, X.L., Huang, X.N., and Liu, S.W., 2000b, Tectonic framework of North China Block and its cratonization in the early Precambrian: *Acta Petrologica Sinica*, v. 16, no. 1, p. 1-10.
- Li, X.H., Li, W.X., Li, Z.X., Lo, C.H., Wang, J., Ye, M.F., and Yang, Y.H., 2009, Amalgamation between the Yangtze and Cathaysia Blocks in South China: constraints from SHRIMP U–Pb zircon ages, geochemistry and Nd–Hf isotopes of the Shuangxiwu volcanic rocks. *Precambrian Research*, v. 174, no. 1, p. 117-128.
- Li, X.H., Li, Z.X., Ge, W., Zhou, H., Li, W., Liu, Y., and Wingate, M.T., 2003, Neoproterozoic granitoids in South China: crustal melting above a mantle plume at ca. 825 Ma?: *Precambrian Research*, v. 122, no. 1, p. 45-83.
- Li, X.H., Su, L., Chung, S.L., Li, Z.X., Liu, Y., Song, B., and Liu, D.Y., 2005, Formation of the Jinchuan ultramafic intrusion and the world's third largest Ni-Cu sulfide deposit: Associated with the ~825 Ma south China mantle plume?: *Geochemistry, Geophysics, Geosystems*, v. 6, no. 11.
- Li, Y., Li, Y., Sharps, R., McWilliams, M., and Gao, Z., 1991, Sinian paleomagnetic results from the Tarim block, western China. *Precambrian Research*, v. 49, no. 1, p. 61-71.
- Li, Z.X. et al., 2008, Assembly, configuration, and break-up history of Rodinia: A synthesis: *Precambrian Research*, v. 160, p. 179–210.
- Li, Z.X., Zhang, L., and Powell, C.M., 1995, South China in Rodinia: part of the missing link between Australia–East Antarctica and Laurentia?: *Geology*, v. 23, no. 5, p. 407-410.
- Liao, F.X., Zhang, L., Chen, N.S., Sun, M., Santosh, M., Wang, Q.Y., and Mustafa, H.A., 2014, Geochronology and geochemistry of meta-mafic dykes in the Quanji Massif, NW China: Paleoproterozoic evolution of the Tarim Craton and implications for the assembly of the Columbia supercontinent: *Precambrian Research*, v. 249, p. 33-56.
- Lin C., Yang Q. and Li S., 1995, Basin Filling and Evolution Analysis of Helan Aulacogen, Northwest China: Geological Publishing House, Beijing, 143 p.
- Lin, C., Liu, J., Eriksson, K., Yang, H., Cai, Z., Li, H., Yang, Z., and Rui, Z., 2014, Late Ordovician, deep-water gravity-flow deposits, palaeogeography and tectonic setting, Tarim Basin, Northwest China: *Basin Research*, v. 26, no. 2, p. 297-319.

- Lin, Y.H., Zhang, L.F., Ji, J.Q., and Song, S.G., 2010,  $^{40}\text{Ar}/^{39}\text{Ar}$  age of Jiugequan lawsonite blueschists in northern Qilian Mountains and its petrologic significance: Chinese Science Bulletin, v. 55, p. 2021–2027, doi: 10.1007/s11434-010-3239-8.
- Lindsay, J.F., Brasier, M.D., Shields, G., Khomentovsky, V. V., and Bat-Ireedui, Y.A, 1996, Glacial facies associations in a Neoproterozoic back-arc setting, Zavkhan Basin, western Mongolia: Geological Magazine, v. 133, no. 04, p. 391-402.
- Ling, W., Gao, S., Zhang, B., Li, H., Liu, Y. and Cheng, J., 2003, Neoproterozoic tectonic evolution of the northwestern Yangtze craton, South China: implications for amalgamation and break-up of the Rodinia Supercontinent: Precambrian Research, v. 122, p. 111–140.
- Liou, J. G. et al., 1989, Proterozoic blueschist belt in western China: best documented Precambrian blueschists in the world: Geology, v. 17, no. 12, p. 1127-1131.
- Litvinova, T.P., 2000. Karta Anomalnogo Magnitnogo Polya ( $\Delta T$ )<sub>a</sub> Rossii, Sopredelnykh Gosudarstv (v Granitsax Byvshego SSSR) i Prilegayuschikh Akvatorii (1:5,000,000), VSEGEI.
- Liu, S., Hu, R., Gao, S., Feng, C., Coulson, I. M., Feng, G., Qi, Y., Yang, Y., Yang, C., and Tang, L., 2012, U–Pb zircon age, geochemical and Sr–Nd isotopic data as constraints on the petrogenesis and emplacement time of the Precambrian mafic dyke swarms in the North China Craton (NCC): Lithos, v. 140, p. 38-52.
- Liu, S.W., Guo, Z.J., Zhang, Z.C., Li, Q.G., and Zheng, H.F., 2004, Nature of Precambrian metamorphic blocks in eastern segment of the Central Tianshan: constraints from geochronology and Nd geochemistry: Science in China Series D: Earth Sciences, v. 47, p. 1085–1094.
- Liu, Y. J., Neubauer, F., Genser, J., Takasu, A., Ge, X. H., and Handler, R., 2006,  $^{40}\text{Ar}/^{39}\text{Ar}$  ages of blueschist facies pelitic schists from Qingshuigou in the Northern Qilian Mountains, western China: Island Arc, v. 15, no. 1, p. 187-198.
- Long, X., Yuan, C., Sun, M., Kröner, A., and Zhao, G., 2014, New geochemical and combined zircon U-Pb and Lu-Hf isotopic data of orthogneisses in the northern Altyn Tagh, northern margin of the Tibetan plateau: Implication for Archean evolution of the Dunhuang Block and crust formation in NW China: Lithos, v. 200, p. 418-431.
- Long, X., Yuan, C., Sun, M., Kröner, A., Zhao, G., Wilde, S., and Hu, A., 2011, Reworking of the Tarim Craton by underplating of mantle plume-derived magmas: evidence from Neoproterozoic granitoids in the Kuluketage area, NW China: Precambrian Research, v. 187, no. 1, p. 1-14.
- Long, X., Yuan, C., Sun, M., Zhao, G., Xiao, W., Wang, Y., Yang, Y., and Hu, A., 2010, Archean crustal evolution of the northern Tarim craton, NW China: Zircon U-Pb and Hf isotopic constraints: Precambrian Research, v. 180, no. 3, p. 272-284.
- Lu, S., 2002. The Precambrian Geology of Northern Tibet: Geological Publishing.

- Lu, S., Chunliang, Y., Huaikun, L., and Humin, Li., 2002, A group of rifting events in the terminal Paleoproterozoic in the North China Craton: *Gondwana Research*, v. 5, no. 1, p. 123-131.
- Lu, S., Li, H., Zhang, C., and Niu, G., 2008, Geological and geochronological evidence for the Precambrian evolution of the Tarim Craton and surrounding continental fragments: *Precambrian Research*, v. 160, no. 1, p. 94-107.
- Lu, S.N., 2002, Preliminary Study of Precambrian Geology in the north Tibet-Qinghai Plateau: Beijing, Geological Publishing House, pp. 1–125 (in Chinese).
- Lu, S.N., Yu, H.F., and Li, H.K., 2006, Research on Precambrian Major Problems in China: Beijing, Geological Publishing Press, pp. 1–206 (in Chinese).
- Lund, K., Aleinikoff, J.N., Evans, K.V., and Fanning, C.M., 2003, SHRIMP U-Pb geochronology of Neoproterozoic Windermere Supergroup, central Idaho: Implications for rifting of western Laurentia and synchronicity of Sturtian glacial deposits: *Geological Society of America Bulletin*, v. 115, no. 3, p. 349-372.
- Lund, K., Aleinikoff, J.N., Evans, K.V., Dewitt, E.H., and Unruh, D M., 2010, SHRIMP U-Pb dating of recurrent Cryogenian and Late Cambrian–Early Ordovician alkalic magmatism in central Idaho: Implications for Rodinian rift tectonics: *Geological Society of America Bulletin*, v. 122, no. 3-4, p. 430-453.
- Lyberis, N., Manby, G., Poli, J. T., Kalougin, V., Yousouphocaev, H., and Ashirov, T., 1998, Post-Triassic evolution of the southern margin of the Turan plate: *Earth and Planetary Sciences*, v. 326, no. 2, p. 137-143.
- Lyon-Caen, H., and Molnar, P., 1984, Gravity anomalies and the structure of western Tibet and the southern Tarim basin: *Geophysical Research Letters*, v. 11, no. 12, p. 1251-1254.
- Ma, X., Shu, L., Jahn, B. M., Zhu, W., and Faure, M., 2011, Precambrian tectonic evolution of Central Tianshan, NW China: Constraints from U–Pb dating and in situ Hf isotopic analysis of detrital zircons: *Precambrian Research*, v. 222-223, p. 450-473.
- Ma, X., Shu, L., Santosh, M., and Li, J., 2012, Detrital zircon U–Pb geochronology and Hf isotope data from Central Tianshan suggesting a link with the Tarim Block: implications on Proterozoic supercontinent history: *Precambrian Research*, v. 206, p. 1-16.
- Macdonald, F.A., Jones, D.S., and Schrag, D.P., 2009, Stratigraphic and tectonic implications of a newly discovered glacial diamictite–cap carbonate couplet in southwestern Mongolia: *Geology*, v. 37, no. 2, p. 123-126.
- Marcinowski, R., Walaszczyk, I., and Olszewska-Nejbert, D., 1996, Stratigraphy and regional development of the mid-Cretaceous (Upper Albian through Coniacian) of the Mangyshlak Mountains, Western Kazakhstan: *Acta Geologica Polonica*, v. 46, no. 1-2, p. 1-60.
- Markova, N.G., 1982, *Tektonika Kazakhstana*, 139 p.

- Maslov, A.V., Erdtmann, B.D., Ivanov, K.S., Ivanov, S.N., and Krupenin, M.T., 1997, The main tectonic events, depositional history, and the palaeogeography of the southern Urals during the Riphean-early Palaeozoic: *Tectonophysics*, v. 276, no. 1, p. 313-335.
- McKenzie, N.R., Hughes, N.C., Myrow, P.M., Choi, D.K., and Park, T.Y., 2011, Trilobites and zircons link north China with the eastern Himalaya during the Cambrian: *Geology*, v. 39, no. 6, p. 591-594.
- Meert, J.G., 2014, Strange attractors, spiritual interlopers and lonely wanderers: the search for pre-Pangean supercontinents: *Geoscience Frontiers*, v. 5, no. 2, p. 155-166.
- Meert, J.G., Gibsher, A.S., Levashova, N.M., Grice, W.C., Kamenov, G.D., and Ryabinin, A.B., 2011, Glaciation and ~ 770Ma Ediacara (?) Fossils from the Lesser Karatau Microcontinent, Kazakhstan: *Gondwana Research*, v. 19, no. 4, p. 867-880.
- Mei, H., Yu, H., Lu, S., and Li, H., 1998, The Archaean tonalite in Dunhuang, Gansu Province: single-zircon U–Pb age and Nd isotope. *Adv. Precambrian Research*, v. 21, p. 41-45 (in Chinese with English abstract).
- Meng, X., Ge, M., and Tucker, M.E., 1997, Sequence stratigraphy, sea-level changes and depositional systems in the Cambro-Ordovician of the North China carbonate platform: *Sedimentary Geology*, v. 114, p. 189–222.
- Meng, Q.R., Wei, H.H., Qu, Y. Q., and Ma, S.X., 2011, Stratigraphic and sedimentary records of the rift to drift evolution of the northern North China craton at the Paleo-to Mesoproterozoic transition: *Gondwana Research*, v. 20, no.1, p. 205-218.
- Menold, C.A., Manning, C.E., Yin, A., Tropper, P., Chen, X. H., and Wang, X.F., 2009, Metamorphic evolution, mineral chemistry and thermobarometry of orthogneiss hosting ultrahigh-pressure eclogites in the North Qaidam metamorphic belt: Western China. *Journal of Asian Earth Sciences*, v. 35, no. 3, p. 273-284.
- Metcalf, I., 2011, Palaeozoic–Mesozoic history of SE Asia: Geological Society, London, Special Publications, v. 355, no. 1, p. 7-35.
- Metelkin, D.V., Vernikovskiy, V.A., Kazansky, A.Y., Bogolepova, O.K., and Gubanov, A.P., 2005, Paleozoic history of the Kara microcontinent and its relation to Siberia and Baltica: paleomagnetism, paleogeography and tectonics: *Tectonophysics*, v. 398, no. 3, p. 225-243.
- Molnar, P., and Tapponnier, P., 1975, Cenozoic tectonics of Asia: effects of a continental collision: *Science*, v. 189, no. 4201, p. 419-426.
- Monger, J.W.H., Souther, J.G., and Gabrielse, H., 1972, Evolution of the Canadian Cordillera; a plate-tectonic model: *American Journal of Science*, v. 272, no. 7, p. 577-602.
- Mossakovsky, A.A., Ruzhentsev, S.V., Samygin, S.G., and Kheraskova, T.N., 1993, Geodynamic evolution of the Central-Asia folded belt and history of its development: *Geotectonics*, v. 27, no. 6, p. 3-32.

- Mossakovsky, A.A., Pushcharovsky, Y.M., and Ruzhentsev, S.V., 1998, The Earth's Major Structural Asymmetry: *Geotectonics*, v. 32, no. 5, p. 339-353.
- Mueller, P.A., Heatherington, A.L., Kelly, D.M., Wooden, J.L., and Mogk, D.W., 2002, Paleoproterozoic crust within the Great Falls tectonic zone: Implications for the assembly of southern Laurentia: *Geology*, v. 30, no. 2, p. 127-130.
- Mukhin, P.A., Karimov, Kh.K., Savchuk, Yu.S., 1991. Paleozoic Geodynamics of Kyzylkum. FAN, Tashkent, p. 147 (In Russian).
- Müller, R.D., Gaina, C., Roest, W. R., and Hansen, D.L., 2001, A recipe for microcontinent formation: *Geology*, v. 29, no. 3, p. 203-206.
- Murphy, M. A., Yin, A., Harrison, T.M., Dürr, S.B., Chen, Z., Ryerson, F.J., Kidd, W.S.F., Wang, X., and Zhou, X., 1997, Did the Indo-Asian collision alone create the Tibetan plateau?: *Geology*, v. 25, no. 8, p.719-722.
- Myrow, P.M., Chen, J., Snyder, Z., Leslie, S., Fike, D.A., Fanning, C.M., Yuan, J., and Tang, P., 2015, Depositional history, tectonics, and provenance of the Cambrian-Ordovician boundary interval in the western margin of the North China block: *Geological Society of America Bulletin*, v. 127, no. 9-10, p. 1174-1193.
- Najman, Y., Appel, E., Boudagher-Fadel, M., Bown, P., Carter, A., Garzanti, E., ... & Parrish, R. (2010). Timing of India-Asia collision: Geological, biostratigraphic, and palaeomagnetic constraints. *Journal of Geophysical Research: Solid Earth*, 115(B12).
- Nakajima, T., Maruyama, S., Uchiumi, S., Liou, J. G., Wang, X., Xiao, X., & Graham, S. A. (1990). Evidence for late Proterozoic subduction from 700-Myr-old blueschists in China. *Nature*, 346(6281), 263-265.
- Natal'in, B. A., & Şengör, A. C. (2005). Late Palaeozoic to Triassic evolution of the Turan and Scythian platforms: the pre-history of the Palaeo-Tethyan closure. *Tectonophysics*, 404(3), 175-202.
- Nie, S., Yin, A., Rowley, D.B., and Jin, Y., 1994, Exhumation of the Dabie Shan ultra-high-pressure rocks and accumulation of the Songpan-Ganzi flysch sequence, central China: *Geology*, v. 22, no. 11, p. 999-1002.
- Nikishin, A.M., et al., 1996 Late Precambrian to Triassic history of the East European Craton: dynamics of sedimentary basin evolution: *Tectonophysics*, v. 268, no. 1, p. 23-63.
- Norin, E., 1937, *Geology of Western Quruq Tagh, Eastern Tien-Shan: Reports from the Scientific Expedition to the Northwestern Provinces of China under the Leadership of Dr. Sven Hedin: The Sino-Swedish Expedition*, 194 p.
- Norin, E., 1946, *Geological explorations in western Tibet: The Sino-Swedish Expedition*, 214 p.

- Pan, G., Ding, J., Yao, D., and Wang, L., 2004, Geological map of Qinghai-Xiang (Tibet) plateau and adjacent areas, scale 1:1,500,000: Chengdu, China, Chengdu Institute of Geology and Mineral Resources, China Geological Survey, Chengdu Cartographic Publishing House.
- Pease, V., Daly, J.S., Elming, S. Å., Kumpulainen, R., Moczydlowska, M., Puchkov, V., Roberts, D., Saintot, A., and Stephenson, R., 2008, Baltica in the Cryogenian, 850–630Ma: *Precambrian Research*, v. 160, no. 1, p. 46-65.
- Pei, J., Yang, Z., and Zhao, Y., 2006, A Mesoproterozoic paleomagnetic pole from the Yangzhuang Formation, North China and its tectonics implications: *Precambrian Research*, v. 151, no. 1, p. 1-13.
- Polat, A., Kusky, T., Li, J., Fryer, B., Kerrich, R., and Patrick, K., 2005, Geochemistry of Neoproterozoic (ca. 2.55–2.50 Ga) volcanic and ophiolitic rocks in the Wutaishan greenstone belt, central orogenic belt, North China craton: implications for geodynamic setting and continental growth: *Geological Society of America Bulletin*, v. 117, no. 11-12, p. 1387-1399.
- Polat, A., et al., 2006, Geochemical and petrological evidence for a suprasubduction zone origin of Neoproterozoic (ca. 2.5 Ga) peridotites, central orogenic belt, North China craton: *Geological Society of America Bulletin*, v. 118, no. 7-8, p. 771-784.
- Portnyagin, E.A., 1974, Parallel dike complex of the southern Gissar: *Dok. Akad. Nauk SSSR*, v. 219, p. 67-69.
- Proust, J.N., Chuvashov, B.I., Vennin, E., and Boisseau, T., 1998, Carbonate platform drowning in a foreland setting: the mid-carboniferous platform in western urals (Russia): *Journal of Sedimentological Research*, v. 68, p. 1175-1188.
- Puchkov, V.N., 1997, Structure and geodynamics of the Uralian orogen: *Geological Society London Special Publications*, v. 121, no. 1, p. 201-236.
- Puchkov, V.N., 2000, Paleogeodynamics of the Southern and Middle Urals: *Dauria Ufa*.
- Puchkov, V.N., 2009, The diachronous (step-wise) arc–continent collision in the Urals: *Tectonophysics*, v. 479, no. 1, p. 175-184.
- Puchkov, V.N., et al., 2013, The ca. 1380Ma Mashak igneous event of the Southern Urals: *Lithos*, v. 174, p. 109-124.
- Pullen, A., Kapp, P., Gehrels, G. E., Vervoort, J. D., and Ding, L., 2008, Triassic continental subduction in central Tibet and Mediterranean-style closure of the Paleo-Tethys Ocean: *Geology*, v. 36, no. 5, p. 351-354.
- Qi, X.X., 2003, Large size ductile strike-slip shearing and the formation of Qilian Caledonian Orogen [Ph.D Thesi]: Chinese Academy of Geological Sciences, Beijing, 119 p.

- Qian, Q., Wang, Y.M., Li, H.M., Jia, X.Q., Han, S., and Zhang, Q., 1998, Geochemical characteristics and genesis of diorites from Laohushan, Gansu Province: *Yanshi Xuebao*, v. 14, p. 520-528 [in Chinese with English abstract].
- Qinghai BGMR (Bureau of Geology and Mineral Resources), 1991, Regional geology of Qinghai Province: Beijing, China, Geological Publishing House, 662 p.
- Quan, S., Jia, Q., Guo, Z., and Wang, W., 2006, Basic characteristics of granitoids related to tungsten mineralization in the Qilian mountain: *Mineralium Deposita*, v. 25, p. 143-146.
- Rainbird, R.H., Stern, R.A., Khudoley, A.K., Kropachev, A.P., Heaman, L.M., and Sukhorukov, V.I., 1998, U–Pb geochronology of Riphean sandstone and gabbro from southeast Siberia and its bearing on the Laurentia–Siberia connection: *Earth and Planetary Science Letters*, v. 164, no. 3, p. 409-420.
- Ratschbacher, L., et al., 2003, Tectonics of the Qinling (Central China): tectonostratigraphy, geochronology, and deformation history: *Tectonophysics*, v. 366, no. 1, p. 1-53.
- Reith, R.C., 2013, Structural geology of a central segment of the Qilian Shan-Nan Shan thrust belt: Implications for the magnitude of Cenozoic shortening in the northeastern Tibetan Plateau [M.S. thesis]: Los Angeles, University of California, 73 p.
- Remizov, D., & Pease, V. (2004). The Dzela complex, Polar Urals, Russia: a Neoproterozoic island arc. *Geological Society, London, Memoirs*, 30(1), 107-123.
- Ren, J.S., Wang, Z.X., Chen, B.W., Jiang, C.F., Niu, B.G., Li, J.Y., Xie, G.L., He, Z.J., Liu, Z.G., 1999, The Tectonics of China from a Global View: a Guide to the Tectonic Map of China and Adjacent Regions: Geological Publishing House, Beijing. 32 p.
- Ren, J., Tamaki, K., Li, S., and Junxia, Z., 2002, Late Mesozoic and Cenozoic rifting and its dynamic setting in Eastern China and adjacent areas: *Tectonophysics*, v. 344, no. 3, p. 175-205.
- Ren, J., Niu, B., Wang, J., Jin, X., Zhao, L., and Liu, R., 2013, Advances in research of Asian geology—A summary of 1: 5M International Geological Map of Asia project: *Journal of Asian Earth Sciences*, v. 72, p. 3-11.
- Rojas-Agramonte, Y., Kröner, A., Demoux, A., Xia, X., Wang, W., Donskaya, T., Liu, D., and Sun, M., 2011, Detrital and xenocrystic zircon ages from Neoproterozoic to Palaeozoic arc terranes of Mongolia: significance for the origin of crustal fragments in the Central Asian Orogenic Belt: *Gondwana Research*, v. 19, no. 3, p. 751-763.
- Ronov, A., Khain, V., and Seslavinski, A., 1984, Atlas of lithological paleogeographical maps of the world: Late Precambrian and Paleozoic of the Continents: USSR Academy of Science, 70 p.

- Ross, G.M., and Eaton, D.W., 2002, Proterozoic tectonic accretion and growth of western Laurentia: results from Lithoprobe studies in northern Alberta: *Canadian Journal of Earth Sciences*, v. 39, no. 3, p. 313-329.
- Ross, G.M., and Villeneuve, M., 2003, Provenance of the Mesoproterozoic (1.45 Ga) Belt basin (western North America): Another piece in the pre-Rodinia paleogeographic puzzle: *Geological Society of America Bulletin*, v. 115, no. 10, p. 1191-1217.
- Ross, G.M., Parrish, R.R., and Winston, D., 1992, Provenance and U-Pb geochronology of the Mesoproterozoic Belt Supergroup (northwestern United States): Implications for age of deposition and pre-Panthalassa plate reconstructions: *Earth and Planetary Science Letters*, v. 113, no. 1-2, p. 57-76.
- Saidi, A., Brunet, M. F., and Ricou, L.E., 1997, Continental accretion of the Iran Block to Eurasia as seen from Late Paleozoic to Early Cretaceous subsidence curves: *Geodynamica Acta*, v. 10, no. 5, p. 189-208.
- Santosh, M., 2010, Assembling North China Craton within the Columbia supercontinent: the role of double-sided subduction: *Precambrian Research*, v. 178, no. 1, p. 149-167.
- Santosh, M., Sajeev, K., and Li, J.H., 2006, Extreme crustal metamorphism during Columbia supercontinent assembly: evidence from North China Craton: *Gondwana Research*, v. 10, no. 3, p. 256-266.
- Santosh, M., Wilde, S.A., and Li, J.H., 2007, Timing of Paleoproterozoic ultrahigh-temperature metamorphism in the North China Craton: evidence from SHRIMP U-Pb zircon geochronology: *Precambrian Research*, v. 159, no. 3, p. 178-196.
- Savelieva, G.N., Sharaskin, A.Y., Saveliev, A.A., Spadea, P., Pertsev, A.N., and Babarina, I.I., 2002, Ophiolites and zoned mafic-ultramafic massifs of the Urals: a comparative analysis and some tectonic implications: *Mountain building in the Uralides: Pangea to the present*, p. 135-153.
- Scarrow, J.H., Pease, V., Fleutelot, C., and Dushin, V., 2001, The late Neoproterozoic Engenepe ophiolite, Polar Urals, Russia: an extension of the Cadomian arc?: *Precambrian Research*, v. 110, no. 1, p. 255-275.
- Schubert, G., and Tackley, P.J., 1995, Mantle dynamics: The strong control of the spinel-perovskite transition at a depth of 660 km. *Journal of Geodynamics*, v. 20, p. 417-428.
- Scotese, C.R., and McKerrow, W.S., 1990, Revised world maps and introduction: *Geological Society, London, Memoirs*, v. 12, no. 1, p. 1-21.
- Sears, J.W., and Price, R.A., 1978, The Siberian connection: a case for Precambrian separation of the North American and Siberian cratons: *Geology*, v. 6, no. 5, p. 267-270.



- Seltmann, R., Konopelko, D., Biske, G., Divaev, F., and Sergeev, S., 2011, Hercynian post-collisional magmatism in the context of Paleozoic magmatic evolution of the Tien Shan orogenic belt: *Journal of Asian Earth Sciences*, v. 42, no. 5, p. 821-838.
- Sengör, A.M.C., 1984, The cimmeride orogenic system and the tectonics of Eurasia: *Geological Society of America Special paper*, v. 195, 82 pp.
- Şengör, A.M.C., and Natal'in, B.A., 1996, Paleotectonics of Asia: fragments of a synthesis, *in* Yin, A. and Harrison, T.M., eds., *Tectonic Evolution of Asia*: New York, Cambridge Univ. Press, p. 486-640.
- Şengör, A.M.C., Natal'in, B.A., and Burtman, V.S., 1993, Evolution of the Altaid Tectonic Collage and Paleozoic Crustal Growth in Eurasia: *Nature*, v. 364, no. 6435, p. 299–307, doi: 10.1038/364299a0.
- Shchipansky, A.A., Samsonov, A.V., Petrova, A.Y., and Larionova, Y.O., 2007, Geodynamics of the Eastern Margin of Sarmatia in the Paleoproterozoic: *Geotectonics*, v. 41, no. 1, p 38-62.
- Shu, L.S., Deng, X.L., Zhu, W.B., Ma, D.S., and Xiao, W.J., 2011, Precambrian tectonic evolution of the Tarim Block, NW China: New geochronological insights from the Quruqtagh domain: *Journal of Asian Earth Science*, v. 42, p. 774–790.
- Shu, L.S., Yu, J.H., Charvet, J., Laurent-Charvet, S., Zhang, R.G., and Sang, H.Q., 2004, Geological, geochronological and geochemical features of granulites in the Eastern Tianshan, NW China: *Journal of Asian Earth Sciences*, v. 24, no. 1, p. 25–41.
- Smith, A.D., 2006, The geochemistry and age of ophiolitic strata of the Xinglongshan Group: Implications for the amalgamation of the Central Qilian belt: *Journal of Asian Earth Sciences*, v. 28, p. 133-142.
- Sobel, E.R., and Arnaud, N., 1999, A possible middle Paleozoic suture in the Altyn Tagh, NW China: *Tectonics*, v. 18, no. 1, p. 64-74.
- Sone, M., and Metcalfe, I., 2008, Parallel Tethyan sutures in mainland Southeast Asia: new insights for Palaeo-Tethys closure and implications for the Indosinian orogeny: *Comptes Rendus Geoscience*, v. 340, no. 2, p. 166-179.
- Song, C., 2006, *Sedimentary system and sedimentary features of central Junggar Basin*: Beijing, Geological Publishing House.
- Song, S., Niu, Y., Su, L., and Xia, X., 2013, Tectonics of the North Qilian orogen, NW China: *Gondwana Research*, v. 23, no. 4, p. 1378-1401.
- Song, S., Niu, Y., Su, L., Zhang, C., and Zhang, L., 2014, Continental orogenesis from ocean subduction, continent collision/subduction, to orogen collapse, and orogen recycling: The example of the North Qaidam UHPM belt, NW China: *Earth-Science Reviews*, v. 129, p. 59-84.

- Sovetov, Y.K., 1990, The Precambrian–Cambrian Boundary and Precambrian Sedimentary Assemblages in the Lesser Karatau: Stratigraphic, Sedimentologic and Paleotectonic Aspects: Russian Academy of Sciences, Novosibirsk, Preprint 14, 36 p. (in Russian).
- Stampfli, G. M. (2000). Tethyan oceans: Geological Society of London, Special Publications, v.173, no. 1, p. 1-23.
- Stampfli, G.M., and Borel, G.D., 2002, A plate tectonic model for the Paleozoic and Mesozoic constrained by dynamic plate boundaries and restored synthetic oceanic isochrons: *Earth and Planetary Science Letters*, v. 196, no. 1, p. 17-33.
- Stampfli, G.M., Hochard, C., V  rard, C., and Wilhem, C., 2013, The formation of Pangea: *Tectonophysics*, v. 593, p. 1-19.
- Stampfli, G.M., Von Raumer, J., and Wilhem, C., 2011, The distribution of Gondwana derived terranes in the early Paleozoic, *in* Guti  rrez-Marco, J.C., R  bano, I., and Garc  a-Bellido, D., eds., *Ordovician of the world. Cuadernos del Museo Geominero*, v.14, p. 567-574.
- Stewart, J.H., 1972, Initial deposits in the Cordilleran geosyncline: Evidence of a late Precambrian (< 850 my) continental separation: *Geological Society of America Bulletin*, v. 83, no. 5, p. 1345-1360.
- Stewart, J.H., 1976, Late Precambrian evolution of North America: plate tectonics implication: *Geology*, v. 4, no. 1, p. 11-15.
- Su, J.P., Zhang, X.H., Hu, N.G., Fu, G.M., and Zhang, H.F., 2004, Geochemical characteristics and genesis of adakite-like granites at Yema Nanshan in the western segment of the Central Qilian Mountains: *Chinese Geology*, v. 31, no. 1, p. 365-371 (in Chinese with English abstract).
- Suess, E., 1901, *The face of the Earth (Das Antlitz der Erde)*, v. 3, pt. 1., trans. H.B.C. Sollas and W.J. Sollas: Oxford, Clarendon Press.
- Sun, J.F., Yang, J. H., Wu, F.Y., and Wilde, S.A., 2012, Precambrian crustal evolution of the eastern North China Craton as revealed by U–Pb ages and Hf isotopes of detrital zircons from the Proterozoic Jing’eryu Formation: *Precambrian Research*, v. 200, p. 184-208.
- Tam, P.Y., Zhao, G., Liu, F., Zhou, X., Sun, M., and Li, S., 2011, Timing of metamorphism in the Paleoproterozoic Jiao-Liao-Ji Belt: new SHRIMP U–Pb zircon dating of granulites, gneisses and marbles of the Jiaobei massif in the North China Craton: *Gondwana Research*, v. 19, no. 1, p. 150-162.
- Tapponnier, P., Peltzer, G., Le Dain, A. Y., Armijo, R., and Cobbold, P., 1982, Propagating extrusion tectonics in Asia: New insights from simple experiments with plasticine: *Geology*, v. 10, no. 12, 611-616.

- Thomas, J.C., Cobbold, P.R., Shein, V.S., and Le Douaran, S., 1999a, Sedimentary record of late Paleozoic to Recent tectonism in central Asia—analysis of subsurface data from the Turan and south Kazakh domains: *Tectonophysics*, v. 313, no. 3, p. 243-263.
- Thomas, J.C., Grasso, J.R., Bossu, R., Martinod, J., and Nurtaev, B., 1999b, Recent deformation in the Turan and South Kazakh platforms, western central Asia, and its relation to Arabia-Asia and India-Asia collision: *Tectonics*, v. 18, no. 2, p. 201-214.
- Torsvik, T. H., & Andersen, T. B. (2002). The Taimyr fold belt, Arctic Siberia: timing of prefold remagnetisation and regional tectonics. *Tectonophysics*, 352(3), 335-348.
- Torsvik, T. H., Smethurst, M. A., Meert, J. G., Van der Voo, R., McKerrow, W. S., Brasier, M. D., ... & Walderhaug, H. J. (1996). Continental break-up and collision in the Neoproterozoic and Palaeozoic—a tale of Baltica and Laurentia. *Earth-Science Reviews*, 40(3), 229-258.
- Trap, P., Faure, M., Lin, W., and Monié, P., 2007, Late Paleoproterozoic (1900–1800 Ma) nappe-stacking and polyphase deformation in the Hengshan–Wutaishan area: implications for the understanding of the Trans-North-China Belt, North China Craton: *Precambrian Research*, v. 156, p. 85–106.
- Trap, P., Faure, M., Lin, W., Bruguier, O., and Monié, P., 2008, Contrasted tectonic styles for the Paleoproterozoic evolution of the North China Craton. Evidence for a ~2.1Ga thermal and tectonic event in the Fuping Massif: *Journal of Structural Geology*, v. 30, p. 1109–1125.
- Trap, P., Faure, M., Lin, W., Le Breton, N., and Monié, P., 2011, Paleoproterozoic tectonic evolution of the Trans-North China Orogen: toward a comprehensive model: *Precambrian Research*, v. 222-223, p. 191-211.
- Trap, P., Faure, M., Lin, W., Le Breton, N., and Monié, P., 2012, Paleoproterozoic tectonic evolution of the Trans-North China Orogen: Toward a comprehensive model: *Precambrian Research*, v. 222-223, p. 191–211.
- Trap, P., Faure, M., Lin, W., Monié, P., and Meffre, S., 2009b, The Lüliang Massif: a key area for the understanding of the Palaeoproterozoic, in, Evans, D., Reddy, S., Collins, A., eds., *Palaeoproterozoic Supercontinents and Global Evolution: Geological Society of London Special Publication*, v. 323 p. p. 99–125.
- Trap, P., Faure, M., Lin, W., Monié, P., Meffre, S., and Melleton, J., 2009a, The Zhanhuang Massif, the second and eastern suture zone of the Paleoproterozoic Trans-North China Orogen: *Precambrian Research*, v. 172, p. 80–98.
- Traynor, J.J., and Sladen, C., 1995, Tectonic and stratigraphic evolution of the Mongolian People's Republic and its influence on hydrocarbon geology and potential: *Marine and Petroleum Geology*, v. 12, no. 1, p. 35-52.
- Tseng, C.Y., Yang, H. J., Yang, H.Y., Liu, D., Tsai, C.L., Wu, H., and Zuo, G., 2007, The Dongcaohe ophiolite from the North Qilian Mountains: a fossil oceanic crust of the Paleoproterozoic ocean: *Chinese Science Bulletin*, v. 52, no. 17, p. 2390-2401.

- Tseng, C.Y., Yang, H.J., Yang, H. Y., Liu, D., Wu, C., Cheng, C.K., Chen, C.H., and Ker, C. M., 2009, Continuity of the North Qilian and North Qinling orogenic belts, Central Orogenic System of China: evidence from newly discovered Paleozoic adakitic rocks; *Gondwana Research*, v. 16, no. 2, p. 285-293.
- Tseng, C.Y., Yang, H.Y., Yusheng, W., Dunyi, L., Wen, D.J., Lin, T.C., and Tung, K. A., 2006, Finding of Neoproterozoic (~ 775 Ma) magmatism recorded in metamorphic complexes from the North Qilian orogen: Evidence from SHRIMP zircon U-Pb dating: *Chinese Science Bulletin*, v. 51, no. 8, p. 963-970.
- Tung, K., Yang, H.J., Yang, H.Y., Liu, D., Zhang, J., Wan, Y., and Tseng, C.Y., 2007, SHRIMP U-Pb geochronology of the zircons from the Precambrian basement of the Qilian Block and its geological significances: *Chinese Science Bulletin*, v. 52, no. 19, p. 2687-2701.
- Tung, K.A., Yang, H. Y., Liu, D.Y., Zhang, J.X., Yang, H.J., Shau, Y.H., and Tseng, C.Y., 2013, The Neoproterozoic granitoids from the Qilian block, NW China: evidence for a link between the Qilian and South China blocks: *Precambrian Research*, v. 235, p. 163-189.
- Turner, S.A., 2010, Sedimentary record of late Neoproterozoic rifting in the NW Tarim Basin, China: *Precambrian Research*, v. 181, no. 1, p. 85-96.
- Ulmishek, G. F., 2001a, Petroleum geology and resources of the Middle Caspian Basin, former Soviet Union: *U.S. Geological Survey Bulletin*, no. 2201-A, 38 p.
- Ulmishek, G. F., 2001b, Petroleum geology and resources of the North Ustyurt Basin, Kazakhstan and Uzbekistan: *U.S. Geological Survey Bulletin*, no. 2201-D, 14 p.
- Van Der Woerd, J., Ryerson, F.J., Tapponnier, P., Meriaux, A.S., Gaudemer, Y., Meyer, B., Finkel, R.C., Caffee, M.W., Guoguang, Z., and Zhiqin, X., 2000, Uniform slip-rate along the Kunlun Fault: Implications for seismic behaviour and large-scale tectonics: *Geophysical Research Letters*, v. 27, no. 16, p. 2353-2356.
- Van Der Woerd, J., Tapponnier, P., Ryerson, F.J., Meriaux, A.S., Meyer, B., Gaudemer, Y., Finkel, R.C., Caffee, M.W., Guoguan, Z. and Zhiqin, X., 2002, Uniform postglacial slip-rate along the central 600 km of the Kunlun Fault (Tibet), from <sup>26</sup>Al, <sup>10</sup>Be, and <sup>14</sup>C dating of riser offsets, and climatic origin of the regional morphology: *Geophysical Journal International*, v. 148, no. 3, p.356-388.
- Van Hinsbergen, D.J., Kapp, P., Dupont-Nivet, G., Lippert, P. C., DeCelles, P.G., and Torsvik, T.H., 2011, Restoration of Cenozoic deformation in Asia and the size of Greater India: *Tectonics*, v. 30, no. 5.
- Vernikovsky, V.A., 1997. Neoproterozoic and late Paleozoic Taimyr Orogenic and ophiolitic belts, North Asia: a review and models for their formation: *Proceedings of the 30th International Geologic Congress, Beijing, China*, v. 7, p. 121-138.
- Vervoort, J.D., Lewis, R.S., Fisher, C., Gaschnig, R.M., Jansen, A.C., and Brewer, R., 2016, Neoproterozoic and Paleoproterozoic crystalline basement rocks of north-central Idaho:

- Constraints on the formation of western Laurentia: *Geological Society of America Bulletin*, v. 128, no. 1-2, p. 94-109.
- Volkova, N.I., and Budanov, V.I., 1999, Geochemical discrimination of metabasalt rocks of the Fan–Karategin transitional blueschist/greenschist belt, South Tianshan, Tajikistan: seamount volcanism and accretionary tectonics: *Lithos*, v. 47, no. 3, p. 201-216.
- Volozh, Y., Talbot, C., and Ismail-Zadeh, A., 2003, Salt structures and hydrocarbons in the Pricaspian basin: *AAPG bulletin*, v. 87, no. 2, p. 313-334.
- Volozh, Y.A., Antipov, M.P., Leonov, Y.G., Moroz, A.F., Yurov, Y.A., 1999, Structure of the Karpinsky Range: *Geotectonics*, v. 33, p. 28-43.
- Volvovsky, I.S., Garetzkiy, R.G., Shlezinger, A.E., Shraybman, V.N., 1966, *Tektonika Turanskoy Plity*. Nauka, Moscow.
- von Raumer, J.F., and Stampfli, G.M., 2008, The birth of the Rheic Ocean—Early Palaeozoic subsidence patterns and subsequent tectonic plate scenarios: *Tectonophysics*, v. 461, no. 1, p. 9-20.
- Wan, Y.S., Xu, Z.Q., Yan, J.S., and Zhang, J.X., 2001. Ages and compositions of the Precambrian high-grade basement of the Qilian Terrane and its adjacent areas: *Acta Geologica Sinica*, v. 75, p. 375-384.
- Wan, Y.S., Xu, Z.Q., Yang, J.S., and Zhang, J.X., 2003a. The Precambrian high-grade basement of the Qilian terrane and neighboring areas: its ages and compositions: *Acta Geoscientia Sinica*, v. 24, no. 4, p. 319-324 (in Chinese with English abstract).
- Wan, Y., Zhang, Q., and Song, T., 2003b, SHRIMP ages of detrital zircons from the Changcheng System in the Ming Tombs area, Beijing: constraints on the protolith nature and maximum depositional age of the Mesoproterozoic cover of the North China Craton: *Chinese Science Bulletin*, v. 48, no. 22, p. 2500-2506.
- Wan, Y., Song, B., Liu, D., Wilde, S. A., Wu, J., Shi, Y., Yin, X., and Zhou, H., 2006, SHRIMP U–Pb zircon geochronology of Palaeoproterozoic metasedimentary rocks in the North China Craton: evidence for a major Late Palaeoproterozoic tectonothermal event: *Precambrian Research*, v. 149, no. 3, p. 249-271.
- Wan, Y., Liu, D., Wang, W., Song, T., Kröner, A., Dong, C., Zhou, H., and Yin, X., 2011, Provenance of Meso- to Neoproterozoic cover sediments at the Ming Tombs, Beijing, North China Craton: an integrated study of U–Pb dating and Hf isotopic measurement of detrital zircons and whole-rock geochemistry: *Gondwana Research*, v. 20, no. 1, p. 219-242.
- Wang, Q., and Liu, X.Y., 1976, The ancient oceanic crust and its tectonic implications, North Qilian Mountains, China: *Scientia Geologica Sinica*, v. 1, p. 42–55 (in Chinese with English abstract).

- Wang, Q., Liu, X.Y., 1981. On Caledonian polycyclic paired metamorphic belts of Qilian Mountains, northwest China, *in* Huang, T.K., and Li, C.Y. (eds.): Contributions to Tectonics of China and Adjacent Regions, Geological Publishing House, Beijing, p. 92–101 (in Chinese with English abstract).
- Wang, G.P., Wu, G.T., Lun, Zh. Q., and Zhu, Y.Y., 1993, Regional geology of Xinjiang Uygur Autonomous Region: Bureau of Geology and Mineral Resources of Xinjiang Uygur Autonomous Region, Geological Memoirs Series, v. 1, 841 p.
- Wang, A.G., Zhang, C.L., and Guo, K.Y., 2004. Depositional types and its tectonic significance of lower member of Nanhuan System in North margin of West Kunlun: Journal of Stratigraphy, v. 28, p. 248-256 (in Chinese with English abstract).
- Wang, T., Hong, D.W., Jahn, B.M., Tong, Y., Wang, Y.B., Han, B.F., and Wang, X.X., 2006, Timing, petrogenesis, and setting of Paleozoic synorogenic intrusions from the Altai Mountains, Northwest China: implications for the tectonic evolution of an accretionary orogen: The Journal of Geology, v. 114, no. 6, p. 735-751.
- Wang, Q., Chen, N., Li, X., Hao, S., and Chen, H., 2008, LA-ICPMS zircon U-Pb geochronological constraints on the tectonothermal evolution of the Early Paleoproterozoic Dakendaban Group in the Quanji Block, NW China: Chinese Science Bulletin, v. 53, no. 18, p. 2849-2858.
- Wang, H., Gao, R., Zeng, L., Kuang, Z., Xue, A., Li, W., Xiong, X., and Huang, W., 2014, Crustal structure and Moho geometry of the northeastern Tibetan plateau as revealed by SinoProbe-02 deep seismic-reflection profiling: Tectonophysics, v. 636, p. 32-39.
- Wang, C., Liu, L., Wang, Y. H., He, S. P., Li, R. S., Li, M., Yang, W.Q., Cao, Y.T., Collins, A.S., Shi, C., and Wu, Z.N., 2015a, Recognition and tectonic implications of an extensive Neoproterozoic volcano-sedimentary rift basin along the southwestern margin of the Tarim Craton, northwestern China: Precambrian Research, v. 257, p. 65-82.
- Wang, C., Zhang, J.H., Li, M., Li, R.S., and Peng, Y., 2015b, Generation of ca. 900–870Ma bimodal rifting volcanism along the southwestern margin of the Tarim Craton and its implications for the Tarim–North China connection in the early Neoproterozoic: Journal of Asian Earth Sciences, v. 113, p. 610-625.
- Wang, J., Hu, X., Jansa, L., and and Huang, Z., 2011a, Provenance of the Upper Cretaceous–Eocene deep-water sandstones in Sangdanlin, southern Tibet: Constraints on the timing of initial India-Asia collision: The Journal of Geology, v. 119, no. 3, p. 293-309.
- Wang, L.Q., Pan, G.T., Ding, J., and Yao, D.S. (compiler), 2013, Geological map of the Tibetan plateau at a scale of 1:1.5 M with explanations: Geological Publishing House, Beijing, 288 p.
- Wang, X.L., Jiang, S.Y., Dai, B.Z., Griffin, W.L., Dai, M.N., and Yang, Y.H., 2011b, Age, geochemistry and tectonic setting of the Neoproterozoic (ca 830Ma) gabbros on the southern margin of the North China Craton: Precambrian Research, v. 190, no. 1, p. 35-47.

- Webb, L.E., Hacker, B.R., Ratschbacher, L., McWilliams, M.O., and Dong, S., 1999, Thermochronologic constraints on deformation and cooling history of high-and ultrahigh-pressure rocks in the Qinling-Dabie orogen, eastern China: *Tectonics*, v. 18, no. 4, p. 621-638.
- Whitmeyer, S.J., and Karlstrom, K.E., 2007, Tectonic model for the Proterozoic growth of North America: *Geosphere*, v. 3, no. 4, p. 220-259.
- Windley, B.F., Alexeiev, D., Xiao, W., Kröner, A., and Badarch, G., 2007, Tectonic models for accretion of the Central Asian Orogenic Belt: *Journal of the Geological Society*, v. 164, no. 1, p. 31-47.
- Wu, C., Yang, J., Wooden, J. L., Shi, R., Chen, S., Meibom, A., and Mattinson, C., 2004, Zircon U-Pb SHRIMP dating of the Yematan batholith in Dulan, north Qaidam, NW China: *Chinese Science Bulletin*, v. 49, no. 16, p. 1736-1740.
- Wu, C.L., Yao, S., Zeng, L., Yang, J., Wooden, J., Chen, S., and Mazadab, F., 2006, Double subduction of the early Paleozoic North Qilian oceanic plate: Evidence from granites in the central segment of North Qilian, NW China: *Geology in China*, v. 33, p. 1197–1208.
- Wu, C.L., Xu, X.Y., Gao, Q.M., Li, X.M., Lei, M., Gao, Y.H., Frost, B.R., and Wooden, J., 2010, Early Palaeozoic granitoid magmatism and tectonic evolution in North Qilian, NW China: *Yanshi Xuebao*, v. 26, p. 1027–1044 (in Chinese with English abstract).
- Wu, C., Yin, A., Zuza, A. V., Zhang, J., Liu, W., Ding, L., 2016, Pre-Cenozoic Geologic History of the Central and Northern Tibetan Plateau and the Role of Wilson Cycles in Constructing the Tethyan Orogenic System: *Lithosphere*, in press.
- Xia, X., and Song, S., 2010, Forming age and tectono-petrogenises of the Jiugequan ophiolite in the North Qilian Mountain, NW China: *Chinese Science Bulletin*, v. 55, no. 18, p. 1899-1907.
- Xiang, Z.Q., Lu, S.N., Li, H.K., Li, H.M., Song, B., and Zheng, J.K., 2007, SHRIMP U-Pb zircon age of gabbro in Aoyougou in the western segment of the North Qilian Mountains, China and its geological implications: *Geological Bulletin of China*, v. 26, p. 1686–1691.
- Xiao, X.C., Chen, G.M., Zhu, Z.Z., 1974, Some knowledge about the paleo-plate tectonics of the Qilian Mountains: *Geological Science and Technology*, v. 3, p. 73-78 (in Chinese with English abstract).
- Xiao, X.C., Chen, G.M., and Zhu, Z.Z., 1978, A preliminary study on the tectonics of ancient ophiolites in the Qilian Mountain, Northwest China: *Acta Geologica Sinica*, v. 52, no. 4, p. 281-295.
- Xiao, W., Windley, B. F., Hao, J., and Zhai, M., 2003, Accretion leading to collision and the Permian Solonker suture, Inner Mongolia, China: termination of the central Asian orogenic belt: *Tectonics*, v. 22, no. 6.

- Xiao, W., Han, C., Yuan, C., Sun, M., Lin, S., Chen, H., Li, Z., Li, J., and Sun, S., 2008, Middle Cambrian to Permian subduction-related accretionary orogenesis of Northern Xinjiang, NW China: implications for the tectonic evolution of central Asia: *Journal of Asian Earth Sciences*, v. 32, no. 2, p. 102-117.
- Xiao, W.J., Kröner, A., and Windley, B., 2009a, Geodynamic evolution of Central Asia in the Paleozoic and Mesozoic: *International Journal of Earth Sciences*, v. 98, no. 6, p. 1185-1188.
- Xiao, W.J., Windley, B.F., Huang, B.C., Han, C.M., Yuan, C., Chen, H.L., Sun, M., Sun, S., and Li, J.L., 2009b, End-Permian to mid-Triassic termination of the accretionary processes of the southern Altaids: implications for the geodynamic evolution, Phanerozoic continental growth, and metallogeny of Central Asia: *International Journal of Earth Sciences*, v. 98, no. 6, p. 1189-1217.
- Xiao, W., Windley, B.F., Yong, Y., Yan, Z., Yuan, C., Liu, C., and Li, J., 2009c, Early Paleozoic to Devonian multiple-accretionary model for the Qilian Shan, NW China: *Journal of Asian Earth Sciences*, v. 35, p. 323–333.
- Xiao, W., Huang, B., Han, C., Sun, S., and Li, J., 2010, A review of the western part of the Altaids: a key to understanding the architecture of accretionary orogens: *Gondwana Research*, v. 18, no. 2, p. 253-273.
- Xiao, L.L., Wu, C.M., Zhao, G.C., Guo, J.H., and Ren, L.D., 2011, Metamorphic P–T paths of the Zhanhuang amphibolites and metapelites: constraints on the tectonic evolution of the Paleoproterozoic Trans-North China Orogen: *International Journal of Earth Sciences*, v. 100, no. 4, p. 717-739.
- Xiao, W., Windley, B.F., Allen, M.B., and Han, C., 2013, Paleozoic multiple accretionary and collisional tectonics of the Chinese Tianshan orogenic collage: *Gondwana Research*, v. 23, no. 4, p. 1316-1341.
- Xiao, W., Windley, B.F., Sun, S., Li, J., Huang, B., Han, C., Yuan, C., Sun, M., and Chen, H., 2015, A tale of amalgamation of three Permo-Triassic collage systems in central asia: oroclinal sutures, and terminal accretion: *Annual Review of Earth and Planetary Sciences*, v. 43, p. 477-507.
- Xiong, Z., Zhang, H., and Zhang, J., 2012, Petrogenesis and tectonic implications of the Maozangsi and Huangyanghe granitic intrusions in Lenglongling area, the eastern part of North Qilian Mountain, NW China: *Earth Science Frontiers*, v. 19, p. 214–227.
- Xu, B., Jian, P., Zheng, H., Zou, H., Zhang, L., and Liu, D., 2005, U–Pb zircon geochronology and geochemistry of Neoproterozoic volcanic rocks in the Tarim Block of northwest China: implications for the breakup of Rodinia supercontinent and Neoproterozoic glaciations: *Precambrian Research*, v. 136, no. 2, p. 107-123.
- Xu, X.Y., He, S.P., Wang, H.L., Chen, J.X., Zhang, E.P., Feng, Y.M., 2008, *An Outline to Geology in Northwest China*: Science Press, Beijing, 1-167 p.



- Xu, Y.J., Du, Y.S., Cawood, P. A., Guo, H., Huang, H., and An, Z.H., 2010, Detrital zircon record of continental collision: assembly of the Qilian Orogen, China: *Sedimentary Geology*, v. 230, no. 1, p. 35-45.
- Yakubchuk, A., 2002, The Baikalide-Altai, Transbaikal-Mongolian and North Pacific orogenic collages: similarity and diversity of structural patterns and metallogenic zoning: *Geological Society, London, Special Publications*, v. 204, no. 1, p. 273-297.
- Yan, Z., Xiao, W., Wang, Z., and Li, J., 2007, Integrated analyses constraining the provenance of sandstones, mudstones, and conglomerates, a case study: the Laojunshan conglomerate, Qilian orogen, northwest China: *Canadian Journal of Earth Sciences*, v. 44, no. 7, p. 961-986.
- Yan, Z., Xiao, W.J., Windley, B.F., Wang, Z.Q., and Li, J.L., 2010, Silurian clastic sediments in the North Qilian Shan, NW China: Chemical and isotopic constraints on their forearc provenance with implications for the Paleozoic evolution of the Tibetan Plateau: *Sedimentary Geology*, v. 231, no. 3, p. 98-114.
- Yang, J., Xu, Z., Zhang, J., Chu, C., Zhang, R., and Liou, J. G., 2001, Tectonic significance of Caledonian high pressure rocks in the Qilian-Qaidam-Altun mountains, NW China, *in* Hendrix, M. S., and Davis, G. A. (eds.): *Paleozoic and Mesozoic tectonic evolution of central and eastern Asia: From continental assembly to intracontinental deformation*, *Geological Society of America Memoir* 194, p. 151-170.
- Yang, J.H., Wu, F.Y., Liu, X.M., and Xie, L.W., 2005, Zircon U–Pb ages and Hf isotopes and their geological significance of the Miyun rapakivi granites from Beijing, China: *Acta Petrologica Sinica*, v. 21, p. 1633-1644 (in Chinese with English abstract).
- Yang, J., Du, Y., Cawood, P. A., and Xu, Y., 2012a, Modal and geochemical compositions of the Lower Silurian clastic rocks in North Qilian, NW China: implications for provenance, chemical weathering, and tectonic setting: *Journal of Sedimentary Research*, v. 82, no. 2, p. 92-103.
- Yang, X.F., He, D.F., Wang, Q.C., and Tang, Y., 2012b, Tectonostratigraphic evolution of the Carboniferous arc-related basin in the East Junggar Basin, northwest China: insights into its link with the subduction process: *Gondwana Research*, v. 22, no. 3, p. 1030-1046.
- Yang, J.H., Du, Y.S., Cawood, P.A., and Xu, Y.J., 2009, Silurian collisional suturing onto the southern margin of the North China Craton: detrital zircon geochronology constraints from the Qilian Orogen: *Sedimentary Geology*, v. 220, no. 1, p. 95-104.
- Yao, J., Shu, L., and Santosh, M., 2011, Detrital zircon U–Pb geochronology, Hf-isotopes and geochemistry—new clues for the Precambrian crustal evolution of Cathaysia Block, South China: *Gondwana Research*, v. 20, no. 2, p. 553-567.
- Yin, A., 2002, Passive-roof thrust model for the emplacement of the Pelona-Orocopia Schist in southern California, United States: *Geology*, v. 30, no. 2, p. 183-186.

- Yin, A., 2010, Cenozoic tectonic evolution of Asia: A preliminary synthesis: *Tectonophysics*, v. 488, no. 1, p. 293-325.
- Yin, A., and Harrison, T.M., 2000, Geologic evolution of the Himalayan-Tibetan orogen: *Annual Review of Earth and Planetary Sciences*, v. 28, no. 1, p. 211-280.
- Yin, A., and Nie, S., 1993, An indentation model for the North and South China collision and the development of the Tan-Lu and Honam fault systems, eastern Asia: *Tectonics*, v. 12, no. 4, p. 801–813.
- Yin, A., and Nie, S., 1996, A Phanerozoic palinspastic reconstruction of China and its neighboring regions, *in* Yin, A., and Harrison, T.M., eds., *The tectonics of Asia*: New York, Cambridge University Press, p. 442-485.
- Yin, A., Dang, Y.-Q., Wang, L.-C., Jiang, W.-M., Zhou, S.-P., Chen, X.-H., Gehrels, G.E., and McRivette, M.W., 2008a, Cenozoic tectonic evolution of Qaidam Basin and its surrounding regions (part 1): The southern Qilian Shan–Nan Shan thrust belt and northern Qaidam Basin: *Geological Society of America Bulletin*, v. 120, p. 813-846.
- Yin, A., Dang, Y.Q., Zhang, M., Chen, X.H., and McRivette, M.W., 2008b, Cenozoic tectonic evolution of the Qaidam basin and its surrounding regions (Part 3): Structural geology, sedimentation, and regional tectonic reconstruction: *Geological Society of America Bulletin*, v. 120, p. 847-876.
- Yin, A., Dang, Y.-Q., Zhang, M., McRivette, M.W., Burgess, W.P., and Chen, X.-H., 2007a, Cenozoic tectonic evolution of Qaidam Basin and its surrounding regions (part 2): Wedge tectonics in southern Qaidam Basin and the Eastern Kunlun Range, *in* Sears, J.W., et al., eds., *Whence the Mountains? Inquiries into the evolution of orogenic systems: A volume in honor of Raymond A. Price*: Geological Society of America Special Paper 433, p. 369–390.
- Yin, A., Manning, C.E., Lovera, O., Menold, C.A., Chen, X., and Gehrels, G.E., 2007b, Early Paleozoic tectonic and thermomechanical evolution of ultrahigh-pressure (UHP) metamorphic rocks in the northern Tibetan Plateau, northwest China: *International Geology Review*, v. 49, p. 681-716.
- Ying, J.F., Zhou, X. H., Su, B.X., and Tang, Y.J., 2011, Continental growth and secular evolution: Constraints from U-Pb ages and Hf isotope of detrital zircons in Proterozoic Jixian sedimentary section (1.8–0.8 Ga), North China Craton: *Precambrian Research*, v. 189, no. 3, p. 229-238.
- Yong, W., Zhang, L., Hall, C.M., Mukasa, S.B., and Essene, E. J., 2013, The  $^{40}\text{Ar}/^{39}\text{Ar}$  and Rb–Sr chronology of the Precambrian Aksu blueschists in western China: *Journal of Asian Earth Sciences*, v. 63, p. 197-205.
- Zanchi, A., Zanchetta, S., Garzanti, E., Balini, M., Berra, F., Mattei, M., and Muttoni, G., 2009, The Cimmerian evolution of the Naxhlak–Anarak area, Central Iran, and its bearing for the reconstruction of the history of the Eurasian margin: *Geological Society of London, Special Publications*, v. 312, no. 1, p. 261-286.

- Zhang, C.L., Li, Z.X., Li, X.H., Ye, H., Wang, A., and Guo, K.Y., 2006a, Neoproterozoic bimodal intrusive complex in the southwestern Tarim Block, Northwest China: age, geochemistry, and implications for the rifting of Rodinia: *International Geology Review*, v. 48, no. 2, p. 112-128.
- Zhang, S., Li, Z.X., and Wu, H., 2006b, New Precambrian palaeomagnetic constraints on the position of the North China Block in Rodinia. *Precambrian Research*, v. 144, no. 3, p. 213-238.
- Zhang, C.L., Li, H.K., Santosh, M., Li, Z.X., Zou, H.B., Wang, H., and Ye, H., 2012, Precambrian evolution and cratonization of the Tarim Block, NW China: Petrology, geochemistry, Nd-isotopes and U–Pb zircon geochronology from Archaean gabbro-TTG–potassic granite suite and Paleoproterozoic metamorphic belt: *Journal of Asian Earth Sciences*, v. 47, p. 5-20.
- Zhang, C.L., Zou, H.B., Li, H.K., and Wang, H.Y., 2013, Tectonic framework and evolution of the Tarim Block in NW China: *Gondwana Research*, v. 23, no. 4, p. 1306-1315.
- Zhang, S.C., Hanson, A.D., Moldowan, J.M., Graham, S.A., Liang, D.G., Chang, E., and Fago, F., 2000, Paleozoic oil–source rock correlations in the Tarim basin, NW China: *Organic Geochemistry*, v. 31, no. 4, p. 273-286.
- Zhang, C.L., Li, X.H., Li, Z.X., Lu, S.N., Ye, H.M., and Li, H.M., 2007, Neoproterozoic ultramafic–mafic-carbonatite complex and granitoids in Quruqtagh of northeastern Tarim Block, western China: Geochronology, geochemistry and tectonic implications: *Precambrian Research*, v. 152, no. 3, p. 149-169.
- Zhang, K.J., 1997, North and South China collision along the eastern and southern North China margins: *Tectonophysics*, v. 270, no. 1-2, p. 145-156.
- Zhang, S.H., Zhao, Y., Davis, G. A., Ye, H., and Wu, F., 2014, Temporal and spatial variations of Mesozoic magmatism and deformation in the North China Craton: implications for lithospheric thinning and decratonization: *Earth-Science Reviews*, v. 131, p. 49-87.
- Zhao, G., 2009, Metamorphic evolution of major tectonic units in the basement of the North China Craton: key issues and discussion: *Acta Petrologica Sinica*, v. 25, p. 1772–1792.
- Zhao, G., and Cawood, P.A., 2012, Precambrian geology of China: *Precambrian Research*, v. 222-223, p. 13–54.
- Zhao, G., Cawood, P.A., Li, S., Wilde, S.A., Sun, M., Zhang, J., He, Y., Yin, C., 2012, Amalgamation of the North China Craton: key issues and discussion: *Precambrian Research*, v. 222-223, p. 55-76.
- Zhao, G., Cawood, P.A., Wilde, S.A., and Sun, M., 2002. Review of global 2.1-1.8 Ga orogens: Implications for a pre-Rodinia supercontinent, *Earth-Science Reviews*, 59, 125-162.

- Zhao, G.C., Cawood, P.A., Wilde, S.A., and Lu, L.Z., 2000a, Metamorphism of basement rocks in the Central Zone of the North China Craton: implications for Paleoproterozoic tectonic evolution: *Precambrian Research*, v. 103, p. 55–88.
- Zhao, G.C., Cawood, P.A., Wilde, S.A., and Lu, L.Z., 2001b, High-pressure granulites (retrograded eclogites) from the Hengshan Complex North China Craton: petrology and tectonic implications: *Journal of Petrology*, v. 42, p. 1141–1170.
- Zhao, G.C., Kroner, A., Wilde, S.A., Sun, M., Li, S.Z., Li, X.P., Zhang, J., Xia, X.P., and He, Y.H., 2007, Lithotectonic elements and geological events in the Hengshan–Wutai–Fuping belt: a synthesis and implications for the evolution of the Trans-North China Orogen: *Geologic Magazine*, v. 144, p. 753–775.
- Zhao, G.C., Sun, M., Wilde, S.A., and Guo, J.H., 2004, Late Archean to Palaeoproterozoic evolution of the Trans-North China Orogen: insights from synthesis of existing data from the Hengshan–Wutai–Fuping belt, in Malpas, J., Fletcher, C.J.N., Ali, J.R., Aitchison, J.C., eds., *Aspects of the Tectonic Evolution of China*: Geological Society of London, p. 27–55.
- Zhao, G.C., Sun, M., Wilde, S.A., and Li, S.Z., 2005, Late Archean to Paleoproterozoic evolution of the North China Craton: key issues revisited: *Precambrian Research*, v. 136, p. 177–202.
- Zhao, G.C., Wilde, S.A., Cawood, P.A., and Lu, L.Z., 1998, Thermal evolution of Archean basement rocks from the eastern part of the North China Craton and its bearing on tectonic setting: *International Geology Review*, v. 40, p. 706–721.
- Zhao, G.C., Wilde, S.A., Cawood, P.A., and Lu, L.Z., 1999, Tectonothermal history of the basement rocks in the western zone of the North China Craton and its tectonic implications: *Tectonophysics*, v. 310, p. 37–53.
- Zhao, G.-C., Wilde, S.A., Cawood, P.A., and Lu, L.-Z., 2000b, Petrology and P–T–t path of the Fuping mafic granulites: implications for tectonic evolution of the central zone of the North China Craton: *Journal of Metamorphic Geology*, v. 18, p. 375–391.
- Zhao, G.C., Wilde, S.A., Cawood, P.A., and Sun, M., 2001a, Archean blocks and their boundaries in the North China Craton: lithological, geochemical, structural and P–T path constraints and tectonic evolution: *Precambrian Research*, v. 107, p. 45–73.
- Zhao, G.C., Wilde, S.A., Guo, J.H., Cawood, P.A., Sun, M., and Li, X.P., 2010, Single zircon grains record two Paleoproterozoic collisional events in the North China Craton: *Precambrian Research*, v. 177, p. 266–276.
- Zhao, X., and Coe, R.S., 1987, Palaeomagnetic constraints on the collision and rotation of North and South China: *Nature*, v. 327, no. 6118, p. 141–144.
- Zhao, G., and Zhai, M., 2013, Lithotectonic elements of Precambrian basement in the North China Craton: review and tectonic implications: *Gondwana Research*, v. 23, no.4, p. 1207–1240.

- Zheng, B., and Ma, Z., 1991, Fault block tectonics in the northern part of North China and the structural detachment in the mid-lower crust: *Earthquake Research of China*, v. 5, p. 267-280.
- Zheng, B., Zhu, W., Jahn, B.M., Shu, L., Zhang, Z., and Su, J., 2010, Subducted Precambrian oceanic crust: geochemical and Sr–Nd isotopic evidence from metabasalts of the Aksu blueschist, NW China: *Journal of the Geological Society*, v. 167, no. 6, p. 1161-1170.
- Zheng, Y. F., Xiao, W.J., and Zhao, G., 2013, Introduction to tectonics of China: *Gondwana Research*, v. 23, no. 4, p. 1189-1206.
- Zhou, J.B., Wilde, S.A., Zhang, X.Z., Zhao, G.C., Zheng, C.Q., Wang, Y.J., and Zhang, X.H., 2009, The onset of Pacific margin accretion in NE China: evidence from the Heilongjiang high-pressure metamorphic belt: *Tectonophysics*, v. 478, no. 3, p. 230-246.
- Zhou, J.B., Wilde, S.A., Zhang, X.Z., Ren, S.M., and Zheng, C.Q., 2011, Early Paleozoic metamorphic rocks of the Erguna block in the Great Xing'an Range, NE China: Evidence for the timing of magmatic and metamorphic events and their tectonic implications: *Tectonophysics*, v. 499, no. 1, p. 105-117.
- Zhou, D., and Graham, S.A., 1996a, Extrusion of the Altyn Tagh wedge: A kinematic model for the Altyn Tagh fault and palinspastic reconstruction of northern China: *Geology*, v. 24, no. 5, p. 427-430.
- Zhou, D., and Graham, S.A., 1996b, The Songpan-Ganzi complex of the West Qinling Shan as a Triassic remnant ocean basin: *World and Regional Geology*, v. 1, no. 8, p. 281-299.
- Zhu, B., Kidd, W.S., Rowley, D.B., Currie, B.S., and Shafique, N., 2005, Age of initiation of the India-Asia collision in the east-central Himalaya: *The Journal of Geology*, v. 113, no. 3, p. 265-285.
- Zhu, G., Jiang, D., Zhang, B., and Chen, Y., 2012, Destruction of the eastern North China Craton in a backarc setting: Evidence from crustal deformation kinematics: *Gondwana Research*, v. 22, no. 1, p. 86-103.
- Zhu, W., Zhang, Z., Shu, L., Lu, H., Su, J., and Yang, W., 2008, SHRIMP U–Pb zircon geochronology of Neoproterozoic Korla mafic dykes in the northern Tarim Block, NW China: implications for the long-lasting breakup process of Rodinia: *Journal of the Geological Society*, v. 165, no. 5, p. 887-890.
- Ziegler, P.A., 1989, *Evolution of Laurussia: a study in late Palaeozoic plate tectonics*: Springer Science & Business Media, 102 p.
- Zonenshain, L.P., Kononov, M.V., and Savostin, L.A., 1987, Pacific and Kula/Eurasia relative motions during the last 130 Ma and their bearing on orogenesis in northeast Asia: *Circum-Pacific orogenic belts and evolution of the Pacific Ocean basin*.

- Zonenshain, L.P., Korinevsky, V.G., Kazmin, V.G., Pechersky, D.M., Khain, V.V., and Matveenkov, V.V., 1984, Plate tectonic model of the South Urals development: *Tectonophysics*, v. 109, no. 1-2, p. 95-135.
- Zonenshaĭn, L.P., Kuz'min, M.I., and Natapov, L.M., 1990, *Geology of the USSR: a plate-tectonic synthesis (Vol. 21)*: American Geophysical Union.
- Zong, K.Q., Zhang, Z. M., He, Z. Y., Hu, Z. C., Santosh, M., Liu, Y.S., and Wang, W., 2012, Early Palaeozoic high-pressure granulites from the Dunhuang block, northeastern Tarim Craton: constraints on continental collision in the southern Central Asian Orogenic Belt: *Journal of Metamorphic Geology*, v. 30, no. 8, p. 753-768.
- Zuza, A. V., Cheng, X., and Yin, A., 2016, Testing models of Tibetan Plateau formation with Cenozoic shortening estimates across the Qilian Shan-Nan Shan thrust belt: *Geosphere*, v. 12, no. 2, p. 501-5032.
- Zuza, A., Reith, R., Yin A., Dong, S., Liu, W., Zhang, Y., and Wu, C., 2013, Structural and Tectonic Framework of the Qilian Shan-Nan Shan Thrust belt, Northeastern Tibetan Plateau: *Acta Geologica Sinica (English Edition)*, v. 87, no. s1, p. 1-2.
- Zuza, A.V., and Yin, A., 2013, Testing the TWINS hypothesis: Were Greater North China and Western Laurentia linked in the Archean and Proterozoic?: *GSA Annual Meeting*, v. 45, no. 7, p. 463.
- Zuza, A.V., and Yin, A., 2014, Initial and boundary conditions for the evolution of the Central Asian orogenic system (CAOS): The Balkatach hypothesis: *Geological Society of America Abstracts with Programs*, v. 46, no. 6, p. 789.
- Zuza, A.V., and Yin, A., 2016, Continental deformation accommodated by non-rigid passive bookshelf faulting: An example from the Cenozoic tectonic development of northern Tibet: *Tectonophysics*, in press.

**-Appendices-**

**Auxiliary figures, text, and data tables**



**Figure A.1.** Uninterpreted seismic reflection profiles from Chapter 2.



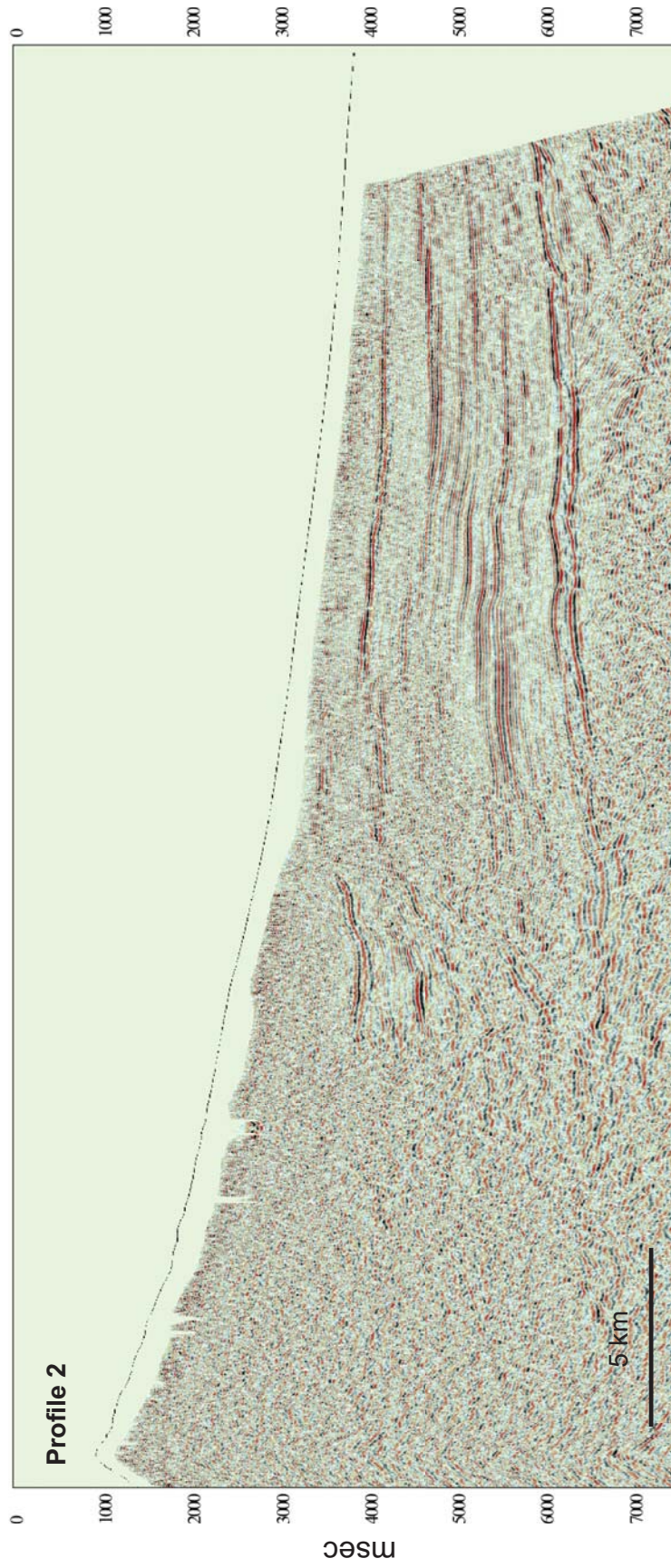


**Figure A.1 (continued).** Uninterpreted seismic reflection profiles from Chapter 2.



Figure A.1 (*continued*). Uninterpreted seismic reflection profiles from Chapter 2.

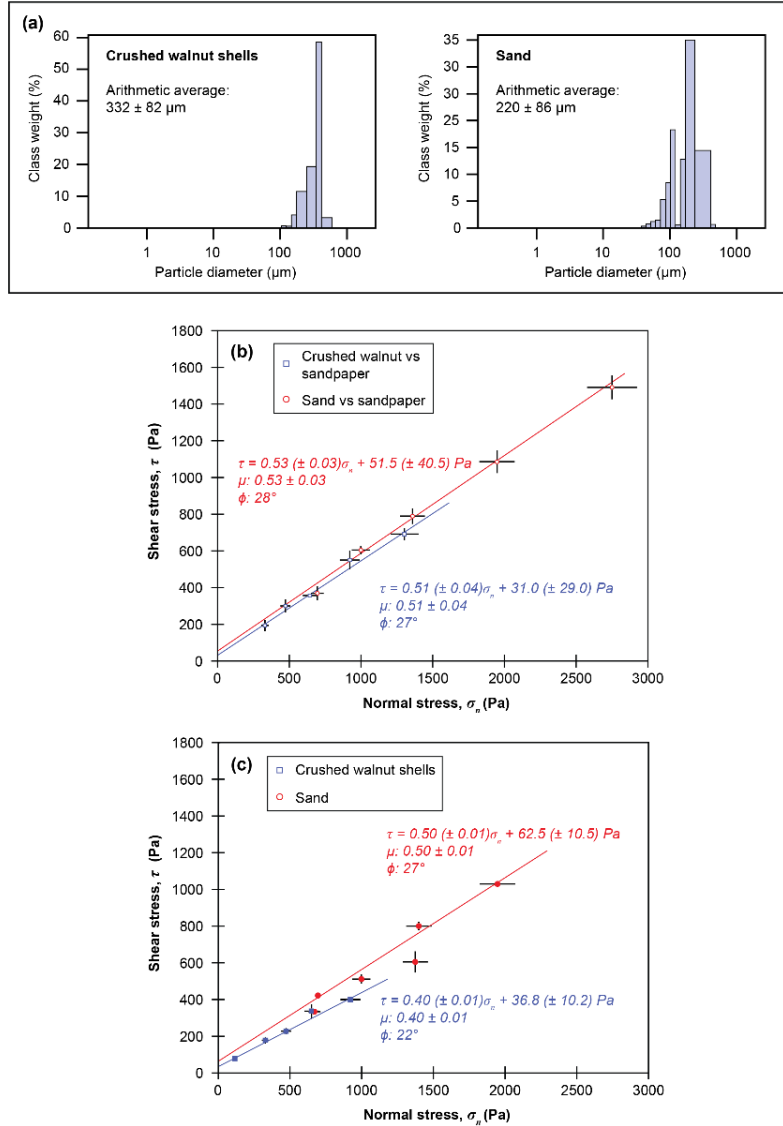


**Figure A.2.** Physical and mechanical properties of experimental materials. (a) Measured grain size distributions for dry crushed walnut shells and dry sand using the methods of Blott and Pye (2001). (b) Measured relationships between shear stress and normal stress for both dry crushed walnut shells and dry sand against P100 sandpaper. (c) Measure relationship between shear stress and normal stress for dry crushed walnut shells and dry sand. For both (b) and (c), the best-fit linear regression for each material yields the cohesive strength, coefficient of internal friction, and angle of internal friction, which are shown in Table 4.1 of the main text. Previous studies report an angle of internal friction ( $\phi$ ) of  $30.3\text{--}32.8^\circ$  and a cohesive strength ( $C_0$ ) of  $80 \pm 22 \text{ Pa}$  for dry sand (Maillot and Koyi, 2006) and  $\phi$  and  $C_0$  of  $38.5\text{--}40.8^\circ$  and  $23\text{--}13 \text{ Pa}$  for crushed walnut shells (Cruz et al., 2008). The procedure of the Hubbert-type experiments in (b) and (c) are described in greater detail by Hubbert (1951), Schellart (2000), Maillot and Koyi (2006), and Cruz et al. (2008).

### Text A.3. The stress-shadow model applied to the analogue experiments

First I determine the shear stress on a vertical plane parallel to the movement direction of the sliding plate (Fig. A2). The stress equilibrium equation in the sliding plate direction  $x$  can be written as

$$\frac{\partial \sigma_{xx}}{\partial x} + \frac{\partial \sigma_{xy}}{\partial y} + \frac{\partial \sigma_{zx}}{\partial z} = 0 \quad (\text{A1})$$

where  $\sigma_{xx}$  is the normal stress on vertical planes perpendicular to the sliding plate,  $\sigma_{xy}$  is the shear stress on vertical planes parallel to the movement direction of the sliding plate, and  $\sigma_{zx}$  is the shear stress on planes parallel to the sliding plate and in the direction of the sliding plate motion (Fig. A.3a). Assuming that  $\sigma_{xx}$  is in a state of lithostatic stress,  $\sigma_{xx} = -\rho g z$  (using the sign convention that compressive stress is negative). Based on the symmetry of the problem,  $\sigma_{xy}(y = 0) = 0$  (i.e., on the vertical plane along the middle dividing line of the sliding plate) because on the vertical plane of  $y = 0$  the shear sense switches. Finally, the measurements of the frictional properties between sand/crushed walnut shells against the underlying sand paper require that  $\sigma_{zx} = -\mu_b \rho g z - C_b$ , and  $\sigma_{zx}(z = h) = -\mu_b \rho g h - C_b$ , where  $\mu_b$  is the friction coefficient of sand/crushed walnut shells against the sand paper, and  $C_b$  is the corresponding cohesive strength of the dry sand/crushed walnut shells. The negative signs in the expression of  $\sigma_{zx} = -\mu_b \rho g z - C_b$  are the results of our assigned sign convention.

Under the aforementioned conditions, one can solve equation (A1) and obtain the “sidewall” shear stress on a plane perpendicular to the sliding plate and parallel to the movement direction of the sliding plate (Fig. A2a). Specifically,

$$\frac{\partial \sigma_{xx}}{\partial x} = 0 \quad (\text{A2})$$

$$\frac{\partial \sigma_{zx}}{\partial z} = -\mu_b \rho g \quad (\text{A3})$$

Inserting (A2) and (A3) into equation (A1), we have

$$\frac{\partial \sigma_{xy}}{\partial y} = -\mu_b \rho g \quad (\text{A4})$$

Equation (A4) yields

$$\sigma_{xy} = -\mu_b \rho g y + f(x, z) + a_0 \quad (\text{A5})$$

where  $f(x, z)$  is an arbitrary function of  $x$  and  $z$  when solving  $\sigma_{xy}$  and  $a_0$  is a constant. The boundary condition of  $\sigma_{xy}(y = 0) = 0$  requires that  $f(x, z) + a_0 = 0$ , which leads to a simplified equation (A5) as

$$\sigma_{xy} = \sigma_{sidewall} = \mu_b \rho g y \quad (\text{A6})$$

The above equation, which is given as equation (15) in the Chapter 4, indicates that the sidewall shear stress depends on the coefficient of basal friction, the density of the experimental material, and the surface gravity. Equation (A6) also shows that the sidewall shear stress increases with its

distance from the central dividing line of the sliding plate, where  $y = 0$  (Fig. A.3). I wish to determine the magnitude of the shear stress parallel to the Riedel shears, which trend at an angle of  $\theta$  from  $\sigma_{sidewall}$  (Fig. A.3b). A transformation of coordinates allows us to determine the “fault parallel” stress,  $\sigma_{fp}$ . The shear stress applied on planes parallel to the Riedel shear fractures can be expressed as

$$\sigma_{fp}^{sand} = \sigma_{sidewall}^{sand} \times \cos 2\theta \quad (A7)$$

and

$$\sigma_{fp}^{walnut} = \sigma_{sidewall}^{walnut} \times \cos 2\theta \quad (A8)$$

where  $\theta \approx 16^\circ$  as observed in the experiments (i.e., the angle between the sliding direction and the trend of the Riedel shear fractures) (Fig. A.3b). Although  $\sigma_{xy} = \sigma_{sidewall} = \mu_b \rho g y$  goes to infinite as  $y \rightarrow \infty$  (Fig. A2c), its induced shear stress  $\sigma_{fp}$  parallel to the Riedel shear stress is finite. This finite value can be evaluated at  $y = d$ , which marks the edge of the shear zone (Fig. A.3):

$$\sigma_{fp}^{sand/walnut} = \sigma_{sidewall}^{sand/walnut}(y = d) \times \cos(2\theta) = \mu_b \rho g d \cos(2\theta) \quad (A9)$$

where  $\sigma_{fp}(y = d)$  is greater than the yield strength of the experimental material, creating a shear zone in which Riedel shear fractures are created (Figs. A.3c and A.3d). In the above interpretation,  $\sigma_{fp}$  is equivalent to the regional stress  $\sigma_s^r = \sigma^{bc}$  used in equation (1b) of Chapter 4.

As the dry sand/crushed walnut shells are both Coulomb materials, their shear strengths increase with normal stress and thus depth. That is, at the surface, the shear strengths of the dry sand/crushed walnut shells are the lowest and equal to the cohesive strength of the experimental materials (Table 4.1). On the other hand, the shear stress generated by the basal shearing that is parallel to the Riedel shear fractures is vertically uniform, as expressed by  $\sigma_{fp} = \mu_b \rho g d \cos(2\theta)$ , which is independent of  $z$ . Under such a stress state, Riedel shear fractures will break first at the surfaces, where the yield strengths of the experimental Coulomb materials are weakest and equal to the cohesive strengths. In this scenario, our stress shadow model from equation (5) of the Chapter 4, relating fault spacing  $S$  to brittle layer thickness  $h$ , may be written as

$$S = \frac{\bar{y} - \bar{\sigma}^f}{\sigma^{bc} - \bar{y}} h = \frac{C_Y - C_f}{\sigma_{fp} - C_Y} h \quad (A10)$$

where  $\sigma_{fp} = \mu_b \rho g d \cos(2\theta)$  is the fault-parallel regional shear stress,  $C_Y$  is the cohesive strength of the experimental material (same as  $C_0$  in equation [7] in Chapter 4), and  $C_f$  is the cohesive strength of the Riedel shear fractures (equal to  $C_1$  in equation (6) in Chapter 4). The interpretation that the spacing of the observed Riedel shear spacing is controlled by the cohesive strength only, as expressed in equation (A10), explains why the  $S/h$  ratio is constant in the experiments regardless of changes in the thickness of the experimental materials (i.e.,  $h$ ). This would not be the case if a frictional term depending on  $h$  is involved in equation (A10).

The values of  $C_Y$  for dry sand and crushed walnut shells were measured in the study (Table 4.1), whereas the values of  $C_f$  are unknown for both experimental materials. However, from equation (A10), I can estimate  $C_f$  if the  $S/h$  ratio defined in equation (A10) is known.

Based on our experiments with only granular materials, the  $S/h$  ratio is  $\sim 0.68$  for dry sand and  $\sim 0.82$  for crushed walnut shells, respectively (Fig. 4.5d). In the sand and viscous putty experiments, the  $S/h$  ratio is 0.45-0.56 (average 0.51). Visual observations indicate that  $d \approx W/3 \approx 2$  cm, which defines the position of the inner boundary of the shear zone, where fault-parallel shear stress ( $\sigma_{fp}$ ) exceeds the yield strength of the experimental materials leading to the formation of the Riedel shear fractures. In the experiments, the shear zone boundary location  $y = d$  can be determined by the bending segments of the originally straight reference lines that were perpendicular to the movement direction of the sliding plate (e.g., Fig. 4.5c). This estimate is likely a maximum value.

Using  $d = 2$  cm,  $\mu_b = 0.53$  (Table 4.1), a sand density of  $1670 \text{ kg/m}^3$ ,  $\theta = 16^\circ$ , and  $g = 9.8 \text{ m/s}^2$ , we obtain

$$\sigma_{fp} = \mu_b \rho g d \cos(2\theta) = 147 \text{ Pa} \quad (\text{A11})$$

Rearranging equation (A10) and inserting known  $C_Y = 62.5 \text{ Pa}$  (Table 4.1),  $\sigma_{fp} = 147 \text{ Pa}$  from (A11), and  $S/h = 0.68$  from Fig. 4.5d, I estimate the cohesive strength of the Riedel shear fractures formed in our dry sand experiments as:

$$C_f^{sand} = C_Y - \frac{S}{h} (\sigma_{fp} - C_Y) = 5 \text{ Pa} \quad (\text{A12})$$

For the sand-putty experiments  $\mu_b$  is  $\sim 0.73$  (Table 4.1) and  $d$  is expected to be smaller because of the effects of distributed basal shear. Using  $S/h = 0.52$ ,  $\mu_b = 0.73$ ,  $d = 1.5$  cm, a sand density of  $1670 \text{ kg/m}^3$ ,  $\theta = 16^\circ$ , and  $g = 9.8 \text{ m/s}^2$ , and  $C_Y = 62.5 \text{ Pa}$ , we estimate  $C_f^{sand\_putty} = 15 \text{ Pa}$ .

For crushed walnut shell experiments, I use  $\mu_b = 0.51$  (Table 4.1), a density of  $800 \text{ kg/m}^3$ ,  $\theta = 16^\circ$ , and  $g = 9.8 \text{ m/s}^2$  to calculate the fault parallel shear stress as

$$\sigma_{fp} = \mu_b \rho g d \cos(2\theta) = 68 \text{ Pa} \quad (\text{A13})$$

Using a  $S/h$  ratio of 0.82 (Fig. 4.5d) and a cohesive strength of  $36.8 \text{ Pa}$  (Table 4.1), I obtain the corresponding cohesive strength of the Riedel shears that formed in the crushed walnut shells under basal shearing as

$$C_f^{walnut} = C_Y - \frac{S}{h} (\sigma_{fp} - C_Y) = 11 \text{ Pa} \quad (\text{A14})$$

I believe that the estimated cohesive strengths of the newly created fractures in both dry sand and crushed walnut shells are reasonable: (1) they are all positive values, and (2) they are smaller than the cohesive strength of materials in which the shear fractures formed. The above consistency provides validation of the proposed stress-shadow model in Chapter 4.

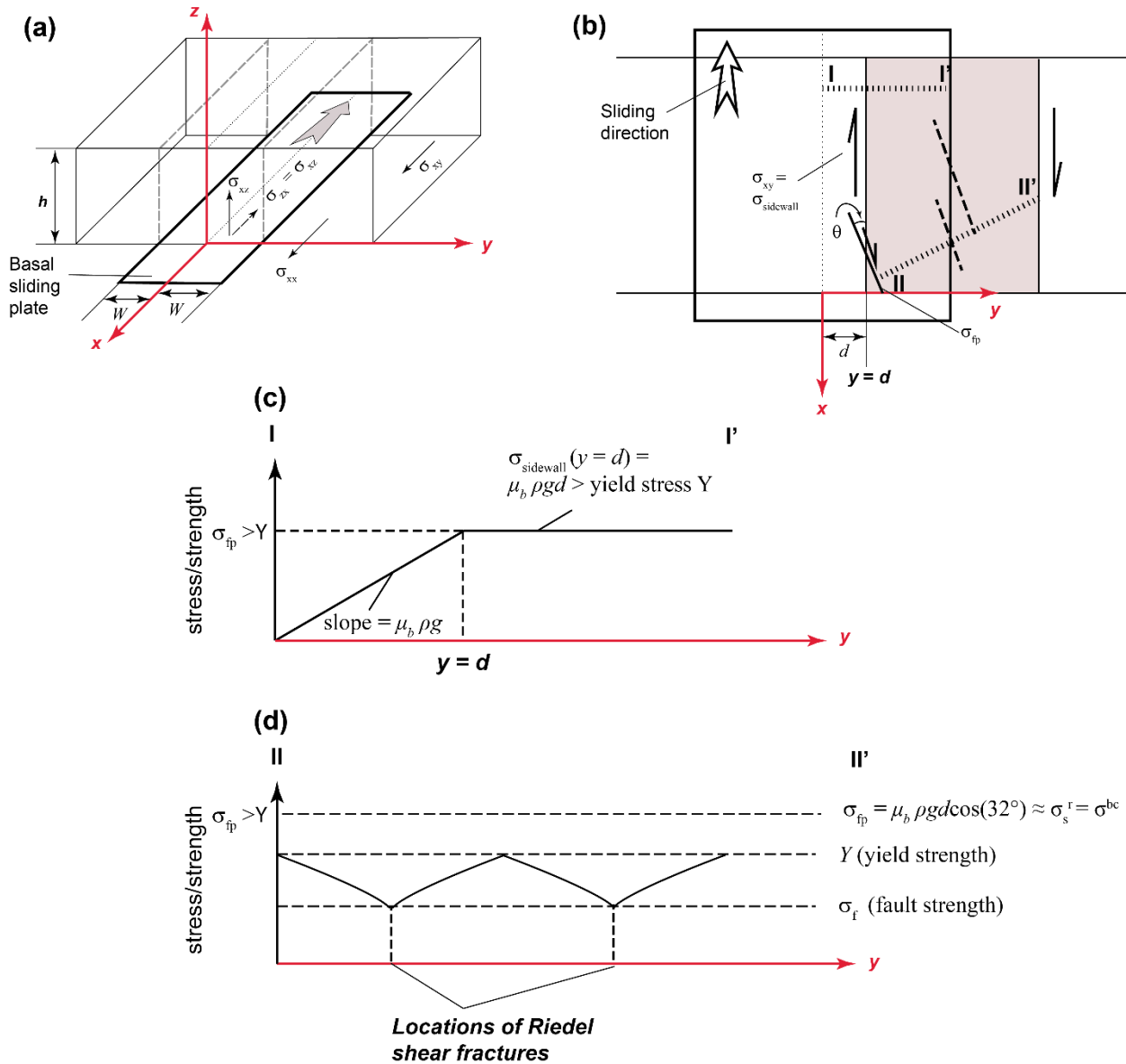
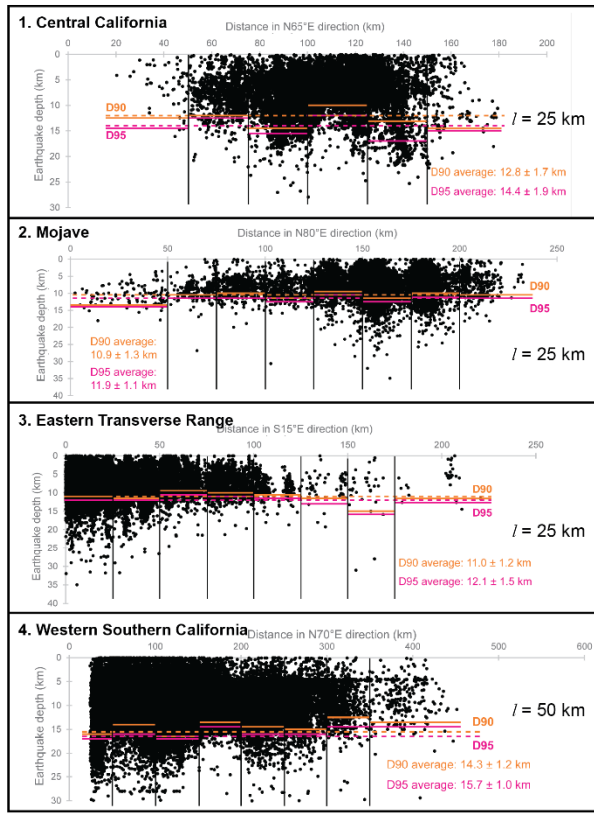


**Figure A.4.** (a) Coordinate system of reference. The box represents the region occupied by the experimental materials (i.e., dry sand and crushed walnut shells).  $h$ , thickness of the experimental material;  $W$ , the half width of the basal sliding plate;  $x$ - $y$  plane lies at the base of the experimental set up and  $y = 0$  represents the central dividing line of the sliding plate. (b) Plan view of the sidewall shear stress on a vertical plane at the edge of the shear zone that is parallel to the sliding plate direction and perpendicular to the basal plane. Also shown is the angular relationship between the sidewall shear stress and the fault-parallel shear stress. The location of the inner boundary of the shear zone is marked by  $y = d$ . Lines I-I' and II-II' are cross sections along which the stress distributions are shown in (c) and (d). (c) Postulated magnitude distribution of the sidewall shear stress across the shear zone. (d) Postulated magnitude distribution of the fault-parallel shear stress across the Riedel shear fractures in the shear zone.

(a) California



(b) Asia

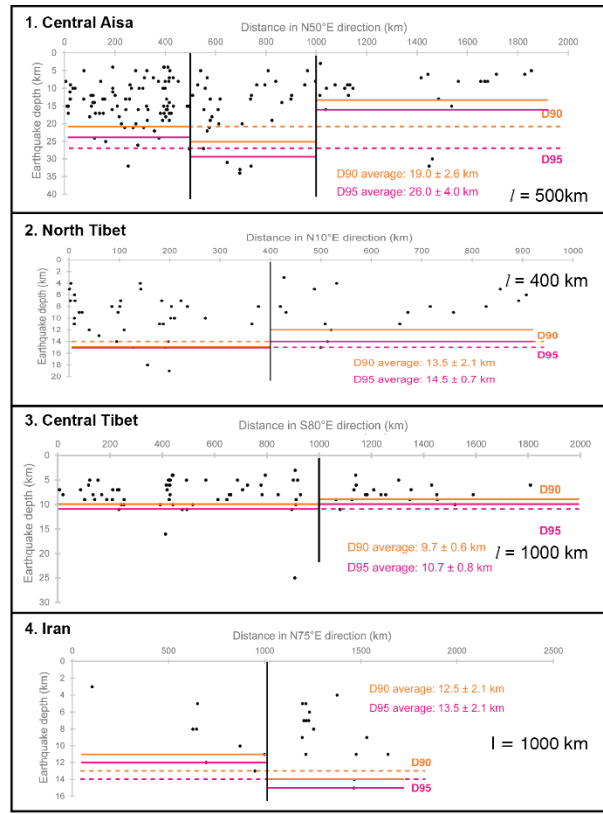


**Figure A.5.** Earthquake depth plotted as a function of horizontal distance along a profile line perpendicular to the fault strike of each domain from (a) California and (b) Asia. For this plot, the cutoff depth above which 95% (D95) and 90% (D90) seismicity is contained in the crust was calculated (e.g., Sibson, 1982) (Table 4.2 of main text). Dashed lines represent the bulk averaged D90 (orange) and D95 (pink) depths without dividing each profile into segments. In contrast, the solid lines represent D90 (orange) and D95 (pink) depths in each segment with a segment length  $l$ .



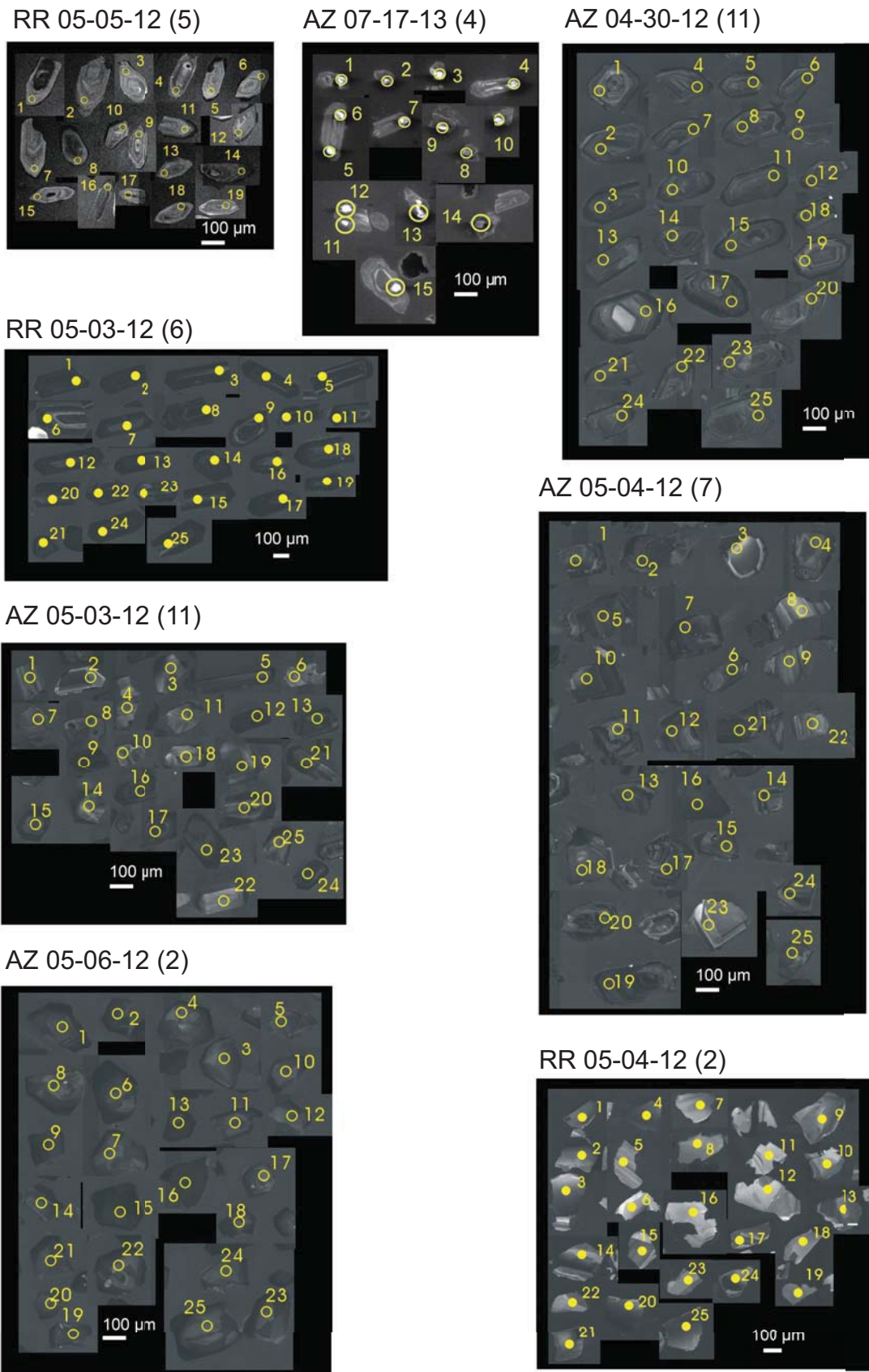
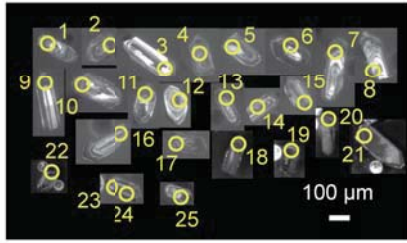
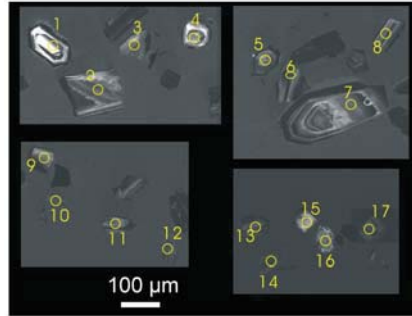


**Figure A.6.** Cathodoluminescence (CL) images of zircon and locations of U-Pb spot analyses.

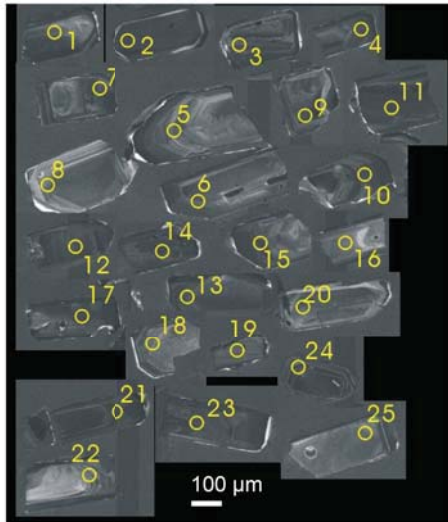
AY 09-21-11 (4)



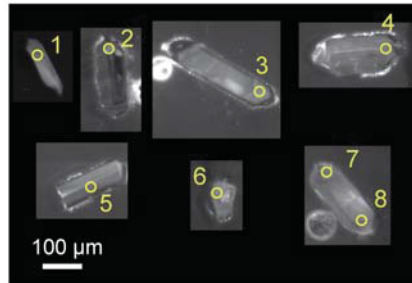
AZ 04-30-12 (4)



AZ 05-01-12 (1)



AZ 07-24-13 (9)



AZ 09-14-14 (8)

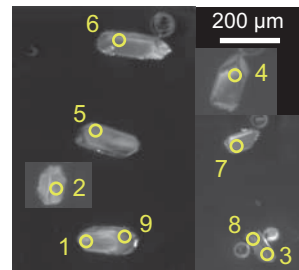


**Figure A.6 (continued).** Cathodoluminescence (CL) images of zircon and locations of U-Pb spot analyses.

**Table A.7. U-Pb isotopic data for central Qilian Shan igneous samples**

| Spot  | <sup>206</sup> Pb/ <sup>238</sup> U |      | Age   |      | <sup>207</sup> Pb/ <sup>235</sup> U |       | <sup>206</sup> Pb/ <sup>206</sup> Pb |       | <sup>206</sup> Pb* 206Pb*/ <sup>238</sup> U |       | Isotopic ratios |       | p <sup>i</sup> | Th/U | Conc. # | Exc. \$ | Remarks <sup>%</sup> |         |
|---|-------------------------------------|------|-------|------|-------------------------------------|-------|--------------------------------------|-------|---|-------|-----------------|-------|----------------|------|---------|---------|----------------------|---------|
|   | 1 σ                                 | 1 σ  | 1 σ   | 1 σ  | 1 σ                                 | 1 σ   | 1 σ                                  | 1 σ   | 1 σ   | 1 σ   | 1 σ             | 1 σ   |                |      |         |         |                      | 1 σ     |
| RR 05-05-12 (5), 38° 34.698' N 98° 31.760' E (4584 m)     |                                     |      |       |      |                                     |       |                                      |       |   |       |                 |       |                |      |         |         |                      |         |
| (5)-5   | 435.1                               | 7.7  | 436.5 | 8.3  | 463.8                               | 123.9 | 99.7                                 | 0.070 | 0.0013                                      | 0.542 | 0.0319          | 0.056 | 0.0031         | 0.31 | 0.47    | 0.94    |                      |         |
| (5)-6   | 437.9                               | 7.4  | 439.6 | 8.0  | 374.8                               | 55.1  | 99.7                                 | 0.070 | 0.0012                                      | 0.524 | 0.0158          | 0.054 | 0.0013         | 0.58 | 0.42    | 1.17    |                      |         |
| (5)-10  | 438.7                               | 6.9  | 440.0 | 7.4  | 445.3                               | 77.6  | 99.6                                 | 0.070 | 0.0011                                      | 0.542 | 0.0209          | 0.056 | 0.0019         | 0.42 | 0.42    | 0.99    |                      |         |
| (5)-8   | 441.4                               | 7.1  | 440.4 | 7.5  | 534.8                               | 36.8  | 100.0                                | 0.071 | 0.0012                                      | 0.568 | 0.0134          | 0.058 | 0.0010         | 0.70 | 0.48    | 0.83    |                      |         |
| (5)-12  | 441.9                               | 7.0  | 443.6 | 7.3  | 382.7                               | 69.4  | 99.1                                 | 0.071 | 0.0012                                      | 0.531 | 0.0186          | 0.054 | 0.0017         | 0.47 | 0.40    | 1.15    |                      |         |
| (5)-16  | 443.9                               | 7.5  | 444.2 | 7.8  | 428.9                               | 54.8  | 99.5                                 | 0.071 | 0.0012                                      | 0.545 | 0.0164          | 0.055 | 0.0014         | 0.58 | 0.42    | 1.03    |                      |         |
| (5)-11  | 445.8                               | 6.8  | 445.1 | 7.2  | 494.2                               | 30.0  | 100.0                                | 0.072 | 0.0011                                      | 0.563 | 0.0117          | 0.057 | 0.0008         | 0.76 | 0.51    | 0.90    |                      |         |
| (5)-1   | 445.8                               | 7.4  | 447.8 | 7.9  | 418.7                               | 82.4  | 100.0                                | 0.072 | 0.0012                                      | 0.545 | 0.0222          | 0.055 | 0.0020         | 0.42 | 0.34    | 1.06    |                      |         |
| (5)-14  | 446.8                               | 6.8  | 449.6 | 7.4  | 403.2                               | 42.4  | 100.0                                | 0.072 | 0.0011                                      | 0.542 | 0.0133          | 0.055 | 0.0010         | 0.64 | 0.38    | 1.11    |                      |         |
| (5)-19  | 447.0                               | 7.2  | 448.3 | 7.7  | 382.6                               | 88.5  | 99.5                                 | 0.072 | 0.0012                                      | 0.537 | 0.0230          | 0.054 | 0.0021         | 0.39 | 0.44    | 1.17    |                      |         |
| (5)-2   | 447.7                               | 7.2  | 450.1 | 7.7  | 407.3                               | 52.6  | 100.0                                | 0.072 | 0.0012                                      | 0.544 | 0.0157          | 0.055 | 0.0013         | 0.58 | 0.33    | 1.10    |                      |         |
| (5)-15  | 448.1                               | 7.3  | 451.7 | 7.7  | 282.5                               | 108.7 | 99.8                                 | 0.072 | 0.0012                                      | 0.515 | 0.0260          | 0.052 | 0.0025         | 0.33 | 0.29    | 1.59    |                      |         |
| (5)-18  | 448.2                               | 6.9  | 449.8 | 7.4  | 426.5                               | 45.9  | 99.5                                 | 0.072 | 0.0012                                      | 0.550 | 0.0143          | 0.055 | 0.0011         | 0.61 | 0.53    | 1.05    |                      |         |
| (5)-9   | 448.3                               | 7.0  | 448.2 | 7.4  | 508.3                               | 39.1  | 99.8                                 | 0.072 | 0.0012                                      | 0.570 | 0.0137          | 0.057 | 0.0010         | 0.67 | 0.57    | 0.88    |                      |         |
| (5)-4   | 448.3                               | 7.1  | 449.2 | 7.7  | 441.0                               | 52.2  | 99.4                                 | 0.072 | 0.0012                                      | 0.553 | 0.0158          | 0.056 | 0.0013         | 0.57 | 0.40    | 1.02    |                      |         |
| (5)-13  | 450.0                               | 8.5  | 452.6 | 9.3  | 390.9                               | 88.7  | 99.9                                 | 0.072 | 0.0014                                      | 0.543 | 0.0239          | 0.054 | 0.0022         | 0.44 | 0.29    | 1.15    |                      |         |
| (5)-7   | 451.9                               | 7.9  | 450.0 | 8.6  | 487.4                               | 61.9  | 97.0                                 | 0.073 | 0.0013                                      | 0.570 | 0.0190          | 0.057 | 0.0016         | 0.54 | 0.37    | 0.93    |                      | (4),(5) |
| (5)-17  | 519.6                               | 8.7  | 522.2 | 9.1  | 501.9                               | 177.3 | 99.7                                 | 0.084 | 0.0015                                      | 0.663 | 0.0546          | 0.057 | 0.0046         | 0.21 | 0.40    | 1.04    | X                    | (1)     |
| (5)-3   | 643.4                               | 10.0 | 438.2 | 25.3 | 3525.0                              | 45.6  | 99.7                                 | 0.105 | 0.0017                                      | 4.498 | 0.1518          | 0.311 | 0.0092         | 0.48 | 0.39    | 0.18    | X                    | (1)     |
| <b>Weighted mean age: 445 ± 3 Ma (n = 17); MSWD: 0.38</b> |                                     |      |       |      |                                     |       |                                      |       |   |       |                 |       |                |      |         |         |                      |         |
| AZ 07-17-13 (4), 38° 28.546' N 98° 49.882' E (4290m)      |                                     |      |       |      |                                     |       |                                      |       |   |       |                 |       |                |      |         |         |                      |         |
| (4)-1   | 475.8                               | 23.7 | 462.2 | 19.3 | 394.9                               | 17.8  | 99.9                                 | 0.077 | 0.0040                                      | 0.577 | 0.0300          | 0.055 | 0.0004         | 0.99 | 0.24    | 1.20    |                      |         |
| (4)-2   | 485.3                               | 28.3 | 478.5 | 23.5 | 446.3                               | 40.9  | 98.1                                 | 0.078 | 0.0047                                      | 0.602 | 0.0370          | 0.056 | 0.0010         | 0.95 | 0.31    | 1.09    |                      |         |
| (4)-3   | 360                                 | 20.5 | 355.1 | 60.5 | 322.9                               | 423   | 82.6                                 | 0.057 | 0.0034                                      | 0.419 | 0.0846          | 0.053 | 0.0098         | 0.41 | 0.21    | 1.11    | X                    | (2)     |
| (4)-4   | 453.2                               | 26.4 | 432   | 33.2 | 320.8                               | 172   | 90.6                                 | 0.073 | 0.0044                                      | 0.530 | 0.0500          | 0.053 | 0.0040         | 0.60 | 1.68    | 1.41    |                      |         |
| (4)-5   | 314.3                               | 16.4 | 358.2 | 102  | 652.9                               | 689   | 68.9                                 | 0.050 | 0.0027                                      | 0.423 | 0.1420          | 0.061 | 0.0197         | 0.36 | 0.28    | 0.48    | X                    | (1),(2) |
| (4)-6   | 455.6                               | 23   | 448.9 | 19.4 | 414.9                               | 28.6  | 99.9                                 | 0.073 | 0.0038                                      | 0.556 | 0.0298          | 0.054 | 0.0024         | 0.97 | 0.30    | 1.10    |                      |         |
| (4)-7   | 473                                 | 26.2 | 452.6 | 21   | 350                                 | 21.5  | 99.8                                 | 0.076 | 0.0044                                      | 0.562 | 0.0323          | 0.054 | 0.0005         | 0.99 | 0.20    | 1.35    |                      |         |
| (4)-8   | 679.7                               | 164  | 628.2 | 142  | 446.8                               | 156   | 99.4                                 | 0.111 | 0.0282                                      | 0.857 | 0.2600          | 0.056 | 0.0039         | 0.98 | 0.28    | 1.52    | X                    | (1),(3) |
| (4)-9   | 419.5                               | 20   | 446.4 | 31.4 | 587.1                               | 154   | 93.2                                 | 0.067 | 0.0033                                      | 0.552 | 0.0480          | 0.060 | 0.0042         | 0.58 | 0.37    | 0.71    |                      |         |
| (4)-10  | 413.3                               | 22.1 | 449.1 | 27.4 | 636.8                               | 112   | 94.7                                 | 0.066 | 0.0037                                      | 0.556 | 0.0420          | 0.061 | 0.0032         | 0.72 | 0.21    | 0.65    |                      |         |
| (4)-11  | 439.3                               | 20.3 | 453.6 | 27   | 526.9                               | 114   | 90.3                                 | 0.071 | 0.0034                                      | 0.563 | 0.0416          | 0.058 | 0.0030         | 0.71 | 0.70    | 0.83    |                      |         |

|  |       |      |       |      |       |      |      |       |        |       |        |       |        |      |      |        |
|--|-------|------|-------|------|-------|------|------|-------|--------|-------|--------|-------|--------|------|------|--------|
| (4)-12   | 455   | 26.7 | 441.9 | 27.8 | 374.1 | 99.7 | 92.6 | 0.073 | 0.0044 | 0.545 | 0.0423 | 0.055 | 0.0007 | 0.82 | 0.30 | 1.22   |
| (4)-13   | 437.6 | 22.7 | 434   | 18.8 | 414.7 | 15.2 | 99.8 | 0.070 | 0.0038 | 0.533 | 0.0284 | 0.055 | 0.0004 | 0.99 | 0.11 | 1.06   |
| (4)-14   | 483.4 | 27.1 | 468.5 | 22.3 | 396   | 22.2 | 99.8 | 0.078 | 0.0045 | 0.586 | 0.0348 | 0.055 | 0.0005 | 0.99 | 0.99 | 1.22   |
| (4)-15   | 442.8 | 24   | 441.8 | 23.7 | 436.7 | 68.1 | 92.4 | 0.071 | 0.0040 | 0.545 | 0.0360 | 0.056 | 0.0017 | 0.89 | 1.45 | 1.01   |
| <b>Weighted mean age: 449 ± 13 Ma (n = 12); MSWD: 0.99</b> |       |      |       |      |       |      |      |       |        |       |        |       |        |      |      |        |
| AZ 04-30-12 (11), 38° 34.473' N 98° 58.035' E (3911 m)     |       |      |       |      |       |      |      |       |        |       |        |       |        |      |      |        |
| (11a)-1  | 451.4 | 2.8  | 452.4 | 6.5  | 457.3 | 33.5 | 80.1 | 0.073 | 0.0004 | 0.561 | 0.0081 | 0.056 | 0.0008 | 0.43 | 0.63 | 0.99   |
| (11a)-2  | 450.5 | 2.9  | 450.6 | 5.1  | 451.0 | 28.3 | 80.2 | 0.072 | 0.0005 | 0.559 | 0.0063 | 0.056 | 0.0007 | 0.57 | 0.68 | 1.00   |
| (11a)-3  | 450.8 | 2.7  | 452.6 | 4.7  | 461.7 | 22.7 | 82.3 | 0.072 | 0.0004 | 0.562 | 0.0059 | 0.056 | 0.0006 | 0.57 | 0.56 | 0.98   |
| (11a)-4  | 450.1 | 2.6  | 448.5 | 4.3  | 440.0 | 20.9 | 81.0 | 0.072 | 0.0004 | 0.555 | 0.0053 | 0.056 | 0.0005 | 0.61 | 0.63 | 1.02   |
| (11a)-5  | 449.4 | 2.7  | 450.8 | 8.6  | 458.3 | 38.0 | 77.1 | 0.072 | 0.0004 | 0.559 | 0.0107 | 0.056 | 0.0010 | 0.31 | 0.74 | 0.98   |
| (11a)-6  | 448.5 | 2.7  | 447.4 | 8.9  | 441.7 | 40.3 | 79.7 | 0.072 | 0.0004 | 0.554 | 0.0110 | 0.056 | 0.0010 | 0.30 | 0.59 | 1.02   |
| (11a)-7  | 440.5 | 2.5  | 448.8 | 4.3  | 491.5 | 20.3 | 76.7 | 0.071 | 0.0004 | 0.556 | 0.0053 | 0.057 | 0.0005 | 0.60 | 1.11 | 0.90   |
| (11a)-8  | 450.3 | 2.6  | 449.8 | 7.4  | 447.5 | 35.5 | 78.3 | 0.072 | 0.0004 | 0.557 | 0.0092 | 0.056 | 0.0009 | 0.35 | 0.68 | 1.01   |
| (11a)-9  | 450.5 | 2.6  | 454.3 | 6.3  | 473.4 | 29.6 | 76.5 | 0.072 | 0.0004 | 0.564 | 0.0079 | 0.057 | 0.0008 | 0.42 | 0.76 | 0.95   |
| (11a)-10   | 450.2 | 2.6  | 454.1 | 5.7  | 474.0 | 27.3 | 79.1 | 0.072 | 0.0004 | 0.564 | 0.0071 | 0.057 | 0.0007 | 0.46 | 0.62 | 0.95   |
| (11a)-11   | 450.7 | 2.6  | 450.9 | 5.7  | 452.0 | 27.1 | 79.2 | 0.072 | 0.0004 | 0.559 | 0.0071 | 0.056 | 0.0007 | 0.45 | 0.67 | 1.00   |
| (11a)-12   | 451.0 | 2.7  | 452.1 | 8.3  | 457.6 | 37.2 | 77.3 | 0.072 | 0.0004 | 0.561 | 0.0103 | 0.056 | 0.0009 | 0.32 | 0.73 | 0.99   |
| (11a)-13   | 449.5 | 2.6  | 447.3 | 5.6  | 435.5 | 27.3 | 76.4 | 0.072 | 0.0004 | 0.553 | 0.0069 | 0.056 | 0.0007 | 0.46 | 0.82 | 1.03   |
| (11a)-14   | 469.8 | 2.7  | 468.3 | 5.1  | 460.7 | 23.2 | 78.3 | 0.076 | 0.0004 | 0.586 | 0.0064 | 0.056 | 0.0006 | 0.53 | 0.74 | 1.02 X |
| (11a)-15   | 470.9 | 2.8  | 473.1 | 5.8  | 483.8 | 26.5 | 80.5 | 0.076 | 0.0004 | 0.594 | 0.0073 | 0.057 | 0.0007 | 0.48 | 0.67 | 0.97 X |
| (11a)-16   | 467.5 | 2.8  | 470.4 | 8.5  | 484.7 | 35.6 | 80.8 | 0.075 | 0.0005 | 0.589 | 0.0106 | 0.057 | 0.0009 | 0.34 | 0.54 | 0.96 X |
| (11a)-17   | 450.0 | 2.8  | 448.4 | 6.0  | 440.0 | 32.2 | 78.1 | 0.072 | 0.0004 | 0.555 | 0.0074 | 0.056 | 0.0008 | 0.46 | 0.66 | 1.02   |
| (11a)-18   | 470.3 | 2.8  | 470.4 | 7.6  | 471.3 | 32.1 | 77.5 | 0.076 | 0.0004 | 0.589 | 0.0095 | 0.056 | 0.0008 | 0.37 | 0.69 | 1.00 X |
| (11a)-19   | 497.0 | 3.2  | 578.3 | 12.7 | 911.9 | 39.2 | 91.6 | 0.080 | 0.0005 | 0.767 | 0.0169 | 0.069 | 0.0013 | 0.30 | 0.06 | 0.55 X |
| (11a)-20   | 522.4 | 3.0  | 581.7 | 9.6  | 820.6 | 34.2 | 77.6 | 0.084 | 0.0005 | 0.773 | 0.0128 | 0.066 | 0.0011 | 0.35 | 0.76 | 0.64 X |
| (11a)-21   | 449.6 | 2.6  | 452.7 | 4.8  | 468.6 | 23.6 | 80.9 | 0.072 | 0.0004 | 0.562 | 0.0059 | 0.056 | 0.0006 | 0.55 | 0.58 | 0.96   |
| (11a)-22   | 451.4 | 2.7  | 452.1 | 4.6  | 455.4 | 22.2 | 79.1 | 0.073 | 0.0004 | 0.561 | 0.0057 | 0.056 | 0.0006 | 0.58 | 0.69 | 0.99   |
| (11a)-23   | 452.0 | 2.7  | 454.2 | 4.9  | 465.5 | 25.6 | 77.6 | 0.073 | 0.0004 | 0.564 | 0.0061 | 0.056 | 0.0007 | 0.56 | 0.59 | 0.97   |
| (11a)-24   | 451.6 | 2.6  | 447.6 | 7.4  | 427.3 | 35.7 | 78.3 | 0.073 | 0.0004 | 0.554 | 0.0091 | 0.055 | 0.0009 | 0.35 | 0.63 | 1.06   |
| (11a)-25   | 451.0 | 2.7  | 453.6 | 6.5  | 467.0 | 28.7 | 78.4 | 0.072 | 0.0004 | 0.563 | 0.0081 | 0.056 | 0.0007 | 0.41 | 0.65 | 0.97   |
| <b>Weighted mean age: 450 ± 1 Ma (n = 19); MSWD: 0.92</b>  |       |      |       |      |       |      |      |       |        |       |        |       |        |      |      |        |
| RR 05-03-12 (6), 38° 29.415' N 98° 54.218' E (3982 m)      |       |      |       |      |       |      |      |       |        |       |        |       |        |      |      |        |
| (6a)-1   | 472.6 | 2.7  | 486.6 | 4.6  | 552.8 | 19.9 | 84.2 | 0.076 | 0.0004 | 0.615 | 0.0059 | 0.059 | 0.0005 | 0.59 | 0.48 | 0.86 X |
| (6a)-2   | 458.7 | 7.5  | 464.8 | 10.1 | 494.7 | 25.9 | 84.5 | 0.074 | 0.0012 | 0.580 | 0.0126 | 0.057 | 0.0007 | 0.75 | 0.43 | 0.93   |
| (6a)-3   | 457.0 | 4.3  | 463.4 | 9.5  | 494.9 | 30.8 | 80.8 | 0.073 | 0.0007 | 0.578 | 0.0119 | 0.057 | 0.0008 | 0.46 | 0.54 | 0.92   |
| (6a)-4   | 457.4 | 2.7  | 461.1 | 6.0  | 479.6 | 26.7 | 72.9 | 0.074 | 0.0004 | 0.575 | 0.0075 | 0.057 | 0.0007 | 0.44 | 1.16 | 0.95   |

|         |       |     |       |      |       |      |      |       |        |       |        |       |        |      |      |            |
|---------|-------|-----|-------|------|-------|------|------|-------|--------|-------|--------|-------|--------|------|------|------------|
| (6a)-5  | 454.0 | 2.6 | 458.5 | 5.3  | 481.4 | 25.2 | 79.0 | 0.073 | 0.0004 | 0.571 | 0.0066 | 0.057 | 0.0006 | 0.49 | 0.65 | 0.94       |
| (6a)-6  | 464.6 | 2.9 | 471.5 | 5.1  | 505.1 | 21.9 | 67.5 | 0.075 | 0.0005 | 0.591 | 0.0064 | 0.057 | 0.0006 | 0.57 | 1.38 | 0.92 (7)   |
| (6a)-7  | 452.6 | 2.8 | 460.5 | 7.6  | 500.0 | 31.1 | 80.3 | 0.073 | 0.0005 | 0.574 | 0.0095 | 0.057 | 0.0008 | 0.38 | 0.55 | 0.91 (4)   |
| (6a)-8  | 486.2 | 3.0 | 491.1 | 4.3  | 514.3 | 17.8 | 83.1 | 0.078 | 0.0005 | 0.622 | 0.0055 | 0.058 | 0.0005 | 0.70 | 0.58 | 0.95 X     |
| (6a)-9  | 451.5 | 2.8 | 456.3 | 4.2  | 480.4 | 19.7 | 76.7 | 0.073 | 0.0005 | 0.567 | 0.0052 | 0.057 | 0.0005 | 0.68 | 0.89 | 0.94 (7)   |
| (6a)-10 | 457.3 | 3.5 | 463.6 | 6.7  | 494.8 | 24.0 | 73.2 | 0.074 | 0.0006 | 0.579 | 0.0083 | 0.057 | 0.0006 | 0.53 | 1.03 | 0.92 (7)   |
| (6a)-11 | 456.7 | 2.8 | 468.4 | 4.7  | 526.0 | 19.5 | 77.9 | 0.073 | 0.0005 | 0.586 | 0.0058 | 0.058 | 0.0005 | 0.62 | 0.62 | 0.87 (4)   |
| (6a)-12 | 504.4 | 3.8 | 510.1 | 12.9 | 535.4 | 42.1 | 74.7 | 0.081 | 0.0006 | 0.653 | 0.0165 | 0.058 | 0.0011 | 0.29 | 0.96 | 0.94 X (7) |
| (6a)-13 | 453.6 | 2.7 | 464.1 | 4.3  | 516.5 | 21.1 | 70.2 | 0.073 | 0.0004 | 0.579 | 0.0054 | 0.058 | 0.0006 | 0.64 | 1.37 | 0.88 (7)   |
| (6a)-14 | 463.3 | 3.0 | 469.7 | 4.1  | 501.5 | 16.4 | 74.7 | 0.075 | 0.0005 | 0.588 | 0.0051 | 0.057 | 0.0004 | 0.74 | 1.00 | 0.92 (7)   |
| (6a)-15 | 465.3 | 3.2 | 473.8 | 6.7  | 515.3 | 22.6 | 83.8 | 0.075 | 0.0005 | 0.595 | 0.0083 | 0.058 | 0.0006 | 0.49 | 0.45 | 0.90 (7)   |
| (6a)-16 | 455.6 | 2.8 | 460.5 | 5.0  | 485.1 | 20.7 | 79.5 | 0.073 | 0.0005 | 0.574 | 0.0062 | 0.057 | 0.0005 | 0.58 | 0.73 | 0.94 (7)   |
| (6a)-17 | 454.1 | 3.1 | 460.3 | 4.6  | 491.4 | 24.3 | 93.6 | 0.073 | 0.0005 | 0.574 | 0.0057 | 0.057 | 0.0006 | 0.69 | 0.32 | 0.92 (7)   |
| (6a)-18 | 451.8 | 2.6 | 457.0 | 5.1  | 482.7 | 23.5 | 75.9 | 0.073 | 0.0004 | 0.568 | 0.0063 | 0.057 | 0.0006 | 0.52 | 0.84 | 0.94 (7)   |
| (6a)-19 | 452.6 | 2.7 | 457.1 | 5.7  | 479.8 | 29.9 | 79.7 | 0.073 | 0.0004 | 0.569 | 0.0071 | 0.057 | 0.0008 | 0.48 | 0.66 | 0.94 (7)   |
| (6a)-20 | 462.8 | 2.6 | 469.9 | 4.2  | 504.9 | 18.5 | 93.0 | 0.074 | 0.0004 | 0.588 | 0.0052 | 0.057 | 0.0005 | 0.64 | 0.06 | 0.92 (7)   |
| (6a)-21 | 461.9 | 2.8 | 467.9 | 4.0  | 497.5 | 17.4 | 77.1 | 0.074 | 0.0004 | 0.585 | 0.0051 | 0.057 | 0.0005 | 0.69 | 0.86 | 0.93 (7)   |
| (6a)-22 | 461.7 | 2.7 | 469.4 | 4.3  | 507.5 | 17.6 | 87.2 | 0.074 | 0.0004 | 0.588 | 0.0054 | 0.057 | 0.0005 | 0.65 | 0.33 | 0.91 (7)   |
| (6a)-23 | 455.8 | 2.7 | 464.8 | 8.4  | 509.4 | 40.7 | 79.0 | 0.073 | 0.0004 | 0.581 | 0.0105 | 0.057 | 0.0011 | 0.33 | 0.78 | 0.89 (7)   |
| (6a)-24 | 443.4 | 3.2 | 451.4 | 13.6 | 492.5 | 56.8 | 84.0 | 0.071 | 0.0005 | 0.560 | 0.0168 | 0.057 | 0.0015 | 0.24 | 0.47 | 0.90 (7)   |
| (6a)-25 | 465.4 | 2.8 | 468.7 | 4.9  | 485.2 | 19.6 | 79.5 | 0.075 | 0.0004 | 0.587 | 0.0061 | 0.057 | 0.0005 | 0.57 | 0.56 | 0.96 (7)   |

**Weighted mean age: 457 ± 2 Ma (n = 22); MSWD: 3.5**

AZ 09-14-14 (8), 37° 37.658' N 101° 49.904' E (3198 m)

|       |       |      |       |      |       |      |      |        |        |        |        |       |        |      |      |          |
|-------|-------|------|-------|------|-------|------|------|--------|--------|--------|--------|-------|--------|------|------|----------|
| (8)-1 | 461.1 | 17.7 | 454.6 | 17.5 | 421.8 | 48.4 | 100  | 0.0742 | 0.0030 | 0.5647 | 0.0269 | 0.055 | 0.0012 | 0.89 | 0.88 | 1.09 (1) |
| (8)-2 | 465.8 | 19.2 | 459.3 | 25   | 426.5 | 92.8 | 99.8 | 0.0749 | 0.0032 | 0.5719 | 0.0387 | 0.055 | 0.0023 | 0.81 | 0.6  | 1.09 (1) |
| (8)-3 | 580.4 | 20.2 | 865.9 | 21.3 | 1690  | 18.3 | 100  | 0.0942 | 0.0034 | 1.346  | 0.0491 | 0.104 | 0.0010 | 0.96 | 0.47 | 0.34 (1) |
| (8)-4 | 457.8 | 19   | 457.6 | 24.3 | 456.9 | 126  | 99.6 | 0.0736 | 0.0032 | 0.5694 | 0.0376 | 0.056 | 0.0032 | 0.53 | 0.89 | 1.00 (1) |
| (8)-5 | 437.7 | 15.9 | 450.2 | 17.6 | 514.2 | 60.4 | 99.9 | 0.0703 | 0.0026 | 0.5579 | 0.0270 | 0.058 | 0.0016 | 0.82 | 0.5  | 0.85 (1) |
| (8)-6 | 452   | 15.4 | 416.3 | 30.3 | 223   | 182  | 99.4 | 0.0726 | 0.0026 | 0.5068 | 0.0450 | 0.051 | 0.0040 | 0.47 | 0.56 | 2.03 (1) |
| (8)-7 | 507.7 | 21.2 | 492.6 | 19   | 423   | 55.6 | 99.9 | 0.0819 | 0.0036 | 0.6244 | 0.0304 | 0.055 | 0.0014 | 0.86 | 0.81 | 1.20 (1) |
| (8)-8 | 503.6 | 22.1 | 506   | 20.7 | 516.7 | 46.2 | 100  | 0.0813 | 0.0037 | 0.646  | 0.0335 | 0.058 | 0.0012 | 0.91 | 0.54 | 0.97 (1) |
| (8)-9 | 499.1 | 26.7 | 490.4 | 18.2 | 449.9 | 59.6 | 99.9 | 0.0805 | 0.0045 | 0.6209 | 0.0291 | 0.056 | 0.0015 | 0.88 | 0.93 | 1.11 (1) |

**Weighted mean age: 462 ± 14 Ma (n = 7); MSWD: 1.2**

AZ 05-04-12 (7), 38° 41.752' N 98° 45.627' E (3850 m)

|       |       |     |       |     |       |      |      |       |        |       |        |       |        |      |      |          |
|-------|-------|-----|-------|-----|-------|------|------|-------|--------|-------|--------|-------|--------|------|------|----------|
| (7)-1 | 470.2 | 2.8 | 467.9 | 6.9 | 456.5 | 30.7 | 81.8 | 0.076 | 0.0005 | 0.585 | 0.0086 | 0.056 | 0.0008 | 0.40 | 0.59 | 1.03 (7) |
| (7)-2 | 471.4 | 2.9 | 470.9 | 7.9 | 468.6 | 31.6 | 83.5 | 0.076 | 0.0005 | 0.590 | 0.0098 | 0.056 | 0.0008 | 0.37 | 0.43 | 1.01 (7) |
| (7)-3 | 471.1 | 2.9 | 475.4 | 8.9 | 496.3 | 40.1 | 76.0 | 0.076 | 0.0005 | 0.597 | 0.0112 | 0.057 | 0.0010 | 0.33 | 0.82 | 0.95 (7) |

|        |       |     |       |      |       |      |      |       |        |       |        |       |        |      |      |        |          |
|--------|-------|-----|-------|------|-------|------|------|-------|--------|-------|--------|-------|--------|------|------|--------|----------|
| (7)-4  | 472.5 | 2.7 | 472.1 | 5.2  | 470.2 | 23.8 | 88.4 | 0.076 | 0.0004 | 0.592 | 0.0066 | 0.056 | 0.0006 | 0.52 | 0.24 | 1.00   |          |
| (7)-5  | 490.1 | 2.9 | 488.0 | 5.0  | 478.1 | 23.2 | 72.7 | 0.079 | 0.0005 | 0.617 | 0.0063 | 0.057 | 0.0006 | 0.58 | 1.01 | 1.03 X | (4), (7) |
| (7)-6  | 471.0 | 2.9 | 472.3 | 4.3  | 478.2 | 19.6 | 75.4 | 0.076 | 0.0005 | 0.592 | 0.0054 | 0.057 | 0.0005 | 0.67 | 0.99 | 0.98   |          |
| (7)-7  | 471.0 | 3.0 | 473.8 | 4.3  | 487.3 | 20.4 | 79.1 | 0.076 | 0.0005 | 0.595 | 0.0054 | 0.057 | 0.0005 | 0.70 | 0.69 | 0.97   |          |
| (7)-8  | 419.7 | 2.9 | 422.4 | 13.1 | 436.9 | 62.7 | 74.9 | 0.067 | 0.0005 | 0.516 | 0.0160 | 0.056 | 0.0016 | 0.22 | 0.78 | 0.96 X | (8)      |
| (7)-9  | 470.7 | 2.8 | 468.9 | 6.8  | 460.1 | 32.5 | 74.9 | 0.076 | 0.0004 | 0.587 | 0.0085 | 0.056 | 0.0008 | 0.41 | 0.89 | 1.02   |          |
| (7)-10 | 470.4 | 2.8 | 467.7 | 8.0  | 454.8 | 34.9 | 73.0 | 0.076 | 0.0005 | 0.585 | 0.0100 | 0.056 | 0.0009 | 0.35 | 1.03 | 1.03   |          |
| (7)-11 | 470.2 | 2.8 | 474.1 | 5.9  | 493.1 | 26.7 | 86.7 | 0.076 | 0.0004 | 0.595 | 0.0074 | 0.057 | 0.0007 | 0.47 | 0.32 | 0.95   |          |
| (7)-12 | 469.6 | 2.8 | 471.1 | 4.3  | 478.7 | 20.4 | 72.7 | 0.076 | 0.0004 | 0.590 | 0.0054 | 0.057 | 0.0005 | 0.64 | 1.12 | 0.98   | (7)      |
| (7)-13 | 473.0 | 2.8 | 471.4 | 4.7  | 463.3 | 22.1 | 79.6 | 0.076 | 0.0004 | 0.591 | 0.0059 | 0.056 | 0.0006 | 0.58 | 0.71 | 1.02   |          |
| (7)-14 | 480.3 | 2.8 | 484.4 | 4.9  | 503.6 | 22.1 | 80.5 | 0.077 | 0.0005 | 0.611 | 0.0062 | 0.057 | 0.0006 | 0.58 | 0.66 | 0.95   |          |
| (7)-15 | 480.8 | 2.9 | 483.0 | 4.5  | 493.3 | 19.7 | 85.1 | 0.077 | 0.0005 | 0.609 | 0.0057 | 0.057 | 0.0005 | 0.64 | 0.43 | 0.97   |          |
| (7)-16 | 483.1 | 2.8 | 480.3 | 4.8  | 467.3 | 20.8 | 77.8 | 0.078 | 0.0005 | 0.605 | 0.0060 | 0.056 | 0.0005 | 0.59 | 0.85 | 1.03   |          |
| (7)-17 | 501.5 | 3.1 | 507.0 | 6.3  | 531.7 | 23.5 | 77.1 | 0.081 | 0.0005 | 0.648 | 0.0081 | 0.058 | 0.0006 | 0.50 | 0.77 | 0.94 X | (4)      |
| (7)-18 | 483.2 | 2.8 | 477.9 | 4.7  | 452.9 | 21.2 | 79.6 | 0.078 | 0.0005 | 0.601 | 0.0059 | 0.056 | 0.0005 | 0.59 | 0.68 | 1.07   |          |
| (7)-19 | 472.0 | 2.9 | 475.9 | 4.3  | 495.1 | 19.1 | 92.7 | 0.076 | 0.0005 | 0.598 | 0.0054 | 0.057 | 0.0005 | 0.69 | 0.06 | 0.95   |          |
| (7)-20 | 416.2 | 3.7 | 421.5 | 5.0  | 450.7 | 20.7 | 85.8 | 0.067 | 0.0006 | 0.515 | 0.0061 | 0.056 | 0.0005 | 0.74 | 0.38 | 0.92 X | (8)      |
| (7)-21 | 510.6 | 3.4 | 514.6 | 4.9  | 532.2 | 19.7 | 80.2 | 0.082 | 0.0006 | 0.660 | 0.0062 | 0.058 | 0.0005 | 0.71 | 0.63 | 0.96 X | (4)      |
| (7)-22 | 481.3 | 3.0 | 482.1 | 7.5  | 485.9 | 33.1 | 78.2 | 0.078 | 0.0005 | 0.608 | 0.0094 | 0.057 | 0.0009 | 0.40 | 0.70 | 0.99   |          |
| (7)-23 | 480.7 | 2.9 | 474.9 | 7.0  | 446.8 | 31.9 | 76.9 | 0.077 | 0.0005 | 0.596 | 0.0088 | 0.056 | 0.0008 | 0.41 | 0.76 | 1.08   |          |
| (7)-24 | 490.5 | 3.0 | 490.7 | 5.2  | 491.8 | 22.1 | 66.6 | 0.079 | 0.0005 | 0.621 | 0.0066 | 0.057 | 0.0006 | 0.57 | 1.40 | 1.00 X | (4), (7) |
| (7)-25 | 471.1 | 2.8 | 470.5 | 4.3  | 467.4 | 19.6 | 71.3 | 0.076 | 0.0004 | 0.589 | 0.0054 | 0.056 | 0.0005 | 0.64 | 1.09 | 1.01   | (7)      |

**Weighted mean age: 474 ± 3 Ma (n=19); MSWD: 3.2**

AZ 05-06-12 (2), 38° 36.800' N 98° 58.482' E (4509 m)

|        |       |     |       |     |       |      |      |       |        |       |        |       |        |      |      |        |     |
|--------|-------|-----|-------|-----|-------|------|------|-------|--------|-------|--------|-------|--------|------|------|--------|-----|
| (6)-1  | 529.4 | 3.2 | 530.2 | 5.9 | 533.6 | 23.0 | 80.7 | 0.086 | 0.0005 | 0.686 | 0.0076 | 0.058 | 0.0006 | 0.72 | 0.73 | 0.99   |     |
| (6)-2  | 525.1 | 3.0 | 517.1 | 5.9 | 481.8 | 24.0 | 81.7 | 0.085 | 0.0005 | 0.664 | 0.0076 | 0.057 | 0.0006 | 0.40 | 0.68 | 1.09   |     |
| (6)-3  | 518.1 | 3.1 | 518.8 | 4.9 | 521.9 | 18.9 | 79.1 | 0.084 | 0.0005 | 0.667 | 0.0063 | 0.058 | 0.0005 | 0.59 | 0.90 | 0.99   |     |
| (6)-4  | 520.8 | 3.2 | 519.8 | 5.2 | 515.7 | 20.2 | 82.0 | 0.084 | 0.0005 | 0.669 | 0.0067 | 0.058 | 0.0005 | 0.57 | 0.72 | 1.01   |     |
| (6)-5  | 520.1 | 3.0 | 518.2 | 5.4 | 509.7 | 22.2 | 79.1 | 0.084 | 0.0005 | 0.666 | 0.0070 | 0.057 | 0.0006 | 0.72 | 0.92 | 1.02   |     |
| (6)-6  | 533.4 | 3.3 | 526.3 | 7.8 | 495.3 | 28.2 | 84.3 | 0.086 | 0.0005 | 0.679 | 0.0101 | 0.057 | 0.0007 | 0.43 | 0.59 | 1.08   | (4) |
| (6)-7  | 565.8 | 3.3 | 567.3 | 6.3 | 573.0 | 23.7 | 81.4 | 0.092 | 0.0005 | 0.748 | 0.0084 | 0.059 | 0.0006 | 0.84 | 0.69 | 0.99 X | (4) |
| (6)-8  | 549.7 | 3.7 | 550.1 | 8.1 | 552.2 | 29.0 | 82.3 | 0.089 | 0.0006 | 0.719 | 0.0105 | 0.059 | 0.0008 | 0.60 | 0.71 | 1.00 X | (4) |
| (6)-9  | 543.3 | 3.3 | 539.7 | 6.2 | 524.3 | 21.7 | 81.0 | 0.088 | 0.0005 | 0.702 | 0.0081 | 0.058 | 0.0006 | 0.71 | 0.81 | 1.04 X | (4) |
| (6)-10 | 542.0 | 3.2 | 543.6 | 6.4 | 550.7 | 24.6 | 80.9 | 0.088 | 0.0005 | 0.708 | 0.0083 | 0.059 | 0.0007 | 0.59 | 0.79 | 0.98 X | (4) |
| (6)-11 | 510.8 | 3.0 | 507.5 | 4.8 | 492.6 | 20.2 | 80.1 | 0.082 | 0.0005 | 0.648 | 0.0061 | 0.057 | 0.0005 | 0.81 | 0.85 | 1.04   |     |
| (6)-12 | 519.5 | 3.1 | 520.5 | 4.8 | 524.7 | 19.1 | 81.3 | 0.084 | 0.0005 | 0.670 | 0.0061 | 0.058 | 0.0005 | 0.43 | 0.74 | 0.99   |     |
| (6)-13 | 522.7 | 3.1 | 516.2 | 4.5 | 487.5 | 17.1 | 78.7 | 0.084 | 0.0005 | 0.663 | 0.0057 | 0.057 | 0.0004 | 0.72 | 0.86 | 1.07   |     |
| (6)-14 | 520.1 | 3.2 | 523.8 | 4.9 | 540.1 | 19.0 | 81.7 | 0.084 | 0.0005 | 0.675 | 0.0064 | 0.058 | 0.0005 | 0.69 | 0.55 | 0.96   |     |

|        |       |     |       |     |       |      |      |       |        |       |        |        |      |      |        |
|--------|-------|-----|-------|-----|-------|------|------|-------|--------|-------|--------|--------|------|------|--------|
| (6)-15 | 519.7 | 3.0 | 520.1 | 4.5 | 521.6 | 18.0 | 79.9 | 0.084 | 0.0005 | 0.669 | 0.0058 | 0.0005 | 0.51 | 0.65 | 1.00   |
| (6)-16 | 521.0 | 3.1 | 517.5 | 4.5 | 502.0 | 17.7 | 76.5 | 0.084 | 0.0005 | 0.665 | 0.0057 | 0.0005 | 0.81 | 0.83 | 1.04   |
| (6)-17 | 520.0 | 3.1 | 520.2 | 5.3 | 521.5 | 21.1 | 77.6 | 0.084 | 0.0005 | 0.669 | 0.0069 | 0.0006 | 0.67 | 0.71 | 1.00   |
| (6)-18 | 522.3 | 3.1 | 520.0 | 4.9 | 509.6 | 19.0 | 78.4 | 0.084 | 0.0005 | 0.669 | 0.0062 | 0.0005 | 0.60 | 0.67 | 1.02   |
| (6)-19 | 519.9 | 3.1 | 522.9 | 4.8 | 536.0 | 18.2 | 92.6 | 0.084 | 0.0005 | 0.674 | 0.0062 | 0.0005 | 0.60 | 0.06 | (6)    |
| (6)-20 | 520.3 | 3.1 | 519.3 | 6.2 | 515.0 | 25.6 | 77.2 | 0.084 | 0.0005 | 0.668 | 0.0080 | 0.0007 | 0.52 | 0.64 | 1.01   |
| (6)-21 | 522.5 | 3.1 | 522.9 | 4.5 | 524.7 | 17.6 | 80.8 | 0.084 | 0.0005 | 0.674 | 0.0058 | 0.0005 | 0.74 | 0.52 | 1.00   |
| (6)-22 | 539.2 | 3.2 | 537.3 | 4.9 | 529.0 | 18.4 | 77.3 | 0.087 | 0.0005 | 0.697 | 0.0064 | 0.0005 | 0.76 | 0.63 | 1.02 X |
| (6)-23 | 520.8 | 3.1 | 520.0 | 5.1 | 516.5 | 19.9 | 78.4 | 0.084 | 0.0005 | 0.669 | 0.0065 | 0.0005 | 0.61 | 0.55 | 1.01   |
| (6)-24 | 520.9 | 3.1 | 522.3 | 5.4 | 528.3 | 21.6 | 78.3 | 0.084 | 0.0005 | 0.673 | 0.0070 | 0.0005 | 0.88 | 0.59 | 0.99   |
| (6)-25 | 520.5 | 3.2 | 521.1 | 6.3 | 523.5 | 24.6 | 78.6 | 0.084 | 0.0005 | 0.671 | 0.0081 | 0.0005 | 0.38 | 0.59 | 0.99   |

**Weighted mean age: 521 ± 2 Ma (n = 20); MSWD: 1.3**

AZ 05-03-12 (11), 38° 36.640' N 98° 59.398' E (4442 m)

|         |        |      |        |      |        |      |      |       |        |       |        |       |        |      |      |        |          |
|---------|--------|------|--------|------|--------|------|------|-------|--------|-------|--------|-------|--------|------|------|--------|----------|
| (11)-1  | 1587.7 | 9.7  | 1724.2 | 14.5 | 1894.2 | 13.8 | 70.0 | 0.279 | 0.0017 | 4.464 | 0.0376 | 0.116 | 0.0009 | 0.72 | 1.24 | 0.84 X | (1)      |
| (11)-2  | 115.8  | 0.7  | 141.8  | 2.2  | 601.2  | 32.9 | 80.1 | 0.018 | 0.0001 | 0.150 | 0.0023 | 0.060 | 0.0009 | 0.40 | 0.65 | 0.19 X | (1)      |
| (11)-3  | 551.3  | 3.5  | 552.0  | 5.9  | 555.0  | 22.5 | 83.9 | 0.089 | 0.0006 | 0.722 | 0.0078 | 0.059 | 0.0006 | 0.59 | 0.54 | 0.99   | (8)      |
| (11)-4  | 501.3  | 2.9  | 501.3  | 5.2  | 501.7  | 22.1 | 78.9 | 0.081 | 0.0005 | 0.638 | 0.0066 | 0.057 | 0.0006 | 0.57 | 0.87 | 1.00 X | (8)      |
| (11)-5  | 551.9  | 3.4  | 551.6  | 4.8  | 550.4  | 18.5 | 83.6 | 0.089 | 0.0006 | 0.722 | 0.0062 | 0.059 | 0.0005 | 0.72 | 0.78 | 1.00   | (1)      |
| (11)-6  | 550.4  | 3.3  | 846.8  | 11.8 | 1731.5 | 23.3 | 73.4 | 0.089 | 0.0005 | 1.303 | 0.0181 | 0.106 | 0.0013 | 0.43 | 0.75 | 0.32 X | (1)      |
| (11)-7  | 1585.9 | 13.2 | 2033.5 | 20.1 | 2524.3 | 12.3 | 74.1 | 0.279 | 0.0023 | 6.409 | 0.0634 | 0.167 | 0.0012 | 0.84 | 1.58 | 0.63 X | (1)      |
| (11)-8  | 517.2  | 3.1  | 516.8  | 5.1  | 515.1  | 20.1 | 80.0 | 0.084 | 0.0005 | 0.664 | 0.0066 | 0.058 | 0.0005 | 0.60 | 1.02 | 1.00 X | (8)      |
| (11)-9  | 528.6  | 3.1  | 531.0  | 4.4  | 541.5  | 16.6 | 82.1 | 0.085 | 0.0005 | 0.687 | 0.0057 | 0.058 | 0.0004 | 0.71 | 0.86 | 0.98   | (8)      |
| (11)-10 | 530.6  | 3.7  | 527.6  | 6.2  | 514.9  | 23.6 | 78.6 | 0.086 | 0.0006 | 0.681 | 0.0080 | 0.058 | 0.0006 | 0.59 | 1.11 | 1.03   | (1), (4) |
| (11)-11 | 1721.1 | 18.3 | 1884.8 | 24.6 | 2070.2 | 15.4 | 70.1 | 0.306 | 0.0033 | 5.400 | 0.0706 | 0.128 | 0.0011 | 0.81 | 1.72 | 0.83 X | (1), (4) |
| (11)-12 | 529.2  | 4.4  | 532.2  | 10.3 | 545.2  | 28.5 | 75.5 | 0.086 | 0.0007 | 0.689 | 0.0134 | 0.058 | 0.0008 | 0.43 | 1.16 | 0.97   | (4)      |
| (11)-13 | 529.8  | 3.1  | 528.8  | 4.3  | 524.4  | 16.5 | 80.1 | 0.086 | 0.0005 | 0.683 | 0.0055 | 0.058 | 0.0004 | 0.72 | 0.81 | 1.01   | (4)      |
| (11)-14 | 572.5  | 3.9  | 574.7  | 5.7  | 583.5  | 16.8 | 88.3 | 0.093 | 0.0006 | 0.761 | 0.0075 | 0.059 | 0.0005 | 0.69 | 0.26 | 0.98 X | (4)      |
| (11)-15 | 549.7  | 3.2  | 548.6  | 6.3  | 544.2  | 23.8 | 79.2 | 0.089 | 0.0005 | 0.717 | 0.0082 | 0.058 | 0.0006 | 0.51 | 0.54 | 1.01   | (8)      |
| (11)-16 | 511.1  | 3.9  | 509.1  | 4.8  | 499.9  | 16.6 | 80.3 | 0.083 | 0.0006 | 0.651 | 0.0062 | 0.057 | 0.0004 | 0.81 | 0.71 | 1.02 X | (8)      |
| (11)-17 | 553.0  | 3.3  | 547.3  | 4.8  | 523.9  | 17.8 | 83.3 | 0.090 | 0.0005 | 0.714 | 0.0063 | 0.058 | 0.0005 | 0.67 | 0.46 | 1.06   | (6)      |
| (11)-18 | 531.7  | 3.9  | 529.5  | 6.5  | 519.8  | 21.0 | 77.7 | 0.086 | 0.0006 | 0.684 | 0.0083 | 0.058 | 0.0006 | 0.60 | 0.74 | 1.02   | (6)      |
| (11)-19 | 532.6  | 3.1  | 532.8  | 5.2  | 533.7  | 20.7 | 92.6 | 0.086 | 0.0005 | 0.690 | 0.0067 | 0.058 | 0.0005 | 0.60 | 0.06 | 1.00   | (6)      |
| (11)-20 | 551.0  | 3.3  | 546.8  | 6.2  | 529.1  | 23.4 | 76.8 | 0.089 | 0.0005 | 0.713 | 0.0081 | 0.058 | 0.0006 | 0.52 | 0.67 | 1.04   | (6)      |
| (11)-21 | 529.6  | 3.3  | 528.2  | 4.4  | 522.4  | 16.3 | 75.2 | 0.086 | 0.0005 | 0.682 | 0.0057 | 0.058 | 0.0004 | 0.74 | 0.91 | 1.01   | (7), (4) |
| (11)-22 | 1670.5 | 10.1 | 1682.3 | 13.3 | 1696.9 | 13.1 | 71.0 | 0.296 | 0.0018 | 4.242 | 0.0336 | 0.104 | 0.0007 | 0.76 | 1.10 | 0.98 X | (7), (4) |
| (11)-23 | 551.5  | 3.6  | 552.8  | 5.9  | 558.2  | 19.4 | 82.5 | 0.089 | 0.0006 | 0.724 | 0.0077 | 0.059 | 0.0005 | 0.61 | 0.46 | 0.99   | (7), (4) |
| (11)-24 | 549.0  | 6.5  | 546.9  | 7.3  | 538.2  | 17.6 | 83.7 | 0.089 | 0.0010 | 0.714 | 0.0095 | 0.058 | 0.0005 | 0.88 | 0.66 | 1.02   | (7), (4) |
| (11)-25 | 553.1  | 3.3  | 549.4  | 8.7  | 534.4  | 32.9 | 81.5 | 0.090 | 0.0005 | 0.718 | 0.0113 | 0.058 | 0.0009 | 0.38 | 0.74 | 1.03   | (7), (4) |

**Weighted mean age: 541 ± 6 Ma (n = 15); MSWD: 10.1**

*RR 05-04-12 (2), 38° 32.708' N 99° 00.082' E (4060 m)*

|         |        |      |        |       |        |       |      |       |        |       |        |       |        |      |      |        |
|---------|--------|------|--------|-------|--------|-------|------|-------|--------|-------|--------|-------|--------|------|------|--------|
| (1a)-1  | 832.8  | 4.7  | 845.1  | 12.1  | 877.8  | 29.1  | 79.5 | 0.138 | 0.0008 | 1.299 | 0.0186 | 0.068 | 0.0010 | 0.40 | 0.51 | 0.95   |
| (1a)-2  | 807.9  | 4.7  | 828.5  | 10.9  | 884.3  | 27.6  | 79.6 | 0.134 | 0.0008 | 1.261 | 0.0166 | 0.069 | 0.0009 | 0.44 | 0.54 | 0.91   |
| (1a)-3  | 835.3  | 4.7  | 840.5  | 10.4  | 854.3  | 25.1  | 78.2 | 0.138 | 0.0008 | 1.288 | 0.0159 | 0.068 | 0.0008 | 0.46 | 0.59 | 0.98   |
| (1a)-4  | 843.8  | 4.7  | 863.3  | 9.3   | 913.8  | 21.4  | 78.3 | 0.140 | 0.0008 | 1.340 | 0.0145 | 0.070 | 0.0007 | 0.52 | 0.57 | 0.92   |
| (1a)-5  | 764.5  | 5.3  | 774.2  | 26.8  | 802.2  | 62.4  | 83.8 | 0.126 | 0.0009 | 1.144 | 0.0396 | 0.066 | 0.0020 | 0.20 | 0.40 | 0.95   |
| (1a)-6  | 829.6  | 5.7  | 832.4  | 35.5  | 840.1  | 80.6  | 79.9 | 0.137 | 0.0009 | 1.270 | 0.0541 | 0.067 | 0.0026 | 0.16 | 0.37 | 0.99   |
| (1a)-7  | 883.8  | 6.1  | 892.1  | 35.7  | 912.4  | 72.7  | 76.0 | 0.147 | 0.0010 | 1.407 | 0.0564 | 0.069 | 0.0025 | 0.17 | 0.46 | 0.97   |
| (1a)-8  | 859.7  | 6.4  | 886.5  | 43.7  | 953.8  | 85.8  | 74.0 | 0.143 | 0.0011 | 1.394 | 0.0687 | 0.071 | 0.0030 | 0.15 | 0.62 | 0.90   |
| (1a)-9  | 654.8  | 5.9  | 669.6  | 42.4  | 719.9  | 128.4 | 74.6 | 0.107 | 0.0010 | 0.934 | 0.0592 | 0.063 | 0.0038 | 0.14 | 0.04 | 0.91 X |
| (1a)-10 | 823.9  | 7.2  | 829.0  | 35.3  | 842.8  | 73.6  | 78.0 | 0.136 | 0.0012 | 1.262 | 0.0538 | 0.067 | 0.0024 | 0.21 | 0.50 | 0.98   |
| (1a)-11 | 1074.1 | 26.4 | 1106.2 | 198.9 | 1169.8 | 515.4 | 55.1 | 0.181 | 0.0045 | 1.972 | 0.3546 | 0.079 | 0.0205 | 0.14 | 0.29 | 0.92 X |
| (1a)-12 | 915.4  | 8.9  | 926.7  | 77.4  | 953.9  | 167.5 | 76.4 | 0.153 | 0.0015 | 1.491 | 0.1246 | 0.071 | 0.0058 | 0.12 | 0.34 | 0.96   |
| (1a)-13 | 995.4  | 10.0 | 1010.8 | 43.4  | 1044.4 | 77.6  | 76.2 | 0.167 | 0.0017 | 1.706 | 0.0732 | 0.074 | 0.0028 | 0.23 | 0.52 | 0.95 X |
| (1a)-14 | 1029.8 | 8.4  | 1074.1 | 23.1  | 1165.2 | 38.6  | 71.4 | 0.173 | 0.0014 | 1.880 | 0.0405 | 0.079 | 0.0015 | 0.38 | 0.68 | 0.88 X |
| (1a)-15 | 1203.9 | 18.8 | 1247.3 | 94.5  | 1323.2 | 136.6 | 67.2 | 0.205 | 0.0032 | 2.416 | 0.1829 | 0.085 | 0.0060 | 0.21 | 0.43 | 0.91 X |
| (1a)-16 | 1074.1 | 23.2 | 1100.6 | 61.2  | 1153.4 | 108.8 | 70.2 | 0.181 | 0.0039 | 1.956 | 0.1088 | 0.078 | 0.0043 | 0.39 | 0.31 | 0.93 X |
| (1a)-17 | 797.0  | 4.5  | 814.3  | 10.6  | 862.1  | 26.6  | 86.7 | 0.132 | 0.0007 | 1.230 | 0.0160 | 0.068 | 0.0009 | 0.43 | 0.32 | 0.92   |
| (1a)-18 | 776.5  | 4.7  | 787.3  | 29.3  | 818.1  | 77.3  | 85.6 | 0.128 | 0.0008 | 1.171 | 0.0437 | 0.066 | 0.0025 | 0.16 | 0.34 | 0.95   |
| (1a)-19 | 792.1  | 4.6  | 802.4  | 15.1  | 831.2  | 38.3  | 81.5 | 0.131 | 0.0008 | 1.204 | 0.0227 | 0.067 | 0.0012 | 0.31 | 0.57 | 0.95   |
| (1a)-20 | 813.7  | 4.7  | 820.4  | 8.7   | 838.7  | 20.8  | 92.1 | 0.135 | 0.0008 | 1.243 | 0.0132 | 0.067 | 0.0007 | 0.55 | 0.06 | 0.97   |
| (1a)-21 | 748.8  | 4.3  | 768.3  | 16.1  | 825.5  | 42.7  | 84.6 | 0.123 | 0.0007 | 1.131 | 0.0237 | 0.067 | 0.0014 | 0.27 | 0.40 | 0.91   |
| (1a)-22 | 805.8  | 4.8  | 827.8  | 21.9  | 887.1  | 54.1  | 86.3 | 0.133 | 0.0008 | 1.260 | 0.0334 | 0.069 | 0.0018 | 0.22 | 0.31 | 0.91   |
| (1a)-23 | 802.4  | 4.7  | 821.1  | 20.9  | 872.1  | 51.7  | 81.2 | 0.133 | 0.0008 | 1.245 | 0.0317 | 0.068 | 0.0017 | 0.23 | 0.58 | 0.92   |
| (1a)-24 | 800.9  | 4.8  | 819.3  | 10.8  | 869.7  | 26.7  | 81.6 | 0.132 | 0.0008 | 1.241 | 0.0164 | 0.068 | 0.0009 | 0.45 | 0.56 | 0.92   |
| (1a)-25 | 882.6  | 6.7  | 902.2  | 40.1  | 950.5  | 71.2  | 78.1 | 0.147 | 0.0011 | 1.432 | 0.0636 | 0.071 | 0.0025 | 0.17 | 0.58 | 0.93   |

**Weighted mean Pb-Pb age: 868 ± 16 Ma (n = 19); MSWD: 0.79**

*AY 09-21-11 (4), 38° 41.418' N 98° 37.762' E (3624 m)*

|       |       |      |       |      |       |      |       |       |        |       |        |       |        |      |      |      |
|-------|-------|------|-------|------|-------|------|-------|-------|--------|-------|--------|-------|--------|------|------|------|
| (4)-1 | 974.0 | 80.8 | 956.1 | 56.0 | 915.0 | 17.1 | 100.0 | 0.163 | 0.0146 | 1.564 | 0.1410 | 0.070 | 0.0006 | 1.00 | 0.40 | 1.06 |
| (4)-2 | 882.4 | 54.6 | 886.3 | 41.9 | 896.0 | 27.1 | 99.9  | 0.147 | 0.0097 | 1.394 | 0.0988 | 0.069 | 0.0009 | 0.98 | 0.39 | 0.98 |
| (4)-3 | 855.8 | 49.6 | 873.1 | 36.7 | 917.4 | 33.1 | 99.9  | 0.142 | 0.0088 | 1.363 | 0.0854 | 0.070 | 0.0011 | 0.97 | 0.39 | 0.93 |
| (4)-4 | 903.0 | 60.7 | 895.1 | 44.7 | 875.8 | 25.2 | 99.9  | 0.150 | 0.0108 | 1.415 | 0.1060 | 0.068 | 0.0008 | 0.99 | 0.29 | 1.03 |
| (4)-5 | 902.7 | 46.7 | 892.4 | 33.0 | 867.1 | 20.2 | 99.8  | 0.150 | 0.0083 | 1.408 | 0.0782 | 0.068 | 0.0007 | 0.98 | 0.49 | 1.04 |
| (4)-6 | 956.2 | 57.8 | 947.2 | 39.2 | 926.4 | 18.6 | 100.0 | 0.160 | 0.0104 | 1.542 | 0.0982 | 0.070 | 0.0006 | 0.99 | 0.37 | 1.03 |
| (4)-7 | 888.6 | 53.4 | 903.7 | 39.3 | 940.9 | 17.2 | 100.0 | 0.148 | 0.0095 | 1.435 | 0.0943 | 0.070 | 0.0006 | 0.99 | 0.40 | 0.94 |
| (4)-8 | 906.2 | 63.4 | 918.4 | 43.2 | 947.8 | 32.1 | 100.0 | 0.151 | 0.0113 | 1.471 | 0.1050 | 0.071 | 0.0011 | 0.98 | 0.37 | 0.96 |



|  |        |      |        |      |        |       |       |       |        |       |        |       |        |      |      |                 |
|--|--------|------|--------|------|--------|-------|-------|-------|--------|-------|--------|-------|--------|------|------|-----------------|
| (4)-9  | 989.1  | 69.4 | 948.5  | 47.2 | 855.5  | 33.9  | 99.8  | 0.166 | 0.0125 | 1.545 | 0.1180 | 0.068 | 0.0011 | 0.98 | 0.38 | 1.16            |
| (4)-10   | 917.0  | 46.8 | 909.1  | 33.5 | 889.9  | 20.5  | 100.0 | 0.153 | 0.0084 | 1.448 | 0.0807 | 0.069 | 0.0007 | 0.98 | 0.34 | 1.03            |
| (4)-11   | 956.7  | 61.0 | 935.0  | 41.5 | 884.3  | 18.0  | 100.0 | 0.160 | 0.0110 | 1.511 | 0.1030 | 0.069 | 0.0006 | 0.99 | 0.36 | 1.08            |
| (4)-12   | 1085.0 | 96.4 | 1037.0 | 62.4 | 937.9  | 31.1  | 99.9  | 0.183 | 0.0177 | 1.777 | 0.1710 | 0.070 | 0.0011 | 0.99 | 0.72 | 1.16            |
| (4)-13   | 894.7  | 58.5 | 901.9  | 41.8 | 919.4  | 25.4  | 100.0 | 0.149 | 0.0104 | 1.431 | 0.1000 | 0.070 | 0.0009 | 0.98 | 0.17 | 0.97            |
| (4)-14   | 966.0  | 59.8 | 953.6  | 42.0 | 925.1  | 14.7  | 100.0 | 0.162 | 0.0108 | 1.558 | 0.1060 | 0.070 | 0.0005 | 0.99 | 0.32 | 1.04            |
| (4)-15   | 950.6  | 51.8 | 941.6  | 35.9 | 920.8  | 13.2  | 100.0 | 0.159 | 0.0093 | 1.528 | 0.0895 | 0.070 | 0.0004 | 0.99 | 0.30 | 1.03            |
| (4)-16   | 993.9  | 61.9 | 974.3  | 41.1 | 930.3  | 21.9  | 100.0 | 0.167 | 0.0112 | 1.610 | 0.1060 | 0.070 | 0.0007 | 0.99 | 0.58 | 1.07            |
| (4)-17   | 962.0  | 55.4 | 944.4  | 38.5 | 903.8  | 16.0  | 99.9  | 0.161 | 0.0100 | 1.535 | 0.0960 | 0.069 | 0.0005 | 0.99 | 0.44 | 1.06            |
| (4)-18   | 895.7  | 65.0 | 794.5  | 57.2 | 520.2  | 140.0 | 98    | 0.149 | 0.0116 | 1.187 | 0.1230 | 0.058 | 0.0037 | 0.79 | 0.01 | 1.72 X (1)      |
| (4)-19   | 1022.0 | 51.6 | 984.4  | 39.0 | 901.4  | 34.2  | 100   | 0.172 | 0.0094 | 1.637 | 0.1010 | 0.069 | 0.0012 | 0.97 | 0.30 | 1.13            |
| (4)-20   | 1007.0 | 37.7 | 980.6  | 24.6 | 920.9  | 16.9  | 99.9  | 0.169 | 0.0068 | 1.627 | 0.0638 | 0.070 | 0.0006 | 0.98 | 0.19 | 1.09            |
| (4)-21   | 934.1  | 39.4 | 925.2  | 30.3 | 903.9  | 19.5  | 100   | 0.156 | 0.0071 | 1.487 | 0.0743 | 0.069 | 0.0007 | 0.99 | 0.35 | 1.03            |
| (4)-22   | 1014.0 | 55.1 | 982.4  | 37.9 | 913.3  | 21.5  | 100   | 0.170 | 0.0100 | 1.631 | 0.0982 | 0.069 | 0.0007 | 0.98 | 0.46 | 1.11            |
| (4)-23   | 964.9  | 49.1 | 941.8  | 34.8 | 888.1  | 15.1  | 99.8  | 0.162 | 0.0088 | 1.528 | 0.0868 | 0.069 | 0.0005 | 0.99 | 0.15 | 1.09            |
| (4)-24   | 803.9  | 28.7 | 828.8  | 23.1 | 896.1  | 16.2  | 99.9  | 0.133 | 0.0050 | 1.262 | 0.0516 | 0.069 | 0.0005 | 0.98 | 0.23 | 0.90            |
| (4)-25   | 930.8  | 37.2 | 918.6  | 26.2 | 889.3  | 8.8   | 99.9  | 0.155 | 0.0067 | 1.471 | 0.0638 | 0.069 | 0.0003 | 1.00 | 0.17 | 1.05            |
| <b>Weighted mean Pb-Pb age: 905 ± 7 Ma (n = 24); MSWD: 1.3</b>   |        |      |        |      |        |       |       |       |        |       |        |       |        |      |      |                 |
| AZ 04-30-12 (4), 38° 33.522' N 98° 55.447' E (3778 m)            |        |      |        |      |        |       |       |       |        |       |        |       |        |      |      |                 |
| (4a)-1   | 38.2   | 0.2  | 39.9   | 0.9  | 148.1  | 51.8  | 66.6  | 0.006 | 0.0000 | 0.040 | 0.0009 | 0.049 | 0.0011 | 0.26 | 1.65 | 0.26 X (1)      |
| (4a)-2   | 909.5  | 5.9  | 909.6  | 7.2  | 909.8  | 15.0  | 78.7  | 0.152 | 0.0010 | 1.449 | 0.0115 | 0.069 | 0.0005 | 0.81 | 0.70 | 1.00            |
| (4a)-3   | 909.8  | 5.3  | 911.8  | 8.4  | 916.7  | 18.6  | 82.3  | 0.152 | 0.0009 | 1.455 | 0.0135 | 0.070 | 0.0006 | 0.62 | 0.53 | 0.99            |
| (4a)-4   | 658.0  | 3.8  | 783.8  | 11.5 | 1160.8 | 25.5  | 73.2  | 0.107 | 0.0006 | 1.164 | 0.0171 | 0.079 | 0.0010 | 0.40 | 1.04 | 0.57 X (1)      |
| (4a)-5   | 472.5  | 2.9  | 712.6  | 21.8 | 1567.7 | 51.2  | 69.7  | 0.076 | 0.0005 | 1.017 | 0.0312 | 0.097 | 0.0027 | 0.20 | 0.92 | 0.30 X (1)      |
| (4a)-6   | 1066.7 | 11.7 | 1747.1 | 68.0 | 2697.6 | 47.9  | 63.4  | 0.180 | 0.0020 | 4.588 | 0.1787 | 0.185 | 0.0054 | 0.28 | 0.46 | 0.40 X (1)      |
| (4a)-7   | 907.8  | 5.4  | 907.9  | 13.8 | 908.1  | 27.5  | 81.9  | 0.151 | 0.0009 | 1.445 | 0.0220 | 0.069 | 0.0009 | 0.39 | 0.50 | 1.00            |
| (4a)-8   | 1116.6 | 10.4 | 2157.0 | 53.8 | 3376.9 | 27.2  | 49.3  | 0.189 | 0.0018 | 7.367 | 0.1836 | 0.283 | 0.0049 | 0.38 | 0.97 | 0.33 X (1)      |
| (4a)-9   | 944.8  | 7.6  | 1448.8 | 39.3 | 2293.0 | 36.8  | 69.0  | 0.158 | 0.0013 | 3.165 | 0.0859 | 0.145 | 0.0031 | 0.30 | 0.35 | 0.41 X (1)      |
| (4a)-10  | 2036.1 | 15.1 | 2287.0 | 47.3 | 2519.4 | 25.9  | 68.3  | 0.371 | 0.0028 | 8.510 | 0.1759 | 0.166 | 0.0026 | 0.36 | 0.76 | 0.81 X (1)      |
| (4a)-11  | 1967.3 | 11.8 | 1961.3 | 15.3 | 1954.9 | 12.9  | 84.5  | 0.357 | 0.0021 | 5.900 | 0.0460 | 0.120 | 0.0009 | 0.77 | 0.31 | 1.01 X (4)      |
| (4a)-12  | 1810.3 | 11.9 | 1814.8 | 14.9 | 1819.8 | 12.9  | 66.9  | 0.324 | 0.0021 | 4.973 | 0.0409 | 0.111 | 0.0008 | 0.80 | 2.29 | 0.99 X (4), (7) |
| (4a)-13  | 1065.0 | 6.3  | 1410.1 | 24.3 | 1978.7 | 27.1  | 74.1  | 0.180 | 0.0011 | 3.010 | 0.0519 | 0.122 | 0.0018 | 0.34 | 0.47 | 0.54 X (1)      |
| (4a)-14  | 1842.2 | 14.3 | 1848.5 | 17.6 | 1855.7 | 13.3  | 73.0  | 0.331 | 0.0026 | 5.175 | 0.0493 | 0.113 | 0.0008 | 0.81 | 1.67 | 0.99 X (4)      |
| (4a)-15  | 622.3  | 6.4  | 716.4  | 14.9 | 1023.6 | 28.5  | 82.3  | 0.101 | 0.0010 | 1.025 | 0.0213 | 0.073 | 0.0010 | 0.50 | 0.51 | 0.61 X (1)      |
| (4a)-16  | 460.3  | 2.6  | 512.8  | 6.5  | 754.3  | 27.3  | 81.07 | 0.074 | 0.0004 | 0.657 | 0.0083 | 0.064 | 0.0008 | 0.45 | 0.63 | 0.61 X (1)      |
| <b>Weighted mean Pb-Pb age: 912 ± 21 Ma (n = 3); MSWD: 0.053</b> |        |      |        |      |        |       |       |       |        |       |        |       |        |      |      |                 |
| AZ 05-01-12 (1), 38° 39.452' N 98° 41.372' E (3624 m)            |        |      |        |      |        |       |       |       |        |       |        |       |        |      |      |                 |

|   |        |      |        |      |        |      |       |       |        |       |        |       |        |      |      |        |
|---|--------|------|--------|------|--------|------|-------|-------|--------|-------|--------|-------|--------|------|------|--------|
| (1)-1   | 950.5  | 5.8  | 949.0  | 9.4  | 945.5  | 19.6 | 81.1  | 0.159 | 0.0010 | 1.546 | 0.0154 | 0.071 | 0.0007 | 0.61 | 0.55 | 1.01   |
| (1)-2   | 948.8  | 5.7  | 950.2  | 7.8  | 953.3  | 15.3 | 76.1  | 0.159 | 0.0010 | 1.549 | 0.0128 | 0.071 | 0.0005 | 0.73 | 0.82 | 1.00   |
| (1)-3   | 951.8  | 5.6  | 954.5  | 10.1 | 960.7  | 19.3 | 78.7  | 0.159 | 0.0009 | 1.560 | 0.0165 | 0.071 | 0.0007 | 0.56 | 0.61 | 0.99   |
| (1)-4   | 949.0  | 5.7  | 948.6  | 9.3  | 947.7  | 17.5 | 83.2  | 0.159 | 0.0009 | 1.545 | 0.0151 | 0.071 | 0.0006 | 0.61 | 0.39 | 1.00   |
| (1)-5   | 949.8  | 5.6  | 953.3  | 8.6  | 961.4  | 16.8 | 83.1  | 0.159 | 0.0009 | 1.557 | 0.0140 | 0.071 | 0.0006 | 0.65 | 0.40 | 0.99   |
| (1)-6   | 970.7  | 5.8  | 975.7  | 8.1  | 987.1  | 15.7 | 79.6  | 0.163 | 0.0010 | 1.614 | 0.0134 | 0.072 | 0.0006 | 0.71 | 0.60 | 0.98   |
| (1)-7   | 959.9  | 5.6  | 960.1  | 8.5  | 960.7  | 16.5 | 82.9  | 0.161 | 0.0009 | 1.574 | 0.0139 | 0.071 | 0.0006 | 0.66 | 0.42 | 1.00   |
| (1)-8   | 944.8  | 5.6  | 955.4  | 10.3 | 979.7  | 21.0 | 80.0  | 0.158 | 0.0009 | 1.562 | 0.0168 | 0.072 | 0.0007 | 0.55 | 0.55 | 0.96   |
| (1)-9   | 959.3  | 5.7  | 963.3  | 9.9  | 972.5  | 19.4 | 79.6  | 0.160 | 0.0010 | 1.582 | 0.0163 | 0.072 | 0.0007 | 0.58 | 0.51 | 0.99   |
| (1)-10  | 987.5  | 5.8  | 989.1  | 8.3  | 992.4  | 16.1 | 80.6  | 0.166 | 0.0010 | 1.649 | 0.0138 | 0.072 | 0.0006 | 0.70 | 0.47 | 1.00   |
| (1)-11  | 982.2  | 5.7  | 984.4  | 8.1  | 989.5  | 15.6 | 77.9  | 0.165 | 0.0010 | 1.637 | 0.0135 | 0.072 | 0.0006 | 0.70 | 0.60 | 0.99   |
| (1)-12  | 999.1  | 5.8  | 1000.3 | 8.6  | 1002.8 | 16.3 | 77.1  | 0.168 | 0.0010 | 1.678 | 0.0144 | 0.073 | 0.0006 | 0.67 | 0.64 | 1.00   |
| (1)-13  | 995.4  | 5.8  | 1001.7 | 9.5  | 1015.5 | 18.1 | 81.0  | 0.167 | 0.0010 | 1.682 | 0.0160 | 0.073 | 0.0007 | 0.61 | 0.44 | 0.98   |
| (1)-14  | 949.4  | 5.8  | 948.8  | 7.6  | 947.6  | 15.7 | 76.9  | 0.159 | 0.0010 | 1.546 | 0.0124 | 0.071 | 0.0005 | 0.76 | 0.62 | 1.00   |
| (1)-15  | 949.4  | 5.6  | 946.8  | 8.2  | 940.6  | 16.4 | 80.6  | 0.159 | 0.0009 | 1.541 | 0.0134 | 0.070 | 0.0006 | 0.68 | 0.51 | 1.01   |
| (1)-16  | 948.8  | 5.7  | 955.6  | 12.8 | 971.2  | 26.6 | 76.9  | 0.159 | 0.0010 | 1.563 | 0.0210 | 0.071 | 0.0009 | 0.45 | 0.70 | 0.98   |
| (1)-17  | 947.4  | 5.6  | 952.5  | 8.1  | 964.4  | 15.9 | 82.2  | 0.158 | 0.0009 | 1.555 | 0.0132 | 0.071 | 0.0006 | 0.70 | 0.44 | 0.98   |
| (1)-18  | 948.7  | 6.2  | 949.5  | 8.8  | 951.5  | 17.8 | 78.3  | 0.159 | 0.0010 | 1.548 | 0.0143 | 0.071 | 0.0006 | 0.71 | 0.66 | 1.00   |
| (1)-19  | 949.3  | 5.5  | 954.6  | 10.2 | 966.9  | 20.7 | 91.6  | 0.159 | 0.0009 | 1.560 | 0.0167 | 0.071 | 0.0007 | 0.54 | 0.06 | 0.98   |
| (1)-20  | 885.2  | 5.7  | 1071.4 | 24.4 | 1472.9 | 36.3 | 73.7  | 0.147 | 0.0009 | 1.872 | 0.0426 | 0.092 | 0.0018 | 0.28 | 0.56 | 0.60 X |
| (1)-21  | 958.9  | 5.5  | 958.8  | 8.9  | 958.5  | 18.2 | 82.0  | 0.160 | 0.0009 | 1.571 | 0.0146 | 0.071 | 0.0006 | 0.62 | 0.46 | 1.00   |
| (1)-22  | 935.0  | 5.4  | 933.9  | 10.2 | 931.3  | 21.4 | 81.2  | 0.156 | 0.0009 | 1.509 | 0.0165 | 0.070 | 0.0007 | 0.53 | 0.48 | 1.00   |
| (1)-23  | 899.8  | 6.0  | 900.3  | 8.5  | 901.7  | 17.5 | 79.0  | 0.150 | 0.0010 | 1.427 | 0.0134 | 0.069 | 0.0006 | 0.71 | 0.78 | 1.00   |
| (1)-24  | 920.0  | 5.5  | 918.5  | 7.6  | 915.1  | 16.0 | 79.6  | 0.153 | 0.0009 | 1.471 | 0.0122 | 0.070 | 0.0005 | 0.71 | 0.78 | 1.01   |
| (1)-25  | 918.2  | 5.6  | 921.6  | 8.8  | 929.9  | 18.5 | 83.3  | 0.153 | 0.0009 | 1.478 | 0.0142 | 0.070 | 0.0006 | 0.64 | 0.55 | 0.99   |
| <b>Weighted mean Pb-Pb age: 961 ± 12 Ma (n = 24); MSWD: 2.4</b> |        |      |        |      |        |      |       |       |        |       |        |       |        |      |      |        |
| AZ 07-24-13 (9), 38° 42.472' N 98° 38.763' E (3554 m)           |        |      |        |      |        |      |       |       |        |       |        |       |        |      |      |        |
| (9)-1   | 924.9  | 42.0 | 924.6  | 31.6 | 923.7  | 16.8 | 100.0 | 0.154 | 0.0075 | 1.486 | 0.0774 | 0.070 | 0.0006 | 0.99 | 0.30 | 1.00   |
| (9)-2   | 1102.0 | 56.6 | 1039.0 | 37.2 | 909.0  | 12.2 | 99.8  | 0.186 | 0.0104 | 1.783 | 0.1020 | 0.069 | 0.0004 | 0.99 | 0.15 | 1.21   |
| (9)-3   | 989.9  | 43.0 | 961.6  | 29.5 | 897.5  | 13.3 | 99.9  | 0.166 | 0.0078 | 1.578 | 0.0749 | 0.069 | 0.0004 | 0.99 | 0.26 | 1.10   |
| (9)-4   | 1015.0 | 45.9 | 986.6  | 30.8 | 923.5  | 14.7 | 100.0 | 0.171 | 0.0083 | 1.642 | 0.0802 | 0.070 | 0.0005 | 0.99 | 0.20 | 1.10   |
| (9)-5   | 913.8  | 35.1 | 916.4  | 23.4 | 922.6  | 15.5 | 100.0 | 0.152 | 0.0063 | 1.466 | 0.0568 | 0.070 | 0.0005 | 0.98 | 0.42 | 0.99   |
| (9)-6   | 1055.0 | 48.7 | 1003.0 | 33.5 | 890.5  | 26.0 | 100.0 | 0.178 | 0.0089 | 1.685 | 0.0886 | 0.069 | 0.0009 | 0.97 | 0.27 | 1.18   |
| (9)-7   | 931.3  | 45.3 | 936.6  | 31.6 | 949.0  | 10.6 | 99.8  | 0.155 | 0.0081 | 1.515 | 0.0783 | 0.071 | 0.0004 | 1.00 | 0.17 | 0.98   |
| (9)-8   | 846.1  | 38.8 | 863.6  | 30.2 | 908.9  | 18.9 | 99.5  | 0.140 | 0.0069 | 1.341 | 0.0695 | 0.069 | 0.0006 | 0.99 | 0.21 | 0.93   |
| <b>Weighted mean Pb-Pb age: 921 ± 10 Ma (n = 8); MSWD: 1.8</b>  |        |      |        |      |        |      |       |       |        |       |        |       |        |      |      |        |

(7)  
(1)

<sup>1</sup>Concordia coefficient

# Concordance

\$ Excluded from weighted mean calculation; See explanation of Remarks column and text for further details

% Explanation of Remarks column:

- (1) Discordant
- (2) Low % radiogenic  $^{206}\text{Pb}$  relative to other analyses
- (3) Outside UO/U calibration range
- (4) Outside main age population; Possibly inherited
- (5) High  $^{204}\text{Pb}$
- (6) Low Th/u
- (7) High Th/u
- (8) Distinct young age possibly due to Pb loss

**Table A.8. Representative electron-microprobe analyses metamorphic samples for thermobarometry**

| Sample                         | AY 09-21-2011 (1A) [garnet-mica schist] |               |           |                |       |               |           |             |       |         |                |                    |       |                   |                |               |
|--------------------------------|---|---------------|-----------|----------------|-------|---------------|-----------|-------------|-------|---------|----------------|--------------------|-------|-------------------|----------------|---------------|
| Mineral                        | Grt                                     | Bt            | Ms        | Pl             | Grt   | Bt            | Ms        | Pl          | Grt   | Chl     | Ms             | Pl                 | Grt   | Bt                | Ms             | Pl            |
| Descr. #                       | 1; p                                    | 1; mean hi-Ti | 1; low-Si | 1, 2; adj. grt | 2; p  | 2; mean hi-Ti | 2; low-Si | 3; adj. grt | 3; p  | 4; mean | 4; mean low-Si | 4; adj. grt, hi-Ca | 5; p  | 5; Ti, low Al(vi) | 5; mean low-si | 5; mean hi-Ca |
| Interp. <sup>1</sup> n*        | 1                                       | 3             | 1         | 5              | 1     | 2             | 3         | 2           | 1     | 5       | 2              | 1                  | 1     | 1                 | 3              | 2             |
|                                | Peak                                    | Peak          | Peak      | Peak           | Peak  | Peak          | Peak      | Peak        | Peak  | Peak    | Peak           | Peak               | Peak  | Peak              | Peak           | Peak          |
| SiO <sub>2</sub>               | 37.16                                   | 34.82         | 44.98     | 62.55          | 37.08 | 35.42         | 45.11     | 63.25       | 37.12 | 24.38   | 45.52          | 62.20              | 37.06 | 35.41             | 45.82          | 63.80         |
| TiO <sub>2</sub>               | 0.05                                    | 1.50          | 0.35      | 0.02           | 0.08  | 1.27          | 0.39      | 0.02        | 0.13  | 0.07    | 0.38           | 0.01               | 0.08  | 1.68              | 0.47           | 0.00          |
| Al <sub>2</sub> O <sub>3</sub> | 21.90                                   | 19.76         | 37.05     | 23.08          | 22.01 | 19.75         | 36.50     | 22.72       | 21.63 | 23.62   | 36.76          | 23.36              | 21.57 | 20.20             | 37.76          | 23.02         |
| Cr <sub>2</sub> O <sub>3</sub> | 0.00                                    | 0.06          | 0.07      | 0.02           | 0.00  | 0.08          | 0.08      | 0.05        | 0.00  | 0.12    | 0.06           | 0.00               | 0.08  | 0.06              | 0.07           | 0.02          |
| Fe <sub>2</sub> O <sub>3</sub> | 35.22                                   | 20.24         | 1.86      | 0.26           | 35.08 | 20.94         | 1.12      | 0.13        | 35.77 | 26.45   | 1.20           | 0.08               | 35.67 | 20.28             | 1.08           | 0.09          |
| MgO                            | 1.82                                    | 9.17          | 0.68      | 0.00           | 2.36  | 9.55          | 0.43      | 0.01        | 1.82  | 13.74   | 0.49           | 0.00               | 1.74  | 9.27              | 0.52           | 0.00          |
| CaO                            | 4.05                                    | 0.01          | 0.02      | 3.83           | 3.36  | 0.03          | 0.02      | 4.11        | 4.13  | 0.02    | 0.03           | 3.93               | 4.07  | 0.00              | 0.03           | 3.29          |
| MnO                            | 1.11                                    | 0.03          | 0.00      | 0.02           | 1.68  | 0.05          | 0.01      | 1.25        | 0.99  | 0.07    | 0.00           | 0.02               | 1.13  | 0.04              | 0.01           | 0.00          |
| Na <sub>2</sub> O              | 0.02                                    | 0.34          | 1.41      | 9.58           | 0.00  | 0.28          | 1.55      | 0.02        | 0.04  | 0.01    | 1.39           | 9.51               | 0.00  | 0.33              | 1.27           | 9.86          |
| K <sub>2</sub> O               | 0.02                                    | 8.77          | 8.52      | 0.07           | 0.04  | 8.76          | 9.24      | 0.06        | 0.00  | 0.03    | 9.03           | 0.09               | 0.01  | 8.99              | 8.78           | 0.09          |
| Total                          | 101.3                                   | 94.7          | 94.9      | 99.4           | 101.7 | 96.1          | 94.4      | 99.5        | 101.6 | 88.5    | 94.9           | 99.2               | 101.4 | 96.3              | 95.8           | 100.2         |
| No. O                          | 12                                      | 11            | 11        | 8              | 12    | 11            | 11        | 8           | 12    | 14      | 11             | 8                  | 12    | 11                | 11             | 8             |
| Si                             | 2.96                                    | 2.67          | 2.99      | 2.79           | 2.94  | 2.68          | 3.02      | 2.81        | 2.95  | 2.56    | 3.02           | 2.78               | 2.96  | 2.67              | 3.00           | 2.81          |
| Ti                             | 0.00                                    | 0.09          | 0.02      | 0.00           | 0.00  | 0.07          | 0.02      | 0.00        | 0.01  | 0.01    | 0.02           | 0.00               | 0.00  | 0.10              | 0.02           | 0.00          |
| Al                             | 2.06                                    | 1.79          | 2.90      | 1.21           | 2.06  | 1.76          | 2.88      | 1.19        | 2.02  | 2.92    | 2.88           | 1.23               | 2.03  | 1.79              | 2.92           | 1.20          |
| Cr                             | 0.00                                    | 0.00          | 0.00      | 0.00           | 0.00  | 0.00          | 0.00      | 0.00        | 0.00  | 0.01    | 0.00           | 0.00               | 0.00  | 0.00              | 0.00           | 0.00          |
| Fe                             | 2.35                                    | 1.30          | 0.10      | 0.01           | 2.33  | 1.32          | 0.06      | 0.01        | 2.37  | 2.32    | 0.07           | 0.00               | 2.38  | 1.28              | 0.06           | 0.00          |
| Mg                             | 0.22                                    | 1.05          | 0.07      | 0.00           | 0.28  | 1.08          | 0.04      | 0.00        | 0.24  | 2.15    | 0.05           | 0.00               | 0.21  | 1.04              | 0.05           | 0.00          |
| Ca                             | 0.35                                    | 0.00          | 0.00      | 0.18           | 0.29  | 0.00          | 0.00      | 0.16        | 0.39  | 0.00    | 0.00           | 0.19               | 0.35  | 0.00              | 0.00           | 0.16          |
| Mn                             | 0.08                                    | 0.00          | 0.00      | 0.00           | 0.11  | 0.00          | 0.00      | 0.00        | 0.07  | 0.01    | 0.00           | 0.00               | 0.08  | 0.00              | 0.00           | 0.00          |
| Na                             | 0.00                                    | 0.05          | 0.18      | 0.83           | 0.00  | 0.04          | 0.20      | 0.85        | 0.00  | 0.00    | 0.18           | 0.82               | 0.00  | 0.05              | 0.16           | 0.84          |
| K                              | 0.00                                    | 0.86          | 0.72      | 0.00           | 0.00  | 0.85          | 0.79      | 0.00        | 0.00  | 0.00    | 0.77           | 0.01               | 0.00  | 0.86              | 0.74           | 0.00          |
| Cations                        | 8.01                                    | 7.80          | 6.99      | 5.02           | 8.02  | 7.81          | 7.02      | 6.99        | 8.03  | 9.98    | 6.99           | 5.02               | 8.02  | 7.79              | 6.96           | 5.01          |
| XMg                            | 0.08                                    | 0.45          | 0.39      | 0.02           | 0.11  | 0.45          | 0.41      | 0.10        | 0.09  | 0.48    | 0.42           | 0.00               | 0.08  | 0.45              | 0.46           | 0.00          |
| XCa                            | -                                       | -             | -         | 0.18           | -     | -             | -         | 0.16        | -     | -       | -              | 0.19               | -     | -                 | -              | 0.15          |
| Al(IV)                         | -                                       | 1.33          | 1.01      | -              | -     | 1.32          | 0.98      | -           | -     | 1.44    | 0.98           | -                  | -     | 1.33              | 1.00           | -             |
| Al(vi)                         | -                                       | 0.46          | 1.89      | -              | -     | 0.44          | 1.90      | -           | -     | 1.48    | 1.90           | -                  | -     | 0.46              | 1.92           | -             |
| Alm                            | 0.79                                    | -             | -         | -              | 0.77  | -             | -         | -           | 0.77  | -       | -              | -                  | 0.79  | -                 | -              | -             |
| Prp                            | 0.07                                    | -             | -         | -              | 0.09  | -             | -         | -           | 0.08  | -       | -              | -                  | 0.07  | -                 | -              | -             |
| Grs                            | 0.12                                    | -             | -         | -              | 0.10  | -             | -         | -           | 0.13  | -       | -              | -                  | 0.12  | -                 | -              | -             |
| Sps                            | 0.03                                    | -             | -         | -              | 0.04  | -             | -         | -           | 0.02  | -       | -              | -                  | 0.03  | -                 | -              | -             |

<sup>#</sup>Description; number indicates different garnets in same sample; p is inferred peak-metamorphism position based on garnet compositional zoning

<sup>1</sup>Interpretation

\* n = number of analyses in average

**Table A.8 (continued). Representative electron-microprobe analyses metamorphic samples for thermobarometry**

| Sample                         | AZ 04-18-12 (4b) [garnet-mica schist] |                  |       |                  | AZ 07-21-13 (5) [garnet amphibolite] |          |       |       |       |        |         |                        |                    |
|--------------------------------|---------------------------------------|------------------|-------|------------------|--------------------------------------|----------|-------|-------|-------|--------|---------|------------------------|--------------------|
|                                | Grt                                   | Bt               | Grt   | Bt               | Grt                                  | Pl       | Amph  | Grt   | Pl    | Amph   | Grt     | Pl                     | Amph               |
| Mineral                        |                                       |                  |       |                  |                                      |          |       |       |       |        |         |                        |                    |
| Descr.#                        | 1; p                                  | 1; mean<br>hi-Ti | 2; p  | 2; mean<br>hi-Ti | 1; p                                 | 1; hi-Ca | 1     | 2; p  | 2     | 2; rim | 3; Core | 3;<br>matrix<br>relict | 3; low-<br>Al core |
| Interp. <sup>1</sup>           | Peak                                  | Peak             | Peak  | Peak             | Peak                                 | Peak     | Peak  | Late  | Late  | Late   | Early   | Early                  | Early              |
| n*                             | 2                                     | 4                | 2     | 4                | 2                                    | 7        | 10    | 1     | 2     | 2      | 15      | 3                      | 2                  |
| SiO <sub>2</sub>               | 36.95                                 | 33.60            | 36.99 | 34.81            | 37.08                                | 59.32    | 42.12 | 37.29 | 61.04 | 42.98  | 37.15   | 58.46                  | 42.72              |
| TiO <sub>2</sub>               | 0.01                                  | 1.73             | 0.01  | 2.85             | 0.15                                 | 0.01     | 0.75  | 0.10  | 0.02  | 0.68   | 0.22    | 0.02                   | 0.66               |
| Al <sub>2</sub> O <sub>3</sub> | 22.08                                 | 21.44            | 21.85 | 20.46            | 21.44                                | 25.16    | 11.83 | 21.56 | 23.77 | 10.81  | 21.32   | 25.79                  | 11.23              |
| Cr <sub>2</sub> O <sub>3</sub> | 0.00                                  | 0.01             | 0.01  | 0.04             | 0.00                                 | 0.01     | 0.03  | 0.01  | 0.00  | 0.03   | 0.02    | 0.01                   | 0.07               |
| Fe <sub>2</sub> O <sub>3</sub> | 33.48                                 | 21.54            | 32.48 | 20.31            | 27.89                                | 0.19     | 21.78 | 27.58 | 0.22  | 21.62  | 25.55   | 0.13                   | 21.48              |
| MgO                            | 3.37                                  | 7.85             | 2.90  | 7.60             | 0.98                                 | 0.00     | 6.79  | 1.05  | 0.01  | 7.11   | 0.71    | 0.00                   | 7.05               |
| CaO                            | 1.30                                  | 0.04             | 1.30  | 0.01             | 9.63                                 | 6.27     | 11.41 | 9.22  | 4.73  | 11.41  | 10.27   | 7.14                   | 11.42              |
| MnO                            | 3.90                                  | 0.29             | 5.47  | 0.23             | 3.19                                 | 0.01     | 0.29  | 3.31  | 0.02  | 0.28   | 5.11    | 0.02                   | 0.29               |
| Na <sub>2</sub> O              | 0.00                                  | 0.08             | 0.00  | 0.22             | 0.04                                 | 8.48     | 1.43  | 0.07  | 9.41  | 1.39   | 0.04    | 7.88                   | 1.35               |
| K <sub>2</sub> O               | 0.01                                  | 8.19             | 0.00  | 9.79             | 0.00                                 | 0.05     | 0.71  | 0.00  | 0.06  | 0.59   | 0.01    | 0.06                   | 0.64               |
| Total                          | 101.1                                 | 94.8             | 101.0 | 96.3             | 100.4                                | 99.5     | 97.1  | 100.2 | 99.3  | 96.9   | 100.4   | 99.5                   | 96.9               |
| No. O                          | 12                                    | 11               | 12    | 11               | 12                                   | 8        | 23    | 12    | 8     | 23     | 12      | 8                      | 23                 |
| Si                             | 2.94                                  | 2.58             | 2.96  | 2.64             | 2.96                                 | 2.66     | 6.50  | 2.98  | 2.73  | 6.63   | 2.97    | 2.63                   | 6.59               |
| Ti                             | 0.00                                  | 0.10             | 0.00  | 0.16             | 0.01                                 | 0.00     | 0.09  | 0.01  | 0.00  | 0.08   | 0.01    | 0.00                   | 0.08               |
| Al                             | 2.07                                  | 1.94             | 2.06  | 1.83             | 2.02                                 | 1.33     | 2.15  | 2.03  | 1.26  | 1.97   | 2.01    | 1.37                   | 2.04               |
| Cr                             | 0.00                                  | 0.00             | 0.00  | 0.00             | 0.00                                 | 0.00     | 0.00  | 0.00  | 0.00  | 0.00   | 0.00    | 0.00                   | 0.01               |
| Fe                             | 2.23                                  | 1.39             | 2.17  | 1.29             | 1.86                                 | 0.01     | 2.81  | 1.84  | 0.01  | 2.79   | 1.71    | 0.00                   | 2.77               |
| Mg                             | 0.40                                  | 0.90             | 0.35  | 0.86             | 0.12                                 | 0.00     | 1.56  | 0.12  | 0.00  | 1.63   | 0.08    | 0.00                   | 1.62               |
| Ca                             | 0.11                                  | 0.00             | 0.11  | 0.00             | 0.82                                 | 0.30     | 1.89  | 0.79  | 0.23  | 1.89   | 0.88    | 0.34                   | 1.89               |
| Mn                             | 0.26                                  | 0.02             | 0.37  | 0.02             | 0.22                                 | 0.00     | 0.04  | 0.22  | 0.00  | 0.04   | 0.35    | 0.00                   | 0.04               |
| Na                             | 0.00                                  | 0.01             | 0.00  | 0.03             | 0.01                                 | 0.74     | 0.43  | 0.01  | 0.82  | 0.42   | 0.01    | 0.69                   | 0.40               |
| K                              | 0.00                                  | 0.80             | 0.00  | 0.95             | 0.00                                 | 0.00     | 0.14  | 0.00  | 0.00  | 0.12   | 0.00    | 0.00                   | 0.13               |
| Cations                        | 8.02                                  | 7.75             | 8.01  | 7.77             | 8.02                                 | 5.04     | 15.61 | 8.01  | 5.05  | 15.57  | 8.02    | 5.03                   | 15.57              |
| XMg                            | 0.15                                  | 0.39             | 0.14  | 0.40             | 0.06                                 | 0.02     | 0.36  | 0.06  | 0.10  | 0.37   | 0.05    | 0.02                   | 0.37               |
| XCa                            | -                                     | -                | -     | -                | -                                    | 0.29     | -     | -     | 0.22  | -      | -       | 0.33                   | -                  |
| Al(IV)                         | -                                     | 1.42             | -     | 1.36             | -                                    | -        | 1.50  | -     | -     | 1.37   | -       | -                      | 1.41               |
| Al(VI)                         | -                                     | 0.53             | -     | 0.47             | -                                    | -        | 0.66  | -     | -     | 0.60   | -       | -                      | 0.64               |
| Alm                            | 0.74                                  | -                | 0.72  | -                | 0.62                                 | -        | -     | 0.62  | -     | -      | 0.56    | -                      | -                  |
| Prp                            | 0.13                                  | -                | 0.12  | -                | 0.04                                 | -        | -     | 0.04  | -     | -      | 0.03    | -                      | -                  |
| Grs                            | 0.04                                  | -                | 0.04  | -                | 0.27                                 | -        | -     | 0.26  | -     | -      | 0.29    | -                      | -                  |
| Sps                            | 0.09                                  | -                | 0.12  | -                | 0.07                                 | -        | -     | 0.07  | -     | -      | 0.11    | -                      | -                  |

<sup>#</sup>Description; number indicates different garnets in same sample; p is inferred peak-metamorphism position based on garnet compositional zoning

<sup>1</sup>Interpretation

\* n = number of analyses in average

**Table A.8 (continued). Representative electron-microprobe analyses metamorphic samples for thermobarometry**

| Sample                         | AZ 04-18-12 (4) [garnet-epidote amphibolite gneiss] |          |       |       |       |          |          |           |          |           |
|--------------------------------|---|----------|-------|-------|-------|----------|----------|-----------|----------|-----------|
|                                | Mineral   | Grt      | Pl    | Amph  | Ep    | Grt      | Pl       | Amph      | Pl       | Amph      |
| Descr.#                        | 1; p  | 1; hi-Ca | 1     | 1;2   | 2; p  | 2; hi-Ca | 2; hi-Ca | 2; low-Al | 2; hi-Ca | 2; low-Al |
| Interp. <sup>1</sup>           | Peak  | Peak     | Peak  | Peak  | Peak  | Peak     | Peak     | Peak      | Peak     | Peak      |
| n*                             | 4   | 4        | 3     | 10    | 3     | 6        | 6        | 3         | 6        | 3         |
| SiO <sub>2</sub>               | 37.77   | 46.80    | 43.10 | 41.14 | 37.73 | 46.99    | 46.99    | 43.13     | 46.99    | 43.13     |
| TiO <sub>2</sub>               | 0.06  | 0.02     | 1.39  | 0.03  | 0.03  | 0.02     | 0.02     | 1.33      | 0.02     | 1.33      |
| Al <sub>2</sub> O <sub>3</sub> | 22.05   | 34.11    | 13.00 | 31.82 | 22.00 | 34.01    | 34.01    | 12.74     | 34.01    | 12.74     |
| Cr <sub>2</sub> O <sub>3</sub> | 0.02  | 0.00     | 0.00  | 0.02  | 0.02  | 0.01     | 0.01     | 0.02      | 0.01     | 0.02      |
| Fe <sub>2</sub> O <sub>3</sub> | 28.81   | 0.13     | 18.63 | 2.54  | 28.60 | 0.12     | 0.12     | 19.25     | 0.12     | 19.25     |
| MgO                            | 2.86  | 0.00     | 8.68  | 0.02  | 2.93  | 0.00     | 0.00     | 8.43      | 0.00     | 8.43      |
| CaO                            | 7.69  | 16.79    | 11.13 | 22.65 | 7.89  | 16.67    | 16.67    | 10.93     | 16.67    | 10.93     |
| MnO                            | 2.06  | 0.03     | 0.23  | 0.04  | 1.97  | 0.02     | 0.02     | 0.26      | 0.02     | 0.26      |
| Na <sub>2</sub> O              | 0.00  | 2.05     | 1.20  | 0.72  | 0.01  | 2.13     | 2.13     | 1.24      | 2.13     | 1.24      |
| K <sub>2</sub> O               | 0.00  | 0.02     | 0.93  | 0.05  | 0.00  | 0.03     | 0.03     | 0.84      | 0.03     | 0.84      |
| Total                          | 101.3   | 100.0    | 98.3  | 99.0  | 101.2 | 100.0    | 100.0    | 98.2      | 100.0    | 98.2      |
| No. O                          | 12  | 8        | 23    | 12.5  | 12    | 8        | 8        | 23        | 8        | 23        |
| Si                             | 2.96  | 2.15     | 6.45  | 3.10  | 2.96  | 2.16     | 2.16     | 6.48      | 2.16     | 6.48      |
| Ti                             | 0.00  | 0.00     | 0.16  | 0.00  | 0.00  | 0.00     | 0.00     | 0.15      | 0.00     | 0.15      |
| Al                             | 2.04  | 1.85     | 2.29  | 2.83  | 2.04  | 1.84     | 1.84     | 2.25      | 1.84     | 2.25      |
| Cr                             | 0.00  | 0.00     | 0.00  | 0.00  | 0.00  | 0.00     | 0.00     | 0.00      | 0.00     | 0.00      |
| Fe                             | 1.89  | 0.00     | 2.33  | 0.16  | 1.88  | 0.00     | 0.00     | 2.42      | 0.00     | 2.42      |
| Mg                             | 0.33  | 0.00     | 1.94  | 0.00  | 0.34  | 0.00     | 0.00     | 1.89      | 0.00     | 1.89      |
| Ca                             | 0.65  | 0.83     | 1.78  | 1.83  | 0.66  | 0.82     | 0.82     | 1.76      | 0.82     | 1.76      |
| Mn                             | 0.14  | 0.00     | 0.03  | 0.00  | 0.13  | 0.00     | 0.00     | 0.03      | 0.00     | 0.03      |
| Na                             | 0.00  | 0.18     | 0.35  | 0.10  | 0.00  | 0.19     | 0.19     | 0.36      | 0.19     | 0.36      |
| K                              | 0.00  | 0.00     | 0.18  | 0.00  | 0.00  | 0.00     | 0.00     | 0.16      | 0.00     | 0.16      |
| Cations                        | 8.01  | 5.02     | 15.51 | 8.04  | 8.02  | 5.02     | 5.02     | 15.50     | 5.02     | 15.50     |
| XMg                            | 0.15  | 0.05     | 0.45  | 0.02  | 0.15  | 0.04     | 0.04     | 0.44      | 0.04     | 0.44      |
| XCa                            | -   | 0.82     | -     | 0.94  | -     | 0.81     | 0.81     | -         | -        | -         |
| Al(IV)                         | -   | -        | 1.55  | -     | -     | -        | -        | 1.52      | -        | 1.52      |
| Al(VI)                         | -   | -        | 0.75  | -     | -     | -        | -        | 0.73      | -        | 0.73      |
| Alm                            | 0.63  | -        | -     | -     | 0.62  | -        | -        | -         | -        | -         |
| Prp                            | 0.11  | -        | -     | -     | 0.11  | -        | -        | -         | -        | -         |
| Grs                            | 0.21  | -        | -     | -     | 0.22  | -        | -        | -         | -        | -         |
| Sps                            | 0.05  | -        | -     | -     | 0.04  | -        | -        | -         | -        | -         |

<sup>#</sup>Description; number indicates different garnets in same sample; p is inferred peak-metamorphism position based on garnet compositional zoning

<sup>1</sup>Interpretation

\* n = number of analyses in average

**Table A.8 (continued). Representative electron-microprobe analyses metamorphic samples for thermobarometry**

| Sample                         |       | RR 05-05-2012 (8) [gneiss] |               |                 |                   |         |                  |               |               |                  |                  |               |       |              |      |                  |      |      |               |      |      |               |      |      |      |
|--------------------------------|-------|----------------------------|---------------|-----------------|-------------------|---------|------------------|---------------|---------------|------------------|------------------|---------------|-------|--------------|------|------------------|------|------|---------------|------|------|---------------|------|------|------|
| Mineral                        | Grt   | Bt                         | Ms            | Pl              | Kfs               | Grt     | Bt               | Ms            | 2; low-<br>Si | Peak             | 2; mean<br>hi-Ti | Peak          | Grt   | 3; p<br>Peak | Bt   | 3; Mean<br>hi-Ti | Peak | Ms   | 3; low-<br>Si | Peak | Pl   | 3; high<br>Ca | Peak | Kfs  |      |
| Descr.#                        | 1; p  | 1                          | 1; low-<br>Si | 1,2; high<br>Ca | 1,2,3<br>Peak     | 2; p    | 2; mean<br>hi-Ti | 2; low-<br>Si | 3; p<br>Peak  | 3; Mean<br>hi-Ti | 3; low-<br>Si    | 3; high<br>Ca | 3     |              |      |                  |      |      |               |      |      |               |      |      |      |
| Interp. <sup>1</sup>           | Peak  | Peak                       | Peak          | Peak            | Peak              | Peak    | Peak             | Peak          | Peak          | Peak             | Peak             | Peak          | Peak  | Peak         | Peak | Peak             | Peak | Peak | Peak          | Peak | Peak | Peak          | Peak | Peak | Peak |
| n*                             | 3     | 1                          | 1             | 2               | 4                 | 2       | 2                | 1             | 5             | 2                | 2                | 1             | 2     | 5            | 2    | 2                | 2    | 3    | 3             | 3    | 5    | 5             | 2    | 2    |      |
| SiO <sub>2</sub>               | 37.05 | 33.21                      | 45.00         | 60.62           | 63.67             | 37.03   | 34.30            | 45.63         | 36.83         | 33.12            | 45.18            | 61.75         | 36.40 |              |      |                  |      |      |               |      |      |               |      |      |      |
| TiO <sub>2</sub>               | 0.07  | 3.05                       | 0.71          | 0.01            | 0.03              | 0.02    | 3.67             | 0.95          | 0.02          | 3.36             | 0.30             | 0.03          | 0.03  |              |      |                  |      |      |               |      |      |               |      |      |      |
| Al <sub>2</sub> O <sub>3</sub> | 21.87 | 19.30                      | 36.16         | 24.80           | 18.87             | 21.80   | 19.20            | 36.29         | 21.67         | 18.63            | 35.06            | 23.98         | 18.82 |              |      |                  |      |      |               |      |      |               |      |      |      |
| Cr <sub>2</sub> O <sub>3</sub> | 0.00  | 0.12                       | 0.01          | 0.00            | 0.00              | 0.03    | 0.03             | 0.03          | 0.02          | 0.01             | 0.03             | 0.00          | 0.00  |              |      |                  |      |      |               |      |      |               |      |      |      |
| Fe <sub>2</sub> O <sub>3</sub> | 32.36 | 25.59                      | 1.35          | 0.09            | 0.25              | 32.97   | 24.35            | 1.14          | 33.81         | 23.91            | 1.55             | 0.16          | 0.25  |              |      |                  |      |      |               |      |      |               |      |      |      |
| MgO                            | 1.73  | 5.31                       | 0.41          | 0.00            | 0.00              | 1.95    | 5.46             | 0.42          | 2.05          | 5.54             | 0.63             | 0.00          | 0.00  |              |      |                  |      |      |               |      |      |               |      |      |      |
| CaO                            | 1.65  | 0.00                       | 0.03          | 6.21            | 0.04              | 1.52    | 0.00             | 0.01          | 1.58          | 0.02             | 0.02             | 4.89          | 0.02  |              |      |                  |      |      |               |      |      |               |      |      |      |
| MnO                            | 6.84  | 0.50                       | 0.03          | 0.04            | 0.06              | 6.21    | 0.32             | 0.02          | 4.69          | 0.39             | 0.03             | 0.01          | 0.05  |              |      |                  |      |      |               |      |      |               |      |      |      |
| Na <sub>2</sub> O              | 0.02  | 0.03                       | 0.53          | 8.76            | 0.69              | 0.01    | 0.11             | 0.55          | 0.01          | 0.05             | 0.48             | 9.28          | 0.60  |              |      |                  |      |      |               |      |      |               |      |      |      |
| K <sub>2</sub> O               | 0.01  | 9.18                       | 11.01         | 0.26            | 16.04             | 0.00    | 9.66             | 11.08         | 0.01          | 9.09             | 10.79            | 0.18          | 16.24 |              |      |                  |      |      |               |      |      |               |      |      |      |
| Total                          | 101.6 | 96.3                       | 95.2          | 100.8           | 99.6              | 101.5   | 97.1             | 96.1          | 100.7         | 94.1             | 94.1             | 100.3         | 99.4  |              |      |                  |      |      |               |      |      |               |      |      |      |
| No. O                          | 12    | 11                         | 11            | 8               | 8                 | 12      | 11               | 11            | 12            | 11               | 11               | 8             | 8     |              |      |                  |      |      |               |      |      |               |      |      |      |
| Si                             | 2.96  | 2.56                       | 3.01          | 2.69            | 2.96              | 2.96    | 2.64             | 3.02          | 2.97          | 2.63             | 3.06             | 2.74          | 2.96  |              |      |                  |      |      |               |      |      |               |      |      |      |
| Ti                             | 0.00  | 0.17                       | 0.04          | 0.00            | 0.00              | 0.00    | 0.21             | 0.05          | 0.00          | 0.20             | 0.02             | 0.00          | 0.00  |              |      |                  |      |      |               |      |      |               |      |      |      |
| Al                             | 2.06  | 1.79                       | 2.85          | 1.30            | 1.04              | 2.06    | 1.74             | 2.83          | 2.06          | 1.74             | 2.80             | 1.25          | 1.04  |              |      |                  |      |      |               |      |      |               |      |      |      |
| Cr                             | 0.00  | 0.00                       | 0.00          | 0.00            | 0.00              | 0.00    | 0.00             | 0.00          | 0.00          | 0.00             | 0.00             | 0.00          | 0.00  |              |      |                  |      |      |               |      |      |               |      |      |      |
| Fe                             | 2.16  | 1.73                       | 0.08          | 0.00            | 0.01              | 2.21    | 1.56             | 0.06          | 2.28          | 1.59             | 0.09             | 0.01          | 0.01  |              |      |                  |      |      |               |      |      |               |      |      |      |
| Mg                             | 0.21  | 0.67                       | 0.04          | 0.00            | 0.00              | 0.23    | 0.63             | 0.04          | 0.25          | 0.65             | 0.06             | 0.00          | 0.00  |              |      |                  |      |      |               |      |      |               |      |      |      |
| Ca                             | 0.14  | 0.00                       | 0.00          | 0.29            | 0.00              | 0.13    | 0.00             | 0.00          | 0.14          | 0.00             | 0.00             | 0.23          | 0.00  |              |      |                  |      |      |               |      |      |               |      |      |      |
| Mn                             | 0.46  | 0.03                       | 0.00          | 0.00            | 0.00              | 0.42    | 0.02             | 0.00          | 0.32          | 0.03             | 0.00             | 0.00          | 0.00  |              |      |                  |      |      |               |      |      |               |      |      |      |
| Na                             | 0.00  | 0.01                       | 0.07          | 0.75            | 0.06              | 0.00    | 0.02             | 0.07          | 0.00          | 0.01             | 0.06             | 0.80          | 0.05  |              |      |                  |      |      |               |      |      |               |      |      |      |
| K                              | 0.00  | 0.81                       | 0.94          | 0.01            | 0.95              | 0.00    | 0.95             | 0.94          | 0.00          | 0.92             | 0.93             | 0.01          | 0.97  |              |      |                  |      |      |               |      |      |               |      |      |      |
| Cations                        | 8.01  | 7.78                       | 7.03          | 5.05            | 5.03              | 8.01035 | 7.76             | 7.02          | 8.01          | 7.77             | 7.02             | 5.04          | 5.03  |              |      |                  |      |      |               |      |      |               |      |      |      |
| XMg                            | 0.09  | 0.28                       | 0.35          | 0.04            | 0.00              | 0.10    | 0.29             | 0.40          | 0.10          | 0.29             | 0.42             | 0.04          | 0.00  |              |      |                  |      |      |               |      |      |               |      |      |      |
| XCa                            | -     | -                          | -             | 0.28            | 0.94 <sup>^</sup> | -       | -                | -             | -             | -                | -                | 0.22          | 0.00  |              |      |                  |      |      |               |      |      |               |      |      |      |
| Al(IV)                         | -     | 1.44                       | 0.99          | -               | -                 | -       | 1.36             | 0.98          | -             | 1.37             | 0.94             | -             | -     |              |      |                  |      |      |               |      |      |               |      |      |      |
| Al(VI)                         | -     | 0.35                       | 1.86          | -               | -                 | -       | 0.37             | 1.86          | -             | 0.37             | 1.86             | -             | -     |              |      |                  |      |      |               |      |      |               |      |      |      |
| Alm                            | 0.73  | -                          | -             | -               | -                 | 0.74    | -                | -             | 0.76          | -                | -                | -             | -     |              |      |                  |      |      |               |      |      |               |      |      |      |
| Prp                            | 0.07  | -                          | -             | -               | -                 | 0.08    | -                | -             | 0.08          | -                | -                | -             | -     |              |      |                  |      |      |               |      |      |               |      |      |      |
| Grs                            | 0.05  | -                          | -             | -               | -                 | 0.04    | -                | -             | 0.05          | -                | -                | -             | -     |              |      |                  |      |      |               |      |      |               |      |      |      |
| Sps                            | 0.16  | -                          | -             | -               | -                 | 0.14    | -                | -             | 0.11          | -                | -                | -             | -     |              |      |                  |      |      |               |      |      |               |      |      |      |

<sup>#</sup>Description; number indicates different garnets in same sample; p is inferred peak-metamorphism position based on garnet compositional zoning

<sup>1</sup>Interpretation

\* n = number of analyses in average

<sup>^</sup> XK or Or# instead of XCa

**Table A.8 (continued). Representative electron-microprobe analyses metamorphic samples for thermobarometry**

| Sample Mineral                 | RR 05-05-12 (12) [garnet amphibolite] |          |       |        |                |       |         |                |         |         |         |        |        |
|--------------------------------|---------------------------------------|----------|-------|--------|----------------|-------|---------|----------------|---------|---------|---------|--------|--------|
|                                | Grt                                   | Pl       | Amph  | Grt    | Pl             | Amph  | Grt     | Pl             | Grt     | Pl      | Grt     | Pl     | Amph   |
| Descr.#                        | 1; p                                  | 1; Hi-Ca | 1     | 4; p   | 4; Adj. to grt | 4     | 1; core | 1; Low-Ca core | 4; core | 4; core | 4; core | 1; rim | 1      |
| Interp. <sup>1</sup> n*        | Peak 3                                | Peak 1   | 1     | Peak 1 | Peak 2         | 3     | Early 4 | Early 3        | Early 2 | Early 3 | Early 2 | Late 2 | Late 1 |
| SiO <sub>2</sub>               | 38.00                                 | 56.88    | 43.55 | 38.30  | 54.47          | 43.11 | 38.12   | 58.23          | 37.82   | 58.18   | 38.01   | 54.47  | 48.35  |
| TiO <sub>2</sub>               | 0.08                                  | 0.03     | 0.49  | 0.14   | 0.02           | 1.52  | 0.16    | 0.01           | 0.10    | 0.04    | 0.08    | 0.02   | 0.30   |
| Al <sub>2</sub> O <sub>3</sub> | 22.00                                 | 27.93    | 12.81 | 22.17  | 29.59          | 12.33 | 21.90   | 27.11          | 21.79   | 26.83   | 21.98   | 29.59  | 8.32   |
| Cr <sub>2</sub> O <sub>3</sub> | 0.00                                  | 0.02     | 0.08  | 0.00   | 0.01           | 0.01  | 0.02    | 0.00           | 0.03    | 0.02    | 0.00    | 0.01   | 0.00   |
| Fe <sub>2</sub> O <sub>3</sub> | 27.80                                 | 0.32     | 17.64 | 26.89  | 0.30           | 17.83 | 26.57   | 0.48           | 27.71   | 0.49    | 27.12   | 0.30   | 15.18  |
| MgO                            | 2.70                                  | 0.00     | 9.77  | 2.92   | 0.01           | 9.42  | 1.65    | 0.01           | 1.99    | 0.00    | 2.97    | 0.01   | 13.06  |
| CaO                            | 10.93                                 | 9.31     | 11.49 | 10.85  | 11.31          | 11.57 | 10.71   | 8.23           | 11.30   | 8.19    | 10.57   | 11.31  | 11.71  |
| MnO                            | 0.26                                  | 0.00     | 0.10  | 0.37   | 0.01           | 0.06  | 2.87    | 0.01           | 0.95    | 0.00    | 0.58    | 0.01   | 0.06   |
| Na <sub>2</sub> O              | 0.01                                  | 6.13     | 1.45  | 0.02   | 5.07           | 1.54  | 0.04    | 6.96           | 0.02    | 7.00    | 0.02    | 5.07   | 1.00   |
| K <sub>2</sub> O               | 0.00                                  | 0.12     | 1.03  | 0.01   | 0.18           | 1.12  | 0.02    | 0.10           | 0.00    | 0.07    | 0.01    | 0.18   | 0.48   |
| Total                          | 101.8                                 | 100.7    | 98.4  | 101.7  | 101.0          | 98.5  | 102.1   | 101.1          | 101.7   | 100.8   | 101.3   | 101.0  | 98.5   |
| No. O                          | 12                                    | 8        | 23    | 12     | 8              | 23    | 12      | 8              | 12      | 8       | 12      | 8      | 23     |
| Si                             | 2.96                                  | 2.54     | 6.49  | 2.97   | 2.44           | 6.44  | 2.97    | 7.74           | 2.96    | 2.59    | 2.96    | 2.44   | 7.04   |
| Ti                             | 0.00                                  | 0.00     | 0.05  | 0.01   | 0.00           | 0.17  | 0.01    | 0.00           | 0.01    | 0.00    | 0.00    | 0.00   | 0.03   |
| Al                             | 2.02                                  | 1.47     | 2.25  | 2.03   | 1.56           | 2.17  | 2.01    | 4.25           | 2.01    | 1.41    | 2.02    | 1.56   | 1.43   |
| Cr                             | 0.00                                  | 0.00     | 0.01  | 0.00   | 0.00           | 0.00  | 0.00    | 0.00           | 0.00    | 0.00    | 0.00    | 0.00   | 0.00   |
| Fe                             | 1.81                                  | 0.01     | 2.20  | 1.74   | 0.01           | 2.23  | 1.73    | 0.05           | 1.81    | 0.02    | 1.77    | 0.01   | 1.85   |
| Mg                             | 0.31                                  | 0.00     | 2.17  | 0.34   | 0.00           | 2.10  | 0.19    | 0.00           | 0.23    | 0.00    | 0.35    | 0.00   | 2.84   |
| Ca                             | 0.91                                  | 0.44     | 1.84  | 0.90   | 0.54           | 1.85  | 0.90    | 1.17           | 0.95    | 0.39    | 0.88    | 0.54   | 1.83   |
| Mn                             | 0.02                                  | 0.00     | 0.01  | 0.02   | 0.00           | 0.01  | 0.19    | 0.00           | 0.06    | 0.00    | 0.04    | 0.00   | 0.01   |
| Na                             | 0.00                                  | 0.53     | 0.42  | 0.00   | 0.44           | 0.45  | 0.01    | 1.80           | 0.00    | 0.60    | 0.00    | 0.44   | 0.28   |
| K                              | 0.00                                  | 0.01     | 0.20  | 0.00   | 0.01           | 0.21  | 0.00    | 0.02           | 0.00    | 0.00    | 0.00    | 0.01   | 0.09   |
| Cations                        | 8.03                                  | 5.00     | 15.63 | 8.01   | 5.01           | 15.63 | 8.02    | 15.04          | 8.03    | 5.01    | 8.03    | 5.01   | 15.40  |
| XMg                            | 0.15                                  | 0.00     | 0.50  | 0.16   | 0.04           | 0.48  | 0.10    | 0.03           | 0.11    | 0.01    | 0.16    | 0.04   | 0.61   |
| XCa                            | -                                     | 0.45     | -     | -      | 0.55           | -     | -       | 0.39           | -       | 0.39    | -       | 0.55   | -      |
| Al(IV)                         | -                                     | -        | 1.51  | -      | -              | 1.56  | -       | -              | -       | -       | -       | -      | 0.96   |
| Al(VI)                         | -                                     | -        | 0.74  | -      | -              | 0.61  | -       | -              | -       | -       | -       | -      | 0.47   |
| Alm                            | 0.59                                  | -        | -     | 0.58   | -              | -     | 0.57    | -              | 0.59    | -       | 0.58    | -      | -      |
| Prp                            | 0.10                                  | -        | -     | 0.11   | -              | -     | 0.06    | -              | 0.08    | -       | 0.11    | -      | -      |
| Grs                            | 0.30                                  | -        | -     | 0.30   | -              | -     | 0.30    | -              | 0.31    | -       | 0.29    | -      | -      |
| Sps                            | 0.01                                  | -        | -     | 0.01   | -              | -     | 0.06    | -              | 0.02    | -       | 0.01    | -      | -      |

<sup>#</sup>Description; number indicates different garnets in same sample; p is inferred peak-metamorphism position based on garnet compositional zoning

<sup>1</sup>Interpretation

\* n = number of analyses in average



**Table A.8 (continued). Representative electron-microprobe analyses metamorphic samples for thermobarometry**

| Sample                         | AY 09-21-11 (6A) [garnet amphibolite] |       |                    |       |       |       |          |         |       |              |       |       |
|--------------------------------|---------------------------------------|-------|--------------------|-------|-------|-------|----------|---------|-------|--------------|-------|-------|
| Mineral                        | Grt                                   | Amph  | Pl                 | Amph  | Grt   | Amph  | Pl       | Grt     | Amph  | Pl           | Amph  | Pl    |
| Descr.#                        | 1; p                                  | 1     | 1; adj; grt; hi-Ca | 2     | 2; p  | 2     | 2; hi-Ca | 3; core | 3     | 3; inclusion |       |       |
| Interp. <sup>1</sup>           | Peak                                  | Peak  | Peak               | Peak  | Peak  | Peak  | Peak     | Early   | Early | Early        | Early | Early |
| n*                             | 2                                     | 3     | 2                  | 2     | 2     | 2     | 2        | 2       | 1     | 2            | 1     | 2     |
| SiO <sub>2</sub>               | 37.58                                 | 44.35 | 52.95              | 42.94 | 38.16 | 42.94 | 52.91    | 37.86   | 47.96 | 58.36        |       |       |
| TiO <sub>2</sub>               | 0.11                                  | 0.63  | 0.00               | 1.92  | 0.13  | 1.92  | 0.01     | 0.09    | 1.05  | 0.00         |       |       |
| Al <sub>2</sub> O <sub>3</sub> | 21.87                                 | 12.31 | 30.26              | 12.68 | 22.01 | 12.68 | 30.85    | 21.85   | 8.34  | 26.75        |       |       |
| Cr <sub>2</sub> O <sub>3</sub> | 0.07                                  | 0.04  | 0.06               | 0.13  | 0.01  | 0.13  | 0.02     | 0.00    | 0.01  | 0.01         |       |       |
| Fe <sub>2</sub> O <sub>3</sub> | 27.60                                 | 15.55 | 0.41               | 16.16 | 27.82 | 16.16 | 0.38     | 28.88   | 16.79 | 0.68         |       |       |
| MgO                            | 2.81                                  | 10.61 | 0.01               | 9.26  | 2.70  | 9.26  | 0.01     | 2.68    | 11.12 | 0.01         |       |       |
| CaO                            | 10.12                                 | 11.65 | 12.04              | 11.63 | 10.79 | 11.63 | 12.47    | 9.60    | 11.18 | 7.86         |       |       |
| MnO                            | 0.63                                  | 0.08  | 0.02               | 0.05  | 0.32  | 0.05  | 0.03     | 0.59    | 0.08  | 0.01         |       |       |
| Na <sub>2</sub> O              | 0.05                                  | 1.29  | 4.66               | 1.43  | 0.03  | 1.43  | 4.43     | 0.02    | 0.95  | 7.07         |       |       |
| K <sub>2</sub> O               | 0.00                                  | 0.93  | 0.10               | 1.19  | 0.01  | 1.19  | 0.11     | 0.01    | 0.58  | 0.10         |       |       |
| Total                          | 100.8                                 | 97.4  | 100.5              | 97.4  | 102.0 | 97.4  | 101.2    | 101.6   | 98.1  | 100.9        |       |       |
| No. of O                       | 12                                    | 23    | 8                  | 23    | 12    | 23    | 8        | 12      | 23    | 8            |       |       |
| Si                             | 2.95                                  | 6.59  | 2.39               | 6.44  | 2.96  | 6.44  | 2.37     | 2.96    | 7.06  | 2.59         |       |       |
| Ti                             | 0.01                                  | 0.07  | 0.00               | 0.22  | 0.01  | 0.22  | 0.00     | 0.01    | 0.12  | 0.00         |       |       |
| Al                             | 2.02                                  | 2.16  | 1.61               | 2.24  | 2.01  | 2.24  | 1.63     | 2.01    | 1.45  | 1.40         |       |       |
| Cr                             | 0.00                                  | 0.00  | 0.00               | 0.01  | 0.00  | 0.01  | 0.00     | 0.00    | 0.00  | 0.00         |       |       |
| Fe                             | 1.81                                  | 1.93  | 0.02               | 2.03  | 1.81  | 2.03  | 0.01     | 1.89    | 2.07  | 0.03         |       |       |
| Mg                             | 0.33                                  | 2.35  | 0.00               | 2.07  | 0.31  | 2.07  | 0.00     | 0.31    | 2.44  | 0.00         |       |       |
| Ca                             | 0.85                                  | 1.86  | 0.58               | 1.87  | 0.90  | 1.87  | 0.60     | 0.80    | 1.76  | 0.37         |       |       |
| Mn                             | 0.04                                  | 0.01  | 0.00               | 0.01  | 0.02  | 0.01  | 0.00     | 0.04    | 0.01  | 0.00         |       |       |
| Na                             | 0.01                                  | 0.37  | 0.41               | 0.42  | 0.00  | 0.42  | 0.38     | 0.00    | 0.27  | 0.61         |       |       |
| K                              | 0.00                                  | 0.18  | 0.01               | 0.23  | 0.00  | 0.23  | 0.01     | 0.00    | 0.11  | 0.01         |       |       |
| Cations                        | 8.03                                  | 16.28 | 5.01               | 15.54 | 8.03  | 15.54 | 5.01     | 8.03    | 15.29 | 5.01         |       |       |
| XMg                            | 0.15                                  | 0.55  | 0.03               | 0.51  | 0.15  | 0.51  | 0.03     | 0.14    | 0.54  | 0.03         |       |       |
| XCa                            | -                                     | -     | 0.58               | -     | -     | -     | 0.60     | -       | -     | 0.38         |       |       |
| Al(IV)                         | -                                     | 1.41  | -                  | 1.56  | -     | -     | -        | -       | 0.94  | -            |       |       |
| Al(VI)                         | -                                     | 0.75  | -                  | 0.68  | -     | -     | -        | -       | 0.51  | -            |       |       |
| Alm                            | 0.60                                  | -     | -                  | -     | 0.59  | -     | -        | 0.62    | -     | -            |       |       |
| Prp                            | 0.11                                  | -     | -                  | -     | 0.10  | -     | -        | 0.10    | -     | -            |       |       |
| Grs                            | 0.28                                  | -     | -                  | -     | 0.30  | -     | -        | 0.26    | -     | -            |       |       |
| Sps                            | 0.01                                  | -     | -                  | -     | 0.01  | -     | -        | 0.01    | -     | -            |       |       |

<sup>#</sup>Description; number indicates different garnets in same sample; p is inferred peak-metamorphism position based on garnet compositional zoning

<sup>1</sup>Interpretation

\* n = number of analyses in average

## **Auxiliary References**

- Blott, S. J., and Pye, K., 2001, GRADISTAT: a grain size distribution and statistics package for the analysis of unconsolidated sediments: *Earth surface processes and Landforms*, v. 26, no. 11, p. 1237-1248.
- Cruz, L., Teyssier, C., Perg, L., Take, A., and Fayon, A., 2008, Deformation, exhumation, and topography of experimental doubly-vergent orogenic wedges subjected to asymmetric erosion: *Journal of Structural Geology*, v. 30, no. 1, p. 98-115.
- Hubbert, M. K., 1951, Mechanical basis for certain familiar geologic structures: *Geological Society of America Bulletin*, v. 62, no. 4, p. 355-372.
- Jaeger, J. C., Cook, N. G., and Zimmerman, R., 2009, *Fundamentals of rock mechanics*: John Wiley & Sons.
- Maillot, B., and Koyi, H., 2006,. Thrust dip and thrust refraction in fault-bend folds: analogue models and theoretical predictions: *Journal of Structural Geology*, v. 28, no. 1, p. 36-49.
- Schellart, W. P., 2000, Shear test results for cohesion and friction coefficients for different granular materials: scaling implications for their usage in analogue modelling: *Tectonophysics*, v. 324, no. 1, p. 1-16.
- Sibson, R. H., 1982, Fault zone models, heat flow, and the depth distribution of earthquakes in the continental crust of the United States: *Bulletin of the Seismological Society of America*, v. 72, no. 1, p. 151-163.